

**Polymer Vol. 52, No. 5, 1 March 2011**

**Contents**

**POLYMER PAPERS**

**Poly(ethoxytriethyleneglycol acrylate) cryogels as novel sustained drug release systems for oral application**

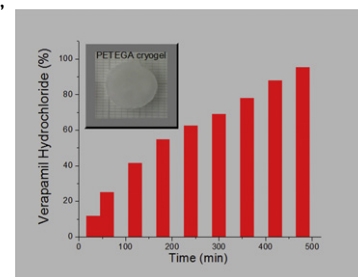
**pp 1217–1222**

Bistra Kostova<sup>a</sup>, Denitsa Momekova<sup>a</sup>, Petar Petrov<sup>b,\*</sup>, Georgi Momekov<sup>c</sup>, Natalia Toncheva-Moncheva<sup>b</sup>, Christo B. Tsvetanov<sup>b</sup>, Nikolai Lambov<sup>a</sup>

<sup>a</sup> Department of Pharmaceutical Technology and Biopharmaceutics, Faculty of Pharmacy, Medical University-Sofia, 2 Dunav Str., 1000 Sofia, Bulgaria

<sup>b</sup> Institute of Polymers, Bulgarian Academy of Sciences, Akad. G. Bonchev Str. 103A, 1113 Sofia, Bulgaria

<sup>c</sup> Department of Pharmacology, Pharmacotherapy and Toxicology, Faculty of Pharmacy, Medical University-Sofia, 2 Dunav Str., 1000 Sofia, Bulgaria



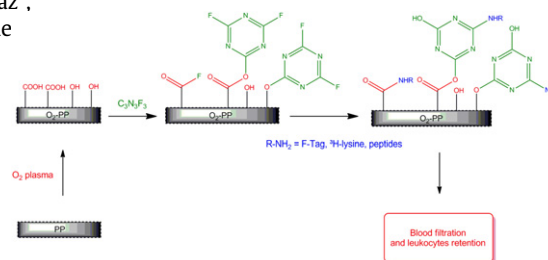
**Surface modifications of polypropylene membranes used for blood filtration**

**pp 1223–1233**

Estelle Gérard<sup>a</sup>, Emilie Bessy<sup>b</sup>, Claudio Salvagnini<sup>a</sup>, Vincent Rerat<sup>a</sup>, Maryam Momtaz<sup>a</sup>, Grégory Hénard<sup>b</sup>, Pascal Marmey<sup>b</sup>, Thierry Verpoort<sup>b</sup>, Jacqueline Marchand-Brynae

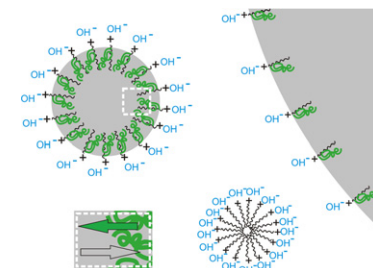
<sup>a</sup> Université catholique de Louvain, Institut de la Matière Condensée et des Nanosciences, Bâtiment Lavoisier, place L. Pasteur n° 1, B-1348 Louvain-la-Neuve, Belgium

<sup>b</sup> MacoProductions, chaussée Fernand Forest n° 200, F-59200 Tourcoing, France



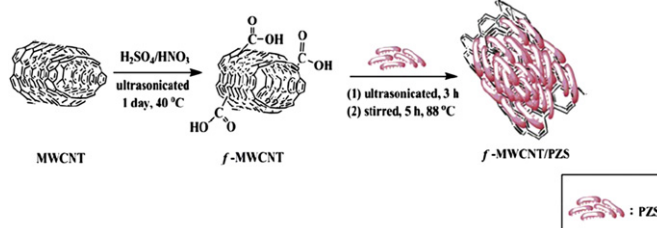
### Anionic ring-opening polymerization of octamethylcyclotetrasiloxane in emulsion above critical micelle concentration

pp 1234–1240

Ines Mohorič<sup>a</sup>, Urška Šebenik<sup>b,\*</sup><sup>a</sup>Hidria Institute for Materials and Technology, Sp. Kanomlja 23, 5281 Sp. Idrija, Slovenia<sup>b</sup>University of Ljubljana, Faculty of Chemistry and Chemical Technology, Aškerčeva cesta 5, 1000 Ljubljana, Slovenia

### Synthesis and characterization of soluble multi-walled carbon nanotube/poly(organophosphazene) composites

pp 1241–1248

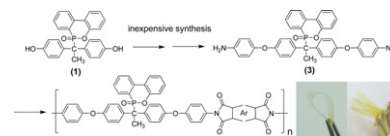
Elif Okutan<sup>a</sup>, Gülsah Ozan Aydın<sup>a</sup>, Ferda Hacivelioglu<sup>a,c</sup>, Adem Kılıç<sup>a,\*</sup>, Saadet Kayıran Beyaz<sup>b</sup>, Serkan Yesilot<sup>a</sup><sup>a</sup>Department of Chemistry, Gebze Institute of Technology, 41400, Gebze, Kocaeli, Turkey<sup>b</sup>Department of Chemistry, Kocaeli University, Izmit, Turkey<sup>c</sup>University of Southampton, School of Chemistry, Southampton, SO17 1BJ, UK

### Dietheramine from an alkaline-stable phosphinated bisphenol for soluble polyetherimides

pp 1249–1255

Ching Hsuan Lin<sup>\*</sup>, Sheng Lung Chang, Po Wen Cheng

Department of Chemical Engineering, National Chung Hsing University, Taichung 402, Taiwan

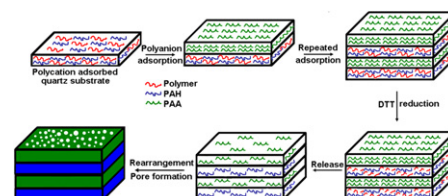


### Fabrication and stability of porous poly(allylamine) hydrochloride (PAH)/poly(acrylic acid) (PAA) multilayered films via a cleavable-polycation template

pp 1256–1262

Na Peng, Xi-Ming Xia, Wen-Tao He, Wen-Ming Liu, Shi-Wen Huang<sup>\*</sup>, Ren-Xi Zhuo<sup>\*</sup>

Key Laboratory of Biomedical Polymers of Ministry of Education, Department of Chemistry, Wuhan University, Wuhan 430072, PR China



**pH-change protective PB-b-PEO polymersomes**

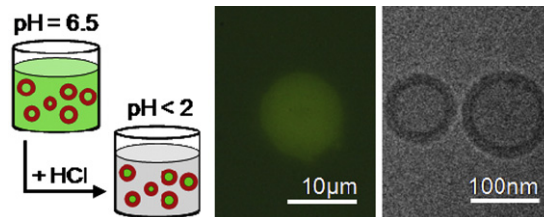
pp 1263–1267

Waltraut Mueller<sup>a,c</sup>, Kaloian Koynov<sup>b</sup>, Sebastien Pierrat<sup>a</sup>, Raphael Thiermann<sup>c</sup>, Karl Fischer<sup>a</sup>, Michael Maskos<sup>a,c,\*</sup>

<sup>a</sup>Institute of Physical Chemistry, University Mainz, Jakob-Welder-Weg 11, D-55128 Mainz, Germany

<sup>b</sup>Max-Planck-Institute of Polymer Research, D-55021 Mainz, Germany

<sup>c</sup>BAM Federal Institute for Materials Research and Testing, Unter den Eichen 87, D-12205 Berlin, Germany



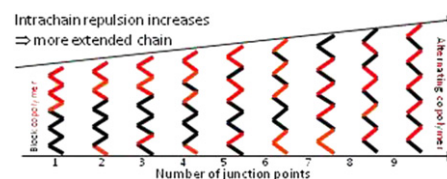
**How does sequence length heterogeneity affect the dilute solution conformation of copolymers?**

pp 1268–1277

Imad A. Haidar Ahmad<sup>a</sup>, Deborah A. Striegel<sup>b</sup>, André M. Striegel<sup>a,\*</sup>

<sup>a</sup>Department of Chemistry & Biochemistry, Florida State University, Tallahassee, FL 32306-4390, USA

<sup>b</sup>Department of Mathematics, Florida State University, Tallahassee, FL 32306-4510, USA



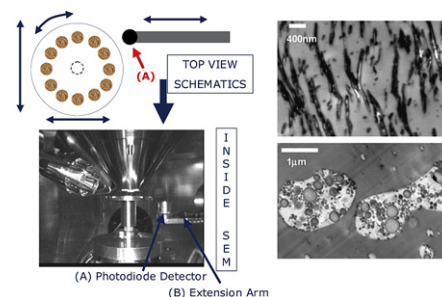
**STEM-in-SEM method for morphology analysis of polymer systems**

pp 1278–1285

Olivier Guise<sup>a,\*</sup>, Carl Strom<sup>a</sup>, Nisha Preschilla<sup>b</sup>

<sup>a</sup>SABIC Innovative Plastics, Technology Department, 1 NORYL Avenue, Selkirk, NY 12158, USA

<sup>b</sup>Reliance Technology Group, Reliance Corporate Park, Reliance Industries Limited, Ghansoli, Navi Mumbai 400701, India



**Preparation and characterization of nanocomposite polyelectrolyte membranes based on Nafion<sup>®</sup> ionomer and nanocrystalline hydroxyapatite**

pp 1286–1296

Mohammad Mahdi Hasani-Sadrabadi<sup>a,b</sup>, Nassir Mokarram<sup>c</sup>, Mahmoud Azami<sup>d,e</sup>, Erfan Dashtimoghadam<sup>a</sup>, Fatemeh Sadat Majedi<sup>b,d</sup>, Karl I. Jacob<sup>c,\*</sup>

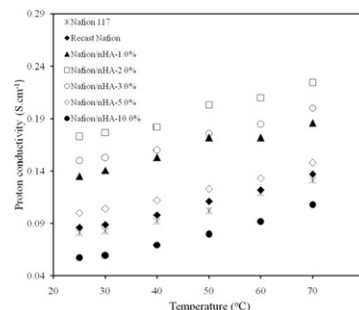
<sup>a</sup>Department of Polymer Engineering and Color Technology, Amirkabir University of Technology, Tehran, Iran

<sup>b</sup>Institute of Bioengineering, Swiss Federal Institutes of Technology, Lausanne (EPFL), CH-1015 Lausanne, Switzerland

<sup>c</sup>School of Materials Science and Engineering, Georgia Institute of Technology, Atlanta, GA, USA

<sup>d</sup>Department of Biomedical Engineering, Amirkabir University of Technology, Tehran, Iran

<sup>e</sup>Tissue Engineering and Cell Therapy Group, School of Advanced Medical Technologies, Tehran University of Medical Sciences, Tehran, Iran

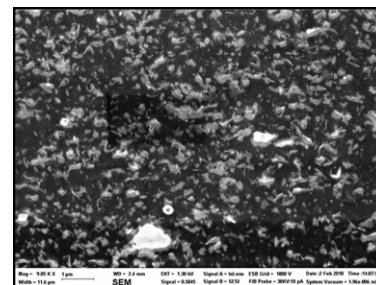


**Unique morphology of dispersed clay particles in a polymer nanocomposite**

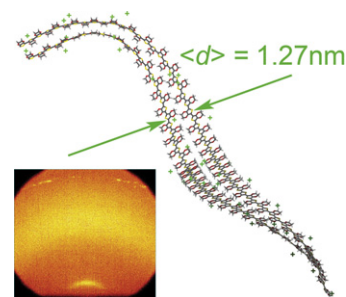
pp 1297–1301

Thomas Malwela, Suprakas Sinha Ray\*

National Centre for Nano-Structured Materials, Council for Scientific and Industrial Research, Pretoria 0001, South Africa

**Structural, chemical and electrochemical characterization of poly(3,4-Ethylendioxythiophene) (PEDOT) prepared with various counter-ions and heat treatments**

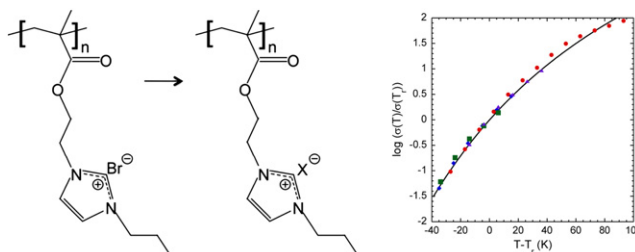
pp 1302–1308

Zachary A. King<sup>a</sup>, Charles M. Shaw<sup>b</sup>, Sarah A. Spanning<sup>a,b</sup>, David C. Martin<sup>a,b,c,d,\*</sup><sup>a</sup> Department of Biomedical Engineering, The University of Michigan, 2200 Bonisteel Blvd., Ann Arbor, MI 48109-2099, USA<sup>b</sup> Macromolecular Science and Engineering Center, The University of Michigan, 2300 Hayward Ave., Ann Arbor, MI 48109-2136, USA<sup>c</sup> Department of Materials Science and Engineering, The University of Michigan, 2300 Hayward Ave., Ann Arbor, MI 48109-2136, USA<sup>d</sup> Department of Materials Science and Engineering, The University of Delaware, 201C DuPont Hall, Newark, DE 19716, USA**Anion exchanged polymerized ionic liquids: High free volume single ion conductors**

pp 1309–1317

Yuesheng Ye, Yossef A. Elabd\*

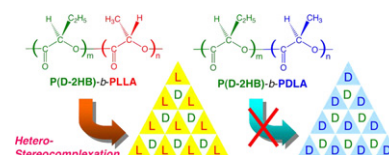
Department of Chemical and Biological Engineering, Drexel University, Philadelphia, PA 19104, United States

**Hetero-stereocomplex formation of stereoblock copolymer of substituted and non-substituted poly(lactide)s**

pp 1318–1325

Hideto Tsuji\*, Kenta Shimizu, Yuzuru Sakamoto, Ayaka Okumura

Department of Environmental and Life Sciences, Graduate School of Engineering, Toyohashi University of Technology, Tempaku-cho, Toyohashi, Aichi 441-8580, Japan



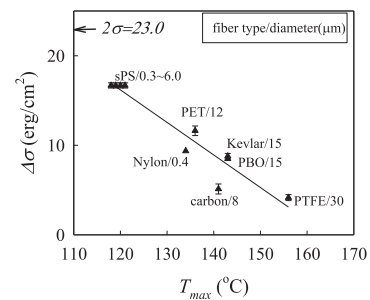


**Electrospun-fiber induced transcrystallization of isotactic polypropylene matrix**

pp 1326-1336

Chi Wang\*, Fwu-Hung Liu, Wei-Hung Huang

Department of Chemical Engineering, National Cheng Kung University, Tainan 70101, Taiwan, ROC

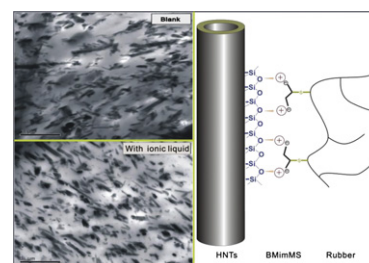


**Functional thiol ionic liquids as novel interfacial modifiers in SBR/HNTs composites**

pp 1337-1344

Yanda Lei, Zhenghai Tang, Lixin Zhu, Baochun Guo\*, Demin Jia

Department of Polymer Materials and Engineering, South China University of Technology, Guangzhou 510640, China



\*Corresponding author



Full text of this journal is available, on-line from **ScienceDirect**. Visit [www.sciencedirect.com](http://www.sciencedirect.com) for more information.

Abstracted/indexed in: AGRICOLA, Beilstein, BIOSIS Previews, CAB Abstracts, Chemical Abstracts. Current Contents: Life Sciences, Current Contents: Physical, Chemical and Earth Sciences, Current Contents Search, Derwent Drug File, Ei compendex, EMBASE/ Excerpta Medica, Medline, PASCAL, Research Alert, Science Citation Index, SciSearch. Also covered in the abstract and citation database SCOPUS®. Full text available on ScienceDirect®

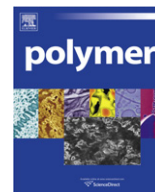


ELSEVIER

ISSN 0032-3861

**Author Index**

- Aydın, G. O. 1241  
Azami, M. 1286
- Bessy, E. 1223  
Beyaz, S. K. 1241
- Chang, S. L. 1249  
Cheng, P. W. 1249
- Dashtimoghadam, E. 1286
- Elabd, Y. A. 1309
- Fischer, K. 1263
- Gérard, E. 1223  
Guise, O. 1278  
Guo, B. 1337
- Hacıvelioğlu, F. 1241  
Haidar Ahmad, I. A. 1268  
Hasani-Sadrabadi, M. M. 1286  
He, W.-T. 1256  
Hénard, G. 1223  
Huang, S.-W. 1256  
Huang, W.-H. 1326
- Jacob, K. I. 1286  
Jia, D. 1337
- Kılıç, A. 1241  
King, Z. A. 1302  
Kostova, B. 1217  
Koynov, K. 1263
- Lambov, N. 1217  
Lei, Y. 1337  
Lin, C. H. 1249  
Liu, F.-H. 1326  
Liu, W.-M. 1256
- Majedi, F. S. 1286  
Malwela, T. 1297  
Marchand-Brynaert, J. 1223  
Marmey, P. 1223  
Martin, D. C. 1302  
Maskos, M. 1263  
Mohorič, I. 1234  
Mokarram, N. 1286  
Momekov, G. 1217  
Momekova, D. 1217  
Momtaz, M. 1223  
Mueller, W. 1263
- Okumura, A. 1318  
Okutan, E. 1241
- Peng, N. 1256  
Petrov, P. 1217  
Pierrat, S. 1263  
Preschilla, N. 1278
- Rerat, V. 1223
- Sakamoto, Y. 1318  
Salvagnini, C. 1223  
Šebenik, U. 1234  
Shaw, C. M. 1302  
Shimizu, K. 1318  
Sinha Ray, S. 1297  
Spanninga, S. A. 1302  
Striegel, A. M. 1268  
Striegel, D. A. 1268  
Strom, C. 1278
- Tang, Z. 1337  
Thiermann, R. 1263  
Toncheva-Moncheva, N. 1217  
Tsuji, H. 1318  
Tsvetanov, C. B. 1217
- Verpoort, T. 1223
- Wang, C. 1326
- Xia, X.-M. 1256
- Ye, Y. 1309  
Yeşilot, S. 1241
- Zhu, L. 1337  
Zhuo, R.-X. 1256



## Poly(ethoxytriethyleneglycol acrylate) cryogels as novel sustained drug release systems for oral application

Bistra Kostova<sup>a</sup>, Denitsa Momekova<sup>a</sup>, Petar Petrov<sup>b,\*</sup>, Georgi Momekov<sup>c</sup>, Natalia Toncheva-Moncheva<sup>b</sup>, Christo B. Tsvetanov<sup>b</sup>, Nikolai Lambov<sup>a</sup>

<sup>a</sup> Department of Pharmaceutical Technology and Biopharmaceutics, Faculty of Pharmacy, Medical University-Sofia, 2 Dunav Str., 1000 Sofia, Bulgaria

<sup>b</sup> Institute of Polymers, Bulgarian Academy of Sciences, Akad. G. Bonchev Str. 103A, 1113 Sofia, Bulgaria

<sup>c</sup> Department of Pharmacology, Pharmacotherapy and Toxicology, Faculty of Pharmacy, Medical University-Sofia, 2 Dunav Str., 1000 Sofia, Bulgaria

### ARTICLE INFO

#### Article history:

Received 9 December 2010

Received in revised form

17 January 2011

Accepted 22 January 2011

Available online 1 February 2011

#### Keywords:

Cryogels

Drug release

Temperature sensitive

### ABSTRACT

Novel temperature sensitive cryogels of poly(ethoxytriethyleneglycol acrylate) (PETEGA), with *in situ* entrapped active substance, are synthesized employing the UV irradiation technique and tested as matrix for controlled release of the hydrophilic drug verapamil hydrochloride. PETEGA cryogels are non-toxic materials and, due to the macroporous structure, exhibit a reversible, ultra-rapid volume phase transition at temperature *ca.* 31 °C. Carriers based on PETEGA cryogels possess sustained release of verapamil hydrochloride over a period of more than 8 h, which is attributed to the hydrophobic state of the polymer network at physiological temperature and the method of drug immobilization. Drug release characteristics of PETEGA cryogels are compared with another cryogel systems, based on polyacrylamide (PAAm), poly(N-isopropylacrylamide) (PNIPAAm) and poly(2-hydroxyethyl methacrylate) (PHEMA), obtained via the same method.

© 2011 Elsevier Ltd. All rights reserved.

### 1. Introduction

Polymer matrices are one of the most widely investigated and used in practice materials for modified-release drug delivery systems [1,2]. The efforts are focused on both elaboration of novel advanced polymeric carriers and modification of the methods for obtaining the system itself [3–7]. From a technological stand-point a crucial stage in the elaboration of such systems is the method for drug loading. The most common technique is the physical mixing of the active ingredient with the matrix carrier. Another approach for drug loading is based on chemical bonding between the drug and the polymer.

In particular, hydrogels are main class of polymeric materials commonly used in clinical practice and experimental medicine for a wide range of applications such as tissue engineering and regenerative medicine, diagnostics, cellular immobilization, drug release, etc [1,2]. Currently, there is an increasing interest in super-macroporous polymer hydrogels with unique heterogeneous open-porous structure, which opens new perspectives for development of innovative systems for biomedical and pharmaceutical applications [1]. Among different techniques, the cryotropic gelation is an efficient method for preparation of super-macroporous polymer hydrogels, also named cryogels [8].

Cryogels are formed as a result of consequent freezing, reaction of cross-linking and thawing of low- or high molar mass precursors dissolved most often in water. In the process of cryogenic treatment most of the water forms ice crystals while the bound water and the soluble substances are accumulated in a non-frozen liquid microphase (NFLMP). The gel formation occurs in this liquid microphase and the ice crystals perform as porogens. The spongy-like structure of cryogels, i.e. the oriented and interconnected pores with their very smooth wall interface, facilitates dramatically the diffusion of species and, thereby, the mass and heat transfer, respectively.

Several years ago a method for preparation of cryogels based on the UV irradiation technique [9] was developed by our team. The advantages of UV irradiation are the very low capital outlay and the extremely short time for efficient gel formation. Thus, cryogels of poly(ethylene oxide) [9] and various cellulose derivatives [10,11] were prepared by only 2 min of UV irradiation (irradiation dose rate of 5.7 J/cm<sup>2</sup>.min) of moderately frozen polymer systems in the presence of photoinitiator. Very recently, Petrov et al. reported on the synthesis of temperature sensitive PNIPAAm and hydroxypropylcellulose cryogels via UV irradiation that exhibit reversible, ultra-rapid volume phase transition within 10–15 s [12].

The present study aims at reporting on the preparation of novel temperature sensitive cryogels of poly(ethoxytriethyleneglycol acrylate) (PETEGA) and their utilization as matrices for loading and sustained release of hydrophilic drug. Verapamil hydrochloride,

\* Corresponding author. Tel.: +359 2 979 6335.

E-mail address: [ppetrov@polymer.bas.bg](mailto:ppetrov@polymer.bas.bg) (P. Petrov).

a representative L-type calcium channel blocker widely used as antihypertensive, antiarrhythmic and antianginal drug [13] is selected as a model drug. To the best of our knowledge, this is the first work describing how the combination of the *in situ* incorporation of hydrophilic drug into temperature sensitive cryogel and the hydrophobic state of the matrix at physiological temperature causes a sustained drug release profile. Drug release characteristics of PETEGA cryogels are compared with another cryogel systems based on polyacrylamide, poly(N-isopropylacrylamide) and poly(2-hydroxyethyl methacrylate).

## 2. Experimental section

### 2.1. Materials

Acrylamide, N-isopropylacrylamide, 2-hydroxyethyl methacrylate, acryloyl chloride, N,N'-methylenebisacrylamide, poly(ethylene glycol) diacrylate (aver. mol. wt. 575 g/mol), Dulbecco's modified Eagle's medium (DMEM), fetal calf serum (FCS), ethylenediaminetetraacetic acid (EDTA) and PBS tablets (phosphate buffered saline, pH 6.8) were purchased from Sigma–Aldrich and used without purification. Tri(ethylene glycol) monoethyl ether (Sigma–Aldrich), and triethylamine (Sigma–Aldrich) were distilled before using. H<sub>2</sub>O<sub>2</sub> (30 vol.% aqueous solution), trypsin, 3-(4,5-dimethylidiazol-2-yl)-2,5-diphenyltetrazolium bromide (MTT), 2-propanol were obtained from Merck and used without purification. Verapamil hydrochloride was provided by Knoll AG, Ludwigshafen, Germany. Ninety six well flat-bottomed microplates are products of Nunc, Roskilde, Denmark. The solvents (dichloromethane, hexane, ethyl acetate, tetrahydrofuran) were purified by distillation before using.

### 2.2. Syntheses of ETEGA

Ethoxytriethyleneglycol acrylate was synthesized according to the procedure described in Ref [14]. Briefly, tri(ethylene glycol) monoethyl ether (40 mL, 0.2 mol) and triethylamine (29.8 mL, 0.2 mol) were dissolved in 50 mL of dichloromethane in a 3-necked round-bottom flask in an ice/water bath under nitrogen atmosphere. Then, acryloyl chloride (18.53 mL, 0.2 mol) dissolved in 20 mL of dichloromethane was added drop-wise. The reaction was carried out at room temperature overnight. The precipitate was filtered off, whereas the filtrate was transferred in a separating funnel and washed subsequently with 50 mL of a 10 wt % aqueous solution of sodium bicarbonate, 50 mL of water, and 50 mL of a saturated aqueous solution of sodium chloride. The organic layer was collected and dried over anhydrous sodium sulfate. The crude product was concentrated using rotary vacuum evaporation and purified by passing through a silica gel column using ethyl acetate as an eluent. The solvent was removed and the product was purified by vacuum distillation at 110 °C and 45 mTorr in the presence of small quantities of hydroquinone. The monomer was then dissolved in 150 mL of dichloromethane and washed with 0.1 M aqueous solution of NaOH until the aqueous layer became colorless. The organic layer was washed with water to neutral pH and dried over anhydrous sodium sulfate. The monomer was obtained as a colorless liquid (yield 60%, 23.0 g). The purity of the monomer (>98%) was checked by gas chromatography.

### 2.3. Synthesis of cryogels with *in situ* immobilized drug

0.6 g of monomer was dissolved in 6 mL distilled water under stirring to obtain homogeneous aqueous solution (10 wt.%). Then, 0.1 mL H<sub>2</sub>O<sub>2</sub> initiator, 0.18 g (0.06 g) cross-linking agent (BisAAM or PEGDA) and 0.06 g verapamil hydrochloride were added under

stirring at room temperature. Portions of 1 mL of the resulting homogeneous solution were poured into 6 Teflon dishes (20 mm diameter) forming a 4 mm thick layer, which were then kept in a freezer at minus 20 °C for 2 h. The dishes were irradiated with full spectrum UV–vis light with a “Dymax 5000-EC” UV curing equipment with 400 W metal halide flood lamp for 5 min (irradiation dose rate: 5.7 J/cm<sup>2</sup> min; input power: 93 mW/cm<sup>2</sup>). PETEGA cryogels used for the determination of degree of swelling and cytotoxicity assessment were synthesized without verapamil hydrochloride.

### 2.4. Measurements of gel fraction yield and degree of swelling

Gel fraction (GF) yield and degree of swelling (DS) of cryogels were determined gravimetrically. To calculate the GF content, the samples were extracted in distilled water for 6 days at room temperature. After that, the samples were freeze dried in an “Alpha 1–2 Freeze drier” (Martin Christ) at minus 55 °C and 0.06 mbar for 24 h, weighed and the GF was calculated by the relationship:

$$\text{GF yield (\%)} = \frac{\text{weight of dried sample}}{\text{weights of monomer and crosslinking agent}} \times 100$$

The degree of swelling was determined gravimetrically at equilibrium water uptake. The DS was measured in water in a temperature range from 20 to 50 °C. Disks of cryogel, equilibrated at 20 °C, were weighed and transferred to water at a given, elevated temperature for 10 min and weighed again. Prior to weighing, the cryogels were blotted with filter paper. Finally, the samples were freeze dried.

$$\text{DS} = \frac{\text{weight of swollen sample}}{\text{weight of dried sample}}$$

The experimental errors of the GF yields and the DS calculations were in the range of 2–5%.

### 2.5. Surface morphology

The extracted cryogels were frozen in liquid nitrogen, fractured and freeze dried in an “Alpha 1–2 Freeze drier” (Martin Christ) at minus 55 °C and 0.06 mbar for 24 h. Then the specimens were fixed on a glass substrate and coated with gold for 60 s. The interior morphology of the gels was studied by using a JEOL JSM-6390 scanning electron microscope operating at 10 kV.

#### 2.5.1. Cytotoxicity assessment

The cytotoxicity of PETEGA cryogel (without drug) was evaluated using a modification of the USP *In vitro* biological reactivity elution test in a panel of human cell lines. In brief, extracts of the tested materials were freshly prepared in RPMI-1640 medium (200 mg/mL) for 24 h at 37 °C. The tested cells were exposed to extract from stock PETEGA cryogel (200 mg/mL) in RPMI-1640 growth medium and its serial dilutions (1:1; 1:2, 1:4, 1:8). Following 72 h continuous exposure the cellular viability was determined using the standard MTT-dye reduction assay [15,16].

### 2.6. Drug release studies

Drug release profiles were evaluated using a dissolution test apparatus (Erweka DT 600, Heusenstamm, Germany). The modified USP paddle method was selected. Six freeze-dried samples were immersed in PBS (pH 6.8) and the test was carried out at a paddle rotation speed of 50 rpm, at temperature = 37 ± 0.5 °C, in 500 mL dissolution medium. The quantity of verapamil hydrochloride in sample solutions was analyzed by UV absorbance at 278 nm using DU 800 spectrophotometer (Beckman Coulter). The

**Table 1**  
Model systems based on three different polymer carriers.

Sample code	Polymer cryogel	Cross-linking agent (mass %)	Verapamil hydrochloride (mass %)
M1	PETEGA	BisAAm 30	10
M2	PETEGA	PEGDA 30	10
M3	PNIPAA	BisAAm 10	10
M4	PNIPAA	BisAAm 30	10
M5	PHEMA	BisAAm 10	10
M6	PHEMA	BisAAm 30	10

cumulative percentage of drug release was calculated and the average of six determinations was used in the data analysis. The statistical analysis of dissolution data of the samples based on systems M1–M6 (Table 1) at pH = 6.8 showed a statistical difference ( $p < 0.05$ ) using *t*-test by Origin Plot software.

### 3. Results and discussion

#### 3.1. Syntheses and characterization

Macroporous PETEGA cryogels containing the hydrophilic drug verapamil hydrochloride were synthesized by the UV irradiation technique [9–12]. So far, this is the first work reporting on the synthesis, swelling behavior and release properties of drug caring system based on temperature-responsive PETEGA cryogel. The procedure involves preparation of homogeneous aqueous solution of ETEGA, H<sub>2</sub>O<sub>2</sub>, cross-linking agent (BisAAm or PEGDA) and drug, followed by freezing at a defined negative temperature, an extremely short UV irradiation and thawing (or freeze drying for drug release studies). Finally, opalescent cryogels (aerogels in case of freeze dried samples) with an open-porous structure (Fig. 1) were obtained. Importantly, to localize the hydrophilic drug into the polymer matrix, verapamil was dissolved in water and mixed with the reagents before freezing and cross-linking, respectively.

Due to the cryostructuration effect [8] this method predetermines incorporation of drug molecules predominantly into the polymer walls, without significant accumulation of drug in the channels of as-synthesized material. One has to mention that the applied irradiation dose did not affect the drug, as confirmed by proton NMR and UV–vis spectroscopy. On the other hand, the presence of verapamil (up to 10 mass % to the monomer) did not disturb the reaction of cross-linking and practically quantitative GF yield were calculated (GF > 99%). Since the materials obtained are foreseen for peroral application, it is a critical issue to avoid any contamination of initial monomer and cross-linking agent. Therefore, an additional test for detection of monomer into the final cryogels was carried out. The cryogels were extracted with water and, then, the liquid, after concentration, was analyzed by gas chromatography. No apparent traces of monomer in each sample after UV irradiation were detected, which is in good agreement with the gel fraction measurements.

It was reported that linear PETEGA polymer is a temperature-responsive polymer [17]. In this work, we describe the swelling/deswelling properties of PETEGA cryogel in the 20–50 °C temperature range. It was found that PETEGA cryogels obtained from 10 mass % monomer solution undergo a reversible volume phase transition (VPT) from hydrophilic to hydrophobic state roughly in the interval of 28–42 °C, and decreased the apparent degree of swelling from 14 at 20 °C to 8 at 50 °C (Fig. 2). The temperature of VPT,  $T_{VPT}$ , estimated as the maximum of first derivative of swelling vs. temperature curve, is equal to 31 °C. For comparison, DS of PNIPAAm cryogel were 17 at 20 °C and 5 at 50 °C, respectively [12]. As seen from Fig. 1 (bottom), the network collapse reduces the size of the pores, but as a whole the material maintains its open-porous structure at temperature above VPT. Typically for temperature-responsive cryogels [18,19], PETEGA cryogel reversibly swells and shrinks for extremely short time below and above the VPT temperature, respectively. Namely, equilibrated at 20 °C, PETEGA cryogel immediately decreased its apparent degree of swelling

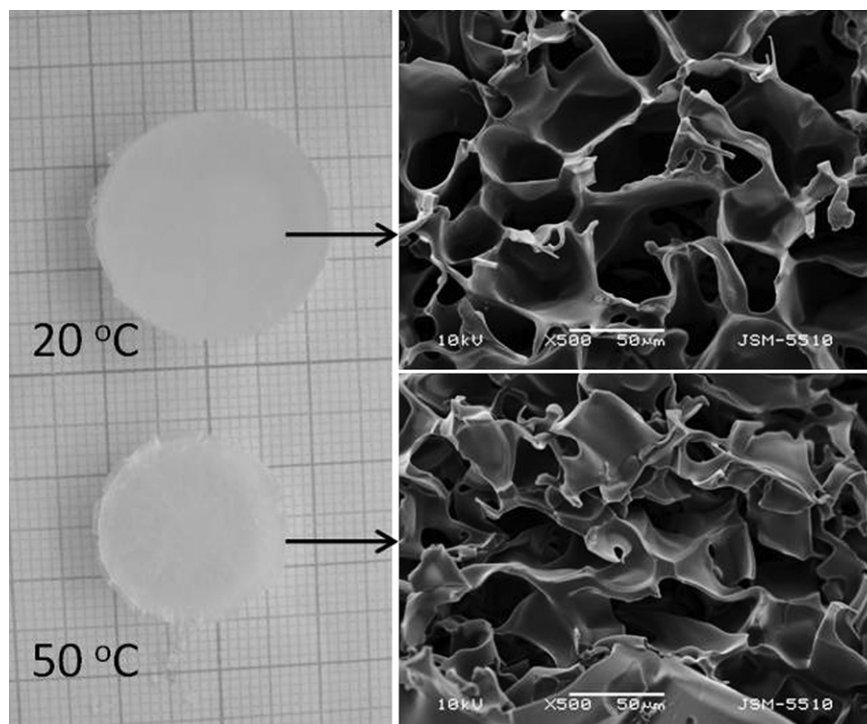


**Fig. 1.** Digital and SEM photographs of PETEGA cryogel at 20 °C (top) and 50 °C (bottom), synthesized via UV irradiation of moderately frozen system (10 mass % solution of ETEGA; temperature of freezing –20 °C; 5 mass % H<sub>2</sub>O<sub>2</sub> and 30 mass % PEGDA to the monomer).



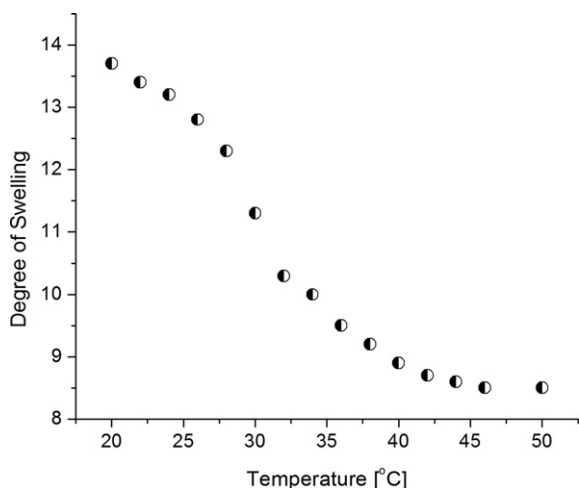


**Fig. 2.** Temperature dependence of the swelling properties of PETEGA cryogel, synthesized via UV irradiation of moderately frozen system (10 mass % solution of ETEGA; temperature of freezing  $-20\text{ }^{\circ}\text{C}$ ; 5 mass %  $\text{H}_2\text{O}_2$  and 30 mass % PEGDA to the monomer).

when transferred to hot water ( $50\text{ }^{\circ}\text{C}$ ) and reached nearly equilibrium state in 20 s (Fig. 3). Vice versa, immersed again in water at  $20\text{ }^{\circ}\text{C}$  the cryogels did uptake approximately 90 vol.% of its equilibrium water content for the same time.

Definitely, the regular open-porous structure of cryogel and the existence of large amount of free water in the pores alleviate the mass transport and heat exchange and, thereby, essentially contribute to the fast response of the system. It was established that PETEGA cryogels obtained with the two different cross-linking agents, PEGDA and BisAAm (Table 1), exhibit identical swelling behavior.

In addition, in order to evaluate the applicability of the method for drug entrapment into other cryogel matrices as well as to compare the release properties of PETEGA carriers to another similar systems, our study was extended to the synthesis of different biocompatible PAAm, PNIPAAm and PHEMA cryogels employing the same procedure.

### 3.2. Cytotoxicity assessment

Very important issues for a drug delivery system are its biocompatibility and biodegradability. Since our materials are

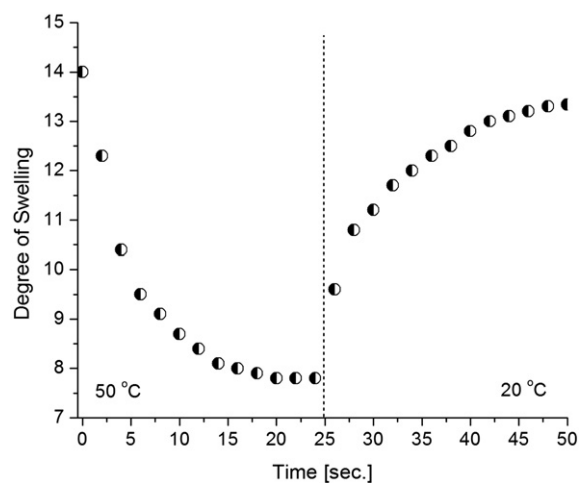


**Fig. 3.** Deswelling–reswelling kinetics of PETEGA cryogel above ( $50\text{ }^{\circ}\text{C}$ ) and below ( $20\text{ }^{\circ}\text{C}$ ) the temperature of volume phase transition (10 mass % solution of ETEGA; temperature of freezing  $-20\text{ }^{\circ}\text{C}$ ; 5 mass %  $\text{H}_2\text{O}_2$  and 30 mass % PEGDA to the monomer).

foreseen for peroral application a biodegradable matrix is not necessary. The cytotoxicity of PETEGA cryogels, without loaded drug, was tested on human cell lines, representative for different cellular populations/tissues, namely HT-29 (colon epithelium), BV-173 (pre-B-cell), SKW-3 (T-cell) and HL-60 (myeloid). The cellular viability after 72 h exposure to extracts of the tested materials in RPMI-1640 medium was assessed using the MTT-dye reduction assay (data not shown) and by light microscopy, as described by USP. Throughout the panel of human cell lines the tested polymers proved to be devoid of cytotoxic activity (Fig. 4) and can be exploited as drug delivery system.

### 3.3. Drug release studies

In many cases, when a controlled release of drug from hydrogel matrix is considered, an unwanted burst release is observed [20]. We found that verapamil hydrochloride was successfully entrapped in all cryogel carriers described in the present work, however, the swelling behavior of the polymer matrices at physiological temperature play a key role for the drug release profile. Our preliminary studies with the highly hydrophilic polyacrylamide cryogels showed a substantial burst release within the first hour. In fact, the macroporous structure of freeze-dried systems allows very fast water uptake by the pores due to the capillary effects and, in the case of hydrophilic PAAm, the network rapidly swells upto DS 17–20. In contrast, PETEGA and PNIPAAm cryogels are in hydrophobic state at  $37\text{ }^{\circ}\text{C}$  and have DS = 8 and 5, respectively, while PHEMA cryogel in general does not swell to a great extent (DS ca. 6)[12].

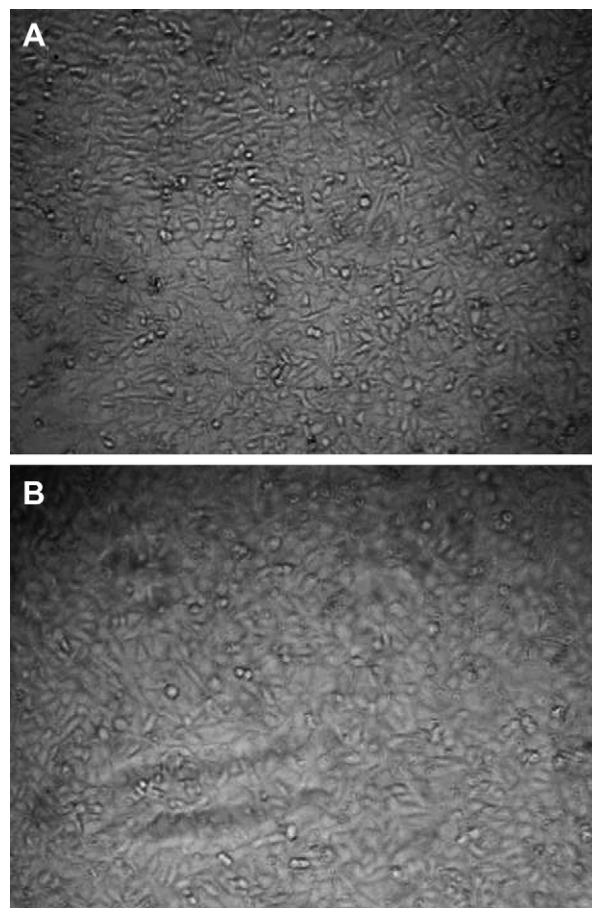


**Fig. 4.** HT-29 (colon epithelium) human cells before (A) and after 72 h exposure to extract from PETEGA cryogel (200 mg/mL) in RPMI-1640 medium (B).



Our findings indicate that the systems based on PETEGA, PNIPAAm and PHEMA (Table 1) allow controlled release of verapamil hydrochloride over a period of more than 8 h (Fig. 5).

The results from the *in vitro* drug release investigation of PETEGA-based samples are presented in Fig. 5a. It is clear that both systems (M1 and M2), obtained with two different cross-linking agents, have almost equivalent rate and extent of drug release. Following a slight initial burst effect, from the 2nd hour post incubation the drug release process is characterized by a time-independent kinetics (zero order kinetic with correlation coefficient  $R = 0.998$ ).

It was suggested that the active ingredient is incorporated predominantly in the walls of the porous matrix, but probably a small fraction is adsorbed on the surface of the matrix. Thus, immersing the freeze-dried disk in the dissolution medium (PBS), most probably the adsorbed fraction is rapidly released, while the embedded fraction of the drug is thereafter released much more slowly. The release of the drug which is immobilized in the polymeric walls is directly dependent on the swelling ability of the matrix. As far as PETEGA is concerned as a carrier, at temperature of 37°C, the polymer is in a hydrophobic state, which slows down the rate of drug release. In other words, the rate of this process depends substantially on the localization of the drug during the synthesis of the cryogel as well as on the degree of swelling of the polymer network, which is related to the time for polymer chain relaxation. From this point of view, the behavior of cryogel system in the drug release process is not governed by the typical diffusion-controlled release patterns and probably follows an anomalous mechanism.

The samples based on the other thermo-sensitive polymer, PNIPAAm, exhibited similar trend (Fig. 5b). In this case, no prominent difference between the two model systems containing different amounts of the cross-linking agent was established. Nevertheless, there is difference in the release rate and extent of verapamil hydrochloride, as compared to the cryogels based on PETEGA (Fig. 5a). In the very beginning of the *in vitro* release experiment, the samples M1 and M2 are characterized with a greater rate and extent of verapamil hydrochloride release, as compared to M3 and M4, and this trend is maintained until the end of the incubation period. The amount of released drug by M1 and M2 for 8 h is 98%, whereas the PNIPAAm-based carriers released approximately 75%. Hence it could be concluded that cryogels based on PNIPAAm would be more applicable either for active ingredients requiring more prolonged drug release period (ca. 12 h), or for drugs which are more soluble in water than verapamil hydrochloride.

The systems based on PHEMA cryogels (Fig. 5c) exhibited more pronounced differences in the release kinetics as a function of the content of cross-linking agent, in contrast to the aforementioned systems M1–M4.

PHEMA is hydrophilic at physiological temperature and most probably the density of polymer network, determined by the content of BisAAm, influence the release profile. It is plausible that when the content of the cross-linking agent is 10 mass % the polymer network is less dense and, hence, the release process is faster as compared to the cryogel containing 30 mass % cross-linking agent. The larger amount of BisAAm leads to a denser polymer network which hinders the release of the active compound immobilized in the polymer wall. On this ground, the amount of the drug released from M6 for 8 h is 80%, whereas in case of M5 (10 mass % cross-linking agent) the amount of released verapamil hydrochloride is 97%.

#### 4. Conclusions

Temperature-responsive PETEGA cryogels, containing verapamil hydrochloride, were synthesized and tested as drug release

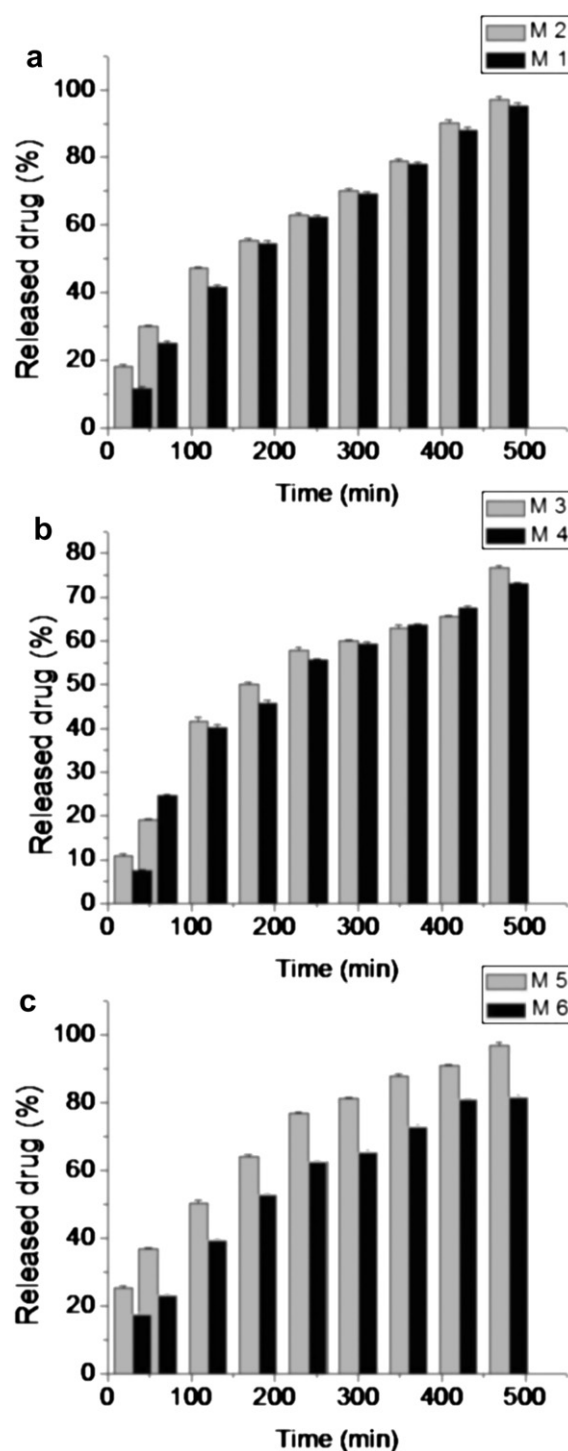


Fig. 5. Release kinetics of verapamil hydrochloride from model systems based on: a) PETEGA cryogels obtained with 30 mass % BisAAm (M1) and 30 mass % PEGDA (M2); b) PNIPAAm cryogels obtained with 10 mass % BisAAm (M3) and 30 mass % BisAAm (M4); c) PHEMA cryogels obtained with 10 mass % BisAAm (M5) and 30 mass % BisAAm (M6); Mean  $\pm$  SD,  $n = 6$ .

systems. The lack of cytotoxicity of PETEGA cryogels was confirmed by tests on several human cell lines with different cell type and origin. The results from the *in vitro* drug release investigations were compared to other biocompatible cryogel systems. The systems based on PETEGA, PNIPAAm and PHEMA allow efficient controlled release of verapamil hydrochloride over a period of more than 8 h.

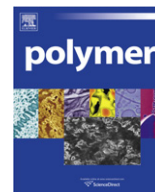
In case of temperature-responsive PETEGA- (M1, M2) and PNI-PAAm-based systems (M3, M4), there was no significant influence of the type and content of the cross-linking agent on the drug release patterns, i.e. the delayed release of the drug is due to the hydrophobic state of the polymer carrier at physiological temperature. In a dissimilar fashion, for PHEMA based systems (M5 and M6) the increase of the content of cross-linking agent from 10 to 30 mass % resulted in 17% decrease of the amount of drug released for 8 h incubation. The results indicate that PETEGA and PHEMA (10 mass % BisAAm) based systems could be considered as optimal drug delivery systems for sustained release of verapamil hydrochloride.

### Acknowledgement

The authors acknowledge the financial support by the National Science Fund of Bulgaria (National Centre for New Materials UNION, contract no. DCVP-02/2).

### References

- [1] Ravi Kumar MNV, Kumar N, Domb AJ, Arora MA. *Adv Polym Sci* 2002; 160:45–117.
- [2] Hoare TR, Kohane DS. *Polymer* 2008;49(8):1993–2007.
- [3] Brannon-Peppas L. *Med Plast Biomat* 1997;4:34–44.
- [4] Kim H, Fassihi R. *Pharm Res* 1997;14:1415–21.
- [5] Kostova B, Kamenska E, Ivanov I, Momekov G, Rachev D, Georgiev G. *Pharm Dev Tech* 2008;13(6):311–21.
- [6] Kamenska E, Kostova B, Ivanov I, Rachev D, Georgiev G. *J Biomat Sci Polym Ed* 2009;20:181–97.
- [7] Gil EC, Colarte AI, Bataille B, Pedráz JL, Heinämäki J. *Int J Pharm* 2006;317(1):32–9.
- [8] Lozinsky VI. *Russ Chem Rev* 2002;71(6):489–511.
- [9] Doycheva M, Petrova E, Stamenova R, Tsvetanov ChB, Riess G. *Macromol Mater Eng* 2004;289(7):676–80.
- [10] Petrov P, Petrova E, Stamenova R, Tsvetanov ChB, Riess G. *Polymer* 2006;47(19):6481–4.
- [11] Petrov P, Petrova E, Tsvetanov CB. *Polymer* 2007;48:4943–9.
- [12] Petrov P, Petrova E, Tsvetanov CB. *Polymer* 2009;50(5):1118–23.
- [13] Kasim A, Whitehouse M, Ramachandran C, Bermejo M, Lennernäs H, Hussain S, et al. *Mol Pharm* 2004;1:85–96.
- [14] Jiang XG, Lavender CA, Woodcock JW, Zhao B. *Macromolecules* 2008;41(7):2632–43.
- [15] Mosmann TJ. *Immunol Methods* 1983;65:55–63.
- [16] Konstantinov SM, Eibl H, Berger MR. *Br J Haematol* 1999;107:365–80.
- [17] Dimitrov P, Toncheva N, Weda P, Rangelov S, Trzebicka B, Dworak A, et al. *Macromol Symposia* 2009;278(1):89–95.
- [18] Lozinskii VI, Kalinina EV, Grinberg VYa, Grinberg NV, Chupov VV, Platé NA. *Polym Sci* 1997;A 39(12):1300–5.
- [19] Zhang X-Z, Zhuo R-X. *Macromol Chem Phys* 1999;200(12):2602–5.
- [20] Huang X, Brazel CS. *J Control Release* 2001;73:121–36.



## Surface modifications of polypropylene membranes used for blood filtration

Estelle Gérard<sup>a</sup>, Emilie Bessy<sup>b</sup>, Claudio Salvagnini<sup>a</sup>, Vincent Rerat<sup>a</sup>, Maryam Momtaz<sup>a</sup>, Grégory Hénard<sup>b</sup>, Pascal Marmey<sup>b</sup>, Thierry Verpoort<sup>b</sup>, Jacqueline Marchand-Brynaert<sup>a,\*</sup>

<sup>a</sup> Université Catholique de Louvain, Institut de la Matière Condensée et des Nanosciences, Bâtiment Lavoisier, place L. Pasteur n° 1, B-1348 Louvain-la-Neuve, Belgium

<sup>b</sup> MacoProductions, Chaussée Fernand Forest n° 200, F-59200 Tourcoing, France

### ARTICLE INFO

#### Article history:

Received 27 October 2010

Received in revised form

13 January 2011

Accepted 13 January 2011

Available online 21 January 2011

#### Keywords:

Polypropylene membrane

Surface chemistry

Blood filtration

### ABSTRACT

The surface of two commercial meltblown polypropylene (PP) membranes, used for the filtration of blood products, were modified by wet chemistry treatments (carbodiimide, tosyl chloride and trihalogeno-triazines) in the case of the oxygen-plasma treated membrane ( $O_2$ -PP), and by photochemistry using molecular clips in the case of the native PP membrane. The most efficient technique uses trifluorotriazine reagent for the activation of both hydroxyl- and carboxyl-functions of  $O_2$ -PP. It enables the fixation of amine-terminated molecules with high degrees of derivatization ( $\sim 700$  pmol/cm<sup>2</sup>), without inducing modification of the membrane morphology nor cytotoxicity. Only a weak decrease of surface hydrophilicity was measured after the treatments and steam-sterilization. This method was applied for the grafting of peptides (Gly-Gly-Gly-Gly-Gly, Gly-Arg-Gly-Asp-Ser, home-made modified Leu-Asp-Val) on  $O_2$ -PP membranes incorporated into multi-layer filter devices. These modified filters showed improved properties of leukocyte depletion in blood filtration experiments, principally due to the wetting properties of the membranes.

© 2011 Elsevier Ltd. All rights reserved.

### 1. Introduction

Polypropylene (PP) membranes are used in a large variety of industrial applications such as wastewater treatment, desalination of sea water, ultra-pure water in the semiconductor industry, electrode separation in secondary battery, sterilization of beverages and pharmaceuticals, because of their good mechanical properties, good chemical resistance, good thermal stability and low cost [1,2]. Polypropylene membranes are also increasingly considered for biomedical applications, namely hemodialysis, plasmapheresis, blood oxygenation and leukodepletion [3,4].

Nowadays, different layers of non-woven polymer fibers are used as materials for leukodepletion filters and can be easily processed by meltblowing. The filtration of leukocytes from blood by means of filters can be regarded as a depth filtration process [5,6]. Two main mechanisms are involved: the mechanical entrapment (or sieving), depending on the pores sizes and the deformability of the cells, and the physico-chemical entrapment (or adhesion). Different factors can be responsible for the non-specific adhesion of white cells to surfaces such as the surface chemistry and charge, the wettability and the morphology of the surface (porosity,

roughness...). The specific adhesion could be promoted by the use of selective ligands recognized by the cell receptors, mainly integrins. However, this concept largely developed in the field of tissue engineering [7,8], is not applied to industrial filters yet, in our knowledge, but only studied at the laboratory scale [9].

In this article, we are interested in the surface modification of two meltblown polypropylene membranes: a native PP membrane and an oxygen-plasma treated PP membrane ( $O_2$ -PP) currently used as part of industrial filtration devices of blood products.

Different methods have been reported to modify the wettability or the hydrophilicity of polypropylene surfaces in order to improve the cell adhesion phenomena [10], reduce the proteins adsorptions [11] and enhance the permeation flux of aqueous solutions [12–14]. The most usual methods are various plasma treatments [15–18] and mainly oxygen-plasma [10,19–23], coatings with surfactants [3,14,24], and graft-polymerizations of hydrophilic monomers using peroxide [25,26], UV [27–29] and plasma-induced [30–32] processes. Tailor-made surfaces have been prepared by combining plasma treatment and wet-chemistry [33] for the covalent coupling of heparin [34] and chitosan [35], among others, in the development of blood compatible materials.

Here, we describe a novel wet process aiming at the covalent post-derivatization of oxygen-plasma treated polypropylene membranes ( $O_2$ -PP). Our method is based on the simultaneous activation of the hydroxyl- and carboxyl-functions, displayed on

\* Corresponding author. Tel.: +32 10 47 27 46; fax: +32 10 47 41 68.

E-mail address: [jacqueline.marchand@uclouvain.be](mailto:jacqueline.marchand@uclouvain.be) (J. Marchand-Brynaert).

the  $O_2$ -PP surface with trihalogeno-triazine reagents [36]. The protocol validity has been established by coupling  $^3\text{H}$ - and F-tagged molecules, and then analyzing the samples by Liquid Scintillation Counting (LSC) and X-ray Photoelectron Spectroscopy (XPS), respectively. Comparatively to classical reagents dedicated to the separate activation of hydroxyl- and carboxyl-functions, namely tosyl chloride [37] and carbodiimides [34,35,38], the use of trifluoro-triazine allowed to reach higher degrees of derivatization.

Moreover, a simple and mild protocol for the functionalization of native polypropylene membranes is also presented. It consists in the photo-grafting of arylazide or diazirine derivatives, also called “molecular clips”, which enable the introduction of active functional groups onto inert polypropylene surfaces [39]. These clips are commonly used for the immobilization of enzymes [40,41] on polypropylene surfaces or for improving their biocompatibility by the conjugation to biopolymers or dedicated molecules [42–44]. Degrees of derivatization have been determined by the coupling of  $^3\text{H}$ -tagged molecules onto the clips and subsequent LSC analysis. The photo-functionalization of PP appeared less effective than the activation of  $O_2$ -PP functions with trifluoro-triazine.

This latter method has been optimized and further applied to the grafting of a hydrophobic small pentapeptide and two active peptides recognized by the cell-receptor integrins involved in the cellular adhesion phenomena. Physico-chemical and morphological characteristics of the surface modified membranes have been compared to native and blank samples, before and after steam-sterilization. Lastly, blood filtration experiments have been performed at the laboratory scale. Different parameters have been studied: the effect of the wettability of the polypropylene membrane on the retention of the white cells and the phenomena of specific adhesion by the presence of different peptides on the surface of the membranes. Finally, the efficiency of leukocyte depletion could be correlated to the membrane wetting properties as the main parameter.

## 2. Experimental

### 2.1. Materials

Custom polypropylene (PP) membranes (0.30–0.35 mm of thickness) from MacoProductions (Tourcoing, France) were used. They were obtained by the meltblown technique. It consists in melting the polymer and forcing it through a linear nozzle with small holes; heated compressed air is directed at the primary fibers, at a specific angle of attack, to stretch the fibers and reduce their diameter. The membrane displays a heterogeneous distribution in fiber diameter sizes, from 0.5 to 2.0  $\mu\text{m}$ . The two faces of the membrane are visually different: the face named A appears pattern-like, while the face named B is more fibrous. The native membrane is referred to as PP, with A or B indicated in index, if one particular face was analyzed. For the leukodepletion application, an oxygen-plasma treatment was performed (MacoProductions, in-house facilities), giving the hydrophilic membrane named  $O_2$ -PP, i.e. oxygen-plasma treated polypropylene membrane. Moreover, the membranes were steam-sterilized before blood filtration experiments, giving the  $O_2$ -PP-*st* membranes. Steam-sterilization (MacoProductions, in-house facilities) consists in an autoclave treatment with two successive phases of rise in temperature, followed by a phase of 24 min at 121–124  $^\circ\text{C}$  and two phases of cooling.

Samples for surface modifications and analyses were cut in disks of 12 mm of diameter. The apparent surface is 1.13  $\text{cm}^2$ /sample. Samples for blood filtration assays were cut in squares of 6  $\times$  6  $\text{cm}^2$ . Samples for morphological analyses (Air permeability, Critical

Wetting Surface Tension (CWST), Mean Flow Pore Diameter (MFPD) and Thickness) were cut in squares of 10  $\times$  10  $\text{cm}^2$ . Samples for cytotoxicity measurements were cut in squares of 5  $\times$  5  $\text{cm}^2$ .

### 2.2. Surface chemistry

#### 2.2.1. Reagents and solutions

Reagents and solvents were of analytical grade and purchased from Acros (Beerse, Belgium), Sigma–Aldrich–Fluka (Bornem, Belgium), Janssen (Beerse, Belgium), Lancaster (Windham, NH, USA), or Molecular Probes–Invitrogen (Merelbeke, Belgium). Pyridine was obtained in extra dry grade from Merck (Bruxelles, Belgium). Water was obtained with a Milli-Q system (Millipore, Bedford, MA). (L)-4,5- $^3\text{H}$ -lysine was purchased from Amersham Pharmacia Biotech (Little Chalfont, UK) in aqueous solution of 89 Ci/mmol activity.

Phosphate buffer (PB, pH 8) was prepared from  $\text{Na}_2\text{HPO}_4 \cdot 2\text{H}_2\text{O}$  (16.86 g),  $\text{NaH}_2\text{PO}_4 \cdot \text{H}_2\text{O}$  (0.826 g) dissolved in water (1 L). For the preparation of PB– $\text{CH}_3\text{CN}$  solution (1/1), equal volumes of PB and acetonitrile were mixed under vigorous magnetic stirring until precipitation of salt excess occurred; the filtered solution was still at pH 8 and sufficiently buffered for our experimental working conditions. 2-(*N*-morpholino) ethanesulfonic acid (MES) buffer (pH 3.5) was obtained from MES (9.76 g) dissolved in water (500 mL).

The lysine solution ( $10^{-3}$  M) for surface labeling and LSC analysis was prepared as follows: 187.5  $\mu\text{L}$  of commercial radioactive lysine and 250  $\mu\text{L}$  of 0.1 M lysine [lysine monohydrochloride (0.183 g) in water (10 mL)] were dissolved in 25 mL of PB– $\text{CH}_3\text{CN}$  solution.

The F-tagged solution ( $10^{-3}$  M) for XPS analysis was prepared as follows: 2.43 mg of 3,5-bis(trifluoromethyl)benzylamine were dissolved in 10 mL of PB– $\text{CH}_3\text{CN}$  solution.

The reactive and rinsing solutions containing the polymer samples were shaken (150 rpm) with an Edmund Bühler stirrer (model KL-2) or a Heidolph stirrer (Unimax 1010). The heating of the reactive solutions at 37  $^\circ\text{C}$  was performed by a Heidolph incubator (Inkubator 1000).

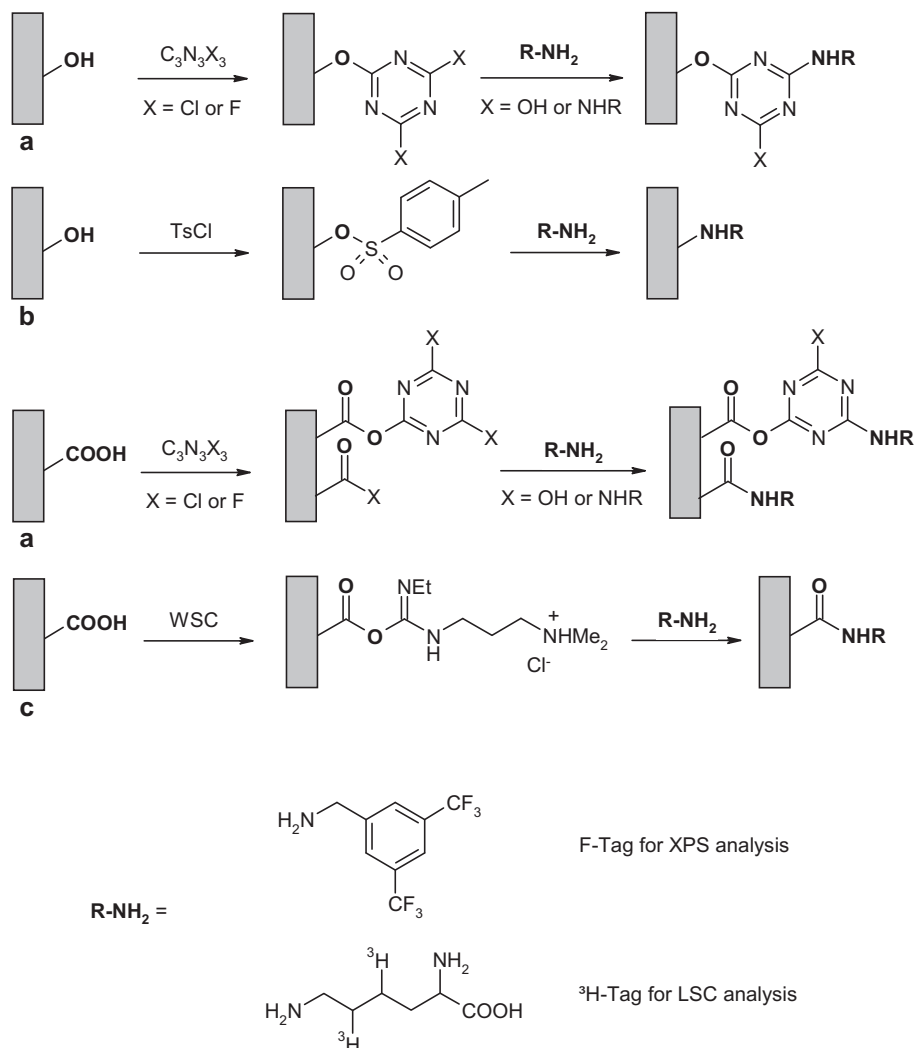
#### 2.2.2. Surface wet chemistry on oxygen-plasma treated polypropylene membranes (see also Scheme 1)

Protocols for the activation with Water-Soluble-Carbodiimide (WSC), tosyl chloride (TsCl) and trichloro-triazine ( $\text{C}_3\text{N}_3\text{Cl}_3$ ) are given in Supplementary Information (SI).

**2.2.2.1. Activation with trifluoro-triazine ( $\text{C}_3\text{N}_3\text{F}_3$ ).** The polymer samples were treated individually in a 24-well polystyrene plate (1 mL of solution/well). They were rinsed with water (1  $\times$  10 min) and acetonitrile (2  $\times$  10 min) before use. Then, they were activated under argon atmosphere by a freshly prepared solution of  $\text{C}_3\text{N}_3\text{F}_3$  in dry acetonitrile (1.25 g/25 mL) for 1 h at 20  $^\circ\text{C}$ . The samples were washed with acetonitrile (4  $\times$  10 min) and dried under vacuum. The blank samples were similarly prepared, but omitting  $\text{C}_3\text{N}_3\text{F}_3$ .

**2.2.2.2. Coupling to the molecular probes.** The activated and blank samples were directly submitted to the labeling protocol (treatments in 24-well polystyrene plate).

The samples were individually immersed in 1 mL of a  $10^{-3}$  M solution of  $^3\text{H}$ -tagged compound ((L)-4,5- $^3\text{H}$ -lysine) in a PB– $\text{CH}_3\text{CN}$  mixture (1/1) and incubated for 2 h at 20  $^\circ\text{C}$  under shaking. The solution was removed by suction and samples were immersed in 1 mL of different washing solutions to remove adsorbed reagents. After each incubation, the solution was removed by suction, the sample and the well were carefully dried also by suction. The samples were washed with PB– $\text{CH}_3\text{CN}$  (1/1, v/v, 2  $\times$  5 min,



**Scheme 1.** Activation of hydroxyl- and carboxyl functions of O<sub>2</sub>-PP membranes: (a) trichloro- or trifluoro-triazine; (b) tosyl chloride; (c) water-soluble carbodiimide; and then coupling to molecular probes.

2 × 10 min), H<sub>2</sub>O–CH<sub>3</sub>CN (1/1, v/v, 2 × 5 min), 5.10<sup>−3</sup> M HCl–CH<sub>3</sub>CN (1/1, v/v, 1 × 5 min) and again H<sub>2</sub>O–CH<sub>3</sub>CN (1/1, v/v, 1 × 5 min, 1 × 10 min). The resulting samples were finally dried over filter paper and submitted to LSC analysis (see Section 2.3.1). The apparent surface is 2.26 cm<sup>2</sup>/sample (considering both faces). The results obtained are collected in Table 2.

**2.2.2.3. Optimization of the grafting protocol with trifluoro-triazine.** After rinsing with water (1 mL, 1 × 10 min) and acetonitrile (1 mL, 2 × 10 min), activation by C<sub>3</sub>N<sub>3</sub>F<sub>3</sub> treatment (1 mL, 1 h or 2 h, 20 °C) and washing with acetonitrile (1 mL, 4 × 10 min), polymer samples were submitted to various incubation conditions into the tagged solutions (1 mL of solution/well): concentration of 10<sup>−3</sup> M or 10<sup>−4</sup> M, reaction during 1 h–24 h, at 20 °C or 37 °C. The samples were rinsed as follows: PB–CH<sub>3</sub>CN (1/1, v/v, 4 × 10 min); H<sub>2</sub>O–CH<sub>3</sub>CN (1/1, v/v, 2 × 10 min); HCl 5.10<sup>−3</sup> M–CH<sub>3</sub>CN (1/1, v/v, 1 × 10 min); H<sub>2</sub>O–CH<sub>3</sub>CN (1/1, v/v, 2 × 10 min). The samples were dried under vacuum and directly analyzed by LSC or XPS (see Section 2.3). The selected conditions for grafting molecules of interest are: activation with C<sub>3</sub>N<sub>3</sub>F<sub>3</sub> during 2 h at 20 °C, incubation overnight at 20 °C with a 10<sup>−3</sup> M solution or incubation 1 h at 37 °C with a 10<sup>−4</sup> M solution (see Table 3).

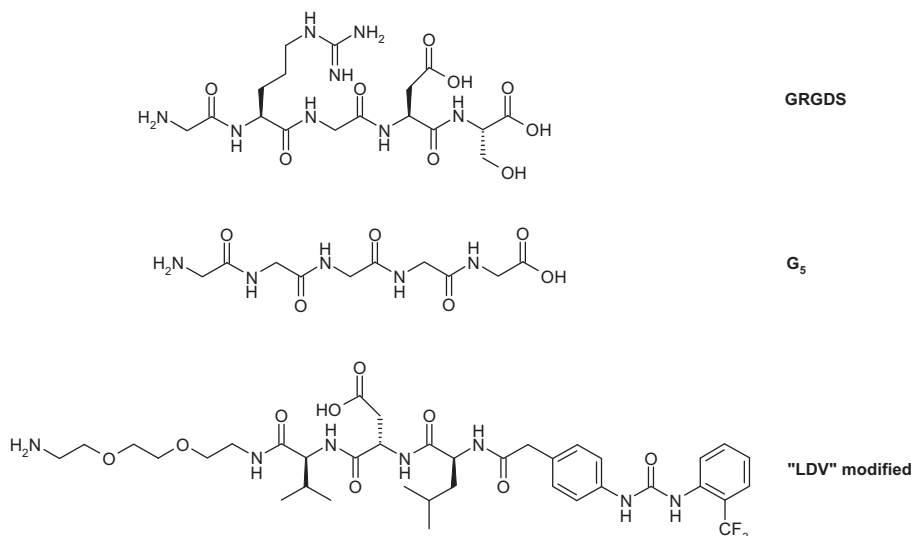
**2.2.2.4. Grafting of the peptides G<sub>5</sub>, GRGDS and “LDV”.** The peptides grafted on the membranes for filtration experiments were the following (see also Scheme 3):

G<sub>5</sub>: Gly-Gly-Gly-Gly-Gly pentapeptide was purchased from Bachem Group (Weil am Rhein, Germany).

GRGDS: Gly-Arg-Gly-Asp-Ser pentapeptide was purchased from PolyPeptide Group (Strasbourg, France).

“LDV”: This Leu-Asp-Val (LDV) tripeptide derivative, with a diarylurea moiety at N-terminus and a triethyleneglycol spacer-arm at C-terminus, was prepared by standard peptide synthesis in solution, according to protocols adapted from the literature (see Section 3.3). The structural characterization of this peptide is given in SI.

Activated polymer samples (C<sub>3</sub>N<sub>3</sub>F<sub>3</sub>, 2 h, 20 °C, see above) were incubated for 1 h at 37 °C into a 10<sup>−4</sup> M solution of G<sub>5</sub> (3.03 mg of peptide dissolved in 100 mL of PB–CH<sub>3</sub>CN) or GRGDS (4.90 mg of peptide dissolved in 100 mL of PB–CH<sub>3</sub>CN) or overnight at 20 °C into a 10<sup>−3</sup> M solution of G<sub>5</sub> (30.33 mg of peptide dissolved in 100 mL of PB–CH<sub>3</sub>CN) or “LDV” (79.59 mg of peptide dissolved in 100 mL of PB–CH<sub>3</sub>CN). We used 10 mL of activation,



**Scheme 3.** Peptides grafted on  $O_2$ -PP membranes (with trifluoro-triazine as cross-linking reagent) for filtration experiments.

incubation or washing solution per square sample of  $6 \times 6 \text{ cm}^2$ . The samples were washed as above, dried under vacuum and stored at  $4 \text{ }^\circ\text{C}$ . XPS analyses realized on these membranes are given in Table 5.

### 2.2.3. Photochemical grafting on native polypropylene membranes

Three different molecular clips, *O*-succinimidyl 4-(*p*-azido-phenyl)butanoate ( $N_3\text{Ar}$ ), *O*-succinimidyl 4-azido-2,3,5,6-tetrafluorobenzoate ( $N_3\text{ArF}_4$ ) and *O*-succinimidyl 4-(3-(trifluoromethyl)-3*H*-diazirin-3-yl)benzoate (diazirine), were prepared according to protocols adapted from the literature (see Section 3.1.) and then tested in the photochemical grafting of native PP membranes (see Scheme 2 and SI for the photo-grafting protocols and results).

### 2.2.4. Samples nomenclature

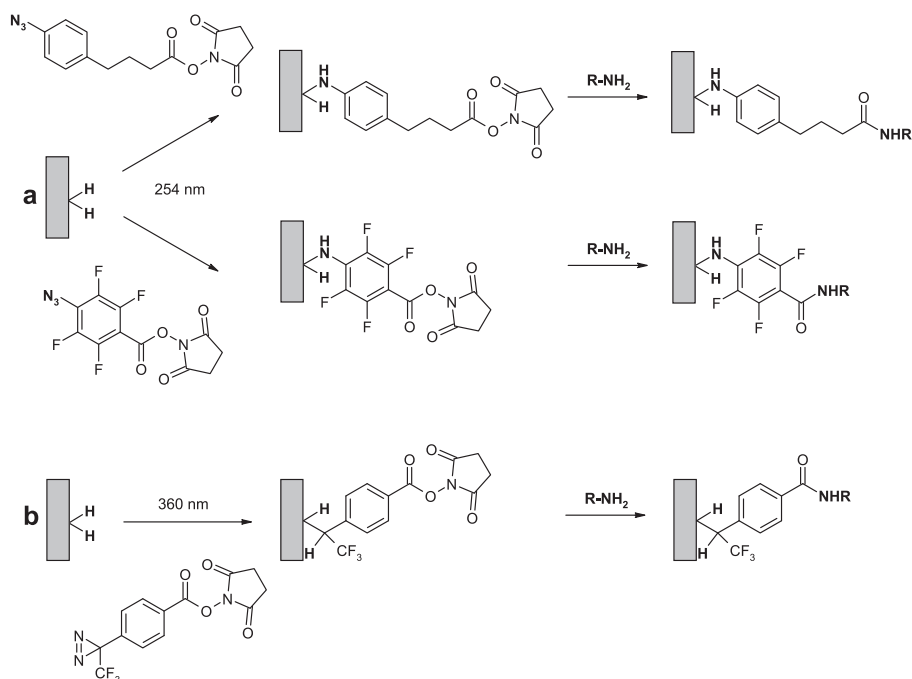
#### 2.2.4.1. Fully treated membranes.

$O_2$ -PP-TsCl- $^3\text{H}$  = oxygen-plasma treated polypropylene activated with tosyl chloride and grafted with  $^3\text{H}$ -tag

$O_2$ -PP-WSC- $^3\text{H}$  = oxygen-plasma treated polypropylene activated with Water Soluble Carbodiimide and grafted with  $^3\text{H}$ -tag

$O_2$ -PP-TrzCl- $^3\text{H}$  = oxygen-plasma treated polypropylene activated with trichloro-triazine and grafted with  $^3\text{H}$ -tag

$O_2$ -PP-TrzF- $^3\text{H}$  = oxygen-plasma treated polypropylene activated with trifluoro-triazine and grafted with  $^3\text{H}$ -tag



**Scheme 2.** Functionalization of native PP membranes by photochemical grafting: (a) arylazides  $N_3\text{Ar}$  and  $N_3\text{ArF}_4$  or (b) diazirine deposition and UV irradiation, then coupling to molecular probes ( $\text{R-NH}_2$ ). See SI for experimental details.



$O_2$ -PP-G<sub>5</sub> = oxygen-plasma treated polypropylene activated with trifluoro-triazine and grafted with pentapeptide G<sub>5</sub>

$O_2$ -PP-GRGDS = oxygen-plasma treated polypropylene activated with trifluoro-triazine and grafted with pentapeptide GRGDS

$O_2$ -PP-LDV = oxygen-plasma treated polypropylene activated with trifluoro-triazine and grafted with peptide "LDV"

#### 2.2.4.2. Blank samples.

NAI = polypropylene not activated with WSC, TsCl, C<sub>3</sub>N<sub>3</sub>Cl<sub>3</sub> or C<sub>3</sub>N<sub>3</sub>F<sub>3</sub> but incubated with tags

NAG<sub>5</sub> = polypropylene not activated with C<sub>3</sub>N<sub>3</sub>F<sub>3</sub> but incubated with G<sub>5</sub>

NAGRGDS = polypropylene not activated with C<sub>3</sub>N<sub>3</sub>F<sub>3</sub> but incubated with GRGDS

ANI = polypropylene activated with trifluoro-triazine but not incubated with tags or peptides

NANI = not activated polypropylene and not incubated with tags or peptides

These samples have been treated with all the washing solutions.

2.2.4.3. *Other encodings.* When oxygen-plasma treated PP is used as starting material, the surface modified sample is indicated with the prefix  $O_2$ -.

The steam-sterilized samples are indicated by the suffix *-st*.

### 2.3. Surface characterization

Two methods were used to analyze the open surface (LSC) and the apparent surface (XPS), respectively. No correlation could be established between the LSC and XPS values. Indeed, the specific surface area of  $O_2$ -PP obtained by BET analysis (physisorption of N<sub>2</sub>) is very low (0.2852 m<sup>2</sup>/g) because the material is not mesoporous (the free space between the irregular fibers is about 9.5 μm, see Table 4).

#### 2.3.1. Liquid Scintillation Counting (LSC)

The radioactivity associated to the <sup>3</sup>H-lysine grafted on PP samples was measured by Liquid Scintillation Counting. The liquid scintillator analyzer (TRI-CARB 1600 TR, from Packard Instruments, San Diego, CA, USA) provides counting results in terms of absolute values of disintegrations per minute (dpm). Polymer samples were individually introduced in 20 mL polyethylene vials (MILLIQ 20, Packard, San Diego, CA) containing 5 mL of scintillator cocktail (Aqualuma<sup>®</sup> from Lumac. LSC B.V., Groningen, The Netherlands). Vials with treated samples were individually counted for 5 min, whereas the vials with blank samples were counted for 10 min. A vial containing only Aqualuma was used as ground reference, while two vials containing 20 μL and 40 μL of <sup>3</sup>H-lysine solution, respectively, were used to determine the conversion factor between dpm and fixed molecules of lysine. Considering 2 × 10<sup>-8</sup> mol of <sup>3</sup>H-lysine contained in 20 μL of 10<sup>-3</sup> M solution (2 × 10<sup>-9</sup> mol in 20 μL of 10<sup>-4</sup> M solution), and DPM<sub>20</sub>, the counting result for this sample, we determined that 1 dpm corresponds to

2 × 10<sup>-8</sup> mol/DPM<sub>20</sub> (or 1 dpm = 2 × 10<sup>-9</sup> mol/DPM<sub>20</sub> for a 10<sup>-4</sup> M solution). Similarly, 1 dpm corresponds to 4 × 10<sup>-8</sup> mol/DPM<sub>40</sub>. The average of the two controls was used. The collected data in dpm/sample were converted in pmol/sample and then in pmol/cm<sup>2</sup> of apparent surface (two faces).

Three samples for each condition were analyzed. Final results are presented as average of at least three measures with the standard deviation. Corrected results are obtained by subtracting the respective blank values.

The PP membranes were swollen but not dissolved in the scintillator cocktail. Accordingly, the LSC values could be underestimated because of a loss of emission by surface quenching. This probable systematic error does not prevent to compare samples (maximum underestimation: factor 2–3).

#### 2.3.2. X-ray Photoelectron Spectroscopy (XPS)

The surface atomic composition of the PP samples was obtained by X-ray Photoelectron Spectroscopy. The XPS analyses were performed on a Kratos Axis Ultra spectrometer (Kratos Analytical – Manchester – UK) equipped with a monochromatised aluminum X-ray source (powered at 10 mA and 15 kV) and an eight channeltrons detector. The spectrometer was interfaced with a Sun Ultra 5 workstation for instrument control and data acquisition with the Vision2 program.

The samples were fixed on a stainless steel multispecimen holder by using double sided conductive tape. The pressure in the analysis chamber was around 10<sup>-6</sup> Pa. The angle between the normal to the sample surface and the lens axis was 0°. The X-ray bombarded area was ~2000 μm × 800 μm. The hybrid lens magnification mode, a combination of magnetic and electrostatic lenses, was used with the slot aperture (10 mm × 3.7 mm) and the iris drive position set at 0.5 (8.4 mm diameter) resulting in an analyzed area of 700 μm × 300 μm. The constant pass energy was set at 40 eV. In these conditions, the energy resolution gives a full width at half maximum (FWHM) of the Ag 3d<sub>5/2</sub> peak of about 1.0 eV. Charge stabilization was achieved by using the Kratos Axis device.

The following sequence of spectra was recorded: survey spectrum, C 1s, O 1s, N 1s, F 1s, (Si 2p) and C 1s again to check the stability of charge compensation in function of time and the absence of degradation of the sample during the analyses. The binding energies were calculated with respect to the C–(C,H) component of the C 1s peak of adventitious carbon fixed at 284.8 eV.

The spectra were decomposed with the CasaXPS program (Casa Software Ltd., UK) with a Gaussian/Lorentzian (70/30) product function and after subtraction of a linear baseline.

Molar fractions were calculated using peak areas normalized on the basis of acquisition parameters, sensitivity factors provided by the manufacturer and the transmission function (depending on kinetic energy, analyzer pass energy and lens combination).

The peak deconvolution was done in two steps: a first fitting was imposed on components placed at their corresponding energy without constraints. In order to improve reproducibility of the deconvolution process, the peak width at half height (FWHM) of the principal component of a peak was imposed to the others. Deconvolutions of C 1s peak was done fixing the following energies for the different components: (a) C–(C,H): 284.8 eV; (b) C–O: 284.36 eV (a + 1.56 eV); (c) C=O: 287.74 (a + 2.94 eV); (d) O–C=O: 288.8 eV (a + 4.3 eV). Final results (corrected) are the average of at least three measures with standard deviation. Corrected results are obtained by subtracting the respective blank values.

#### 2.4. Bulk analysis

The PP membranes were manufactured from industrial PP pellets (mp = 160–170 °C, d<sub>20°C</sub> = 0.89–0.91 g/cm<sup>3</sup>) and made

hydrophilic by O<sub>2</sub> plasma treatment (home-made treatments by MacoProductions, Tourcoing, France). The bulk characteristics of the native PP material were not significantly modified by the two successive industrial treatments, as shown by the following analyses: Infra-Red (FTIR) spectroscopy, Gel Permeation Chromatography (GPC), Nuclear Magnetic Resonance (NMR) spectroscopy (<sup>1</sup>H and <sup>13</sup>C), X-ray diffraction analysis (WAXS), and Differential Scanning Calorimetry (DSC). All these experimental data are given in SI.

## 2.5. Filter characterization

Before and after wet chemistry, and steam-sterilization, the polypropylene filters (10 × 10 cm<sup>2</sup>, 20 mL of solution/sample in the treatments) were characterized by four main parameters. The results obtained are collected in Table 4.

### 2.5.1. Thickness

The thickness was determined thanks to an electronic micrometer of type MTS MI 20. The applied strength was 10 kPa, the contact area was 10 cm<sup>2</sup> and the time elapsed between the contact with the sample and the reading of the measure was 2 s.

### 2.5.2. Pore diameter

The Mean Flow Pore Diameter (MFPD) or the distribution of the average size of the pores of the material was determined by a porometer PMI.

### 2.5.3. Air permeability

The permeability of a non-woven material is the capacity of this material to allow itself to be crossed by air at constant pressure. It is expressed in volume of air, per unit of surface and per unit of time, which the material allows to pass when a difference of specified pressure is created between the two surfaces. This test was made on a TEXTEST 3300 instrument at a pressure of 196 Pa.

### 2.5.4. Wettability (test for macroporous materials)

The determination of the Critical Wetting Surface Tension (CWST) was realized by means of a series of test inks of type ARCOTEST<sup>®</sup> presenting given surface tensions from 30 to 105 mN/m. Three drops of a liquid possessing a low surface tension were placed on representative portions of the macroporous media. Between the 10th and the 11th minute following the deposit of the drops, a visual observation allowed to count the drops still present on the surface of the material. The test was continued by using liquids possessing surface tensions higher and higher, until the identification of the pair of liquids, which the surface tensions were the closest, among which one wetted the material and not the other. The wettability was defined by the absorption or the spreading of at least 2 of the 3 drops deposited. The non-wettability was defined by the presence on the surface of the material of at least 2 of the 3 drops deposited. The Critical Wetting Surface Tension was then included between the two surface tensions of the pair of liquids. It was arbitrarily chosen as the average of the two values. In this scale, high CWST values correspond to hydrophilic surfaces.

## 2.6. Cytotoxicity

The cytotoxicity of O<sub>2</sub>-PP-TrzF-Lys-st (activation by C<sub>3</sub>N<sub>3</sub>F<sub>3</sub> and grafting with non labeled lysine) was assayed according to standard protocols ISO 10993-5 or EN 30993-5 using L-929 cell line. Results showed the absence of cytotoxicity (see SI).

## 2.7. Blood filtration

### 2.7.1. Device and protocol

The filtering materials (6 × 6 cm<sup>2</sup>) were tested by means of a filter having a shape of diamond. The filter was composed of 14 or 17 layers according to the filtration experiment:

- *Figs. 1 and 3*: 14 layers = 2 layers of pre-filter of PET (spunbond oxygen-plasma treated polyethylene terephthalate), 10 layers of O<sub>2</sub>-PP and 1 layer of O<sub>2</sub>-PP modified by wet chemistry and finally 1 layer of pre-filter of O<sub>2</sub>-PET.
- *Fig. 2*: 17 layers = 2 layers of pre-filter of PET, 13 layers of O<sub>2</sub>-PP and 1 layer of O<sub>2</sub>-PP modified by wet chemistry and finally 1 layer of pre-filter of O<sub>2</sub>-PET or 2 layers of pre-filter of PET, 10 layers of O<sub>2</sub>-PP and 4 layers of O<sub>2</sub>-PP modified by wet chemistry and finally 1 layer of pre-filter of O<sub>2</sub>-PET.

The filter was then inserted in a PVC bag and integrated in a kit of filtration. The composition of this kit was: a pipe, the filter, a ring, a pipe and a bag of recovery. The kits were sterilized by steam-sterilization in an autoclave (see Section 2.1).

Then, a bag containing 140 mL (*Figs. 1 and 2*) or 105 mL (*Fig. 3*) of freshly collected total blood was integrated to the kit of filtration. The kit was hung on a support and the filtration was realized by gravity.

The bags of whole blood containing also an anti-clotting solution were obtained from the Etablissement Français du Sang (EFS, Lille). They were received the day of their taking. The preparation and the filtration of the blood took place the same day in MacoProductions (Tourcoing, France).

### 2.7.2. Performance parameters

Two parameters were considered:

- *The total filtration time*: defined as the time elapsed between the opening of the upstream clamp releasing the blood and the total draining of the filter. The taking of measure was manually made with a chronometer.
- *The amount of leukocytes in the filtrate*: a cell counting realized by means of two automatons, the day of the filtration experiment or one day after. An ABX Micros 60 (Horiba) automatic hematology analyzer was used for the counting of red cells, white cells and platelets present in blood before filtration (variation of impedance measure). A FACSCalibur (BD Biosciences) flow cytometer enabled the counting of the residual leukocytes present in the blood after filtration.

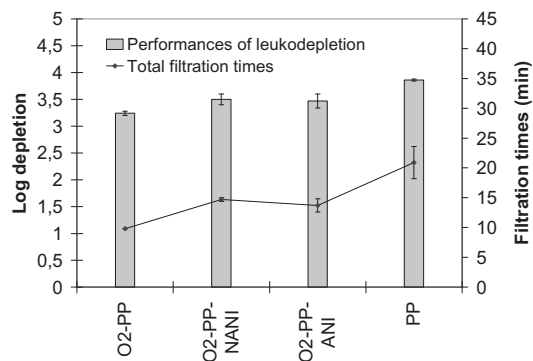


**Fig. 1.** Leukocytes retention on O<sub>2</sub>-PP or native PP membranes sterilized. The filter was composed of 10 layers of O<sub>2</sub>-PP and 1 last layer modified: O<sub>2</sub>-PP or NANI or ANI or PP. 140 mL of blood were filtered ( $7.45 \pm 0.05 \times 10^8$  leukocytes). See also Table S2.

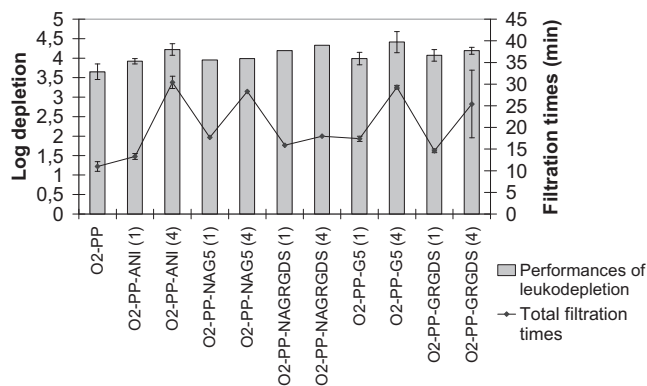


**Fig. 2.** Leukocytes retention on  $O_2$ -PP membranes modified with peptides  $G_5$  and GRGDS and sterilized. The filter was composed of 13 layers of  $O_2$ -PP and 1 last layer of  $O_2$ -PP modified with peptides  $G_5$  or GRGDS (1) at the concentration  $10^{-4}$  M or 10 layers of  $O_2$ -PP and 4 last layers of  $O_2$ -PP modified with the same peptides (4). 140 mL of blood were filtered ( $7.42 \pm 0.08 \times 10^8$  leukocytes). See also Table S3.

The performances of leukodepletion were evaluated in function of the number of residual leukocytes by blood bag and also by the logarithm of depletion defined by the formula below:

$$\log \text{ depletion} = \log \left( \frac{\text{leukocytes per bag before filtration}}{\text{leukocytes per bag after filtration}} \right)$$

The results are represented in Figs. 1–3, (see also SI for more details), each value corresponds to the mean of 2–7 different experiments with standard deviation.

### 3. Results and discussion

#### 3.1. Surface modification

The native PP membrane is devoid of functional groups and thus inadequate for surface derivatization. After oxygen-plasma treatment, the material displays oxygen-containing functions (Table 1), mainly hydroxyl- (9–12%), carbonyl- (3–6%), and carboxyl groups (2–4%), as assessed by XPS analysis [19,22,45]. The same functionalities have been detected during the investigation of PP natural aging under ambient atmosphere and light [46]. The upper most oxidized surface layer is not firm: it slowly rearranges under air to minimize the interfacial energy [47], and can be easily etched by washing with water and other polar solvents [13]. However, the XPS data collected in Table 1 (entries 2–7) clearly show that there are still

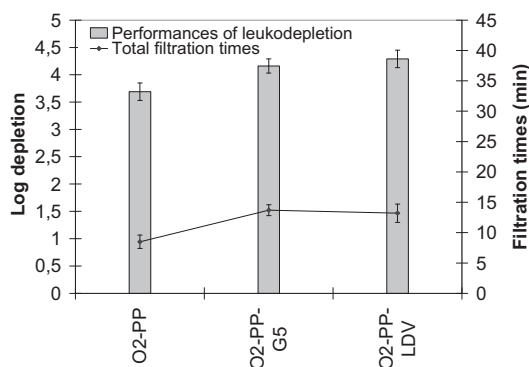


**Fig. 3.** Leukocytes retention on  $O_2$ -PP membranes modified with peptides  $G_5$  and LDV and sterilized. The filter was composed of 10 layers of  $O_2$ -PP and 1 last layer of  $O_2$ -PP modified with peptides  $G_5$  or LDV at the concentration  $10^{-3}$  M. 105 mL of blood were filtered ( $5.77 \pm 0.05 \times 10^8$  leukocytes). See also Table S4.

**Table 1**  
XPS analyses of PP membranes.

Entry	Sample	Atom. Compos. (%)			C 1s peak deconvolution (%)			
		C 1s	O 1s	N 1s	C-(C,H)	C-O	C=O	O-C=O
1	PP	100			100			
2	$O_2$ -PP <sub>A</sub> (1) <sup>a,b</sup>	87.4	12.6		85.5	9.2	3.2	2.1
3	$O_2$ -PP <sub>B</sub> (1) <sup>a,b</sup>	86.9	13.1		82.7	10.6	4.1	2.6
4	$O_2$ -PP <sub>A</sub> -w <sup>c</sup>	94.2	5.8		92.3	5.9	1.2	0.5
5	$O_2$ -PP <sub>B</sub> -w <sup>c</sup>	93.7	6.3		92.4	6.0	1.0	0.6
6	$O_2$ -PP <sub>B</sub> (2) <sup>b</sup>	85.55	14.45		78.28	11.79	6.01	3.92
7	$O_2$ -PP <sub>B</sub> -st <sup>d</sup>	94.22	5.78		91.47	5.43	1.85	1.25
8	$O_2$ -PP <sub>B</sub> -NANI <sup>e</sup>	96.40	3.60		93.62	4.81	1.08	0.49
9	$O_2$ -PP <sub>B</sub> -NANI-st <sup>d,e</sup>	98.06	1.94		93.47	5.65	0.64	0.24
10	$O_2$ -PP <sub>B</sub> -ANI <sup>e</sup>	96.40	3.46	0.14	93.92	4.55	1.02	0.51
11	$O_2$ -PP <sub>B</sub> -ANI-st <sup>d,e</sup>	97.87	2.06	0.07	95.85	3.50	0.38	0.27

<sup>a</sup> Face A (pattern-like) or B (fibrous) of a sample.

<sup>b</sup> Samples from different batches (1) or (2).

<sup>c</sup> Samples washed in water ( $2 \times 1$  h) and dried in an oven for 1 h.

<sup>d</sup> Samples steam-sterilized.

<sup>e</sup> Blank samples (see experimental part).

remaining polar groups, firmly linked to the membrane surface, even after steam-sterilization, the autoclave treatment recommended for the sterilization of blood compatible PP devices [48]. The O 1s atomic compositions range within 12–15%, when directly measured after plasma treatment, and within 5–7% after etching or sterilization; both sides of the membranes (patterned A and fibrous B) appear quite similar and feature mainly hydroxyl functions.

Our objective is to take advantage of the surface functionality of  $O_2$ -PP membrane to covalently graft molecules in order to increase its capacity of retaining leukocytes during blood filtration.

Starting from our expertise in the surface chemistry of “Dura-pore DV PP” membranes [36] and PET track-etched membranes [49], a series of activation reagents and coupling conditions were tested and assayed by radiolabeling, using 4,5-<sup>3</sup>[H]-lysine as radioactive probe. Briefly,  $O_2$ -PP samples were activated into solutions of carbodiimide (activation of the carboxyl functions), tosyl chloride (activation of the hydroxyl functions), trichloro-triazine and trifluoro-triazine (activation of both hydroxyl- and carboxyl functions), followed by incubation during 2 h into the labeling solution ( $10^{-3}$  M) and counting of the sample-associated radioactivity by LSC. Blank samples (same preparation as fully treated samples but omitting the activation reagent) were also prepared to measure the non-specific label adsorption and the coupling to the carbonyl functions which does not require any activation step. Scheme 1 summarizes the surface chemistry performed on  $O_2$ -PP. Results of Table 2 are given as pmol of grafted lysine per cm<sup>2</sup> of apparent surface; corrected values are obtained by subtracting the respective blanks. Clearly, the activation of  $O_2$ -PP with trifluoro-

**Table 2**  
Surface chemistry on  $O_2$ -PP – LSC assay.

Entry	Sample <sup>a</sup>	pmol/cm <sup>2</sup> <sup>b</sup>	Corrected (pmol/cm <sup>2</sup> )	Comment
1	$O_2$ -PP- <sup>3</sup> H	$38 \pm 7$	$38 \pm 7$	C=O labeling and adsorption
2	$O_2$ -PP-WSC- <sup>3</sup> H	$80 \pm 13$		
3	Blank (NAI) of entry 2	$35 \pm 13$	$45 \pm 0$	CO <sub>2</sub> H labeling
4	$O_2$ -PP-TsCl- <sup>3</sup> H	$183 \pm 11$		
5	Blank (NAI) of entry 4	$83 \pm 7$	$100 \pm 4$	OH labeling
6	$O_2$ -PP-TrzCl- <sup>3</sup> H	$96 \pm 13$		
7	Blank (NAI) of entry 6	$26 \pm 3$	$70 \pm 10$	OH + CO <sub>2</sub> H labeling
8	$O_2$ -PP-TrzF- <sup>3</sup> H	$263 \pm 24$		
9	Blank (NAI) of entry 8	$25 \pm 2$	$238 \pm 22$	OH + CO <sub>2</sub> H labeling

<sup>a</sup> See experimental part.

<sup>b</sup> Mean of 3 independent experiments  $\pm$  standard deviation.

triazine ( $C_3N_3F_3$ ) allowed to reach the highest level of lysine grafting ( $\sim 240$  pmol/cm<sup>2</sup>). Indeed, this reagent enables to activate both the hydroxyl and carboxyl functions, and two <sup>3</sup>H-tag molecules can be theoretically fixed on the triazine core.

Then, we tried to optimize the grafting protocol with trifluoro-triazine by varying the conditions of activation (1 h, 20 °C or 2 h, 20 °C) and incubation, i.e. the coupling to two amine-terminated molecular probes, namely 3,5-bis(trifluoromethyl)benzylamine ((F)-tag) and 4,5-<sup>3</sup>[H]-lysine (<sup>3</sup>H-tag). Two concentrations of tag-solution were tested ( $10^{-3}$  M and  $10^{-4}$  M), two temperatures ( $T = 20$  °C or  $37$  °C) and different incubation times ( $t = 1$  h, 2 h, 4 h, 19 h or 24 h). Blank samples were also prepared (same conditions of activation and incubation as the fully treated samples but omitting the addition of trifluoro-triazine) to determine the quantity of non-specific adsorption. The results obtained are collected in Table 3 and are given as pmol of grafted lysine per cm<sup>2</sup> for the LSC analysis and as N/C or F/C atomic ratios for the XPS analysis. The highest degrees of grafting ( $\sim 700$  pmol/cm<sup>2</sup>, determined by LSC) were obtained for 2 h activation at 20 °C and 19 h incubation at 20 °C in a  $10^{-3}$  M solution (entry 10). The XPS analysis confirmed the presence of the (F)-tag on the surface of the O<sub>2</sub>-PP membrane by the detection of fluorine and nitrogen atoms which are only present on this molecule regarding the polymer substrate. However, no real evolution of the F/C and N/C ratios was observed by changing the conditions of the grafting protocol. Indeed, the XPS analysis probes the outermost layer of the apparent surface, whereas LSC analysis concerns the open surface, that is, the apparent surface and the internal surface of the pores. Thus, considering the XPS analysis, the treatments of entry 10 (selected by LSC analysis) and entry 16 (2 h activation at 20 °C and 1 h incubation at 37 °C in a  $10^{-4}$  M tag-solution) gave similar surfaces.

We were also interested in the surface modification of the native PP membrane, which contains only C–C or C–H functions; no oxygen atoms were detected by XPS (Table 1, entry 1). We applied a method based on the photo-grafting of three different molecular clips: *O*-succinimidyl 4-(*p*-azido-phenyl)butanoate (N<sub>3</sub>Ar) [50], *O*-succinimidyl 4-azido-2,3,5,6-tetrafluorobenzoate (N<sub>3</sub>ArF<sub>4</sub>) [51], *O*-succinimidyl 4-(3-(trifluoromethyl)-3*H*-diazirin-3-yl)benzoate (diazirine) [52], and inspired by the photoaffinity

labeling technique in biochemistry, for the introduction of activated ester functions onto the PP surface. Further reactions with amines allow the covalent fixation of <sup>3</sup>H-tag molecules via an amide bond resulting from *N*-hydroxy-succinimide (NHS) displacement (Scheme 2). Under light excitation, arylazide derivatives transform into arylnitrenes (for  $\lambda = 254$  nm) and diazine compounds into carbenes (for  $\lambda = 360$  nm) with loss of nitrogen. These intermediates rapidly react by insertion into hydrocarbon chains, either as singlet or triplet species.

Practically, the polymer samples were coated with a solution of arylazide, fluoro arylazide or diazine compounds at different concentrations, the solvent was evaporated and then an irradiation (254 nm or 360 nm) was realized during different times ( $t = 5$  min, 10 min, 30 min or 2 h). Several washings were performed to remove the non-grafted products and excess of clips, before incubating the samples with 4,5-<sup>3</sup>[H]-lysine (2 h, 20 °C or 2 h, 37 °C) (see SI). Two series of blank samples were prepared: blank 1 was obtained by omitting the clip reagent, for determining the effect of UV irradiation alone on the fixation of the <sup>3</sup>H-tag; blank 2 resulted from the above treatment, but without irradiation for measuring the non-specific fixation of <sup>3</sup>H-tag. Fully treated and blank samples were analyzed by LSC (see Table S1 for complete results in SI). It appeared clearly that the photo-activation method enables to immobilize less <sup>3</sup>H-lysine on native PP than the activation of O<sub>2</sub>-PP with trifluoro-triazine (maximum of 157 pmol/cm<sup>2</sup> of lysine grafted with the arylazide clip). The immersion of the samples into clip solutions followed by the irradiation of both sides of the samples, did not improve the grafting degrees. The irradiation only (254 nm or 360 nm, without clip) had no significant effect on the PP surface and particularly did not cause oxidation (verified by XPS), a phenomenon previously described [53], most probably because we applied UV-treatments of short times.

### 3.2. Filter characterization

The O<sub>2</sub>-PP samples modified according to the trifluoro-triazine optimized protocol were submitted to morphological analyses to determine the effects of the washings and reagents on the bulk characteristics of these filtration membranes. Two blank samples

**Table 3**  
Optimization of the protocol of grafting with trifluoro-triazine on O<sub>2</sub>-PP – LSC and XPS studies.

Entry	Activation conditions	Incubation conditions		pmol/cm <sup>2</sup> <sup>b</sup>	Corrected (pmol/cm <sup>2</sup> )	F/C × 100 <sup>c</sup>	N/C × 100 <sup>c</sup>
		Concentration	Time, Temperature				
1	1 h, 20 °C	$10^{-3}$ M	2 h, 20 °C	263 ± 24	238 ± 22	0.28	0.22
2 <sup>a</sup>				25 ± 2			
3			19 h, 20 °C	500 ± 18			
4 <sup>a</sup>				96 ± 9			
5	2 h, 20 °C	$10^{-3}$ M	19 h, 37 °C	487 ± 13	396 ± 8	0.32	0.21
6 <sup>a</sup>				91 ± 5			
7			1 h, 20 °C	358 ± 50			
8	2 h, 20 °C	$10^{-3}$ M	2 h, 20 °C	442 ± 31	291 ± 42	0.39	0.21
9			4 h, 20 °C	478 ± 23			
10			19 h, 20 °C	774 ± 37			
11 <sup>a</sup>				67 ± 8			
12			2 h, 20 °C	71 ± 1			
13	2 h, 20 °C	$10^{-4}$ M	19 h, 20 °C	79 ± 0	61 ± 1	0.39	0.14
14			24 h, 20 °C	86 ± 10			
15 <sup>a</sup>				10 ± 0			
16			1 h, 37 °C	97 ± 9			
17			2 h, 37 °C	123 ± 9			
18			4 h, 37 °C	134 ± 9			
19	2 h, 20 °C	$10^{-4}$ M	19 h, 37 °C	142 ± 8	85 ± 8	0.39	0.14
20 <sup>a</sup>				12 ± 1			

<sup>a</sup> Blank samples (NAI), see experimental part.

<sup>b</sup> Mean of 3 independent experiments ± standard deviation.

<sup>c</sup> Corrected F/C and N/C ratios from XPS = F/C (N/C) treated samples – F/C (N/C) blank.



**Table 4**  
Filter characterization.

Entry	Sample	Air permeability (L/m <sup>2</sup> /s)	Thickness (μm)	MFPD (μm)	CWST (mN/m)
1	O <sub>2</sub> -PP (1) <sup>a</sup>	130.0 ± 5.6	326 ± 6	9.10 ± 0.39	n.d.
2	O <sub>2</sub> -PP (2) <sup>a</sup>	132.8 ± 5.0	315 ± 14	n.d.	71
3	O <sub>2</sub> -PP-st (2) <sup>b</sup>	149.0 ± 4.7	355 ± 18	n.d.	44
4	O <sub>2</sub> -PP-NANI (1)	131.5 ± 2.1	309 ± 6	9.22 ± 0.20	52
5	O <sub>2</sub> -PP-NANI-st (1) <sup>b</sup>	156.8 ± 5.9	311 ± 15	9.73 ± 0.17	39
6	O <sub>2</sub> -PP-ANI (1)	139.0 ± 5.5	284 ± 11	9.45 ± 0.20	52
7	O <sub>2</sub> -PP-ANI-st (1) <sup>b</sup>	141.5 ± 2.1	329 ± 8	9.69 ± 0.21	39
8	PP (3) <sup>a</sup>	121.3 ± 4.1	294 ± 10	9.24 ± 0.13	35

<sup>a</sup> Samples from different batches (1), (2) or (3).

<sup>b</sup> Samples steam-sterilized.

prepared in the same way as the fully treated samples and with the same number of rinsing cycles were studied as well: blank “NANI” (for Non Activated with trifluoro-triazine and Non Incubated with a tag molecule) and blank “ANI” (for Activated with trifluoro-triazine and Non Incubated with a tag molecule) and compared to native PP and O<sub>2</sub>-PP membranes. Four different parameters were measured (see experimental part for details): the air permeability, the thickness, the mean flow pore diameter (MFPD) and the wettability by the CWST (Critical Wetting Surface Tension) method dedicated to fibrous supports [54]. The results obtained are collected in Table 4. No obstruction of the pores of the materials was observed since the treatments did not modify the air permeability, thickness and porosity. However, a low decrease of the hydrophilicity of the O<sub>2</sub>-PP membranes was detected due to the washings (CWST = 71 mN/m for native O<sub>2</sub>-PP and 52 mN/m for “NANI” and “ANI” samples), but the hydrophilicity of the blank samples remains still superior to that of native PP (35 mN/m).

Materials dedicated to the blood filtration require a steam-sterilization before application. This sterilization led to a low increase of the air permeability, thickness and porosity, but also to a significant decrease of the hydrophilicity with CWST values around 40 mN/m.

These results are in accordance with the XPS observations (Table 1): the treatments decrease the percentage of oxygen present on the surface of O<sub>2</sub>-PP membranes as well as the sterilization (entries 6–11), resulting in a drop of the hydrophilicity.

The incubation with tag molecules (“fully treated sample”) does not modify the results obtained for the blank sample “ANI” and in particular the CWST values.

### 3.3. Filtration assays

For blood filtration experiments, two commercial pentapeptides, GRGDS and G<sub>5</sub>, and a home-made modified LDV peptide (referred to as “LDV”) were fixed on the O<sub>2</sub>-PP membranes (Scheme 3) using trifluoro-triazine as cross-linking reagent. G<sub>5</sub> (Gly<sub>5</sub>) is a hydrophobic

peptide susceptible of tuning the membrane wettability without raising specific biological activity. GRGDS contains the active sequence RGD (Arg-Gly-Asp) widely used in biomaterials science for stimulating cellular adhesion on surfaces via the integrin receptors. Indeed, the RGD molecules mimic the cell attachment sites of various extracellular matrix (ECM) proteins and target a lot of integrin sub-types [7]. The synthetic peptide is a derivative of the LDV (Leu-Asp-Val) sequence specifically recognized by the leukocyte integrins β<sub>1</sub>. The diarylurea moiety enables to improve the affinity and the selectivity towards the integrins β<sub>1</sub> [55]; the triethyleneglycol spacer-arm is useful for surface conjugation [56].

The three peptides have been grafted on O<sub>2</sub>-PP membranes by using the conditions previously selected that were: (i) activation with 1 N solution of trifluoro-triazine in CH<sub>3</sub>CN for 2 h at 20 °C and (ii) incubation in 10<sup>-3</sup> M solutions of GRGDS, G<sub>5</sub> or “LDV” in PB/CH<sub>3</sub>CN for 19 h at 20 °C, or, as preferred option for using tenuous quantities of peptides, (ii) incubation in 10<sup>-4</sup> M solutions of GRGDS or G<sub>5</sub> in PB/CH<sub>3</sub>CN for 1 h at 37 °C. Blank samples have also been prepared: NAG<sub>5</sub> and NAGRGDS (Not Activated with trifluoro-triazine but Incubated with peptides G<sub>5</sub> and GRGDS respectively), for measuring the non-specific adsorption of G<sub>5</sub> and GRGDS.

The samples were analyzed by XPS (Table 5). The detection of nitrogen atoms in the fully treated samples confirmed the grafting of the three peptides, exclusively via the triazine linker. Indeed, no nitrogen was measured for the blank samples (entries 2 and 4). However, no fluorine atoms could be detected for the “LDV” peptide featuring a CF<sub>3</sub> substituent (entry 1). This suggests a lower immobilization yield for this peptide or a higher fixation inside the membrane pores. An evolution of the N/C atomic ratios was observed between the two concentrations of grafting of the peptide G<sub>5</sub> (entries 5 and 6).

Then, different filtration experiments with whole blood were performed after sterilization of the filtration kits (see experimental part for details). The different filters were evaluated towards their capacity of retaining the white cells.

The objective of such assays was the research of improvements, even small, of commercial filters already used for the leukodepletion of whole blood and satisfying the norms at the moment. These improvements should enable to modify the size and the shape of the commercial filters and also the number of layers of O<sub>2</sub>-PP composing the filters and thus to reduce the loss of blood products and the costs.

The filtrations described in this article were realized on filters with a different size and composition from the commercial filters in order to obtain severe experimental conditions (see experimental part and SI for Tables of results).

In the first series of filtration (Fig. 1), the last layer of the 11 layers of polypropylene composing the filter was modified by the blank samples corresponding to the grafting protocol with trifluoro-triazine: “ANI” (Activated, Not Incubated with molecules) or “NANI” (Not Activated, Not Incubated with molecules). The

**Table 5**  
XPS analyses of O<sub>2</sub>-PP membranes modified with peptides GRGDS, G<sub>5</sub> and LDV.

Entry	Sample	Atom. Compos. (%) <sup>d</sup>				N/C × 100
		C 1s	O 1s	N 1s	F 1s	
1	O <sub>2</sub> -PP-LDV (10 <sup>-3</sup> M) <sup>a</sup>	96.12 ± 0.07	3.59 ± 0.06	0.28 ± 0.13	0.01 ± 0.00	0.29
2	Blank of entry 1 <sup>c</sup>	95.97 ± 0.06	4.01 ± 0.04	0.01 ± 0.00	0.01 ± 0.01	0.01
3	O <sub>2</sub> -PP-GRGDS (10 <sup>-3</sup> M) <sup>a</sup>	94.72 ± 0.95	4.86 ± 0.97	0.42 ± 0.08	0.00 ± 0.00	0.45
4	Blank of entry 3 <sup>c</sup>	95.88 ± 0.63	4.08 ± 0.60	0.03 ± 0.03	0.01 ± 0.01	0.03
5	O <sub>2</sub> -PP-G <sub>5</sub> (10 <sup>-4</sup> M) <sup>b</sup>	95.66 ± 0.04	3.98 ± 0.06	0.36 ± 0.06	0.00 ± 0.00	0.37
6	O <sub>2</sub> -PP-G <sub>5</sub> (10 <sup>-3</sup> M) <sup>a</sup>	95.63 ± 0.90	3.87 ± 0.72	0.50 ± 0.19	0.00 ± 0.00	0.52

<sup>a</sup> Incubation in a solution of peptides at the concentration 10<sup>-3</sup> M, 20 °C, 19 h.

<sup>b</sup> Incubation in a solution of G<sub>5</sub> at the concentration 10<sup>-4</sup> M, 37 °C, 1 h.

<sup>c</sup> Blank samples NAI (see experimental part).

<sup>d</sup> XPS values from 3 independent experiments ± standard deviation.

performances of these filters for the retention of leukocytes were compared with filters composed of  $O_2$ -PP or native PP as the last layer. The number of leukocytes recovered in the filtrates was determined by flow cytometry. The logarithm of depletion (see Section 2.7.2.) is 3.24 ( $\pm 0.04$ ) with a last layer of  $O_2$ -PP and 3.86 ( $\pm 0.02$ ) with a last layer of native PP. The samples “NANI” and “ANI” have intermediate performances with a logarithm of depletion of 3.50 ( $\pm 0.10$ ) and 3.47 ( $\pm 0.13$ ). We can also notice that the efficiency of retention of these membranes is directly correlated to the filtration time. Indeed, the longer the filtration is, the better the leukodepletion is, since the contact time between the fibers and the cells is favored. But this filtration time is itself correlated to the wetting properties of the membranes (Table 5) since the native PP is the most hydrophobic, the  $O_2$ -PP the most hydrophilic, and the samples “NANI” and “ANI” after sterilization have a hydrophilicity comprised between  $O_2$ -PP-*st* and native PP.

In order to reduce the filtration time (below 20 min) while maintaining comparable performances to native PP, in the second filtration series (Fig. 2), we decided to increase the number of  $O_2$ -PP layers composing the filter to 14 layers. Filtering the same volume of blood (140 mL), we observe a better retention of leukocytes (log depletion =  $3.65 \pm 0.20$ ) by the  $O_2$ -PP membrane ( $3.24 \pm 0.04$  in Fig. 1). By modifying the last layer with the peptides  $G_5$  and GRGDS grafted at the smallest concentration of  $10^{-4}$  M, the number of leukocytes in the filtrate is reduced (log depletion = 3.99 and  $4.07 \pm 0.15$  respectively) and comparable to native PP ( $3.86 \pm 0.02$  in Fig. 1) with a shorter filtration time.

By modifying the four last layers of the filter, the retention of the leukocytes is still enhanced but the filtration time becomes too long. The grafting of the active peptide GRGDS on the last layers improves only weakly the filter performance. The results obtained range in the same order of magnitudes as for the non selective and hydrophobic peptide  $G_5$  or the blank samples.

In order to verify the possible effect of a selective ligand of the leukocyte integrins on the filtration, we performed a last series of experiments (Fig. 3) to compare the performance of filters with one modified layer being native  $O_2$ -PP,  $O_2$ -PP grafted with the inactive peptide  $G_5$  and  $O_2$ -PP grafted with the active peptide “LDV”. We reduced the number of layers of the filter to 11 layers of polypropylene and used smaller volume of blood (105 mL instead of 140 mL). Peptides  $G_5$  and “LDV” were grafted at the highest concentration of  $10^{-3}$  M. The logarithm of depletion for a last layer of  $O_2$ -PP is 3.69 ( $\pm 0.16$ ) compared to 4.16 ( $\pm 0.13$ ) and 4.29 ( $\pm 0.16$ ) for a last layer modified with peptides  $G_5$  or “LDV” respectively. A small difference in leukodepletion was observed in favor of the  $\beta_1$  integrin ligand. Nevertheless, the non selective physico-chemical interactions, in particular the wettability, seem to be principally responsible of the efficiency of the modified PP membranes.

### 3.4. Discussion

Trifluoro-triazine reagent has been used for the surface functionalization of  $O_2$ -PP membrane. This method enables to immobilize molecules of interest, but slightly modifies the wettability of the membrane.

Removal of leukocytes from blood by filters can be considered as a depth filtration process. The mechanisms that are probably involved include blocking or straining, bridging, interception and adhesion of cells [6]. Different factors are recognized to be responsible of non-specific adhesion: the chemical composition of the filter surface, the surface charge (leukocytes have a negative surface charge), the surface wettability, the surface morphology (porosity, curvature, texture, roughness...), the protein adsorption and the platelet adhesion. But the composition, the age and temperature of the blood component play also a role in the

adhesive capacity and deformability of the leukocytes. Flow rate and temperature at filtration will also affect the filter performance.

For a blood filtration application, a membrane requires a certain hydrophilicity to allow the flux of aqueous solutions and to avoid the adsorption of proteins or platelets. Our filtration experiments have shown that the wettability of the PP membrane influences the retention of the leukocytes. Indeed, the best results were obtained with a multi-layer filter modified with the last layer being hydrophobic native PP. However, the filtration times are too long for an industrial application in the biomedical field. The same efficiency was reproduced by increasing the number of  $O_2$ -PP layers of the filter, with the last layer modified by the trifluoro-triazine method. We also proposed to change a little bit the characteristics of the  $O_2$ -PP membrane by grafting the hydrophobic peptide  $G_5$  in very small quantities [57]. On the other hand, two biologically active peptides were similarly fixed: the first one is a promoter of cell adhesion by the recognition of the integrin receptors; the second is more particularly specific of leukocyte integrins  $\beta_1$  [58]. Weak differences in their capacity to retain white cells were observed in comparison with peptide  $G_5$ . Finally, for similar filtration times, the adhesion of leukocytes on PP materials depends mainly of the wetting properties of the membranes, a parameter also noticed and studied in other substrates such as polyurethane [59] or glass [60].

## 4. Conclusions

In this article, we propose new methods to immobilize molecular probes and peptides on the surface of PP meltblown membranes via their activation by photo-grafting in the case of native PP membranes or by wet-chemistry treatments for oxygen-plasma treated PP membranes ( $O_2$ -PP). The most efficient technique makes use of trifluoro-triazine reagent for the activation of both hydroxyl- and carboxyl-functions of  $O_2$ -PP. The following protocol: (i)  $C_3N_3F_3$  (1 N) in dry  $CH_3CN$ , 2 h, 20 °C; (ii)  $10^{-3}$  M peptide in (1/1, v/v) PB/ $CH_3CN$ , 19 h, 20 °C, allowed the grafting of 700 pmol/cm<sup>2</sup> from LSC analysis. With a view to reduce the costs for applications, an alternative protocol using tiny amounts of peptides and short reaction time is also proposed: (iii)  $10^{-4}$  M peptide in (1/1, v/v) PB/ $CH_3CN$ , 1 h, 37 °C.

The morphological characteristics of the resulting membranes are not modified; just a weak decrease of the hydrophilicity was measured after the treatments and steam-sterilization. Moreover, the PP membranes modified via the trifluoro-triazine method are not cytotoxic.

This method was applied for the modification of  $O_2$ -PP membranes entering in the composition of filters dedicated to the filtration of blood products. The expected effect of enhanced leukocytes adhesion on RGD- and LDV-modified membranes was not very pronounced under our severe experimental conditions, i.e. whole blood filtration through multi-layer filters with only one or four modified layers at low peptide concentration. The specific effect of these peptides was also masked by the prevailing physico-chemical effects of the  $O_2$ -PP membranes modified according to the trifluoro-triazine protocol. Indeed, the wetting properties of these membranes (hydrophilicity between those of  $O_2$ -PP and native PP) increase the filtration times i.e. the times of contact between the fibers and the white cells, and thus promote the non-specific retention of leukocytes.

## Acknowledgments

This work has been supported by MacoProductions (Tourcoing, France) and the F.R.S.-FNRS (Belgium) (J. Marchand-Brynaert is senior research associate). The authors thank Ir. M. Genet for advice and access to the XPS facilities (UCL), S. Devouge for XPS analyses



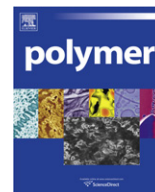
(UCL), D. Rousseaux and X. Drooghaag for bulk analyses (UCL) and the technicians of MacoProductions for morphological analyses, filtration experiments and cytotoxicity measurements.

## Appendix. Supplementary information

Supplementary data related to this article can be found online at doi:10.1016/j.polymer.2011.01.029

## References

- [1] Mulder M. Basic principles of membrane technology. Dordrecht: Kluwer Academic; 1996 [Chapter 6].
- [2] Baker RW. Membrane technology and applications. 2nd ed. Chichester: Wiley & Sons Ltd.; 2004.
- [3] Ulbricht M. *Polymer* 2006;47:2217–62.
- [4] Stamatialis DF, Papenburg BJ, Gironés M, Saiful S, Bettahalli SNM, Schmitmeier S, et al. *J Membr Sci* 2008;308:1–34.
- [5] Pietersz RNI, Van Der Meer PF, Seghatchian MJ. *Transfus Sci* 1998;19(4):321–8.
- [6] Bruil A, Beugeling T, Feijen J, Van Aken WG. *Transfus Med Rev* 1995;9(2):145–66.
- [7] Hersel U, Dahmen C, Kessler H. *Biomaterials* 2003;24(24):4385–415.
- [8] Zhu J. *Biomaterials* 2010;31:4639–56.
- [9] Momtaz M, Rerat V, Gharbi S, Gérard E, Pourcelle V, Marchand-Brynaert J. *Bioorg Med Chem Lett* 2008;18:1084–90.
- [10] Tamada Y, Ikada Y. *Polymer* 1993;34(10):2208–12.
- [11] Sun S, Yue Y, Huang X, Meng D. *J Membr Sci* 2003;222:3–18.
- [12] Wei Q, Wang Y, Hou D, Huang F. *J Appl Polym Sci* 2007;104:2157–60.
- [13] Yang YF, Wan LS, Xu ZK. *J Membr Sci* 2009;326:372–81.
- [14] Bratskaya S, Marinin D, Nitschke M, Pleul D, Schwarz S, Simon F. *J Adhes Technol* 2004;18:1173–86.
- [15] Yu HY, Hu MX, Xu ZK, Wang JL, Wang SY. *Sep Purif Technol* 2005;45:8–15.
- [16] Yu HY, He XC, Liu LQ, Gu JS, Wei XW. *Water Res* 2007;41:4703–9.
- [17] Yu HY, Xie YJ, Hu MX, Wang JL, Wang SY, Xu ZK. *J Membr Sci* 2005;254:219–27.
- [18] Bae B, Chun BH, Kim D. *Polymer* 2001;42:7879–85.
- [19] Wei QF. *Mater Character* 2004;52:231–5.
- [20] Huang F, Wei Q, Wang X, Xu W. *Polym Test* 2006;25:22–7.
- [21] Wei QF, Mather RR, Wang XQ, Fotheringham AF. *J Mater Sci* 2005;40:5387–92.
- [22] Morent R, De Geyter N, Leys C, Gengembre L, Payen E. *Surf Interface Anal* 2008;40:597–600.
- [23] Gross T, Lippitz A, Unger WES, Friedrich JF, Woll C. *Polymer* 1994;35(25):5590–4.
- [24] Xie YJ, Yu HY, Wang SY, Xu ZK. *J Environ Sci* 2007;19:1461–5.
- [25] Xu Z, Wang J, Shen L, Men D, Xu Y. *J Membr Sci* 2002;196:221–9.
- [26] Bamford CH, Al-Lamee KG. *Polymer* 1996;37(22):4885–9.
- [27] Xu ZK, Dai QW, Wu J, Huang XJ, Yan Q. *Langmuir* 2004;20:1481–8.
- [28] Yang Q, Xu ZK, Dai ZW, Wang JL, Ulbricht M. *Chem Mater* 2005;17:3050–8.
- [29] Yu HY, Liu LQ, Tang ZQ, Yan MG, Gu JS, Wei XW. *J Membr Sci* 2008;310:409–17.
- [30] Kou RQ, Xu ZK, Deng HT, Liu ZM, Seta P, Xu Y. *Langmuir* 2003;19:6869–75.
- [31] Liu ZM, Xu ZK, Wan LS, Wu J, Ulbricht M. *J Membr Sci* 2005;249:21–31.
- [32] Okamura A, Itayagoshi M, Hagiwara T, Yamaguchi M, Kanamori T, Schinbo T, et al. *Biomaterials* 2005;26:1287–92.
- [33] Friedrich J, Kühn G, Mix R, Hoffmann K, Resch-Genger U. *Progr Colloid Polym Sci* 2006;132:62–71.
- [34] Tyan YC, Liao JD, Wu YT, Klauser R. *J Biomater Appl* 2002;17:153–78.
- [35] Tyan YC, Liao JD, Lin SP. *J Mater Sci Mater Med* 2003;14:775–81.
- [36] Momtaz M, Dewez JL, Marchand-Brynaert J. *J Membr Sci* 2005;250:29–37.
- [37] Salvagnini C, Roback A, Momtaz M, Pourcelle V, Marchand-Brynaert J. *J Biomater Sci Polym Ed* 2007;18:1491–516.
- [38] Aumsuwan N, Mc Connell MS, Urban MW. *Biomacromolecules* 2009;10:623–9.
- [39] He D, Susanto H, Ulbricht M. *Prog Polym Sci* 2009;34:62–98.
- [40] Tomohiro T, Tachi N, Azuma Y, Hatanaka Y. *Heterocycles* 2009;79:897–908.
- [41] Naqvi A, Nahar P, Gandhi RP. *Anal Biochem* 2002;306:74–8.
- [42] Mao C, Zhang C, Qui Y, Zhu A, Shen J, Lin S. *Appl Surf Sci* 2004;228:26–33.
- [43] Tseng YC, Mullins WM, Park K. *Biomaterials* 1993;14(5):392–400.
- [44] Patrick E. U.S. patent 4973493.
- [45] Vesel A, Moztetic M. *J Phys Conf Ser* 2009;162:1–20. doi:10.1088/1742-6596/162/1/012015.
- [46] Rjeb A, Letarte S, Tajoute L, El Idrissi MC, Adnot A, Roy D, et al. *J Electron Spectrosc Relat Phenom* 2000;107:221–30.
- [47] Occhiello E, Morra M, Morini G, Garbassi F, Humphrey P. *J Appl Polym Sci* 1991;42:551–9.
- [48] Sato H, Watanabe K, Minezawa T, Hori M. *Artif Organs* 1984;8:97–104.
- [49] Rerat V, Pourcelle V, Devouge S, Nysten B, Marchand-Brynaert J. *J Appl Polym Sci Part A Polym Chem* 2010;48(1):195–208.
- [50] Devouge S, Salvagnini C, Marchand-Brynaert J. *Bioorg Med Chem Lett* 2005;15:3252–6.
- [51] Keana JFW, Cai SX. *J Org Chem* 1990;55(11):3640–7.
- [52] Nassal M. *Liebigs Ann Chem* 1983;9:1510–23.
- [53] Gryta M, Grzechulska-Damszel J, Markowska A, Karakulski K. *J Membr Sci* 2009;326:493–502.
- [54] Pall DB. Patent WO 8903717.
- [55] Lin K, Ateeq HS, Hsiung SH, Chong LT, Zimmerman CN, Castro A, et al. *J Med Chem* 1999;42(5):920–34.
- [56] Fievez V, Plapied L, Des Rieux A, Pourcelle V, Freichels H, Wascotte V, et al. *Eur J Pharm Biopharm* 2009;73(1):16–24.
- [57] Deng HT, Xu ZK, Liu ZM, Wu J, Ye P. *Enzym Microb Technol* 2004;35:437–43.
- [58] Groth T, Altankov G, Klosz K. *Biomaterials* 1994;15(6):423–8.
- [59] Bruil A, Brenneisen LM, Terlingen JGA, Beugeling T, Van Aken WG, Feijen J. *J Colloid Interface Sci* 1994;165:72–81.
- [60] Yayapour N, Nygren H. *Colloids Surf B Biointerfaces* 1999;15:127–38.



# Anionic ring-opening polymerization of octamethylcyclotetrasiloxane in emulsion above critical micelle concentration

Ines Mohorič<sup>a</sup>, Urška Šebenik<sup>b,\*</sup>

<sup>a</sup>Hidria Institute for Materials and Technology, Sp. Kanomlja 23, 5281 Sp. Idrija, Slovenia

<sup>b</sup>University of Ljubljana, Faculty of Chemistry and Chemical Technology, Aškerčeva cesta 5, 1000 Ljubljana, Slovenia

## ARTICLE INFO

### Article history:

Received 19 November 2010

Received in revised form

23 December 2010

Accepted 12 January 2011

Available online 20 January 2011

### Keywords:

Polysiloxanes

Emulsion polymerization

Anionic polymerization

## ABSTRACT

Batch anionic ring-opening polymerization of octamethylcyclotetrasiloxane in emulsion using nonionic and cationic emulsifiers was studied. The concentration of emulsifiers was set above their critical micelle concentration. Effects of emulsifier concentration, nonionic/cationic emulsifier ratio and cationic emulsifier/initiator (KOH) ratio on the kinetics, average particle size and distribution and on the average molecular weight and distribution were investigated and discussed. At the beginning of the polymerization, empty micelles, active micelles (polymer particles) and monomer droplets co-exist in emulsion. The transport of monomer from monomer droplets toward empty micelles was confirmed by monomer droplets and empty micelles disappearance and by formation of smaller particles. The transport of monomer from monomer droplets toward polymer particles was not confirmed, since the average polymer particle size did not increase during polymerization. It was proposed, that at lower conversions, monomer diffuses from polymer particle interior to particle surface, while at higher conversions, the monomer diffuses from larger to smaller polymer particles. Emulsifier concentration, nonionic/cationic emulsifier ratio and cationic emulsifier/KOH ratio have an evident effect on the kinetics and on the average molecular weight, thus demonstrating that cationic emulsifier participates to the initiation reaction.

© 2011 Elsevier Ltd. All rights reserved.

## 1. Introduction

Polysiloxanes are widely used in industry because of their excellent properties such as resistance to high and low temperatures, weather-ability, good hydrophobicity, good electrical insulation properties and good biocompatibility [1]. In 1959, Hyde and Wehrly demonstrated a possibility of carrying out ring-opening polymerization (ROP) of cyclosiloxanes in water emulsion [2]. Since then, the anionically initiated ring-opening polymerization of cyclosiloxanes has been one of the most promising methods for preparing polysiloxane emulsions. Particularly, a number of studies have focused on the polymerization of cyclosiloxanes using cationic [3–10], anionic [11,12] and nonionic [6,13,14] emulsifiers.

Systematic studies of anionic ring-opening polymerization (AROP) in emulsion [7,9,10] showed that the process differs significantly from free-radical emulsion polymerization. Mechanism of the anionic ring-opening polymerization is more complex. During AROP in emulsion, different chemical reactions take place on the polymer particle surface and inside the particle. These chemical reactions are presented in Fig. 1 [9]. Main chemical reactions by which polymer is

formed (initiation, propagation and termination) occur on the particle surface. Chain growth is initiated by hydroxide anion of water-soluble initiator which is coupled with cationic emulsifier on the particle surface. The emulsifier cation remains associated to the active center (hydroxide anion) of growing polymer chain during the propagation step. Termination occurs through protonation by water to give silanol end-groups. The reversibility of termination reaction is a key factor for long chain generation [9]. Backbiting reactions produce small oligomeric cycles accumulating on the particle surface, where the steric constraints imposed by the ion-pairing limit the size of the obtained rings. Indeed, it was observed [7] that polydimethylsiloxane (PDMS) polymer obtained by AROP in emulsion contained only relatively small amounts of small cycles, such as octamethylcyclotetrasiloxane ( $D_4$ ), dodecamethylcyclopentasiloxane ( $D_5$ ) and dodecamethylcyclohexasiloxane ( $D_6$ ), when compared to bulk polymerization, and only traces of higher cycles. When a growing polymer chain reaches a critical degree of polymerization (DP) and its termination occurs, the chain penetrates into the particle interior. For PDMS a critical DP value 30 D units was determined [9]. Once the chains have penetrated into the particle core, they cannot undergo further propagation due to the absence of the active center. In the particle interior, condensation and redistribution reactions take place. De Gunzbourg et al. [7,15] and Zhang et al. [3–5], who

\* Corresponding author. Tel.: +386 1 2419 543; fax: +386 1 2419 541.

E-mail address: [urska.sebenik@fktk.uni-lj.si](mailto:urska.sebenik@fktk.uni-lj.si) (U. Šebenik).

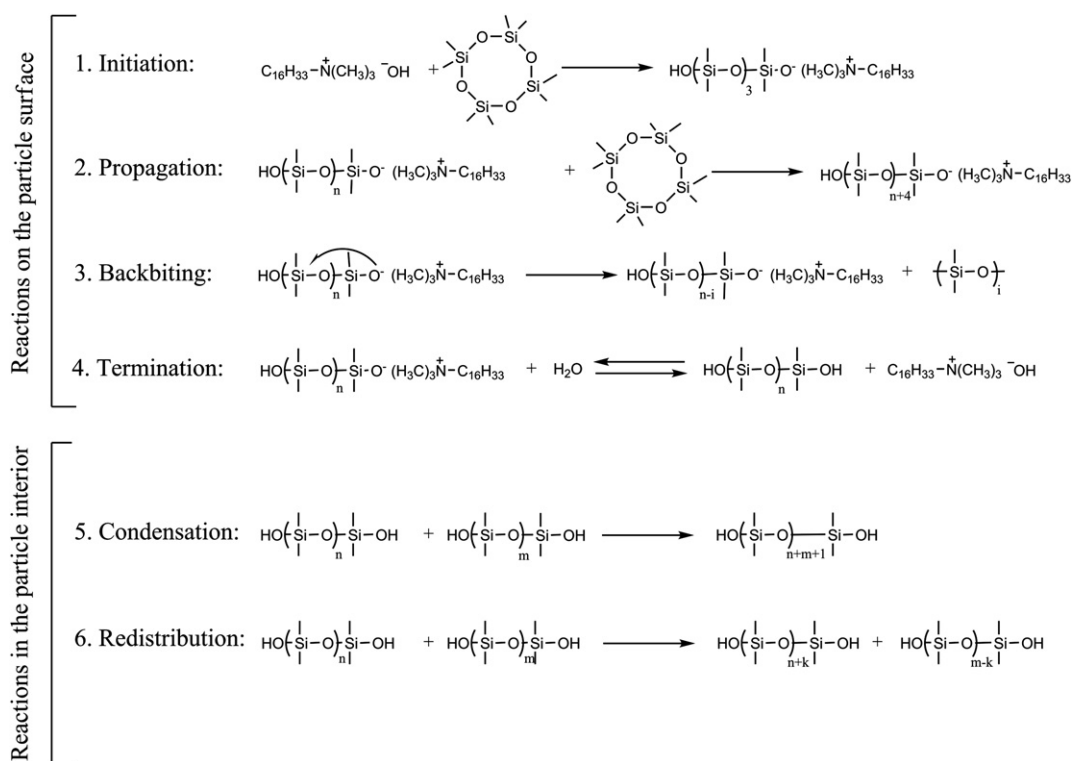


Fig. 1. Chemical reactions [9] on the particle surface and in the particle interior.

studied polymerization of D<sub>4</sub>, observed a significant increase in average molecular weight and polydispersity index above 70 and 60% monomer conversion, respectively, what clearly indicated condensation reactions. Redistribution reactions are difficult to follow as they do not affect the number of polymer chains or monomer conversion nor the cycle formation [9]. For a polymer with narrow molecular weight distribution to be prepared, backbiting, condensation and redistribution reactions have to be controlled. Nevertheless, condensation reactions are not always undesirable since by them polymer of higher average molecular weight is formed.

D<sub>4</sub> has been the most widely used cyclosiloxane monomer in academic researches [1,4,7,9,16], patents [17–19] and in organo-silicone industry. First detailed studies of AROP polymerization of D<sub>4</sub> in emulsion were done by Zhang et al. [3] who studied the anionic polymerization of D<sub>4</sub> in emulsion with potassium hydroxide (KOH) as an initiator and benzyldimethylammonium bromide (NBr) as a cationic emulsifier. They proposed a hypothetical mechanism for AROP of D<sub>4</sub>. On the basis of their results [3–5], De Gunzbourg et al. [7] used benzyldimethyldodecylammonium hydroxide which acted as initiator and emulsifier. One of the main issues has been to find conditions for better emulsion stability. To obtain stable monomer droplets dispersed in the water phase many research groups [7,9,15,20] used sonication previous to polymerization. Benefit of pre-emulsification of the system is monomer scattering to smaller droplets, which can act as independent mini-reactors during polymerization process. To prepare emulsions of small and monodisperse particles with high polymer content various parameters like monomer [10,15,21,22], initiator [14] and emulsifier [13–15,21] concentrations, type of emulsifier [13–15,21], combinations of different emulsifiers [13–15,21] and monomer feeding rate during semi-batch process [21,22] were varied and controlled.

So far, most research groups investigated how the properties of the final products depend on the emulsion recipe and/or process parameters. Fewer groups studied kinetics of the polymerization and/or emulsion properties, such as particle size and distribution

[21,22] or molecular weight and distribution [21,22], during the polymerization process. They [7,9,15] were interested in the control of molecular weight distribution and in the prediction of the amount of linear and cyclic compounds formed during AROP polymerization of D<sub>4</sub>. Barrère et al. [21] compared particle sizes and distributions of polysiloxane emulsions during batch and semi-batch AROP and cationic ROP (CROP) of D<sub>4</sub> using photon correlation spectroscopy, while Lin et al. [20] studied Ostwald ripening effect and size evolution of PDMS particles during CROP by using dynamic light scattering (DLS). Recently, Zhuang et al. [16] investigated the kinetics and physical mechanism of micro emulsion polymerization of D<sub>4</sub>. In their research [16] light transparency of the emulsion, monomer conversion and particle sizes and distributions were recorded as a function of polymerization time.

In this work, batch AROP of octamethylcyclotetrasiloxane in emulsion was investigated. Cationic emulsifier, hexadecyltrimethylammonium bromide (CTAB), and nonionic emulsifier, secondary alcohol ethoxylate, were used. The concentration of emulsifiers was above their critical micelle concentration (CMC). Effects of emulsifier mixture concentration, nonionic/cationic emulsifier ratio and cationic emulsifier/initiator (KOH) ratio on the kinetics, on the evolution of average particle size and distribution with time and on the evolution of average molecular weights and distribution with time were studied and discussed. The results obtained contribute to a better understanding of the complex mechanism of batch emulsion AROP with emulsifier concentration above CMC.

## 2. Experimental

### 2.1. Materials

Octamethylcyclotetrasiloxane (D<sub>4</sub>, 98%) was used as received from Aldrich, without further purification. The cationic emulsifier, hexadecyltrimethylammonium bromide (CTAB, Aldrich, ≥98%) and nonionic emulsifier, secondary alcohol ethoxylate, with trade name

Tergitol, Type 15-S-9 (p.a., Aldrich) were used as received. Deionized water was used to prepare all the solutions and emulsions. Potassium hydroxide (p.a., Merck) was used as initiator. Hydrochloric acid (p.a., Merck, 0.5 M) was used in order to stop the reaction.

## 2.2. Emulsification and polymerization

Polysiloxane emulsions were synthesized isothermally at 80 °C by batch emulsion polymerization in a 250 ml glass reactor with four necks equipped with a reflux condenser, a mechanical stirrer, a digital thermometer, and a nitrogen gas inlet. An adjustable cooling temperature system was used.

The monomer pre-emulsion was prepared at room temperature by dissolution of ionic and nonionic emulsifiers in various proportions in deionized water in the reactor. Monomer was added to the emulsifier solution and the pre-emulsion was stirred at 1000 rpm for 15 min. After 15 min, the mixture was heated up to 80 °C and the stirring speed was lowered to 500 rpm. To initiate the polymerization KOH was added. The reactor content was sampled during the polymerization at scheduled times. To stop the polymerization pH value of the withdrawn samples and emulsion at the end of the process was adjusted to 7.5–8 using HCl (0.5 M). Detailed recipes for the preparation of polysiloxane emulsions are given in Table 1.

## 2.3. Monomer conversion determination

The conversion was determined by gravimetric analysis. The samples, which were taken out of the reactor during the polymerization and neutralized in order to stop the polymerization, were dried to constant mass at 50 °C in vacuum oven. During drying all volatile components, water, monomer and small oligomeric cycles, were removed from the sample. To obtain the polymer mass, the masses of emulsifiers and inorganic salts were subtracted from the mass of dried sample. Therefore, by the gravimetric method only the amount of monomer converted to large, non-volatile polymeric chains was determined and the monomer conversion should be interpreted accordingly.

## 2.4. Emulsion and polymer characterization

<sup>29</sup>Si NMR spectra were recorded on a Varian Unity Inova 300 NMR Spectrometer equipped with a <sup>29</sup>Si probe (5 mm diameter) at 60.19 MHz. The dried samples were diluted in chloroform containing TMS which was used as a chemical reference. Samples of PDMS emulsions were measured directly, without solvent use.

The particle size of emulsion samples was measured on 3D DLS Spectrometer, LS Instruments. The experimental setup consisted of an Ar laser (wavelength  $\lambda = 670$  nm), a thermostated sample holder and a photomultiplier mounted at a detection angle of 90°. The measurement temperature was 25 °C. Before each particle size

measurement, emulsion samples were diluted by deionized water to rule out interaction and multiple scattering effects. Average particle diameters were calculated from the intensity of auto-correlation function by Stokes-Einstein equation using the Contin method. The diameter measured by DLS was a hydrodynamic diameter.

Average molecular weights of polymer were determined by gel permeation chromatography (GPC) using polystyrene standards (between 1060 and 750,000 g/mol). The determination of average molecular weights was performed with a Waters 2690 (separations module) instrument with a refractive-index detector. Three Waters Styragel columns (300 × 4.6 mm) were used in series. The 0.2% (w/v) solutions were prepared in tetrahydrofuran (THF), which was also used as carrier solvent at a rate of 0.2 ml min<sup>-1</sup>.

## 3. Results and discussion

### 3.1. Polymer formation and conversion of monomer

The formation of PDMS was confirmed by <sup>29</sup>Si NMR analysis of emulsions and dried samples. NMR spectra of PDMS emulsions showed signals at -19, 64 ppm and -22, 28 ppm, which were attributed [23] to D<sub>4</sub> and PDMS unit of polymer chain, respectively. In the NMR spectra of dried samples, the D<sub>4</sub> signal was absent, which proved that the monomer was efficiently removed by drying.

By gravimetric analysis only the amount of monomer converted to large non-volatilizable polymeric chains was determined. Here, all volatile oligomeric cycles, which are formed during polymerization [7,9,21,22], were treated as monomer in conversion calculations. De Gunzbourg et al. [7], who studied AROP of D<sub>4</sub>, observed that the amount of other than D<sub>4</sub> cycle species reached only 4.2 wt% at equilibrium and it was essentially composed of D<sub>5</sub> (3.3 wt%), D<sub>6</sub> (0.8 wt%) and D<sub>7</sub> (0.1 wt%).

The conversion curves of D<sub>4</sub> at different reaction temperatures are presented in Fig. 2. Increasing the reaction temperature significantly increased the polymerization rate. On the basis of these results, the reaction temperature of 80 °C was used for further investigations. Raising the temperature above 80 °C was not reasonable due to water evaporation.

The conversion of D<sub>4</sub> at 80 °C versus polymerization time curves for syntheses PDMS1, PDMS2, PDMS3 and PDMS4 are presented in Fig. 3. These syntheses differed in the total amount of emulsifier used, while the ratio between nonionic and cationic emulsifier remained unchanged. It was observed (Fig. 3) that polymerization rate of D<sub>4</sub> increased with increasing concentration of emulsifiers. After 4 h of polymerization the reached conversions for samples PDMS1, PDMS2, PDMS3 and PDMS4 were 42%, 59%, 65% and 68%, respectively.

Also the effect of cationic/nonionic emulsifier ratio on the polymerization rate was investigated. The syntheses PDMS2, PDMS2a, and PDMS2b did not differ in the total amount of emulsifier used, but in the ratio between nonionic and cationic emulsifier (Fig. 4).

**Table 1**  
Recipes of PDMS emulsions.

PDMS emulsions	PDMS1	PDMS2	PDMS2a	PDMS2b	PDMS2c	PDMS2d	PDMS2e	PDMS2f	PDMS3	PDMS4
D <sub>4</sub> (g)	10.0	10.0	10.0	10.0	10.0	10.0	10.0	10.0	10.0	10.0
CTAB (g)	0.251	0.504	0.756	0.255	0.503	0.508	0.503	0.503	0.624	0.750
Tergitol (g)	0.263	0.501	0.260	0.763	0.503	0.494	0.515	0.511	0.626	0.759
KOH (g)	0.260	0.205	0.204	0.201	0.300	0.078	0.043	0.022	0.201	0.213
Deionized water (g)	60.0	60.4	60.0	60.0	60.0	60.0	60.0	60.0	60.7	60.6
Overall mass (g)	70.7	71.6	71.3	71.2	71.3	71.1	71.1	71.1	72.1	72.3
CTAB/Tergitol mass ratio	1.0:1.0	1.0:1.0	3.0:1.0	1.0:3.0	1.0:1.0	1.0:1.0	1.0:1.0	1.0:1.0	1.0:1.0	1.0:1.0
Monomer/Emulgators mass ratio	10:0.5	10:1.0	10:1.0	10:1.0	10:1.0	10:1.0	10:1.0	10:1.0	10:1.25	10:1.5
KOH/CTAB molar ratio	6.7:1.0	2.6:1.0	1.8:1.0	5.1:1.0	3.9:1.0	1.0:1.0	0.6:1.0	0.3:1.0	2.1:1.0	1.9:1.0



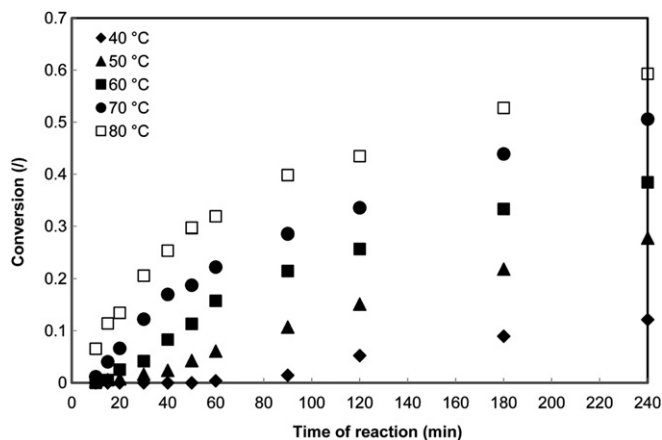


Fig. 2. Conversion versus polymerization time plot for PDMS2 syntheses at different temperatures.

It can be observed in the Fig. 4, that the conversions for syntheses with higher amount of cationic emulsifier were higher.

The increase of monomer conversion and therefore the increase of polymerization rate with overall emulsifiers' concentration and with increasing ratio between cationic and nonionic emulsifier at fixed overall emulsifier concentration may be explained by the polymerization mechanism proposed by Zhang [3] and De Gunzbourg [7]. The AROP in emulsion has been explained by the kinetic scheme (Fig. 1), which involves three reactions, which effect the monomer consumption: initiation, propagation and reversible termination. As it was stated previously, all the three reactions take place at the particle/water interface [7]. The polymerization is initiated by hydroxide anions which are coupled with CTAB cations. Chains propagate by adding monomer molecules on the active centers associated with CTAB cations. Reversible termination occurs through active center protonation by water to give silanol end-groups. Usually, when the emulsifier concentration in the emulsion is increased smaller particles are formed and their number is higher [4,7,16]. Consequently, also the surface areas of the particle/water interface where above mentioned reactions occur is larger, what enables higher monomer consumption rate. Moreover, in the case of AROP, the use of higher amount of CTAB increases the number of polymerization sites and therefore also the polymerization rate. To investigate solely the effect of CTAB concentration on polymerization kinetics the total amount of emulsifiers was kept constant and the ratio between cationic and

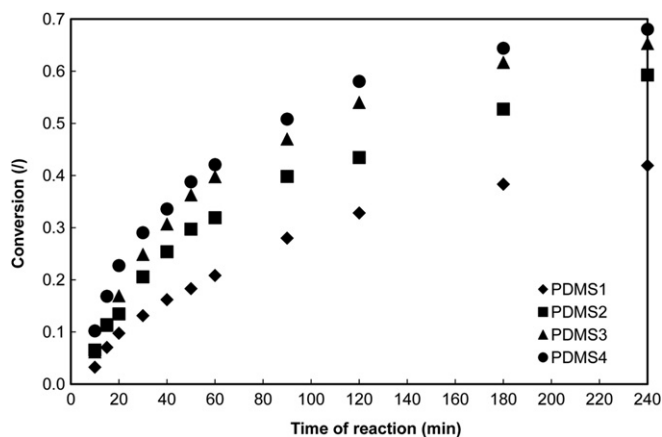


Fig. 3. Conversion versus polymerization time plot for samples containing different amount of emulsifiers at 80 °C.

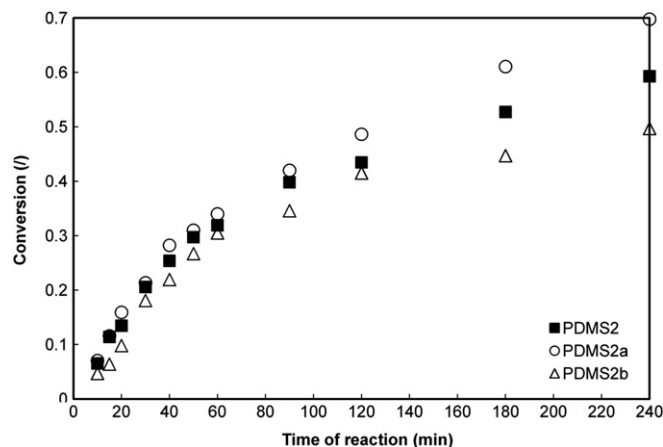


Fig. 4. Effect of cationic/nonionic emulsifier ratio on the conversion as a function of the polymerization time at 80 °C.

nonionic emulsifier was varied (Fig. 4). As mentioned before, the polymerization rate decreased with decreasing cationic/nonionic emulsifier ratio. This result is consistent with competitive adsorption between nonionic and cationic emulsifiers on the particle surface. The instantaneous concentration of silanolate active centers, which determined the propagation rate, was a function of the number of hydroxide anions localized at the interface (first ionic layer) [15]. By decreasing the amount of cationic emulsifier the concentration of hydroxide anions on the particle surface was reduced, therefore also the initiation and propagation rates were decreased. However, the differences between samples with different nonionic/cationic emulsifier ratio were minimal at low reaction times, but they became important when the monomer conversion between 30 and 40% was reached. This observation may be explained by free emulsifier consumption and empty micelle disappearance. The existence and disappearance of empty micelles at these conversions was confirmed by particle size and distribution evolutions, which are presented in the next section.

To prove that the number of hydroxide anions localized at the interface is a function of concentration of CTAB, the molar ratio between initiator and CTAB was varied. The syntheses PDMS2, PDMS2c, PDMS2d, PDMS2e and PDMS2f differ in the molar ratio between initiator and cationic emulsifier. The curves of  $D_4$  conversion versus time are presented in Fig. 5. It was observed that the polymerization rate was practically the same when equimolar ratio (synthesis PDMS2d,  $n_{\text{KOH}} = n_{\text{CTAB}}$ ) and higher initiator/CTAB molar ratios (syntheses PDMS2 and PDMS2c,  $n_{\text{KOH}} > n_{\text{CTAB}}$ ) were used. Nevertheless, when the molar amount of initiator was lower than the molar amount of CTAB (syntheses PDMS2e and PDMS2f,  $n_{\text{KOH}} < n_{\text{CTAB}}$ ) the polymerization rate decreased. Therefore it may be stated, that the KOH concentration affected polymerization kinetics only when the ratio KOH/CTAB was lower than equimolar ratio.

### 3.2. Average particle size and distribution

For polysiloxane emulsions obtained by experiments PDMS1, PDMS2, PDMS3 and PDMS4 average particle size and particle size distribution (PSD) during polymerization were followed. It was observed, that the average particle size altered significantly between 60 and 130 nm during the initial period of the polymerization (Fig. 6). Similar behavior was observed by Lin et al. [17]. After the initial period the particle size stabilized when conversion of monomer was between 30 and 40%. Thereafter, for emulsions PDMS1, PDMS2 and PDMS3 the average particle size of polymer particles remained relatively constant (between 70 and 85 nm).

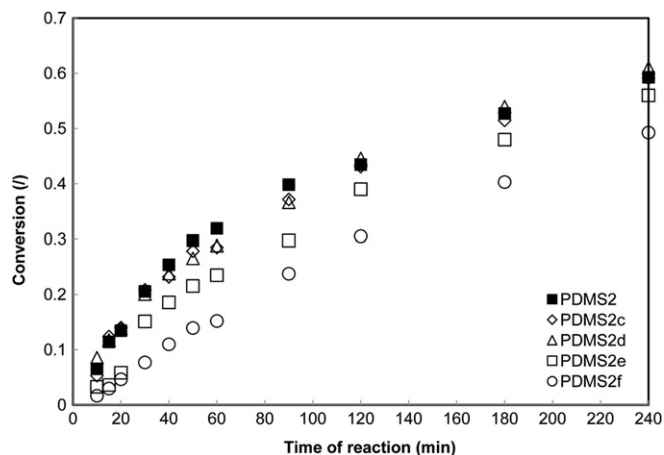


Fig. 5. Effect of molar ratio between initiator and cationic emulsifier on the monomer conversion as a function of the polymerization time at 80 °C.

On the other hand, the average particle size for emulsion PDMS4, which contained the higher amount of emulsifiers, continued to decrease slowly with time of reaction (at about 68% conversion the particle size value of about 50 nm was reached).

It seems that at the beginning of the polymerization, when the monomer conversion was still low, the particles were not stable. The observed increase in average particle size during initial period may be explained by particle coalescence through collision and by Ostwald ripening effect (transfer of monomer from small particles to larger particles to reduce the surface energy of the system) [21]. The ripening was a consequence of the absence of a hydrophobic stabilizer in the reaction mixture. However, upon polymerization, polymer molecules were formed and particles containing enough hydrophobic polysiloxane became stabilized against ripening. Thereafter, a decrease in average particle size was observed. The decrease may be related to an increase of the number of particles and may be explained by the relatively high amount of emulsifier used in our research. In all the syntheses, concentrations of cationic emulsifier were above the critical micelle concentration (CMC) which is 1 mM at room temperature (producer's data) and about 2 mM at 80 °C (CMC was determined in our lab by performing conductivity measurements.).

Multimodal PSD curves shown in Fig. 7a,b clearly indicate that after 10 min of polymerization three different kinds of particles co-existed in the emulsion. The three peaks detected in PSDs were

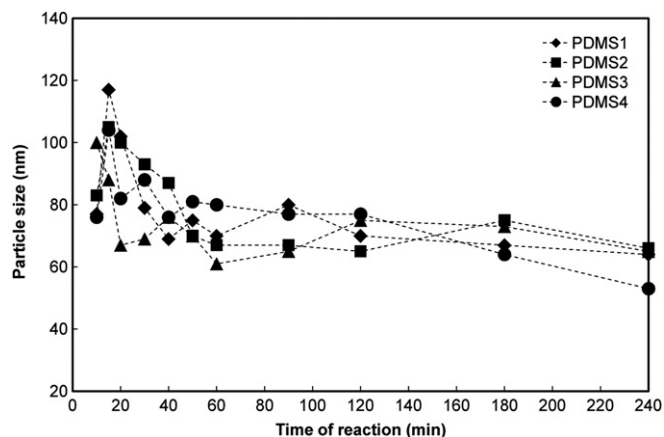


Fig. 6. Average particle size versus polymerization time plot for samples containing different amount of emulsifiers at 80 °C.

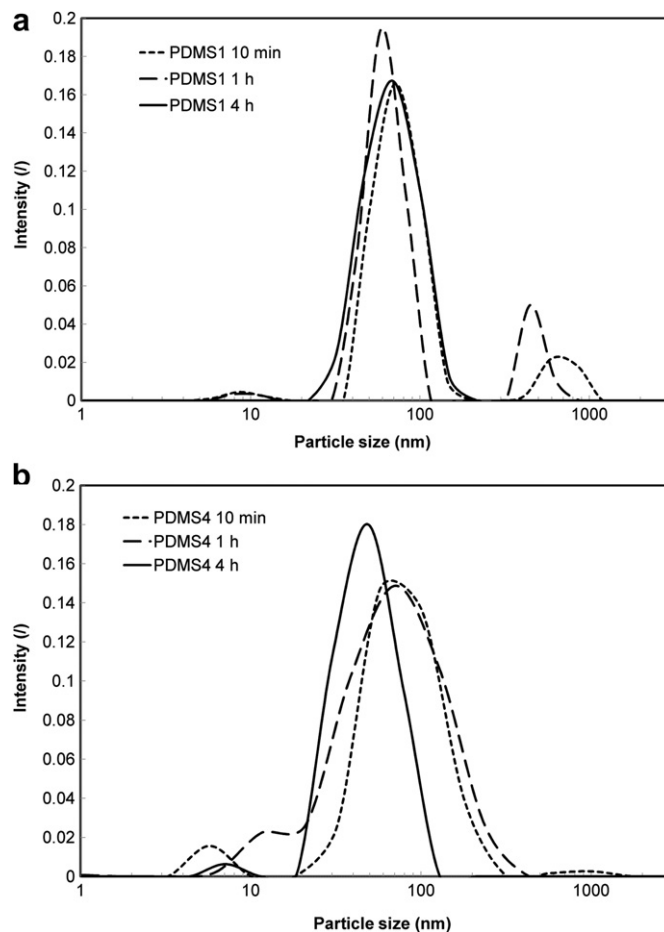


Fig. 7. a. Particle size distributions of sample PDMS1 after 10 min, 1 h and 4 h of polymerization. b. Particle size distributions of sample PDMS4 after 10 min, 1 h and 4 h of polymerization.

attributed to empty micelles (3–15 nm), active micelles or polymer particles (30–120 nm), and monomer droplets (>300 nm). It was observed (from the number and volume PSDs of these samples not presented in figures), that after 10 min of polymerization the great majority of the particles had a diameter between 3 and 15 nm, that there was a smaller fraction of particles with size between 30 and 300 nm and that only a limited number of particles was larger than 300 nm. The average sizes shown in Fig. 6 correspond to average sizes of polymer particles (active micelles). Since the initiation and propagation take place on the particle surface, where the cationic emulsifier participates in the initiation process, polymerization took place in all kinds of particles that contained monomer and were stabilized by emulsifier molecules. After 10 min of polymerization polymer particles and monomer droplets contained mainly monomer and only small percent of polymer (monomer conversion was about 10% for PDMS4, 6.5% for PDMS3, 4.5% for PDMS2 and only about 3% for PDMS1). Because the total surface of polymer particles was higher than that of monomer droplets, monomer droplets contained even lower percent of polymer than polymer particles. Consequently, the following processes, which could contribute to the decrease of average particle size of polymer particles, were envisaged: (i) nucleation of new particles via monomer diffusion from monomer droplets and larger polymer particles toward empty micelles [16]; (ii) monomer diffusion from larger polymer particles toward smaller polymer particles to compensate for their rapid monomer consumption by interfacial polymerization, which is



faster in particles exhibiting large specific surface [16]; (iii) re-nucleation due to emulsifier diffusion from empty micelles toward large polymer particles (containing mainly monomer) and/or monomer droplets. Increased emulsifier density on the particles and droplets surface together with continuous stirring of the emulsion may enable the formation of smaller particles from larger ones.

To investigate the observed phenomena further and to prove the likelihood of all above listed options PSDs of emulsions at different times of polymerization were compared. In Fig. 7a,b PSDs of samples PDMS1 and PDMS4 after 10 min, 1 h and 4 h of polymerization are shown. As explained above, after 10 min of reaction, when the conversions for samples PDMS1 and PDMS4 were 3 and 10%, respectively, three peaks corresponding to empty micelles, polymer particles and monomer droplets in PSDs were observed. After 1 h of polymerization conversion of sample PDMS1 was around 21% and its PSD curve did not differ significantly from that after 10 min. The main difference was in monomer droplets size which was smaller. However, after 4 h the conversion was above 40% and the PSD curve changed noticeably, although the average size of polymer particles did not change significantly; after 4 h the PSD was monomodal and no peaks corresponding to either empty micelles or monomer droplets were observed. For sample PDMS4 no peak corresponding to monomer droplets was noticed already after 1 h of polymerization, when the monomer conversion was already about 42%. On the other hand, a shoulder between 15 and 30 nm was observed which indicated the probability of nucleation of new particles via monomer diffusion toward empty micelles. However, the empty micelles in sample PDMS4 existed yet after 4 h (at 68% conversion) because of the very high emulsifier concentration in the synthesis. PSDs of samples PDMS2 and PDMS3, which are not presented in the figure, showed intermediate behavior between samples PDMS1 and PDMS4.

The results of particle size and distribution analysis showed that the size of monomer droplets and the number of empty micelles was decreasing during polymerization, while the average size of polymer particles was not increasing. Despite extremely low monomer solubility in water ( $2.4 \times 10^{-7}$  mol/l) and slow diffusion rates of cyclosiloxanes in a high ionic strength medium [22], the transport of monomer from monomer droplets and larger polymer particles toward empty micelles was confirmed by monomer droplets disappearance, by formation of smaller particles (see PSD of PDMS4 after 1 h of polymerization) and by empty micelles disappearance (see PSD of PDMS1 after 4 h of polymerization). On the other hand, the transport of monomer from monomer droplets toward polymer particles, which is typical for classical emulsion polymerization and causes polymer particle growth, could not be confirmed, since the average size of polymer particles did not increase. However, driving force for monomer diffusion toward polymer particles is to compensate for rapid monomer consumption by interfacial polymerization. Therefore, there are two possibilities for this compensation to occur; monomer diffusion from monomer droplets through water toward particle surface and/or monomer diffusion from polymer particle interior toward particle surface. Especially at lower conversions the second possibility is more plausible, due to extremely low monomer solubility in water. At higher conversions the first possibility becomes likely, of course, if monomer droplets still exist. If there are no monomer droplets left, the monomer can diffuse from larger polymer particles toward smaller polymer particles, as the monomer consumption by interfacial polymerization is faster in particles exhibiting larger specific surface. This process narrows PSD, while the decrease of average particle size would happen only, if the number of smaller particles was significantly higher than that of larger particles and/or if empty micelles still exist. This explains the differences between PSDs of sample PDMS4 after 1 and 4 h of polymerization and why the

average particle size for emulsion PDMS4 continued to decrease slowly with time of reaction. A change in particle size due to density increase as a consequence of polymerization is not expected, since monomer and polymer exhibit comparable densities [22].

Even though the above discussion, which justifies experimental observations by monomer diffusion, seems very feasible and for this reason most of the research articles explain such observations exclusively by monomer diffusion, the possibility of emulsifier diffusion and its continuous rearrangements between phases cannot be ignored. Nevertheless, empty micelles are dynamic entities and an individual emulsifier molecule might only reside for  $10^{-6}$  s in a particular micelle [24]. Therefore, it is also possible that, when the conversion of monomer is still low, free emulsifier molecules (from empty micelles) diffuse toward large polymer particles and even larger monomer droplets, where they adsorb on their surface. Consequently, the increased emulsifier density on the surface, together with continuous stirring of the emulsion, could enable the formation of smaller particles from larger ones.

### 3.3. Average molecular weights and distributions

Fig. 8 shows the evolution of the number average molecular weight ( $\bar{M}_n$ ) and polydispersity index (PDI) as a function of conversion for samples PDMS1, PDMS2 and PDMS4. As it was expected, and as it has been shown elsewhere [3,4], both  $\bar{M}_n$  and PDI increased with conversion and time of reaction continuously. The continuous increase of average molecular weights and polydispersity index was explained by chain growth by successive polyaddition of  $D_4$  and reversible termination on active centers at the particle surface and by chain growth by condensation reactions in the particle interior. In Fig. 8, at given monomer conversion values,  $\bar{M}_n$  values of samples containing higher amount of emulsifier were lower than values for samples containing less emulsifier. By raising the amount of emulsifiers, the number of initiation sites increased what resulted in an increased number of polymer chains. Hence, at a given conversion, i.e. when an explicit part of monomer was consumed, the average length of chains was smaller while their number was larger.

The evolution of the number of polymer chains ( $N$ ) with polymerization time is shown in Fig. 9. It can be observed how  $N$  increases during polymerization and how the increase depends on the amount of emulsifier used; the higher the ratio between emulsifier and monomer, the faster the initiation reaction at the

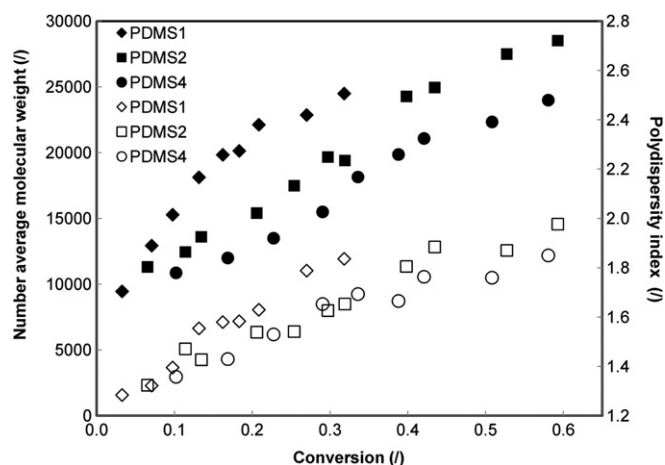


Fig. 8. Number average molecular weight (plain symbols) and polydispersity index (open symbols) as a function of monomer conversion for syntheses PDMS1, PDMS2 and PDMS4.

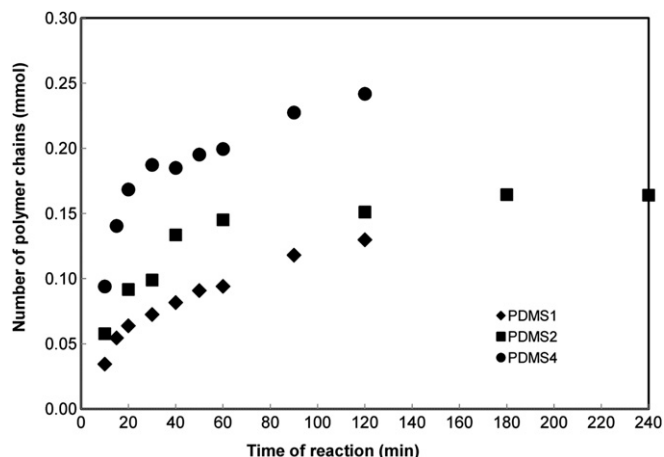


Fig. 9. Number of polymer chains as a function of polymerization time for syntheses PDMS1, PDMS2 and PDMS4.

beginning of the polymerization and the larger the number of polymer chains formed. However, the initiation is not the only reaction that affects the  $N$  value. Especially at higher conversions, condensation reactions become important as well. Each initiation reaction leads to the formation of one chain and each condensation reaction leads to the disappearance of one chain. Since  $N$  increased during the entire time (4 h) and conversion interval (up to 68%), it may be concluded that initiation reactions prevailed over the condensation reactions during the period under investigation. Nevertheless, the rate of  $N$  growth slowed down with time (Fig. 9) and conversion. In other words, condensation reactions became important when the concentration of polymer was high enough. Similar behavior was observed by Zhang et al. [3] and De Gunzbourg et al. [7]. De Gunzbourg et al. [7] noticed a linear increase in  $N$  up to 10% conversion, a slow down in the  $N$  growth between 10 and 70% conversion and a sharp decrease in  $N$  above 70% monomer conversion. However, we believe that the monomer conversion is not the only factor that affects the extent of condensation reactions. Since it has been proved that condensation reactions take place in the particle interior, the particle size must play an important role as well. In our study, average particle sizes of different samples under investigation were similar and the effect of particle sizes on molecular weight could not be studied in detail.

#### 4. Conclusions

Batch emulsion AROP of octamethylcyclotetrasiloxane using nonionic and cationic emulsifiers above their critical micelle concentration was studied. At the beginning of the polymerization, three different kinds of dispersed objects containing emulsifier were detected in the reaction system: empty micelles, active micelles (polymer particles), and monomer droplets. The transport of monomer from monomer droplets and larger polymer particles toward empty micelles was confirmed by monomer droplets and free micelles disappearance and by formation of smaller particles. On the other hand, the transport of monomer from monomer droplets toward polymer particles, which is typical for classical emulsion polymerization, was not confirmed, since the average particle size of polymer particles did not increase during polymerization. It was proposed that at lower conversions, monomer diffuses from polymer particle interior toward particle surface to compensate for rapid

monomer consumption by interfacial polymerization. This seems reasonable also due to the extremely low monomer solubility in water. However, at higher conversions, when the possibility of monomer migration from monomer droplets toward polymer particles becomes more likely, the monomer droplets vanished. Thereafter, the observed changes in particle size distributions pointed toward the monomer diffusion from larger polymer particles toward smaller ones, because the monomer consumption by interfacial polymerization is faster in particles exhibiting large specific surface.

Emulsifier concentration, nonionic/cationic emulsifier ratio and cationic emulsifier/initiator (KOH) ratio have an evident effect on the kinetics and on the average molecular weights, clearly showing that cationic emulsifier has an important function in initiation reaction, as it was stated previously. An increase of KOH molar concentration above the cationic emulsifier molar concentration did not affect the polymerization rate.

To conclude, when batch emulsion AROP is compared to a batch free-radical emulsion polymerization, particular attention must be paid to the significant differences between the processes and the comparison may not be done straightforwardly. We believe that the results of the present study contribute to a better understanding of the complex mechanism of the batch emulsion AROP with emulsifier concentration above critical micelle concentration.

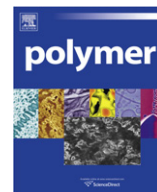
#### Acknowledgments

The financial support of this work by the Slovenian Ministry of Higher Education, Science and Technology (Grant P2-0191) is gratefully acknowledged.

Operation part was financed by the European Union, European Social Fund. Operation implemented in the framework of the Operational Programme for Human Resources Development for the Period 2007–2013, Priority axis 1: Promoting entrepreneurship and adaptability, Main type of activity 1.1.: Experts and researchers for competitive enterprises.

#### References

- [1] Zhang Z, Zhou N, Xu C, Xie Z. *Chin J Polym Sci* 2001;19:7–11.
- [2] Hyde JF, Wehrly JR. U.S. Patent 2,891,920, June 23, 1959.
- [3] Zhang X, Yang Y, Dai D. *Polym Comm (China)* 1982;2:154–7.
- [4] Zhang X, Yang Y, Liu X. *Polym Comm (China)* 1982;2:104–11.
- [5] Zhang X, Yang Y, Liu X. *Polym Comm (China)* 1984;4:226–32.
- [6] Landfester K, Bechtold N, Tiarks F, Antonietti M. *Macromolecules* 1999;32:2679–83.
- [7] De Gunzbourg A, Favier J-C, Hémerly P. *Polym Int* 1994;35:179–88.
- [8] Hsieh HL, Quirk RP. *Anionic polymerization: principles and practical applications*. New York: Marcel Dekker; 1996. 699–702.
- [9] Barrère M, Ganachaud F, Bendejacq D, Dourges MA, Maitre C, Hémerly P. *Polymer* 2001;42:7239–46.
- [10] Barrère M, Maitre C, Dourges MA, Hémerly P. *Macromolecules* 2001;34:7276–80.
- [11] Maisonnier S, Favier J-C, Masure M, Hémerly P. *Polym Int* 1999;48:159–64.
- [12] Palaprat G, Ganachaud F, Mauzac M, Hémerly P. *Polymer* 2005;46:11213–8.
- [13] Silas JA, Kaler EW, Hill RM. *Langmuir* 2001;17:4534–9.
- [14] Zhang D, Jiang X, Yang C. *J Appl Polym Sci* 2002;89:3587–93.
- [15] De Gunzbourg A, Maisonnier S, Favier J-C, Maitre C, Masure M, Hémerly P. *Macromol Symp* 1998;132:359–70.
- [16] Zhuang Y-Q, Ke X, Zhan X-L, Luo Z-H. *Powder Technol* 2010;201:146–52.
- [17] Gee RP. U.S. Patent 5,925,469, Jul 20, 1999.
- [18] Gee RP, Wrolson BM, Zimmerman BL. U.S. Patent 6,465,568 B1, Oct 15, 2002.
- [19] Ferritto MS, Schulz WJ. U.S. Patent 6,294,634 B1, Sep 25, 2001.
- [20] Lin M, Chu F, Bourgeat-Lami E, Guyot A. *J Dispersion Sci and Technol* 2004;25:827–35.
- [21] Barrère M, Capitaio da Silva S, Balic R, Ganachaud F. *Langmuir* 2002;18:941–4.
- [22] Palaprat G, Ganachaud F. *CR Chim* 2003;6:1385–92.
- [23] LaRochelle RW, Cargioli JD, Williams EA. *Macromolecules* 1976;9:85–8.
- [24] Gilbert RG. *Emulsion polymerization: a mechanistic approach*. London: Academic Press; 1995 (chapter 1).



## Synthesis and characterization of soluble multi-walled carbon nanotube/poly-(organophosphazene) composites

Elif Okutan<sup>a</sup>, Gülşah Ozan Aydın<sup>a</sup>, Ferda Hacivelioglu<sup>a,c</sup>, Adem Kılıç<sup>a,\*</sup>, Saadet Kayıran Beyaz<sup>b</sup>, Serkan Yeşilot<sup>a</sup>

<sup>a</sup> Department of Chemistry, Gebze Institute of Technology, 41400, Gebze, Kocaeli, Turkey

<sup>b</sup> Department of Chemistry, Kocaeli University, Izmit, Turkey

<sup>c</sup> University of Southampton, School of Chemistry, Southampton, SO17 1BJ, UK

### ARTICLE INFO

#### Article history:

Received 13 September 2010

Received in revised form

3 January 2011

Accepted 9 January 2011

Available online 19 January 2011

#### Keywords:

Polyphosphazene  
Carbon nanotubes  
Nanocomposites

### ABSTRACT

Poor solubility of carbon nanotubes (CNTs) in water and organic solvents offers a significant problem for their applications. Macromolecules can be suitable solubilizing agents and a structural component of composite materials for CNTs. Several polymers were tested for the preparation of CNT dispersions. In this study, a poly[(4-pyridineoxy)(phenoxy)phosphazene] (3) was prepared by sequential treatment of poly(dichlorophosphazene) (2) with sodium 4-pyridineoxy and sodium phenoxide in THF. Multi-walled carbon nanotube/poly(organophosphazene) composites (*f*-MWCNT/PZS) with different feed ratios [ $R_{\text{feed}} = 1:1, 1:3, 1:5$  and  $1:10$  (w/w)] were obtained by the treatment of the functionalized multi-walled carbon nanotube (*f*-MWCNT) with the protonated poly(organophosphazene) (PZS). Excellent dispersions of the *f*-MWCNT/PZS nanocomposites in water and common organic solvents were achieved. The influence of feed ratio on polymer coating and the stability of composites were investigated by thermal gravimetric analysis (TGA). *f*-MWCNT/PZS<sub>1:5</sub> nanocomposite was characterized by <sup>31</sup>P, <sup>1</sup>H NMR, FTIR, XRD, EDX and Raman Spectroscopy. The morphologic characterizations of *f*-MWCNT/PZS<sub>1:5</sub> were carried out by HRTEM and SEM methods.

© 2011 Elsevier Ltd. All rights reserved.

### 1. Introduction

CNTs exhibit unique electronic, mechanical, and thermal properties [1]. Due to their wide range of applications in nanotechnology, they have attracted attention in materials science, electronics, and biomedical devices [2–6]. Unfortunately, the key problem for the application of CNTs in industry is still their poor wettability/dispersibility which reduces their great potential. The surface functionalization and modification of CNTs, improve their dispersibility in liquids, which gave them new properties for different applications. In this regard diverse strategies for CNTs functionalization continue to emerge for functionalization of CNTs [7]. The functionalization of CNTs with polymers may yield samples compatible with solvents and with feasible applications. Many polymers have been successfully used for the coating of CNTs by this approach, based on the  $\pi$ – $\pi$  stacking and ionic interactions between polymers and the graphitic surface of the CNTs [8].

Phosphazene-containing polymers are a class of organic–inorganic hybrid materials. Depending upon the nature of their substituents, stable or hydrolytically degradable polymers can be prepared [9]. The mechanical properties and the rate of degradation can be varied by a proper choice of chemical composition of the polymer backbone. The presence of –P=N– structural units in the macromolecular backbone provide tremendous flexibility to functionalize the materials through chemical modification for various applications. It is known that phosphazene-containing materials have been used as biomaterials, [10,11] membranes, [12] electrical and electrochromic materials, [13] ceramics, [14] and hybrid materials [15]. Even though the researches about polymer/CNT composites grow rapidly, the preparation of polyphosphazene/CNT composites remains rare. Unfortunately, little research has been reported for the fabrication of polyphosphazene/CNT containing hybrid materials. Recently, cyclomatrix-type polyphosphazenes have been used to functionalize MWCNTs [16,17]. The use of linear type polyphosphazene as a dispersing agent of single-walled carbon nanotubes (SWCNTs) has been reported by Park et al. [18]. They used noncovalent method for dispersing SWCNTs in water solution of sulfonated polyorganophosphazene by supramolecular association between the single-walled carbon nanotube and the

\* Corresponding author. Tel.: +90 2626053105; fax: +90 2626053101.  
E-mail address: [kilic@gyte.edu.tr](mailto:kilic@gyte.edu.tr) (A. Kılıç).

sulfonated poly(organophosphazene) which was soluble in DMSO and water. Therefore, designing a poly(organophosphazene) by a simple synthetic route to modify MWCNTs and preparing *f*-MWCNT/PZS composites with better solubility and thermal property could be an attractive approach.

In this paper the *f*-MWCNT and protonated poly(organophosphazene) (PZS) were used for synthesizing *f*-MWCNT/PZS composites with different feed ratios. The surface activation (–COOH groups) of MWCNTs was obtained by acid treatment [19–22] which also imparts strong negative charge to MWCNT dispersions. Poly[(4-pyridineoxy)(phenoxy)phosphazene] (3) was prepared by sequential treatment of poly(dichlorophosphazene) (2) with sodium phenoxide and sodium 4-pyridineoxy in THF. Protonated poly(organophosphazene) (PZS) was obtained by the reaction of compound (3) with HCl<sub>(g)</sub>. *f*-MWCNT/PZS composites with different feed ratios from PZS and *f*-MWCNT were prepared by stirring and sonicating in dichloroethane. The influence of feed ratio on polymer coating and the stability of composites were investigated by TGA. An example of prepared nanocomposites, *f*-MWCNT/PZS<sub>1:5</sub> was characterized by <sup>31</sup>P, <sup>1</sup>H NMR (Nuclear Magnetic Resonance Spectroscopy), SEM (Scanning Electron Microscopy), HRTEM (High Resolution Transmission Electron Microscopy), FTIR (Fourier Transform Infrared Spectroscopy), XRD (X-Ray Diffraction), EDX (Energy-dispersive X-ray) and Raman Spectroscopy. The morphologic characterizations of the (*f*-MWCNT/PZS<sub>1:5</sub>) nanocomposite were carried out by HRTEM and SEM methods.

## 2. Experimental section

### 2.1. Materials

Hexachlorocyclotriphosphazene (Otsuka Chemical Co., Ltd) was purified by fractional crystallization from *n*-hexane. The crystallized hexachlorocyclotriphosphazene was further purified by vacuum sublimation before the ring opening polymerization and only 60% of the material was allowed to be sublimed. Sodium hydride, (60% dispersion in mineral oil Merck); prior to use the oil was removed by washing with dry heptane followed by decantation. The deuterated solvents [CDCl<sub>3</sub> (≥99.8%) and THF-*d*<sub>8</sub> (≥99.5%)], tetrahydrofuran (≥99.0%), dichloromethane (≥99.0%), *n*-hexane (≥95.0%), acetone (≥99.8%), phenol (≥99%), Ni (NO<sub>3</sub>)<sub>2</sub>·6H<sub>2</sub>O, MgO, H<sub>2</sub>SO<sub>4</sub> (95–98%) and HNO<sub>3</sub> (65%) were obtained from Merck. 4-Hydroxypyridine (≥95.0%) was obtained from Fluka. Acetylene (99.8%), helium (99.98%), hydrogen (99.998%) gases were purchased from Yalız Industrial Medical Gases Inc. All other solvents and reagents were reagent grade and obtained from commercial suppliers.

### 2.2. Methods

The structures of PZS and *f*-MWCNT/PZS<sub>1:5</sub> were characterized by Nuclear Magnetic Resonance and Fourier Transform Infrared spectroscopy. Infrared spectra were recorded on a Bruker Tensor 27 spectrophotometer in the range 4000–400 cm<sup>-1</sup>, with a 2 cm<sup>-1</sup> resolution over 30 scans, using Ge ATR. <sup>31</sup>P and <sup>1</sup>H NMR spectra were recorded in CDCl<sub>3</sub> and tetrahydrofurane-*d*<sub>8</sub> solutions on a Varian 500 MHz spectrometer. Morphology of the *f*-MWCNT/PZS<sub>1:5</sub> composite was characterized using a Philips XL30 SFEG SEM and JEOL 2100 HRTEM. Gel permeation chromatography was performed with an Agilent 1100 series GPC system equipped with CHEMSTATION with the addition of 'GPC Add On' software to calculate the average molecular weights (Mw and Mn) against to polystyrene standards. Thermal properties of compounds were investigated on a Mettler Toledo TGA/SDTA 851 Thermogravimetric Analysis (TGA) equipped with METTLER TOLEDO STAR<sup>®</sup> software at

a heating rate of 10 °C min<sup>-1</sup> under nitrogen flow (50 ml min<sup>-1</sup>). The glove box (Plas Labs. 855-AC/220) was equipped with spectrograde N<sub>2</sub>. The structural analysis was performed on HORIBA Jobin-Yvon HR 800UV Raman Spectrometer. The X-ray diffraction (XRD) patterns of samples were taken at room temperature between 2 = 5–40° on a Bruker C2 X-ray diffractometer equipped with a sealed tube copper target (I<sub>Cu</sub>–k<sub>α</sub> = 1.54056 Å) and driven by Bruker GADDS software.

### 2.3. Synthesis

Poly(dichlorophosphazene) (2) was prepared by ring opening polymerization of hexachlorocyclotriphosphazatriene (1) at 250 °C in a sealed tube as described elsewhere [23,24].

### 2.4. Synthesis of poly[(4-pyridineoxy)(phenoxy)phosphazene] (3)

Phenol (1.2 g, 12.7 mmol) was dissolved in 5 mL of THF and added dropwise to a suspension of NaH (0.31 g, 12.9 mmol) in 15 mL THF and let to stir over 2 h. 4-hydroxypyridine (1.22 g, 12.8 mmol) was dissolved in 10 mL of THF and added dropwise to a suspension of NaH (0.31 g, 12.9 mmol) in 15 mL THF and let to stir over 3 h. The sodium phenoxide was added dropwise a stirring solution of poly(dichlorophosphazene) (2) (1.48 g, 12.7 mmol) in 100 mL of THF and stirred for 1 h. The sodium salt of 4-hydroxypyridine was then added dropwise and the reaction heated to reflux for 5 days. The polymer solution was then cooled to room temperature and concentrated by using rotary evaporator until becoming viscous. The polymer (3) was precipitated into 500 mL of water and washed with ultra pure water (2 × 250 mL) and ethanol (2 × 100 mL) and *n*-hexane (2 × 100 mL) respectively. Then the polymer (3) was dried in a vacuum oven for 36 h at 60 °C to yield 2.43 g (82.4%) of pale yellow solid (Anal. Calc. for [C<sub>11</sub>H<sub>9</sub>N<sub>2</sub>O<sub>2</sub>P]<sub>n</sub>: C, 56.91; H, 3.91; N, 12.07. Found: C, 56.88; H, 3.95; N, 12.02%). <sup>1</sup>H NMR (*d*<sub>8</sub>-THF) δ = 8.64 (br.s, aromatic protons). <sup>31</sup>P NMR (*d*<sub>8</sub>-THF) δ = –19 to –16 (br.m, phosphazene phosphorus). GPC: Mw = 2.32 × 10<sup>5</sup> with PDI = 2.6.

### 2.5. Synthesis of PZS

HCl<sub>(g)</sub> was generated by dropwise addition of H<sub>2</sub>SO<sub>4</sub> with a dropping funnel onto NaCl powder [25] placed in a two necked round bottomed 250 mL flask and generated HCl<sub>(g)</sub> was directly fed into the THF solution of poly[(4-pyridineoxy)(phenoxy)phosphazene] and allowed to bubble for 2 h. The protonation reaction of poly[(4-pyridineoxy)(phenoxy)phosphazene] with HCl<sub>(g)</sub> was confirmed by the precipitation of PZS in the solution.

### 2.6. Synthesis and functionalization of MWCNT

MWCNTs were synthesized by the catalytic decomposition of acetylene (C<sub>2</sub>H<sub>2</sub>) over the nickel/magnesium oxide catalyst (Ni/MgO, 5 wt% Ni). The catalyst was prepared via impregnation method from Ni(NO<sub>3</sub>)<sub>2</sub>·6H<sub>2</sub>O solution in ethanol. Supported catalyst was placed in a horizontal fixed-bed flow reactor in a quartz boat which was inserted in a quartz tube and was calcined in air at 600 °C. After the calcination, the catalyst was reduced in hydrogen flow (20 mL/min) for 2 h at 600 °C. To grow the MWCNTs, the decomposition of acetylene flow (60 mL/min) was carried out at 650 °C for 30 min, after that the reactor was cooled to room temperature under helium atmosphere and MWCNTs were collected from the quartz boat. The MWCNTs were oxidized thermally at 350 °C and sonicated in a mixture of concentrated sulfuric and nitric acid (3:1 by volume) for 24 h at 40 °C. The solution was centrifuged at 4000 rpm for 1 h and the excess of acid was removed.



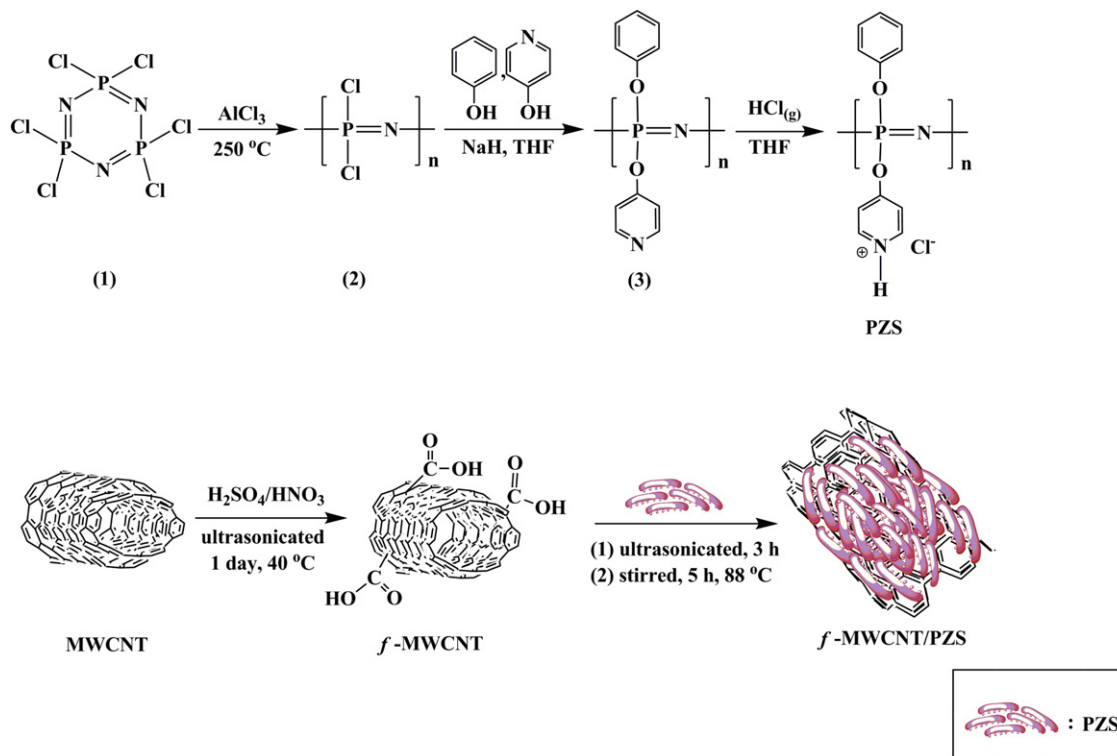


Fig. 1. Schematic formation mechanism of *f*-MWCNT/PZS nanocomposite.

The acid treated material was redispersed in ethanol to remove the acid by at least 5 times and with the help of ultrasonic bath. The *f*-MWCNTs were collected by centrifugation at 4500 rpm for 30 min and dried under vacuum overnight at 60 °C.

### 2.7. Preparation of *f*-MWCNT/PZS nanocomposites

*f*-MWCNT/PZS composites were prepared by similar synthetic procedure at different feed ratios [ $R_{\text{feed}} = 1:1; 1:3; 1:5; 1:10$  (w/w)] of the PZS. In a typical experiment *f*-MWCNTs and PZS were placed in a 50 mL round bottomed flask in dichloroethene. The mixture was treated with an ultrasonic bath for 3 h and then placed on a magnetic stirrer with an oil bath. The reaction mixture was then heated and maintained around 88 °C for 5 h. After cooling to room temperature the product was isolated by precipitation into acetone. The resulting precipitates were redispersed in acetone with the aid of an ultrasonic bath and then collected by centrifugation. This centrifugation was repeated until the upper layer was nearly colorless. The separated solid was sequentially redispersed in water and dichloromethane and purified by at least 5 centrifugation cycles. All these centrifugations were performed at a rotation speed of 4500 rpm for 1 h. The supernatant was decanted and the black solid was dried under vacuum at 60 °C overnight to give *f*-MWCNT/PZS composite.

## 3. Results and discussion

Diverse strategies designed to functionalize CNTs continuously emerge, such as end and defect-chemistry [26], endohedral functionalization [27], ionic chemistry (doping) [28], covalent sidewalls functionalization [29,30], noncovalent functionalization [31] and ionic functionalization [32]. In this study the ionic functionalization has been preferred over other strategies, depending on the following advantages. For example ionic functionalization approach generally gives much higher yield than the covalent

functionalization approach [33]. Furthermore the presence of ionic interactions can significantly improve the solubility of *f*-MWCNTs [34,35]. And also the acid–base reaction represents the simplest possible route to soluble MWCNTs and can be readily scaled-up at low cost. Unlike the covalent amide bond, the cation PZS in the ionic bond of *f*-MWCNT/PZS composite can be easily exchanged with other organic or inorganic cations. Thus it is possible to adjust the solubility of the MWCNTs and use soluble *f*-MWCNTs as versatile building blocks for advanced MWCNT-based materials. Furthermore, such ionic feature may allow electrostatic interactions between MWCNTs and PZS and serve as the basis for direct methanol fuel cells because interactions between polymer and CNT may enable homogeneous distribution of the CNT [8,36,37].

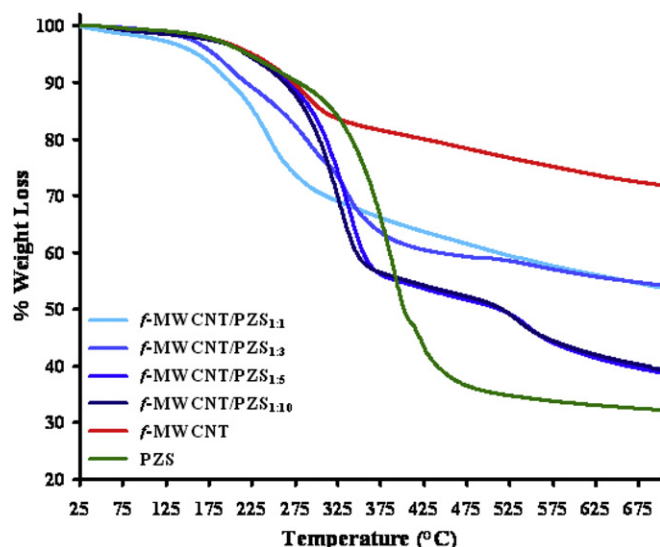


Fig. 2. TGA results of PZS, *f*-MWCNT and *f*-MWCNT/PZS composites.



Linear type poly(organophosphazene)s are synthesized by three principal routes [24]. First route is the reaction of organophosphorus halides with ammonium halides or metal azide. The polymers produced by this method generally contained very low number of monomer units. The second and third routes involve both the thermal ring opening polymerization and condensation reactions. The second route is the thermal polymerization of hexachlorocyclotriphosphazene ( $\text{NPCl}_2$ )<sub>3</sub>, to hydrolytically unstable, high molecular weight polydichlorophosphazene,  $[\text{NPCl}_2]_n$ , followed by replacement of the halogen atoms in the polymer by organic groups. Within the third route polymerization of cyclic organophosphazene trimers and tetramers are carried out under similar conditions with route two. By this route open-chain low molecular weight polymers have been prepared. Hence, poly(dichlorophosphazene) (2) have been prepared by the second route to obtain high molecular weight polymer. Poly[(4-pyridineoxy)(phenoxy)phosphazene] (3) has been prepared by sequential treatment of poly(dichlorophosphazene) (2) with sodium phenoxide and sodium salt of 4-hydroxypyridine in THF. We have chosen phenoxide, a bulky aromatic hydrophobic group as a substituent to enhance  $\pi$ - $\pi$ -interaction between the polymer and *f*-MWCNT and also as to impart flexibility [24]. 4-hydroxypyridine have been chosen to impart ionic interaction between protonated poly(organophosphazene) (PZS) and *f*-MWCNT. All *f*-MWCNT/PZS composites were prepared according to Fig. 1 with selected feed ratio of the PZS.

Thermal gravimetric analysis (TGA) is extensively used method to determine the percentage of organic groups in the functionalized CNTs [38]. The thermal stability of *f*-MWCNT, PZS and all *f*-MWCNT/PZS composites were investigated by determining the weight loss of a sample upon linearly increasing the temperature by conventional TGA at a heating rate of 10 °C/min up to 700 °C under nitrogen flow (Fig. 2). TGA curve of *f*-MWCNT shows ~20% initial decomposition between 220 and 320 °C, which can be attributed to the loss of -COOH functionality. The calculation of weight loss at this temperature range (220–320 °C) gives ~52 -COOH groups per

1000 C atoms. TGA curve of PZS shows a preliminary decomposition between the 220–270 °C with a 12% weight loss. This low temperature decomposition can be attributed to the loss of HCl moiety bonded to quaternary nitrogen atom of 4-hydroxypyridine groups on the PZS chain which gives a ratio of 0.75 HCl group per repeating monomer unit. However, under vigorous reaction conditions higher protonation of PZS could not be achieved more than 0.75 HCl per monomer unit (the reason can be the insolubility of the precipitated polymer form the THF solution). Further heating of PZS gives main decomposition in two steps between 320 and 450 °C and this is in the expected decomposition temperature range of poly(aryloxyphosphazenes) [20]. Thermal decomposition of the prepared materials varies by the supplied PZS ratio in the *f*-MWCNT/PZS composites which can be related to the interaction between the *f*-MWCNT and PZS. For eg., when the *f*-MWCNT and PZS supplied in a 1:1 (w/w) ratio, the resulting material [*f*-MWCNT/PZS<sub>1:1</sub>] has one step decomposition from 100 °C to 300 °C in a similar tendency but lower decomposition temperatures that we observe for *f*-MWCNT. The thermal stability of *f*-MWCNT/PZS<sub>1:3</sub> is better than the *f*-MWCNT/PZS<sub>1:1</sub> but still lower than the starting materials. However, thermal stability of the *f*-MWCNT/PZS<sub>1:5</sub> is better than the lower feed ratios and shows similar thermal decomposition character of parent materials and decomposition temperature increases to 270–360 °C range. As expected increasing the feed ratio of PZS after a certain limit does not affect the thermal behavior of the resulting material due to the followed synthetic procedure which includes washing, centrifugation and drying. Hence there is no major thermal behavior difference between the *f*-MWCNT/PZS<sub>1:5</sub> and *f*-MWCNT/PZS<sub>1:10</sub>. When the percent weight loss of all the samples calculated roughly between 25 and 500 °C are evaluated together by considering PZS and *f*-MWCNT as part of *f*-MWCNT/PZS composites it can be seen that *f*-MWCNT/PZS<sub>1:5</sub> and *f*-MWCNT/PZS<sub>1:10</sub> have ~1:3(w/w) composition ratio in the beginning of TGA experiment. Therefore at the beginning of the preparation reaction at least 1:5 (w/w) feed ratio should be used to ensure better interaction and thermal stability of designed

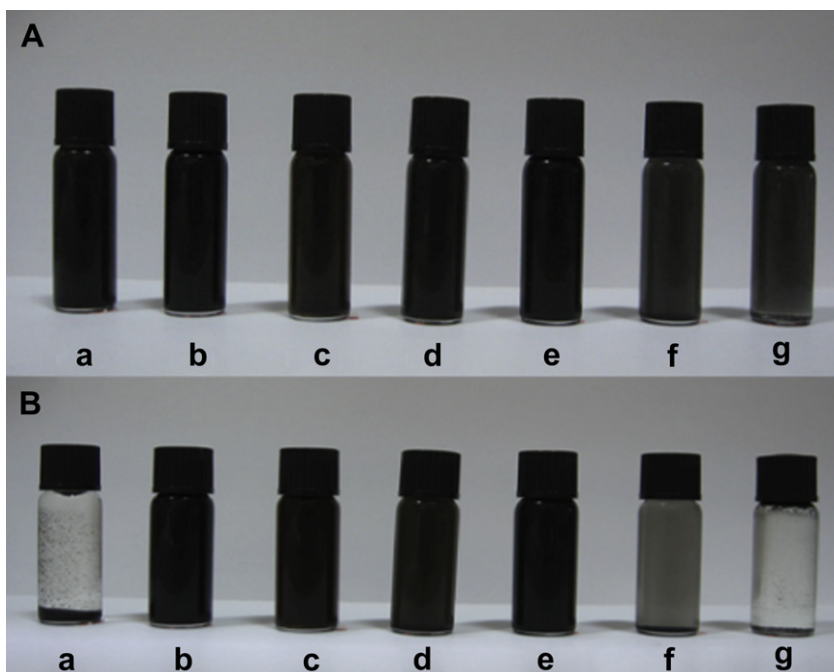


Fig. 3. Photographs of *f*-MWCNT/PZS<sub>1:5</sub> nanocomposite (A) after ultrasonication, (B) after 3 weeks, in seven different solvents: (a) acetone (b) water (c) tetrahydrofuran (d) N,N-dimethylformamide (e) dimethyl sulfoxide (f) 1,2-dichloroethane (g) chloroform.

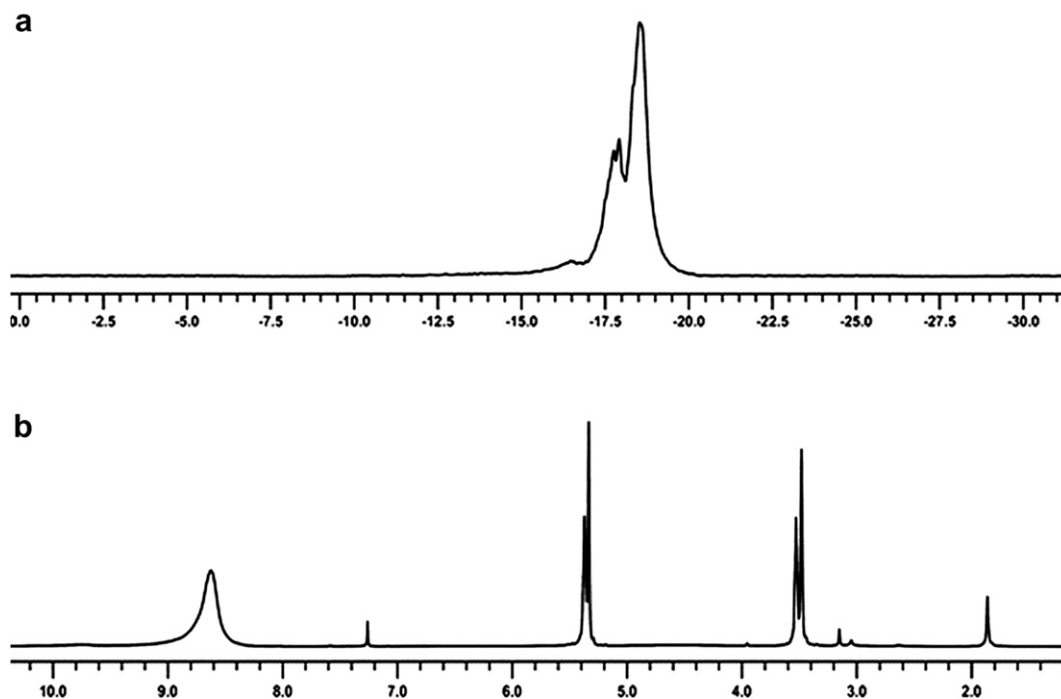


Fig. 4. (a)  $^{31}\text{P}$  NMR, (b)  $^1\text{H}$  NMR spectra of *f*-MWCNT/PZS<sub>1.5</sub> in  $d_8$ -THF.

composite. Thus *f*-MWCNT/PZS<sub>1.5</sub> has been selected for the structural characterization of composite because it combines the given properties.

The solubility test shows that the *f*-MWCNT/PZS nanocomposites are soluble in common solvents such as tetrahydrofuran, *N,N*-dimethylformamide, dimethyl sulfoxide, and water. It is well known that the solubility of poly(organophosphazenes) depend mainly on the nature of the side groups [24] and the high efficiency of the polymeric dispersing agent can be achieved on the basis of structural optimization of the macromolecule. Hence, the surface of *f*-MWCNT is wrapped with poly(organophosphazene) (PZS) possessing hydrophilic protonated pyridine groups. The hydrophobic part of the chain (phenoxide groups) is bound to the CNT surface via intermolecular interactions and provides solubility in organic solvents, while the hydrophilic parts provide solubility in polar

organic solvents and water. Solution of *f*-MWCNT/PZS<sub>1.5</sub> composite in different solvents such as acetone, deionized water, tetrahydrofuran, *N,N*-dimethylformamide, dimethyl sulfoxide, 1,2-dichloroethene and chloroform with same concentration (5 mg/mL) was prepared. *f*-MWCNT/PZS<sub>1.5</sub> composite was dispersed in each solvent by sonication in an ultrasonic bath for 10 min (Fig. 3a). After 3 weeks from the preparation, the *f*-MWCNT/PZS solutions showed great solubility in tetrahydrofuran, *N,N*-dimethylformamide, dimethyl sulfoxide, and water while the *f*-MWCNT/PZS<sub>1.5</sub> was less soluble in 1,2-dichloroethene and not soluble in chloroform and acetone (Fig. 3b).

Since *f*-MWCNT/PZS<sub>1.5</sub> has good solubility in tested solvents, the structure of *f*-MWCNT/PZS<sub>1.5</sub> is investigated by NMR spectroscopy. The  $^{31}\text{P}$  NMR spectrum of *f*-MWCNT/PZS<sub>1.5</sub> clearly shows that there is only one phosphorus resonance in the spectrum which is in the expected resonance region of poly(aryloxyphosphazene)s [39] (Fig. 4a). The aromatic hydrogen resonance of both pyridine and

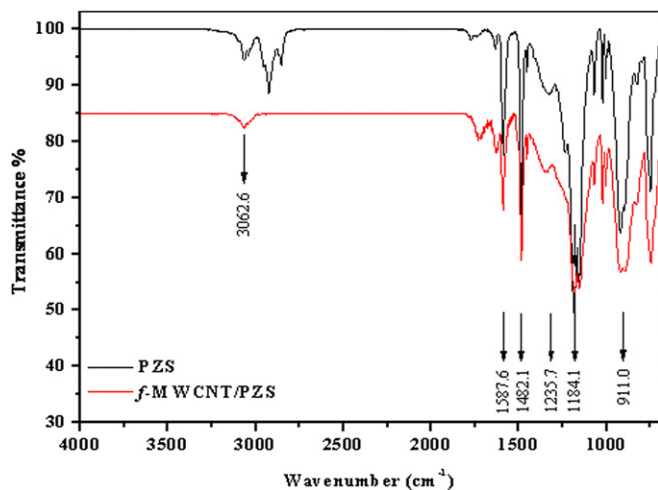


Fig. 5. FTIR spectra of PZS and *f*-MWCNT/PZS<sub>1.5</sub>.

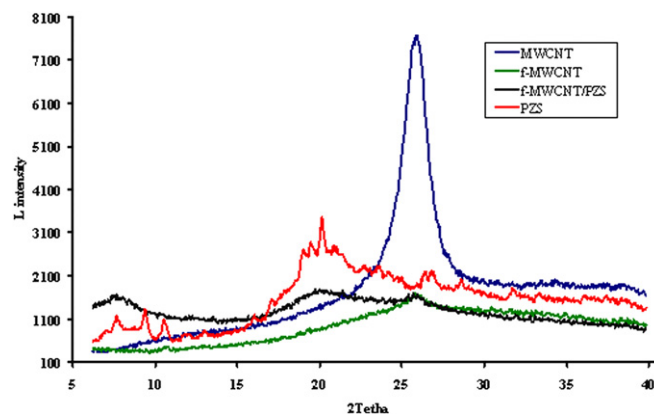


Fig. 6. The X-ray diffraction patterns of the MWCNT, *f*-MWCNT, *f*-MWCNT/PZS<sub>1.5</sub> and PZS.

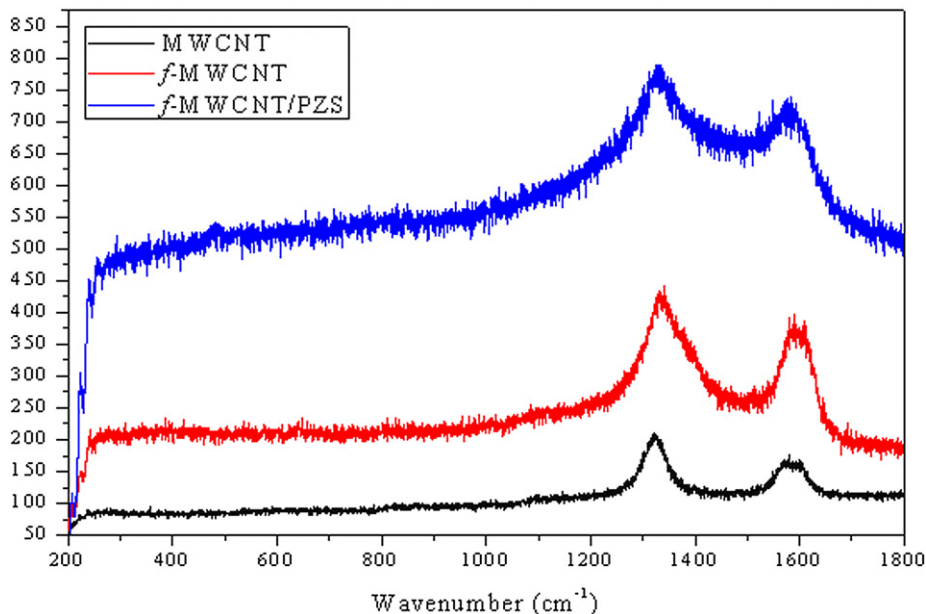


Fig. 7. Raman spectra of MWCNT, *f*-MWCNT and *f*-MWCNT/PZS<sub>1.5</sub>.

phenoxy groups of PZS units are clearly observed as overlapping broad resonance in 8.6–9.0 ppm region in the <sup>1</sup>H NMR spectrum (Fig. 4b).

The FTIR spectra of PZS and *f*-MWCNT/PZS<sub>1.5</sub> can be seen in Fig. 5. FTIR spectrum of *f*-MWCNT/PZS<sub>1.5</sub> shows the structural features of phosphazene, phenylene and P–O–Ph moieties in the PZS. Comparing these two curves, the strong absorptions at 1587.6

and 1482.1 cm<sup>-1</sup> are attributed to the vibrations of the benzene ring skeleton. The characteristic peaks centered at 1235.7, 1184.1 and 911.0 cm<sup>-1</sup> correspond to C–O–C, P=N and P–O–Ph respectively. The characteristic absorption peak located at 3062.6 cm<sup>-1</sup> can be indexed to aromatic C–H moieties.

The X-ray diffraction patterns of the MWCNT, *f*-MWCNT, *f*-MWCNT/PZS<sub>1.5</sub> and PZS polymer are represented on Fig. 6. The

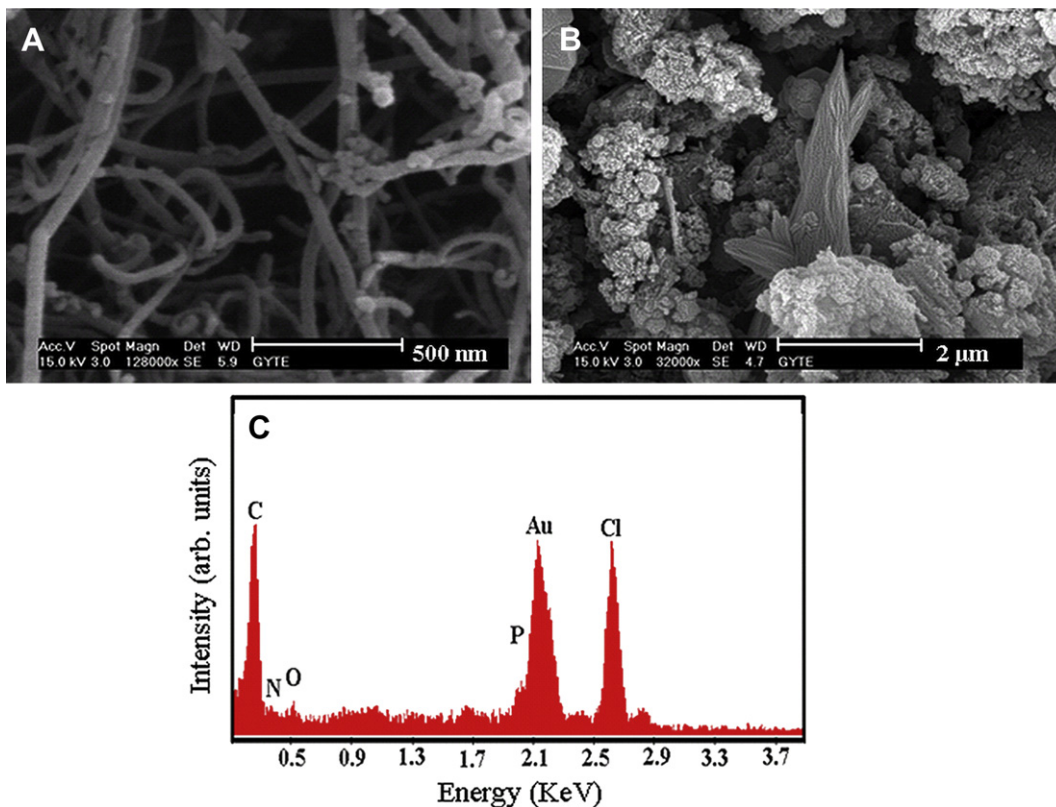


Fig. 8. SEM images of (A) *f*-MWCNT, (B) *f*-MWCNT/PZS<sub>1.5</sub>, (C) EDX analysis of *f*-MWCNT/PZS<sub>1.5</sub> nanocomposite.



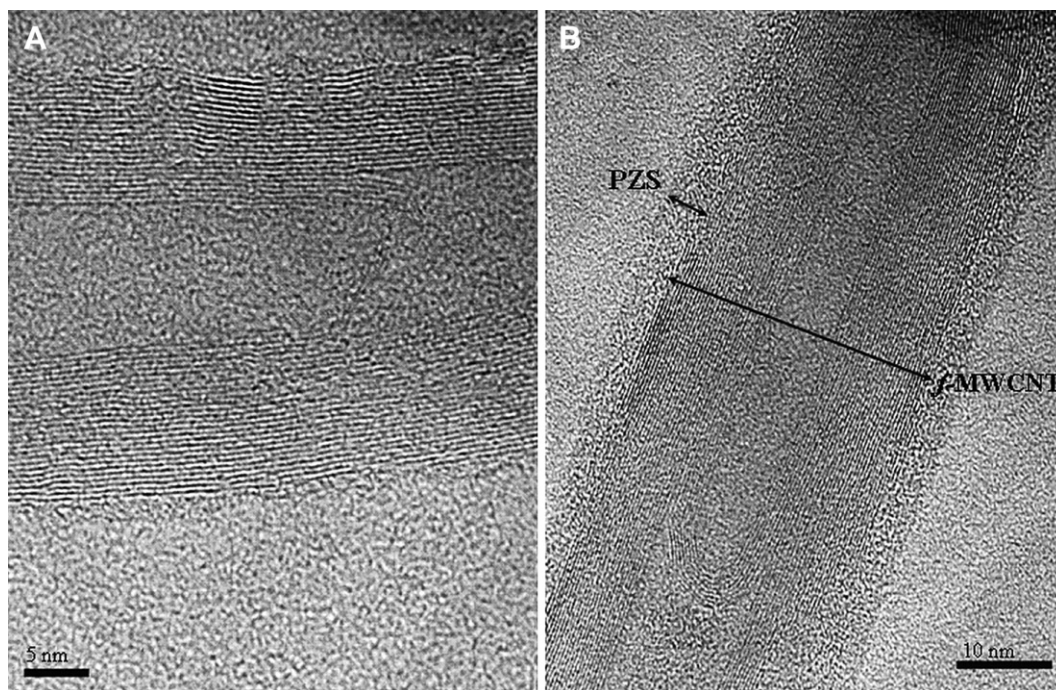


Fig. 9. HRTEM images of (A) MWCNT, (B) *f*-MWCNT/PZS<sub>1.5</sub> nanocomposite.

typical peak of MWCNT structure centered at  $2\theta = 26^\circ$  is clearly observed and the influence of acid treatment and polymer attachment of *f*-MWCNT and *f*-MWCNT/PZS<sub>1.5</sub> composite. After functionalization process, *f*-MWCNT exhibits a broad and low peak situated at  $2\theta = 26^\circ$ , corresponding to low structural organization carbons as expected [40,41]. Hence, we can say attachment of  $-\text{COOH}$  functional groups on the surface of nanotube have created disorder. This peak also indicates that the interplanar distance is about 0.342 nm. The PZS polymer shows two low and broad peaks at  $2\theta = 7^\circ$  and  $2\theta = 20^\circ$ . *f*-MWCNT/PZS<sub>1.5</sub> sample shows the characteristics of parent (PZS and *f*-MWCNT) compounds. Indeed, it exhibits three broad peaks situated at  $2\theta = 7^\circ$ ,  $20^\circ$  and  $26^\circ$ .

The Raman spectra of MWCNT, *f*-MWCNT and *f*-MWCNT/PZS<sub>1.5</sub> composite are represented on Fig. 7. MWCNT exhibits two peaks at  $1345\text{ cm}^{-1}$  and  $1580\text{ cm}^{-1}$ . The first peak situated at  $1345\text{ cm}^{-1}$  is identified as D band and is assigned to disordered structures. The second peak, centered at  $1580\text{ cm}^{-1}$  is identified as G band and is assigned to the active  $\text{E}_{2g}$  vibration of graphite [42]. By determining the intensity ratio between these two bands ( $I_{1350}/I_{1580}$ ), a quantitative measure of defect density in the CNT sidewall can be determined [42]. The Raman spectrum of *f*-MWCNT indicates that the *f*-MWCNT have long-range order with defect sites along the sidewall. The Raman spectrum of the *f*-MWCNT/PZS<sub>1.5</sub> nanocomposite shows that D band is displaced to  $1325\text{ cm}^{-1}$  and the G band is displaced to  $1590\text{ cm}^{-1}$ . It is interesting to notice that the intensity ratio of the D and G bands is increased after the formation of composite material. This result may indicate that the formation of defect sites on the sidewalls and the enveloping of the polymer on nanotube surface as observed on XRD pattern on Fig. 6. The peaks of RBM mode have appeared for two samples between  $210\text{ cm}^{-1}$  and  $240\text{ cm}^{-1}$ .

The morphological characterizations were carried out by HRTEM and SEM methods. The SEM image of *f*-MWCNT (Fig. 8A) shows homogeneously distributed nanotubes. The diameter of nanotubes varies between 25 and 30 nm. The SEM image of *f*-MWCNT/PZS<sub>1.5</sub> (Fig. 8A) shows that the nanotubes are enveloped

by the PZS. Hence the mean diameter of the nanotubes increased to 35 nm in the nanocomposite material. Comparison of Fig. 8A and B illustrates that a film of polymer is deposited homogeneously on the nanotube surface. Energy-dispersive X-ray (EDX) analysis shows that *f*-MWCNT/PZS<sub>1.5</sub> nanocomposite possess an identical composition with PZS whereas the nanotubes are composed of carbon and oxygen (Fig. 8C).

HRTEM micrographs of the MWCNT and *f*-MWCNT/PZS<sub>1.5</sub> are shown in Fig. 9. Measured MWCNT diameter is 28.3 nm, and the internal diameter is about 5.8 nm in Fig. 9A. However, it is clearly observed that PZS shell uniformly covered the *f*-MWCNT surface with the shell thickness of 3.3–4.7 nm and the lengths of several micrometers in Fig. 9B. Hence, it is obvious that for surface modification of MWCNT using PZS is quite effective.

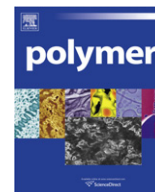
#### 4. Conclusion

In conclusion, poly(organophosphazene)s are very attractive candidate for an advanced dispersing agent of carbon nanotubes because of the synthetic advantages allowing to control their hydrophilic-hydrophobic balance by variation of side groups. *f*-MWCNT/PZS composites with different mass ratios have been fabricated. Comparative TGA experiments showed that when feed ratio of PZS has been increased the thermal stability of the composite increased until  $R_{\text{feed}} = 1:5$  (w:w). The maximum coating result of the polymer have been reached at  $R_{\text{feed}} = 1:5$  (w:w). Based on the structural and morphological analysis of the composite material (*f*-MWCNT/PZS<sub>1.5</sub>), we have succeeded in evenly coating poly(organophosphazene) (PZS) onto the *f*-MWCNT surface. We have demonstrated that functionalized multi-walled carbon nanotubes (*f*-MWCNT) can be soluble in common organic solvents and water. Solubility of the *f*-MWCNT/PZS composite material driven by the ionic interaction between the  $-\text{COO}^-$  and  $^+\text{NHR}_2$  (quaternary pyridine) groups bonded to *f*-MWCNT surface and PZS polymer respectively. It should be noted that the solubility of *f*-MWCNT/PZS composite appears to be promising candidates for applications in fuel cells and solar cells.

## References

- [1] Dresselhaus MS, Dresselhaus G, Avouris P. Carbon nanotubes: synthesis, structure, properties and applications. Springer-Verlag; 2001.
- [2] Coleman JN, Khan U, Blau WJ, Gun'ko YK. Carbon 2006;44:1624–52.
- [3] Avouris P. Acc Chem Res 2002;35:1026–34.
- [4] Wang J. Electroanal 2005;17:7–14.
- [5] Baughman RH, Zakhidov AA, de Heer WA. Science 2002;297:787–92.
- [6] Bianco A, Kostarelos K, Partidos CD, Prato M. Chem Commun; 2005:571–7.
- [7] Breuer O, Uttandaraman S. Polym Compos 2004;25(6):630–45.
- [8] O'Connell MJ. Carbon nanotubes properties and applications. Taylor & Francis; 2006 [chapter 8].
- [9] Mark JE, Allcock HR, West R. Inorganic polymers. New Jersey: Prentice Hall, Englewood Cliffs; 1992 [chapter 3].
- [10] Greish YE, Bender JD, Lakshmi S, Brown PW, Allcock HR, Laurencin CT. Biomaterials 2005;26(1):1–9.
- [11] Kim JK, Toti US, Song R, Sohn YS. Bioorg Med Chem Lett 2005;15(15):3576–9.
- [12] Orme CJ, Stewart FF. J Membr Sci 2005;253(1–2):243–9.
- [13] Morales E, Acosta J L. Solid State Ionics 1997;96(1–2):99–106.
- [14] Allcock HR, Welker MF, Parvez M. Chem Mater 1992;4(2):296–307.
- [15] Guglielmi M, Brusatin G, Facchin G, Gleria M. Appl Organomet Chem 1999;13(5):339–51.
- [16] Fu J, Huang X, Huang Y, Zhang J, Tang X. Chem Commun 2009;9:1049–51.
- [17] Zhang P, Huang X, Fu J, Huang Y, Tang X. Macromol Mater Eng 2010;295(5):437–41.
- [18] Park HJ, Heo HY, Lee SC, Park M, Lee SS, Kim J, et al. J Inorg Organomet Pol Mater 2006;16(4):359–64.
- [19] Liu J, Rinzler AG, Dai H, Hafner JH, Bradley RK, Boul PJ, et al. Science 1998;280:1253–6.
- [20] Zhao W, Song C, Pehrsson PE. J Am Chem Soc 2002;124:12418–9.
- [21] Hiura H, Ebbesen TW, Tanigaki K. Adv Mater 1995;7(3):275–6.
- [22] Mickelson ET, Chiang IW, Zimmerman JL, Boul PJ, Lozano J, Liu J, et al. J Phys Chem B 1999;103:4318–22.
- [23] Sohn YS, Cho YH, Baek H, Jung OS. Macromolecules 1995;28(22):7566–8.
- [24] Allcock HR. Chemistry and applications of polyphosphazenes. New Jersey: Wiley-Interscience; 2003.
- [25] Francisco JA. J Chem Ed 1995;72(12):1139–46.
- [26] Banerjee S, Hemraj-Benny T, Wong SS. Adv Mater 2005;17(1):17–29.
- [27] Hirsch A. Angew Chem. Int Ed 2002;41(11):1853–9.
- [28] Niyogi S, Hamon MA, Hu H, Zhao B, Bhowmik P, Sen R, et al. Acc Chem Res 2002;35(12):1105–13.
- [29] Blake R, Gun'ko YK, Coleman J, Cadek M, Fonseca A, Nagy JB, et al. J Am Chem Soc 2004;126:10226–7.
- [30] Liang F, Sadana AK, Peera A, Chattopadhyay J, Gu ZN, Hauge RH, et al. Nano Lett 2004;4(7):1257–60.
- [31] Holzinger M, Abbramo J, Whelan P, Graupner R, Ley L, Hennrich F, et al. J Am Chem Soc 2003;125(28):8566–80.
- [32] Hamon MA, Chen J, Hu H, Chen Y, Itkis ME, Rao AM, et al. Adv Mater 1999;11(10):834–40.
- [33] Chen J, Hamon MA, Hu H, Chen Y, Rao AM, Eklund PC, et al. Science 1998;282:95–8.
- [34] Chattopadhyay D, Lastella S, Kim S, Papadimitrakopoulos F. J Am Chem Soc 2002;124(5):728–9.
- [35] Chattopadhyay D, Galeska I, Papadimitrakopoulos F. J Am Chem Soc 2003;125(11):3370–5.
- [36] Hacivelioglu F, Ozden S, Unugur Celik S, Yesilot S, Kilic A, Bozkurt A. J Mater Chem 2011;21:1020–7.
- [37] Joo SH, Pak C, Kim EA, Lee YH, Chang H, Seung D, et al. J Power Sources 2008;180:63–70.
- [38] Kong H, Gao C, Yan DY. Macromolecules 2004;37(11):4022–30.
- [39] Takegoshi K, Tanaka I, Hikichi K, Higashida S. Macromolecules 1992;25:3392–8.
- [40] Onyestyák Gy, Valyon J, Hernadi K, Kiricsi I, Rees LVC. Carbon 2003;41(6):1241–8.
- [41] Reznik D, Olk CH, Neumann DA, Copley JRD. Phys Rev B 1995;52(1):116–24.
- [42] Wepasnick KA, Smith BA, Bitter JL, Fairbrother HD. Anal Bioanal Chem 2010;396:1003–14.





# Dietheramine from an alkaline-stable phosphinated bisphenol for soluble polyetherimides

Ching Hsuan Lin\*, Sheng Lung Chang, Po Wen Cheng

Department of Chemical Engineering, National Chung Hsing University, Taichung 402, Taiwan

## ARTICLE INFO

### Article history:

Received 16 September 2010

Received in revised form

7 January 2011

Accepted 18 January 2011

Available online 25 January 2011

### Keywords:

Polyetherimide

Phosphinate

Phosphorus

## ABSTRACT

This study focuses on economic preparation of a phosphinated dietheramine for soluble polyetherimides. For this purpose, a phosphinated dietheramine, 1,1-bis(4-(4-aminophenoxy)phenyl)-1-(6-oxido-6H-dibenz <c,e> <1,2> oxaphosphorin-6-yl)ethane (**3**), was prepared from the nucleophilic substitution of an alkaline-stable biphenol, 1,1-bis(4-hydroxyphenyl)-1-(6-oxido-6H-dibenz <c,e> <1,2> oxaphosphorin-6-yl)ethane (**1**), with 4-chloronitrobenzene using inexpensive potassium carbonate as catalyst, followed by catalytic hydrogenation. Light color, and foldable polyetherimides (PEIs) with good thermal stability, improved organo-solubility, and good flame retardancy were synthesized from the condensation of (**3**) with various aromatic dianhydrides in DMAc, followed by thermal imidization. Properties of the resulting PEIs were evaluated and compared with those of PEIs based on a commercially available dietheramine, 2,2-bis(4-(4-aminophenoxy)phenyl) propane (BAPP). The  $T_g$ s of the resulting PEIs range from 271 °C to 314 °C by dynamic mechanical analysis. The degradation temperatures ( $T_d$  5%) range from 453 to 467 °C in  $N_2$  atmosphere, and 435–451 °C in air atmosphere. The resulting PEIs also show good flame retardancy.

© 2011 Elsevier Ltd. All rights reserved.

## 1. Introduction

Due to the high glass transition temperature, high thermal stability and good mechanical properties, aromatic polyimides are widely applied in electronics and composites [1–8].

However, aromatic polyimides (PIs) are difficult to process due to their poor solubility in organic solvents. It has been reported that incorporating bulky pendants [9–13] in PIs can enhance the organo-solubility without sacrificing  $T_g$ .

According to this principle, we developed phosphinated PIs [14] with  $T_g$  as high as 392 °C. However, although a bulky phosphinate pendent was present, the organo-solubility of the resulting PIs was not good. Very recently [15], we developed asymmetric phosphinated PIs with high  $T_g$  and excellent solubility. However, due to the intramolecular charge transfer interaction between the alkyl and phosphorus, the asymmetric PIs showed unexpected darker color, limiting their applications.

It is well known that PIs with flexible ether linkages can impart good solubility and lighter color [16–18]. In our another work [19], we reported a phosphinated PIs based on a dietheramine, 1,4-bis(4-aminophenoxy)-2-(6-oxido-6H-dibenz <c,e> <1,2> oxaphosphorin-6-yl) phenylene (**3'**) (Fig. 1), which was prepared by the nucleophilic aromatic substitution of 2-(6-oxido-6H-dibenz <c,e>

<1,2> oxaphosphorin-6-yl)-1,4-dihydroxy phenylene (**1'**) with 4-fluoronitrobenzene, followed by catalytic hydrogenation. However, due to cleavage of P–Ar bond at alkaline condition, the catalyst for the nucleophilic substitution is limited to cesium fluoride, which is very expensive compared with common inorganic bases such as potassium carbonate. The expensive catalyst prohibits the application potential of the resulting PIs. In addition, the nucleophilic substitution did not succeed unless 4-fluoronitrobenzene, instead of 4-chloronitrobenzene, was selected as reactant. It is known that the former exhibits higher reactivity, but is much more expensive than the latter. As shown in Fig. 1, the reactivity of one phenol group of (**1'**) was reduced due to the steric hindrance and electro-withdrawing P=O bond of the ortho-substituted phosphinate pendent, so the nucleophilic substitution of biphenol (**1'**) did not occur when using less reactive 4-chloronitrobenzene. To reduce the steric hindrance of phenol group, the phosphinate pendent must be distanced from the phenol groups. In our recent work, we developed a new phosphinated biphenol, 1,1-bis(4-hydroxyphenyl)-1-(6-oxido-6H-dibenz <c,e> <1,2> oxaphosphorin-6-yl)ethane (**1**). As shown in Fig. 1, the two phenol groups of (**1**) were distanced from the phosphinate pendent, so less steric hindrance and higher reactivity for the nucleophilic substitution is expected.

Here, continuing our work in organo-soluble, flame-retardant phosphinated PIs, a phosphinated dietheramine, 1,1-bis(4-(4-aminophenoxy)phenyl)-1-(6-oxido-6H-dibenz <c,e> <1,2> oxaphosphorin-6-yl)ethane (**3**), was economically prepared from the

\* Corresponding author. Tel.: +886 4 22850180; fax: +886 4 2285 4734.  
E-mail address: [linch@nchu.edu.tw](mailto:linch@nchu.edu.tw) (C.H. Lin).

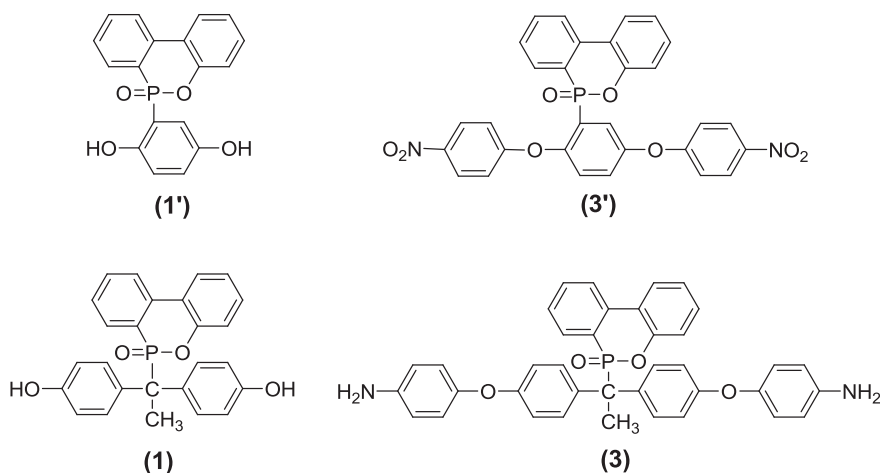


Fig. 1. Structures of (1'), (1), (3') and (3).

nucleophilic aromatic substitution of (1) with 4-chloronitrobenzene using inexpensive potassium catalyst as catalyst, followed by catalytic hydrogenation. Base on dietheramines (3), a series of phosphinated PEIs (5) were prepared. The chemical structures, solubility, crystallinity, thermal properties, and thermal stability of the PEIs were investigated and compared with those of PEIs based on a commercially available dietheramine, 2,2-bis[4-(4-amino-phenoxy)phenyl] propane (BAPP), which exhibits a similar structure with (3) except for the phosphinate pendent.

## 2. Experimental

### 2.1. Materials

(1) was prepared according to a published procedure [20]. Potassium carbonate 10% palladium on carbon (Pd/C, from Acros), 4-chloronitrobenzene (from Acros), 2,2-bis(4-(4-amino-phenoxy)phenyl)propane (BAPP) (from Chriskev) and calcium hydride (from Acros) were used as received. Pyromellitic dianhydride (PMDA, from Acros) was dried at 170 °C overnight before use. 3,3',4,4'-Benzophenonetetracarboxylic dianhydride (BTDA, from Acros), 4,4'-oxydiphthalic anhydride (ODPA, from Chriskev), and 3,3',4,4'-biphenyltetracarboxylic dianhydride (BPDA, from Chriskev) were recrystallized from acetic anhydride. *N,N*-dimethylacetamide (DMAc, from TEDIA) was purified by distillation under reduced pressure over calcium hydride (from Acros) and stored over molecular sieves. The other solvents used are commercial products (HPLC grade) and used without further purification.

### 2.2. Characterization

NMR measurements were performed using a Varian Inova 600 NMR in DMSO- $d_6$ , and the chemical shift was calibrated by setting the chemical shift of DMSO- $d_6$  as 2.49 ppm. The assignment of individual peak of (2–3) is assisted by the correlations shown in the  $^1\text{H}$ – $^1\text{H}$  COSY and  $^1\text{H}$ – $^{13}\text{C}$  HETCOR NMR spectra. IR Spectra were measured by Perkin–Elmer RX1 infrared spectrophotometer. High-resolution mass (HRMS) measurements were performed by a Finnigan/Thermo Quest MAT 95XL mass spectrometer by fast atom bombardment. Elemental analysis was performed on an Elementar Vario EL III. Wide-angle X-ray diffraction measurements were performed at room temperature by a MAC Science DMAX2000 X-ray diffractometer with monochromatic Cu K $\alpha$  radiation ( $\lambda = 1.5418 \text{ \AA}$ , operating at 40 kV and 30 mA). The scanning rate was 3°/min over a range of  $2\theta = 5$ – $40^\circ$ . The stress–strain behavior of the polyimides

was characterized by an EZ tester at room temperature with film specimens of 0.5 cm wide, 6 cm long and about 25  $\mu\text{m}$  in thickness. Differential scanning calorimeter (DSC) scans were obtained by a Perkin–Elmer DSC 7 in a nitrogen atmosphere at a heating rate of 20 °C/min.  $T_g$  was taken as the midpoint of the heat capacity transition between the upper and lower points of deviation from the extrapolated liquids and glass lines. Dynamic mechanical analysis (DMA) was performed by a Perkin–Elmer Pyris Diamond DMA at a heating rate of 5 °C/min. Thermo mechanical analysis (TMA) was performed by a SII TMA/SS6100 at a heating rate of 5 °C/min. Thermal gravimetric analysis (TGA) was performed by a Seiko Exstar 600 at a heating rate of 20 °C/min in a nitrogen or air atmosphere. Flame retardancy of polyimides was performed by a UL-94VTM vertical thin test. In that test, an 8"  $\times$  2" sample was wrapped around a 1/2" mandrel, and then taped on one end. The mandrel was removed, leaving a cone-shaped sample that was relatively rigid. The two flame applications were 3 s instead of 10 s. After the first ignition, the flame was removed and the time for the polymer to self-extinguish ( $t_1$ ) was recorded. Cotton ignition was noted if polymer dripping occurred during the test. After cooling, the second ignition was performed on the same sample and the self-extinguishing time ( $t_2$ ) and dripping characteristics were recorded. If  $t_1$  plus  $t_2$  was less than 10 s without any dripping, the polymer was considered to be a VTM-0 material. If  $t_1$  plus  $t_2$  was in the range of 10–30 s without any dripping, the polymer was considered to be a VTM-1 material.

### 2.3. Synthesis of (2)

To a round-bottom 100 mL glass flask equipped with a nitrogen inlet, a condenser and a magnetic stirrer, (1) 10.0 g (23.3 mmol), 4-chloronitrobenzene 7.25 g (51.4 mmol), potassium carbonate 6.45 g (47 mmol) and DMAc 46 mL were introduced. The reaction mixture was heated to 120 °C and maintained at that temperature for 12 h. Then, the reaction mixture was filtered, and the filtrate was poured into 450 mL of ethanol/water (1/2, V/V) solution under stirring. The precipitate was filtered and recrystallized from acetic anhydride, and then dried in a vacuum oven at 110 °C. Light yellow crystals 8.61 g (55% yield) were obtained. HR-MS(EI)  $m/z$ : calcd. for  $\text{C}_{38}\text{H}_{27}\text{O}_8\text{N}_2\text{P}$  670.1505; anal., 670.1509 for  $\text{C}_{38}\text{H}_{27}\text{O}_8\text{N}_2\text{P}$ . FTIR (KBr): 920  $\text{cm}^{-1}$  (P–O–Ph), 1203  $\text{cm}^{-1}$  (P=O), 1339  $\text{cm}^{-1}$  ( $\text{NO}_2$  symmetric stretch), 1543  $\text{cm}^{-1}$  ( $\text{NO}_2$  asymmetric stretch), 1591  $\text{cm}^{-1}$  (P–Ph).  $^1\text{H}$  NMR (ppm, DMSO- $D_6$ ),  $\delta = 1.82$  (3H,  $\text{H}^1$ ), 7.00 (2H,  $\text{H}^{17}$ ), 7.03 (2H,  $\text{H}^{17}$ ), 7.06 (2H,  $\text{H}^{20}$ ), 7.08 (2H,  $\text{H}^{20}$ ), 7.17 (1H,  $\text{H}^{13}$ ), 7.20 (1H,  $\text{H}^{11}$ ), 7.38 (1H,  $\text{H}^{12}$ ), 7.40 (1H,  $\text{H}^7$ ), 7.41 (2H,  $\text{H}^{16}$ ), 7.47 (1H,  $\text{H}^6$ ), 7.49 (2H,  $\text{H}^{16}$ ), 7.75 (1H,  $\text{H}^5$ ), 8.06 (1H,  $\text{H}^{10}$ ), 8.26 (2H,  $\text{H}^{21}$ ), 8.29 (2H,  $\text{H}^{21}$ ).  $^{13}\text{C}$

NMR (ppm, DMSO- $D_6$ ),  $\delta = 24.39$  ( $C^1$ ), 52.94 ( $C^2$ ), 117.49 ( $C^{20,20'}$ ), 119.06 ( $C^{13}$ ), 119.72 ( $C^{17,17'}$ ), 120.60 ( $C^3$ ), 121.56 ( $C^9$ ), 123.50 ( $C^4$ ), 124.18 ( $C^{11}$ ), 125.34 ( $C^{10}$ ), 128.33 ( $C^6$ ), 126.18 ( $C^{21,21'}$ ), 128.33 ( $C^6$ ), 130.65 ( $C^7$ ), 130.83 ( $C^{16}$ ), 131.60 ( $C^{16}$ ), 132.11 ( $C^{12}$ ), 133.99 ( $C^5$ ), 136.40 ( $C^{15,15'}$ ), 139.15 ( $C^8$ ), 142.41 ( $C^{22,22'}$ ), 150.92 ( $C^{19,19'}$ ), 153.26 ( $C^{14}$ ), 162.39 ( $C^{18,18'}$ ).

#### 2.4. Synthesis of (3)

(2) 6 g, 10% Pd/C 0.18 g, and DMF 50 mL were introduced into a Parr autoclave at room temperature. The reaction system was purged with nitrogen for 30 min before introducing hydrogen. The pressure of the autoclave was maintained at about 140 psi under hydrogen atmosphere for 24 h. Then, the reaction mixture was filtered to remove Pd/C, and the filtrate was poured into 500 mL of water under stirring. The precipitate was filtered and then dried in a vacuum oven at 70 °C. Off white powders 4.37 g (80% yield) were obtained. HR-MS(EI)  $m/z$ : calcd. for  $C_{38}H_{31}O_4N_2P$  610.2021; anal., 610.2028 for  $C_{38}H_{31}O_4N_2P$ . FTIR (KBr): 920  $cm^{-1}$  (P–O–Ph), 1203  $cm^{-1}$  (P=O), 1591  $cm^{-1}$  (P–Ph), 1616  $cm^{-1}$  (NH bend), 3339  $cm^{-1}$  (NH symmetric stretch), 3439  $cm^{-1}$  (NH asymmetric stretch).  $^1H$  NMR (ppm, DMSO- $D_6$ ),  $\delta = 1.67$  (3H,  $H^1$ ), 4.97 (4H,  $NH_2$ ), 6.59 (2H,  $H^{21}$ ), 6.62 (2H,  $H^{21'}$ ), 6.63 (2H,  $H^{17}$ ), 6.68 (2H,  $H^{17'}$ ), 6.71 (2H,  $H^{20}$ ), 6.73 (2H,  $H^{20'}$ ), 7.11 (1H,  $H^{13}$ ), 7.16 (2H,  $H^{16}$ ), 7.20 (1H,  $H^{11}$ ), 7.26 (1H,  $H^{16}$ ), 7.28 (1H,  $H^7$ ), 7.33 (1H,  $H^{12}$ ), 7.40 (1H,  $H^6$ ), 7.70 (1H,  $H^5$ ), 7.95 (1H,  $H^{10}$ ), 8.07 (1H,  $H^4$ ).  $^{13}C$  NMR (ppm, DMSO- $D_6$ ),  $\delta = 24.34$  ( $C^1$ ), 52.38 ( $C^2$ ), 114.99 ( $C^{17,17'}$ ), 115.75 ( $C^{21,21'}$ ), 120.76 ( $C^9$ ), 121.02 ( $C^{20,20'}$ ), 121.35 ( $C^8$ ), 122.11 ( $C^3$ ), 123.45 ( $C^4$ ), 124.09 ( $C^{11}$ ), 125.36 ( $C^{10}$ ), 128.18 ( $C^6$ ), 129.88 ( $C^{16}$ ), 130.71 ( $C^{12}$ ), 130.90 ( $C^{16}$ ), 132.09 ( $C^{15}$ ), 132.53 ( $C^{15'}$ ), 133.81 ( $C^7$ ), 135.58 ( $C^{22,22'}$ ), 136.41 ( $C^5$ ), 145.40 ( $C^{19,19'}$ ), 150.95 ( $C^{14}$ ), 1157.82 ( $C^{18,18'}$ ).

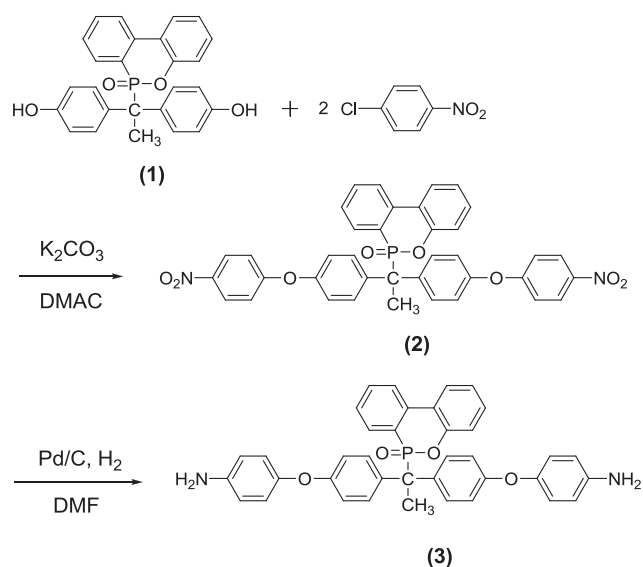
#### 2.5. Preparation of PEIs

Phosphinated PEIs were prepared by reacting (3) with equal mole of dianhydrides (a–d). PEIs syntheses are exemplified by specific synthesis of (5a) from the condensation of (3) and PMDA. To a 100-mL three-neck round-bottom flask equipped with a magnetic stirrer, nitrogen inlet, (3) 1.013 g (2 mmol), and  $CaH_2$ -dried DMAC 5.82 g were added. After the monomer had dissolved completely, the reactor was placed into an ice-bath cooling system. After the reaction mixture reached 3–5 °C, PMDA 0.436 g (2 mmol) was added quickly and reacted at that temperature for 2 h. Then, the viscous poly(amic acid) (4a) was diluted with DMAC 2.40 g and then casted on glass by an automatic film applicator. The film was dried at 80 °C overnight, and then imidized at 100 °C (1 h), 200 °C (1 h) and 300 °C (1 h), respectively.

### 3. Results and discussion

#### 3.1. Synthesis and characterization of (2)

(2) was synthesized from the nucleophilic substitution of (1) and 4-chloronitrobenzene at 120 °C using potassium carbonate as catalyst (Scheme 1). Liou and Hsiao [21] attempted to synthesize a phosphorus-containing bis(ether-benzonitrile) from (1') and p-fluorobenzonitrile by the fluoro-displacement in the present of potassium carbonate. However, according to the NMR and X-ray analyses, the side-chain P–Ar bond was cleaved by alkaline hydrolysis during the nucleophilic fluoro-displacement reaction. Furthermore, the cleavage of P–Ar bond was observed when (1') was reacted with 4-chloronitrobenzene in the presence of potassium carbonate [22]. Hoffmann et al. synthesized phosphinated polyetherketones and polyethersulfones [23], and the cleavage of



Scheme 1. Synthesis of (2) and (3).

P–Ar bond was reported. Therefore, alkaline hydrolysis of P–Ar bond seems to be a problem for (1') derivative compounds.

However, in this study, (2) can easily be prepared by a  $K_2CO_3$ -catalyzed nucleophilic substitution of (1) and 4-chloronitrobenzene. Fig. 2 shows the  $^1H$  NMR spectrum of (2). Signals from  $H^{20}$ – $H^{20'}$  and  $H^{21}$ – $H^{21'}$  indicate that (2) was successfully prepared. Due to the inductive and anisotropic deshielding effect of the nitro group,  $H^{21}$  and  $H^{21'}$  (ortho to the nitro group) show the largest chemical shift at around 8.3 ppm. In contrast,  $H^{17}$  and  $H^{17'}$  (ortho to the ether group) show the smallest chemical shift at 7.0 ppm because of the shielding effect of the electron-donating ether group. The other spectroscopic data such as  $^{13}C$  NMR,  $^{31}P$ ,  $^1H$ – $^{13}C$  COSY, and  $^1H$ – $^{13}C$  HETERCOSY spectra (Supporting information Fig. S1–S4) support the structure and purity of (1). Biphenol (1) exhibits a P–C (aliphatic carbon) bond, which is different from the P–Ar bond in (1'), might be responsible for the alkaline resistance of (1). In addition, the nucleophilic substitution can be carried out using less reactive 4-chloronitrobenzene. The less steric hindrance of phosphinate on phenol groups might also be the reason for the improved reactivity.

#### 3.2. Synthesis and characterization of (3)

(3) was readily obtained by catalytic reduction of (2). Fig. 3 shows the  $^1H$  NMR spectrum of (3). An amino peak at 4.97 ppm was observed. Because of the shielding effect of the electron-donating amino groups, signals of  $H^{21}$  and  $H^{21'}$  upshifted from 8.3 ppm in (2) to 6.6 ppm in (3), demonstrating the successful reduction of (2). The other spectroscopic data such as  $^{13}C$  NMR,  $^{31}P$ ,  $^1H$ – $^{13}C$  COSY, and  $^1H$ – $^{13}C$  HETERCOSY spectra (Supporting information Fig. S5–S8) support the structure and purity of (3).

#### 3.3. Polyimide synthesis

PEIs (5) were prepared by the reaction of (3) with various commercially available dianhydrides (a)–(d) in DMAC to form poly(amic acid)s (4), followed by thermal imidization (Scheme 2). According to the principle of NMR, a smaller chemical shift of an amino proton means a higher electron density of nitrogen, corresponding to a higher reactivity. The chemical shift of the amino group of (3) is 5.0 ppm, which is almost the same as that of BAPP. This suggests that the reactivity of (3) is not affected by the

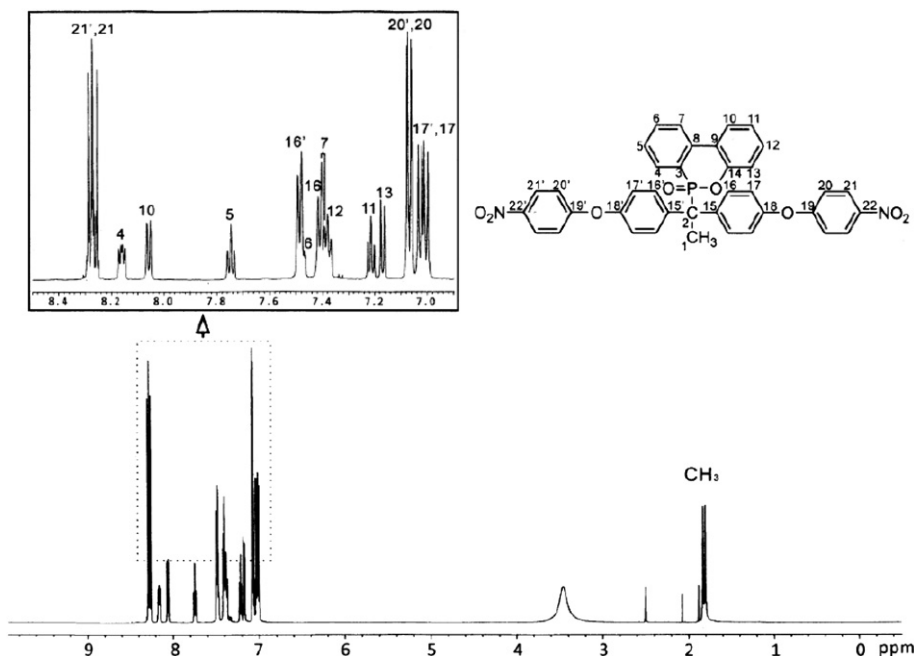


Fig. 2.  $^1\text{H}$  NMR spectrum of (2).

electron-withdrawing  $\text{P}=\text{O}$  group. As a result, PEIs with moderate-to-high inherent viscosity, ranging from 0.59 to 0.80 dL/g (Table 1), can be prepared. Fig. S9 shows the IR spectra of (5), the disappearance of amic acid absorptions at  $1650\text{--}1700\text{ cm}^{-1}$  ( $\text{C}=\text{ONH}$ ) and  $2400\text{--}3400\text{ cm}^{-1}$  ( $\text{C}=\text{OOH}$ ), together with the appearance of characteristic imide absorption bands at  $1776\text{ cm}^{-1}$  ( $\text{C}=\text{O}$  asymmetric stretch),  $1736\text{ cm}^{-1}$  ( $\text{C}=\text{O}$  symmetric stretch),  $1438\text{ cm}^{-1}$  ( $\text{C}-\text{N}$  stretch),  $1118$  and  $717\text{ cm}^{-1}$  (imide ring deformation) indicate the transformation of *o*-carboxyl amide to the imide ring, therefore confirming the complete imidization of the poly(amic acid). Further, the absorptions of  $\text{P}-\text{Ph}$  absorption at  $1583\text{ cm}^{-1}$ ,  $\text{P}=\text{O}$  absorption at  $1206\text{ cm}^{-1}$  and  $\text{P}-\text{O}-\text{Ph}$  absorption at  $922\text{ cm}^{-1}$

indicate that the biphenylene phosphinate pendent did not cleavage in the thermal imidization.

### 3.4. Properties of the PEIs

#### 3.4.1. Organosolubility and crystallinity

The solubility properties of PEIs (5) are listed in Table 1. Compared with the BAPP-based PIs [24], which are insoluble in organic solvent, PEIs (5) show improved solubility. The crystallinity of the prepared PEIs was evaluated by wide-angle X-ray diffraction (Fig. S10). The patterns show that all the PEIs are amorphous. The bulky biphenylene phosphinate, which retards the well-stacking of

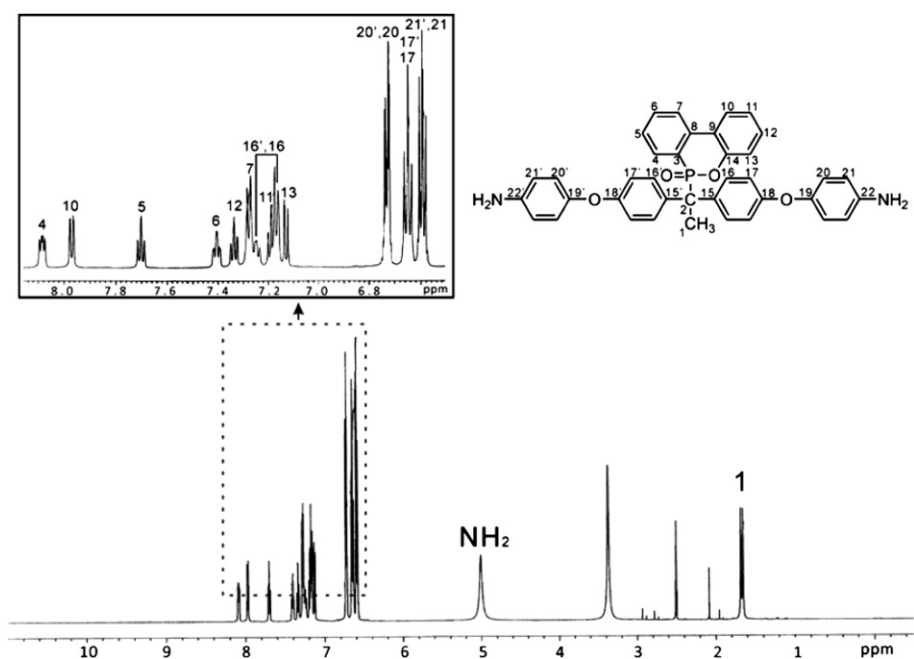
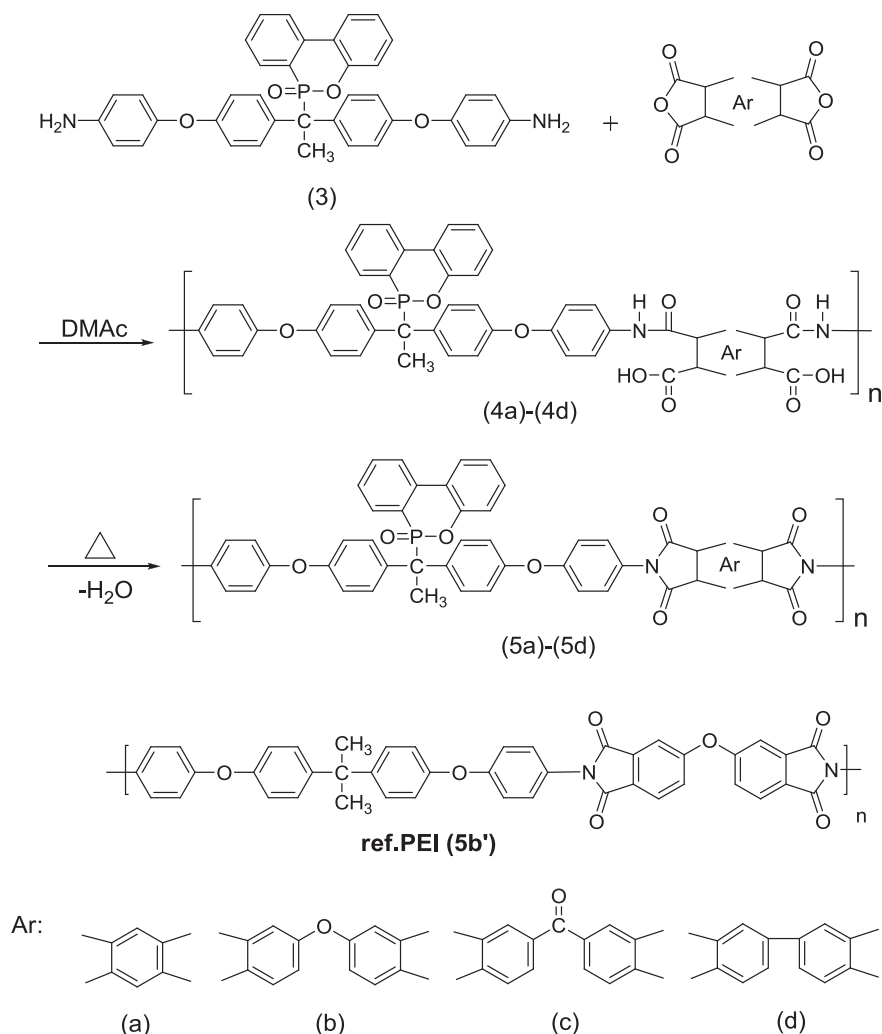


Fig. 3.  $^1\text{H}$  NMR spectrum of (3).



Scheme 2. Synthesis of PEIs (5).

polymer chains, should be responsible for the amorphous characteristic and improved solubility of (5).

### 3.4.2. Film quality and thermal properties

Fig. S11 shows a picture of (5b). As can be seen in the Figure, PEI (5b) displays light color and is foldable. The other PEIs also show light-color and foldable property. The tensile properties of PEIs (5) are summarized in Table 1. The tensile strength, elongation at break, and initial modulus range from 82 to 92 MPa, 8.1–14.2%, and 1.8–2.3 GPa, respectively. Since all PEIs (5) are tough and foldable, DMA and TMA were applied to evaluate their thermal mechanical properties and dimensional stability. Fig. 4 shows the DMA curves of PEIs (5), and the DMA data are listed in Table 2. The  $T_g$  obtained from

the peak temperature of  $\tan(\delta)$  is 314, 271, 278 and 289 °C for (5a)–(5d), respectively. Among the PEIs, (5a) shows the highest  $T_g$  due to the rigid pyromellitic moieties. In contrast, (5b) displays the lowest  $T_g$  because of the flexible ether linkage. The  $T_g$ s of PEIs (5) are much higher than that (215 °C) of a commercially available polyetherimide, ULTEM. It is thought that the bulky phosphinate pendent makes polymer chains PEIs (5) difficult to rotate, increasing the  $T_g$ . Fig. S12 shows the DMA curves of (5b) and (5b'). As can be seen in the Figure, (5b) shows higher  $T_g$  than (5b'). It is thought this phenomenon is related with the asymmetric/symmetric distribution of substituents. The bulky phosphinate pendent makes the polymer chains of (5b) difficult to rotate. In contrast, the symmetric isopropylidene  $-C(CH_3)_2-$  linkage makes PI (5b') chains easier to

**Table 1**  
Inherent viscosity, mechanical and solubility data of PEIs (5).

Polymer	$\eta_{inh}$ (dLg <sup>-1</sup> ) <sup>a</sup>	Tensile strength	Elongation at break	Initial modulus	Solvent for solubility test <sup>b</sup>							
		(MPa)	(%)	(GPa)	NMP	DMAc	DMF	DMSO	m-cresol	CH <sub>2</sub> Cl <sub>2</sub>	CHCl <sub>3</sub>	THF
(5a)	0.59	92	8.1	2.3	+h <sup>c</sup>	+-	+-	-	+-	-	-	-
(5b)	0.69	82	14.2	1.8	+h	+h	+-	-	+h	+-	+-	-
(5c)	0.64	86	12.3	2.1	+h	+-	+-	-	+-	+-	+-	-
(5d)	0.78	86	9.6	1.9	+h	+-	+-	+h	+-	+-	+-	-
(5d')	-	-	-	-	-	-	-	-	-	-	-	-

<sup>a</sup> Measured at a polymer concentration of 0.5 g/dL in NMP at 30 °C.

<sup>b</sup> Solubility was tested with a 5 mg sample in 0.5 g of solvent at room temperature.

<sup>c</sup> +, soluble at room temperature; +h, soluble on heating; +-, partially soluble on heating; -, insoluble on heating.



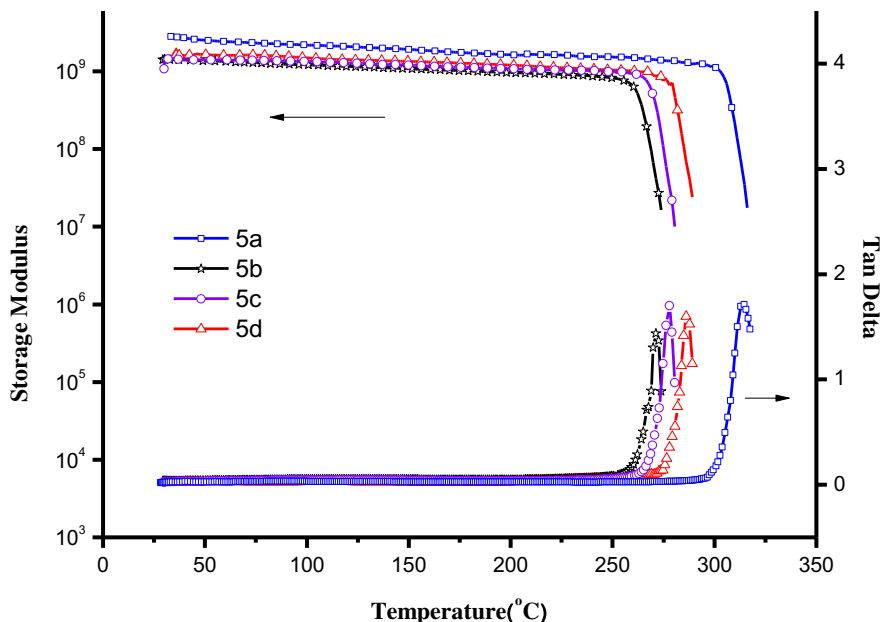


Fig. 4. DMA curves of PEIs (5).

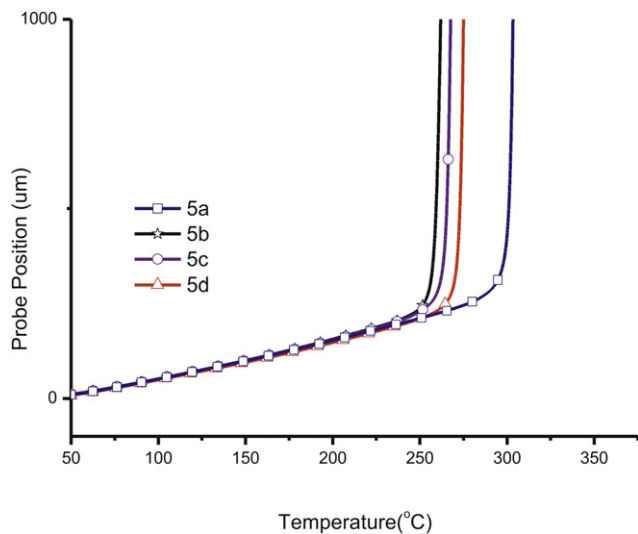


Fig. 5. TMA curves PEIs (5).

rotate. The lowering of  $T_g$  by symmetric distribution of substituents can be supported by the fact that the  $T_g$  of poly(vinyl dichloride) ( $T_g \sim -17^\circ\text{C}$ ) is much lower than that of poly(vinyl chloride) ( $T_g \sim 89^\circ\text{C}$ ). Another example is that the  $T_g$  of poly(vinyl difluoride) ( $T_g \sim -40^\circ\text{C}$ ) is much lower than that of poly(vinyl fluoride) ( $T_g \sim 40^\circ\text{C}$ ). Fig. 5 shows the TMA curves of PEIs (5), and the TMA data are listed in Table 2.  $T_g$ s measured by TMA are in the range of 266–302  $^\circ\text{C}$ , which is slightly lower than those measured by DMA. CTE at 100–200  $^\circ\text{C}$  are in the range of 49–53 ppm/ $^\circ\text{C}$ , displaying moderate dimensional stability. Fig. S13 shows the TMA curves of (5b) and (5b'). As shown in the Figure, (5b) show higher  $T_g$  and lower thermal expansion, indicating that introducing the bulky phosphinate pendent not only enhance the glass transition but also enhance the dimensional stability. This result is rarely seen in the literature.

### 3.4.3. Thermal stability

The thermal stability of PEIs (5) was evaluated by TGA (Table 2). The 5 wt% degradation temperatures of PEIs (5) in nitrogen atmosphere range from 453 to 467  $^\circ\text{C}$ , and the char yields are in the range of 56–58 wt%. In air atmosphere, the 5 wt% degradation temperatures of polyimides 5 range from 435 to 451  $^\circ\text{C}$ , and the char yields are in the range of 30–41 wt%. The degradation temperature is relatively high compared with those of main-chain type phosphinates [25,26].

**Table 2**  
Thermal Properties of PEIs (5).

Sample	Film quality	E'(GPa) <sup>a</sup>	Tan $\delta$ ( $^\circ\text{C}$ )	$T_g$ ( $^\circ\text{C}$ ) (DSC) <sup>b</sup>	$T_g$ ( $^\circ\text{C}$ ) (TMA) <sup>c</sup>	CTE (ppm/ $^\circ\text{C}$ ) <sup>d</sup>	$T_{d5\%}$ ( $^\circ\text{C}$ ) <sup>e</sup>		Char yield <sup>f</sup>	
							N <sub>2</sub>	air	N <sub>2</sub>	air
(5a)	foldable	2.5	314	306	302	50	459	450	56	38
(5b)	foldable	1.3	271	261	260	53	467	451	56	41
(5c)	foldable	1.4	278	268	266	51	453	431	58	35
(5d)	foldable	1.6	289	286	274	49	459	441	58	30
(5b')	foldable	1.3	241	234	231	64	522	537	30	21

<sup>a</sup> Measured by DMA at a heating rate of 5  $^\circ\text{C}/\text{min}$ .

<sup>b</sup> From the second DSC heating scan at a heating rate of 20  $^\circ\text{C}/\text{min}$ .

<sup>c</sup> Measured by TMA at a heating rate of 5  $^\circ\text{C}/\text{min}$ .

<sup>d</sup> Coefficient of thermal expansion are recorded from 100  $^\circ\text{C}$  to 200  $^\circ\text{C}$ .

<sup>e</sup> Temperature corresponding to 5% weight loss by thermogravimetry at a heating rate of 20  $^\circ\text{C}/\text{min}$ .

<sup>f</sup> Residual weight % at 800  $^\circ\text{C}$ .

**Table 3**  
Data of UL-94 test for PEIs (**5**) series and Kapton.

Sample code	1st burning time(sec)	2nd burning time(sec)	dripping	UL-94 grade
<b>5a</b>	0.6	0.1	No	V-0
<b>5b</b>	1.4	0.3	No	V-0
<b>5c</b>	1.1	0.3	No	V-0
<b>5d</b>	0.8	0.2	No	V-0
Kapton	4.6	1.8	No	V-0

The reason for the relatively high thermal stability of polyimides **5** may be attributed to the O=P–O group being protected by the two phenylene groups, and therefore the cyclic O=P–O chain was more thermally stable than the open O=P–O chain. In addition, on heating, the decomposition of the weak P–O bond decreases the molecular weight rapidly for main-chain type phosphinates. In contrast, the cleavage of the phosphorus pendent has little effect on the integrity of polymer main chains, so they are thermally more stable than the main-chain type phosphinates. The thermal decomposition temperatures of PEIs (**5**) are higher than those of our previous synthesized polyimides [15]. In our previous studies [27,28], we reported that the thermal stability of phosphorus-containing thermosets is related to the electron density of the carbon adjacent to the phosphorus. The lower the electron density of the carbon is, the lower its thermal stability. It is speculated that PEIs (**5**), with two electron-donating ether groups, increased the electron density of the carbon next to phosphorus, so they display the higher degradation temperatures than the polyimides prepared in our previous work [15]. However, although with higher 5% degradation temperatures, the char yields of PEIs (**5**) are lower than those of polyimides prepared in our previous work.<sup>15</sup> It is speculated the ether linkage reduces the oxidative resistance. As to the flame retardancy, according to the UL-94VTM vertical thin test, the  $t_1 + t_2$  is less than 2 s for PEIs (**5**), so they belong to the VTM-0 grade (Table 3). In contrast, the  $t_1 + t_2$  is higher than 6 s for Kapton. Although wholly aromatic polyimides usually possess VTM-0 grade without halogen and phosphorus components, they are usually organo-insoluble. The combination of organo-solubility and flame retardancy makes PEIs (**5**) attractive for industrial application.

#### 4. Conclusions

We report an economic synthesis of phosphinated dietheramine (**3**), which was prepared from a  $K_2CO_3$ -catalyzed nucleophilic aromatic substitution of (**1**) with less reactive 4-chloronitrobenzene,

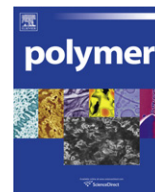
followed by catalytic hydrogenation. Biphenol (**1**) exhibiting an alkaline-stable P–C (aliphatic carbon) bond might be responsible for the alkaline resistance of (**1**). In addition, the steric hindrance of phenolic OH in (**1**) is less than that in (**1'**), so the nucleophilic substitution can occur using less reactive (but inexpensive) 4-chloronitrobenzene. All the PEIs (**5**) are light-color, tough and foldable. When compared with BAPP-based PEIs, PEIs (**5**) shows higher  $T_g$ , lower thermal expansion, improved solubility, and better flame retardancy. The combination of organo-solubility and flame retardancy makes PEIs (**5**) attractive for industrial application.

#### Appendix. Supporting information

Supplementary data related to this article can be found online at doi:10.1016/j.polymer.2011.01.035.

#### References

- [1] Chung CL, Yang CP, Hsiao SH. *J Polym Sci Part A Polym Chem* 2006;44:3092.
- [2] Li HS, Liu JG, Rui JM, Fan L, Yang SY. *J Polym Sci Part A Polym Chem* 2006;44:2665.
- [3] Kwark SM, Yeon JH, Yoon TH. *J Polym Sci Part A Polym Chem* 2006;44:2567.
- [4] Ogura T, Higashihara T, Ueda M. *J Polym Sci Part A Polym Chem* 2010;48:1317.
- [5] Wang CY, Li G, Jiang JM. *Polymer* 2009;50:1709.
- [6] Tao L, Yang H, Liu J, Fan L, Yang S. *Polymer* 2009;50:6009.
- [7] Liou GS, Lin PH, Yen HJ, Yu YY, Chen WC. *J Polym Sci Part A Polym Chem* 2010;48:1433.
- [8] Kurose T, Yudin VE, Otaigbe JU, Svetlichnyi VM. *Polymer* 2007;48:7130.
- [9] Liu Y, Xing Y, Zhang Y, Guan S, Zhang H, Wang Y, et al. *J Polym Sci Part A Polym Chem* 2010;48:3281.
- [10] Kung YC, Liou GS, Hsiao SH. *J Polym Sci Part A Polym Chem* 2009;47:1740.
- [11] Wu S, Hayakawa T, Kakimoto M, Oikawa H. *Macromolecules* 2008;41:3481.
- [12] Chern YT, Tsai JY, Wang JJ. *J Polym Sci Part A Polym Chem* 2009;47:2443.
- [13] Mathews AS, Kim D, Kim Y, Kim I, Ha CS. *J Polym Sci Part A Polym Chem* 2008;46:8117.
- [14] Chang CW, Lin CH, Cheng PW, Hwang HJ, Dai SA. *J Polym Sci Part A Polym Chem* 2009;47:2486.
- [15] Lin CH, Chang SL, Peng LA, Peng SP, Chuang YH. *Polymer* 2010;51:3899.
- [16] Hsiao SH, Guo WJ, Chung CL, Chen WT. *Eur Polym J* 2010;46:1878.
- [17] Yang CP, Su YY. *J Polym Sci Part A Polym Chem* 2006;44:3140.
- [18] Liaw DJ, Chang FC. *J Polym Sci Part A Polym Chem* 2004;42:5766.
- [19] Lin CH, Lin CH. *J Polym Sci Part A Polym Chem* 2007;45:2897.
- [20] Lin CH, Chang SL, Wei TP, Ding SH, Su WC. *Polym Deg Stab* 2010;95:1167.
- [21] Liou GS, Hsiao SH. *J Polym Sci Part A Polym Chem* 2002;40:459.
- [22] Liou GS, Hsiao SH. *High Perform Polym* 2001;13:137.
- [23] Hoffmann T, Pospiech D, Haußler L, Komber H, Voigt D, Harnisch C, et al. *Macromol Chem Phys* 2005;206:423.
- [24] Yang CP, Hung KS, Chen RSJ. *J Polym Sci Part A Polym Chem* 2000;38:3954.
- [25] Liu YL, Hsiu GH, Lee RH, Chiu YS. *J Appl Polym Sci* 1997;63:895.
- [26] Liou GS, Hsiao SH. *J Polym Sci Part A Polym Chem* 2001;39:1786.
- [27] Wang CS, Lin CH. *J Appl Polym Sci* 2000;78:228.
- [28] Wang CS, Lin CH. *J Appl Polym Sci* 2000;75:429.



## Fabrication and stability of porous poly(allylamine) hydrochloride (PAH)/poly-(acrylic acid) (PAA) multilayered films via a cleavable-polycation template

Na Peng, Xi-Ming Xia, Wen-Tao He, Wen-Ming Liu, Shi-Wen Huang\*, Ren-Xi Zhuo\*

Key Laboratory of Biomedical Polymers of Ministry of Education, Department of Chemistry, Wuhan University, Wuhan 430072, PR China

### ARTICLE INFO

#### Article history:

Received 9 October 2010

Received in revised form

6 January 2011

Accepted 15 January 2011

Available online 22 January 2011

#### Keywords:

Layer-by-layer

Cleavable-polycation template

Porous

### ABSTRACT

Porous films were fabricated from nonporous layer-by-layer multilayers composed of a blend of positively charged disulfide-containing polyamidoamine and poly(allylamine hydrochloride), and negatively charged poly(acrylic acid), followed by removal of cleavable disulfide-containing polycation after incubation in 1 mM DTT solution. The thickness of original multilayered films decreased with the increase of incubation time in DTT solution. Atomic force microscopy (AFM) measurements and electrochemical analysis demonstrated the formation of nanopores with sizes ranging from 50 to 120 nm. The formed porous films were stable in buffer solution at pHs ranging from 7.4 to 1.6, whereas they showed slight changes in pore number and pore size when incubated in PBS buffer at a pH of 10.0. This research might provide a universal method for the fabrication of noncrosslinked porous multilayered films.

© 2011 Elsevier Ltd. All rights reserved.

### 1. Introduction

The layer-by-layer (LBL) assembly technique, which was first introduced by Decher and co-workers in 1991, has rapidly expanded to become a premier method for the fabrication of nanoscale films with tailored properties [1]. Due to its simplicity, versatility, and systematical control over the structure and the thickness of the obtained films, LBL technique has been extensively applied for the preparation of multilayered films [2,3]. Although a variety of interactions, such as hydrogen-bonding [4,5], charge transfer [6,7], acid–base pairing, metal ion coordination and covalent bonding [8,9], have been employed as driving forces for the LBL assembly, electrostatic interaction has been most widely used to construct multilayered films. These thin films can be prepared on substrates including metals, glass, silicon, and polymers with varying morphologies, such as flat macroscopic surface, nanopatterned surface [10], porous membranes, and colloids [11] by using a variety of compounds including natural and synthetic polyelectrolytes [12], nanoparticles [13], and carbon nanotubes [14]. The formed multilayered films have been widely used in sensing [15], nonlinear optics [16], photoactive films [17], drug delivery [18,19], and selective area patterning [20]. Recently, porous films have received more

and more attention because their permeation properties could be controlled by changing external pH [21], temperature [22], electric field [23], concentration of starting polymers, or ionic strength of their environments [24]. Two kinds of important methods have been developed to fabricate microporous or nanoporous multilayered films. One is to treat the constructed nonporous multilayers at different pH value, temperature or ionic strength to form porous structures by the breakage of the interchain ionic bonds and rearrangement of the polyelectrolytes inside the films. Thus formed pores are often reversible by changing pH, temperature or ionic strength. It is necessary to chemically crosslink the film to fix the formed pores. For example, Rubner et al. prepared microporous thin films from the weak polyelectrolytes PAH and PAA by changing the external pH [25], and found that the external pH affected the morphology of the resulted films [26]. Immersion of PAA/PAH multilayered films in ultrapure water, prepared from salt-containing polyelectrolyte, resulted in the formation of nanopores [27]. Similarly, hydrogen-bonding-directed porous PAA/poly (4-vinylpyridine, P4VP) multilayered film was prepared by post-treatment in basic aqueous solution at different temperatures [28–30]. In the second kind of method, P4VP was used as a template to be incorporated into the multilayered films via layer-by-layer deposition of PAA and a blend of PAH and P4VP. After crosslinking of the constructed multilayers by 1-ethyl-3-(3-dimethylaminopropyl) carbodiimide (EDC) activation, the hydrogen-bonded component (P4VP) was removed from the crosslinked film in a basic solution (pH 10.0) to obtain nanoporous films [31].

\* Corresponding authors. Fax: +86 27 68755317.

E-mail addresses: [swhuang@whu.edu.cn](mailto:swhuang@whu.edu.cn) (S.-W. Huang), [bmp@whu.edu.cn](mailto:bmp@whu.edu.cn) (R.-X. Zhuo).

In our previous work, we have developed a simple method for fabrication of noncrosslinked, porous polyelectrolyte multilayered films via the removal of reducible template from nonporous multilayers prepared by LBL deposition of poly(sodium4-styrenesulfonate) (PSS) and a blend of reducible polycation and nonreducible polycation [32]. The pores in the films, composed of strong polyelectrolyte (PSS) and weak polyelectrolyte (polyamine), are stable and irreversible at pH 5.5–7.4. In this work, we used the reducible template method to fabricate porous multilayers composed of weak polyelectrolyte PAH and PAA (Scheme 1). Different from the porous PAH/PAA films prepared by changing pH or using P4VP template, the pores in the noncrosslinked PAH/PAA films, prepared from reducible template, are stable and irreversible at pH 1.6–10.0.

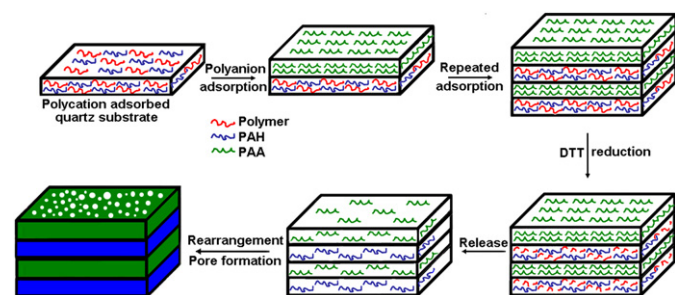
## 2. Experimental part

### 2.1. Materials

Poly (allylamine hydrochloride) (PAH  $M_w = 70,000 \text{ g mol}^{-1}$ ) and poly (acrylic acid) (PAA  $M_w = 100,000 \text{ g mol}^{-1}$  35 wt.% in water) were purchased from Sigma–Aldrich and used without further treatment. Dithiothreitol (DTT, Merk, Germany) was used directly. Other reagents and solvents were of analytical grade and used as received. Polymer 1 ( $M_w = 1.22 \times 10^4 \text{ g mol}^{-1}$ ,  $M_w/M_n = 1.26$ ) was synthesized as previously described [32]. Quartz substrates ( $0.8 \text{ cm} \times 2.0 \text{ cm}$ ) were cleaned with methylene chloride, ethanol, methanol, ultrapure water, and dried under a stream of nitrogen. Subsequently, the surface of quartz substrates was activated by immersion in a 1:1 (v/v) mixture of  $\text{H}_2\text{SO}_4$  and  $\text{H}_2\text{O}_2$  (30 wt.% in water) solution at  $80^\circ\text{C}$  for 2 h, rinsing with ultrapure water, dipping into a 5:1:1 mixture of water,  $\text{H}_2\text{O}_2$  (30 wt.% in water) and a 29 vol.% ammonia solution at  $80^\circ\text{C}$  for 1 h, rinsing again, and drying under a stream of nitrogen.

### 2.2. Preparation of multilayered films

Multilayered films were prepared by the alternate dipping method: the activated quartz substrates were immersed in PBS buffer (0.1 M, pH 7.4) containing  $0.5 \text{ mg ml}^{-1}$  of PAH (polymer 2) and  $0.5 \text{ mg ml}^{-1}$  of polymer 1 (or with one of them) for 10 min, followed by rinsing with ultrapure water for three times and dried with a gentle stream of nitrogen. The substrates were then immersed into the oppositely charged polyelectrolyte solution in PBS buffer (0.1 M, pH 7.4) containing  $1 \text{ mg ml}^{-1}$  of PAA (polymer 3) for 10 min, followed by the same rinsing and drying protocol. This cycle was repeated until the desired number of layers had been built on the activated substrates. Films to be used in thickness measurements, degradation experiments, and AFM measurements were dried under a gentle stream of nitrogen, placed in desiccators and stored dry until use.



**Scheme 1.** Procedure used to produce porous polymer film from (1 + 2)/3 multilayered film. First, a polycation adsorbed quartz substrate is followed by adsorbing PAA in a repeated manner. Then, polymer 1 degraded in DTT solution to disrupt S–S bonds. Finally, polymer 1 and excess PAA released, and films rearranged to form pores.

### 2.3. Thickness measurement

The thickness of multilayered films with different numbers of bilayers was determined in three different locations on the substrate surface by using profilometry (Taylor–Hobson S4C–3D).

### 2.4. Reductive degradation

A quartz substrate coated with ten bilayers of (1 + 2)/3 or 2/3 films was placed in a plastic tube and a sufficient 1 mM solution of DTT in PBS buffer (0.1 M, pH 7.4) was added to cover the substrates. The film-coated substrates were incubated at room temperature for appointed time, and then the films were washed with ultrapure water and dried under a stream of nitrogen. The reductive degradation of multilayered films in 1.5 mM, 2 mM, 2.5 mM DTT solution and PBS without DTT was similar to the procedure described above.

### 2.5. Atomic force microscopy (AFM)

The surface topography of the nitrogen-dried films on quartz substrates after different treatments was recorded by AFM (SPM-9500J3, Shimadzu, Japan) in air, which was operated in tapping mode.

### 2.6. Electrochemical measurements

Cyclic voltammetry was made using a three-electrode standard system consisting of a saturated calomel reference electrode (SEC), a platinum wire counter electrode, and a film-supporting ITO-coated working electrode at a scan rate of 25 mV/s. A CH-Instruments 830 electrochemical analyzer was used to perform cyclic voltammetry measurements. A 0.005 M  $\text{K}_3\text{Fe}(\text{CN})_6$  solution (with 0.1 M KCl, PBS (0.1 M, pH 7.4), as solvent) was purged with a flow of nitrogen for 30 min prior to any measurement.

## 3. Results and discussion

### 3.1. Preparation and thickness analysis of multilayered films

The multilayered films, composed of a blend of polycations including polymer 1 and polymer 2 (PAH), and polyanion (polymer 3, PAA), were fabricated by the alternate dipping method [1]. The chemical structures of polymer 1, 2, and 3 are shown in Fig. 1. It is known that both PAH and PAA are weak polyelectrolytes. The PAA chain could be fully ionized at pH 6.5 or above. In the case of PAH, the polymeric chains are fully ionized under acidic conditions and start to lose protons at a pH of 7.0 [33]. Similarly, the primary amino groups in the side chains of polymer 1 are ionized at a pH of 7.0, however, the tertiary amines in the mainchain of polymer 1 are free. In this work, we used a blend solution of polymer 1 and PAH in PBS (0.1 M, pH 7.4),

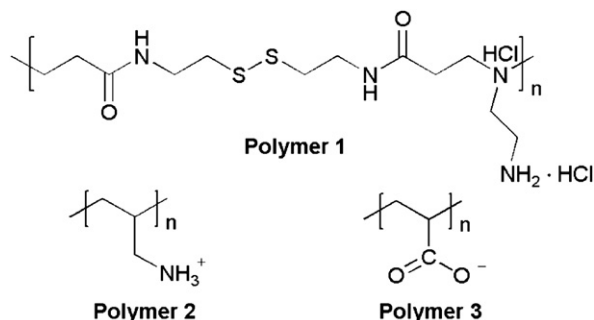


**Fig. 1.** The chemical structures of polymer 1, 2 (PAH) and 3 (PAA).

and the solution of PAA in PBS (0.1 M, pH 7.4) to construct (1 + 2)/3 multilayered films. Under these conditions, the weak polyelectrolyte PAA was fully ionized, and PAH and the side chains of polymer 1 was largely ionized [34]. The complexation of PAH–PAA and polymer 1–PAA were mainly attributed to electrostatic interaction.

The thickness of multilayers prepared by layer-by-layer deposition of the polycation and polyanion onto the activated quartz substrates was measured by profilometry. Fig. 2 displays the increase of thickness as a function of the number of 1/3, 2/3, and (1 + 2)/3 bilayers for films deposited on quartz substrates. The results indicated that the thickness of (1 + 2)/3, 1/3, and 2/3 films gradually increased with the increase of respective bilayer numbers when the activated substrates were submerged alternately into polycation and polyanion solutions. As shown in Fig. 2a, an exponential increase of thickness of the 1/3 films with an increase of deposited bilayer numbers was observed. The possible explanation for this phenomenon was that polymer 1 containing the disulfide linkages in the backbone can diffuse “in and out” of the film during the process of LBL buildup. The hypothesis of polyion’s diffusion “in and out” of the film during the LBL assembly was experimentally confirmed in the PLL/HA system [35]. It was proposed that polymer 1 diffused through-out the film down into the quartz substrate after each new polymer 1 deposition and out of the film after each polymer 1 rinsing and further after each PAA deposition. Because polymer 1 molecules ( $M_w = 1.22 \times 10^4 \text{ g mol}^{-1}$ ) were much smaller than PAA ( $M_w = 1.0 \times 10^5 \text{ g mol}^{-1}$ ), it is possible that polymer 1 was easier to diffuse out of the film in the presence of PAA (polymer 3) in solution, which increased the amount of polycation and the charge density on the surface of the film. This resulted that the amount of PAA adsorbed in the new forming bilayer was larger than that in the former bilayer, leading to a nonlinear increase of film thickness. In contrast, a linear increase of thickness of the 2/3 films on the quartz substrates with an increase of bilayers was observed (shown in Fig. 2b). Because the polyion in the films, either 2 or 3, were difficult to diffuse outside in the process of construction. In the case of (1 + 2)/3 multilayers, similar results were observed. In (1 + 2)/3 film, polymer 1, polymer 2 and PAA entwined to form tighter polyelectrolyte complexes, which

resulted in that polymer 1 was fixed inside the films and difficult to diffuse out. The thickness of 1/3, 2/3 and (1 + 2)/3 (in Fig. 2c) multilayers with 10 bilayers was 258, 75 and 104 nm, respectively. The results indicated that the thickness of polycation/PAA multilayered films was greatly dependent on the chemical structures and molecular weights of polycations used.

### 3.2. Reductive degradation and pores formation in (1 + 2)/3 multilayered films

#### 3.2.1. Film thickness decrease

It is known that the disulfide bond is cleavable under reductive conditions. We first study the effect of incubation of the film in a solution without DTT, and found that there was no significant decrease of thickness when (1 + 2)/3 film was immersed in the solution without DTT. Then, we investigated the thickness change of films incubated in DTT solution. Dry (1 + 2)/3 film on a quartz substrate with 10 bilayers was immersed in PBS (0.1 M, pH 7.4) containing DTT. After 23 h, 26 h, 29 h, and 34 h incubation of the films in PBS (0.1 M, pH 7.4) containing 1 mM of DTT, the thickness of films, measured by profiler, decreased by 44.2%, 65.5%, 66.3%, and 69.4% (shown in Fig. 3) with reference to the original films, respectively. Similar results have also been observed from disulfide-containing polycation/DNA multilayers incubated in DTT solution in our previous work [36]. The disulfide bond in the backbone of polymer 1 in (1 + 2)/3 multilayered film was reduced by DTT to yield low-molecular-weight polycation or small molecules, which lost the ability to bind negatively charged PAA via electrostatic interaction. As a result, low-molecular-weight polycation or small molecules and excess PAA diffused out from the multilayered film. The loss of polymer 1 and part of 3 resulted in the thickness decrease of (1 + 2)/3 film when incubated in reductive solution. The thickness decrease is dependent on the incubation time.

#### 3.2.2. Pores formation

Atomic force microscopy (AFM) was used to monitor the surface morphological change of (1 + 2)/3 film and 2/3 film after incubation

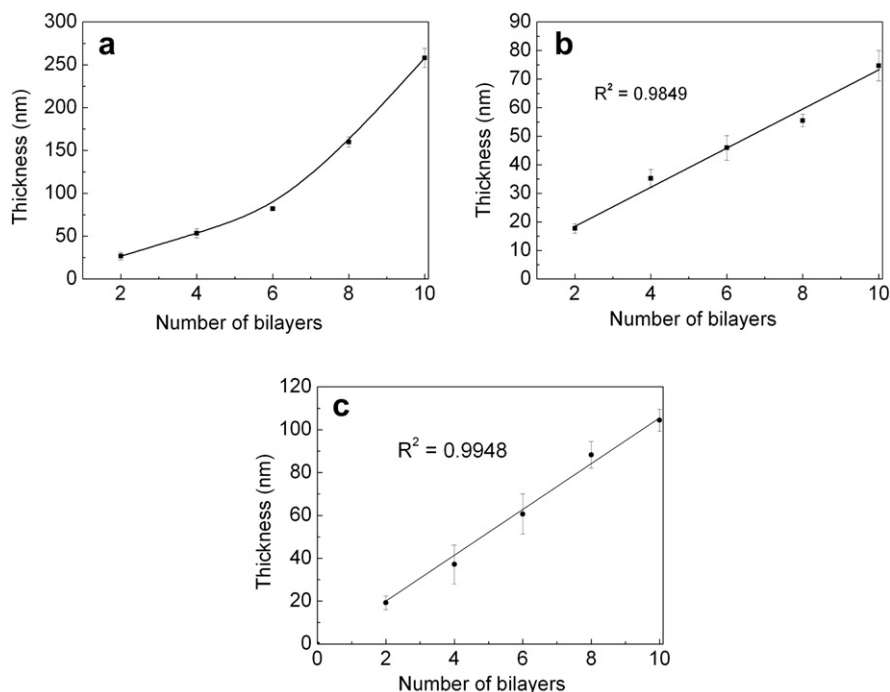
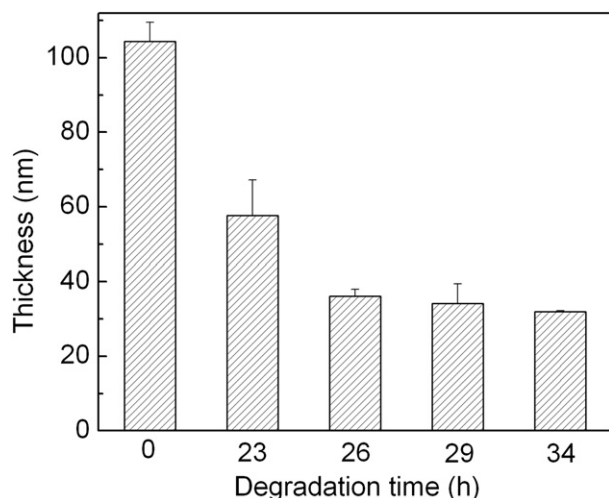


Fig. 2. Thickness of multilayered films as a function of 1/3 (a), 2/3 (b), and (1 + 2)/3 (c) bilayer numbers for films deposited on quartz substrates. The outermost layer was PAA.





**Fig. 3.** Thickness of original (1 + 2)/3 films with 10 bilayers and films after 23 h, 26 h, 29 h, and 34 h incubation in PBS containing 1 mM DTT at room temperature.

in PBS (0.1 M, pH 7.4) containing DTT. Fig. 4 shows AFM images of the surface of (1 + 2)/3 films with 10 bilayers in 1 mM of DTT for different incubation time. Before treated with DTT solution, the surface of the (1 + 2)/3 film was relatively flat, and no pores were observed (Fig. 4a). After incubation of (1 + 2)/3 film in 1 mM of DTT solution for 23 h, a small number of pores formed on the surface of the film (Fig. 4b). With increasing incubation time from 23 h to 26 h, large number of pores formed on the surface of the film. Further increase of incubation time from 26 h to 34 h resulted in neither increasing pore numbers nor significantly changing pore sizes (Fig. 4c–e). The sizes of pores, formed by incubation in 1 mM DTT solution for 26, 29 and 34 h, ranged from 50 to 120 nm.

AFM measurement also provided the surface roughness changes of (1 + 2)/3 multilayered films incubated in 1 mM DTT solution,

which is shown in Fig. 5. The original (1 + 2)/3 multilayered film exhibited very low surface roughness (2.4 nm) before reductive degradation. However, after incubation of the (1 + 2)/3 multilayered film in 1 mM DTT solution for 23 h or longer, the surface roughness increased significantly above 10 nm, accompanying formation of pores. This observation in increasing surface roughness was consistent with the results of surface morphological changes. As a reference, treatment of 2/3 films without disulfide bonds did not result in pores formation. No difference was found in the surface morphologies of 2/3 films before and after incubation in DTT solution (Fig. 6a and b). The results demonstrated that the formation of pores in (1 + 2)/3 films in DTT solution was triggered by the cleavage of disulfide bonds in polymer 1. The mechanism of pore formation using cleavable polymer 1 as a template is similar to that discussed in our previous work [32]. Briefly, polymer 1 was cleaved into small molecules when (1 + 2)/3 multilayered film was incubated in a DTT solution, which lost the ability to bind PAA via electrostatic interaction, and diffused out from the film. Subsequently, the excess of PAA released from the film, and rearrangement of polycation and polyanion occurred, which resulted in the formation of pores inside the film.

### 3.3. Electrochemical analysis

We used cyclic voltammetry to provide further evidence for the formation of nanoporous thin films. We first constructed (1 + 2)/3 films with 10 bilayers on the surface of ITO (indium tin oxide) substrate, and then fabricated porous multilayers by incubating the films in 1 mM DTT solution. The permeability of nonporous and porous multilayers was then electrochemically evaluated using  $K_3Fe(CN)_6$  as a probe.  $K_3Fe(CN)_6$  was widely used as an electrochemical probe to investigate the characteristics of films on the various electrode surfaces [27,31,37,38]. The formation of nanopores in multilayers on the surface of ITO would allow the accessibility of ferricyanide complexes to the surface of the electrode, which

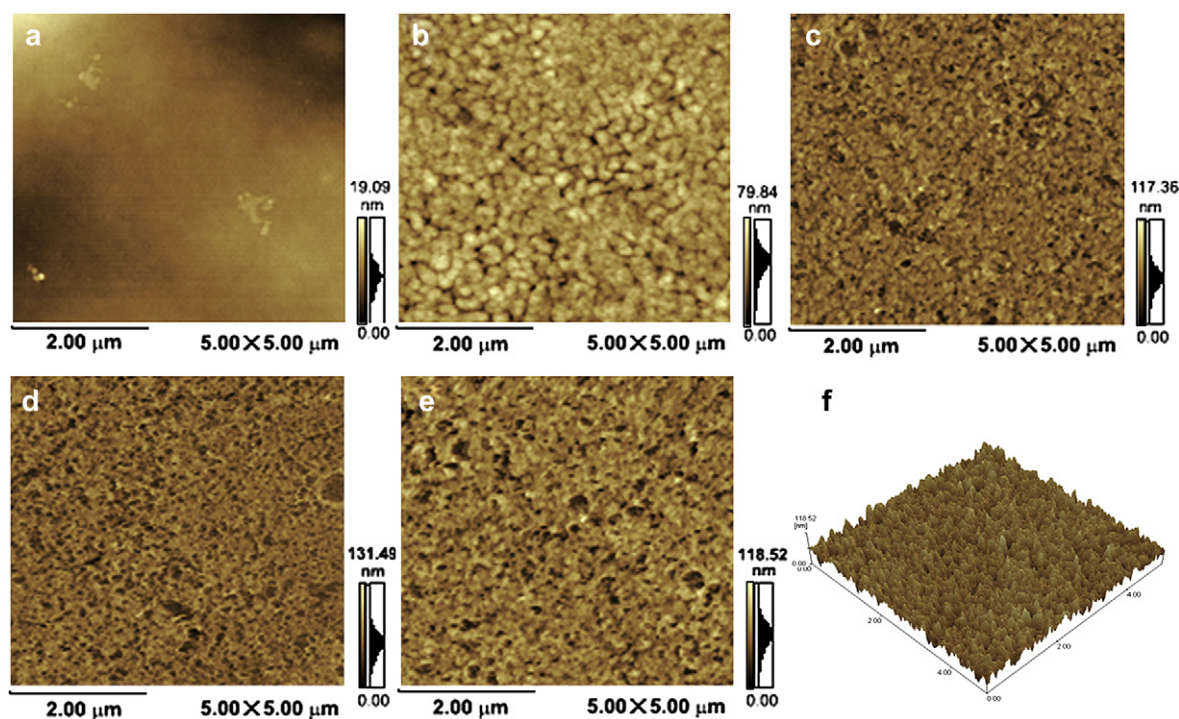


**Fig. 4.** AFM images of (1 + 2)/3 films with 10 bilayers after incubation in 1 mM DTT for (a) 0 h; (b) 23 h; (c) 26 h; (d) 29 h; and (e) 34 h, and 3D-AFM images of (1 + 2)/3 films after immersion in 1 mM DTT for 34 h (f). Image size = 5 × 5 μm.

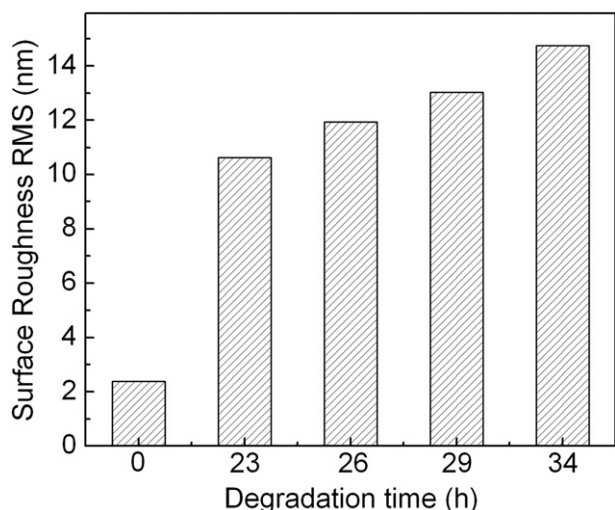


Fig. 5. RMS surface roughness of original (1 + 2)/3 films with 10 bilayers and films after 23 h, 26 h, 29 h, and 34 h incubation in PBS containing 1 mM DTT at room temperature.

resulted in a higher redox current. Fig. 7 shows the change of electrochemical behaviors of multilayered film-coated ITO electrode in the process of pore formation. A freshly-prepared electrode coated with a [(1 + 2)/3]<sub>10</sub> film was first immersed into 0.005 M K<sub>3</sub>Fe(CN)<sub>6</sub> solution containing 0.1 M KCl. A quasi-reversible cyclic voltammetry was detected, with a reduction peak current of 61.4 μA/cm<sup>2</sup> (shown in Fig. 7a). To quantify the influence of cleavage time on the multilayered film structure, the same electrode was re-immersed into 1 mM DTT solution for 23 h and washed with ultrapure water and reused to examine the permeability in the same electrolytic solution. As suggested in Fig. 7b, compared to 7a of original multilayer-coated-ITO electrode, a dramatic increase in reduction peak current (188.6 μA/cm<sup>2</sup>, a 3-fold increasing) after 23 h incubation of (1 + 2)/3 multilayers in 1 mM DTT solution was detected. The degraded [(1 + 2)/3]<sub>10</sub>-coated ITO was incubated for further 11 h in 1 mM DTT solution, and reused in the same electrolytic solution for cyclic voltammetry measurement. The reduction peak current of multilayer-coated-ITO electrode after 34 h cleavage increased to 231.7 μA/cm<sup>2</sup> (Fig. 7c), which was significantly higher than that after 23 h cleavage. The higher current suggested that better diffusion of ferricyanide complexes to the surface of the electrode after cleavage of multilayers when incubated in 1 mM DTT, and the film permeability increased with the increase of incubation time. The electrochemical analysis results provided additional evidences for the pore formation throughout the film after incubation in DTT solution, which is consistent with that measured by AFM.

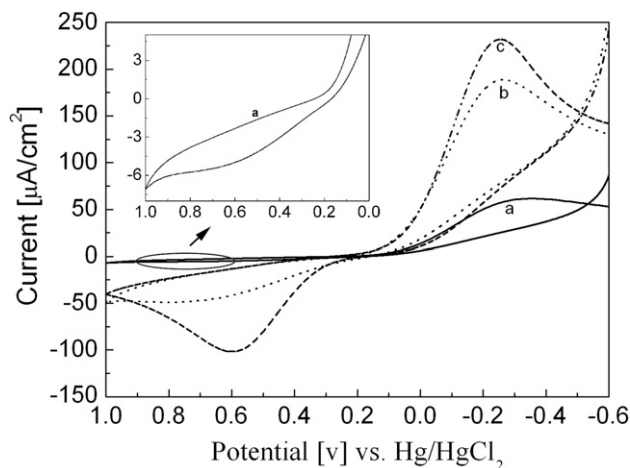


Fig. 7. Cyclic voltammograms of ITO-coated electrodes coated with a ten bilayer (1 + 2)/3 film in a 0.005 M K<sub>3</sub>Fe(CN)<sub>6</sub> solution (with 0.1 M KCl, PBS 7.4, 0.1 M as solvent), prior to (a) and after exposure to 1 mM DTT for 23 h (b), and 34 h (c).

#### 3.4. Effect of DTT concentration on reductive degradation of (1 + 2)/3 multilayered films

To investigate the effects of DTT concentration on reductive degradation of (1 + 2)/3 multilayered films, (1 + 2)/3 multilayered films with 10 bilayers were separately incubated in PBS buffer containing DTT at concentrations of 1.5 mM, 2 mM and 2.5 mM for 23 h. Fig. 8 shows the AFM images of the reductively degraded films. We found that the degradation rate of (1 + 2)/3 films dramatically increased with increasing DTT concentration from 1 mM to 2.5 mM. After 23 h incubation of (1 + 2)/3 multilayered films in DTT solution at 1.5 mM, 2 mM and 2.5 mM, large area of film shed and large pores formed. The results were different from that we previously reported in the case of reductive degradation of multilayers prepared from disulfide-containing polycation and strong polyelectrolytes, such as DNA and poly(sodium 4-styrenesulfonate) [32,36]. Because both of poly(allylamine hydrochloride) and poly(acrylic acid) are weak polyelectrolytes, the weak electrostatic interaction in poly(allylamine hydrochloride)/poly(acrylic acid) multilayered films resulted in shedding of film after rapid cleavage of disulfide when incubated in DTT solution at high concentration. In contrast, relatively slow degradation of disulfide bonds in DTT solution at a concentration of 1 mM allowed the occurrence of polyelectrolyte rearrangement and the formation of nanopores in the multilayers. In this work, we found that only 1 mM DTT solution is suitable for the fabrication of nanoporous PAH/PAA multilayered films.

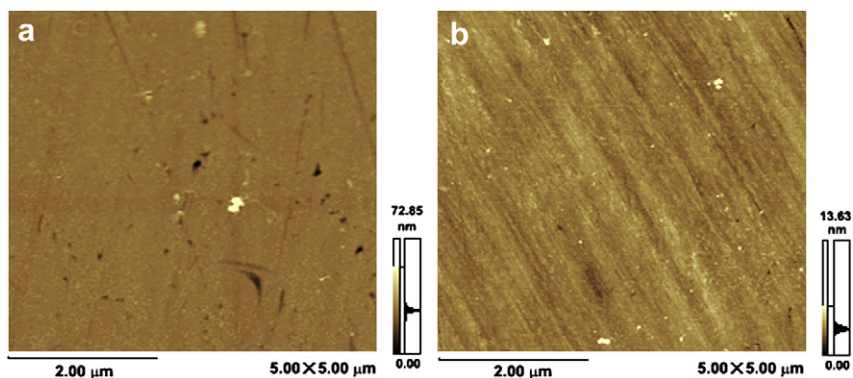
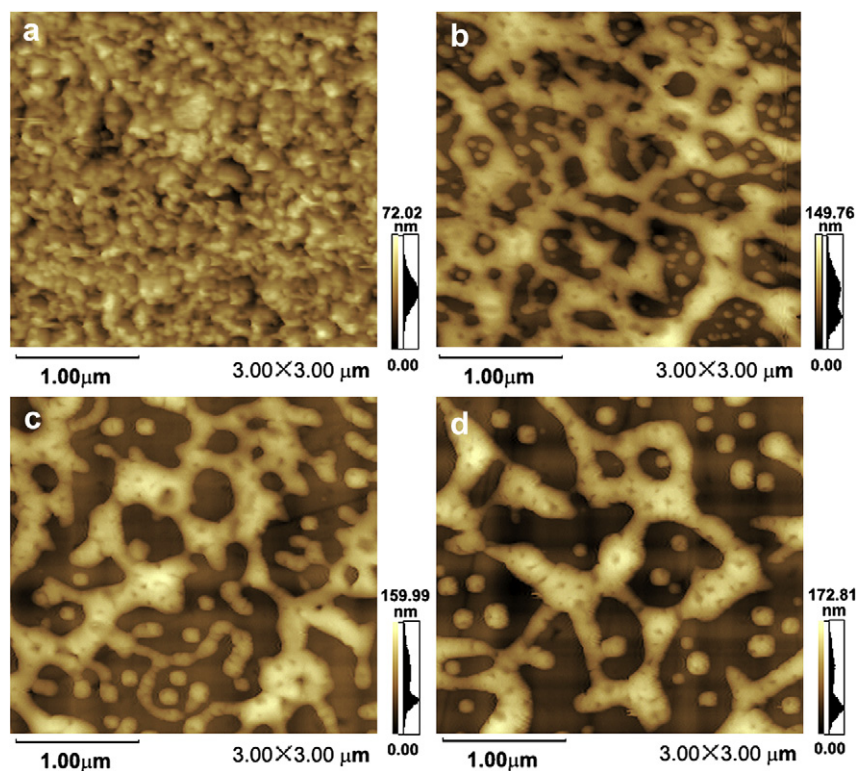
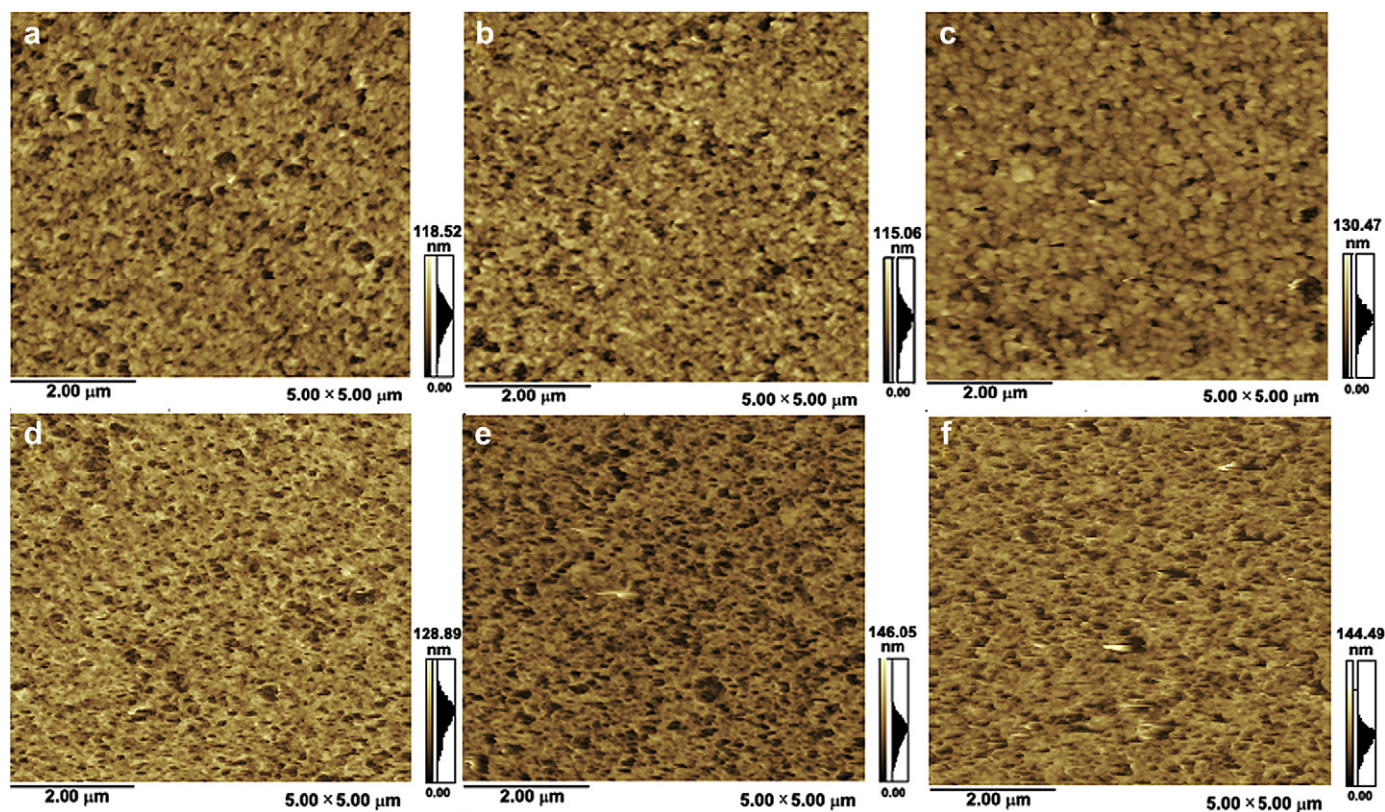


Fig. 6. AFM images of PAH/PAA multilayered films with 10 bilayers: (a) original film; (b) after incubation in 1 mM DTT for 23 h. Image size = 5 × 5 μm.





**Fig. 8.** AFM images of (1 + 2)/3 multilayered films with 10 bilayers after incubation in 1 mM DTT (a), 1.5 mM DTT (b), 2 mM DTT (c), and 2.5 mM DTT (d) solution for 23 h. Image size = 3 × 3 μm.



**Fig. 9.** AFM images of (1 + 2)/3 porous film: original (a); after immersion in PBS 7.4 for 6 h (b); in pH 10.0 for 6 h (c); in pH 2.8 for 4 h (d); in pH 2.1 for 4 h (e); and in pH 1.6 for 4 h (f). Image size = 5 × 5 μm.

### 3.5. Stability of pores formed in PAH/PAA multilayers

The nanopores or micropores in previously reported multilayers composed of weak polyelectrolyte, PAH and PAA, are completely and repeatedly reversed by changing the pH value of incubation buffer solution. It is necessary to heat the films at 180 °C to crosslink the films and lock the pores in the films. To investigate the stability of porous structures in multilayers fabricated from (1 + 2)/3 films by treatment with 1 mM DTT solution for 34 h, we first submerged the porous films in PBS (0.1 M, pH 7.4) at room temperature for 6 h. Then, the films were washed with ultrapure water, blown dried under a stream of nitrogen, and placed in a desiccator for AFM measurement. This film was successively re-incubated in PBS (0.025 M, pH 10) for 6 h, sodium acetate buffer (0.2 M, pH 2.8) for 4 h, sodium acetate buffer (0.2 M, pH 2.1) for 4 h and sodium acetate buffer (0.2 M, pH 1.6) for 4 h at room temperature. After each incubation, the film was washed and dried for AFM measurements. Fig. 9 shows the AFM images of the porous films after incubation in various buffer solution. Compared to the original film (Fig. 9a), the AFM image of the film after 6 h immersion in PBS (0.1 M, pH 7.4) (Fig. 9b) showed no significant surface morphological changes. When the porous film was re-incubated in PBS (0.025 M, pH 10.0), some changes were observed, including the decrease of the pore number and pore size. When the PBS 10.0 treated porous film was successively incubated in sodium acetate buffer (0.2 M, pH 2.8), sodium acetate buffer (0.2 M, pH 2.1) and sodium acetate buffer (0.2 M, pH 1.6), we found that the pore number and pore size became same as that of original film. The results indicated that the noncrosslinked PAH/PAA porous film prepared via a cleavable template is stable in buffer solution at pHs ranging from 7.4 to 1.6. However, the porous film showed slight changes in pore number and pore size when incubated in PBS buffer at a pH of 10.0. The results are greatly different from the porous PAH/PAA film prepared by changing pH value of incubation buffer solution. The reason of the difference is easily understood that the cleavage of disulfide bonds induced loss of polycation and polyanion is irreversible, which resulted that the formed pores are irreversible. The results demonstrated that the cleavable template is suitable not only for the fabrication of stable weak polyelectrolyte/strong polyelectrolyte porous multilayers, but also for stable weak polyelectrolyte/weak polyelectrolyte porous multilayers.

## 4. Conclusions

In conclusion, we have successfully applied the cleavable template for the fabrication of weak polyelectrolyte(PAH)/weak polyelectrolyte (PAA) porous multilayers by selective cleavage of disulfide-containing polycation in the multilayers composed of PAA and a blend of PAH and disulfide-containing polycation. Different from porous PAH/PAA multilayers prepared by changing the pH value of incubation buffer, the pores in porous PAH/PAA multilayers prepared via cleavable template are stable at pHs ranging from 7.4

to 1.6. This study may provide a general cleavable-polycation template for the construction of noncrosslinked porous multilayered films from any kind of polycation/polyanion, either weak polyelectrolytes or strong polyelectrolytes.

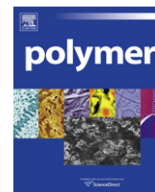
## Acknowledgments

This work was financially supported by National Natural Science Foundation of China (20874076, 21074101), National Basic Research Program of China (2009CB930300) and Program for New Century Excellent Talents in University (08-0410).

## References

- [1] Decher G. *Science* 1997;277(5330):1232–7.
- [2] Boudou T, Crouzier T, Ren K, Blin G, Picart C. *Adv Mater* 2010;22(4):441–67.
- [3] Bernards DA, Desai TA. *Soft Matter* 2010;6(8):1621–31.
- [4] Orozco VH, Kozlovskaya V, Kharlampieva E, López BL, Tsukruk VV. *Polymer* 2010;51(18):4127–39.
- [5] Kharlampieva E, Kozlovskaya V, Tyutina J, Sukhishvili SA. *Macromolecules* 2005;38(25):10523–31.
- [6] Shimazaki Y, Mitsui M, Ito S. *Langmuir* 1997;13(6):1385–7.
- [7] Wang XQ, Naka K, Itoh H, Uemura T, Chujo Y. *Macromolecules* 2003;36(3):533–5.
- [8] Silva R, Muniz EC, Rubira AF. *Polymer* 2008;49(19):4066–75.
- [9] Kinnane CR, Wark K, Such GK, Johnston AP, Caruso F. *Small* 2009;5(4):444–8.
- [10] Li JL, Yan LT, Xie XM. *Polymer* 2009;50(9):2172–80.
- [11] Caruso F, Caruso RA, Möhwald H. *Science* 1998;282(5391):1111–4.
- [12] Crouzier T, Boudou T, Picart C. *Curr Opin Colloid Interface Sci* 2010;15(6):417–26.
- [13] Lan Y, Wang EB, Song YH, Song YL, Kang ZH, Xu L, et al. *Polymer* 2006;47(4):1480–5.
- [14] Zhang C, Liu TX, Lu XH. *Polymer* 2010;51(16):3715–21.
- [15] Sun YP, Zhang X, Sun CQ, Wang B, Shen JC. *Macromol Chem Phys* 1996;197(1):147–53.
- [16] Casson JL, McBranch DW, Robinson JM. *J Phys Chem B* 2000;104(50):11996–2001.
- [17] Zhang TZ, Ge LQ, Wang X, Gu ZZ. *Polymer* 2008;49(12):2898–902.
- [18] Ding ZB, Guan Y, Zhang YJ, Zhu XX. *Polymer* 2009;50(4):4205–11.
- [19] Jiao Q, Yi Z, Cheng YM, Xi F. *Polymer* 2008;49(6):1520–6.
- [20] Lu YX, Sun JQ, Shen JC. *Langmuir* 2008;24(15):8050–5.
- [21] Hester JF, Olugebefola SC, Mayes AM. *J Membr Sci* 2002;208(1–2):375–88.
- [22] Chu LY, Li Y, Zhu JH, Chen WM. *Angew Chem Int Ed* 2005;44(14):2124–7.
- [23] Langer R. *Nature* 1998;392(supp):5–10.
- [24] Ibarz G, Dähne L, Donath E, Möhwald H. *Adv Mater* 2001;13(17):1324–7.
- [25] Mendelsohn JD, Barrett CJ, Chan VV, Pal AJ, Mayes AM, Rubner MF. *Langmuir* 2000;16(11):5017–23.
- [26] Hiller JA, Mendelsohn JD, Rubner MF. *Nat Mater* 2002;1(1):59–63.
- [27] Fery A, Schöler B, Cassagneau T, Caruso F. *Langmuir* 2001;17(11):3779–83.
- [28] Fu Y, Bai SL, Cui SX, Qiu DL, Wang ZQ, Zhang X. *Macromolecules* 2002;35(25):9451–8.
- [29] Bai SL, Wang ZQ, Zhang X. *Langmuir* 2004;20(26):11828–32.
- [30] Bai SL, Wang ZQ, Gao J, Zhang X. *Eur Polymer J* 2006;42(4):900–7.
- [31] Li Q, Quinn JF, Caruso F. *Adv Mater* 2005;17(17):2058–62.
- [32] Chen J, Xia XM, Huang SW, Zhuo RX. *Adv Mater* 2007;19(7):979–83.
- [33] Shiratori SS, Rubner MF. *Macromolecules* 2000;33(11):4213–9.
- [34] Mendelsohn JD, Yang SY, Hiller JA, Hochbaum AI, Rubner MF. *Bio-macromolecules* 2003;4(1):96–106.
- [35] Picart C, Mutterer J, Richert L, Luo Y, Prestwich GD, Schaaf P, et al. *Proc Natl Acad Sci USA* 2002;99(20):12531–5.
- [36] Chen J, Huang SW, Lin WH, Zhuo RX. *Small* 2007;3(4):636–43.
- [37] Harris JJ, Bruening ML. *Langmuir* 2000;16(4):2006–13.
- [38] Yu AM, Liang ZJ, Cho JH, Caruso F. *Nano Lett* 2003;3(9):1203–7.





## pH-change protective PB-b-PEO polymersomes

Waltraut Mueller<sup>a,c</sup>, Kaloian Koynov<sup>b</sup>, Sebastien Pierrat<sup>a</sup>, Raphael Thiermann<sup>c</sup>, Karl Fischer<sup>a</sup>, Michael Maskos<sup>a,c,\*</sup>

<sup>a</sup>Institute of Physical Chemistry, University Mainz, Jakob-Welder-Weg 11, D-55128 Mainz, Germany

<sup>b</sup>Max-Planck-Institute of Polymer Research, D-55021 Mainz, Germany

<sup>c</sup>BAM Federal Institute for Materials Research and Testing, Unter den Eichen 87, D-12205 Berlin, Germany

### ARTICLE INFO

#### Article history:

Received 5 October 2010

Received in revised form

11 January 2011

Accepted 13 January 2011

Available online 21 January 2011

#### Keywords:

Diblock copolymers

Self assembly

Vesicle loading

### ABSTRACT

Poly(butadiene)-*b*-poly(ethylene oxide) vesicles were successfully loaded with hydrophilic dye Phloxine B. Dye addition during vesicle formation leads to Phloxine B encapsulated inside the water filled vesicle core as well as to freely diffusing dye molecules. The removal of unencapsulated substrate involves time consuming methods like dialysis or harsher methods like ultra filtration or selective precipitation, posing the risk of irreversible sample manipulation. Here used Phloxine B as pH sensitive fluorescence indicator allows the characterization of hydrophilic loading without separation procedure by adjusting the pH value. Additionally membrane blocking efficiency can be studied by time dependent fluorescence measurements. Cryogenic TEM studies showed that the self-assembled structure remained unchanged when the hydrophilic dye was incorporated within the vesicles. Fluorescence microscopy imaging proved the encapsulation of the hydrophilic dye inside the core volume. The combination of fluorescence correlation spectroscopy (FCS) and dynamic light scattering (DLS) measurements as ensemble methods confirmed those results additionally.

© 2011 Elsevier Ltd. All rights reserved.

### 1. Introduction

Amphiphilic block copolymers tend to self-assemble in selective solvents like water. Depending on parameters like overall average molecular weight, volume fraction of each block or effective interaction energy between monomers in the blocks, vesicles with bilayer shell and solvent interior volume similar to liposomes can be formed [1]. Such block copolymer vesicles in aqueous media have attracted increasing interest due to their enhanced stability compared to classical liposomes and due to the potential to control vesicle properties like bilayer thickness, permeability or surface functionalities by appropriate chemical copolymer adjustment [2].

The block copolymer poly(butadiene)-block-poly(ethylene oxide) (PB-*b*-PEO) is a frequently studied system under this regard [3–6] as it offers several advantages. For example, the PEO that forms the surface of the assembled structures in water is in general regarded as biocompatible [7,8]. Furthermore, depending on the PB block length the assembled vesicles can exhibit a thicker hydrophobic membrane core and therefore higher stability compared to liposomes [9]. Additionally this copolymer features the possibility of being crosslinked thereby stabilizing the assembled structure [10–12].

Drug delivery is mainly based on successful encapsulation of substrates with different solubility parameters. Micellar structures are favored in case of hydrophobic substrates solubilized within the hydrophobic core of the micelle [13,14]. Hydrophilic substrates are typically encapsulated by solubilization within the water filled cavity of liposomes or vesicles. With the additional hydrophobic domain in the shell, such vesicles offer the possibility of loading hydrophobic and hydrophilic substrates at the same time into the very same particle.

The hydrophobic encapsulation into the vesicle shell of various polymer systems has been reported before [15–24]. For the polymer under study the hydrophobic loading with fluorescent dye Nile Red as well as with hydrophobic semi-conductor nanocrystals was already investigated by our group and published recently [25].

The hydrophilic loading of the vesicles core volume has been successful for several polymer systems including the PB-*b*-PEO [26,27]. By substrate addition into the aqueous media during vesicle formation the hydrophilic substrates are encapsulated inside the vesicles core volume and are also freely diffusing in the surrounding solution. Crucial step is always the removal of unencapsulated substrate for detailed characterization. Such separation procedure involve time consuming methods like dialysis or harsher methods like ultra filtration or selective precipitation, posing the risk of irreversible sample manipulation. We here report on a system allowing the characterization of hydrophilic loading possibilities

\* Corresponding author. Institute of Physical Chemistry, University Mainz, Jakob-Welder-Weg 11, D-55128 Mainz, Germany. Tel.: +49 6131 3924190.

E-mail addresses: [michael.maskos@bam.de](mailto:michael.maskos@bam.de), [maskos@uni-mainz.de](mailto:maskos@uni-mainz.de) (M. Maskos).



without separating procedure. The hydrophilic dye Phloxine B is used whose fluorescence is pH sensitive and quenched at pH values smaller 2. By adjusting the surrounding pH the emission of freely diffusing dye molecules can be quenched and the measurement of fluorescence originating from the encapsulated molecules alone becomes possible. An additional feature is the possibility to monitor the proton diffusion through the vesicles membrane time dependent. Apart from spectroscopic and microscopic techniques we utilized fluorescence correlation spectroscopy in combination with dynamic light scattering to further characterize loading properties.

## 2. Experimental section

### 2.1. Materials

All vesicle solutions were produced in purified water (Waters MilliQ system) and tetrahydrofuran (THF, uvasol grade, Riedel-de Haën, destabilized by distillation). The fluorescent dyes Nile Red (99%, Acros) and Phloxine B (Aldrich) were used without purification. Hydrochloric acid (0.1M, Acros) was used without purification. The synthesis of poly(butadiene)-*b*-poly(ethylene oxide) was published before [6]. The copolymer PB<sub>130</sub>-*b*-PEO<sub>66</sub>-COOH was characterized by MALDI-TOF mass spectrometry and <sup>1</sup>H NMR resulting in  $M_n = 10$  kg/mol,  $M_w/M_n = 1.05$  and 29%w/w PEO (the indices represent the number average degree of polymerization of the individual blocks as determined by <sup>1</sup>H NMR).

### 2.2. Methods

Transmission Electron Microscopy imaging was performed at a FEI Tecnai 12 on carbon coated copper grids. Cryogenic TEM imaging was done under liquid N<sub>2</sub> cryo conditions on holey carbon coated copper grids. The microscope was used with 120 kV acceleration voltage and the images were taken with a CCD camera.

Fluorescence Correlation Spectroscopy was performed with a commercial FCS setup (Zeiss, Germany) consisting of the module ConfoCor 2 and an inverted microscope model Axiovert 200. A Zeiss C-Apochromat 40x/1.2 W water immersion objective was used. The fluorophores were excited by an argon-ion laser at  $\lambda = 488$  nm and emission was collected after filtering with a LP505 long pass filter. For detection, avalanche photodiodes were used to enable single-photon counting [25,28].

The calibration of the confocal observation volume was done using a reference standard with known diffusion coefficient, in our case orange fluorescent carboxylate-modified microspheres (FluoSpheres, Invitrogen) with a hydrodynamic radius of 54 nm (as obtained by dynamic light scattering).

Fluorescence Microscopy imaging was performed at an Axio Imager A1 Microscope (Zeiss, Germany), equipped with a 100×

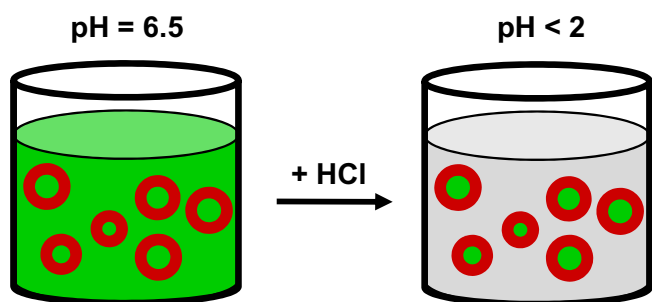


**Fig. 1.** Schematic drawing: (a) vesicle preparation at pH = 6.5, fluorescing PhB (green) and vesicle shell (red); (b) sample after HCl addition, surrounding solution at pH < 2 causes quenched fluorescence of freely diffusing PhB molecules. (For interpretation of the references to colour in this figure legend, the reader is referred to the web version of this article).

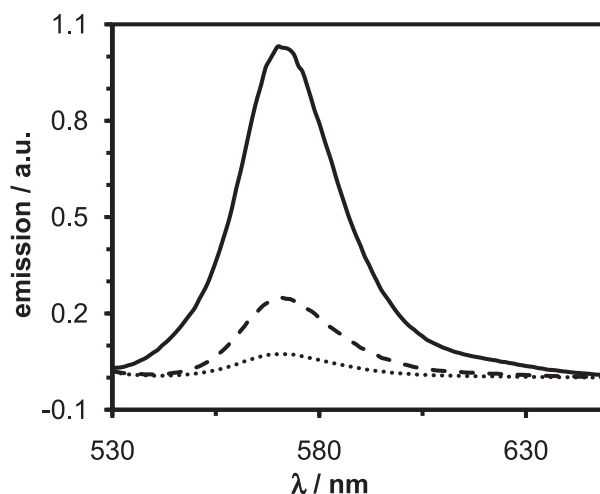


**Fig. 2.** Emission spectra of PhB-loaded vesicle solution P\_VC\_Ph1 after preparation at pH = 6.5 (line) and after HCl addition at pH = 2 (dashed line) and pH = 1.5 (dotted line), normalized at  $\lambda = 560$  nm for pH = 6.5.

water-objective (Zeiss) and an Alexa filter set,  $\lambda_{ex} = 488$  nm,  $\lambda_{em} = 550$  nm with a dichroic plate (Edmund Optics, Germany). Colour pictures were taken using a Canon Camera.

Fluorescence Spectroscopy was performed at a FP-6500 Spectrofluorometer (Jasco, Germany) with external temperature control.

Dynamic Light Scattering was performed with a SpectraPhysics SP2080 argon-ion laser ( $\lambda = 514$  nm), an ALV-SP125 goniometer with single-photon detector SO-SIPD and an ALV-5000 Multiple-Tau digital correlator, or with a JDS Uniphase helium-neon laser ( $\lambda = 623.8$  nm), an ALV-SP-86#060 goniometer with Avalanche photodiodes and an ALV-3000 digital correlator. Angle dependent measurements were carried out between 30° and 150° in steps of 20° at a temperature of 20 °C. Data evaluation was done according to the literature [29,33].

### 2.3. Procedure

Vesicle solutions were produced following two different routes, as already published [25]. The cosolvent method yields small vesicles with narrow size distribution. Standard final polymer

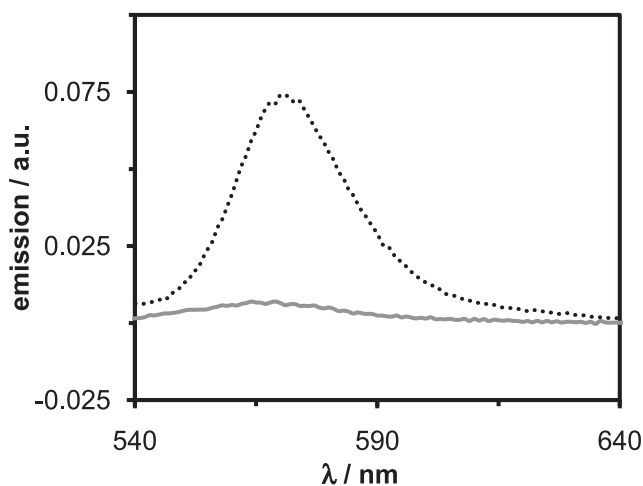


**Fig. 3.** Emission spectra of PhB/H<sub>2</sub>O solution ( $C = 0.1$  mg/l) after HCl addition at pH = 1.5 (gray line) in comparison to PhB-loaded vesicle solution P\_VC\_Ph1 at pH = 1.5 (dotted black line).

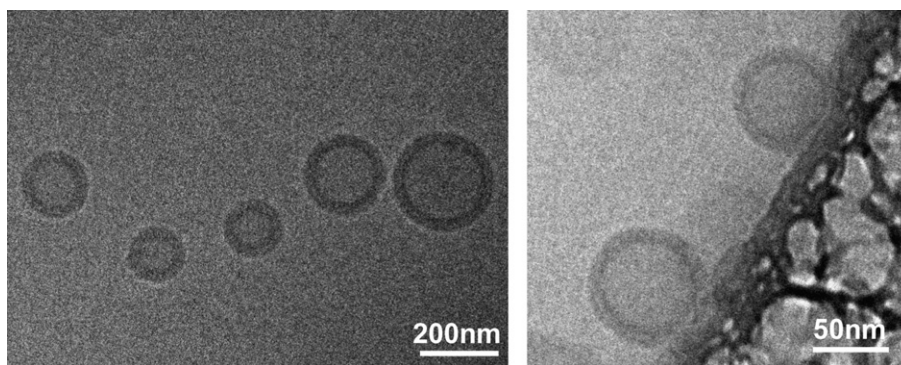


Fig. 4. Cryogenic TEM images of PhB-loaded vesicles P\_VC\_Ph1 in aqueous solution at pH = 6.5 (left) and pH = 1.5 (right).

concentration was  $C_p = 1$  g/L in water. Hydrophilic Phloxine B loading of those vesicles was achieved by addition of dye/water solution ( $C_{PhB} = 0.1$  g/L) to the starting copolymer/THF solution. The rehydration method leads to huge vesicles with broad size distribution. Hydrophilic Phloxine B loading of those vesicles was achieved by addition of dye/water solution ( $C_{PhB} = 0.1$  g/L) to the starting copolymer/THF solution. For additional hydrophobic loading, Nile Red (NR) was added to the starting copolymer/THF solution (final concentration  $c_{NR} = 0.1$  mg/L).

Fluorescence quenching of freely diffusing Phloxine B was achieved by adjusting the pH to a value of  $<2$  by addition of hydrochloric acid.

### 3. Results and discussion

The loading of PB<sub>130</sub>-b-PEO<sub>66</sub> vesicles with the hydrophilic dye Phloxine B (PhB) was successfully realized. The addition of PhB as hydrophilic substrate during vesicle formation leads to an equal distribution of dye molecules inside the water filled vesicle core volume and the surrounding aqueous environment. For characterization of hydrophilic loading properties the separation of freely diffusing dye molecules from encapsulated substrate is essential. The fluorescence of here used PhB is pH sensitive and quenched at pH values  $<2$ . This allows for loading characterization without separation step. By adjusting the surrounding pH after vesicle formation below pH = 2 the fluorescence emission of freely diffusing dye molecules is quenched whereas the polymeric vesicle membrane shields the dye molecules inside the vesicle core volume from proton

contact. Measurement of fluorescence originating from the encapsulated molecules alone becomes possible without physical separation procedure. Fig. 1 shows a schematic drawing.

Hydrophilic loaded vesicles with PhB inside the core volume were prepared using the ‘cosolvent method’ starting from a solution of PB-b-PEO copolymer in THF, dropwise addition of PhB solution in water (0.1 g/l) at pH = 6.5 and THF evaporation as described above. This leads to homogeneous coloured vesicle solutions with average hydrodynamic radii in the range of 60–80 nm (samplesP\_VC\_Ph) and PhB located inside the vesicles core volume and in the surrounding solution. The partial fluorescence quenching is achieved by addition of HCl thereby adjusting the pH to values  $<2$ . Fig. 2 shows the emission spectra in dependence of pH.

The emission of Phloxine B with the maximum at  $\lambda = 560$  nm is decreasing due to the addition of HCl. At pH = 1.5 (dotted line) only 7.2% of the emission intensity of the neutral sample (line) is detected. This effect cannot be attributed to the dilution process alone. An analogous 0.1 mg/l PhB/H<sub>2</sub>O solution as blind sample (blind1) diluted with water to the equivalent content results in an even higher emission intensity as reabsorption occurs at 0.1 mg/l (see SI). The fluorescence emission of this blind sample was also measured after HCl addition at pH = 1.5 (gray line, Fig. 3). The comparison with the emission intensity of the PhB-loaded vesicle sample at pH = 1.5 indicates nearly complete fluorescence quenching in the purely aqueous system as shown in Fig. 3. Normalized to the emission of the

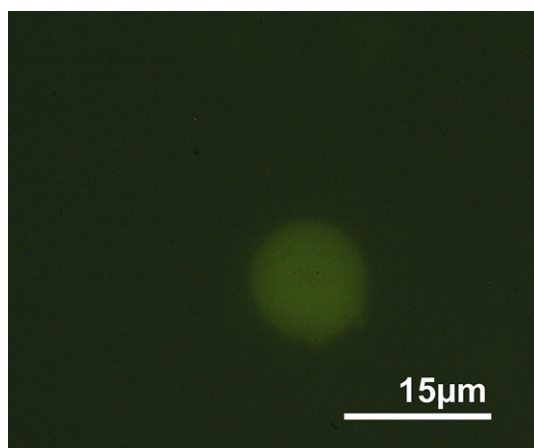


Fig. 5. Fluorescence microscopy image of PhB-loaded vesicles prepared via film rehydration in aqueous solution at pH = 1.5 (true color).

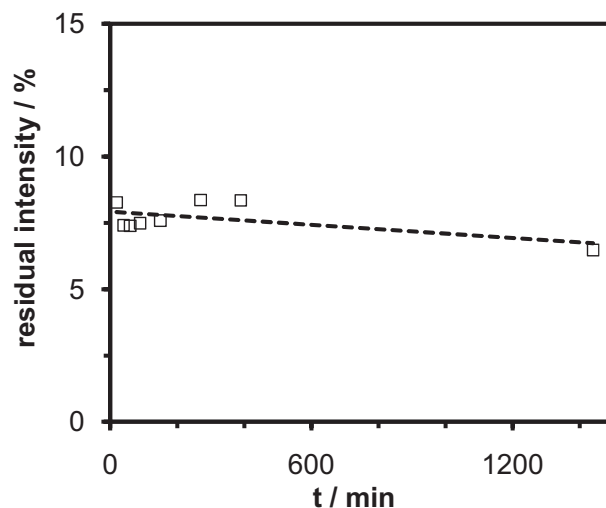


Fig. 6. Residual emission intensity of a PhB-loaded vesicle solution (pH = 1.5) at fluorescence maximum  $\lambda = 572$  nm in percent of the initial intensity (pH = 6.5), measured time dependent after HCl addition at  $t = 0$ .

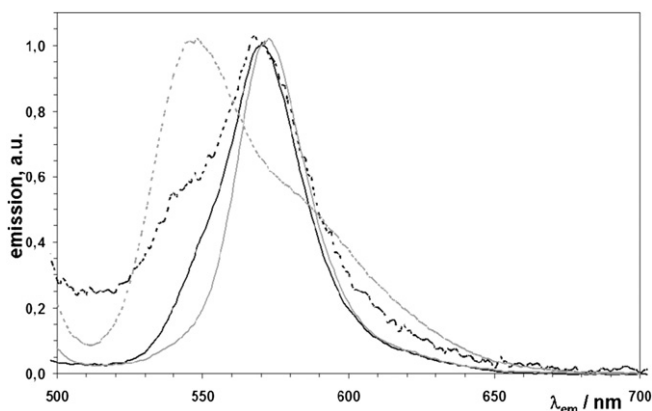


Fig. 7. Normalized emission spectra of PhB- and NR-co-loaded vesicle solution P\_VR\_PhNR after preparation at pH = 6.5 (line, black) and after HCl addition at pH = 1.5 (dotted line, black); additionally shown are the corresponding spectra of individually NR- and PhB-loaded vesicles at pH 1.5 (dotted line, gray; line gray).

PhB/H<sub>2</sub>O solution at pH = 6.5 the intensity decreases to 3% of the initial value due to HCl addition.

Analog experiments were done for a blind sample (blind2) of PhB in PEO/H<sub>2</sub>O solution with  $C_{\text{PEO}} = 2 \text{ g/l}$  ( $M_{\text{PEO}} = 3.5 \text{ kg/mol}$ ) and  $C_{\text{PhB}} = 0.1 \text{ mg/l}$ . The fluorescence intensity after HCl addition was as well below 3% of the initial value at pH = 6.5 (see SI). Dissolving PhB in linear polybutadiene ( $M = 1.5\text{--}2 \text{ kg/mol}$ ) was not possible even by harsh ultrasonic use. This partial protection of PhB molecules from proton contact in the PhB-loaded vesicle sample is therefore not due to interactions with the hydrophilic vesicle shell or incorporation into the hydrophobic polybutadiene area but due to the PhB position inside the vesicles core volume. The vesicular structure could be verified by cryogenic TEM imaging as shown in Fig. 4.

A vesicle sample prepared with pure water and Phloxine B addition after vesicle formation (blind3) could not shield dye molecules from proton contact. After HCl addition only below 3.1% of the initial fluorescence intensity were detected (see SI). Compared to 7.2% detected emission intensity of the loaded vesicle sample, this implies no PhB diffusion through the vesicle membrane within the experimental duration of less than 30 min.

For further investigations, starting from a dried copolymer film as described above, PhB-loaded vesicles were prepared via the 'rehydration method' (sample P\_VR\_Ph). This method leads to vesicles with very broad size distribution and diameters ranging from 60 nm up to several  $\mu\text{m}$ . By fluorescence microscopy imaging the dye loading can be visualized. Fig. 5 shows an image of PhB-loaded vesicles with a size of about 15  $\mu\text{m}$  (far above the microscope resolution limit of about 3  $\mu\text{m}$ , see ref. [25]). The high fluorescence intensity inside the vesicle supports the model of hydrophilic loading into the vesicle core volume and protection from proton contact by the vesicle membrane. Fluorescence originating from PhB molecules in the surrounding solution is not detectable.

To supplement characterization by imaging methods, fluorescence correlation spectroscopy (FCS) was used for measuring diffusion coefficients of fluorescent particles (details see SI) [28,30–32]. The hydrodynamic radii of the PhB-loaded vesicles is  $R_h = 87 \text{ nm}$ . Dynamic light scattering (DLS) measurements of the same solution resulted in an average hydrodynamic radius of  $\langle R_h \rangle = 63 \text{ nm}$  with a very broad size distribution ( $\mu_2 = 0.1$ ). The experimental angle dependent DLS data were evaluated by biexponential fitting and  $q = 0$  extrapolation [29].

The discrepancy between the particle size in FCS and DLS is probably due to the particles very broad size distribution. The DLS

result 'hydrodynamic radius' is the inverse value of a reciprocal z-average ( $R_h = \langle 1/R_h \rangle^{-1}$ ), whereas the FCS theory is derived for monodisperse samples and is highly dependent on equal particle brightness [28]. The bigger PhB-loaded vesicles can superimpose the result as they contain more dye molecules and therefore show brighter fluorescence signals. Nevertheless the FCS result proves, that the PhB molecules do not freely diffuse in the sample solution but travel with bigger particles. These results combined with the cryogenic TEM images showing vesicles with comparable sizes, allow to conclude the successful hydrophilic vesicle loading for Phloxine B without separation procedure.

Additional to loading verification, the proton diffusion through the vesicle membrane can be studied. Time dependent detection of the emitted fluorescence signal after acid addition gives access to the blocking efficiency of the vesicle membrane. Fig. 6 shows the residual fluorescence at  $\lambda = 572 \text{ nm}$  in percent of the initial intensity monitored for the first 24 h after pH adjustment. Most of the PhB molecules inside the vesicles core volume fluoresce unchanged even after 24 h in an acidic environment at pH = 1.5. This proves that those vesicle membranes have an excellent blocking ability for protons.

The pH induced quenching of the PhB outside the vesicles can even be used to detect e.g. Nile red loaded into the hydrophobic vesicle shell, which before acidification is not detectable [25]. An example of the corresponding fluorescence spectra is shown in Fig. 7.

After adjustment of the pH to 1.5, the clearly detected shoulder in the spectrum of P\_VR\_PhNR observed at approximately 540 nm can be related to the presence of NR.

#### 4. Conclusion

Polymeric vesicles of poly(butadiene)-b-poly(ethylene oxide) were successfully loaded with hydrophilic substrates. The hydrophilic dye Phloxine B, whose fluorescence is sensitive to pH, was distributed inside the water filled vesicle core volume and the surrounding solution. By adjusting the pH of the surrounding media the emission of freely diffusing dye molecules could be quenched and fluorescent measurement of the encapsulated substrates alone became possible. In addition, the hydrophobic loading employing small amount of Nile Red becomes detectable after pH sensitive quenching. Time dependent fluorescence measurements showed the membranes efficient blocking ability for proton diffusion. Cryogenic TEM imaging confirmed that the vesicular structure is not affected by the hydrophilic substrates encapsulation. Fluorescence microscopy measurements visualized the substrates positions inside the vesicles core volume. Results of fluorescence correlation spectroscopy and dynamic light scattering measurements as ensemble methods further support these results.

#### Acknowledgments

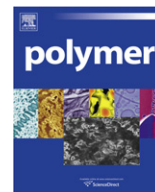
We thank Prof. M. Schmidt, University Mainz for the lab environment and helpful discussions, Dr. U. Kolb and the 'Elektronen Mikroskopie Zentrum' Mainz. For financial support we gratefully acknowledge Deutsche Forschungsgemeinschaft DFG (SFB 625). W.M. thanks Fonds der Chemischen Industrie (FCI) and Polymat 'Polymers in Advanced Materials' Mainz for additional financial support.

#### Appendix A. Supplementary material

Supplementary data associated with this article can be found, in the online version, at doi:10.1016/j.polymer.2011.01.028.

## References

- [1] Discher DE, Eisenberg A. *Science* 2002;297:967–73.
- [2] Lee JC-M, Bermudez H, Discher BM, Sheehan MA, Won Y-Y, Bates FS, et al. *Biotechnology and Bioengineering* 2001;73:135–45.
- [3] Förster S, Berton B, Hentze H-P, Krämer E, Antonietti M, Lindner P. *Macromolecules* 2001;34:4610–23.
- [4] Antonietti M, Förster S. *Advanced Materials* 2003;15:1323–33.
- [5] Jain S, Bates FS. *Science* 2003;300:460–4.
- [6] Maskos M. *Polymer* 2006;47:1172–8.
- [7] Caliceti P, Veronese FM. *Advanced Drug Delivery Reviews* 2003;55:1261–77.
- [8] Haag R. *Angewandte Chemie* 2004;116:280–4.
- [9] Bermudez H, Brannan AK, Hammer DA, Bates FS, Discher DE. *Macromolecules* 2002;35:8203–8.
- [10] Maskos M, Harris JR. *Macromolecular Rapid Communications* 2001;22:271–3.
- [11] Jofre A, Hutchison JB, Kishore R, Locascio LE, Helmerson K. *Journal of Physical Chemistry B* 2007;111:5162–6.
- [12] Chécot F, Lecommandoux S, Klok H-A, Gnanou Y. *European Physical Journal E* 2003;10:25–35.
- [13] Allen C, Maysinger D, Eisenberg A. *Colloids Surface B: Interfaces* 1999;16:3–27.
- [14] Kataoka K, Harada A, Nagasaki Y. *Advanced Drug Delivery Reviews* 2001;47:113–31.
- [15] Lecommandoux S, Sandre O, Chécot F, Rodriguez-Hernandes J, Perzyski R. *Advanced Materials* 2005;17:712–8.
- [16] Krack M, Hohenberg H, Kornowski A, Lindner P, Weller H, Förster S. *Journal of the American Chemical Society* 2008;130:7315–20.
- [17] Ghoroghchian PP, Lin JJ, Brannan AK, Frail PR, Bates FS, Therien MJ, et al. *Soft Matter* 2006;2:973–80.
- [18] Nardin C, Thoeni S, Widmer J, Winterhalter M, Meier W. *Chemical Communications*; 2000:1433–4.
- [19] Binder WH, Sachsenhofer R, Farnik D, Blaas D. *Physical Chemistry Chemical Physics* 2007;9:6435–41.
- [20] Binder WH, Sachsenhofer R. *Macromolecular Rapid Communications* 2008;29:1097–103.
- [21] Lecommandoux S, Sandre O, Chécot F, Perzyski R. *Progress in Solid State Chemistry* 2006;34:171–9.
- [22] Ghoroghchian PP, Frail PR, Susumo K, Park TH, Wu SP, Uyeda HT, et al. *Journal of the American Chemical Society* 2005;127:15388–90.
- [23] Bockstaller MR, Lapetnikov Y, Margel S, Thomas EL. *Journal of the American Chemical Society* 2003;125:5276–7.
- [24] Chiu JJ, Kim BJ, Kramer EJ, Pine DJ. *Journal of the American Chemical Society* 2005;127:5036–7.
- [25] Mueller W, Koynov K, Fischer K, Hartmann S, Pierrat S, Basché Th, et al. *Macromolecules* 2009;42:357–61.
- [26] Choucair A, Soo PL, Eisenberg A. *Langmuir* 2005;21:9308–13.
- [27] Borchert U, Lippbrandt U, Bilanz M, Kimpfler A, Rank A, Pescka-Süss R, et al. *Langmuir* 2006;22:5843–7.
- [28] Rigler R, Elson E. *Fluorescence correlation spectroscopy: theory and applications*. Berlin: Springer-Verlag; 2001.
- [29] Schmidt M. In: Brown W, editor. *Dynamic light scattering*. Oxford: Clarendon Press; 1993 [Chapter 8].
- [30] Haustin E, Schwille P. *Current Opinion in Structural Biology* 2004;14:531–40.
- [31] Koynov K, Mihov G, Mondeshki M, Moon C, Spiess W, Müllen K, et al. *Bio-macromolecules* 2007;8:1745–50.
- [32] Yin M, Sorokina K, Kuhlmann C, Li C, Mihov G, Koynov K, et al. *Bio-macromolecules* 2008;9:1381–9.
- [33] Goodwin AP, Mynar JL, Ma Y, Flemin GR, Fréchet JMJ. *Journal of the American Chemical Society* 2005;127:9952–3.



## How does sequence length heterogeneity affect the dilute solution conformation of copolymers?

Imad A. Haidar Ahmad<sup>a</sup>, Deborah A. Striegel<sup>b</sup>, André M. Striegel<sup>a,\*</sup>

<sup>a</sup>Department of Chemistry & Biochemistry, Florida State University, Tallahassee, FL 32306-4390, USA

<sup>b</sup>Department of Mathematics, Florida State University, Tallahassee, FL 32306-4510, USA

### ARTICLE INFO

#### Article history:

Received 5 November 2010

Received in revised form

7 January 2011

Accepted 16 January 2011

Available online 22 January 2011

#### Keywords:

Multi-detector SEC

Copolymer conformation

Sequence length heterogeneity

### ABSTRACT

Sequence length heterogeneity (SLH) is defined as the change, as a function of copolymer molar mass ( $M$ ), in the average number of continuous monomers of a given repeat unit. SLH can influence polymeric properties such as thermal stability, mechanical behavior, transparency, and the ability of copolymers to reduce interfacial surface tension. Here, we demonstrate the relation between SLH and the change as a function of molar mass of a dimensionless size parameter, the ratio of the viscometric radius and the radius of gyration, irrespective of chemical heterogeneity or molar mass polydispersity. Multi-detector size-exclusion chromatography (SEC) provides for a convenient method by which to experimentally establish this relation and, consequently, a method by which to determine whether SLH is present in a copolymer, whether the degree of randomness of a copolymer changes across the molar mass distribution (MMD), or whether two copolymers differ from each other in degree of randomness at a given  $M$  and/or across their MMDs. Results from our SEC and FT-IR measurements of block, random, alternating, and gradient copolymers of styrene (S) and methyl methacrylate (MMA) and their respective homopolymers agree with results from a probability theory based model of SLH in linear random copolymers. The multi-detector SEC method employs instrumentation available in most polymer separations laboratories and the relations developed should be applicable to copolymers other than the S-MMAs studied here.

© 2011 Elsevier Ltd. All rights reserved.

### 1. Introduction

Sequence length heterogeneity (SLH) is the change with copolymer molar mass ( $M$ ) in the average number of continuous monomers of a given type (i.e., of a given chemistry or of a given repeat unit). This type of heterogeneity exists in the case of a random copolymer, i.e., a polymer comprising two different types of monomers randomly distributed within the chain. A random copolymer is shown in Fig. 1c, along with the other types of copolymers used in this study. The arrangement of monomers in the polymeric chain is uniform in the case of alternating and block copolymers, not so in the case of random copolymers, where the random arrangement of monomers in the chain results in a distribution of the number of continuous monomers of a given type (either white or black, for the generic cases in Fig. 1). The change in this distribution as a function of molar mass is given the term “sequence length heterogeneity” and abbreviated as SLH.

The ability to detect SLH is important for understanding both its sources and its influence on structure-property relationships. Examples of the polymeric properties affected by SLH are the ability to reduce interfacial surface tension via copolymeric adsorption at a liquid–liquid interface [1]; conformation and folding of protein-like copolymers [2–7]; and the thermal stability [8], melting point [9], mechanical behavior [10], and transparency of films [11,12]. Sequence length heterogeneity originates from the different probabilities with which monomers arrange in a copolymeric chain, from chemical heterogeneity (i.e., from the change in the relative percentage of the various monomers among copolymeric chains of different molar mass) [13], and from the change in mutual miscibility of monomers during the copolymerization process. Here, we show a new, semi-quantitative method for determining SLH in random copolymers. This method provides an approach to understanding the “randomness”, and change therein, of a random copolymer, i.e., for determining whether a random copolymer is of preferentially blocky, statistical, or alternating nature, and to ascertaining how this randomness changes as a function of molar mass  $M$ .

In this study, we relate SLH to a change in copolymer solution conformation as a result of intrachain repulsion. This intrachain

\* Corresponding author.

E-mail address: [striegel@chem.fsu.edu](mailto:striegel@chem.fsu.edu) (A.M. Striegel).



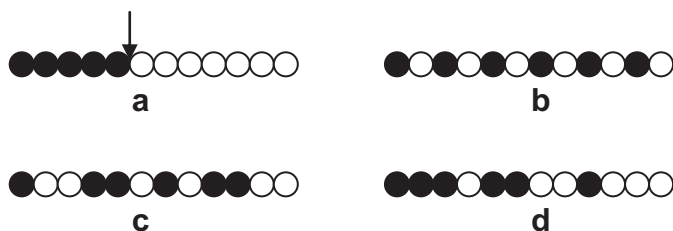


**Fig. 1.** Types of copolymers used in this study. (a) Block copolymer, (b) alternating copolymer, (c) random copolymer, and (d) gradient random copolymer. Arrow indicates junction point in the block copolymer.

repulsion occurs at the junction points between dissimilar monomers (as indicated by the arrow in Fig. 1a) [14–16]. Consequently, the change in the dispersion of the monomers in a copolymeric chain, i.e., the SLH, results in a change in intrachain repulsion along the copolymeric chain due to the variation in the percentage of the number of junction points as a function of the degree of polymerization. These intrachain enthalpic interactions force the chain to adopt a conformation that minimizes intrachain repulsion. The change in enthalpy is therefore balanced by a change in entropy in the form of conformational change [15]. In this project, we use the ratio of the viscometric radius to the radius of gyration,  $R_{\eta}/R_G$ , to determine the conformation of the copolymer in solution and to detect the SLH by detecting the change in conformation (as will be explained subsequently). Our conclusions are supported by results from infrared spectroscopy experiments and from a model based on probability theory.

At this point it is, perhaps, useful to distinguish between SLH and the more commonly encountered parameter “sequence length distribution” or SLD. If the average value of the SLD at each  $M$  in the copolymer is plotted as a function of copolymer  $M$ , and if this average value changes with  $M$ , then the copolymer is said to possess SLH. Conversely, a plot with sequence length as the abscissa and either the differential or cumulative weight fraction as the ordinate, is the SLD. (The distinction between SLD and SLH is thus akin to that between chemical composition distribution and chemical heterogeneity).

The dimensionless ratio  $R_{\eta}/R_G$  is known to depend on polymer architecture and dilute solution conformation. This ratio increases with increasing polymer compactness and decreases as the polymer becomes more extended. Highly extended polymers (e.g., poly( $\gamma$ -benzyl-L-glutamate) in helicogenic solvents) have  $R_{\eta}/R_G$  values in the 0.3–0.4 range [17]. At the other extreme, the  $R_{\eta}/R_G$  for a hard sphere is  $\sqrt{5/3}$ . Random coil polymers adopt a flexible conformation in solution, corresponding to  $R_{\eta}/R_G$  values in the range of approximately 0.7–0.9 [18–21]. Previous work in this area has focused on using either the sequence length distribution [22–24] or the instantaneous monomer sequence length to study how copolymeric randomness changes as a function of  $M$  [25,26]. A distinct advantage of the present method is that it relies solely on physical properties (angular dissymmetry and intrinsic viscosity) of the copolymer solutions; i.e., success is not contingent upon existence of chemical properties such as preferential UV absorption of one monomer over another in a copolymer (except for the case of gradient copolymers, as described in Section 2.6). An additional advantage of the method presented here is that it does not rely on specialized equipment. Rather, it utilizes a type of separation-detector combination that is nowadays commonplace in most polymer characterization laboratories.

Needed for our approach is a separation technique capable of fractionating polymers according to molar mass, and which can also measure  $R_{\eta}$  and  $R_G$  as a continuous function of  $M$ . Size-

exclusion chromatography (SEC) using multi-angle static light scattering (MALS), differential viscometry (VISC), and differential refractometry (DRI) detection meets these requirements and is, thus, our method of choice [27,28]. This triple-detector SEC technique can be used to obtain the  $R_{\eta}/R_G$  ratio as a continuous function of  $M$ , a novel approach which, to our knowledge, provides the first experimentally established link between a dimensionless size parameter and SLH.

## 2. Experimental

### 2.1. Materials

Homopolymers of polystyrene (PS) and poly(methyl methacrylate) (PMMA) were obtained from Varian/Polymer Laboratories (now Agilent) and Toyo Soda; copolymers of styrene (S) and methyl methacrylate (MMA), and of S and *t*-butyl methacrylate (*t*-BMA), were obtained from Polymer Source. Unstabilized THF was obtained from EMD, methylene chloride from VWR. All materials were used as received, without further purification.

### 2.2. Multi-detector size-exclusion chromatography: SEC/MALS/VISC/DRI and SEC/MALS/UV/DRI

For the multi-detector SEC experiments, a concentration of 1 mg/mL of each copolymer in THF was prepared and left on a laboratory wrist-action shaker overnight to ensure dissolution. For increased precision, two different 1 mg/mL solutions of each sample were prepared and, from each dissolution, two 100  $\mu$ L injections were performed, for a total of four injections per sample. The SEC system consisted of a Waters 2695 Separations Module (Waters), three PLgel 10  $\mu$ m particle size Mixed-B SEC columns, (Varian/Polymer Laboratories), and three detectors connected in series: A DAWN EOS multi-angle static light scattering (MALS) photometer (Wyatt Technology Corp.), followed by either a Model 166 UV detector (Beckman-Coulter) or a ViscoStar differential viscometer (Wyatt), followed by an Optilab rEX differential refractometer (Wyatt). The wavelength of the lamp in the UV detector is set to 260 nm, where styrene (S) absorbs strongly and methyl methacrylate (MMA) does not absorb. A 31,400 g/mol narrow polydispersity ( $M_w/M_n = 1.02$ ) linear PS standard was used for normalization of the MALS unit photodiodes as well as for calculating interdetector delays and for inter-detector band broadening correction [29]. Data acquisition was performed using Wyatt's ASTRA software (V.5.3.2.1), plotting and calculations were performed with OriginPro 7.5 (V.7.5885, Origin Lab Corp.).

### 2.3. Specific refractive index increment ( $\partial n/\partial c$ ) determination

The specific refractive index increments ( $\partial n/\partial c$ ) of the polymers in THF at 25 °C are given in Table 1. The samples were dissolved in THF and left overnight on a wrist-action shaker to ensure full dissolution and solvation. For offline  $\partial n/\partial c$  determination, six dilutions of each sample, ranging from 1.0–6.0 mg/mL, were injected directly into the Optilab rEX differential refractometer (Wyatt) using a Razel model A-99EJ syringe pump. Flow rate was 0.08 mL/min. Sample solutions were gently filtered through 0.45  $\mu$ m Teflon syringe filters, neat THF for baseline determination through a 0.02  $\mu$ m Teflon syringe filter. The wavelength of the lamp in the DRI detector is filtered to match the vacuum wavelength of the laser in the MALS detector ( $\lambda_0 = 685$  nm). Data acquisition and processing were done with Wyatt's ASTRA V software (V. 5.3.2.1).

**Table 1**  
Homo and copolymers studied.

Polymer	$M_w/M_n^a$	% of styrene (%S)	$\partial n/\partial c$ (mL/g)	Manufacturer
PS (186k) <sup>b</sup>	1.07	100	0.195 ± 0.002	Toyo Soda
PS (533k) <sup>b</sup>	1.05	100	0.194 ± 0.002	Varian/Polymer Laboratories
PS (723k) <sup>b</sup>	1.05	100	0.198 ± 0.004	Varian/Polymer Laboratories
PMMA (343k) <sup>b</sup>	1.02	0	0.087 ± 0.001	Varian/Polymer Laboratories
PMMA (467k) <sup>b</sup>	1.06	0	0.086 ± 0.002	Varian/Polymer Laboratories
P(S- <i>b</i> -MMA) (46k, 138k) <sup>c</sup>	1.16	25 <sup>d</sup>	0.109 ± 0.001	Polymer Source
P(S- <i>b</i> -MMA) (131k, 46k) <sup>c</sup>	1.10	75 <sup>d</sup>	0.168 ± 0.001	Polymer Source
P(S- <i>ran</i> -MMA) ( $M_n$ 126k) <sup>b</sup>	1.39	20 <sup>a</sup>	0.108 ± 0.004	Polymer Source
P(S- <i>ran</i> -MMA) ( $M_n$ 186k) <sup>b</sup>	1.43	25 <sup>a</sup>	0.111 ± 0.002	Polymer Source
P(S- <i>alt</i> -MMA) ( $M_n$ 235k) <sup>b</sup>	1.85	50 <sup>a</sup>	0.136 ± 0.002	Polymer Source
P(S- <i>co</i> -MMA) ( $M_n$ 140k) <sup>e</sup>	1.42	24.4 <sup>a,f</sup>	0.114 ± 0.002 <sup>g</sup>	Polymer Source
P(S- <i>co</i> - <i>t</i> -BMA) ( $M_n$ 96k) <sup>b</sup>	1.7	50.0 <sup>a</sup>	0.128 ± 0.002 <sup>g</sup>	Polymer Source

<sup>a</sup> Values from the manufacturer.

<sup>b</sup> Value in parenthesis represents number-average molar mass  $M_n$ , as reported by manufacturer.

<sup>c</sup> First value in parenthesis represents  $M_n$  of styrene block, second value represents  $M_n$  of the methyl methacrylate block, both values as reported by manufacturer.

<sup>d</sup> Percentages are calculated using the molar mass of each block.

<sup>e</sup> Gradient random copolymer.

<sup>f</sup> Average value. %S in this copolymer extends from ~30% at the low end of the MMD to ~20% at the high end of the MMD.

<sup>g</sup> Denotes average value. Due to chemical heterogeneity,  $\partial n/\partial c$  varies across the MMD of gradient copolymers.

## 2.4. Fraction collection

To collect elution fractions of the random copolymers for subsequent characterization by FT-IR (see below), we employed the above SEC system with only the MALS photometer and an F203B fraction collector (Gilson). A solution of 6 mg/mL of each the 126k and the 186k random copolymers P(S-*ran*-MMA) (see Table 1) in uninhibited THF was prepared and left on a laboratory wrist-action shaker overnight to ensure dissolution. For each copolymer, twenty injections were performed and, from each injection, three fractions were collected: Fraction 1 was collected between an elution volume range of 35.6 and 39.6 mL, fraction 2 between a range of 40.1 and 42.1 mL, and fraction 3 between a range of 42.6 and 46.6 mL.

## 2.5. FT-IR

The solvent from the fractions collected in the previous experiment was evaporated using a rotary evaporator and the remaining dried polymer was dissolved in ~3 mL of methylene chloride. This solution was then added dropwise to the surface of a KBr crystal and left until the solvent evaporated completely. FT-IR spectra of the copolymer deposited on the surface of the crystal were obtained using a Thermo Nicolet Avatar 360 FT-IR (Thermo Nicolet Corp.). Data acquisition was performed using OMNIC (V.6.0, Thermo Nicolet Corp.), peak fitting and calculation of areas under the peaks at 1074 and 1730 cm<sup>-1</sup> were performed with the PeakFit module of OriginPro 7.5 (V.7.5885, Origin Lab Corp.). Peak fitting was performed to calculate the area under the peak at 1074 cm<sup>-1</sup>, because of the partial overlap of two peaks at 1074 and 1064 cm<sup>-1</sup> in the spectra of the random copolymers. The standard deviations shown in Table 2 represent the precision associated with repeat measurements of peak areas in the IR spectra.

## 2.6. Correction for chemical heterogeneity

A classical approach to obtaining the chemical heterogeneity-corrected molar mass and radius of gyration of a copolymer relies on determining the apparent molar mass (i.e.,  $M$  not corrected for chemical heterogeneity) in two different solvents followed by a correction, as explained in references [30] and [31]. The approach we have taken for the gradient random copolymers P(S-*co*-MMA) and P(S-*co*-*t*-BMA) relies on the fact that only the styrene monomer in these copolymers absorbs at a given UV wavelength. Adding a UV

detector to the experimental SEC set-up thus allows calculation of the molar mass of each SEC elution slice according to the S:MMA ratio of that particular slice (or, more specifically, using the  $\partial n/\partial c$  corrected for this ratio), rather than using the S:MMA ratio of the bulk copolymer (and, thus, using the  $\partial n/\partial c$  of the bulk copolymer). Using the SEC/MALS/UV/DRI and SEC/MALS/VISC/DRI systems described above, we are able to correct the  $M$  averages, MMD, intrinsic viscosity, radius of gyration, and viscometric radius of the gradient random copolymers for the effects of chemical heterogeneity. The magnitude of the correction in  $M$  for the gradient copolymers studied is ~5%, the correction in  $R_{G,z}$  of the bulk copolymers is less than 1 nm (no correction is needed for the  $R_{G,z}$  of the individual slices). No correction for chemical heterogeneity was performed for the alternating, random, and block copolymers, in the first two cases because of a lack of chemical heterogeneity (see Fig. 7), in the latter case due to the narrow  $M$  polydispersity of the block copolymers (Table 1).

## 3. Results and discussion

Polystyrene, poly(methyl methacrylate), and their respective random, block, alternating, and gradient random copolymers were used in this study. Polystyrene is denoted as PS, poly(methyl methacrylate) as PMMA, random copolymers as P(S-*ran*-MMA), block copolymers as P(S-*b*-MMA), alternating copolymer as P(S-*alt*-MMA), and gradient random copolymer as P(S-*co*-MMA). We shall denote the gradient random copolymer of styrene and *tert*-butyl methacrylate as P(S-*co*-*t*-BMA). Table 1 gives relevant properties of

**Table 2**  
Area under FT-IR peak at 1074 cm<sup>-1</sup>, indicative of JPR in copolymer.

Fraction number	Normalized 1074 cm <sup>-1</sup> peak area <sup>a</sup>		
	186k random copolymer	126k random copolymer	Alternating copolymer
Fraction 1 <sup>b</sup>	0.148 ± 0.003 <sup>e</sup>	0.080 ± 0.001	0.216 ± 0.014
Fraction 2 <sup>c</sup>	0.137 ± 0.003	0.057 ± 0.001	
Fraction 3 <sup>d</sup>	0.057 ± 0.002	0.032 ± 0.001	

<sup>a</sup> As per Eq. (4).

<sup>b</sup> For SEC slices eluting between 35.6 mL and 39.6 mL.

<sup>c</sup> For SEC slices eluting between 40.1 mL and 42.1 mL.

<sup>d</sup> For SEC slices eluting between 42.6 mL and 46.6 mL.

<sup>e</sup> Standard deviations based on replicate determinations of peak areas, as described in Section 2.5.

the copolymers used in this study, while Fig. 1 shows generic versions of the different types of copolymers.

Because our study relies on the ratio of the viscometric radius and the radius of gyration, we define both of these briefly. As customary, our study employs the weight-average viscometric radius  $R_{\eta,w}$  and the z-average radius of gyration  $R_{G,z}$ . For simplicity, and because SEC slices are assumed to be virtually monodisperse (i.e.,  $\dots R_{\eta,n,i} \approx R_{\eta,w,i} \approx R_{\eta,z,i} \dots$  and  $\dots R_{G,n,i} \approx R_{G,w,i} \approx R_{G,z,i} \dots$ ), the subscripts  $w$  and  $z$  are omitted throughout the paper.

The radius of gyration  $R_G$ , the square of which is determined via multi-angle static light scattering, is defined as per [19,32–35]:

$$R_G = \left( \frac{1}{n} \sum_i (r_i - R_{cm})^2 \right)^{\frac{1}{2}} \quad (1)$$

where  $n$  is the number of monomers in the chain,  $r_i$  is the location of the  $i$ th monomer, and  $R_{cm}$  is the location of the polymer center of mass. (Strictly speaking, equation (1) should include the molar mass of the constituent homopolymers [30]. This complication can be safely ignored here, however, due to the negligible effect of chemical heterogeneity on  $R_G$ , as explained in Section 2.6).

The viscometric radius  $R_{\eta}$ , determined using MALS, VISC, and DRI detection combined, is the radius of a hard sphere that alters the viscosity of the solvent by the same amount as does the polymer. This radius is defined as [19, 32, 34]:

$$R_{\eta} \equiv \left( \frac{3[\eta]M}{10\pi N_A} \right)^{\frac{1}{3}} \quad (2)$$

where  $[\eta]$  is the intrinsic viscosity of the solution,  $N_A$  is Avogadro's number, and  $M$  is the molar mass of the analyte.

A comparison of the radii of gyration at a given  $M$  (Fig. 2a) helps in determining whether the intrachain repulsion is different among copolymers. The difference in the  $R_G$  values of the different copolymers at a given molar mass can be related to the difference in the degree of polymerization (DP) of the copolymers, in the hydrodynamic volume of the constituent monomers, or in the intrachain repulsion along the copolymeric chain. At any given  $M$ , the difference in DP is expected to be negligible because of the similarity in the molar masses of styrene and methyl methacrylate ( $\sim 4\%$  difference). The two homopolymer polymers, PS and PMMA, occupy very similar hydrodynamic volumes in solution under the present solvent/temperature conditions, as shown in previous work [13]. The similarity between the dilute solution size of PS and that of PMMA is supported by the information obtained from Fig. 2b, the plot of the viscometric radius ( $R_{\eta}$ ) versus molar mass, where the difference in the  $R_{\eta}$  values between the copolymers at any given  $M$  is shown to be negligible. To better judge the relation between the  $R_G$  values and intrachain repulsion, the ratio of the viscometric radius to the radius of gyration will be plotted versus molar mass, for reasons that will be explained subsequently.

In Fig. 3, we observe a variation in the  $R_{\eta}/R_G$  ratio as a function of molar mass for the two random copolymers studied. (The ripples in the plots are due to small pump pressure fluctuations in the chromatographic system used). The ratio varies from a maximum value of 0.94 at low  $M$  to a minimum value of 0.66 at high  $M$ . This result indicates that chains in the low- $M$  portion of the MMD of the random copolymers appear to behave in dilute solution as either homo- or block copolymers, whereas chains in the high  $M$  portion of the MMD appear to adopt a structure resembling that of the alternating copolymer studied (the block and the alternating copolymers are studied here as limiting cases, as are their

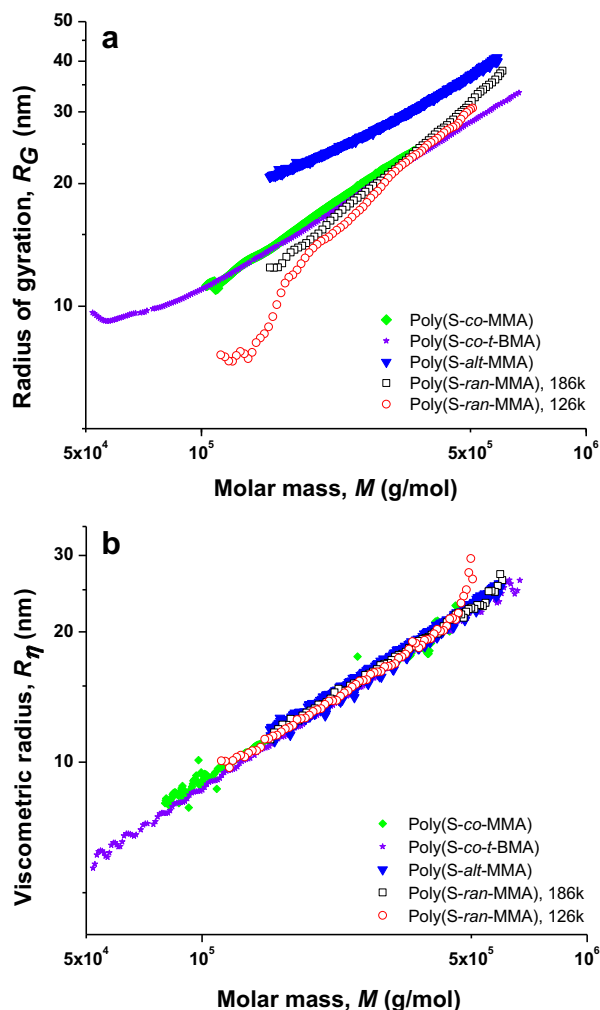


Fig. 2. a) Plot of  $R_G$  versus molar mass of alternating, gradient, and random copolymers studied. b) Plot of  $R_{\eta}$  versus molar mass of alternating, gradient, and random copolymers studied. Data markers represent averages of replicate determinations of each sample, as described in Section 2.2, with standard deviations substantially smaller than data points and, therefore, not shown.

respective homopolymers). We will show that the observed decrease in  $R_{\eta}/R_G$  and the accompanying increase in chain extension are due to sequence length heterogeneity SLH in the copolymers. A change in the  $R_{\eta}/R_G$  ratio as molar mass increases can be related to a change in the degree of polymerization DP of the copolymer (because the number of junction points between S and MMA increases with increasing DP), to the presence of SLH, or to both. To factor out the effect of degree of polymerization, a quantity termed the junction point ratio or  $JPR$  will be used to relate the  $R_{\eta}/R_G$  and supporting FT-IR results to the SLH. The  $JPR$  is explained next.

### 3.1. Junction point ratio ( $JPR$ )

The junction point ratio  $JPR$  of a copolymer is defined as the ratio of the total number of junction points between dissimilar monomers to the total number of junction points between any two monomers in the copolymer. The latter is equivalent to the degree of polymerization minus one (i.e., to  $n-1$ ). For large degrees of polymerization ( $n \gg 1$ ), the total number of junction points between any two monomers is essentially equal to the degree of polymerization. The junction point ratio is defined as per:

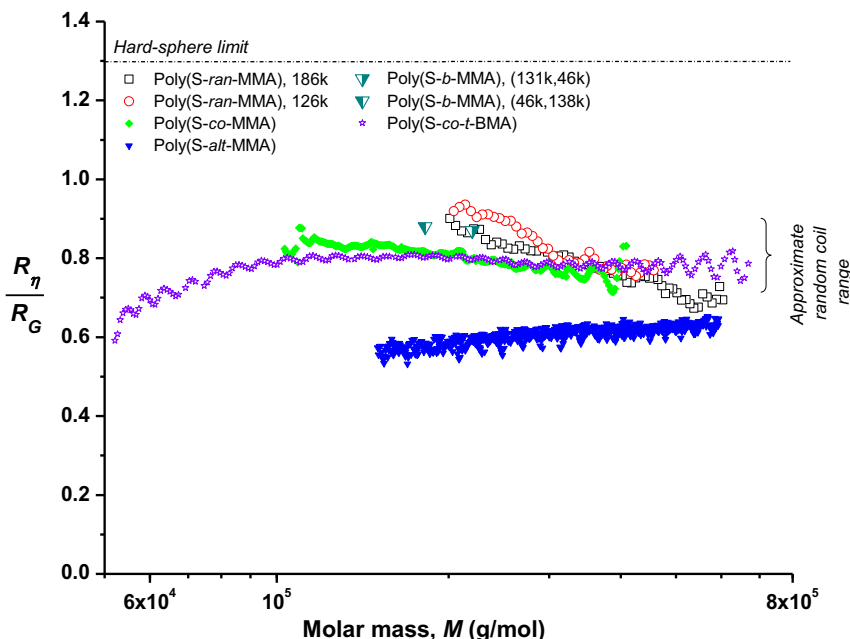


Fig. 3.  $R_{\eta}/R_G$  ratio of block, alternating, random, and gradient random copolymers studied, based on data in Fig. 2. Shown also is the theoretical hard sphere limit.

$$\begin{aligned} \text{Junction point ratio} = JPR &= \frac{\text{total number of junction points between dissimilar monomers}}{\text{total numbers of junction points}} \\ &= \frac{\text{total number of junction points between dissimilar monomers}}{\text{degree of polymerization} - 1} \end{aligned} \quad (3a)$$

and for large degree of polymerization as:

$$\text{Junction point ratio} = JPR \approx \frac{\text{total number of junction points between dissimilar monomers}}{\text{degree of polymerization}} \quad (3b)$$

The value of the  $JPR$  shown in Equation (3b) varies between two limiting cases: Alternating copolymers, for which the  $JPR = 1$ , and block copolymers, for which the  $JPR \approx 0$ . For both types of copolymers, alternating and block, at large  $n$  the  $JPR$  is expected to be molar mass-independent, i.e., to remain constant as a function of  $M$ . In the case of random copolymers, the  $JPR$  changes depending on the distribution of monomers in the chain. As a random copolymer becomes more alternating than blocky, the  $JPR$  approaches 1; as the copolymer becomes more blocky than alternating, the  $JPR$  approaches 0. The change in the  $JPR$  value as a function of  $M$  is indicative of the presence of sequence length heterogeneity in copolymers, as seen in the generic copolymers represented in Fig. 4. In this figure, the SLH is manifested as a change in the  $JPR$  value, as shown in the change from 3a to 3c and from 3a to 3d. The change from 3a to 3c results in an increase in the  $JPR$  value, i.e.,  $\Delta JPR = JPR_{\text{final}} - JPR_{\text{initial}} = 0.83 - 0.64 = 0.19 > 0$ , which indicates that the distribution of monomers in copolymer 3c is more alternating than it is in copolymer 3a. The change from 3a to 3d results in a decrease in the  $JPR$  value, i.e.,  $\Delta JPR = JPR_{\text{final}} - JPR_{\text{initial}} = 0.39 - 0.64 = -0.25 < 0$ , indicating that the distribution of monomers in copolymer 3c is more blocky than that in 3a. The change in the monomeric distribution from 3a to 3b is negligible, i.e.,

$\Delta JPR = JPR_{\text{final}} - JPR_{\text{initial}} = 0.65 - 0.64 = 0.01 \approx 0$ , which indicates a virtual absence of SLH. From the preceding discussion, it should be evident that a change in  $JPR$  as a function of copolymer  $M$  indicates the presence of sequence length heterogeneity in the copolymer.

Using the  $JPR$  as expressed in Equations (3a) and (3b) normalizes out the effect of degree of polymerization on the change in  $R_{\eta}/R_G$  as a function of  $M$ . This isolates the effect of SLH on  $R_{\eta}/R_G$  and on the change in the latter with  $M$  or DP. Additional complications that can arise due to the presence of chemical heterogeneity are addressed in Sections 3.6.4 and 3.6.5.

### 3.2. Quantitative FT-IR analysis of the junction point ratio

As seen in Fig. 5, the FT-IR spectra of alternating copolymers of styrene and methyl methacrylate show a significant peak at  $\sim 1074 \text{ cm}^{-1}$ , which is absent in the spectra of the block copolymers (shown) and of the constituent homopolymers (not shown). As demonstrated by Mori [36], the area under this peak is affected by the presence of a styrene monomer next to a methyl methacrylate monomer. As a result, the area under the peak at  $\sim 1074 \text{ cm}^{-1}$  in a random copolymer of styrene and methyl methacrylate is proportional to the  $JPR$  of the copolymer. For both random



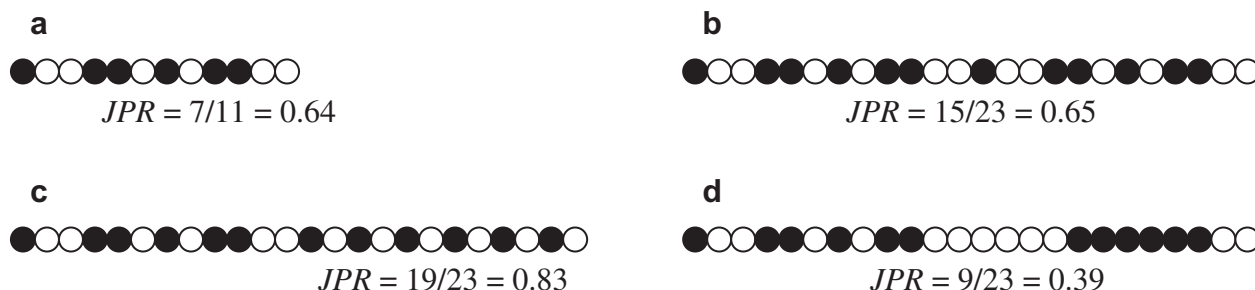


**Fig. 4.** Sequence length heterogeneity SLH and its relation to change in the junction point ratio  $JPR$  of copolymers. (a) Random copolymer of molar mass  $M$ ; (b), (c), and (d) random copolymers of molar mass  $2M$ . There is absence of SLH in the change from (a) to (b), where  $\Delta JPR \approx 0$ , whereas SLH occurs in the change from (a) to (c) and from (a) to (d). In the change from (a) to (c) the copolymer becomes more alternating and  $\Delta JPR > 0$ , whereas in the change from (a) to (d) the copolymer becomes more blocky and  $\Delta JPR < 0$ . (For interpretation of the references to colour in this figure legend, the reader is referred to the web version of this article).

copolymers used in this study, the area under the peak at  $1074\text{ cm}^{-1}$  is expected to increase as a function of molar mass due to the expected increase in  $JPR$  with increasing  $M$ . In order to verify this hypothesis, three fractions of different  $M$  were collected for each of the two random copolymers studied (see Section 2.4); the fractions are numbered according to their elution from the SEC column; i.e., fraction 1 elutes first and has the highest  $M$ , while fraction 3 elutes last and has the lowest molar mass. Fraction 2 is intermediate in both elution volume and molar mass relative to fractions 1 and 3.

Table 2 compares the normalized peak areas of the  $1074\text{ cm}^{-1}$  FT-IR peaks for the alternating copolymer and both random copolymers studied. Normalization (done with respect to the peak at  $\sim 1730\text{ cm}^{-1}$ , which corresponds to the carbonyl stretch in MMA) was performed to account for differences in the concentration of the different fractions while also accounting for the percent MMA in the sample. Normalization was performed as per

$$\text{Normalized } 1074\text{ cm}^{-1} \text{ peak area} = \frac{\text{area under peak at } 1074\text{ cm}^{-1}}{\text{area under peak at } 1730\text{ cm}^{-1}} \times \frac{100\%}{\% \text{ methyl methacrylate}} \quad (4)$$

As seen in Table 2, for both random copolymers the normalized peak area decreases gradually from fraction 1 (highest  $M$ ) to fraction 3 (lowest  $M$ ). This decrease indicates that the percentage of styrene-methyl methacrylate interaction sites in the random copolymers increases with increasing  $M$ . In Table 2 we also observe that the normalized area of the  $1074\text{ cm}^{-1}$  peak of the alternating copolymer is substantially larger than the areas of any of the fractions of either random copolymer. This agrees with the alternating copolymer possessing the maximal junction point ratio of any copolymeric arrangement of dissimilar monomers. All the above results confirm our conclusions regarding the presence of SLH in random copolymers, as discerned from the  $M$ -dependence of the  $R_{\eta}/R_G$  ratio.

Also noted in Table 2 are the larger peak areas of fractions 1–3 of the 186k random copolymer, as compared to the same fraction of the 126k random copolymer. Because each fraction was collected over the same elution volume of each copolymer, an explanation of these differences is warranted. Two main factors contribute to the observed differences in normalized peak areas: First, the percentage of styrene monomer is somewhat ( $\sim 5\%$ ) higher in the 186k random copolymer than in its 126k counterpart. As seen in Fig. 6, this corresponds to a higher percentage of “2 interaction” sites (i.e., sites in which a styrene monomer is bonded to methyl methacrylate monomers at both ends; see Appendix for an explanation of the model) for a particular degree of polymerization in the 186k random copolymer as compared to the 126k random copolymer. It is these “2 interaction” sites that contribute maximally to intrachain repulsion in dilute solution. Therefore, for a given degree

of polymerization, larger normalized FT-IR  $1074\text{ cm}^{-1}$  peak areas are expected for the same fraction of the 186k random copolymer as compared to the 126k copolymer, due to higher styrene content in the former as compared to the latter.

A second, more prosaic reason for the differences in normalized FT-IR peak areas among the same fractions of the different random copolymers is quite simply that, because of differences in chemical composition as well as in MMD of the copolymers, the same fraction (e.g., fraction 1) will encompass a different region of the MMD of each copolymer. As seen in Figs. 2 and 5, all other factors being equal, more intramolecular repulsion (resulting in larger normalized peak areas) is experienced by copolymers of higher  $M$  relative to those of lower  $M$ , with consequent effect on hydrodynamic volume and, thus, SEC retention.

### 3.3. A probability theory model of SLH

The experimental evidence in favor of SLH in random copolymers is supported by results from a probability theory model, details of which are given in the Appendix. The model is based on the change in the percentage of junction points (bonds) between different types of monomers as the degree of polymerization of a linear random copolymer increases. Monomers with different

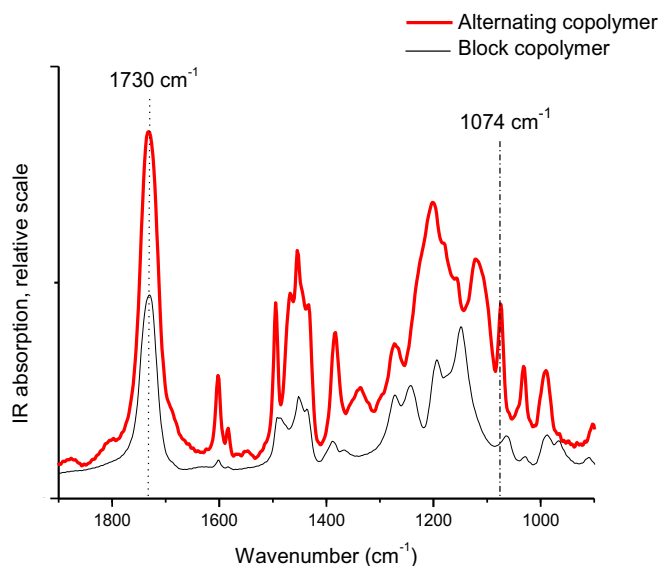


**Fig. 5.** FT-IR spectra of alternating (thick red line) and block (thin black line) copolymers of styrene and methyl methacrylate. See Section 2.5 for experimental details. (For interpretation of the references to colour in this figure legend, the reader is referred to the web version of this article).



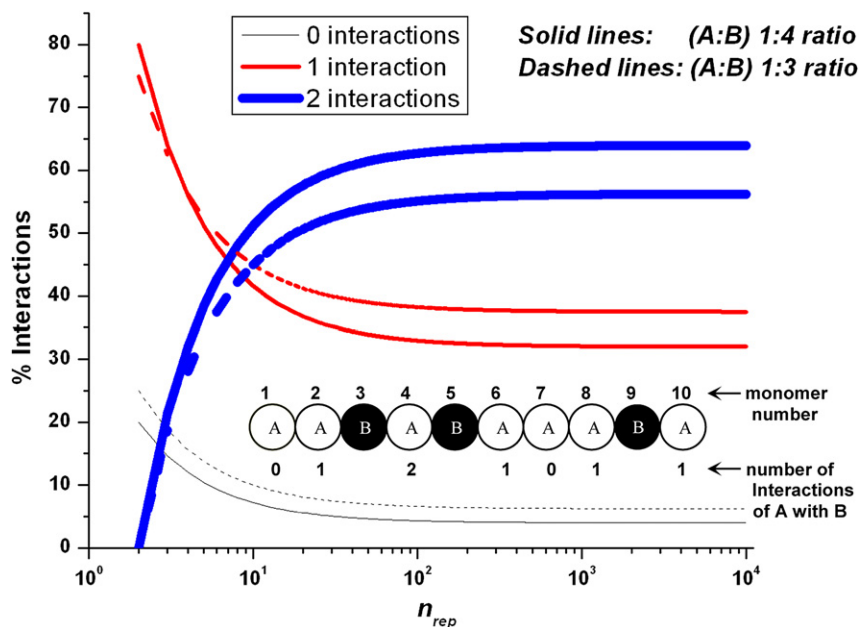


**Fig. 6.** Changes in the percentage of interaction sites of A with B, as a function of molar mass, in a generic random AB linear copolymer, as calculated using the probability theory model described in the Appendix.  $n_{rep}$  represents the number of virtual repeat units, proportional to molar mass. Also shown is the dependence of the number of interaction sites of any particular A monomer on the nature of the neighboring monomers. See Appendix for details.

interaction sites in a copolymeric chain are shown in Fig. 6, where the interactions are of A with respect to B. A monomer with “0 interactions” either corresponds to a monomer located between two monomers of the same type of repeat unit (e.g., monomer 7 in Fig. 6), or to a monomer located at the end of a chain and next to a monomer of the same type (monomer 1 in Fig. 6). A monomer with “1 interaction” is located between two monomers of different chemistries (monomers 2, 6, and 8 in Fig. 6), or at a chain end and next to a monomer of a different chemistry (monomer 10 in Fig. 6). A monomer with “2 interactions” corresponds to a monomer located between two monomers of different chemistry than the monomer itself (monomer 4 in Fig. 6). For a given random copolymeric arrangement, our model predicts the changes in the relative percentages of 0, 1, and 2 interactions as a function of “generic” molar mass, i.e., the latter is expressed in the form of a virtual repeat unit “ $n_{rep}$ ” representing several sequential monomeric units in the copolymeric chain (further specificity is not required at this time, as the model is meant to represent the development of SLH during chain growth, it is not meant to quantitate the SLH). As observed in Fig. 6, which shows the development of SLH in two generic random AB copolymers with 1:3 and 1:4 ratios of A:B, the percentage of “0” and “1” interactions decreases as molar mass increases, while the percentage of “2 interactions” increases with increasing  $M$  (again, interactions are of A with respect to B, though the opposite case can also be derived and plotted. See Appendix for details). The decrease in the percentage of “0” and “1” interaction sites, along with the increase in “2 interaction” sites, as the degree of polymerization increases indicates that, as the chain grows, the monomers are becoming more dispersed within it. These results support the conclusion that the change in  $R_w/R_G$  of random copolymers is related to an increase in the ratio of junction points between dissimilar monomers that accompanies an increase in  $M$ .

### 3.4. Could the observed $R_w/R_G$ change be due to chemical heterogeneity?

Sequence length heterogeneity can originate from the progressive enhancement in the mutual miscibility of two monomeric

solutions during a copolymerization reaction, due to the compatibilizing ability of the synthesized copolymer [38–43]. This gradual enhancement in mutual monomer miscibility impacts the distribution of monomers in solution and during copolymeric chain growth, resulting in SLH. A different source of SLH is chemical heterogeneity, defined as the change in the relative percentages of monomers in a copolymer as a function of molar mass.

To determine whether chemical heterogeneity is responsible for the  $M$ -dependent structural changes (and, consequently, for the  $M$ -dependent changes in the  $R_w/R_G$  ratios) of the random copolymers, we measured the chemical heterogeneity of these copolymers using SEC with on-line MALS, UV, and DRI detection. The detailed procedure for obtaining the percentage composition at each slice eluting from the SEC columns is described in reference [13]. Fig. 7 shows the lack of chemical heterogeneity in the random and

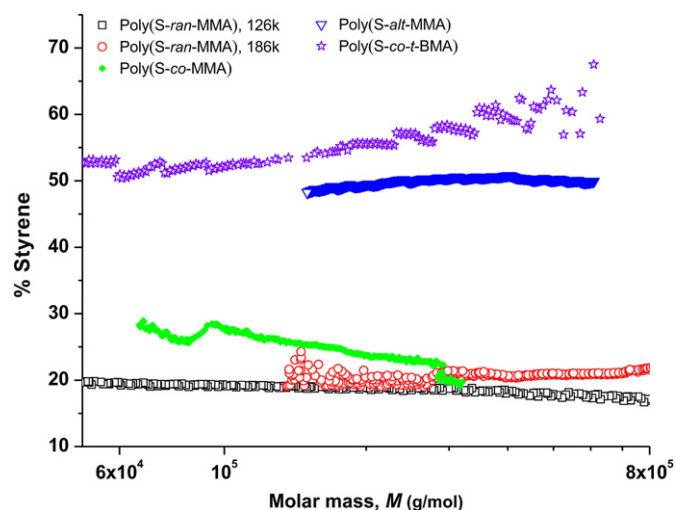


**Fig. 7.** Chemical heterogeneity (given as weight percent styrene) of alternating, gradient, and random copolymers studied, as measured by SEC/MALS/UV/DRI. See Section 2.2 for experimental details.

alternating copolymers. Both random copolymers show a virtual constancy in the % styrene (and, therefore, in the relative percentages of styrene and methyl methacrylate) as a function of molar mass. This indicates that chemical heterogeneity is *not* responsible for the SLH, structural changes, and related  $R_{\eta}/R_G$  variability, of the random copolymers studied.

### 3.5. Behavior of other S-MMA copolymer classes and their constituent homopolymers

#### 3.5.1. Styrene and methyl methacrylate homopolymers

In the case of homopolymers  $JPR = 0$  by definition, due to the absence of junction points between dissimilar species. As shown in Table 3, in spite of differences in chemistry and molar mass the  $R_{\eta}/R_G$  of narrow polydispersity standards of PS and PMMA are all similar to each other (0.81–0.86) and within the range expected for linear random coils in dilute solution ( $\sim 0.7$ – $0.9$ ). The  $R_{\eta}/R_G$  values of the homopolymers are also similar to values of the random copolymers in their low- $M$  region, where the  $JPR$  of the copolymers is smallest. This coincidence agrees with our hypothesis that, when the  $JPR$  of copolymers is minimal, the structure of the copolymers most resembles the homopolymeric structure.

#### 3.5.2. Block copolymers of styrene and methyl methacrylate

Because there is only a single junction point in diblock copolymers (see Fig. 1a), intrachain repulsion should have a negligible effect on the overall solution structure of these macromolecules. If each block adopts a random coil structure at the same given solvent/temperature condition, we would expect the  $R_{\eta}/R_G$  values of the block copolymers to be similar to those of the constituent homopolymers, i.e., in the  $\sim 0.7$ – $0.9$  range. For a set of generic AB block copolymers, this should hold true regardless of the ratio of A–B, as long as the conformation adopted by each block in solution resembles the conformation of both the other block and of the constituent homopolymers.

The above is exactly what we observe when examining two block copolymers of styrene and methyl methacrylate of similar molar masses but with vastly different S:MMA ratios. As seen in Table 3, in spite of their compositional difference the  $R_{\eta}/R_G$  ratios of the two block copolymers are nearly identical to each other, 0.87 and 0.88. These values are quite close to the  $R_{\eta}/R_G$  values of PS and PMMA homopolymers with molar masses similar to those of the respective blocks in the block copolymers, which are in the range 0.81–0.86. This is because THF is a good solvent for both the constituent homopolymers and their resultant diblock copolymers. The near-coincidence in values between the two block copolymers, and between the block copolymers and their respective homopolymers, indicates that the block copolymers adopt a random coil structure in solution that is governed by the structure of the individual blocks and is not influenced by the

minimal intrachain repulsion provided by the single junction point between blocks.

#### 3.5.3. Alternating copolymer of styrene and methyl methacrylate

The  $R_{\eta}/R_G$  versus  $M$  relationship for the S-MMA alternating copolymer examined in this study is shown in Fig. 3. As predicted in Section 3.1, the  $R_{\eta}/R_G$  value is virtually constant as a function of molar mass. The low  $R_{\eta}/R_G$  value of the alternating copolymer ( $\sim 0.65$ ), as compared to the  $R_{\eta}/R_G$  values of the constituent homopolymers and of the block and random S-MMA copolymers (see Table 3 and Fig. 3), is an indication of the relatively extended structure alternating copolymers can adopt in solution. The latter is a direct consequence of the maximal value of the  $JPR$  in alternating copolymers, which results in maximum repulsion between the dissimilar, alternating monomers which constitute the chain. For alternating copolymers, the constancy in  $R_{\eta}/R_G$  as a function of  $M$  is due to the independence of the  $JPR$  on degree of polymerization;  $JPR = 1$ , regardless of  $n$ , in alternating copolymers. As explained in Section 3.1, for the different types of copolymers, block, alternating, and gradient, the  $JPR$  is expected to be highest, and the  $R_{\eta}/R_G$  lowest, for alternating copolymers. This agrees with the results shown in Fig. 3.

#### 3.5.4. Gradient random copolymer of styrene and methyl methacrylate

In a gradient random copolymer, the relative ratio of the two chemical functionalities present changes gradually and unidirectionally with increasing  $M$ . The  $R_{\eta}/R_G$  ratio of a gradient random copolymer of styrene and methyl methacrylate, P(S-co-MMA), was observed to decrease as a function of  $M$ . When compared to the other types of S-MMA copolymers discussed above we see in Fig. 3 that, at low  $M$ , the  $R_{\eta}/R_G$  ratio of the gradient copolymer resembles that of a block copolymer while, at high  $M$ , the  $R_{\eta}/R_G$  ratio of the gradient copolymer resembles that of the alternating copolymer examined. However, the decrease in  $R_{\eta}/R_G$  as a function of  $M$  does not occur as quickly for the gradient copolymer as it does for the random copolymers P(S-ran-MMA) (“non-gradient” random copolymers), i.e., at a given  $M$ , the  $R_{\eta}/R_G$  of the gradient copolymer is smaller than that of the random copolymers, signifying that, at a given  $M$ , the gradient copolymer adopts a slightly more extended structure than do the random copolymers. Moreover, the  $R_{\eta}/R_G$  value of the gradient copolymer approaches that of the random copolymers with increasing  $M$ .

The explanation for the above is as follows. As seen in Fig. 6, the percentage of “2 interaction” sites increases with degree of polymerization. This accounts for the random and gradient copolymers of S and MMA becoming more extended ( $R_{\eta}/R_G$  becoming smaller) as  $M$  increases. We also observe in Fig. 6 that the percentage of “2 interaction” sites increases with decreasing ratio A:B (because the plot and calculations in the Appendix are with respect to A, a smaller percentage of A in the polymer corresponds to a higher probability that a particular A monomer will be between two B monomers, as compared to a polymer with a higher percentage of A. It is these “2 interaction” sites, where an A monomer is located between two B monomers, that contribute maximally toward chain expansion in solution. Equivalent results are obtained if the calculations are performed with respect to B). In Fig. 7, we see that the percentage of styrene (%S) in the gradient copolymer P(S-co-MMA) decreases, from approximately 30 to 20%S, with increasing  $M$ . Two factors are now operational in the gradient copolymer: 1) Probability theory, which indicates that the percentage of “2 interaction” sites will increase with increasing  $M$ , and 2) chemical heterogeneity, which further increases the percentage of these same sites with increasing  $M$  (as, from Fig. 6, we see that as the %S decreases, the percentage of “2 interaction” sites increases). Both

**Table 3**  
 $R_{\eta}/R_G$  value of the homo and block copolymers studied.

Polymer	$R_{\eta}/R_G$
PS (186k)	$0.86 \pm 0.02^a$
PMMA (343k)	$0.82 \pm 0.01$
PMMA (467k)	$0.81 \pm 0.01$
PS (533k)	$0.82 \pm 0.01$
PS (723k)	$0.82 \pm 0.01$
P(S- <i>b</i> -MMA) (46k, 138k)	$0.87 \pm 0.01$
P(S- <i>b</i> -MMA) (131k, 46k)	$0.88 \pm 0.01$

<sup>a</sup> Standard deviations based on measurements of individual radii,  $R_{\eta}$  and  $R_G$ , for repeat injections of duplicate sample dissolutions, as described in Section 2.2.

these factors contribute additively to the gradient random copolymer adopting a more extended conformation in solution, for a given  $M$ , than does a “non-gradient” random copolymer of the same  $M$ . As the %S in the gradient copolymer approaches the %S in the random copolymers, the conformation adopted by the gradient and “non-gradient” random copolymers should be similar to each other. This behavior is evidenced in Fig. 3, where the  $R_{\eta}/R_G$  of the gradient copolymer is seen to (a) decrease with increasing  $M$ , (b) be lower than the  $R_{\eta}/R_G$  of the random copolymers, and (c) to approach the  $R_{\eta}/R_G$  value of the random copolymers as  $M$  increases (i.e., as the %S in the gradient copolymer decreases, approaching the %S in the random copolymers).

### 3.5.5. Gradient random copolymer of styrene and *t*-butyl methacrylate

Seemingly contradictory behavior to that just described for the P(S-co-MMA) gradient copolymer is displayed by a gradient copolymer of styrene and *t*-butyl methacrylate, P(S-co-*t*-BMA). As seen in Fig. 3, the  $R_{\eta}/R_G$  ratio of the latter copolymer increases with increasing  $M$ , from a value close to that of the alternating copolymer to a value close to that of the block copolymers. (Comparison in both cases is to block and alternating copolymers of S and MMA, as we have been unable to obtain block and alternating copolymers of S and *t*-BMA. We expect the difference between the two types of block and of alternating copolymers to be small, however, and the qualitative behavior to be identical).

While probability theory leads to a higher percentage of “2 interaction” sites with increasing  $M$  for the P(S-co-*t*-BMA), from Fig. 6 (assuming, as has been done throughout, that styrene corresponds to A, so that B now corresponds to *t*-butyl methacrylate) we see that 1) A random copolymer with 50%S will have less “2 interaction” sites that will a random copolymer of the same  $M$  with a smaller %S, and 2) the increase in %S (from approximately 50 to 65%S) with increasing  $M$  leads to a concomitant decrease in these same sites. Point 1 means that, at low  $M$ , this particular gradient copolymer of S and *t*-BMA will adopt a more extended structure in solution than will the random P(S-*ran*-MMA) copolymers of the same  $M$ . This corresponds to the  $R_{\eta}/R_G$  of the P(S-co-*t*-BMA) being lower than the  $R_{\eta}/R_G$  of the P(S-*ran*-MMA)s at low  $M$ , which is what is observed in Fig. 3. Point 2 means that the P(S-co-*t*-BMA) which, apparently, possesses a near-alternating structure at low  $M$ , becomes more blocky and experiences less intramolecular repulsion as  $M$  increases. This behavior is reflected in the  $R_{\eta}/R_G$  versus  $M$  relationship: At low  $M$ ,  $R_{\eta}/R_G$  of the P(S-co-*t*-BMA) is 0.59 while, at high  $M$ , the ratio is around 0.82.

## 4. Conclusions

Knowledge of the existence of sequence length heterogeneity SLH in copolymers is important for understanding macromolecular properties that are dependent on the distribution of the monomers in a copolymer. Examples of such properties are the adsorption of copolymers at liquid–liquid interfaces, the conformation and folding of protein-like copolymers, the transparency of films, and the ability of copolymers to compatibilize blends.

In this project, we have employed results from multi-detector SEC and FT-IR experiments, in conjunction with a probability theory model, to relate the decrease in the dimensionless size parameter  $R_{\eta}/R_G$  as a function of molar mass  $M$  to the presence of SLH in random copolymers, independent of molar mass polydispersity and chemical heterogeneity effects. The  $R_{\eta}/R_G$  change with  $M$  can be used as a semi-quantitative metric of the SLH in random copolymers.

Extension of this work to copolymers other than those studied here is contingent upon several factors. First is the ability to

measure the individual radii,  $R_G$  and  $R_{\eta}$ , across the MMD of the copolymer, or across that portion of the MMD of interest in a particular study. Second is the need to determine whether or not chemical heterogeneity is present in the copolymer (accomplished here through the use of SEC/MALS/UV/DRI). Third, the individual homopolymers corresponding to the various chemical functionalities in the copolymer should be well-solvated at the experimental solvent/temperature conditions. Fourth, the intrachain interaction (i.e., the energy of interaction between two monomers due to non-covalent bonding, mismatching size or shape, etc.) between the different types of monomers in the copolymer should be different from the intrachain interactions between monomers of the same type. Lastly, the architecture of the copolymer should remain constant as a function of  $M$ .

To our knowledge, this is the first demonstration of a relationship between a dimensionless size parameter (and its change with  $M$ ) and the existence of SLH in copolymers. This project adds to our understanding of the conformation-dependent properties of random copolymers, of monomeric distribution within copolymers, and of dilute solution thermodynamics, by providing an experimental method by which to detect sequence length heterogeneity.

## Acknowledgments

The authors would like to thank Professors Michael Roper and Joseph Schlenoff for their helpful advice and kind loans of UV and FT-IR detectors, respectively. We would also like to thank Lara Al-Hariri for her assistance in obtaining FT-IR spectra. Acknowledgment is made to the Donors of the American Chemical Society Petroleum Research Fund for partial support of this research through grant 1-1312-0050.

## Appendix 1. Probability theory model of sequence length heterogeneity

Let  $A$  and  $B$  be two species comprising a linear random copolymer. Let  $n$  be the total number of monomers in the chain and  $x_i$ , where  $i \in [1, n]$ , be the  $i$ th monomer. Assuming there is a fixed percentage  $p$  of  $A$  and  $1-p$  of  $B$  found in the copolymer, the probability of the number of interactions  $I$  can be determined. Without loss of generality, the probability of an individual  $A$  monomer  $A_0$  having 0, 1, or 2 interactions with a  $B$  monomer will be found. There are three cases to explore:  $A_0$  has no adjoining  $B$  monomer ( $I = 0$ ),  $A_0$  has one adjoining  $B$  monomer ( $I = 1$ ), and  $A_0$  has two adjoining  $B$  monomers ( $I = 2$ ).

*Case 1:  $I = 0$ .* Zero interactions occur when  $A_0$  is located at an end position and the adjoining monomer is an  $A$  monomer, or when  $A_0$  is located at an interior position and both adjoining monomers are also  $A$ . Hence,

$$P(I = 0) = P(x_1 = A_0 \cap x_2 = A) \cup P(x_n = A_0 \cap x_{n-1} = A) \cup P(x_i = A_0, \text{ where } i \in [2, n-1] \cap x_{i-1} = A \cap x_{i+1} = A)$$

This simplifies to

$$P(I = 0) = \frac{1}{n}p + \frac{1}{n}p + \frac{n-2}{n}p^2 = \frac{p(2+np-2p)}{n} \quad (A1)$$

*Case 2:  $I = 1$ .* One interaction occurs when  $A_0$  is located at an end position and the adjoining monomer is a  $B$  monomer, or when  $A_0$  is located at an interior position and one adjoining monomer is a  $B$  monomer and the other adjoining monomer is an  $A$  monomer. Thus,

$$P(I = 1) = P(x_1 = A_0 \cap x_2 = B) \cup P(x_n = A_0 \cap x_{n-1} = B) \cup P(x_i = A_0, \text{ where } i \in [2, n-1] \cap x_{i-1} = B \cap x_{i+1} = A) \cup P(x_i = A_0, \text{ where } i \in [2, n-1] \cap x_{i-1} = A \cap x_{i+1} = B)$$

This simplifies to

$$P(I = 1) = \frac{1}{n}(1-p) + \frac{1}{n}(1-p) + \frac{n-2}{n}(1-p)p + \frac{n-2}{n}p(1-p) \\ = \frac{2(1-p)(1+np-2p)}{n} \quad (\text{A2})$$

Case 3:  $I = 2$ . Two interactions occur when  $A_0$  is located at an interior position and the adjoining monomers are both  $B$  monomers. Accordingly,

$$P(I = 2) = P(x_i = A_0, \text{ where } i \in [2, n-1] \cap x_{i-1} = B \cap x_{i+1} = B)$$

This simplifies to

$$P(I = 2) = \frac{(n-2)}{n}(1-p)^2 \quad (\text{A3})$$

As the number of monomers in the chain increases (i.e., as  $n \rightarrow \infty$ ), the probability of interactions approaches a steady state. This can be found by taking the limits of Equations (A1)–(A3) as  $n$  approaches  $\infty$ , resulting in

$$\text{for zero interactions } (I = 0), \quad \lim_{n \rightarrow \infty} \frac{p(2+np-2p)}{n} = p^2 \quad (\text{A4})$$

$$\text{for one interaction } (I = 1), \quad \lim_{n \rightarrow \infty} \frac{2(1-p)(1+np-2p)}{n} \\ = 2p(1-p) \quad (\text{A5})$$

$$\text{for two interactions } (I = 2), \quad \lim_{n \rightarrow \infty} \frac{(n-2)(1-p)^2}{n} = (1-p)^2 \quad (\text{A6})$$

Note that the model is based on the population of  $A$ . It describes the number of interactions that  $A$  has. It does not describe the total number of interactions, though this can be calculated using a similar approach.

As an example, let  $n = 10$  and assume there is a 1:4 ratio of monomer  $A$  to monomer  $B$  (hence,  $p = 0.2$ ). Using Equations (A1)–(A3), 7.2% of  $A$  monomers will have no interactions with monomer  $B$ , 41.6% of  $A$  monomers will have one interaction with monomer  $B$ , and 51.2% of  $A$  monomers will have two interactions with monomer  $B$ . When  $n$  is large (using Equations (A4)–(A6)), 4% of monomer  $A$  will have no interactions with monomer  $B$ , 32% of monomer  $A$  will have one interaction with monomer  $B$ , and 64% of monomer  $A$  will have 2 interactions with monomer  $B$ .

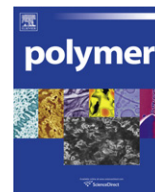
Again, it is an increase in the number of 2 contact point interactions (“2 interaction” sites) that leads to intramolecular repulsion. For a constant ratio of A:B (e.g., of S:MMA; because the reactivity ratios of PS and PMMA are quite similar [37] they need not be included in the model), the number of 2 contact point interactions increases with increasing chain length, while the number of 0 and 1 contact point interactions both decrease with increasing chain length. Letting “ $n_{rep}$ ” denote the total number of virtual repeat units (proportional, though not necessarily equal, to degree of polymerization) and “% Interactions” the relative percentages of 0, 1, and 2 contact point interactions of  $A$  with  $B$ , the probability theory we developed yields the plots in Fig. 6 for cases

of 1:4 and 1:3 ratios of A:B ( $p = 0.2$  and  $0.25$ , respectively), assuming a linear copolymer with a random distribution of monomers. In each case, the number of 2 contact point interactions increases with degree of polymerization (while approaching an asymptotic value that depends on the A:B ratio). This increase leads to increased chain expansion with increasing  $n_{rep}$  (increasing  $M$ ), corresponding to a steady decrease in the ratio  $R_{\eta}/R_G$  as  $M$  increases. As seen in Fig. 3, this is exactly what we observe for the two random copolymers examined.

## References

- [1] Yeung C, Balazs AC, Jasnow D. *Macromolecules* 1992;25(4):1357–60.
- [2] Khokhlov AR, Khalatur PG. *Phys Rev Lett* 1999;82(17):3456–9.
- [3] Khokhlov AR, Khalatur PG. *Physica A* 1998;249:253–61.
- [4] Zheligovskaya EA, Khalatur PG, Khokhlov AR. *Phys Rev E Stat Phys Plasmas Fluids* 1999;59(3-B):3071–8.
- [5] Siu M, Zhang G, Wu C. *Macromolecules* 2002;35(7):2723–7.
- [6] Balazs AC, Sanchez IC, Epstein IR, Karasz FE, MacKnight WJ. *Macromolecules* 1985;18(11):2188–91.
- [7] Balazs AC, Karasz FE, MacKnight WJ, Ueda H, Sanchez IC. *Macromolecules* 1985;18(12):2784–6.
- [8] Brar AS, Kapur GS. *Polym J* 1988;20(5):371–6.
- [9] Dadmun MD. *Macromol Theory Simul* 2001;10(9):795–801.
- [10] Rana D, Mounach H, Halary JL, Monnerie L. *J Mater Sci* 2005;40(4):943–53.
- [11] Galvin ME. *Macromolecules* 1991;24(23):6354–6.
- [12] Shi Y, Wu M. *J Appl Polym Sci* 1995;57(11):1311–4.
- [13] Haidar Ahmad IA, Striegel AM. *Anal Bioanal Chem* 2010;396(4):1589–98.
- [14] Tonelli AE. *Macromolecules* 1977;10:633–5.
- [15] Kent MS, Tirrell M, Lodge TP. *J Polym Sci Part B Polym Phys* 1994;32(3):1927–41.
- [16] Kent MS, Tirrell M, Lodge TP. *Macromolecules* 1992;25(20):5383–97.
- [17] Ostlund SG, Striegel AM. *Polym Degrad Stab* 2008;93(8):1510–4.
- [18] Graessley WW. *Polymeric liquids and networks: structure and properties*. New York: Garland Science; 2003.
- [19] Burchard W. *Adv Polym Sci* 1999;143:113–94.
- [20] Striegel AM. *Biomacromolecules* 2007;8(12):3944–9.
- [21] Roovers J, Martin JE. *J Polym Sci Part B Polym Phys* 1989;27(12):2513–24.
- [22] Denchev Z, Duchesne A, Stamm M, Fakirov S. *J Appl Polym Sci* 1998;68(3):429–40.
- [23] Witt U, Mueller R-J, Deckwer WD. *Macromol Chem Phys* 1996;197(46):1525–35.
- [24] Hoyle CE, Zhao J, Orler B, Kuang W, McDonald CL. *J Macromol Sci Pure Appl Chem* 2001;A38(5&6):527–41.
- [25] Alb AM, Enohnyaket P, Drenski MF, Head A, Reed AW, Reed WF. *Macromolecules* 2006;39(17):5705–13.
- [26] Catalgil-Giz H, Giz A, Alb AM, Koc AO, Reed WF. *Macromolecules* 2002;35(17):6557–71.
- [27] Striegel AM, Yau WW, Kirkland JJ, Bly DD. *Modern size-exclusion liquid chromatography*. 2nd ed. New York: Wiley; 2009.
- [28] Striegel AM. *Anal Chem* 2005;77(5):104A–13A.
- [29] Trainoff, S. P. U.S. Patent 20050075851; 2005.
- [30] Benoit H, Froelich D. In: Huglin MB, editor. *Light scattering from polymer solutions*. New York: Academic Press; 1972. p. 467–501.
- [31] Bushuk W, Benoit H. *Can J Chem* 1958;36:1616–26.
- [32] Smith MJ, Haidar IA, Striegel AM. *Analyst* 2007;132(5):455–60.
- [33] Elias HG. *An introduction to polymers*. Weinheim, Germany: VCH; 1996.
- [34] Mourey T. *Int J Polym Anal Charact* 2004;9(1-3):97–135.
- [35] Flory PJ. *Principles of polymer chemistry*. Ithaca, NY: Cornell University Press; 1953.
- [36] Mori SJ. *Appl Polym Sci* 1989;38(3):547–55.
- [37] Gan LM, Lee KC, Chew CH, Ng SC, Gan LH. *Macromolecules* 1994;27(22):6335–40.
- [38] Lee MS, Lodge TP, Macosko CW. *J Polym Sci B Polym Phys* 1997;35(17):2835–42.
- [39] Jo WH, Kim HC, Baik DH. *Macromolecules* 1991;24(9):2231–5.
- [40] Kim J, Gray MK, Zhou H, Nguyen ST, Torkelson JM. *Macromolecules* 2005;38:1037–40.
- [41] Dadmun M. *Macromolecules* 1996;29(11):3868–74.
- [42] Hellmann GP, Dietz M. *Macromol Symp* 2001;170:1–8.
- [43] Zaremski MY, Kalugin DI, Golubev VB. *Polym Sci Ser A* 2009;51(1):103–22.





## STEM-in-SEM method for morphology analysis of polymer systems

Olivier Guise<sup>a,\*</sup>, Carl Strom<sup>a</sup>, Nisha Preschilla<sup>b</sup>

<sup>a</sup>SABIC Innovative Plastics, Technology Department, 1 NORYL Avenue, Selkirk, NY 12158, USA

<sup>b</sup>Reliance Technology Group, Reliance Corporate Park, Reliance Industries Limited, Ghansoli, Navi Mumbai 400701, India

### ARTICLE INFO

#### Article history:

Received 14 October 2010

Received in revised form

10 January 2011

Accepted 14 January 2011

Available online 22 January 2011

#### Keywords:

STEM-in-SEM

TEM

Microscopy

### ABSTRACT

Applicability of STEM-in-SEM for polymer characterization, particularly for a manufacturing environment, was explored through analysis of a wide range of commercially significant polymer systems. STEM-in-SEM studies of engineering thermoplastic blends and composites, using samples prepared for TEM studies, showed excellent comparison to TEM micrographs. Important structural details of multi-phase polymer systems could be easily obtained, even when using a thermionic SEM. High quality images were obtained from STEM-in-SEM, and enabled the study of commonly monitored features such as overall morphology, identification of component phases, assessment of compatibility between discrete and continuous phases, and the dispersion and distribution of the discrete components. STEM-in-SEM proved to have additional advantages for polymer systems with low contrast between phases, or beam-sensitive samples, which are highly challenging for TEM imaging. Combining the large field of view with the high magnification range in an SEM, it was also possible to successfully study large-scale phenomena, such as crack propagation. High flexibility of STEM-in-SEM over TEM for design changes is also demonstrated to allow for handling of a large number of samples and a lower turnaround time per sample. An increase in productivity by about 50% was obtained for STEM-in-SEM with a 12-sample carousel vs. a conventional single-sample STEM-in-SEM or TEM.

© 2011 Elsevier Ltd. All rights reserved.

### 1. Introduction

The use of polymeric materials in an ever-increasing range of applications has resulted in the growing demand for comprehensive information of morphology of polymer systems in order to derive structure – property correlations. In the microstructure analysis of polymer systems, oftentimes multi-phase blends or composites, the phase structure is studied in detail to generate a mechanistic understanding of the end performance of the material. This, in turn, is critical for optimization of formulations and processing conditions. In a typical multi-phase polymer system, morphological factors such as size, shape and orientation of the phases, identification of the components in the formulation that form continuous or dispersed phase, preferred phase of rubbers, fillers or additives, compatibility and interfaces of the components etc. are sought, usually, with electron microscopy techniques [1].

Transmission electron microscopy (TEM) is the most frequently used technique to study morphology of polymer systems. TEM, however, presents some limitations: the equipment is expensive;

analysis is time-consuming and is somewhat skill-intensive. In addition, many polymer materials are highly beam-sensitive, and imaging them under the acceleration voltage conditions used in conventional TEMs becomes a challenge. Another difficulty with TEM analysis is that – since some of the polymer materials cannot be stained with known standard staining agents – adequate contrast is not observed from the small differences in the inherent density of the component polymer phases. In other words, TEM methods fall short for these materials. Most importantly, in an industrial production environment, where samples need to be analyzed in large numbers for quick morphology analysis as part of quality control, TEM is not always a practical and affordable option.

Alternative methods to obtain fast and detailed morphological information of polymers have been well explored and documented [1–5]. A large fraction of these efforts has been focused on scanning electron microscopy (SEM) methods. SEM is an important tool for polymer analysis, since it is extensively used to study fracture and failure mechanics, particles size and shape, filler orientation and dispersion in polymer matrices. As a result, polymer research and manufacturing laboratories are usually equipped with SEMs. Traditional methods to study micro-structural information of polymer systems via SEM involve preferential etching of phases by exposure to plasma or solvents, in order to generate the necessary

\* Corresponding author. Tel.: +1 518 475 5463; fax: +1 518 475 5101.  
E-mail address: [olivier.guise@sabic-ip.com](mailto:olivier.guise@sabic-ip.com) (O. Guise).



topographical contrast. However, the extent of information that can be obtained is fairly limited with use of these etching methods. Details such as interface adhesion and compatibility of component phases are lost. SEM methods are especially insufficient in the case of polymer systems with three or more components. In the case of solvent etching applied to such formulations, use of multiple solvents is required to identify the phases. In the case of complex microstructures such as co-continuous or heterogeneous morphologies, identification or assignment of phases can be difficult with solvent etching based sample preparation. Use of plasma as an etching medium is a better choice as different phases can be differentially etched. This, though, is quite tedious and intricate, because the etching rate depends on various factors such as the source gas for plasma, the etching parameters (power, rate of etching etc.), the sample composition and also the morphology of the material itself. A large number of experiments and correlations with other techniques are usually required to validate the method.

Another approach for quick morphology analysis of polymers has been achieved through the use of low voltage imaging in special equipment such as the low voltage electron microscope [6]. At such low voltages of the order of units of kV, enhanced imaging contrast of nearly 20 times higher than at 100 kV, has enabled imaging of low-Z materials such as polymers, thus completely evading the need for heavy metal staining [7]. Morphology analysis of a wide range of polymer blends and block copolymers has been reported with excellent phase contrast, and density differences as low as 0.04 g/cm<sup>3</sup> were seen to be sufficient to identify the phase structure. However, resolution of the low voltage electron microscope is lower than that of a conventional TEM, at about 2 nm, being limited by the considerably low accelerating voltage. Preparation of ultra-thin sections of 30–40 nm required for this analysis can also be highly challenging for most polymer systems. Finally, a combination of low voltage imaging with backscatter electron detector on stained blocks was demonstrated [5]. This method is fairly time consuming as it involves block-staining and re-polishing of the blocks prior to imaging. In addition bulk staining of blocks will only work for limited compositions in order to achieve sufficient contrast.

The fairly recent commercial introduction of STEM-in-SEM, i.e. scanning transmission electron microscopy in the scanning electron microscope, presents various benefits over TEM for morphology analysis of polymers, and is particularly suited for an industrial environment. This method combines the advantages of high-contrast generation consequent of low voltage analysis with the information-rich transmission imaging of a TEM, at a resolution equal to that of the host SEM, extending to the sub-nanometer range in a modern day SEM [8–10]. STEM-in-SEM imaging characteristically uses electron detectors positioned side-by-side underneath a thin section of the sample. The detector directly underlying the sample captures electrons that are mostly unaffected by the sample, and forms bright-field images dominated by mass-thickness contrast. Detectors that are offset from the sample, i.e. dark field or high angle annular dark field detectors, capture electrons scattered by interactions with sample electrons or atomic nuclei. Most of the commercially available SEMs now have STEM as an optional attachment, available for a fraction of the cost of a new TEM unit. An unparalleled advantage of STEM-in-SEM over TEM, especially in industrial environment, is its “high output TEM-like imaging”. The extensive, non value-added, downtime between samples in TEM can be eliminated to a great extent in STEM-in-SEM with the addition of a multiple-sample carousel. Thus, STEM-in-SEM can be thought of as an affordable and fast morphology analysis tool, suited for manufacturing as well as research laboratories.

The value of the STEM-in-SEM technique has already been demonstrated in a few published papers in the areas of mineralogy

and petrology [11], semiconductors [12], nanomaterials [13,14], polymers [15,16] and catalysts. STEM-in-SEM was shown to be a quick and easy method for characterizing the morphology and internal structure of mineral and rock samples and was shown to be especially useful in geomicrobiology research [17]. An exhaustive high-resolution STEM-in-SEM study of laser-machined silicon structures was carried out to characterize defects in the crystal lattice, thermal-mechanical damage, internal structure, composition, and dimensions of the laser-machined structures [18]. A powerful extension of STEM-in-SEM – the “wet STEM” in an environmental SEM – has been reported, with high quality analysis of nano-objects embedded in liquid phase [19–21]. Different types of materials suspended in water, such as colloidal gold and silica nanoparticles, nanoclay, carbon nanotubes, soot, acrylic latex, and aqueous emulsions of styrene and polystyrene, grafted colloidal aqueous lattices such as natural rubber, bacteria, etc. could be imaged. A brief study of the method application to polymers and catalysts in a field-emission SEM has also been reported [16]. Another important report discusses three dimensional imaging of filled Polyvinyl chloride and Polyurethane foams using STEM-in-SEM. The capability for obtaining missing information at the mesoscopic scale with STEM-in-SEM was shown, with a very good compromise between the size of the analyzed volume and spatial resolution [22].

In this work, we demonstrate applications of STEM-in-SEM to a wide range of polymer systems of high commercial and scientific importance. Many examples of engineering thermoplastics and composite materials are presented, with emphasis on the study of blend morphology, filler dispersion, etc., which are routinely probed with TEM. Imaging of these materials was carried out in STEM-in-SEM and was compared to the images obtained from a conventional TEM. TEM-like imaging of high quality – both in terms of degree of information and image finesse – was established to be feasible, even with a thermionic SEM. Successful imaging of unstained or highly beam-sensitive materials, which is a real challenge in a TEM, is also established. Finally, design flexibility of STEM-in-SEM to significantly increase productivity is demonstrated by the addition of a custom-made carousel system that can currently hold up to 12 samples.

## 2. Experimental – instruments and materials

### 2.1. Instruments

A Zeiss EVO40 XVP thermionic SEM equipped with a STEM detector from K.E. Developments (KED) was used throughout this study. STEM-in-SEM evaluations were also conducted using the “poor man’s detector” (Ernest Fullam – images not shown) [23–25], however, the signal-to-noise was far better with the KED detector. The STEM detector unit is a cost-effective compact unit containing the specimen and the detector, which consists of a photodiode electron detector mounted at the bottom of a cylinder and positioned under an electron transparent thin specimen in a pre-aligned holder. The specimen, a standard TEM section collected on a copper grid, was mounted at the top of the cylinder and is clamped. The STEM-in-SEM unit was mounted onto the SEM stage and could therefore be precisely positioned under the electron column for imaging. The STEM-in-SEM detector uses the electronic system of the quadrupole back-scattered detector (QBSD) and can be manually connected or disconnected from inside the SEM chamber when vented. When the STEM-in-SEM detector is connected the user simply needs to image in “QBSD mode” to get STEM-in-SEM imaging. Typical operating conditions in STEM-in-SEM mode were 30 kV, and a probe current of ~20 pA. The working distance was optimized at 4 mm. High acceleration voltage of 30 kV

was required, in order to improve the electron penetration and the brightness of the source.

A few STEM-in-SEM studies were also carried out with a Zeiss SUPRA 40VP field-emission electron microscope (FEM), as a way to further compare STEM-in-SEM with a thermionic SEM and FEM with TEM.

TEM studies to compare and validate STEM-in-SEM analysis were done on a FEI Tecnai G<sup>2</sup> TEM with a LaB<sub>6</sub> source, operated at 100–120 kV.

## 2.2. Materials

In this study, a wide range of commercially available grades of engineering thermoplastics and high performance composites manufactured by SABIC Innovative Plastics was investigated. As typical examples of engineering thermoplastics, materials of high commercial importance due their high-volume applications were analyzed, such as blends of Polypropylene/Polyphenylene Ether (PP/PPE), Polyphenylene Ether/Styrene-ethylene-butadiene-styrene (PPE/SEBS), Styrene Acrylonitrile/Acrylonitrile-butadiene-styrene (SAN/ABS), Polyphenylene Ether/Polyamide/Styrene-ethylene-butadiene-styrene (PPE/PA/SEBS), Polycarbonate/Styrene Acrylonitrile/Acrylonitrile-butadiene-styrene (PC/SAN/ABS) and Polycarbonate/

Poly-butylene Terephthalate/Methacrylate-Butadiene-Styrene (PC/PBT/MBS). Some of the high performance polymer composites considered for STEM-in-SEM analysis were single or multi-phase polymers reinforced with inorganic or organic fillers. An example of such composites was a blend of polycarbonate/polybutylene terephthalate and talc (PC/PBT/Talc). All samples mentioned above were prepared on a Leica UCT ultramicrotome, at room temperature or cryo conditions, depending on sample composition. Thin sections of about 80–90 nm were collected on copper TEM grids. For identification of component phases, standard staining procedures, adjusted as a function of sample compositions, were also carried out. For each sample, the same section was used for TEM as well as STEM-in-SEM analysis.

In addition to the above samples, a few polymer systems that are usually very challenging to study by TEM were explored, for instance, highly beam-sensitive materials or those multi-phase polymers wherein differential contrast cannot be introduced into the component phases using standard staining agents. A blend of polyphenylene ether/polyvinylidene difluoride and tri-block copolymer styrene-butadiene-methylmethacrylate (PPE/PVDF/SBM) was chosen as a beam-sensitive candidate, whereas a blend of PPE and siloxane filled with fumed silica was considered as an unstainable system.

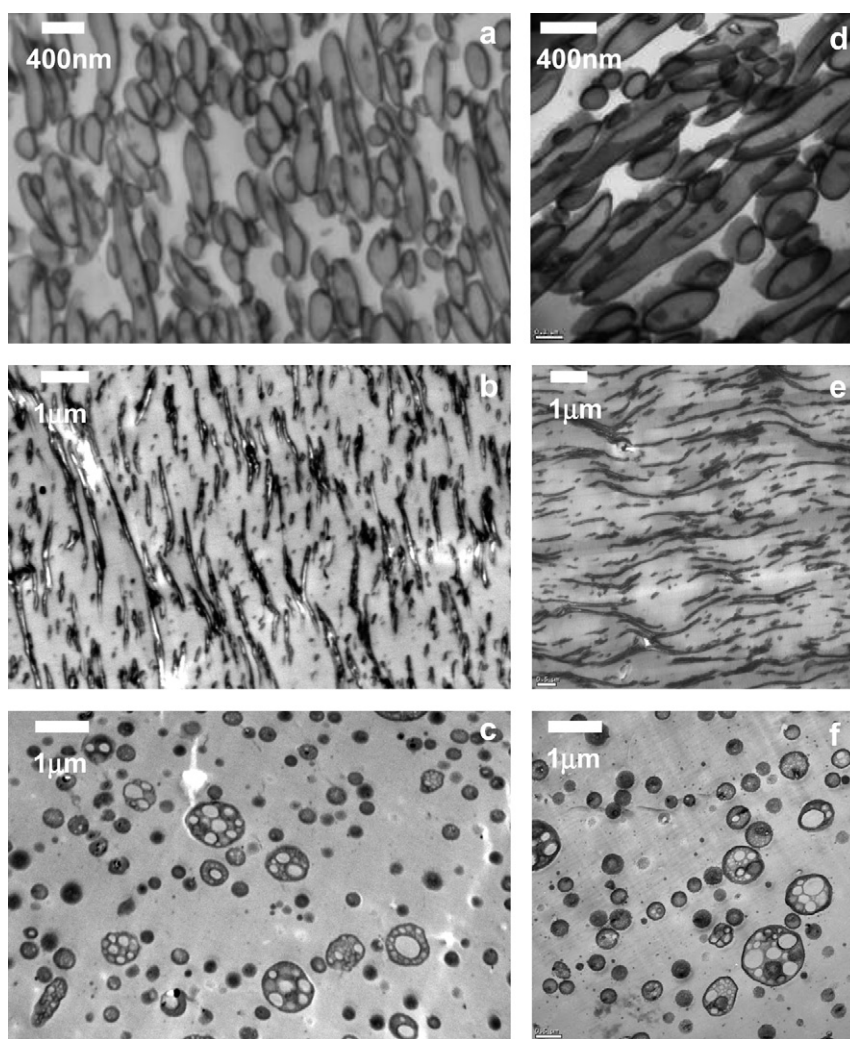


**Fig. 1.** Comparison of STEM-in-SEM and TEM images for two-phase immiscible polymer blends. (a), (b) and (c) are STEM-in-SEM images of PP/PPE, PPE/SEBS and SAN/ABS, respectively, while (d), (e) and (f) are the TEM images of the same samples. In the PP/PPE blend, PP is the matrix phase and PPE is the dispersed phase; in the PPE/SEBS blend, SEBS is dispersed in the continuous PPE phase; finally in the SAN/ABS blend, SAN is the matrix phase while the dispersed phase is bulk ABS rubber.

In order to demonstrate feasibility and benefits of low magnification imaging, a result of the large field of view in the SEM, samples having large micron-scale morphology or those representative of large-scale phenomena such as crack propagation or failure were studied. As an example, an impact-tested sample was imaged in the STEM-in-SEM to understand how the crack propagation affected the surrounding morphology.

### 3. Results and discussion

#### 3.1. (a) Polymer blends

Comparison of STEM-in-SEM and TEM micrographs for three sets of two-phase immiscible polymer blends of PP/PPE, PPE/SEBS and SAN/ABS is shown in Fig. 1. In the PP/PPE blend, PP is the matrix phase and PPE is the dispersed phase; in the PPE/SEBS blend, SEBS is dispersed in the continuous PPE phase; finally in the SAN/ABS blend, SAN is the matrix phase while the dispersed phase is bulk ABS rubber. Comparable image quality and level of information between STEM-in-SEM and TEM were readily seen. All the important morphological details that are sought through with TEM analysis of polymer systems, i.e. phase morphology, dispersion and

distribution of the discrete features, were easily observed by STEM-in-SEM. It should be noted that such high quality information could be attained even when using a thermionic SEM, as was our case throughout this study (unless noted otherwise).

The same approach was successfully applied to image the morphology of more complex systems as highlighted in Fig. 2, which shows three sets of 3-phase immiscible polymer blends of PC/SAN/ABS, PPE/PA/SEBS and PC/PBT/MBS. In the first case, PC is the matrix phase, SAN is the continuous phase, and the features within SAN are emulsion ABS; in the second case PA is the matrix phase, PPE is the discontinuous phase and the features within PPE are SEBS rubber; finally in the third case, PC is the dark gray phase, PBT is the light gray phase and the dispersed particles in the PC phase are MBS rubber. In all three examples, STEM-in-SEM can provide morphological information related to phase morphology, phase dispersion and preferential phase aggregation. It even allows us to distinguish the finer features within a specific phase.

STEM-in-SEM images were also acquired for a few samples with a Field-Emission Microscope as the host SEM, i.e., the STEM-in-FEM. Images displayed in Fig. 3 highlight the differences in image quality between a TEM, thermionic STEM-in-SEM and a STEM-in-FEM. Fig. 3(a) shows the STEM-in-FEM image for a PPE/PE blend,

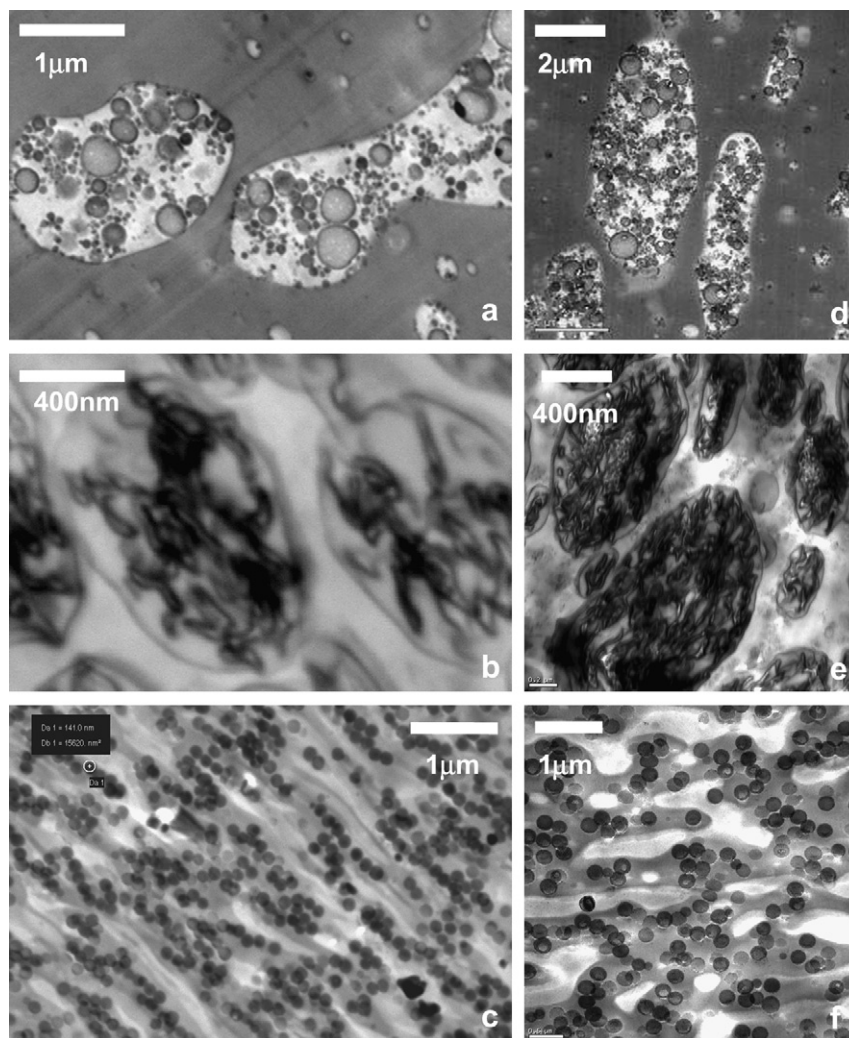


**Fig. 2.** Comparison of STEM-in-SEM and TEM images for three-phase immiscible polymer blends. The left column shows STEM-in-SEM images and the right column shows TEM images. (a) PC/SAN/ABS, with PC as the matrix phase, SAN the discontinuous phase and the dispersed features within the SAN phase are emulsion ABS. (b) PPE/PA/SEBS with PA as the matrix phase, PPE the dispersed phase and SEBS is seen within PPE (c) PC/PBT/MBS, with a co-continuous PC/PBT morphology. PBT is the white/light gray phase and PC is the darker gray phase. MBS is dispersed within the PC phase. (d), (e) and (f) are TEM images for the same samples.



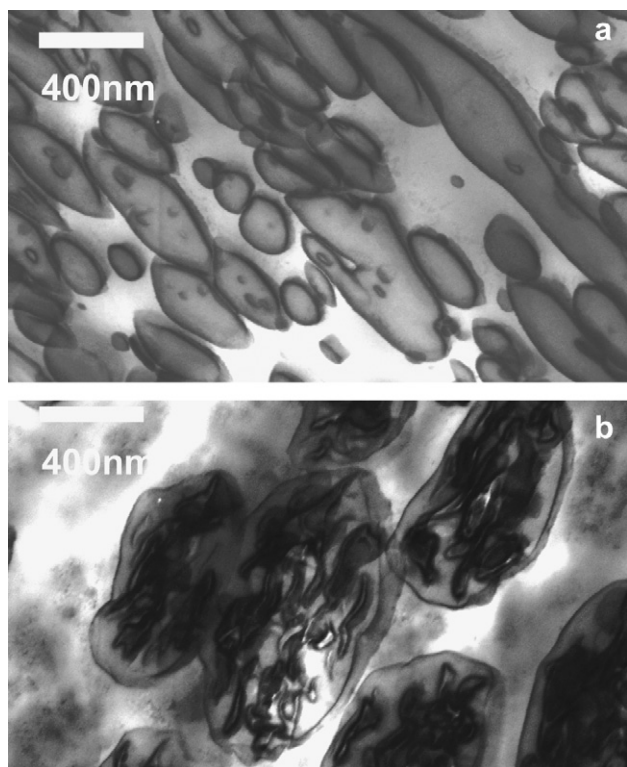


**Fig. 3.** STEM-in-SEM images acquired with a host field-emission microscope. (a) Two-phase immiscible polymer blend of PP/PPE (b) Three-phase immiscible blend of PPE/PA/SEBS.

and the thermionic STEM-in-SEM image for the same sample is given in Fig. 1(a). Similarly, Fig. 3(b) shows the STEM-in-FEM image for a PPE/PA/SEBS material, and can be compared to the thermionic STEM-in-SEM image given in Fig. 2(b). As is readily seen, the FEM provides higher image contrast in combination with improved resolution, compared to the thermionic SEM. Moreover, the image quality of the STEM-in-FEM nearly matches that of the TEM, which is not unexpected, because the resolution of the STEM-in-SEM directly depends on that of the host SEM itself. Nonetheless, at the length scales of interest for common polymer blends, it can be seen that even a thermionic SEM is quite sufficient.

The large magnification range of the SEM, i.e., from very low magnification to very high magnification, combined with high field of view, can also be an important advantage for STEM-in-SEM,

compared to TEM. The large field of view is especially relevant for crack propagation or failure analysis mechanisms, which typically span from mm scale to sub- $\mu\text{m}$  scale. An example for such an application is shown in Fig. 4, where a microtomed thin section of notched sample of PPE/HIPS was collected on a supported grid, and imaged at very low magnification (Fig. 4(a)) to get a clear representation of the crack. The same sample was then imaged at high magnification (Fig. 4(b)), and shows how the dispersed HIPS domains were affected in the vicinity of the crack. Thus, with the STEM-in-SEM, regions of interest from a very large section can be quickly selected, for further analysis at higher magnifications.

### 3.2. (b) High performance polymer composites

Similar STEM-in-SEM analysis was carried out on composite samples, results of which are given in Fig. 5, which shows a PC/PBT/Talc system. In this composite, PC is the continuous phase, PBT is the discrete phase and the dark features within PBT are talc.

Dispersion of the inorganic filler, preferred phase of the filler and overall morphology could be easily observed with this method. In the case of such composites, this method has numerous practical advantages. First, thicker sections can be used for STEM-in-SEM imaging as compared to the TEM. As mentioned earlier, electrons are not required to pass through a lens after crossing the specimen. The spread of velocities caused by absorption in the specimen therefore does not give rise to chromatic aberration induced loss of resolution, as is the case in a conventional transmission microscope: it is thus possible to examine a thicker specimen [26]. Second, in the case of filled samples, especially systems with large micron-size fillers such as  $\text{CaCO}_3$ , glass fiber, talc, mica etc., TEM analysis to obtain comprehensive information is not easily feasible on a routine basis, mainly due to ultramicrotomy limitations. This is because TEM analysis needs sections of less than 100 nm thickness. To obtain such sections of good quality, diamond knives are typically used, and sectioning through inorganic filler particles damages the diamond edge during sectioning and can even tear apart the very thin sections. Even smaller fillers such as ultratalc or silica damage the diamond knife to a great extent. It is often difficult to prepare good TEM sections of the thicknesses needed for TEM analysis with the cheaper alternative, i.e., the “use and throw” glass knives, particularly for samples that are highly crystalline or non-conductive. Therefore, in most cases, such samples are studied with SEM, which leads to limited information pertaining to filler dispersion alone. Etching methods can be employed to obtain further information on preferred phase and overall morphology through SEM, however, they lead to sophistication of sample preparation routes and

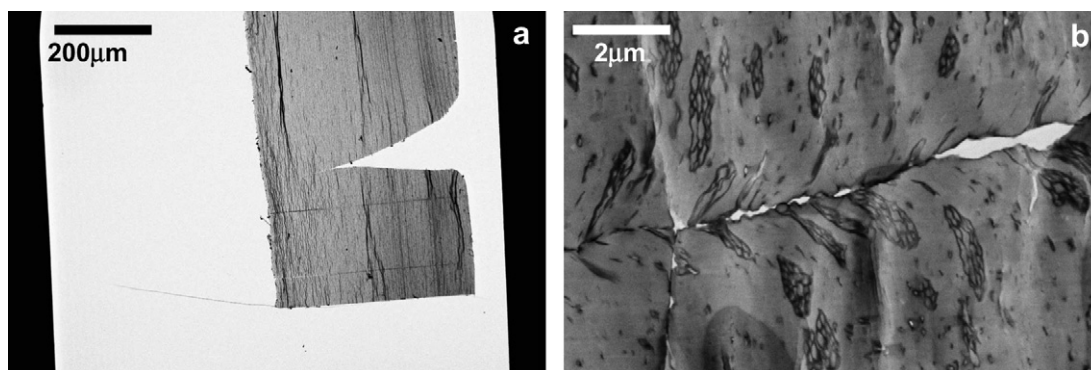


**Fig. 4.** Investigation of a notched PPE/HIPS sample by STEM-in-SEM – a thin section was microtomed in cross-section and deposited on a supported grid. (a) Low magnification STEM-in-SEM image showing the depth of the notch. (b) High magnification STEM-in-SEM image showing the effect of the notch on the surrounding morphology. HIPS is the dispersed phase.



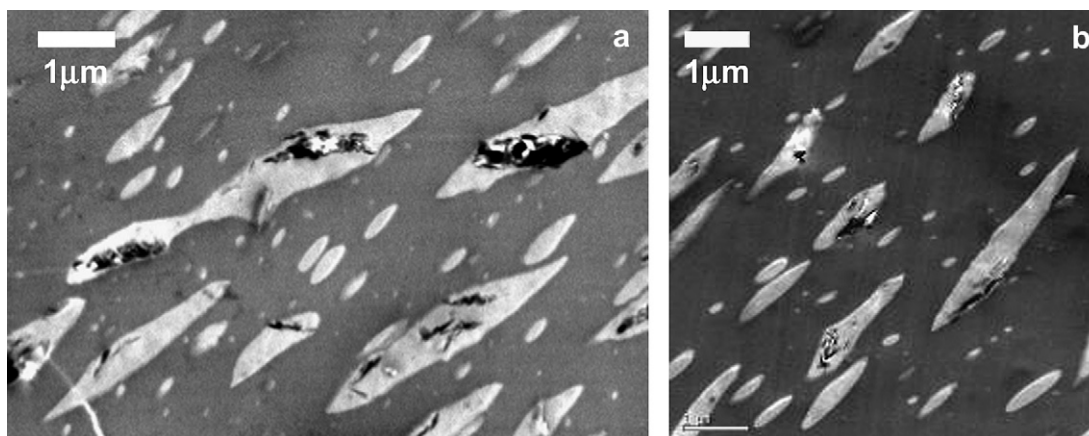


**Fig. 5.** Comparison of (a) STEM-in SEM and (b) TEM images for a typical filled system: PC/PBT/Talc where PC is the matrix phase, PBT is the discrete phase and the dark features within PBT are Talc.

increased time of analysis. With the feasibility to image thicker sections with the STEM-in-SEM method, TEM-like analysis can be performed on sections of thickness much above 100 nm, even up to a micron [21,26], which can be easily prepared with glass knives.

### 3.3. (c) Unstained and beam-sensitive materials

An additional benefit of STEM-in-SEM over TEM could be demonstrated with a class of polymeric materials or polymer blends wherein little or no differential contrast can be induced with standard staining agents, owing to their chemical nature. The lower electron energies used in STEM-in-SEM therefore come to high significance, since considerable contrast enhancement over a TEM can be obtained, resulting from the increased electron scattering cross-section at lower acceleration voltages. This proves to be crucial in the detection of even very small differences in density of the component phases of multi-phase materials, of low atomic number components such as polymer blends, often eliminating the need for heavy metal stain applications. Low voltage imaging of unstained polymer blends has been well exploited with a low voltage TEM, i.e. the LVEM and was demonstrated with many blend systems [7]. As an example the STEM-in-SEM micrograph corresponding to an unstained sample of PPE-siloxane blend is shown in Fig. 6 (a). It can be seen that siloxane (white domains) forms the discrete phase in the continuous PPE phase, and silica particles are found to be dispersed in siloxane domains. In this case of low voltage transmission imaging in the SEM, it may be noted that no specific sample

preparation is involved, contrary to the approach required with the LVEM. Imaging with the LVEM requires preparation of ultra-thin sections of thicknesses in the range of 30–50 nm, which in practice is extremely difficult for most polymer systems. Regular TEM samples with thickness in the range 80–120 nm provide adequate contrast to understand the phase morphology of such un-stainable systems. For these samples, thinner sections of <80 nm is expected to provide improved image contrast in STEM-in-SEM. However, due to the presence of inorganic fillers, sectioning at such low thicknesses generally leads to fall out of fillers and introduces artifacts such as tearing. Another class of challenging polymer systems for traditional TEM imaging is the beam-sensitive polymer material. A number of these materials were successfully imaged with STEM-in-SEM. Fig. 6 (b) shows such an example, a blend of PPE/PVDF/SBM, which is highly beam-sensitive under TEM. It can be seen that STEM-in-SEM imaging of this type of materials, known to collapse on exposure to the electron-beam in TEM in a matter of a few seconds, even under low dose or cryo conditions, could be carried out without any difficulty. We were also able to image fibrillated PTFE samples in the STEM-in-SEM (not shown). Imaging these samples by TEM is a well-known challenge as PTFE fibrils tend to snap under prolonged exposure to the electron-beam.

## 4. Industrial considerations

The main highlight of STEM-in-SEM over TEM is its suitability as the ideal equipment for environments that need rapid morphology

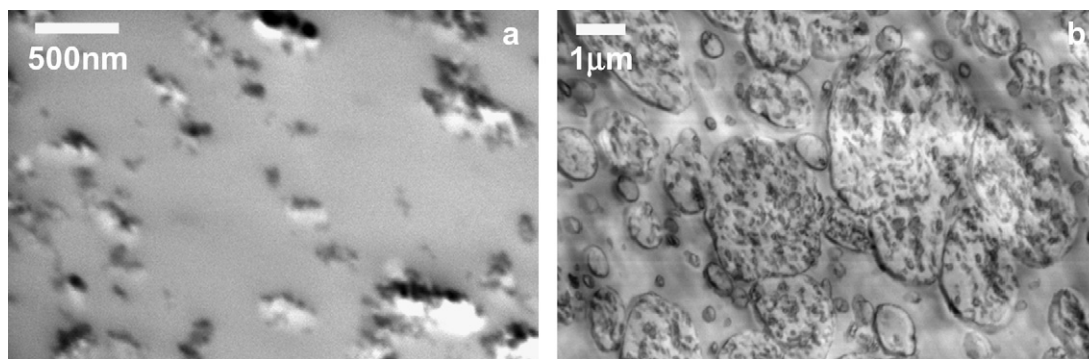


**Fig. 6.** Examples of unstained and beam-sensitive materials imaged by STEM-in-SEM: (a) Unstained PPE/Siloxane material, where PPE is the continuous phase and siloxane is the dispersed phase (white domains). The dark features within siloxane are fumed silica; (b) Beam-sensitive blend of PPE/PVDF/SBM. PPE forms the matrix phase, PVDF is the dispersed phase and SBM are the features seen within PVDF.

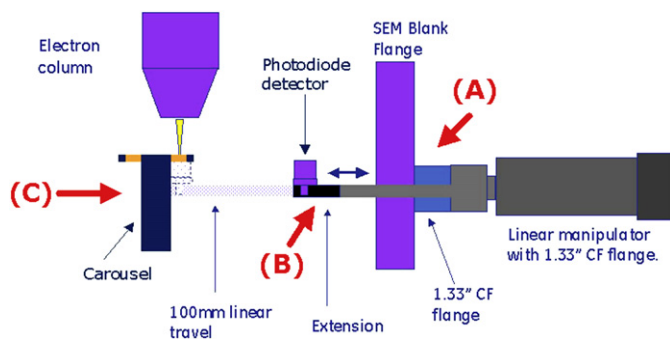


**Fig. 7.** Schematic illustrating the STEM-in-SEM system. The schematics highlights the 3 main parts of the assembly: (A): Flange-manipulator assembly; (B): Manipulator extension and holder for the photodiode detector; (C): 12-sample carousel system.

analysis of samples in large numbers, and at low cost of analysis. Such is the case in a typical production environment of high performance polymers, where morphological parameters need to be monitored and critically controlled as quality control factors in manufacturing processes. In reality, extensive morphology analysis to that extent is not carried out, even in the most advanced manufacturing plants, since it indeed is not practical to carry out TEM analysis in large numbers and with fast turnaround. This situation can be overtly simplified with STEM-in-SEM: manufacturing and quality control laboratories in polymer industry and research laboratories are often equipped with SEM, which can fairly easily be retrofitted with STEM units for a fraction of the cost of a new TEM unit. As mentioned earlier, with the STEM-in-SEM, it is possible to conduct “high throughput, TEM-like imaging” in an industrial environment.

In this work, a single-sample STEM was re-designed to a homemade carousel system, which could handle up to 12 samples

(the same system could easily be expanded to accommodate 24 samples). The throughput of the system was therefore considerably higher than that of a TEM, and without any loss in imaging quality. Most of the commercial SEM manufacturers now offer STEM as an attachment, with the capability to handle up to twelve samples. In our setup, cost incurred for a STEM system with a 12-sample carousel was an order of magnitude lower than the commercial units, and therefore, it could easily be fitted in multiple microscopes as a low-cost and high return-on-investment application. Use of this multi-sample carousel has enabled remarkably higher equipment productivity and better utilization of operator time.

Figs. 7 and 8 provide an overview of the re-designed system and illustration of its principle. The 12-sample carousel is mounted on the SEM stage, which has 5 degrees of freedom, X, Y, Z,  $\theta$  and  $\phi$ , with  $\theta$  and  $\phi$  respectively the rotational degree of freedom and the tilting degree of freedom. By a precise control of the position of the SEM stage, the carousel can be moved to close proximity of the aperture of the electron gun. Because the SEM stage will have to rotate from sample to sample, the detector cannot be mounted on the SEM stage, and hence was physically disconnected from the SEM stage so as to stay in place as the stage is rotated to the next sample. The solution was to mount the detector on a linear manipulator, which itself could be mounted on a flange on the side of the SEM chamber, schematics of which is given in Fig. 7. The linear manipulator carries the detector back and forth between a “rest” position and an “active” position when imaging. In the active imaging mode, the electron gun, the 12-sample carousel and the detector are perfectly aligned (Fig. 8 (right)). In “rest” mode the detector is “parked” away by simply retracting the detector by a safe distance (Fig. 8 (left)).

An estimate of the time saving from deployment of the STEM-in-SEM carousel, in comparison to a single-sample STEM-in-SEM system was derived from a careful analysis of the steps involved in the STEM-in-SEM process, and was compared to TEM. Steps involved in either of these methods can be divided into 3 main

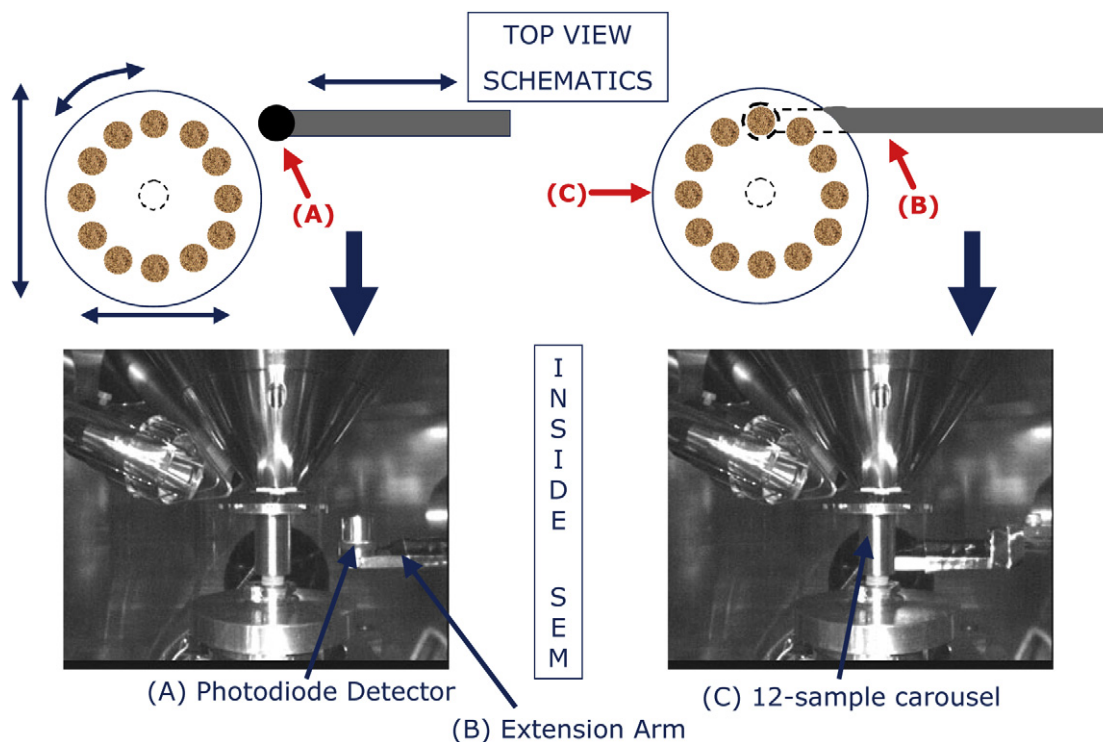


**Fig. 8.** Top part: Schematic showing the top view of parts (A), (B) and (C). Bottom part: Pictures showing the inside of the SEM chamber and corresponding to the schematics of the top part. The 12-sample carousel is aligned with the electron column, and the linear manipulator is extended to bring in the photodiode detector (left). The picture on the right shows the electron column, the 12-sample carousel and the photodiode detector aligned and ready for imaging.

categories. (1) Sample preparation – this step involves the standard microtomy procedures to prepare TEM sections. (2) Staining – using chemicals such as osmium tetroxide ( $\text{OsO}_4$ ) and ruthenium tetroxide ( $\text{RuO}_4$ ) to enhance the contrast between the various phases composing the material. This step is required in most cases. Staining time depends on the composition of the sample, although many samples can be stained in parallel. (3) Imaging – involves loading the specimen holder into the microscope, loading the STEM-in-SEM unit on the SEM sample holder, evacuating the chamber/column and waiting to reach a suitable vacuum level, locating the region of interest and acquiring images of relevant features, and finally removing the sample. While steps 1 and 2 are common for TEM and STEM-in-SEM and were optimized in terms of speed and quality, major differences were seen in productivity estimates between the two techniques when a 12-sample carousel system is added to the STEM-in-SEM. We estimate that the time saving per sample resulted in a 50% increase in imaging productivity vs. TEM imaging. An added benefit of the carousel system is that it contributes to increasing the lifetime of the equipment by limiting the number of occurrences of pumping & venting cycles and by limiting filament warm-up.

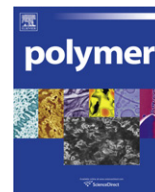
## 5. Conclusion

A STEM-in-SEM system with a 12-sample carousel allowed straightforward analysis of many common polymer systems, matching TEM in terms of quality of information, with remarkable improvement in speed of analysis. This makes the STEM-in-SEM a very practical and affordable alternative to TEM analysis in an industrial environment for the characterization of polymer materials. In addition, STEM-in-SEM was shown to be successful for the study of large-scale phenomena, and for imaging low contrast or beam-sensitive multi-phase samples. Although TEM imaging at higher accelerating voltages is capable of providing more detailed images, analysis of almost all polymer systems could be realized by STEM-in-SEM, with appropriate choice of host SEM. Use of a field-emission SEM was shown to provide only slight improvement in image quality at the magnification up to 50,000X commonly required for most polymer blend systems. High-resolution SEM becomes very relevant for polymer systems composed of nano-sized-phases, as is the case with block copolymers, elastomeric

nanoparticles or nano-fillers. High-resolution STEM-in-SEM could be combined with elemental analysis and high angle annular dark field detectors, so that its analysis capability will ultimately match with that of a 120 kV TEM with high-contrast optics, which is typically used for the majority of polymer applications.

## References

- [1] Sawyer LC, Grubb D. *Polymer microscopy*. Chapman & Hall; 1996.
- [2] Michler GH. *Electron microscopy of polymers*. Berlin: Springer; 2008.
- [3] Butler JH, Joy D, Bradley GF, Krause SJ. *Polymer* 1995;36(9):1781–90.
- [4] Robeson LM. *Polymer blends: a comprehensive review*. Hanser-Gardner; 2007.
- [5] Todd CS, et al. *Microscopy Today* 2008;16(3):24.
- [6] Lednický F, Coufavoła E, Hromádková J, Delong A, Kolrik V. *Polymer* 2000;41:4909–14.
- [7] Drummy LF, Yang J, Martin DC. *Ultramicroscopy* 2004;99:247–56.
- [8] Vanderlinde W. *Electronic Device Failure Analysis* 2004;6(4):32–40.
- [9] Stokes D, Baken E. *Imaging and Microscopy* 2007;2:18–20.
- [10] Stokes D. *Scanning electron microscopy rises to the challenges of the 21st century*. Physicsworld.com; 2008.
- [11] Smith CL, Lee MR, MacKenzie M. *Microscopy & Analysis* 2006;111:17–20.
- [12] Nakagawa M, Dunne R, Koike H, Sato M, Perez-Camacho JJ, Kennedy BJ. *Journal of Electron Microscopy* 2002;51:53–7.
- [13] Russias J, Frizon F, Caudit-Coumes C, Malchere A, Douillard T, Jousot-Dubien C. *Journal of the American Ceramic Society* 2008;91(7):2337–42.
- [14] Acevedo-Reyes D, Perez M, Verdu C, Bogner A, Epicier T. *Journal of Microscopy* 2008;232(1):112–22.
- [15] Vesely D. *Materials World* 2002;10(11):23–4.
- [16] Brown GM, Westwood AD. *Microscopy & Microanalysis* 2003;9(Suppl.2):1020–1.
- [17] Lee MR, Smith CL. *Mineralogical Magazine* 2006;70(5):579–90.
- [18] Coyne E, Magee JP, Mannion P, O'Connor GM, Glynn TJ. *Applied Physics A* 2005;81(2).
- [19] Vermogen A, Masenelli-Varlot K, Vigier G, Sixou B, Thollet G, Duchet-Rumeau J. *Journal of Nanoscience and Nanotechnology* 2007;7(9):3160–71.
- [20] Bogner A, Thollet G, Basset D, Jouneau P-H, Gauthier C. *Ultramicroscopy* 2005;104:290–301.
- [21] Bogner A, Jouneau P-H, Thollet G, Basset D, Gauthier C. *Micron* 2007;38:390–401.
- [22] Jornsano P, Thollet G, Gauthier C, Masenelli-Varlot K. In: Luysberg M, Tillmann K, Weirich T, editors. *EMC 2008 Vol1: instrumentation and methods*; 2008. p. 337–8.
- [23] Cudby PEF. Chapter 3: characterization of vulcanized blends by microscopy. In: Tinker AJ, Jones JP, editors. *Blends of natural rubber: novel techniques for blending with speciality polymers*. London: Chapman & Hall; 1998. p. 21–39.
- [24] Cudby PEF, Gilbey BA. *Rubber Chemistry and Technology* 1995;68(2):342–50.
- [25] Goldstein J, Newbury D, Joy D, Lyman C, Echlin P, Lifshin E, et al. *Scanning electron microscopy and X-ray microanalysis*. 3rd ed. New York: Kluwer Academic/Plenum; 2003. 203–207.
- [26] Oatley CW. *Journal of Applied Physics* 1982;53(2):R1–13.



## Preparation and characterization of nanocomposite polyelectrolyte membranes based on Nafion<sup>®</sup> ionomer and nanocrystalline hydroxyapatite

Mohammad Mahdi Hasani-Sadrabadi<sup>a,b</sup>, Nassir Mokarram<sup>c</sup>, Mahmoud Azami<sup>d,e</sup>, Erfan Dashtimoghadam<sup>a</sup>, Fatemeh Sadat Majedi<sup>b,d</sup>, Karl I. Jacob<sup>c,\*</sup>

<sup>a</sup> Department of Polymer Engineering and Color Technology, Amirkabir University of Technology, Tehran, Iran

<sup>b</sup> Institute of Bioengineering, Swiss Federal Institutes of Technology, Lausanne (EPFL), CH-1015 Lausanne, Switzerland

<sup>c</sup> School of Materials Science and Engineering, Georgia Institute of Technology, Atlanta, GA, USA

<sup>d</sup> Department of Biomedical Engineering, Amirkabir University of Technology, Tehran, Iran

<sup>e</sup> Tissue Engineering and Cell Therapy Group, School of Advanced Medical Technologies, Tehran University of Medical Sciences, Tehran, Iran

### ARTICLE INFO

#### Article history:

Received 31 August 2010

Received in revised form

16 November 2010

Accepted 20 November 2010

Available online 27 November 2010

#### Keywords:

Nanocrystalline hydroxyapatite

Nanocomposite polyelectrolyte membranes

Fuel cell

### ABSTRACT

In this study nanocrystalline hydroxyapatite (nHA) was synthesized and characterized by means of FT-IR, XRD and TEM techniques and a series of proton exchange membranes based on Nafion<sup>®</sup> and nHA were fabricated via solvent casting method. Thermogravimetric analysis confirmed thermal stability enhancement of the Nafion<sup>®</sup> nanocomposite due to the presence of nHA nanopowder. SAXS and TEM analyses confirmed the incorporation of nHA into ionic phase of Nafion<sup>®</sup>. Furthermore, the incorporation of elliptical nHA into the Nafion<sup>®</sup> matrix improved proton conductivity of the resultant polyelectrolyte membrane up to 0.173 S cm<sup>-1</sup> at 2.0 wt% of nHA loading compared to that of 0.086 S cm<sup>-1</sup> for Nafion<sup>®</sup> 117. Also, the inclusion of nHA nanoparticles into nanocomposite membranes resulted in a significant reduction of methanol permeability and crossover in comparison with pristine Nafion<sup>®</sup> membranes. Membrane selectivity parameter of the nanocomposites at 2.0 wt% nHA was calculated and found to be 106,800 S s cm<sup>-3</sup>, which is more than two times than that of Nafion<sup>®</sup> 117. Direct methanol fuel cell tests revealed that Nafion<sup>®</sup>/nHA nanocomposite membranes were able to provide higher fuel cell efficiency and also better electrochemical performance in both low and high concentrations of methanol feed. Thus, the current study shows that nHA enhances the functionality of Nafion<sup>®</sup> as fuel cell membranes.

© 2010 Elsevier Ltd. All rights reserved.

### 1. Introduction

Fuel cell technology is becoming one of the critical technologies of the current century to provide power supply for stationary and portable applications and for transportation [1]. Among the various kinds of fuel cells, polymer electrolyte membrane fuel cells (PEMFCs), direct methanol fuel cells (DMFCs) and biological fuel cells (BFCs) include solid proton conducting membranes [2]. In fact, proton exchange membranes (PEMs) are considered as the central and often the performance-limiting component of such fuel cells [3]. DMFCs, due to their advantages of high-energy density and low weight, are believed to be the most promising energy conversion devices for future portable electronic devices.

Over the past years, Nafion<sup>®</sup> membranes from DuPont have been emerged as the most common and commercially available proton exchange membrane for PEMFC, DMFC and BFC technologies. Nafion<sup>®</sup>, as a perfluorosulfonic acid polymer, combines the high hydrophilicity of the sulfate pendant groups with the high hydrophobicity of the fluorinated backbone. Such an amphiphilic behavior of the Nafion<sup>®</sup> chains enables their nanoscopic phase separation in hydrated state [4,5]. Nafion<sup>®</sup> stands out for its selective permeability to water, intrinsic ion conductivity, dimensional stability in harsh acidic conditions, suitable flexibility and water uptake capacity. However, the high methanol crossover of the Nafion<sup>®</sup> prohibits its large-scale application in DMFC devices [6]. Methanol permeation causes poisoning at the cathode side and consequently diminishes fuel efficiency. Therefore, the development of novel membranes with low methanol permeation rate is in progress and many studies have been employed to synthesize novel polymeric membranes to fulfill low methanol crossover and high proton conductivity [7]. In the meantime, different approaches such as coating with thin polyelectrolyte barrier layers have been also conducted to reduce the methanol permeation

\* Corresponding author. School of Polymer, Textile & Fiber Engineering, Georgia Institute of Technology, Atlanta, GA 30332-0295, USA. Tel.: +1 404 894 2541; fax: +1 404 894 8780.

E-mail address: [karl.jacob@ptfe.gatech.edu](mailto:karl.jacob@ptfe.gatech.edu) (K.I. Jacob).



across the Nafion<sup>®</sup> membranes [8,9]. Another approach to achieve a remarkable reduction in methanol permeability of the PEMs is to modify the size of the proton transport nanochannels through dispersing inorganic fillers and introducing tortuous pathways [10–17]. This is achieved by dispersing inorganic fillers, such as silica [18], titania [19], zirconia [20], zeolite [21–23], zirconium phosphate [24], zirconium hydrogen phosphate [25], laponite [26], montmorillonite [11–17] and carbon nanotube [27,28] into the polymeric matrices.

It has been known that calcium hydroxyl phosphate (Ca<sub>5</sub>(PO<sub>4</sub>)<sub>3</sub>OH) shows proton conductivity [29–31], good compatibility with various polymers [32,33], high thermal stability and high crystallinity. Park and coworkers [34–37] have reported the incorporation of micron-size calcium phosphate particles into Nafion<sup>®</sup> matrix and investigated the morphological and transport properties of fabricated composite membranes.

With recent developments in the nanotechnology related fields, the relationships between filler size and specific properties of the resultant composites have become a subject of great interest [38]. It has been demonstrated that decreasing the size of the filler from micron to nanometer leads to a significant increase of surface-to-volume ratio resulting in high-energy surfaces [39] and enhanced ionic conductivity [40–42]. Moreover, owing to the nanoparticles' high interfacial energy, the bonding between the polymer and filler is enhanced [39].

Our objective in the current study was to develop a series of novel polyelectrolyte membranes by incorporating nanocrystalline hydroxyapatite (nHA) in Nafion<sup>®</sup>. Subsequently, proton conductivity and methanol permeability of the fabricated nanocomposite membranes in the presence of various amounts of nHA were investigated. Finally, the DMFC single cell performance of the pre-determined optimum sample among Nafion<sup>®</sup>/nHA nanocomposite membranes was evaluated.

## 2. Experimental

### 2.1. Synthesis of nanocrystalline hydroxyapatite

The wet chemistry method involving direct precipitation of nanocrystalline hydroxyapatite (nHA) powder from aqueous solutions and a freeze drying step was adapted for the synthesis [32,33]. A 0.09 M diammonium hydrogen phosphate solution [(NH<sub>4</sub>)<sub>2</sub>HPO<sub>4</sub>, 99%, Merck, Germany] and 0.15 M calcium nitrate tetrahydrate solution [Ca(NO<sub>3</sub>)<sub>2</sub>·4H<sub>2</sub>O, 98%, VWR Prolabo, France] were prepared and the pH of both solutions was adjusted to 11 by addition of 1 M sodium hydroxide solution (NaOH, 99%, Merck, Germany). Then, diammonium hydrogen phosphate solution was added drop-wise to calcium nitrate solution at room temperature to provide the precipitation of nanocrystalline HA (nHA). In the next step, the precipitated nHA was centrifuged and washed with deionized water to remove the unwanted ions. The resultant nHA particles were finally dried in a freeze-drier system (Alpha 1-2 LD, Germany) for 10 h.

### 2.2. Nanocomposite preparation

At first, definite amounts of nHA powder were suspended in deionized water (purified with Millipore™) at 25 °C, stirred for 2 h and ultra-sonicated for 1 h. The nHA suspensions were then added to Nafion<sup>®</sup> (Nafion<sup>®</sup> 5 wt% solution in water and low molecular weight alcohols supplied by E.I. DuPont de Nemours company) at 25 °C and stirred for 3 h to obtain various loading weights of 1.0, 2.0, 3.0, 5.0 and 10.0 wt% of nHA to polymer content. The resultant mixtures were ultra-sonicated for six successive intervals of 30 min, cast on glass-made Petri dishes, incubated at 25 °C

overnight and then dried at 70 °C for 12 h. Finally, fabricated membranes were annealed at 120 °C overnight. Subsequently, the newly prepared membranes were treated according to the following procedure: first, all membranes were boiled in 3 vol% hydrogen peroxide (H<sub>2</sub>O<sub>2</sub>, Merck, Germany) for 30 min, washed several times with deionized water and boiled for 1 h in deionized water. Membranes were then boiled in 0.5 M sulfuric acid (H<sub>2</sub>SO<sub>4</sub>, Merck, Germany) for another hour and washed several times with deionized water. The pristine recast Nafion<sup>®</sup> membranes were also treated by the same modification procedure. Nafion<sup>®</sup> 117 membranes, from DuPont were treated similarly and used for comparison of properties.

### 2.3. Characterization

#### 2.3.1. Fourier transform infrared spectroscopy

The FT-IR spectroscopy was performed on the newly synthesized nHA nanoparticles using a Bomem MB 100 spectrometer (ABB Bomem Inc., Quebec, Canada). One milligram of the sample powder was carefully mixed with 300 mg of potassium bromide (KBr) (infrared grade) and pelletized under vacuum. Then, the pellet was analyzed in the range of 500–4000 cm<sup>-1</sup> at the scan speed of 23 scans min<sup>-1</sup> with 4 cm<sup>-1</sup> resolution.

#### 2.3.2. X-ray diffraction

The X-ray diffraction (XRD) analysis was carried out by means of a Siemens–Brucker D5000 diffractometer (Germany) with voltage and current settings of 40 kV and 40 mA, respectively and Cu-K $\alpha$  radiation (1.540600 Å). For qualitative analysis, the XRD patterns were recorded in the interval of 20° ≤ 2θ ≤ 60° at the scan speed of 2° min<sup>-1</sup> and the step size and step time of 0.02° and 1 s, respectively. Crystallographic identification of the synthesized powder was accomplished by comparing the experimental XRD patterns to standards compiled by the International Centre for Diffraction Data (ICDD), in which, card #09-0432 for HA was used. In addition, the average size of the individual crystallites was calculated from XRD data using the Debye–Scherrer approximation

$$t = \frac{0.9\lambda}{\beta_{1/2} \cos \theta}$$

where  $t$  is the crystallite size,  $\lambda$  is the wavelength of Cu-K $\alpha$  radiation (1.540560 Å), and  $\beta_{1/2}$  is full width at half maximum intensity. The crystallinity of nHA based nanocomposite membranes was also investigated using WAXS apparatus as reported by Park et al. [34,35]. Small angle X-ray scattering (SAXS) analysis of the membranes was carried out by using a diffractometer equipped with Cu K source and Kratky SAXS apparatus. The water swelled samples were used in a sealed sample holder at 25 °C. The chamber was maintained under vacuum. The intensity of the X-ray scattering is plotted versus the scattering vector,  $q$ , defined as  $q = (4\pi/\lambda) \sin \theta$ , where  $\lambda$  is the X-ray wavelength and  $2\theta$  is the scattering angle.

#### 2.3.3. Transmission electron microscopy

Transmission electron microscopy (TEM; CM200-FEG-Philips, the Netherlands) was also used to characterize the nHA particles. A dilute suspension of nHA particles in ethanol was prepared from which the particles were deposited onto the Cu grid that supported a carbon film. The particle shape and sizes were characterized via diffraction (amplitude) contrast and, for crystalline materials, by high resolution (phase contrast) imaging.

For the TEM characterization the membrane was embedded into epoxy, and then cut into thin slices using an ultramicrotome (Leica Ultracut E) at room temperature. The thickness of each slice was

50 nm. The slices were examined in a Philips/FEI CM20. TEM with LaB6 source operated at 200 kV accelerating voltage.

### 2.3.4. Water uptake

To study the swelling behavior of the membranes, the dried samples were first soaked in deionized water at room temperature for a day, and then quickly weighed at different time intervals after carefully removing the excess water or methanol with filter paper, and immersed back in the water. This process was repeated several times until no further weight gain was observed. Finally, the water uptake was calculated using the following equation: Water uptake =  $(W_{sw} - W_{dry})/W_{dry} \times 100$ , where  $W_{sw}$  and  $W_{dry}$  are the weights of membranes in the swelled and dried states, respectively.

### 2.3.5. Thermogravimetry analysis (TGA)

The degradation process and thermal stability of the nHA and the nanocomposite membranes were investigated through thermogravimetry analysis (Perkin–Elmer Pyris1) and approximate amounts of 10–20 mg of the fully dried samples were characterized at heating rate of  $10\text{ }^{\circ}\text{C min}^{-1}$ .

### 2.3.6. Proton conductivity

The proton conductivity of the fully hydrated membranes was measured at room temperature via the AC electrochemical impedance spectroscopy method, using a Solartron Interface 1260 gain phase analyzer over the frequency range of  $1\text{--}10^6$  Hz. The conductivity values were calculated from the formula  $\sigma = L \cdot R^{-1} \cdot A_e^{-1}$ , where  $L$  is the membrane thickness,  $A_e$  is the cross-sectional area of the membrane and  $R$  is the resistance. A four-point probe apparatus (Bekktech Conductivity Cell) has been used to measure the in-plane conductivity of membranes. For conductivity measurements, the samples were immersed in water to reach to their equilibrium hydrated state and then put in the conductivity cell equipped with humidity control at 95% RH. The reported data are the average of at least three samples with the standard deviation (S.D.) not been more than 10%. In the case of higher S.D. values, the measurements were repeated with more samples.

### 2.3.7. Methanol permeability

The methanol permeability was determined by means of a two-compartment glass diffusion cell. Prior to testing, the membranes were equilibrated in deionized water for 24 h. Methanol solution was poured into one side of the diffusion cell (cell A) and the other side (cell B) contained pure water. The solution in each compartment was stirred continuously to ensure the homogeneity. The concentration of the methanol in cell B was measured via the gas chromatography method. The methanol permeability was determined using the following equation:

$$P = \frac{1}{C_A} \left( \frac{\Delta C_{B(t)}}{\Delta t} \right) \left( \frac{L \cdot V_B}{A} \right)$$

where  $P$  is the methanol permeability of the membrane ( $\text{cm}^2 \text{ s}^{-1}$ ),  $C_A$  is the methanol concentration in cell A ( $\text{mol L}^{-1}$ ),  $\Delta C_B/\Delta t$  is the slope of the molar concentration variation of methanol in the cell B as a function of time ( $\text{mol L}^{-1} \text{ s}^{-1}$ ),  $V_B$  is the volume of each diffusion reservoir ( $\text{cm}^3$ ),  $A$  is the membrane area ( $\text{cm}^2$ ) and  $L$  is the membrane thickness (cm). The surface area of the membrane samples for permeability measurements was  $2.5 \text{ cm}^2$ , and a 2 M methanol solution was used for methanol permeability measurements. Methanol permeability measurements were performed on at least three separate samples and the results are reported as the average of at least three samples with standard deviation (S.D.) lower than 10%. In the case of higher S.D. values, the measurements were repeated for more samples.

### 2.3.8. Performance tests for a single cell fuel cell

The DMFC single cell was composed of stainless steel as the end plates and flow fields, two carbon papers as the gas diffusion layers (GDL, TGP-H-120 Toray), silicon rubber sheets as the sealants and a membrane electrode assembly (MEA). MEAs were prepared via the catalyst painting technique as same as our previous reports [14–17,20]. Pt and Pt/Ru-black were used as catalysts for the anode and cathode, respectively. The catalysts were mixed with Nafion® solution and several drops of glycerol. The suspension was brushed directly ( $4 \text{ mg cm}^{-2}$ ) onto the membranes, and hot-pressed to increase the contact area between the catalysts and membranes. The area of the tested membranes was  $3 \times 3 \text{ cm}^2$  and MEAs were fabricated using a  $200 \text{ kg cm}^{-2}$  hot-press at  $120\text{ }^{\circ}\text{C}$  for 90 s for each membrane's side.

The performance of the single cell was evaluated at two methanol concentrations (1 and 5 M) and oxygen flow rates into the anode and cathode sides at  $70\text{ }^{\circ}\text{C}$ . The cell temperature as well as the temperature of anode and cathode sides was fixed at  $70\text{ }^{\circ}\text{C}$ , which was controlled by preheating the fuels (air and methanol solution). The relative humidity (RH) was fixed at 70% RH. Methanol was fed to the anode side at 20 psi back pressure for 1 h and oxygen was introduced to the cathode side with gradual pressure increase to 20 psi, and the cell was allowed to run for half an hour before collecting the polarization curves data [43,44]. All single cell performance tests were performed on multiple samples and the results are presented as the mean values.

For methanol crossover measurements, humidified nitrogen was fed to cathode side at  $70\text{ }^{\circ}\text{C}$ , and the fuel cell was performed until a limiting current occurs. This limiting current obtained at the open circuit condition indicates the oxidation current of methanol crossover from anode to cathode.

## 3. Results and discussion

### 3.1. nHA powder

The FT-IR spectrum of the synthesized HA powder is shown in Fig. 1. The characteristic bands are marked, which are: (a) two bands at  $3555 \text{ cm}^{-1}$  and  $622 \text{ cm}^{-1}$  associated with the stretching and vibration mode of hydrogen-bonded  $\text{OH}^-$  ions, respectively, and (b) the band at  $1040 \text{ cm}^{-1}$  arises from  $\nu_3 \text{ PO}_4$ , and the bands at  $603 \text{ cm}^{-1}$  and  $561 \text{ cm}^{-1}$  correspond to  $\nu_4 \text{ PO}_4$ . All of these characteristic bands shown in FT-IR spectrum are typical for hydroxyapatite [32]. The peak around  $1600 \text{ cm}^{-1}$  could be attributed to the formation of carbonated apatite, which indicates carbonate content ( $\text{CO}_3^{2-}$ ) originated from the absorption of carbon dioxide from atmosphere during the reaction.

The straight base line and the sharp peaks of the diffractogram in Fig. 2 confirm that the product was well crystallized. All of the observed peaks in the XRD pattern coincide with typical HA ceramic peaks and trace of no other compound was detected by this technique. According to Debye–Scherrer approximation, crystallite size for this powder was about 12 nm.

TEM was used to examine shape and also estimate size of the synthesized hydroxyapatite crystallites. The TEM micrograph of the hydroxyapatite powder is shown in Fig. 3. As seen, the morphology of nHA nanoparticles presents agglomerated elliptical crystallites. Moreover, it was found that the average dimensions of the single crystallites and agglomerates to be in the range of  $8\text{--}13 \times 20\text{--}40 \text{ nm}$  and  $75\text{--}90 \times 120\text{--}170 \text{ nm}$ , respectively.

### 3.2. Ionomeric nanocomposite

The thermograms of nHA, Nafion® 117 and Nafion®/nHA nanocomposite membranes are plotted in Fig. 4. It can be seen that nHA

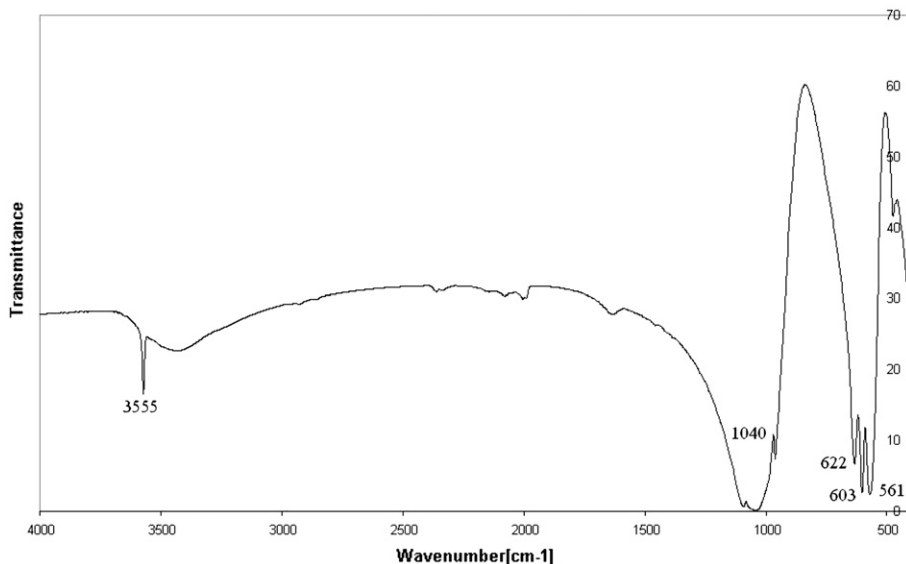


Fig. 1. FT-IR spectra of the synthesized hydroxyapatite powder.

starts to lose weight by increasing temperature to higher than 220 °C (inset of Fig. 4). As displayed in Fig. 4, the first degradation step of Nafion® 117 starts at about 300 °C, which is attributed to the decomposition of the Nafion® sulfonic side chains [12], and a sharp decreasing region occurs after 360 °C due to the degradation of PTFE backbone of the Nafion® polymer. Nafion®/nHA nanocomposite also exhibited a two-step degradation pattern. The weight loss curve of the nanocomposite sample showed a slight falling region at about 330 °C. The enhanced thermal stability of the nanocomposite sample compared to the Nafion® 117 could be ascribed to the possible interactions of active surfaces of nHA particles with ionic side chains of Nafion®.

The TEM micrograph of a nanocomposite sample comprising 5 wt% of nHA is shown in Fig. 5. As seen, the nHA particles are quite homogeneously dispersed in the Nafion® matrix and no significant agglomeration is observed. Accordingly, it could be found out that at lower loadings of the nHA particles, better is achieved.

The swelled nanocomposite membranes were also investigated with the SAXS method to elucidate the contribution of nHA particles into the microstructure of Nafion®. As shown in Fig. 6, the ionomer peak at 2 wt% of nHA has shifted from  $0.6 \text{ nm}^{-1}$  for the pristine Nafion® to  $0.45 \text{ nm}^{-1}$  for the nanocomposite sample. Such an observation implies that the size of Nafion®'s nanochannels in hydrated state has swelled from 10.5 nm to 14 nm in the presence of nHA particles. It should be mentioned that the measured nanochannel size is in accordance with the literature [45]. As mentioned before, the width of the elliptical-shaped nHA particles is in the range of 8–13 nm, which is consistent with the size of swelled ionomeric nanochannels and thus the nHA particles have active contribution into the ionic phase of Nafion®.

The water uptake and membrane thickness values of Nafion®-based nanocomposite membranes as well as crystallinity of these membranes at different nHA loading weights are shown in Table 1. The thickness of all nanocomposite membranes as well as recast Nafion® samples was in the range of 55–66  $\mu\text{m}$ .

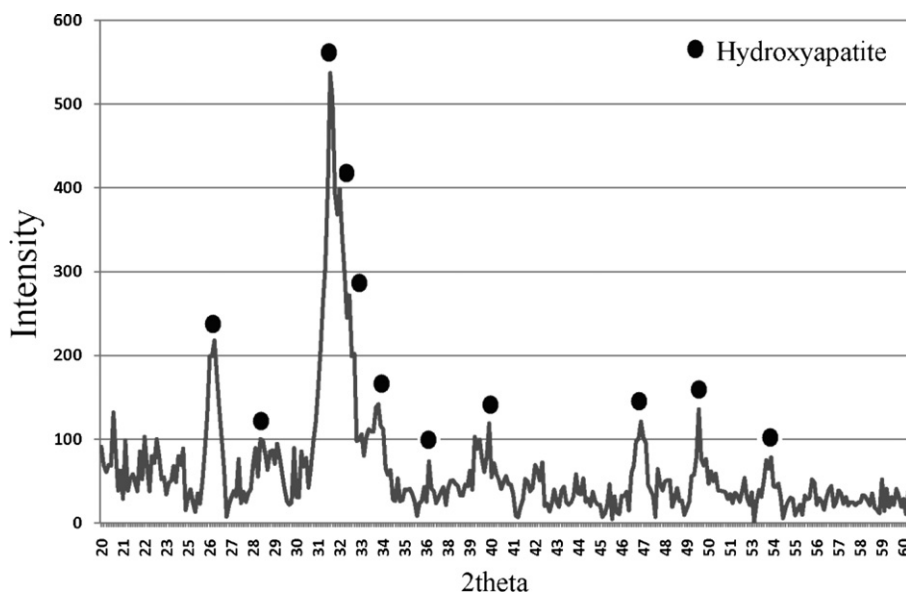


Fig. 2. XRD pattern of the synthesized hydroxyapatite nanopowder.

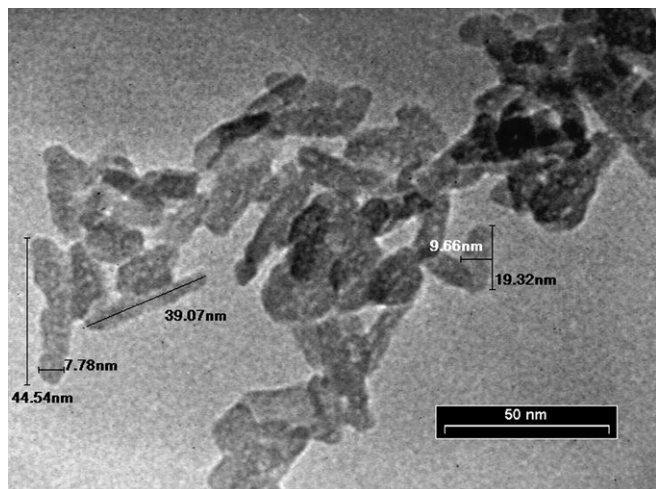


Fig. 3. TEM image of synthesized nHA nanopowder.

It is well known that the water molecules, which reside in the hydrophilic domains of a polyelectrolyte structure, facilitate proton transport [43]. As seen in Table 1, the presence of nHA particles at lower contents (below 5 wt%) does not affect significantly the extent of water swelling ratio and crystallinity.

The crystallinity of nanocomposite samples as well as neat Nafion<sup>®</sup> membranes was investigated using WAXS method and the results are summarized in Table 1. It was found that the crystallinity of Nafion<sup>®</sup> membranes is not considerably affected after inclusion of nHA particles at lower than 5.0 wt% loadings. However, at the higher loading weights (>5.0 wt%) the crystallinity is increased, which is consistent with the previously reported corresponding microparticulate systems [34–37]. Park et al. [34] have speculated that such an observation is attributed to the formation of new crystalline regions in the amorphous domains of Nafion<sup>®</sup> due to the nucleation effect. Proton conductivity in ionomers is considered as

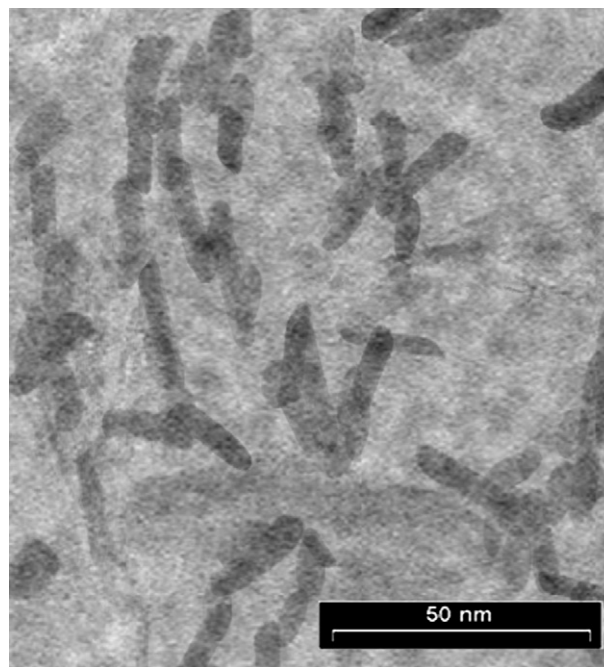


Fig. 5. TEM micrograph of Nafion<sup>®</sup>/nHA-5 wt% nanocomposite membrane.

the key parameter in the development of polymeric electrolyte membrane for fuel cell applications. An ideal electrolyte should be able to conduct protons across itself rapidly. Therefore, conductivity measurements were carried out to assess the contribution of the components of nanocomposite ionomers.

As mentioned in Introduction part the HA structure has an intrinsic ionic conductivity, it has been found that the conductivity of HA is due to the ion hopping ability induced by the ions in the crystal structure of HA, which is increased at elevated temperature [31,46]. Actually, the charge mobility carriers in oxy

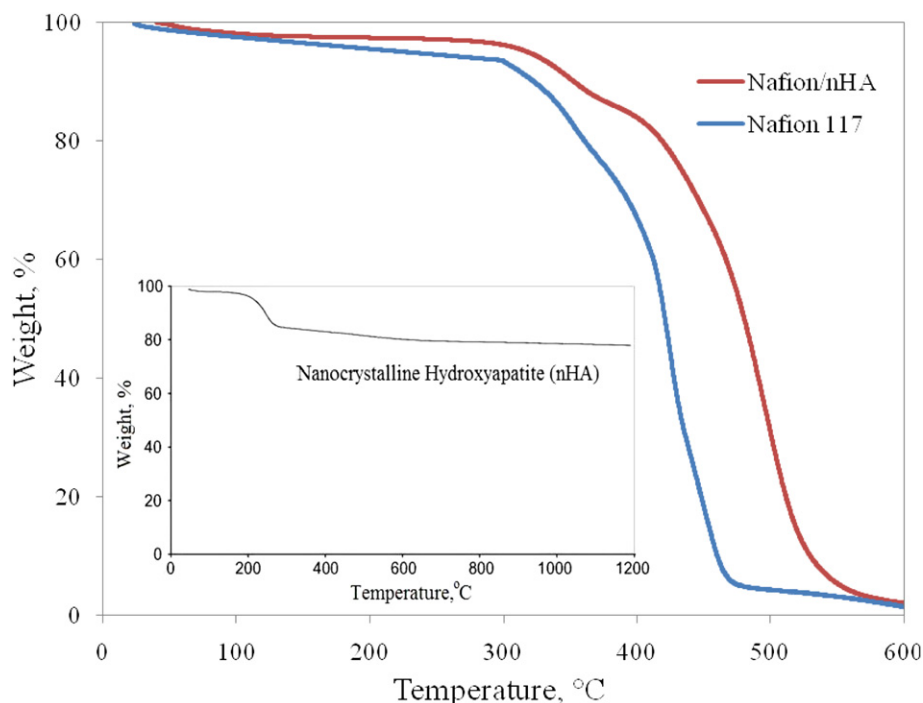


Fig. 4. Thermal stability of Nafion<sup>®</sup>/nHA nanocomposite in comparison with that of Nafion<sup>®</sup> 117. The inset shows the thermogram of nHA.



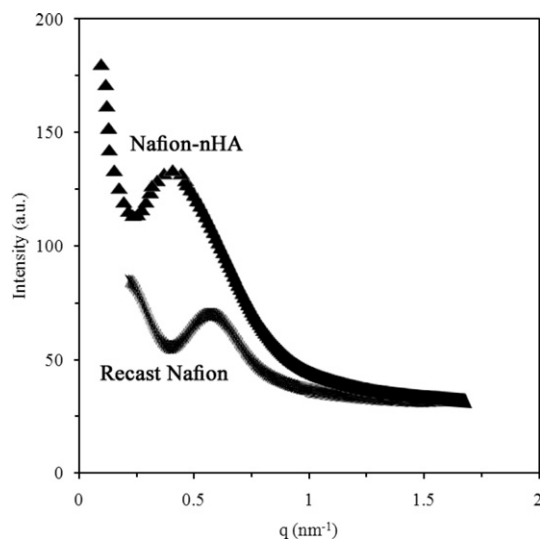


Fig. 6. SAXS of Nafion<sup>®</sup>/nHA-2 wt% at swelled state in comparison with that of recast Nafion<sup>®</sup>.

and hydroxyapatite structures are affected by anionic vacancies in the channels and that of  $O^{2-}$  ions. The analysis of the frequency dependant conductivity allows visualizing the effect of the structurally disordered mobile ions on the conduction properties of these types of materials [47]. At low temperatures (lower than 120 °C), proton conduction is supposed to occur through the adsorbed water molecules. With increasing temperature and gradually elimination of the adsorbed water molecules, the surface conduction is limited, whereas the mobile carriers are increased [48]. The synthesized nHA particles were pressed into a disk with the thickness of 1 mm and characterized via AC two-probe through electrochemical impedance spectroscopy (EIS) at 80 °C. The bulk conductivity of nHA was found to be in the order of  $10^{-9}$  S  $cm^{-1}$ , which is not comparable with that of Nafion<sup>®</sup>. However, proton conductivity characterization of the nanocomposite samples has revealed that the intrinsic conductivity of nHA particles provides a synergistic effect on the total conductivity after their inclusion into the proton conducting nanochannels of Nafion<sup>®</sup>.

The effect of nHA's loading weights on the conductivity of corresponding membranes is shown in Fig. 7. The proton conductivity values are in the same range with the reported results from Park et al. [34,35] which is a work on Nafion<sup>®</sup> and micron-size hydroxyapatite. Moreover and as shown in Table 1, the water uptake of nanocomposite membranes is considerably lower than that of Nafion<sup>®</sup> 117, which implies that the improved conductivity of nanocomposite samples is not associated with the water uptake.

A maximum in conductivity is observed at 2 wt% of nHA content, which is followed by a decrease in conductivity values at higher inorganic filler concentration. Such an observation could be

Table 1

Membrane thickness, water uptake and crystallinity values for Nafion<sup>®</sup>/nHA based nanocomposites.

Sample	nHA loading weight (%)	Membrane thickness ( $\mu$ m)	Water uptake (%)	Crystallinity (%)
Recast Nafion <sup>®</sup>	0.0	60 $\pm$ 4	18 $\pm$ 5	33.5 $\pm$ 6
Nafion <sup>®</sup> /nHA-1.0%	1.0	63 $\pm$ 5	16 $\pm$ 3	31.6 $\pm$ 5
Nafion <sup>®</sup> /nHA-2.0%	2.0	66 $\pm$ 5	18 $\pm$ 5	32.8 $\pm$ 5
Nafion <sup>®</sup> /nHA-3.0%	3.0	55 $\pm$ 4	17 $\pm$ 6	34.1 $\pm$ 4
Nafion <sup>®</sup> /nHA-5.0%	5.0	61 $\pm$ 3	22 $\pm$ 4	35.7 $\pm$ 6
Nafion <sup>®</sup> /nHA-10.0%	10.0	60 $\pm$ 6	24 $\pm$ 3	47.2 $\pm$ 7
Nafion <sup>®</sup> 117	0.0	178 $\pm$ 9	32 $\pm$ 4	18.4 $\pm$ 9

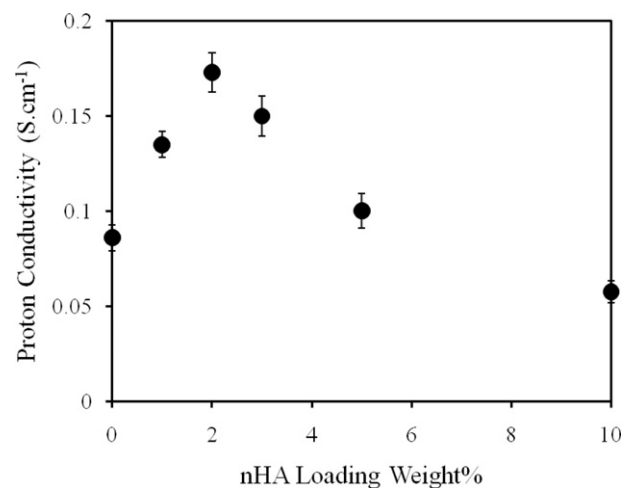
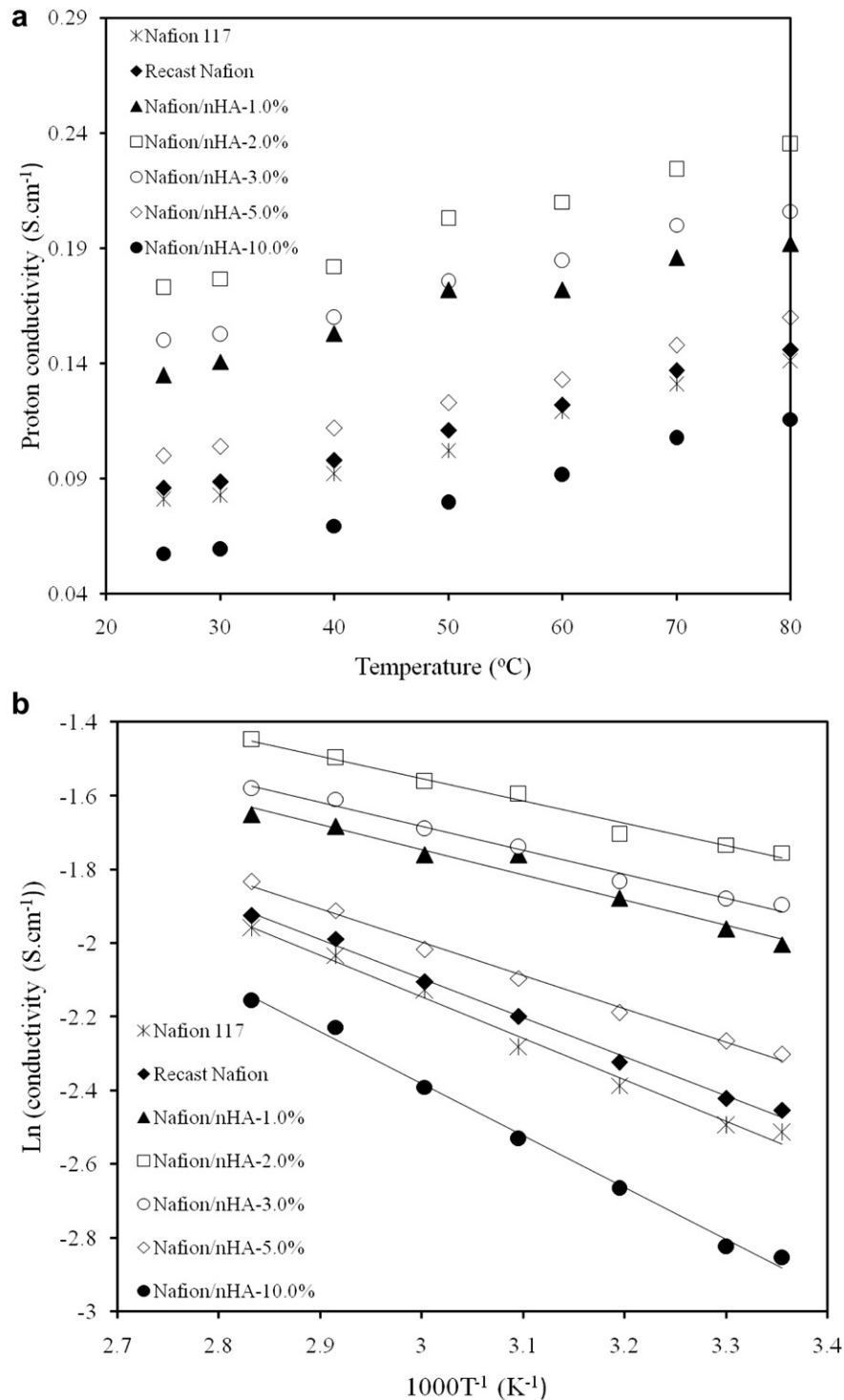


Fig. 7. The effect of nanoparticle's loading weight on the proton conductivity of the Nafion<sup>®</sup>/nHA nanocomposite membranes.

interpreted with the incorporation of the nHA nanoparticles into nanochannels of Nafion<sup>®</sup> ionomers.

Recently, Schmidt-Rohr and Chen have proposed a 3D model for the nanostructure of Nafion<sup>®</sup>, comprising an array of oriented ionomeric nanochannels embedded within a locally aligned polymeric matrix [3]. In accordance with this model, Nafion<sup>®</sup> comprises parallel cylindrical nanochannels with diameters of about 12 nm. Hence and according to SAXS results, it could be expected that the elliptical nHA particles owing to their size to be included into nanochannel of Nafion<sup>®</sup> and provide strong interaction with the ionic cylindrical walls. Accordingly, such a presumptive microstructure of the Nafion<sup>®</sup>/nHA nanocomposite polyelectrolyte is helpful to explain the enhancement of their ionic conductivity at lower contents of nHA. On the other hand, with increasing nHA loading weight to higher than 2 wt%, the conductivity decreases. In fact, at higher contents of nanofiller, nHA particles tend to agglomerate in the Nafion<sup>®</sup> matrices and consequently interfere with the formation well-organized conducting pathways. So, the highest conductivity value of 0.173 S  $cm^{-1}$  at 25 °C among Nafion<sup>®</sup>/nHA nanocomposite membranes is provided at the optimum content of 2.0 wt% nHA. These results are in accordance with the crystallinity values of Nafion<sup>®</sup>.

To get an insight into the temperature dependency of proton conduction across the nanocomposite membranes, proton conductivity measurements were also performed at different temperatures at constant humidity (95% RH). As seen in Fig. 8-a, the proton conductivity is improving remarkably as the temperature increases. The conductivity–temperature relationships of the nanocomposite membranes in the temperature range of 25–80 °C were investigated based on the Arrhenius equation ( $\sigma = \sigma_0 \exp(-E_a/RT)$ ), where  $\sigma$ ,  $\sigma_0$ ,  $E_a$ ,  $R$  and  $T$  are the proton conductivity (in S  $cm^{-1}$ ), pre-exponential parameter, activation energy of proton migration through the sample (in kJ  $mol^{-1}$ ), universal gas constant (8.31 J  $mol^{-1}$  K $^{-1}$ ) and the absolute temperature (in K), respectively. From the Arrhenius plots of conductivity  $C$  depicted in Fig. 8-b, it is found that all the membranes exhibit positive temperature–conductivity dependency, which implies a thermally activated process for proton conduction. Moreover, the activation energy of proton conduction process was calculated based on the Arrhenius equation. The activation energy of nanohybrid membranes, recast Nafion<sup>®</sup> and Nafion<sup>®</sup> 117 is shown in Fig. 9. The lower proton conduction activation energy of recast Nafion<sup>®</sup> compared to that of Nafion<sup>®</sup> 117 originates from the differences in membrane formation via melting



**Fig. 8.** a) Proton conductivity of the Nafion<sup>®</sup>/nHA membranes as a function of temperature at various loading weights of nanofiller. b) Arrhenius plots of proton conductivity for Nafion<sup>®</sup> based nanocomposite membranes.

and solution casting methods. As seen in Fig. 9, the incorporation of nHA up to 5.0 wt% into Nafion<sup>®</sup> matrices results in the lower activation energy of the resultant nanocomposite membranes in comparison with pristine recast Nafion<sup>®</sup> membrane. The activation energy of Nafion<sup>®</sup>/nHA membrane at 2.0 wt% content of nanofiller was obtained to be about 5.05 kJ mol<sup>-1</sup> compared to 8.96 kJ mol<sup>-1</sup> for Nafion<sup>®</sup> 117, which implies that the ionic nanochannels in the Nafion<sup>®</sup> microstructure might have been regulated in the presence of nHA particles.

Since methanol and water molecules have similar properties, these molecules transfer to the cathode through the electro-osmotic drag. Methanol causes mixed potential at the cathode and interferes with the oxygen reduction reaction and consequently the performance of the fuel cell is remarkably decreased [13,20]. Therefore, a methanol barrier property is considered as another major issue of the solid electrolytes for DMFC application. The results of methanol permeability measurements in Fig. 10 clearly demonstrate the methanol crossover of the Nafion<sup>®</sup> matrices has

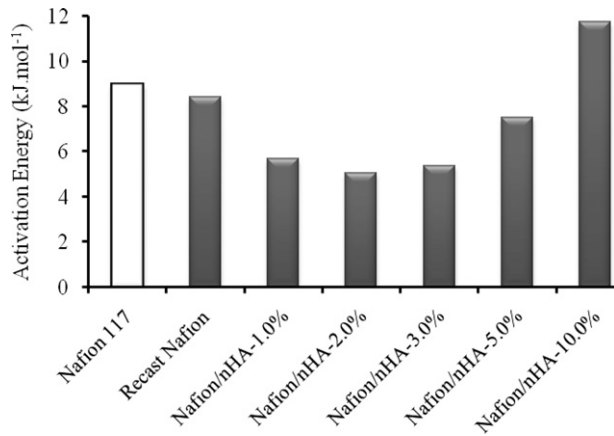


Fig. 9. The activation energies of proton conduction process across the nanocomposite membranes at different nHA content compared to that of recast Nafion<sup>®</sup> and Nafion<sup>®</sup> 117 membranes.

been decreased significantly due to the addition of nHA. In fact, nHA nanoparticles provide longer diffusive pathway against diffusing methanol molecules [14] and also decrease the free volume by occupying amorphous domains, which were originally possessed by water and methanol molecules in Nafion<sup>®</sup> microstructure [37]. Higher loading weights of inorganic filler result in blocking and termination of pathways' formation for penetrant molecules such as methanol.

As discussed above and confirmed by SAXS characterization, the major difference between the nano-sized and micro-sized HA particles is the ability of HA nanoparticles to incorporate into the Nafion<sup>®</sup> nanochannels, which has resulted in the considerably improved transport properties. Such effects are not possible for the corresponding micro-sized particles.

Proton conductivity and methanol permeability are the two transport properties of proton exchange membranes, which determine the performance of the corresponding DMFCs. As both transport properties of the Nafion<sup>®</sup> were affected with the inclusion

of an inorganic component, membrane selectivity parameter (ratio of proton conductivity to methanol permeability) was used to determine the optimum composition of the inorganic filler. The higher selectivity value leads to a better membrane performance in DMFC application. The membrane selectivity of the nanocomposite membranes at various nHA loadings was calculated and is shown in Fig. 10. The maximum selectivity was obtained at 2.0 wt% of nHA loading. Indeed, the nanohybrid membrane at this composition not only provides the highest proton conductivity ( $1.73 \text{ S cm}^{-1}$ ), but also fulfills a low methanol permeability ( $1.62 \times 10^{-6} \text{ cm}^2 \text{ s}^{-1}$ ). In other words, modification of Nafion<sup>®</sup> microstructure with nanocrystalline hydroxyapatite might have led to better nanochannel formation and improvement in membrane selectivity. It has been found that methanol crossover through PEMs at DMFC operational conditions causes catalyst poisoning at cathode, low efficiency of fuel cell due to methanol losses, hindrance of oxygen reduction at cathode and consequently a drastic decrease of open circuit voltage (OCV). Therefore, methanol crossover current density,  $I_C$ , was calculated according to  $I_C = I_{C,OC} (1 - I/I_L)$ , where  $I_{C,OC}$ ,  $I$  and  $I_L$  are methanol crossover current density at open circuit, operating current density and anode mass transport limiting current density, all in  $\text{mA cm}^{-2}$  [49]. The DMFC methanol crossover of Nafion<sup>®</sup>/nHA-2.0% was measured at 1 M (Fig. 11-a) and 5 M (Fig. 11-b) methanol concentrations and compared with recast Nafion<sup>®</sup> and Nafion<sup>®</sup> 117. As shown in Fig. 11, methanol crossover current density at open circuit condition for recast Nafion<sup>®</sup>, Nafion<sup>®</sup> 117 and Nafion<sup>®</sup>/nHA-2 wt% membranes was measured to be 184, 156 and 151  $\text{mA cm}^{-2}$  at 1 M methanol concentration, and 630, 518 and 474  $\text{mA cm}^{-2}$  at 5 M methanol concentration, respectively. Moreover, limiting current density for recast Nafion<sup>®</sup>, Nafion<sup>®</sup> 117 and Nafion<sup>®</sup>/nHA-2 wt% at anode side was obtained as 306, 363 and 376  $\text{mA cm}^{-2}$  at 1 M methanol concentration, and 187, 447 and 525  $\text{mA cm}^{-2}$  at 5 M methanol concentration, respectively. Therefore, methanol crossover experiments revealed that introducing 2 wt% of nHA into Nafion<sup>®</sup> matrix has appreciably reduced its methanol crossover, especially at elevated methanol concentration.

Fuel efficiency of cells,  $\eta_{\text{Fuel}}$ , was also calculated using methanol crossover results via following equation:  $\eta_{\text{Fuel}} = I/(I + I_C)$  [49].

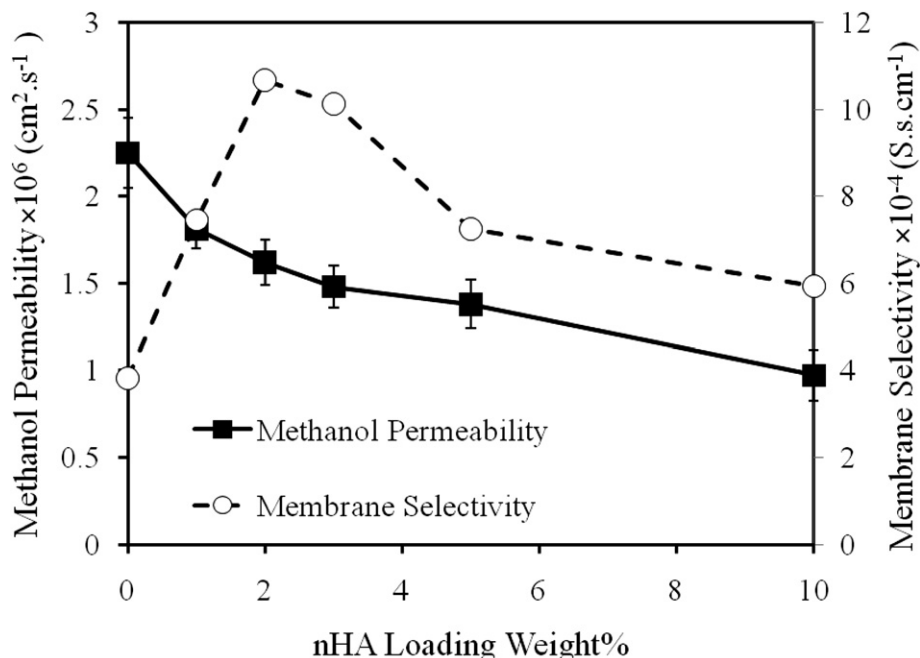
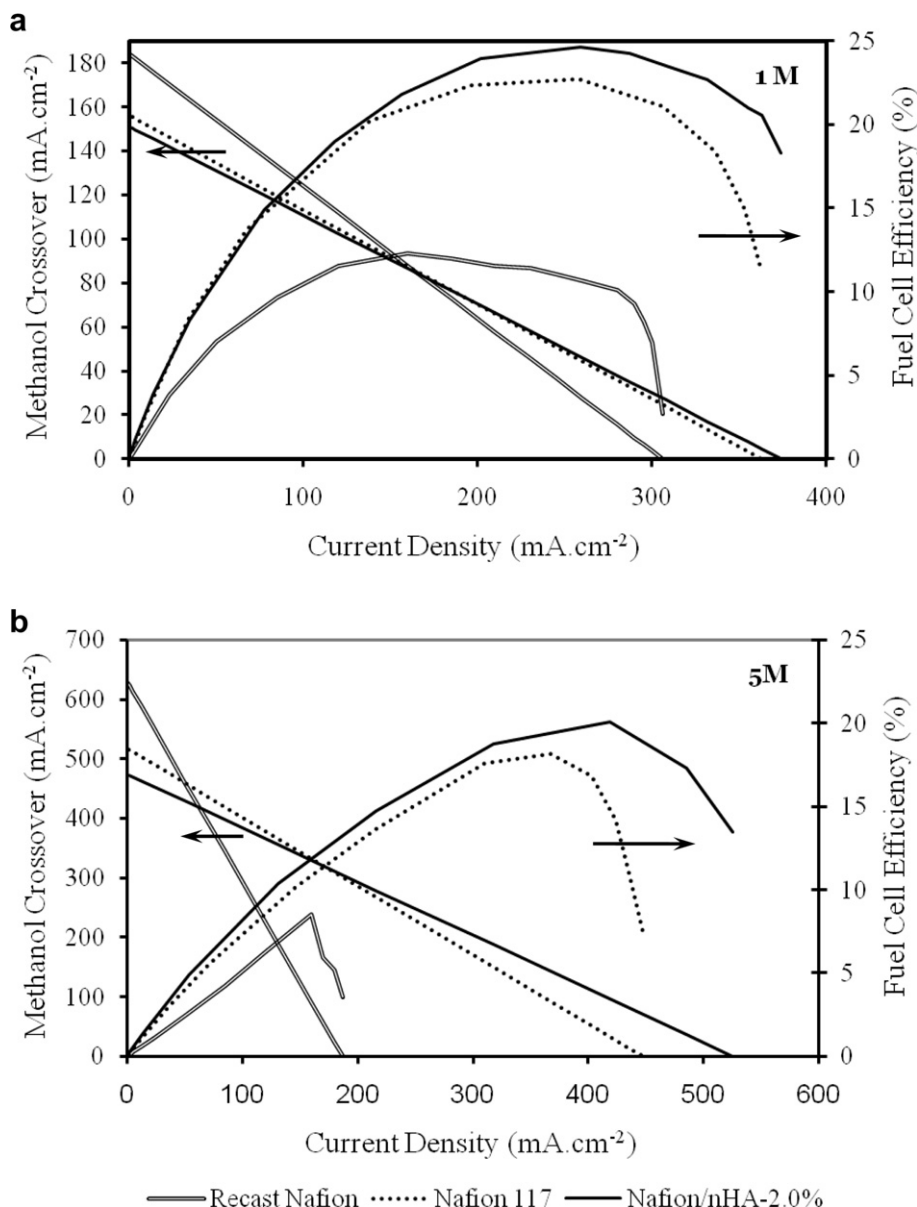


Fig. 10. Effect of nHA loading on methanol permeation and membrane selectivity of Nafion<sup>®</sup> based nanocomposite membranes.



**Fig. 11.** A comparison between methanol crossover current and fuel cell efficiency of recast Nafion<sup>®</sup>, Nafion<sup>®</sup> 117 and Nafion<sup>®</sup>/nHA-2 wt% membranes at two methanol concentrations of 1 M (a) and 5 M (b).

Thermodynamic efficiency,  $\eta_{\text{Therm}}$ , is defined as the ratio of Gibbs free energy change per mole of methanol,  $\Delta g$ , to enthalpy change per mole of methanol,  $\Delta h$ . The voltage efficiency of fuel cell,  $\eta_{\text{Volt}}$ , is determined as ratio of the real operating voltage,  $V_{\text{Cell}}$ , to theoretical maximum voltage,  $V_{\text{Th}}$ , of fuel cell. Accordingly, real efficiency of fuel cell,  $\eta_{\text{Real}}$ , is obtained by the combination of fuel efficiency, thermodynamic efficiency, and voltage efficiency [49]. In this work, the methanol crossover current density and real efficiency of the DMFC were performed and found to depend on methanol concentration and membrane types. The results of real efficiency assessment of fuel cell at 1 M and 5 M methanol concentrations for Nafion<sup>®</sup> 117, recast Nafion<sup>®</sup> and Nafion<sup>®</sup>/nHA-2 wt% have been displayed in Fig. 11. As shown, in the case of recast Nafion<sup>®</sup> and Nafion<sup>®</sup> 117, the maximum efficiency is decreased from 12.2% to 8.5% and from 22.7% to 18.2% as methanol concentration is increased to 5 M. However, lower real fuel cell efficiency reduction from 24.7% to 20.1% is observed with increasing methanol

concentration from 1 M to 5 M, which is associated with the beneficial role of nHA in reduction of methanol crossover through fabricated nanocomposite membrane.

The single cell DMFC performance tests of the fabricated membranes were performed at two methanol concentrations of 1 and 5 M at 70 °C. Fig. 12 shows the polarization curves of Nafion<sup>®</sup>/nHA membranes (with 2.0 wt% nHA loading) compared to Nafion<sup>®</sup> 117 and recast Nafion<sup>®</sup>.

At the potential of 0.5 V and 1 M methanol feed, the current densities for the Nafion<sup>®</sup>/nHA membranes and Nafion<sup>®</sup> 117 were measured as 77 and 68  $\text{mA}\cdot\text{cm}^{-2}$ , and at 5 M methanol concentration the current densities were obtained as 131 and 72  $\text{mA}\cdot\text{cm}^{-2}$ , respectively. In addition, the power density at the potential of 0.5 V for the nanocomposite membranes and Nafion<sup>®</sup> 117 was measured to be 77 and 34  $\text{mW}\cdot\text{cm}^{-2}$  (at 1 M fuel concentration) and 65 and 36  $\text{mW}\cdot\text{cm}^{-2}$  (at 0.5 V potential and 5 M methanol concentration), respectively. Accordingly, 2 wt% nHA filled Nafion<sup>®</sup>



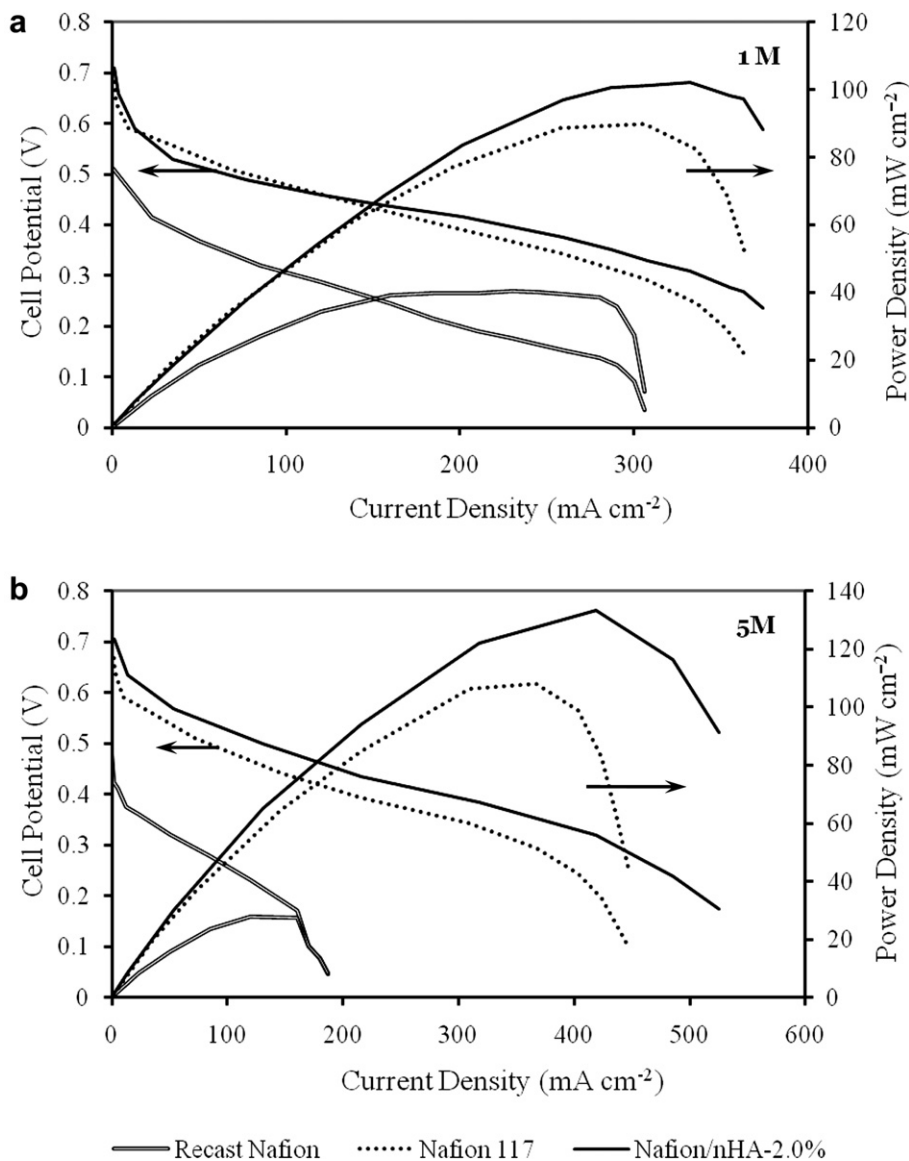


**Fig. 12.** Electrochemical performance of DMFC single cells consisted of Nafion<sup>®</sup>/nHA-2 wt% compared to recast Nafion<sup>®</sup> and Nafion<sup>®</sup> 117 as polyelectrolyte membrane. The performance tests were performed using two methanol concentrations of (a) 1 M and (b) 5 M to anode and oxygen flow to cathode at 70 °C.

membrane is able to supply over 80% more power output than commercial Nafion<sup>®</sup> 117 membrane at a typical operating voltage of 0.5 V and at elevated methanol concentration of 5 M.

The open circuit voltage (OCV) of the single cell for the nanocomposite, Nafion<sup>®</sup> 117 and recast Nafion<sup>®</sup> at 1 M methanol was measured as 0.71, 0.68 and 0.571, and 0.70, 0.66 and 0.571 at 5 M methanol feed, respectively. The OCV for the composite membrane was higher than that of Nafion<sup>®</sup> 117 and recast Nafion<sup>®</sup> at both methanol concentrations. OCV is closely related to the methanol crossover and increases by decreasing methanol crossover. The higher OCV clearly indicates that the Nafion<sup>®</sup>/nHA membrane significantly decreases the rate of methanol crossover, which is in accordance with the already obtained methanol permeability values. Indeed, crossover of methanol hinders oxygen reduction at cathode and consequently leads to a decrease in the OCV of the DMFC single cell comprising Nafion<sup>®</sup> 117 as polyelectrolyte membrane. It has been found that methanol permeation across PEM in DMFCs not only causes catalyst poisoning at the cathode, but also reduces fuel efficiency due to methanol loss. In addition,

methanol crossover hinders oxygen reduction at the cathode and consequently leads to a drastic decrease in open circuit voltage (OCV). So, thick Nafion<sup>®</sup> membranes (Nafion<sup>®</sup> 117 with 178  $\mu\text{m}$  thickness) are usually utilized to alleviate the adverse effects of methanol crossover. Accordingly, it seems that the recast pristine Nafion<sup>®</sup> membranes with same thickness of nanocomposite sample results in remarkably lower power density.

As seen in Fig. 12, nanocomposite membrane is able to provide maximum power density of 102  $\text{mW cm}^{-2}$  and 133  $\text{mW cm}^{-2}$  at 1 M and 5 M methanol concentrations respectively compared to 90  $\text{mW cm}^{-2}$  and 108  $\text{mW cm}^{-2}$  for Nafion<sup>®</sup> 117 and 40  $\text{mW cm}^{-2}$  and 28  $\text{mW cm}^{-2}$  for recast Nafion<sup>®</sup> at the same methanol concentrations.

Generally, from the DMFC performance results, it is found that the presence of nanocrystalline hydroxyapatite has improved the electrochemical performance of the Nafion<sup>®</sup> ionomer at both fuel concentrations, which is not usually observed in the case of layered inorganic nanofillers at the condition of low methanol concentration feed [14–17]. Although two-dimensional structure of layered silicates such as montmorillonite is favorable to reduce methanol

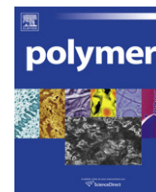
permeability, such impermeable nanosheets also obstruct diffusion pathways of protons across the nanocomposite membranes [12–17]. In spite of layered silicates, the conductivity results in Fig. 7 revealed that hydroxyapatite nanocrystalline particles at the optimum content of 2 wt% improve the conductivity properties of the Nafion<sup>®</sup> matrix. Accordingly, the superior electrochemical performance of the Nafion<sup>®</sup>/nHA membranes compared to Nafion<sup>®</sup> 117 at both tested methanol concentrations might have originated from the conductive nature of the nHA particles.

#### 4. Conclusion

In this work nanocrystalline hydroxyapatite (nHA) was synthesized and incorporated in Nafion<sup>®</sup> matrices. The resulting nanocomposite membranes were investigated for thermal stability, transport properties and DMFC performance as a function of nHA loading. The results indicate that the inclusion of nHA at optimum content not only improves proton conductivity as well as thermal stability of the Nafion<sup>®</sup> matrix, but also reduces methanol permeation and crossover rate. Moreover, performance test of the DMFC single cell comprising Nafion<sup>®</sup>/nHA as polyelectrolyte exhibited higher overall cell efficiency and performance compared to Nafion<sup>®</sup> 117 at both low and high methanol concentrations.

#### References

- [1] Kerres JA. *J Membr Sci* 2001;185(1):3–27.
- [2] Haile SM. *Acta Mater* 2003;51(19):5981–6000.
- [3] Schmidt-Rohr K, Chen Q. *Nat Mater* 2008;7(1):75–83.
- [4] Kreuer KD. *J Membr Sci* 2001;185(1):29–39.
- [5] Mauritz KA, Moore RB. *Chem Rev* 2004;104(10):4535–86.
- [6] Neburchilov V, Martin J, Wang H, Zhang J. *J Power Sources* 2007;169(2):221–38.
- [7] Rikukawa M, Sanui K. *Prog Polym Sci* 2000;25(10):1463–502.
- [8] Wang L, Yi BL, Zhang HM, Liu YH, Xing DM, Shao ZG, et al. *J Power Sources* 2007;164(1):80–5.
- [9] Argun AA, Ashcraft JN, Hammond PT. *Adv Mater* 2008;20(8):1539–43.
- [10] Hasani-Sadrabadi MM, Dashtimoghdam E, Majedi FS, Kabiri K, Mokarram N, Solati-Hashjin M, et al. *Chem Commun* 2010;46:6500–2.
- [11] Hudiono Y, Choi S, Shu S, Koros WJ, Tsapatsis M, Nair S. *Microporous Mesoporous Mater* 2009;118(1–3):427–34.
- [12] Hasani-Sadrabadi MM, Dashtimoghdam E, Majedi FS, Kabiri K. *J Power Sources* 2009;190(2):318–21.
- [13] Hasani-Sadrabadi MM, Emami SH, Ghaffarian R, Moaddel H. *Energy Fuels* 2008;22(4):2539–42.
- [14] Hasani-Sadrabadi MM, Ghaffarian SR, Mokarram-Dorri N, Dashtimoghdam E, Majedi FS. *Solid State Ionics* 2009;180(32–35):1497–504.
- [15] Hasani-Sadrabadi MM, Dashtimoghdam E, Ghaffarian SR, Sadrabadi MHH, Heidari M, Moaddel H. *Renewable Energy* 2010;35(1):226–31.
- [16] Hasani-Sadrabadi MM, Emami SH, Moaddel H. *J Power Sources* 2008;183(2):551–6.
- [17] Hasani-Sadrabadi MM, Dashtimoghdam E, Sarikhani K, Majedi FS, Khanbabaie G. *J Power Sources* 2010;195(9):2450–6.
- [18] Miyake N, Wainright JS, Savinell RF. *J Electrochem Soc* 2001;148(8):898–904.
- [19] Satterfield MB, Majsztzik PW, Ota H, Benziger JB, Bocarsly AB. *J Polym Sci B Polym Phys* 2006;44(16):2327–45.
- [20] Sacca A, Gatto I, Carbone A, Pedicini R, Passalacqua E. *J Power Sources* 2006;163(1):47–51.
- [21] Hasani-Sadrabadi MM, Dashtimoghdam E, Ghaffarian R. *ECS Trans* 2009;17:269–76.
- [22] Bonnet B, Jones DJ, Roziere J, Tchicaya L, Alberti G, Casciola M, et al. *J New Mater Electrochem Syst* 2000;3(2):87–92.
- [23] Byun SC, Jeong YJ, Par JW, Kim SD, Ha HY, Kim WJ. *Solid State Ionics* 2006;177(37–38):3233–43.
- [24] Yang C, Srinivasan S, Bocarsly AB, Tulyani S, Benziger JB. *J Membr Sci* 2004;237(1–2):145–61.
- [25] Hill ML, Kim YS, Einsla BR, McGrath JE. *J Membr Sci* 2006;283(1–2):102–8.
- [26] Bebin P, Caravanier M, Galiano H. *J Membr Sci* 2006;278(1–2):35–42.
- [27] Kannan R, Kakade BA, Pillai VK. *Angew Chem Int Ed* 2008;47(14):2653–6.
- [28] Thomassin JM, Kollar J, Caldarella G, Germain A, Jerome R, Detrembleur C. *J Membr Sci* 2007;303(1–2):252–7.
- [29] Maiti GC, Freund F. *J Chem Soc Dalton Trans* 1981;(4):949–55.
- [30] Yamashita K, Owada H, Nakagawa H, Umegaki T, Kanazawa T. *J Am Ceram Soc* 1986;69(8):590–4.
- [31] Yamashita K, Owada H, Umegaki T, Kanazawa T. *Solid State Ionics* 1990;40(1):918–21.
- [32] Azami M, Moztarzadeh F, Tahriri M. *J Porous Mater* 2010;17(3):313–20.
- [33] Poursamar SA, Rabiee M, Samadikuchaksaraei A, Tahriri M, Karimi M, Azami M. *J Ceram Process Res* 2009;10(5):679–82.
- [34] Park YS, Hatae T, Itoh H, Jang MY, Yamazaki Y. *Electrochim Acta* 2004;50(2–3):595–9.
- [35] Park YS, Yamazaki Y. *Solid State Ionics* 2005;176(11–12):1079–89.
- [36] Park YS, Yamazaki Y. *J Membr Sci* 2005;26(1–2):58–66.
- [37] Park YS, Yamazaki Y. *Eur Polym J* 2006;42(2):375–87.
- [38] Jordana J, Jacob KI, Tannenbaum R, Sharaab MA, Jasiuk I. *Mater Sci Eng A* 2005;393(1–2):1–11.
- [39] Ciprari D, Jacob K, Tannenbaum R. *Macromolecules* 2006;39(19):6565–73.
- [40] Bronstein LM, Karlinsey RL, Stein B, Zwanziger JW. *Solid State Ionics* 2005;176(5–6):559–70.
- [41] Croce F, Appetecchi GB, Persi L, Scrosati B. *Nature* 1998;394(6692):456–8.
- [42] Krawiec W, Scanlon LGJ, Fellner JP, Vaia RA, Vasudevan S, Giannelis EP. *J Power Sources* 1995;54(2):310–5.
- [43] Dashtimoghdam E, Hasani-Sadrabadi MM, Moaddel H. *Polym Adv Technol* 2010;21:726–34.
- [44] Hasani-Sadrabadi MM, Mokarram N, Ghaffarian R, Dashtimoghdam E, Sarikhani K, Majedi FS. *J Appl Polym Sci* 2010;117:1227–33.
- [45] Burgaz E, Lian H, Alonso RH, Estevez L, Kelarakis A, Giannelis EP. *Polymer* 2009;50(11):2384–92.
- [46] Laghzizil A, El Herch N, Bouhaouss A, Lorente G, Macquete J. *J Solid State Chem* 2001;156(1):57–60.
- [47] Bouhaouss A, Laghzizil A, Bensaoud A, Ferhat M, Lorent G, Livage J. *Int J Inorg Mater* 2001;3(7):743–7.
- [48] Tanaka Y, Nakamura M, Nagai A, Toyama T, Yamashita K. *Mater Sci Eng B* 2009;161(1–3):115–9.
- [49] Hasani-Sadrabadi MM, Dashtimoghdam E, Majedi FS, Kabiri K, Solati-Hashjin M, Moaddel H. *J Membr Sci* 2010;365(1–2):286–93.



# Unique morphology of dispersed clay particles in a polymer nanocomposite

Thomas Malwela, Suprakas Sinha Ray\*

National Centre for Nano-Structured Materials, Council for Scientific and Industrial Research, Pretoria 0001, South Africa

## ARTICLE INFO

### Article history:

Received 24 October 2010

Received in revised form

11 January 2011

Accepted 13 January 2011

Available online 21 January 2011

### Keywords:

Polymer nanocomposite

Morphology of dispersed clay particles

Focused-ion beam

## ABSTRACT

This communication reports a unique morphology of dispersed clay particles in a polymer nanocomposite. A nanocomposite of poly[(butylene succinate)-co-adipate] (PBSA) with 3 wt% of organically modified montmorillonite was prepared by melt-blending in a batch mixer. The focused-ion beam cross-sectioning at 36° to the sample surface, followed by delineation etching with water revealed a unique dispersed morphology of the clay particles in PBSA nanocomposite. The scanning electron microscopy image showed a unique structure, where the vertically embedded stacked silicate layers fall down to the PBSA matrix, forming a corn-flake like structure. This unique structured was called as “nano-flake”.

© 2011 Elsevier Ltd. All rights reserved.

## 1. Introduction

Our ongoing research efforts have shown that the mechanical and material properties of poly[(butylene succinate)-co-adipate] (PBSA) increased concurrently upon nanocomposite (PBSACN) formation with a suitable surface modified montmorillonite (OMMT) [1,2]. For example, the flexural storage modulus of PBSACN became ~63% higher than that of neat PBSA. The elongation at break of neat PBSA increased 66% upon nanocomposite formation with 3 wt% OMMT. The oxygen permeability of PBSACN film decreases almost by one-third as compared with the neat PBSA film [3].

The structural analysis by focused-ion beam (FIB) tomography has shown that the clay particles were completely embedded within PBSA matrix and forming an interconnected network like structure [3]. Such an interconnected network is responsible for the effective transfer of load and improved mechanical properties of PBSACN containing 3 wt% OMMT. Tomography results have also supported the significantly improved oxygen-barrier property of PBSACN by creating a long “tortuous path” that slowing down the progress of gas molecules through the PBSA matrix [3].

Recently, small-angle X-ray scattering (SAXS) studies in association with the transmission electron microscopy (TEM) analyses have shown that the enhanced tenacity in the case of the PBSACN is due to the orientation of the dispersed clay layers in the direction of the applied tensile strain [4,5]. Such an orientation allows a better

energy-dissipation mechanism which in turn is responsible for the concurrent improvement in tensile properties.

This communication reports a unique morphology of dispersed clay particles in 3 wt% OMMT containing PBSA nanocomposite using FIB surface delineation etching technique. Previously, Usuki et al. [6] have used oxygen plasma treatment to etch the nylon 6 surface and reported a novel structure of highly delaminated silicate layers. This is the first report where water from FIB gas injection system has been used to etch the surface and imaged a unique morphology using scanning electron microscopy (SEM).

## 2. Experimental part

PBSA is a synthetic aliphatic polyester and is generally synthesized by the polycondensation of butane-1,4-diol in the presence of succinic and adipic acids with relatively low production cost and satisfactory mechanical properties equivalent to that of polyolefins [7–9]. The PBSA used in this study is a commercial product from Showa Highpolymer (Japan), with the designation BIONOLLE #3001. Organoclay used in this study was Cloisite® 30B (C30B). Detailed information about PBSA and C30B can be found in our previous publications [4]. The PBSACN containing 3 wt% of C30B was prepared in a PolyLab Thermohaake-batch mixer at 135 °C (set temperature) and a rotor speed of 60 rpm for 8 min. The dried PBSACN strands were then compression moulded at 135 °C for 10 min to prepare a PBSACN film of ~100 μm thick and ~200 mm wide, using Craver Laboratory compression moulder.

The dispersion characteristic of the clay particles in PBSA matrix was investigated by means of a high-resolution TEM (JEOL

\* Corresponding author. Fax: +27 12 841 2229.

E-mail address: [rsuprakas@csir.co.za](mailto:rsuprakas@csir.co.za) (S. Sinha Ray).

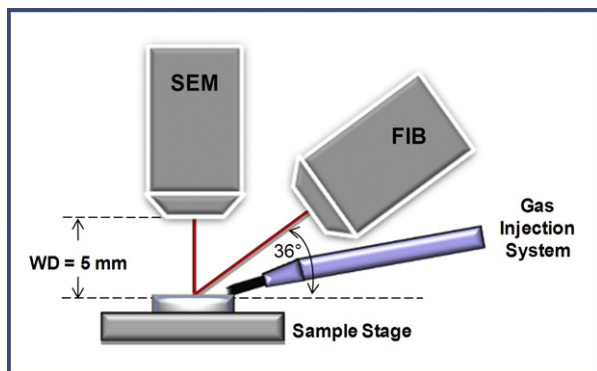


**Fig. 1.** The schematic view of sample stage positioned at  $0^\circ$  tilt and FIB is at  $36^\circ$  with respect to the sample surface. The schematic also show the gas injection system used for water etching.

JEM2100), operated at an accelerating voltage of 100 kV. The ultrathin sections with a thickness of  $\sim 100$  nm were microtomed at  $-80^\circ\text{C}$  using a Reichert Ultracut cryo-ultramicrotome without staining.

To investigate the dispersion of silicate layers in PBSA matrix, the middle section of the compression-moulded film was used for FIB Study. The Zeiss FIB-SEM cross-beam workstation, NVision 40 was used for cross-sectioning. Cross-section milling was conducted using Gallium ion beam which was at  $36^\circ$  to the sample surface, see Fig. 1. To avoid damage that may be caused by the beam, the sample was sputter coated using PtPd alloy for 60 s at 40 mA. Cross-sectioning at  $36^\circ$  to the sample surface using an accelerating voltage of 30 kV was carried out with following successive steps: (i) Coarse milling at 13 nA which was for rough milling, (ii) medium milling at

1.5 nA was used polishing the cross-sectioned area, and (iii) fine milling at 150 pA and 80 pA were employed to get a highly polished cross-sectioned area. SEM imaging was done on the cross-sectioned area. Finally, delineation etching on the sectioned area was performed using water for 240 s and 150 pA current. The water molecule assisted etching process is presented schematically in Fig. 2.

### 3. Results and discussion

In the case of clay-containing polymer nanocomposite, the TEM is one of the most commonly used techniques to determine the dispersed structure of the clay particles. Fig. 3 represents TEM images of PBSACN at two different magnifications, in which dark lines correspond to the stacked and intercalated silicate layers. TEM images show that most of the silicate layers are intercalated and randomly dispersed in the PBSA matrix, and also most of them are overlapping each other, which increase the stacking of the silicate platelets. However, the information along the thickness direction of the sample is an accumulated one which makes it very difficult to conclude on the exact degree of dispersion of silicate layers in the polymer matrix. Such a drawback is due to the fact that TEM projects a three-dimensional (3D) information onto a two-dimensional (2D) plane.

To view the real distribution of dispersed silicate platelets in nanocomposite, the 2D cross-sectioning at  $36^\circ$  to the sample surface by FIB, followed by delineation etching on the cross-sectioned area using water and SEM imaging were conducted. Parts (a)–(c) of Fig. 4, respectively, represent the SEM images of PBSACN sample surface, cross-sectioned, and polished cross-sectioned surface at two different magnifications. From the elemental analysis using energy-dispersive X-ray spectroscopy analysis, Si, Al, Mg, and oxygen were mainly detected and from the elemental compositional analysis, the

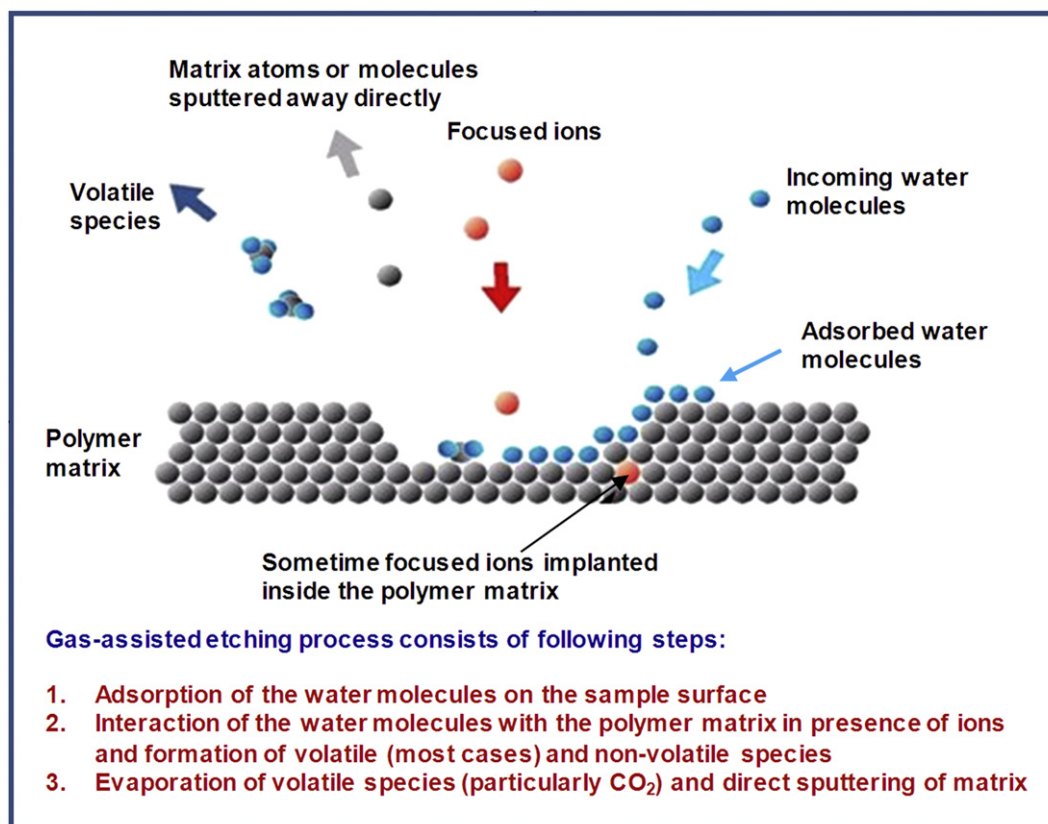


**Fig. 2.** Schematic view of water assisted delineation etching process in focused-ion beam (partially based on information available in wikipedia.org about FIB etching).



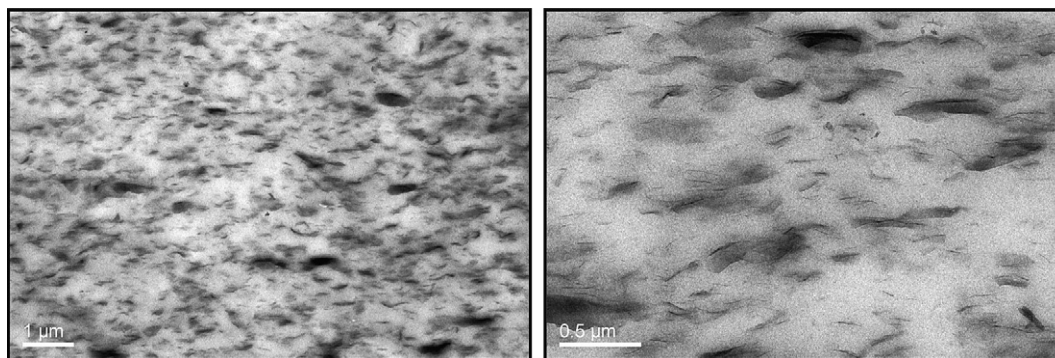


Fig. 3. Transmission electron microscopy images of PBSACN at two different magnifications, in which dark lines correspond to the stacked and intercalated silicate layers.

white particles were found to be MMT used for the preparation of PBSACN. It is clear from the SEM images (Fig. 4c and c') that most of the stacked and intercalated silicate layers embedded vertical to the sectioned surface. However, some faces of stacked silicate layers can be seen. This observation is quite consistent with the FIB-tomography result as recently reported by us [3].

Now to expose the stacked and intercalated silicate layers, the delineation etching process was conducted using water for 240 s at 150 pA current. The SEM images of delineation etched surfaces are reported in Fig. 5. It can be seen from SEM images that vertically embedded silicate layers fall down to the PBSA matrix. Such an observation is natural because during etching process all PBSA matrices around each stacked silicate layers were removed and there was no support for the silicate layers to stand vertically. These

stacked and intercalated silicate layers forming a corn-flake like structure on the matrix surface and such a unique morphology of dispersed clay particles was named as “nano-flake”.

To have a rough idea about the clay particles size distribution in PBSA matrix, Image J software was used to analyze the SEM image of etched surface (Fig. 5(c)). In Fig. 5(d), the size of the stacked silicate layers (in nm) is plotted against the number of the stacked silicate layers. It is clear from the figure that nanocomposite consists of a maximum number of dispersed silicate layers with a size of about 58 nm. This result is not consistent with our previous calculation based on scanning transmission electron microscopy images [4]. This may be due to the fact that previously we have considered only edges (or thickness cross-sections) of the dispersed silicate layers for calculation. However, here mostly faces (length

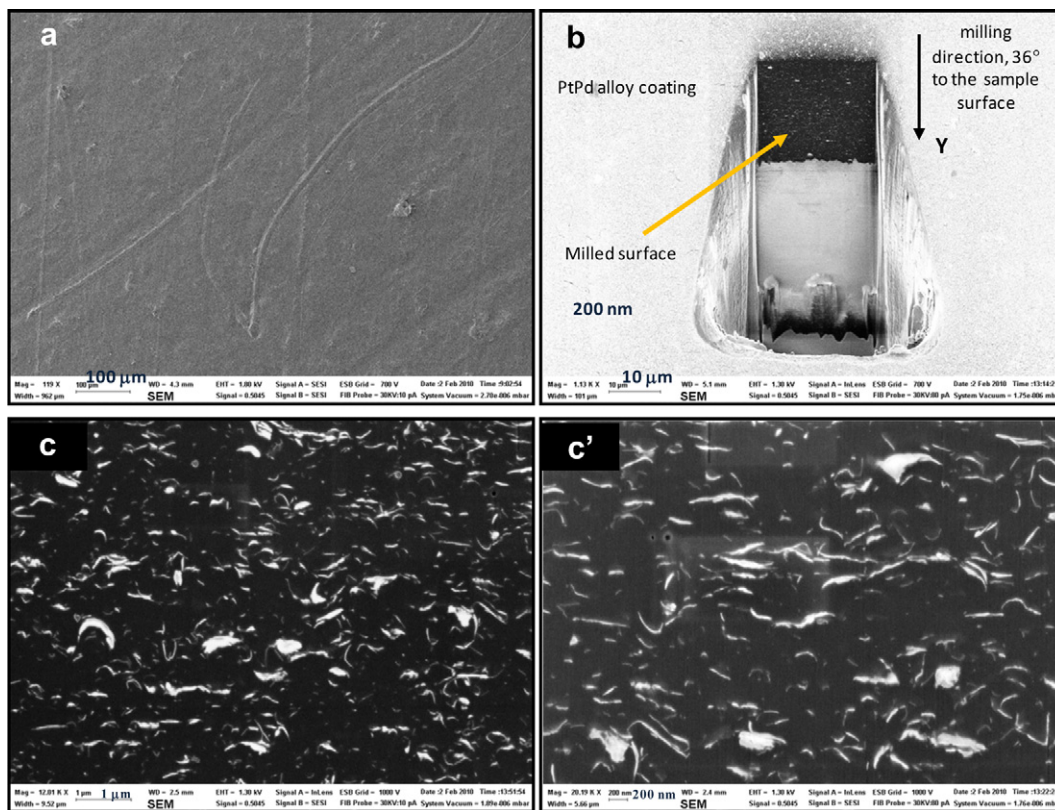
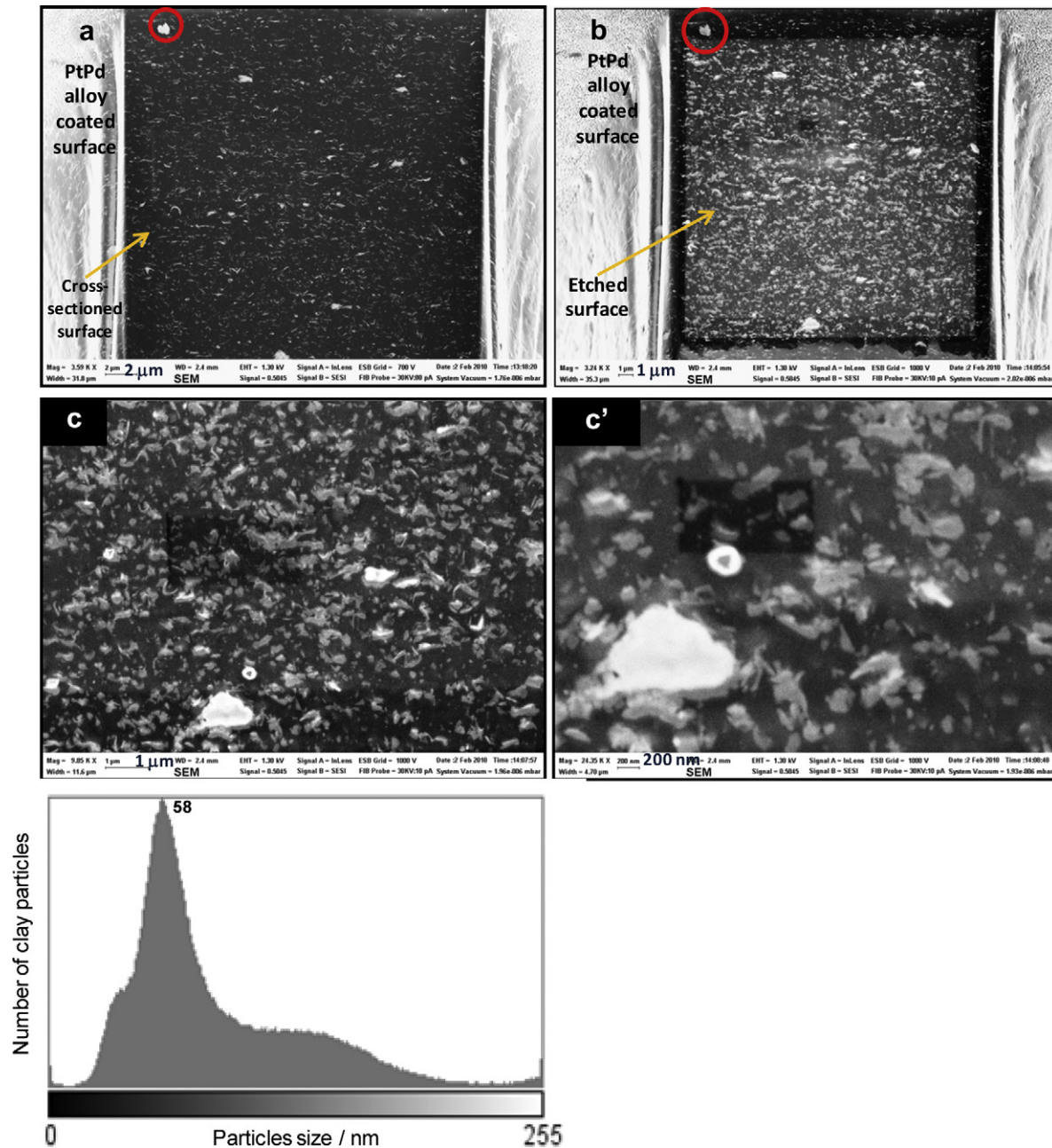


Fig. 4. (a) Scanning electron microscopy image of nanocomposite film surface without protective PtPd alloy coating, (b) scanning electron microscopy images of both PtPd alloy coated and milled surface (cross-sectioned at 36° to the sample surface) of the nanocomposite film, and (c and c') scanning electron microscopy images of polished surface at two different magnifications where white lines are clay particles.



**Fig. 5.** (a) SEM image of cross-sectioned ( $36^\circ$  to the sample surface) nanocomposite film where white lines are silicate layers, (b) SEM image of the same cross-sectioned surface after delineation etching using water, (c and c') SEM images of etched surface at two different magnifications, and (d) dispersed clay particles size distribution (calculated using (c)) histogram analyzed using Image J software. In (a) and (b) the red circle indicates the marked position, i.e. the same sample. (For interpretation of the references to colour in this figure legend, the reader is referred to the web version of this article).

and or width of platelets) of the dispersed silicate layers have taken to account for analysis.

#### 4. Conclusions

This study reports a different but completely new approach to observe the fate of silicate layers in a polymer nanocomposite by FIB delineation etching using water. This work also shows that FIB is a very powerful and versatile instrument in determining the real distribution of nano-fillers in a polymer nanocomposite. Our ongoing research is focusing on finding out the answer of a very challenging but very important question – is it possible to achieve a true exfoliation of silicate layers in a polymer matrix?

#### Acknowledgements

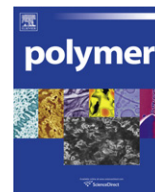
The authors would like to thank the CSIR executive and the DST, South Africa, for financial support. Authors would also like to thank Dr. H. Stegmann for experimental help.

#### References

- [1] Sinha Ray S, Bousmina M. Structure and properties of nanocomposites based on poly(butylene succinate-co-adipate) and organically modified montmorillonite. *Macromol Mater Eng* 2005;290:759–68.
- [2] Sinha Ray S, Bousmina M. Poly[(butylene succinate)-co-adipate]/montmorillonite nanocomposites: effect of organic modifier miscibility on structure, properties, and viscoelasticity. *Polymer* 2005;46:12430–9.

- [3] Sinha Ray S. A new possibility for microstructural investigation of a clay-based polymer nanocomposite by focused ion beam tomography. *Polymer* 2010;51:3966–70.
- [4] Bandyopadhyay J, Sinha Ray S. The quantitative analysis of nano-clay dispersion in polymer nanocomposites by small angle X-ray scattering combined with electron microscopy. *Polymer* 2010;41:1437–49.
- [5] Bandyopadhyay J, Sinha Ray S. Mechanism of enhanced tenacity in a polymer nanocomposite studied by small-angle X-ray scattering and electron microscopy. *Polymer* 2010;51:4860–6.
- [6] Usuki A, Hasegawa N, Kadoura H, Okamoto T. Three-dimensional observation of structure and morphology in nylon-6/clay nanocomposite. *Nano Letts* 2001;1:271–2.
- [7] Ishioka D. Biopolymers, polyesters III. Applications and commercial products, vol. 4. Weinheim: Wiley-VCH Verlag GmbH; 2002. p. 275.
- [8] Nikolic MS, Djonlagic J. Synthesis and characterization of biodegradable poly [(butylene succinate)-co-adipate]. *Polym Degrad Stab* 2001;74:263–70.
- [9] Fujimaki T. Processability and properties of aliphatic polyesters, 'BIONOLLE', synthesized by polycondensation reaction. *Polym Degrad Stab* 1998;59:209–14.





# Structural, chemical and electrochemical characterization of poly(3,4-Ethylenedioxythiophene) (PEDOT) prepared with various counter-ions and heat treatments

Zachary A. King<sup>a</sup>, Charles M. Shaw<sup>b</sup>, Sarah A. Spanninga<sup>b</sup>, David C. Martin<sup>a,b,c,d,\*</sup>

<sup>a</sup> Department of Biomedical Engineering, The University of Michigan, 2200 Bonisteel Blvd., Ann Arbor, MI 48109-2099, USA

<sup>b</sup> Macromolecular Science and Engineering Center, The University of Michigan, 2300 Hayward Ave., Ann Arbor, MI 48109-2136, USA

<sup>c</sup> Department of Materials Science and Engineering, The University of Michigan, 2300 Hayward Ave., Ann Arbor, MI 48109-2136, USA

<sup>d</sup> Department of Materials Science and Engineering, The University of Delaware, 201C DuPont Hall, Newark, DE 19716, USA

## ARTICLE INFO

### Article history:

Received 9 April 2010

Received in revised form

19 January 2011

Accepted 20 January 2011

Available online 28 January 2011

### Keywords:

Conducting polymers

PEDOT

XRD

## ABSTRACT

Electrochemical deposition of the conjugated polymer poly(3,4-ethylenedioxythiophene) (PEDOT) forms thin, conductive films that are especially suitable for charge transfer at the tissue–electrode interface of neural implants. For this study, the effects of counter-ion choice and annealing parameters on the electrical and structural properties of PEDOT were investigated. Films were polymerized with various organic and inorganic counter-ions. Studies of crystalline order were conducted via X-ray diffraction (XRD). Electrochemical impedance spectroscopy (EIS) and cyclic voltammetry (CV) were used to investigate the electrical properties of these films. X-ray photoelectron spectroscopy (XPS) was used to investigate surface chemistry of PEDOT films. The results of XRD experiments showed that films polymerized with certain small counter-ions have a regular structure with strong (100) edge-to-edge correlations of PEDOT chains at  $\sim 1.3$  nm. After annealing at 170 °C for 1 h, the XRD peaks attributed to PEDOT disappeared. PEDOT polymerized with LiClO<sub>4</sub> as a counter-ion showed improved impedance and charge storage capacity after annealing at 160 °C.

© 2011 Elsevier Ltd. All rights reserved.

## 1. Introduction

Poly(3,4-ethylenedioxythiophene) (PEDOT) is an electrically-conducting conjugated polymer that combines excellent conductivity [1] and demonstrated biocompatibility [2]. PEDOT is chemically stable in its oxidized form, is relatively insensitive to pH changes, and can form nearly transparent thin films [1]. These unique characteristics make PEDOT a desirable material in a variety of applications, including solar cells [3], organic light emitting devices [4], and biosensors [5]. Recently, PEDOT has been used as a bioactive coating for the electrode sites of chronic neural implants and other bio-stimulation devices [6].

The electrical characteristics of PEDOT coatings have important consequences for neural stimulation devices. Small electrode areas are desirable for neural stimulation because they provide more spatial selectivity. However, as electrode size decreases, impedance increases and hinders charge transfer for both neural recording and

stimulation [6]. Low-impedance electrodes that have been coated with PEDOT films can therefore be made smaller and can have more-acute neural specificity. In addition to low impedance, a PEDOT film delivers a large charge storage capacity (CSC) and a flat frequency dependence curve. Large CSC values indicate that PEDOT films can mediate the transfer of greater electrical charges between electrical and ionic charge carriers. Flat frequency dependence curves are important to ensure that films maintain low impedance at all relevant frequencies and to improve signal fidelity. The 300–1000 Hz range is especially important because bio-stimulation is most often performed with pulses in this frequency range [7].

Experiments have shown that annealed PEDOT films can have conductivities as much as three times higher than unheated films [8]. Annealing can also decrease surface roughness [9] and induce a phase transition characterized by the loss of long-range  $\pi$ -stacking in the PEDOT films [10]. All these experiments were performed on chemically polymerized PEDOT films. Less is known about the results of annealing electrochemically polymerized PEDOT films, which are more desirable for neural stimulation electrodes because deposition can be targeted directly to electrode sites.

\* Corresponding author. Department of Materials Science and Engineering, The University of Delaware, 201C DuPont Hall, Newark, DE 19716, USA. Tel.: +1 (302) 831 2062; fax: +1 (508) 256 8352.

E-mail address: [milty@udel.edu](mailto:milty@udel.edu) (D.C. Martin).



A number of counter-ions have been used in the electrochemical polymerization of PEDOT, most notably LiClO<sub>4</sub> and PSS [7,11]. Previous work has shown that variation of the counter-ion in PEDOT polymerization changes macroscopic properties such as morphology, color, and electrical impedance [7,11]. The macroscopic differences between PEDOT samples polymerized with different counter-ions can be attributed to differences in the microstructure of the PEDOT samples [12].

PEDOT films polymerized with poly(styrene sulfonate) (PSS) and lithium perchlorate (LiClO<sub>4</sub>) have also been used as ionic actuators that facilitate controlled drug delivery, and these counter-ions have different actuator responses. PEDOT/LiClO<sub>4</sub> films actuate by transporting mobile perchlorate counter-ions, while PEDOT/PSS films have an immobile counter-ion and actuate by transporting cations. These unique actuator responses can make either LiClO<sub>4</sub> or PSS a more desirable counter-ion for the delivery of drugs with different charges [13]. Other considerations—such as the high surface area provided by fibrillar PEDOT polymerized with PAA and LiClO<sub>4</sub>—may also influence counter-ion selection [14].

The selection of a counter-ion for PEDOT deposition is an important consideration, and this selection affects both the electrical properties and morphology of a film. Thus it is valuable to systematically explore how variation of counter-ion affects the microstructure and electrical performance of electrochemically polymerized PEDOT.

In this study, we present work detailing the influence of counter-ion selection and heat treatment steps on the structural and electrochemical properties of electrochemically polymerized films of PEDOT. X-ray diffraction (XRD) of electrochemically polymerized films of PEDOT reveals a strong edge-to-edge (100) correlation at ~1.3 nm in samples containing certain small counter-ions. X-ray photoelectron spectroscopy (XPS) shows that some sulfur oxidation takes place in the PEDOT films above 130 °C. Electrical characterization of PEDOT films polymerized on Pt/Ir ball electrodes indicates that films polymerized with large counter-ions demonstrate lower electrical impedance and higher charge storage capacity than those polymerized with small counter-ions. PEDOT films with large counter-ions show a decrease in charge storage capacity and an increase in impedance when annealed. However, annealing of films polymerized with small counter-ions disrupts the edge-to-edge packing, decreases the impedance, and—in some cases—increases charge storage capacity. Only PEDOT/LiClO<sub>4</sub> films benefit from simultaneous decreases in impedance and increases in charge storage capacity, making these films especially suitable for heat treatment. An even more dramatic improvement was manifested in the decreased saturation frequency at which PEDOT/LiClO<sub>4</sub> films approach their asymptotic, minimum impedances.

## 2. Experimental

### 2.1. Materials

The 3,4-ethylenedioxythiophene (EDOT) monomer was obtained from H. C. Stark, PSS was obtained from Acros Organics, and phosphate buffered solution (PBS) (10× concentration containing KH<sub>2</sub>PO<sub>4</sub>, NaCl, and Na<sub>2</sub>HPO<sub>4</sub>) was obtained from Fisher Scientific. PBS was diluted to a 1× concentration (0.15 M NaCl, 0.0057 M NaH<sub>2</sub>PO<sub>4</sub>, and 0.001 M KH<sub>2</sub>PO<sub>4</sub>). Sodium chloride (NaCl), LiClO<sub>4</sub>, sodium phosphate (NaH<sub>2</sub>PO<sub>4</sub>), heparin, bovine serum albumin (BSA), hyaluronic acid (HA), poly(*D*-lysine) (PDL), *para*-toluenesulfonic acid (PTS), poly(acrylic acid) (PAA) and methylene chloride (CH<sub>2</sub>Cl<sub>2</sub>) were all obtained from Sigma–Aldrich. L-glutamic acid was obtained from M-P Biomedicals, tetrabutylammonium perchlorate (TBAP) was obtained from Fluka, and biotin was obtained from

Pierce. All reagents except PBS—as noted above—were used as received.

Planar substrates for XRD and XPS were fabricated both from SiO<sub>2</sub> glass and poly(styrene) substrates sputtered with Au/Pd to a thickness of approximately 60 nm with a Hummer VI sputter system. Indium-doped tin oxide (ITO) on 25 × 25 × 1.1 mm unpolished float glass from Delta Technologies (R<sub>s</sub> = 6 ± 2 Ω/sq, #CG-40IN-0115) was also used as substrate for some XRD and XPS trials. Pt/Ir ball electrodes were utilized for electrochemical measurements; these substrates were fabricated by flaming the tip of Teflon-coated, 90/10 Pt/Ir wire from A-M Systems with an oxygen torch.

### 2.2. Electrochemical polymerization

PEDOT was electrochemically polymerized on planar substrates under galvanostatic conditions from an aqueous monomer solution containing approximately 0.01 M EDOT and 0.01 M counter-ion. PEDOT films for XRD were grown at a current density of 0.5 mA/cm<sup>2</sup> for 12 min on Au/Pd-sputtered glass and ITO on glass. PEDOT films for electrochemical characterization were deposited at a current of 2 μA for 5 min on Pt/Ir ball electrodes. An AutoLab PGSTAT12 Potentiostat/Galvanostat (EcoChemie, The Netherlands) was used for all electrochemical polymerizations. The counter-ions used were PSS, PBS, NaCl, LiClO<sub>4</sub>, NaH<sub>2</sub>PO<sub>4</sub>, TBAP, and PTS and the biologically derived counter-ions heparin, glutamate, HA, BSA, PDL, and biotin. Methylene chloride was used as solvent for the tetrabutylammonium perchlorate solution. Deionized water was used as solvent for all other EDOT solutions. Fibrillar PEDOT was polymerized with PAA and LiClO<sub>4</sub> as previously reported [14]. All samples were extensively rinsed with deionized water after deposition to wash away excess monomer and counter-ion.

### 2.3. Structural characterization

Structural characterization was performed *via* 2-D XRD using a Bruker D8 Discover diffractometer equipped with a HISTAR 2D wire array area detector. X-rays were generated using a fixed-tube, copper target source operated at 40 kV, 40 mA for all experiments. A 500 μm monochromator was used to generate a point-focused beam. The instrument was calibrated using a NIST1976 flat plate standard or silver behenate powder as appropriate. Data were collected with a camera length of 15 cm.

XPS chemical characterization was performed using a Kratos Axis Ultra DLD X-ray Photon Spectrometer (Kratos Analytical Ltd., Manchester, UK). A Monochromatic Aluminum source was used with the C–C/C–H reference set at 285 eV.

### 2.4. Electrochemical measurements

Pt/Ir ball electrodes were used as the deposition substrate for electrochemical characterization of PEDOT films. Impedance spectroscopy (EIS) and cyclic voltammetry (CV) were performed using an Autolab PGSTAT12. For EIS, the sample acted as the working electrode, a platinum plate as the counter electrode, a saturated Ag/AgCl electrode as the reference electrode, and PBS as the electrolyte. A sinusoidal AC signal with 5 mV amplitude was applied over a frequency range of 1–10<sup>5</sup> Hz. Both impedance and phase angle data were collected over the frequency range. Impedance values at 1 kHz are used as a benchmark when testing PEDOT films because the frequency range of neural activity, from 300 Hz to 1 kHz, is especially important in biological stimulation applications [7,15].

CV was performed with the same electrode setup. The voltage was swept from  $-0.6$  V to  $0.8$  V with a scan rate of  $100$  mV/s. CSC values were calculated by the Autolab software.

### 2.5. Annealing

Planar PEDOT/NaCl samples, which demonstrated the most significant structural regularity as discussed in the results section, were annealed at temperatures up to  $200$  °C in both ambient and  $N_2$  atmospheres. The structural changes of the annealed samples were investigated with XRD. When annealing in  $N_2$  atmosphere at low temperatures, Au/Pd-sputtered poly(styrene) substrates were used. For temperatures above  $90$  °C, Au/Pd-sputtered glass substrates were used. PEDOT films polymerized on ball electrodes with PSS, heparin,  $LiClO_4$ , and NaCl as counter-ions were annealed at temperatures between  $70$  °C and  $220$  °C in ambient atmosphere ovens. Annealing was performed for  $1$  h and all testing was performed after cooling and within three days of annealing.

## 3. Results and discussion

### 3.1. Structural analysis

The 2D XRD patterns for electrochemically polymerized PEDOT films with select counter-ions are shown in Fig. 1a–i. XRD patterns of PEDOT polymerized with NaCl, TBAP, and PTS (Fig. 1a–c) show a distinctive low angle peak near  $\sim 1.3$  nm that is not present in background scans (Fig. 1d). The peak in the PEDOT/NaCl sample (Fig. 1a) corresponds to a first-order  $d$  spacing of  $1.27$  nm. This  $d$  spacing value is similar to the  $1.40$  nm  $d_{100}$  (edge-to-edge) spacing of chemically polymerized PEDOT/Fe(III)Cl<sub>3</sub> reported by Aasmundtveit et al. [16] and the  $d_{100}$  values between  $1.30$  nm and  $1.40$  nm for PEDOT prepared via chemical vapor phase deposition with various counter-ions by Winther-Jensen et al. [10]. Given its similarity to these published results, the diffraction peak observed with electrochemically polymerized PEDOT/NaCl was attributed to intermolecular edge-to-edge (100) correlations between the relatively stiff PEDOT molecules. Fig. 1e shows a diffraction pattern of

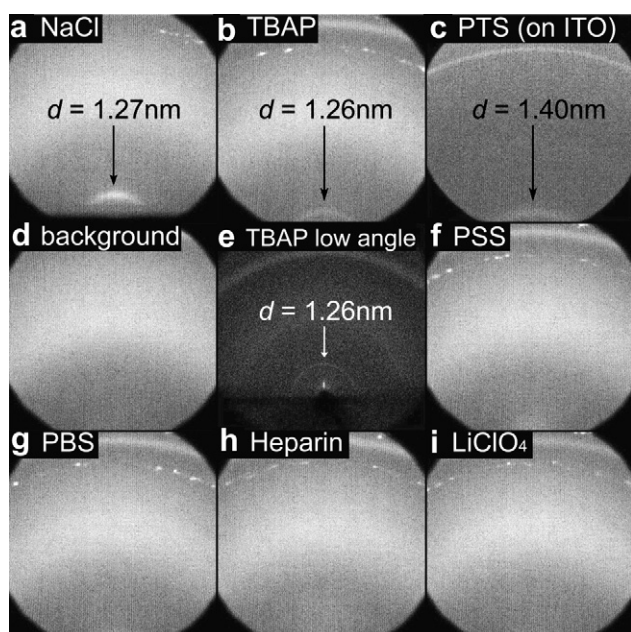


Fig. 1. 2-D X-ray Diffraction data of PEDOT samples electrochemically polymerized with various counter-ions.

PEDOT/TBAP. In this sample, the low angle (100) peak is very uniform in intensity over the observed azimuthal angle range (Fig. 2). PEDOT/PTS shows this same lack of preferred orientation (Fig. 1c). PEDOT/NaCl shows a strong preferred orientation of (100) planes whereas PEDOT/TBAP does not.

These PEDOT diffraction patterns show no indication of  $d_{010}$  or  $d_{001}$  spacings. Diffraction patterns were collected with the samples tilted about the axis of the beam to access diffraction data lying off the meridian; these data also show no indication of (010) or (001) peaks. The lack of evidence for these spacings and the minimal azimuthal variation of the PEDOT/TBAP and PEDOT/PTS (100) peaks indicate that individual PEDOT chains have a regular edge-to-edge correlation with only limited order in the other crystallographic directions. This edge-to-edge (100) correlation indicates a tendency for the chains to organize into ribbon-like structures in which a number of PEDOT chains stack edge-to-edge and remain locally parallel. The absence of other diffraction peaks indicates little or no regularity in face-to-face packing. Therefore, we propose a molecular model of PEDOT chains that are locally organized in the edge-to-edge direction but remain otherwise disordered.

In contrast to PEDOT/TBAP and PEDOT/PTS, Figs. 1a and 2 show the greater azimuthal variation of the peak for PEDOT/NaCl. The PEDOT/NaCl peak has a maximum intensity along the plane perpendicular to the sample stage, which indicates that the chains prefer to organize parallel to the plane of the substrate. XRD patterns of PEDOT films polymerized with PSS and PBS do have faint peaks in the same region as the peaks seen in PEDOT/NaCl, PEDOT/PTS, and PEDOT/TBAP. These faint peaks are evidence of a preferred orientation similar to that found in PEDOT/NaCl. Despite any preferred orientation, films polymerized with NaCl, PSS and PBS have no indication of face-to-face nor backbone regularity, so the model of edge-to-edge packing between PEDOT chains that are otherwise disordered is still applicable to these films.

PEDOT samples prepared with  $LiClO_4$ ,  $NaH_2PO_4$ , and the biologically derived counter-ions—heparin, glutamate, HA, BSA, PDL, and biotin—and fibrillar PEDOT prepared with PAA/ $LiClO_4$  do not show similar low angle peaks to those present in the other samples; for example Fig. 1h and i compare the diffraction pattern for PEDOT/heparin and PEDOT/ $LiClO_4$ . Evidently, in these samples, the larger counter-ions disrupt the lateral order of the PEDOT films.

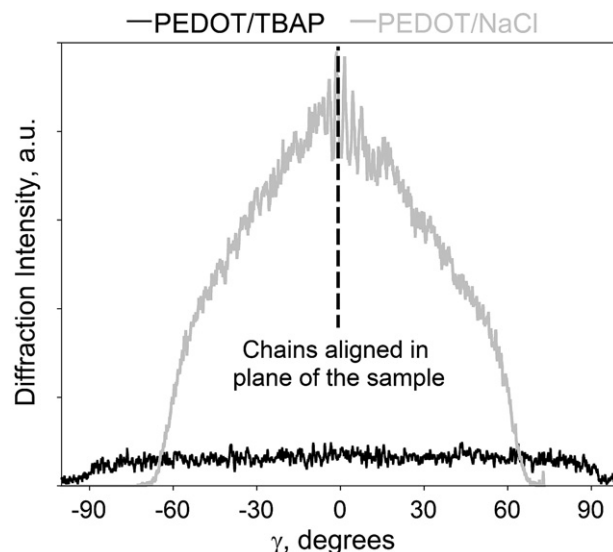


Fig. 2. Azimuthal integration of XRD spectra for low angle (100) peaks of PEDOT/TBAP and PEDOT/NaCl.

### 3.2. Structural analysis after heat treatment

The low angle (100) X-ray diffraction peaks from PEDOT/NaCl samples that have been annealed in ambient atmosphere are shown in Fig. 3a. The (100) diffraction peak in PEDOT/NaCl decreases in intensity when annealed at 150 °C and is completely absent at 200 °C. This monotonic decrease in peak intensity with increased annealing temperature indicates that heat treatment causes a disordering in the PEDOT film. To determine whether this change was due to reactions with the atmosphere, samples were annealed at similar temperatures in N<sub>2</sub> atmosphere. The low angle XRD data for these samples annealed in N<sub>2</sub> atmosphere (Fig. 3b) are consistent with the data from the ambient atmosphere annealing: the intensity of the diffraction peak decreases monotonically as annealing temperature increases. This similarity indicates that the structural changes in the films are not caused by a chemical interaction with atmospheric gasses.

Winther-Jensen et al. reported a similar loss of intensity in X-ray diffraction peaks when PEDOT films were annealed to 140 °C [10]. It is important to note that Winther-Jensen's measurements were taken during the annealing process. Therefore, the complete loss of peak intensity at 140 °C that they reported does not conflict with our findings. Their experiments showed that diffraction peaks

reappeared with less intensity after films had cooled from 140 °C, and this finding is directly comparable to our data for PEDOT annealed to 130 °C and 150 °C and cooled (Fig. 3a and 3b).

Those PEDOT samples that showed no evidence for long-range ordering prior to heat treatment (PEDOT polymerized with heparin, glutamate, HA, BSA, PDL, biotin, LiClO<sub>4</sub>, NaH<sub>2</sub>PO<sub>4</sub>, and PAA/LiClO<sub>4</sub>) did not exhibit any XRD evidence of heat-induced ordering after heat treatments were performed.

In order to analyze the chemical changes that took place during annealing, XPS analysis of the PEDOT/NaCl samples was performed on samples annealed in both ambient atmosphere and N<sub>2</sub> atmosphere. The spectra for unannealed PEDOT are consistent with Spanninga et al. [17]. After annealing at 130 °C in N<sub>2</sub> atmosphere, changes were seen in both sulfur and oxygen spectra (Fig. 4a and b). The sulfur 2p spectra exhibited an increase in intensity in the small, broad peak near 168 eV. This may be an indication of sulfur oxidation in the PEDOT thiophene ring [18]. In the oxygen 1s spectra, an increase was observed in the lower binding energy shoulder at ~532 eV. Similar results were seen for annealing in N<sub>2</sub> atmosphere. These results are not conclusive, but they suggest that some sulfur oxidation is taking place. However, oxidation does not begin to occur until films reach 130 °C. Structural changes in PEDOT/NaCl samples were seen at temperatures as low as 70 °C, indicating that the structural changes observed with XRD cannot be entirely attributed to oxidation.

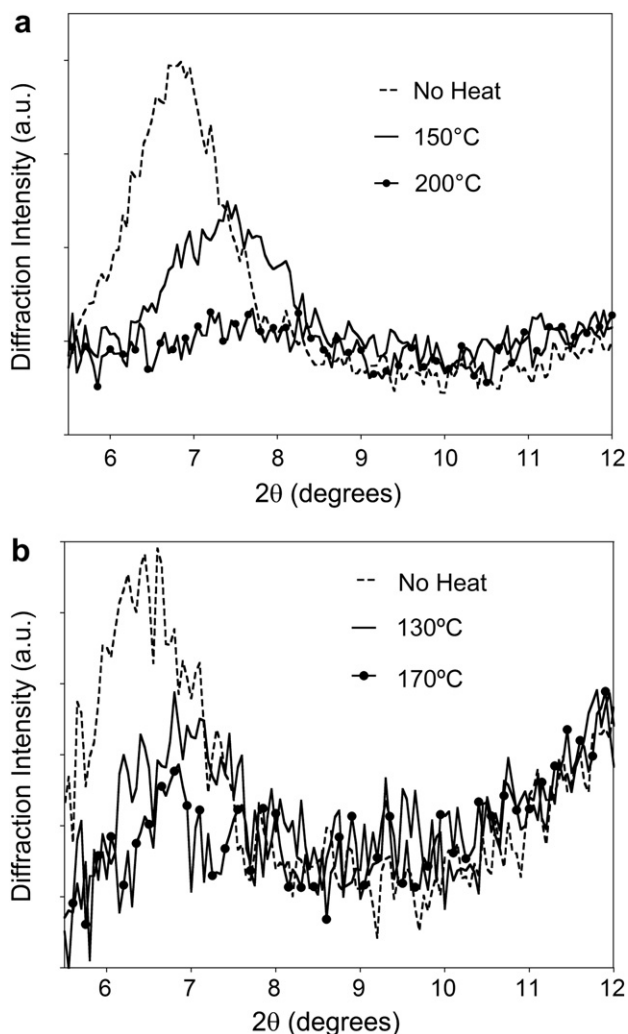


Fig. 3. XRD of PEDOT showing low angle (100) peak of PEDOT/NaCl, (a) annealed in ambient atmosphere and (b) annealed in N<sub>2</sub> atmosphere.

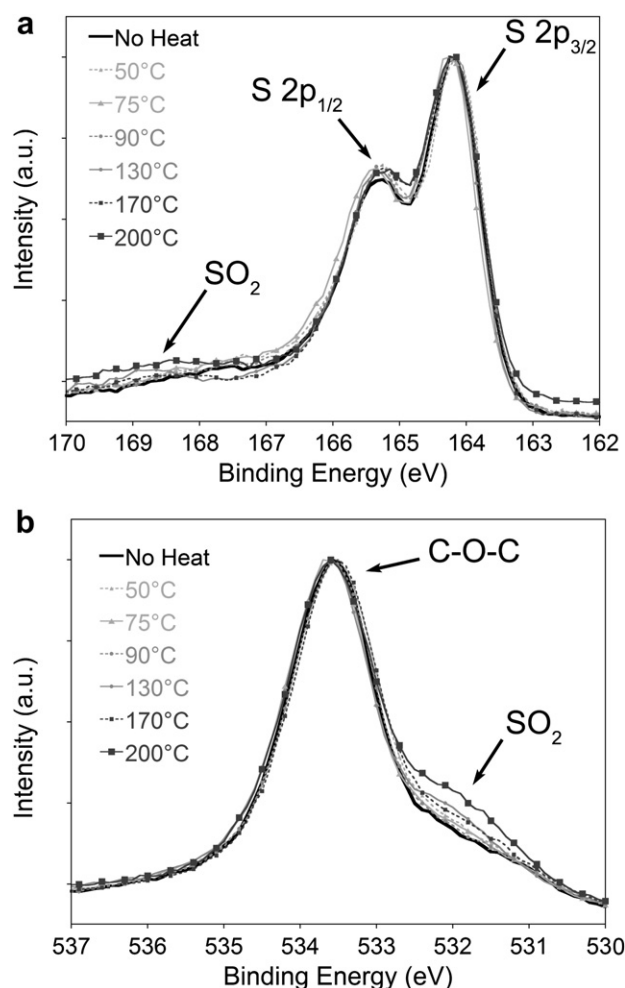


Fig. 4. XPS spectra for PEDOT/NaCl samples annealed in ambient atmosphere; (a) sulfur (2p) and (b) oxygen (1s).



### 3.3. Electrical characterization before and after heat treatment

To further investigate the affects of annealing on PEDOT films, electrical studies were performed on samples before and after annealing. EIS and CV were performed on PEDOT samples polymerized on Pt/Ir ball electrodes with four different counter-ions: PSS, heparin, LiClO<sub>4</sub>, and NaCl. PSS and heparin were chosen for their low impedance and large CSC [1,19,20]. LiClO<sub>4</sub> was chosen for its previous use in neural probe coating and drug delivery investigations [13,14] and NaCl for its interesting structural properties as discussed in the previous section. PEDOT samples polymerized with PSS, heparin, LiClO<sub>4</sub>, and NaCl were annealed at temperatures from 70 °C to 220 °C. Fig. 5 shows EIS impedance at 1 kHz plotted against annealing temperature, and Fig. 6 shows CSC values plotted against annealing temperature. Table 1 provides a summary of electrical data for these counter-ions.

PEDOT/PSS and PEDOT/heparin films show variations in impedance with annealing temperature comparable to the random fluctuations in the untreated films. No significant change in impedance was observed in these films in the temperature ranges examined, save a modest increase in the PEDOT/heparin samples annealed at 220 °C. CV plots of both of these samples show a 44–50% decrease in CSC when annealed at any temperature compared to the unheated sample. These results indicate that heat treatment is detrimental to the electrical performance of PEDOT films polymerized with PSS and heparin. Given the high temperatures involved, thermal degradation of the biological counter-ion heparin could have contributed to these changes in electrical performance.

However, PEDOT films polymerized with LiClO<sub>4</sub> and NaCl, two smaller counter-ions, have much higher impedances and lower CSC values before annealing than PEDOT polymerized with PSS and heparin. These results correspond well with CSC measurements reported by Winther-Jensen et al. [10]. Heat treatment of PEDOT/LiClO<sub>4</sub> causes a decrease in 1 kHz impedance when annealed at

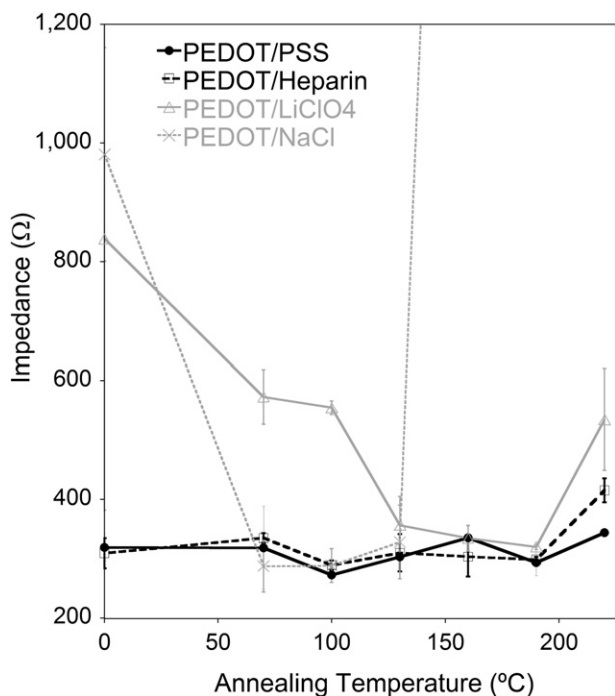


Fig. 5. Magnitude of impedance at 1 kHz as a function of annealing temperature for PEDOT/PSS, PEDOT/Heparin, PEDOT/LiClO<sub>4</sub>, and PEDOT/NaCl. Mean values for three samples are plotted, and error bars indicate one standard deviation.

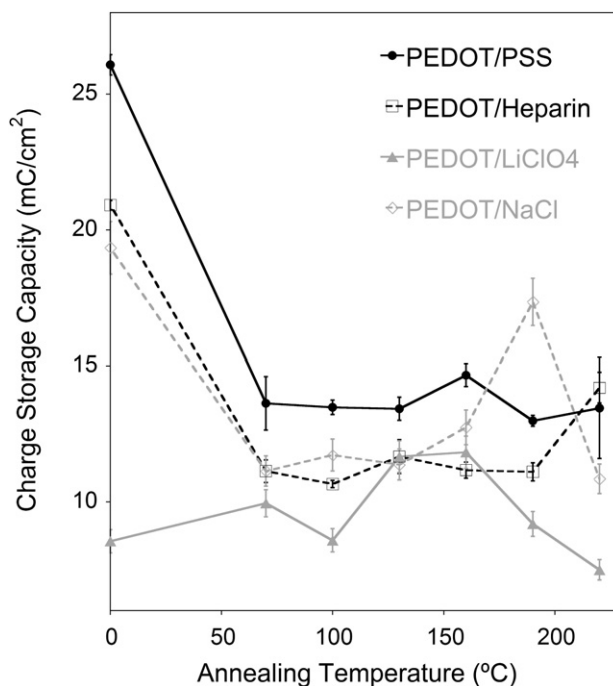


Fig. 6. Total charge storage capacity as a function of annealing temperature for PEDOT/PSS, PEDOT/Heparin, PEDOT/LiClO<sub>4</sub>, and PEDOT/NaCl. Mean values for three samples are plotted, and error bars indicate one standard deviation.

70 °C–190 °C, reaching a minimum of 320 Ω when annealed at 190 °C (Fig. 5). This impedance is comparable to the 319 Ω for unheated PEDOT/PSS.

The large error bars for the impedance of unannealed PEDOT/LiClO<sub>4</sub> are representative of 1 kHz impedance values of 459 Ω, 711 Ω, and 1345 Ω. However, after annealing at 70 °C those films had impedances of 539 Ω, 553 Ω, and 625 Ω, respectively. The impedances of those films retain a low standard deviation (less than 50 Ω) up to 190 °C. It seems that annealing LiClO<sub>4</sub> films both decreases their impedance and results in a tighter distribution of electrical properties. Film stability in annealed films is a potential issue, however; 25% of films annealed between 130 °C and 190 °C failed during electrical testing.

Even more distinct than the decrease in impedance of PEDOT/LiClO<sub>4</sub> samples is the reduction of the frequency at which they approach their lowest impedance. All PEDOT films show similar frequency dependence in their impedance: an asymptotic, low impedance at high frequencies that increases rapidly at frequencies below a critical frequency,  $f_c$  (Fig. 7a). The value of  $f_c$  depends on counter-ion and deposition parameters. It can be arbitrarily represented by the frequency at which the impedance reaches 1000 Ω.

Table 1  
Comparison of PEDOT films polymerized with different counter-ions and annealed.

Counter-ion	Molecular weight	$d_{100}$ spacing	1 kHz impedance and CSC before annealing	1 kHz impedance and CSC after annealing 1 h at 160 °C
PSS	~70,000 Da	~1.3 nm	319 Ω 26.1 mC/cm <sup>2</sup>	335 Ω 14.7 mC/cm <sup>2</sup>
Heparin	12,000–15,000 Da		309 Ω 20.9 mC/cm <sup>2</sup>	304 Ω 11.2 mC/cm <sup>2</sup>
LiClO <sub>4</sub>	106.4 Da		839 Ω 8.6 mC/cm <sup>2</sup>	335 Ω 11.3 mC/cm <sup>2</sup>
NaCl	58.4 Da	1.27 nm	981 Ω 19.3 mC/cm <sup>2</sup>	3168 Ω 12.7 mC/cm <sup>2</sup>



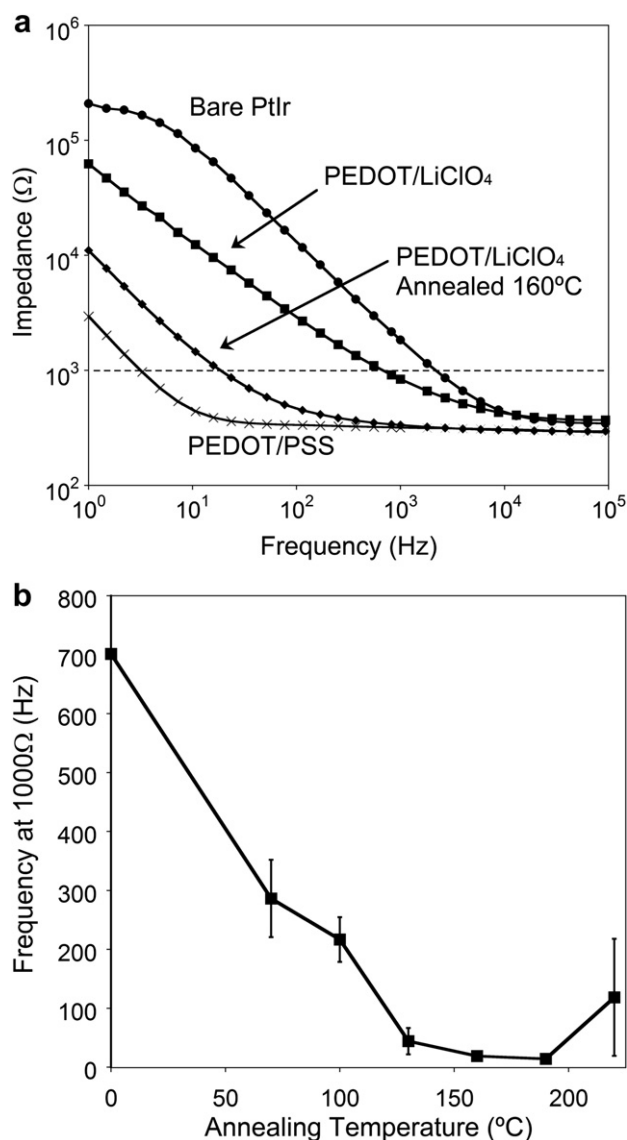


**Fig. 7.** (a) Impedance of bare Pt/Ir, PEDOT/LiClO<sub>4</sub>, PEDOT/LiClO<sub>4</sub> annealed at 160 °C, and PEDOT/PSS on Pt/Ir ball electrodes. Dotted line indicates the 1000 Ω benchmark used to calculate  $f_c$ . (b) Frequency at which PEDOT/LiClO<sub>4</sub> samples reach 1000 Ω versus annealing temperature. Mean values for three samples are plotted, and error bars indicate one standard deviation.

Calculated this way, the  $f_c$  of PEDOT/LiClO<sub>4</sub> films decreases from 698 Hz in the unheated sample to just 14 Hz when the samples are annealed at 190 °C (Fig. 7b). For comparison the  $f_c$  of unheated PEDOT/PSS films is 3.2 Hz.

Cyclic voltammetry of PEDOT/LiClO<sub>4</sub> shows an increase in CSC when samples are annealed, reaching a maximum of 11.3 mC/cm<sup>2</sup> when samples are heated at 160 °C (Fig. 6, Table 1). For comparison, the polymer film with the best electrical properties in our experiments—unheated PEDOT/PSS—has a CSC value of 26.1 mC/cm<sup>2</sup>. Impedance and  $f_c$  values have not reached a minimum when PEDOT/LiClO<sub>4</sub> is annealed at 160 °C, but they are within 15 Ω and 4.9 Hz, respectively, of their minimum values, and above 160 °C the charge storage capacity decreases significantly. Finally, these PEDOT/LiClO<sub>4</sub> films are stable up to 160 °C—the degradation of electrical properties described above only begins at 190 °C. Therefore, 160 °C is an optimal annealing temperature for these PEDOT/LiClO<sub>4</sub> films.

PEDOT/NaCl samples demonstrate considerably lower impedance when annealed at 70–130 °C, with a minimum impedance of just 287 Ω at 70 °C (Fig. 5b). This value is lower than the impedance of unheated PEDOT/PSS, the benchmark for low-impedance PEDOT. The  $f_c$  values are also significantly lower in this range, having decreased from 2200 Hz to only 7 Hz when annealed at 100 °C (see Supp. 2). The CSC in this temperature range, however, is significantly lower, having decreased by more than 40% (Fig. 6). Above 160 °C, the charge storage capacity increases slightly, but the impedance when annealed above 160 °C is much higher than even that of the unheated samples. Thus, impedance of PEDOT/NaCl films can be reduced with heat treatment, but not without a significant loss in charge storage capacity.

### 3.4. Correlation between structural and electrical properties

The observed relationship between structural and electrical properties is quite different for each of the four counter-ions. XRD data shows that planar PEDOT/NaCl films become more disordered when annealed above 150 °C. At these temperatures, the PEDOT/NaCl films on ball electrodes demonstrate both increased impedance and decreased charge storage capacity (Fig. 5b and 6). These results suggest that regular polymer packing in unheated films supports PEDOT's ability to mediate charge transfer at the interface between ionic and electronic conduction. However, Figs. 5 and 6 also show that impedance and charge storage capacity have different relationships to annealing temperature and that neither exhibits a monotonic dependence on annealing temperature. Therefore, some other structural, thermodynamic, or chemical change must also be taking place to account for the complex effects that annealing has on electrical properties.

PEDOT/LiClO<sub>4</sub> shows no evidence of crystallinity before or after annealing, but its electrical properties change dramatically with temperature. PEDOT/PSS and PEDOT/heparin also show no evidence of crystallinity and demonstrate some changes in electrical properties when annealed, though to a lesser extent than the other two PEDOT films. As is the case for PEDOT/NaCl, these changes in electrical properties must be attributable to some structural, thermodynamic, or chemical change. Changes in surface morphology, structural changes within the PEDOT films, and chemical changes at the polymer–substrate interface are all possible causes of the changes seen in these PEDOT films. Investigation of each of these phenomena and its affect on electrical properties could be an avenue for future research.

As demonstrated by Winther-Jensen et al., chemically polymerized films that have been annealed are unstable in their disordered state. After one month with no further heat treatments, annealed films were observed to regain their crystallinity [10]. The effect that this time-dependent return to a more stable thermodynamic state may have on electrochemically polymerized PEDOT was not studied in these experiments and could be another focus of future research.

### 3.5. Application of results

The results discussed here, specifically the improvements in electrical properties seen with annealed PEDOT/LiClO<sub>4</sub> films, could be particularly advantageous for neural stimulation. Stimulation is most often performed in the 300–1000 Hz range and these heat treatments decrease electrode impedances to below 1000 Ω across that entire frequency range ( $f_c$  values decreased from 2200 Hz to 7 Hz for annealed PEDOT/LiClO<sub>4</sub>). Additionally, the heat treatments applied to PEDOT/LiClO<sub>4</sub> films produce extremely flat impedance curves over the relevant frequency range (Fig. 7a). These flatter impedance curves can improve signal fidelity: when impedance

varies across the relevant frequency range, the variations distort output signals. Heat treatment of PEDOT/LiClO<sub>4</sub> films could limit this problem in stimulation devices. Large CSC values are desirable as they indicate the amount of charge available for transfer from electrical to ionic current [19], so the larger CSC values of annealed PEDOT/LiClO<sub>4</sub> films are also advantageous. Empirical studies of this type of heat treatment for PEDOT films on neural devices could ultimately lead to smaller electrode sites that more efficiently stimulate neural tissues.

#### 4. Conclusions

PEDOT samples electrochemically polymerized with NaCl, PTS, and TBAP contain a structural regularity associated with regular (100) edge-to-edge alignment of PEDOT chains. Heat treatment of PEDOT/NaCl between 160 °C and 220 °C causes these edge-to-edge correlations to disappear. Electrical testing indicates that the annealing also decreases impedance and increases CSC of PEDOT samples prepared with LiClO<sub>4</sub> as a counter-ion. In particular, annealing PEDOT/LiClO<sub>4</sub> to 160 °C for 1 h decreases impedance at 1 kHz by 60%, decreases by nearly two orders of magnitude the lowest frequency at which impedance reaches 1 kΩ, and increases CSC by 25%. PEDOT/NaCl films also demonstrate a 39–42% decrease in impedance when samples are annealed in the 70 °C–130 °C range, but this decrease in impedance is accompanied by an undesirable 39–42% decrease in CSC. PEDOT polymerized with larger molecular weight counter-ions (PSS, heparin, etc.) do not show the structural regularity observed in PEDOT polymerized with smaller counter-ions. PEDOT polymerized with large counter-ions also do not exhibit any improvement in electrical properties when annealed.

These findings indicate that PEDOT coatings that have undergone heat treatments may be valuable for neural stimulation devices or any PEDOT application where characteristics such as low impedance, high CSC, and flat frequency dependence curves are important. Annealing of small counter-ion PEDOT films could allow these characteristics to be fine-tuned for particular applications. Further studies will be necessary to determine the usefulness of PEDOT heat treatments for any particular device. Future research could also focus on the deposition and optimization of biological counter-ions such as those investigated here.

LiClO<sub>4</sub> is particularly interesting as a PEDOT counter-ion because it is smaller and more mobile than PSS. Axelsson showed that PEDOT/LiClO<sub>4</sub> films have a larger deflection under actuation than PEDOT/PSS films. Furthermore, PEDOT/LiClO<sub>4</sub> films transport perchlorate anions during actuation whereas PEDOT/PSS films transport cations from solution [13]. This difference could make PEDOT/LiClO<sub>4</sub> films preferable for controlled delivery of certain

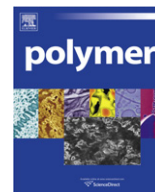
charged drugs. The annealing process described here can improve the electrical properties of PEDOT/LiClO<sub>4</sub> films to levels comparable to PEDOT/PSS. In applications such as neural stimulation devices where both drug delivery and charge delivery are important, annealed PEDOT/LiClO<sub>4</sub> films could prove to be an ideal solution.

#### Acknowledgments

Thanks to Dr. Jeffrey L. Hendricks for his assistance with making Pt/Ir ball electrodes. This research was supported in part by the U. S. Army (MURI) and the National Science Foundation (NSF). DCM is a co-founder and Chief Scientific Officer for Biotectix LLC, a University of Michigan spin-off company actively investigating the use of conducting polymer coatings for biomedical device applications.

#### References

- [1] Groenendaal L, Zotti G, Aubert PH, Waybright SM, Reynolds JR. *Advanced Materials* 2003;15(11):855–79.
- [2] Richardson-Burns SM, Hendricks JL, Foster B, Povlich LK, Kim D, Martin DC. *Biomaterials* 2007;28(8):1539–52.
- [3] Zhang F, Johansson M, Andersson M, Hummelen J, Inganäs O. *Advanced Materials* 2002;14(9):662–5.
- [4] Kulkarni AP, Tonzola CJ, Babel A, Jenekhe SA. *Chemistry of Materials* 2004;16(23):4556–73.
- [5] Rahman MA, Kumar P, Park D, Shim Y. *Sensors* 2008;8(1):118–41.
- [6] Paik S, Park Y, Cho D. *Journal of Micromechanics and Microengineering* 2003;13(3):373–9.
- [7] Cui X, Martin DC. *Sensors and Actuators B: Chemical* 2003;89(1–2):92–102.
- [8] Campbell AJ, Bradley DDC, Antoniadis H. *Journal of Applied Physics* 2001;89(6):3343–51.
- [9] Kim WH, Kushto GP, Kim H, Kafafi ZH. *Journal of Polymer Science Part B: Polymer Physics* 2003;41(21):2522–8.
- [10] Winther-Jensen B, Forsyth M, West K, Andreassen JW, Bayley P, Pas S, et al. *Polymer* 2008;49(2):481–7.
- [11] Yang J, Martin DC. *Sensors and Actuators B: Chemical* 2004;101(1–2):133–42.
- [12] Han D, Yang G, Song J, Niu L, Ivaska A. *Journal of Electroanalytical Chemistry* 2007;602(1):24–8.
- [13] Axelsson R. Mechanisms of mass transport during actuation of poly(3,4-ethylenedioxythiophene) for neural drug delivery devices. Sweden: University of Linköping; 2007.
- [14] Yang J, Lipkin K, Martin DC. *Journal of Biomaterials Science, Polymer Edition* 2007;18(15):1075–89.
- [15] Williams JC. Performance of chronic neural implants: measurement, modeling and intervention strategies. Ph.D. thesis. Arizona State University; 2001.
- [16] Aasmundtveit KE, Samuelsen EJ, Pettersson LAA, Inganäs O, Johansson T, Feidenhans'l R. *Synthetic Metals* 1999;101(1–3):561–4.
- [17] Spanninga SA, Martin DC, Chen Z. *Journal of Physical Chemistry C* 2009;113(14):5585–92.
- [18] Marciniak S, Crispin X, Uvdal K, Trzcinski M, Birgerson J, Groenendaal L, et al. *Synthetic Metals* 2004;141(1–2):67–73.
- [19] Cogan SF. *Annual Review of Biomedical Engineering* 2008;10(1):275–309.
- [20] Paczosa B, Blaz T, Migdalski J, Lewenstam A. *Polish Journal of Chemistry* 2004;78(9):1543–52.



# Anion exchanged polymerized ionic liquids: High free volume single ion conductors

Yuesheng Ye, Yossef A. Elabd\*

Department of Chemical and Biological Engineering, Drexel University, Philadelphia, PA 19104, United States

## ARTICLE INFO

### Article history:

Received 12 October 2010

Received in revised form

11 January 2011

Accepted 14 January 2011

Available online 22 January 2011

### Keywords:

Ionic liquid

Conductivity

Polymer electrolyte

## ABSTRACT

In this study, we investigate the isolated effect of anion type on the chemical, thermal, and conductive properties of imidazolium-based polymerized ionic liquids (PILs). PILs with various anions at constant average chain length were prepared by ion exchange with a water-soluble PIL precursor, (poly(1-[(2-methacryloyloxy)ethyl]-3-butylimidazolium bromide) (poly(MEBIm-Br))). NMR, IR, and elemental analysis confirm that anion exchange of ploy(MEBIm-Br) with bis(trifluoromethanesulfonyl) imide (TFSI), tetrafluoroborate (BF<sub>4</sub>), trifluoromethanesulfonate (Tf), and hexafluorophosphate (PF<sub>6</sub>) in water resulted in nearly fully exchanged PILs. As a function of anion type, the glass transition temperature plays a dominant role, but not the sole role in determining ion conductivity. Other factors affecting ionic conductivity include the size and symmetry of the anion and dissociation energy of the ion pair. Both the Vogel-Fulcher-Tammann (VFT) and Williams-Landel-Ferry (WLF) equations were employed to investigate the temperature dependent ionic conductivities. The  $C_1^g$  (9.03) and  $C_2^g$  (168 K) values obtained from the WLF regression of these PILs greatly deviate from the classical WLF values originally obtained from the mechanical relaxation of uncharged polymers ( $C_1^g = 17.44$ ,  $C_2^g = 51.6$  K) and the WLF values obtained from the conductive properties of other polymer electrolytes. This suggests that the fractional free volume ( $f(T_g) = B/(2.303C_1^g)$ ) and Vogel temperature ( $T_0 = T_g - C_2^g$ ) are strong functions of ion concentration, where high free volume allows for ion mobility at temperatures farther below the glass transition temperature of the polymer.

© 2011 Elsevier Ltd. All rights reserved.

## 1. Introduction

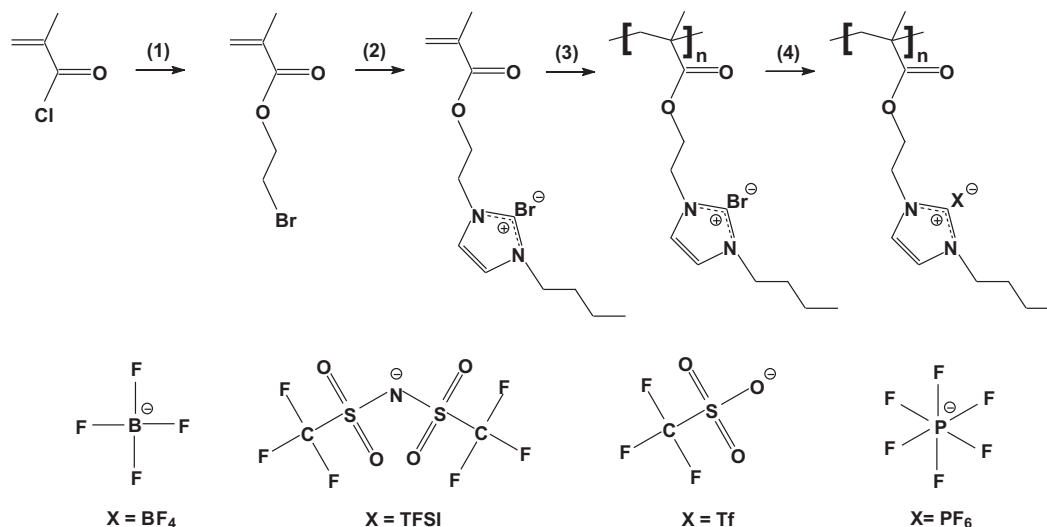
Polymerized ionic liquids (PILs), or polymers synthesized by polymerizing ionic liquid monomers, have attracted recent attention and their application as polymer electrolytes, sorbents, dispersing agents, and nanomaterials has recently been reviewed [1,2]. Overall, the interests in PILs are many fold, but in general, PILs are of interest due to the unique properties of ionic liquids (ILs) (e.g., negligible vapor pressure, nonflammability, high ionic conductivity, a wide electrochemical window, and good chemical and thermal stability) and the broad range of new polymer electrolytes that can be realized with a highly tunable and facile synthesis [3–7]. Unlike ionic liquid (IL)/polymer mixtures, the IL moiety is covalently attached to the macromolecule in a PIL (see Scheme 1). Therefore, PILs differ in that the organic cation or anion is restricted in mobility compared to its more mobile counterion (i.e., single ion conductor), unlike ILs or IL/polymer mixtures where both the cation and anion

are mobile. The former alleviates shortcomings of liquid electrolytes in electrochemical devices (e.g., leakage, stability), but usually results in lower ionic conductivity when compared to the latter. Although PILs are of great interest as solid-state polymer electrolytes, surprisingly, there are relatively few reports on the ionic conductivity of PILs [6–12]. It is evident based on these few investigations that a number of factors can impact ionic conductivity in PILs, such as polymer chemistry, glass transition temperature, molecular weight, and polymer morphology. However, there is still a limited fundamental understanding of ion transport in PILs.

One method for increasing the ionic conductivity in a PIL is to replace the mobile ion with another via ion exchange. Chen et al. [6] observed enhancements in ionic conductivity in a PIL when the tetrafluoroborate (BF<sub>4</sub>) anion was replaced with the bis(trifluoromethanesulfonyl) imide (TFSI) anion. This was the result of a significant reduction in the glass transition temperature of the polymer, which facilitated higher segmental motion of the polymer and therefore higher anion mobility. This is unique to PILs, where these anion differences typically do not have the same effect in ILs. Therefore, with a wide variety of anions available, understanding ion conduction as a function of anion type in PILs is of great interest.

\* Corresponding author. Tel.: +1 215 895 0986; fax: +1 215 895 5837.

E-mail address: [elabd@drexel.edu](mailto:elabd@drexel.edu) (Y.A. Elabd).



**Scheme 1.** Synthesis of anion exchanged PILs (poly(MEBIm-X)). (1) 2-bromoethanol, triethylamine, dichloromethane, room temperature, 18 h. (2) 1-butylimidazole, 40 °C, 24 h. (3) AIBN, DMF, 60 °C, 6 h. (4) salt, DI water, room temperature, 48 h.

However, there are only a few investigations that have focused on the effects of anion type on ionic conductivity in PILs.

In several previous studies [9,13–15], PILs with different anions were prepared by anion exchange of the IL monomer followed by polymerization under different reaction conditions. This resulted in PILs with a variety of molecular weights or different average chain lengths, which also can affect the glass transition temperature and ionic conductivity. Therefore, anion type and molecular weight were convoluted parameters in these studies. These two parameters can be deconvoluted if the PILs undergo anion exchange at the polymer stage. Only a few investigations have produced PILs with this method [16]. However, these investigations did not explore the effect of anion type on ion conduction.

The purpose of this study was to synthesize PILs with different anions at constant average polymer chain length and investigate the effect of anion type on ion conductivity as well as other properties related with these anion exchanged single ion conductors. The effectiveness of exchanging anions at the polymer stage in PILs is largely dependant on the anion type, PIL, and the experimental procedure. In order to achieve a high purity exchange, solubility of the PIL before and after exchange in the solvents used can be a critical issue. In general, imidazolium-based ILs and PILs neutralized with halide anions are water soluble, while these same ILs and PILs neutralized with fluorine-containing anions are water insoluble [17]. We utilize this difference in solubilities to achieve high purity anion exchanged PILs.

Specifically, in this study, an imidazolium-based IL monomer, 1-[(2-methacryloyloxy)ethyl]-3-butylimidazolium bromide (MEBIm-Br), was synthesized and subsequently polymerized using conventional free radical polymerization. This PIL precursor, poly(MEBIm-Br), was subsequently exchanged with other fluoride-containing anions, TFSI, BF<sub>4</sub>, trifluoromethanesulfonate (Tf), and hexafluorophosphate (PF<sub>6</sub>), in water, where the resulting PIL precipitated out of solution. For comparison, the same procedure was also performed on the IL monomer. The chemistry, molecular weight, glass transition temperature, thermal decomposition temperature, and ion conductivity were characterized in all of these PILs, where anion type was the sole variable. The effect of temperature on ion conductivity was explored with the use of regressions to both the VFT and WLF models. Interestingly, the WLF parameters ( $C_1$  and  $C_2$ ) for PILs are uniquely different than neutral polymers and other salt doped polymer electrolytes (e.g., Li salt-poly(ethylene

oxide) (PEO)), which suggest that fractional free volume at the glass transition temperature and Vogel temperature are significantly different in single ion conductor PILs.

## 2. Experimental

### 2.1. Materials

2-Bromoethanol (95%), methacryloyl chloride (97%, stabilized with 200 ppm monomethyl ether hydroquinone (MEHQ)), triethylamine ( $\geq 99.5\%$ ), dichloromethane (ACS reagent,  $\geq 99.5\%$ , contains 50 ppm amylene stabilizer), magnesium sulfate (anhydrous, ReagentPlus<sup>®</sup>, 99%), 1-butylimidazole (98%), 2,6-di-*tert*-butyl-4-methylphenol (99%), diethyl ether (anhydrous,  $\geq 99.7\%$ , contains 1 ppm BHT inhibitor), azobisisobutyronitrile (AIBN, 97%), acetone (HPLC grade,  $\geq 99.9\%$ ), sodium tetrafluoroborate (NaBF<sub>4</sub>, 98%), lithium bis(trifluoromethanesulfonyl) imide (LiTFSI, 97%), lithium trifluoromethanesulfonate (LiTf, 96%), lithium hexafluorophosphate (LiPF<sub>6</sub>, 98%), lithium bromide (LiBr, 99.995% metals basis), acetonitrile (anhydrous, 99.8%), *N,N*-dimethylformamide (DMF, ACS reagent,  $\geq 99.8\%$  and HPLC grade,  $\geq 99.9\%$ ), and methyl sulfoxide-*d*<sub>6</sub> (DMSO-*d*<sub>6</sub>, 99.9%, contains 0.03% v/v TMS) were purchased from Aldrich. Ultrapure deionized (DI) water (resistivity  $\sim 16$  M $\Omega$  cm) was used as appropriate.

### 2.2. Synthesis of ionic liquid (IL) monomer

The synthesis method for the imidazolium-containing monomer, 1-[(2-methacryloyloxy)ethyl]-3-butylimidazolium bromide (MEBIm-Br), is shown in Scheme 1. A typical reaction included adding a mixture of 39.37 g (0.315 mol) of 2-bromoethanol and 50 mL of dichloromethane to a three-neck 500 mL flask in an ice bath. Under nitrogen, a mixture of 33.39 g (0.33 mol) of triethylamine and 50 mL of dichloromethane was slowly added to the flask, followed by a slow addition of a mixture of 31.36 g (0.3 mol) of methacryloyl chloride and 50 mL of dichloromethane using an addition funnel. The reaction mixture was stirred at room temperature for 18 h and then filtered. The liquid filtrate was washed with 300 mL DI water four times. The water layer was removed using a separation funnel and the residual water in the organic layer was further removed with anhydrous magnesium sulfate. The organic



solvent was then removed by vacuum, which yielded a clear liquid of 2-bromoethyl methacrylate (70% yield).

A typical quaternization reaction consisted of adding 40.46 g (0.21 mol) of 2-bromoethyl methacrylate, 26.03 g (0.21 mol, equimolar) of 1-butylimidazole, and a small amount of 2,6-di-*tert*-butyl-4-methylphenol (inhibitor) to a 250 mL flask. The mixture was stirred in an oil bath at 40 °C for 24 h and yielded a viscous liquid. The resulting MEBIm-Br monomer was dissolved in 30 mL dichloromethane and then re-precipitated three times in 200 mL diethyl ether in an ice bath. The purified MEBIm-Br monomer was a clear viscous liquid (82% yield). <sup>1</sup>H NMR (UNITYINOVA 500 MHz, DMSO-*d*<sub>6</sub>, ppm) and elemental analysis: 9.37 (s, 1H, N-CH=N), 7.86–7.88 (d, 2H, N-CH=CH-N), 6.03 (s, 1H, HCH=C(CH<sub>3</sub>)), 5.76 (s, 1H, HCH=C(CH<sub>3</sub>)), 4.53 (m, 2H, N-CH<sub>2</sub>-CH<sub>2</sub>-O), 4.48 (m, 2H, N-CH<sub>2</sub>-CH<sub>2</sub>-O), 4.21 (t, 2H, N-CH<sub>2</sub>-CH<sub>2</sub>-CH<sub>2</sub>-CH<sub>3</sub>), 1.84 (s, 3H, CH<sub>2</sub>=C(CH<sub>3</sub>)), 1.76 (m, 2H, N-CH<sub>2</sub>-CH<sub>2</sub>-CH<sub>2</sub>-CH<sub>3</sub>), 1.22 (m, 2H, N-CH<sub>2</sub>-CH<sub>2</sub>-CH<sub>2</sub>-CH<sub>3</sub>), 0.89 (t, 3H, N-CH<sub>2</sub>-CH<sub>2</sub>-CH<sub>2</sub>-CH<sub>3</sub>). Anal. Found (Anal. Calcd.): C, 46.35 (49.21); H, 7.11 (6.69); O, 14.98 (10.09); N, 8.21 (8.83); Br 23.62 (25.18).

### 2.3. Synthesis of polymerized ionic liquid (PIL)

The imidazolium-containing polymer, poly(MEBIm-Br), was synthesized by the conventional free radical polymerization as shown in Scheme 1. A typical polymerization included adding a mixture of 30.04 g (9.27 × 10<sup>-2</sup> mol) MEBIm-Br monomer and 63.0 g DMF to a 250 mL flask. The reaction mixture was then purged with nitrogen for 30 min followed by an addition of 31.4 mg (1.91 × 10<sup>-4</sup> mol) AIBN initiator to initiate polymerization, which was carried out at 60 °C for 6 h. The reaction mixture was then diluted with DMF and precipitated into acetone followed by washing with fresh acetone several times. The precipitate was then dried under vacuum at 60 °C for 72 h yielding 16.80 g of poly(MEBIm-Br) (56% yield). <sup>1</sup>H NMR (UNITYINOVA 500 MHz, DMSO-*d*<sub>6</sub>, ppm) and elemental analysis: 9.97 (s, 1H, N-CH=N), 8.10–8.17 (d, 2H, N-CH=CH-N), 4.32–4.67 (m, 6H, N-CH<sub>2</sub>-CH<sub>2</sub>-O, N-CH<sub>2</sub>-CH<sub>2</sub>-CH<sub>2</sub>), 1.84 (s, 4H, CH<sub>2</sub>-C(CH<sub>3</sub>), N-CH<sub>2</sub>-CH<sub>2</sub>-CH<sub>2</sub>-CH<sub>3</sub>), 1.30 (s, 5H, N-CH<sub>2</sub>-CH<sub>2</sub>-CH<sub>2</sub>-CH<sub>3</sub>, CH<sub>2</sub>-C(CH<sub>3</sub>)), 0.91 (s, 6H, N-CH<sub>2</sub>-CH<sub>2</sub>-CH<sub>2</sub>-CH<sub>3</sub>, CH<sub>2</sub>-C(CH<sub>3</sub>)), 0.32–0.64 (m, 3H, CH<sub>2</sub>-C(CH<sub>3</sub>)). Anal. Found (Anal. Calcd.): C, 47.69 (49.21); H, 6.89 (6.69); O, 13.08 (10.09); N, 8.10 (8.83); Br 23.64 (25.18).

### 2.4. Anion exchange reactions

The anion exchange reactions for PILs (Scheme 1) and IL monomers (see Supplementary data Scheme S1) were performed in water. A general procedure for the preparation of PILs by anion exchange with poly(MEBIm-Br) is given as follows: 3.16 g (2.87 × 10<sup>-2</sup> mol) NaBF<sub>4</sub> was dissolved in 10 mL of DI water and this solution was then added dropwise into 1.01 g poly(MEBIm-Br) aqueous solution with an anion mole ratio of BF<sub>4</sub>/Br = 9/1 mol/mol. The resulting water-insoluble polymer, poly(MEBIm-BF<sub>4</sub>), precipitated out of the water phase immediately. The reaction mixture was stirred for 48 h, followed by re-precipitating and washing in fresh DI water for 72 h. Silver nitrate testing showed that the Br anion was present in the aqueous phase immediately after the exchange reaction, but no AgBr precipitated after the washing step. The resulting anion exchanged PIL was dried in vacuum oven for at least 24 h. A similar procedure was carried out with other salts, LiTFSI, LiTf, and LiPF<sub>6</sub>, to produce poly(MEBIm-TFSI), poly(MEBIm-Tf), and poly(MEBIm-PF<sub>6</sub>), respectively. <sup>1</sup>H NMR and elemental analysis results for all four PIL samples are shown below, where a residual amount of Br was present in each sample (<4 mol%). <sup>1</sup>H NMR (UNITYINOVA 500 MHz, DMSO-*d*<sub>6</sub>, ppm) and elemental analysis: poly(MEBIm-BF<sub>4</sub>): 9.11 (s, 1H, N-CH=N), 7.70–7.78 (d, 2H, N-CH=

CH-N), 4.20–4.48 (m, 6H, N-CH<sub>2</sub>-CH<sub>2</sub>-O, N-CH<sub>2</sub>-CH<sub>2</sub>-CH<sub>2</sub>), 1.79 (s, 4H, CH<sub>2</sub>-C(CH<sub>3</sub>), N-CH<sub>2</sub>-CH<sub>2</sub>-CH<sub>2</sub>-CH<sub>3</sub>), 1.28 (s, 5H, N-CH<sub>2</sub>-CH<sub>2</sub>-CH<sub>2</sub>-CH<sub>3</sub>, CH<sub>2</sub>-C(CH<sub>3</sub>)), 0.90 (s, 6H, N-CH<sub>2</sub>-CH<sub>2</sub>-CH<sub>2</sub>-CH<sub>3</sub>, CH<sub>2</sub>-C(CH<sub>3</sub>)), 0.40–0.66 (m, 3H, CH<sub>2</sub>-C(CH<sub>3</sub>)). Anal. Found (Anal. Calcd.): F, 21.15 (20.76); Br, 0.51 (0). poly(MEBIm-TFSI): 9.18 (s, 1H, N-CH=N), 7.66–7.78 (d, 2H, N-CH=CH-N), 4.19–4.47 (m, 6H, N-CH<sub>2</sub>-CH<sub>2</sub>-O, N-CH<sub>2</sub>-CH<sub>2</sub>-CH<sub>2</sub>), 1.78 (s, 4H, CH<sub>2</sub>-C(CH<sub>3</sub>), N-CH<sub>2</sub>-CH<sub>2</sub>-CH<sub>2</sub>-CH<sub>3</sub>), 1.27 (s, 5H, N-CH<sub>2</sub>-CH<sub>2</sub>-CH<sub>2</sub>-CH<sub>3</sub>, CH<sub>2</sub>-C(CH<sub>3</sub>)), 0.90 (s, 6H, N-CH<sub>2</sub>-CH<sub>2</sub>-CH<sub>2</sub>-CH<sub>3</sub>, CH<sub>2</sub>-C(CH<sub>3</sub>)), 0.44–0.71 (m, 3H, CH<sub>2</sub>-C(CH<sub>3</sub>)). Anal. Found (Anal. Calcd.): F, 21.09 (22.02); Br, < 0.25 (0). poly(MEBIm-Tf): 9.19 (s, 1H, N-CH=N), 7.74–7.81 (d, 2H, N-CH=CH-N), 4.20–4.50 (m, 6H, N-CH<sub>2</sub>-CH<sub>2</sub>-O, N-CH<sub>2</sub>-CH<sub>2</sub>-CH<sub>2</sub>), 1.79 (s, 4H, CH<sub>2</sub>-C(CH<sub>3</sub>), N-CH<sub>2</sub>-CH<sub>2</sub>-CH<sub>2</sub>-CH<sub>3</sub>), 1.28 (s, 5H, N-CH<sub>2</sub>-CH<sub>2</sub>-CH<sub>2</sub>-CH<sub>3</sub>, CH<sub>2</sub>-C(CH<sub>3</sub>)), 0.89 (s, 6H, N-CH<sub>2</sub>-CH<sub>2</sub>-CH<sub>2</sub>-CH<sub>3</sub>, CH<sub>2</sub>-C(CH<sub>3</sub>)), 0.42–0.69 (m, 3H, CH<sub>2</sub>-C(CH<sub>3</sub>)). Anal. Found (Anal. Calcd.): F, 14.47 (14.75); Br, 0.81 (0). poly(MEBIm-PF<sub>6</sub>): 9.11 (s, 1H, N-CH=N), 7.64–7.75 (d, 2H, N-CH=CH-N), 4.18–4.43 (m, 6H, N-CH<sub>2</sub>-CH<sub>2</sub>-O, N-CH<sub>2</sub>-CH<sub>2</sub>-CH<sub>2</sub>), 1.78 (s, 4H, CH<sub>2</sub>-C(CH<sub>3</sub>), N-CH<sub>2</sub>-CH<sub>2</sub>-CH<sub>2</sub>-CH<sub>3</sub>), 1.28 (s, 5H, N-CH<sub>2</sub>-CH<sub>2</sub>-CH<sub>2</sub>-CH<sub>3</sub>, CH<sub>2</sub>-C(CH<sub>3</sub>)), 0.90 (s, 6H, N-CH<sub>2</sub>-CH<sub>2</sub>-CH<sub>2</sub>-CH<sub>3</sub>, CH<sub>2</sub>-C(CH<sub>3</sub>)), 0.43–0.66 (m, 3H, CH<sub>2</sub>-C(CH<sub>3</sub>)). Anal. Found (Anal. Calcd.): F, 28.47 (29.81); Br, 0.57 (0).

### 2.5. Characterization

<sup>1</sup>H NMR spectra were collected using a UNITYINOVA 500 MHz spectrometer at room temperature with DMSO-*d*<sub>6</sub> as the solvent. Elemental analysis was conducted at Atlantic Microlab, Inc. in Norcross, GA. The infrared spectra were collected at room temperature using a Fourier transform infrared spectroscopy (FTIR) spectrometer (Nicolet 6700 Series; Thermo Electron) equipped with a single-reflection ATR attachment (Specac, Inc., Silver Gate™, zinc selenide crystal). The molecular weights of PILs were determined by gel permeation chromatography (GPC) at 40 °C using a Waters GPC system (breeze 2) equipped with two Styragel columns (Styragel@HR 3 and Styragel@HR 4) and a 2414 reflective index (RI) detector. PILs were dissolved in a mixture of DMF and 0.05 M LiBr. GPC measurements were performed at a flowrate of 1.0 mL/min at 40 °C using polyethylene glycol/polyethylene oxide (PEG/PEO) as standards. Thermal degradation temperatures (*T*<sub>d</sub>) were measured by thermal gravimetric analysis (TGA, TA Instruments, Q50) at a heating rate of 10 °C/min under nitrogen environment. Glass transition temperatures (*T*<sub>g</sub>) were measured with a differential scanning calorimeter (DSC) (TA Instruments, Q2000) under nitrogen environment (50 mL/min) using the method of heat/cool/heat at the same rate of 10 °C/min over a temperature range of -40 to 180 °C. The *T*<sub>g</sub> was determined using the mid-point method on the second heating cycle thermogram. Ionic conductivity of PIL films and IL monomers was measured with an AC impedance system (Solartron, 1260 impedance analyzer, 1287 electrochemical interface, Zplot software) between 10<sup>2</sup> Hz and 10<sup>6</sup> Hz. PIL films with thickness ranging between 100 and 400 μm were prepared by solution casting from acetonitrile on Teflon Petri dishes at ambient conditions. The films were dried in a fume hood at room temperature and films were cut to ~30 mm × 5 mm before they were completely dried. The polymer films were further dried under vacuum at 120 °C for at least 24 h, and then stored in a desiccator until use. The conductivity of IL monomers and PILs was measured in a cell with four-parallel electrodes (four-point method) in an environmental chamber (Tenney, BTRS model) with controlled temperature at the fixed relative humidity of 10%. An alternating current was applied to the outer electrodes and the real impedance or resistance, *R*, was measured between the two inner reference electrodes. Resistance was determined from the *x*-intercept of the imaginary versus real impedance data over a high frequency range. The conductivity

values were calculated from the equation  $\sigma = L/AR$ , where  $\sigma$  is conductivity (S/cm) and  $L$  and  $A$  are the distance between two inner electrodes and cross section area of the polymer film ( $A = Wl$ ,  $W$  is the film strip width and  $l$  is the film thickness), respectively. For conductivity experiments, samples were equilibrated for 2 h at each temperature followed by 12 measurements over 3 h taken over 15 min increments. The values reported are an average of these steady-state measurements. Measurements for PIL films and IL monomers were carried out in a Teflon-coated stainless steel cell and a solid Teflon well-like cell, respectively. More details on these two cells and experimental procedures can be found elsewhere [18]. A small amount of di-*tert*-butyl-4-methylphenol (inhibitor) was added into the cell with the IL monomers to prevent polymerization during conductivity experiments.

### 3. Results and discussion

#### 3.1. Synthesis and chemical characterization of anion exchanged PILs

The synthesis of the IL monomer, MEBIm-Br, is shown in Scheme 1. The resulting IL monomer was a water-soluble clear viscous liquid. The homopolymer, poly(MEBIm-Br), was synthesized by conventional free radical polymerization (also shown in Scheme 1). This resulting polymer was soluble in water or methanol, but not soluble in acetone or diethyl ether. Thus, in this work, poly(MEBIm-Br) was chosen as the PIL precursor to exchange with other anions in water. A general anion exchange reaction scheme is also shown in Scheme 1. The chemical structures of the anion exchanged PILs were confirmed by chemical shifts in the  $^1\text{H}$  NMR spectra as listed in Table 1, e.g., from 9.97 ppm (N-CH=N of poly(MEBIm-Br)) to 9.11 ppm (N-CH=N of poly(MEBIm-BF<sub>4</sub>)). The  $^1\text{H}$  NMR spectra shown in Fig. 1 also indicate that the C(2)-proton peak (9.97 ppm) associated with Br anion is not present in exchanged PILs, suggesting that Br has been replaced with a new anion and the amount of Br was reduced to a low level that was not detectable by  $^1\text{H}$  NMR. Further, elemental analysis shows that the halide residue was negligibly small in the resulting anion exchanged PILs (<4 mol %). This data provides evidence that anion exchange reactions in water resulted in nearly fully exchanged PILs.

Fig. 2 shows the IR spectra for the exchanged PILs at ambient conditions. The characteristic infrared bands found in this study (BF<sub>4</sub>, 1046, 1011 cm<sup>-1</sup>; TFSI, 1346, 1130 cm<sup>-1</sup>; Tf, 1025, 755 cm<sup>-1</sup>; PF<sub>6</sub>, 810 cm<sup>-1</sup>) are consistent with literature (BF<sub>4</sub>, 1045, 1015 cm<sup>-1</sup> [19]; TFSI, 1348, 1136 cm<sup>-1</sup> [20]; Tf, 1032, 755 cm<sup>-1</sup> [21,22]; PF<sub>6</sub>, 808 cm<sup>-1</sup> [20]). Note that at the ambient conditions, there is significant amount of water (O-H stretching band at 3407 cm<sup>-1</sup>) in the precursor, poly(MEBIm-Br), while there is a negligible amount of water in the exchanged PILs.

Molecular weight and distribution of polyelectrolytes is often measured by GPC with a small amount of salt added to screen electrostatic repulsions and therefore minimize polymer chain aggregation [23]. In this work, results from dynamic light scattering (DLS) indicate that the addition of LiBr salt reduced the aggregation

of the PILs in DMF, where there was a monomodal distribution of hydrodynamic size at 0.05 M LiBr salt concentration (see Supplementary data Fig. S2a). A bimodal distribution in hydrodynamic size was observed without the addition of salt (see Supplementary data Fig. S2b). Fig. 3 shows the GPC chromatograms for PILs measured in this study, where monomodal peaks were observed indicating good separation with 0.05 M LiBr salt concentration. In literature, both PS [24] and PEG/PEO [25] have been used as standards for molecular weight measurements on polyelectrolytes. Table 2 lists the molecular weight average and distribution of PILs against both PS and PEG/PEO standards, respectively. Interestingly, the molecular weight average and distribution against PS standards are much higher and narrower than those against PEG/PEO standards. The polydispersities against PS standards ranged from 1.21 to 1.31 and are much smaller than what is typically observed for polymers synthesized by free radical polymerization. The reason for this is that there is a significant interaction between PS and the Styragel packing materials (crosslinked poly(styrene-divinylbenzene) particles) in the DMF solvent [26,27]. As a result, the elution time for polystyrene becomes longer (see Supplementary data Fig. S3). Thus, the molecular weight averages and polydispersities against PS standards are often significantly larger than their true values. In contrast, polydispersity values against the PEG/PEO standards give more reasonable values, ranging from 2.45 to 2.77. This indicates that molecular weights of PILs measured against PEG/PEO standards are closer to their true molecular weights when compared to PS standards, which interact with column packing materials.

#### 3.2. Thermal properties of PILs

Fig. 4 shows the thermal stability of PILs characterized by TGA under nitrogen environment. The thermal decomposition temperatures ( $T_d$ ) of PILs were measured at 5% loss and are listed in Table 3. The precursor PIL with Br anion has the lowest decomposition temperature of all PILs ( $T_d = 534$  K), while the TFSI-exchanged PIL has the highest decomposition temperature ( $T_d = 636$  K). The overall thermal stability of these PILs scales with anion type as: Br < PF<sub>6</sub> < BF<sub>4</sub> < Tf < TFSI. The order of relative stability follows a similar trend reported in literature for ILs [28–30] suggesting that the decomposition temperature of the PIL is strongly dependant on the anion type. With respect to the decomposition mechanism, it is generally accepted that the nucleophilicity of an anion affects the thermal stability and a low decomposition temperature associated with a halide anion is attributed to the attack of highly nucleophilic halide on the primary alkyl group via an S<sub>N</sub>2 reaction with an alkyl halide as a byproduct [31]. As compared with Br anion, it is well known that other anions are more thermally stable than halides. However, the detailed decomposition mechanism for these are still not well understood. For example, the TFSI anion is a weak or non-nucleophilic anion and one possible pathway for the decomposition of the TFSI anion is that it undergoes degradation via sulfur dioxide release instead of dealkylation or proton transfer [32], which makes it more difficult to thermally decompose. Also, from Fig. 4, it is clear that PILs paired with PF<sub>6</sub>, BF<sub>4</sub>, Tf, and TFSI anions undergo a one-step thermal decomposition, while the precursor PIL paired Br appears to undergo a two-step thermal decomposition. The two-step decomposition agrees with the work of Vygodskii et al. [33] For the poly(MEBIm-Br), the first thermal decomposition step ( $T_d = 261$  °C) can be attributed to the degradation of the Br anion, while the second decomposition step at ~ 340 °C is in good agreement with the thermal decomposition temperature of poly(vinylimidazole) ( $T_d \sim 335$  °C) [34].

The glass transition temperatures ( $T_g$ ) of the PILs as a function of anion type are listed in Table 3. For the same polymer chain length, the  $T_g$  values follow the following order: Br > PF<sub>6</sub> > BF<sub>4</sub> > Tf > TFSI.

**Table 1**  
Chemical shifts in  $^1\text{H}$  NMR spectra for PILs.

PIL	N-CH=N (ppm)	N-CH=CH-N (ppm)
Poly(MEBIm-Br)	9.97	8.10, 8.17
Poly(MEBIm-BF <sub>4</sub> )	9.11	7.70, 7.78
Poly(MEBIm-TFSI)	9.18	7.66, 7.78
Poly(MEBIm-Tf)	9.19	7.74, 7.81
Poly(MEBIm-PF <sub>6</sub> )	9.11	7.64, 7.75

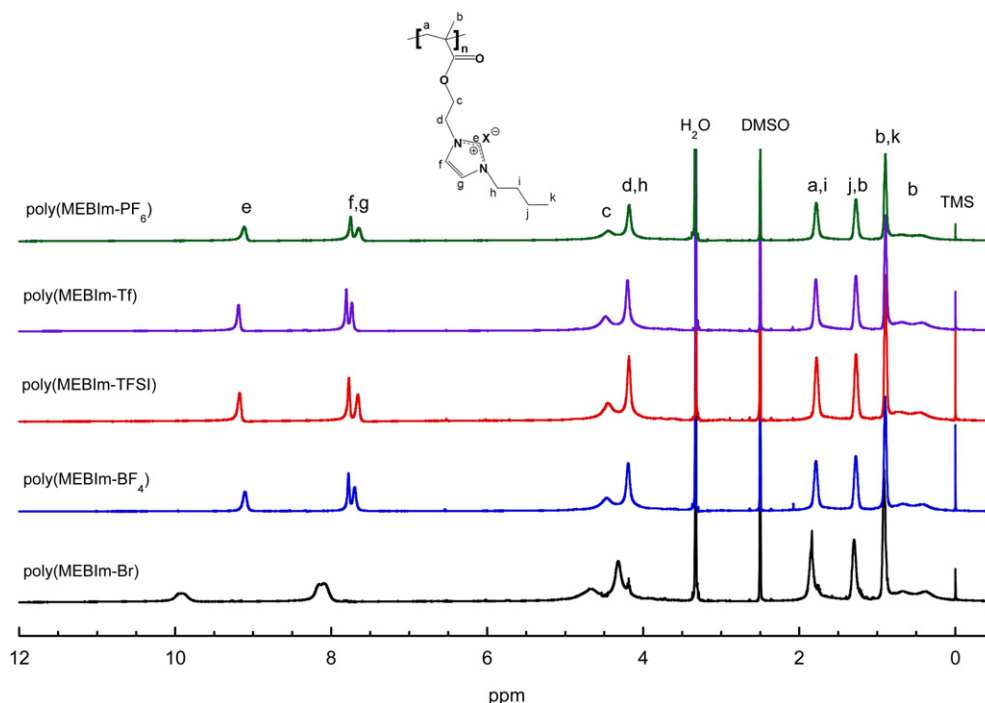


Fig. 1.  $^1\text{H}$  NMR spectra of the PIL precursor and anion exchanged PILs. X on figure represents the corresponding anion.

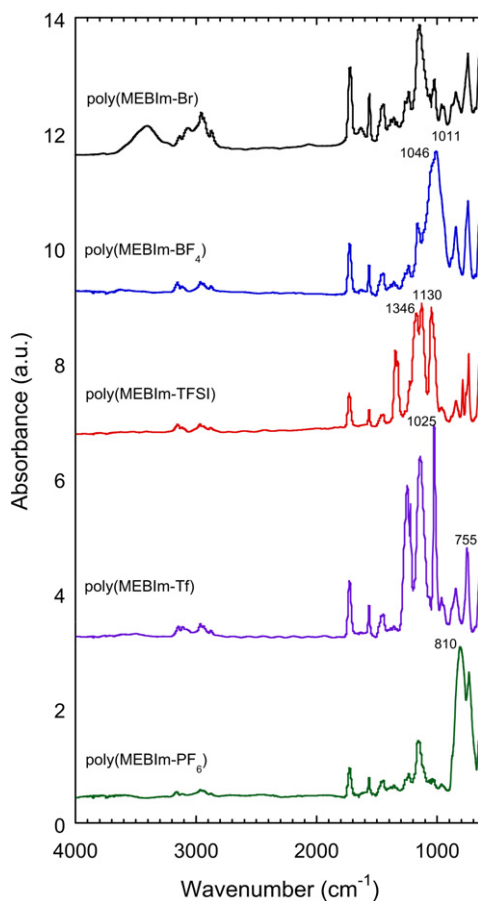


Fig. 2. Infrared spectra of PILs at ambient conditions. Spectra offset for clarity.

Overall, there is a 95 K depression in  $T_g$  from poly(MEBIm-Br) ( $T_g = 375$  K) to poly(MEBIm-TFSI) ( $T_g = 280$  K). Therefore by removing the effect of polymer chain length (each PIL has the same degree of polymerization), the value of  $T_g$  here is largely dependent on the plasticizing effect of the anion. In particular, the TFSI anion has a more significant impact on  $T_g$  depression compared to other anions, such as Tf and  $\text{BF}_4$ . This can be attributed to not only the difference in size, but also lower symmetry, extensive charge delocalization [35], and the flexibility of the TFSI anion [36]. Also, in the temperature range from 233 K to 573 K, no melting behavior

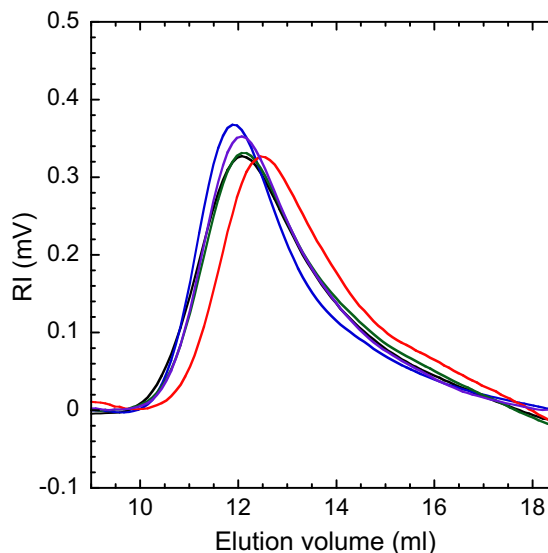


Fig. 3. GPC chromatograms for PILs using DMF columns: poly(MEBIm-Br) (black), poly(MEBIm- $\text{BF}_4$ ) (blue), poly(MEBIm- $\text{PF}_6$ ) (green), poly(MEBIm-Tf) (magenta), poly(MEBIm-TFSI) (red). (For interpretation of the references to color in this figure legend, the reader is referred to the web version of this article).

**Table 2**  
Molecular weights and polydispersities of PILs.

PIL	PEG/PEO standard		PS standard	
	$M_w$	PDI	$M_w$	PDI
Poly(MEBIm–Br)	58,700	2.56	367,000	1.30
Poly(MEBIm–BF <sub>4</sub> )	61,100	2.77	427,000	1.27
Poly(MEBIm–TFSI)	43,080	2.54	312,000	1.21
Poly(MEBIm–Tf)	56,680	2.45	356,000	1.32
Poly(MEBIm–PF <sub>6</sub> )	54,970	2.53	340,000	1.32

was observed for all of these PILs, which suggests that these PILs are amorphous in nature.

### 3.3. Ionic conductivity

Fig. 5a shows the measured ionic conductivities of PILs as a function of temperature. Note that the precursor polymer, (poly (MEBIm–Br)), is water soluble and thus only the hydrophobic PILs are compared here under dry conditions (10% RH). The conductivities of the PILs follow the order: TFSI > Tf > BF<sub>4</sub> > PF<sub>6</sub>, which is the reverse order of  $T_g$  shown in Table 3. These results suggest that polymer chain relaxation plays a dominant role in ion transport. Specifically, the PIL with TFSI is significantly higher in ionic conductivity compared to the other PILs and this coincides with the significantly lower  $T_g$  (Table 3). Also, with increasing temperature, the difference in ionic conductivity between PILs with different anions decreases, suggesting that at a high temperature the importance of  $T_g$  becomes less pronounced.

Compared to the PILs, the IL monomers provide an upper limit of ionic conductivity since the restriction of polymer chain relaxation is eliminated and a large number of ions and their counter ions are available for ion transport. Fig. S4 (see Supplementary data) shows that the ionic conductivity of the IL monomers is approximately two to three orders of magnitude higher than their corresponding PILs. The conductivities of the IL monomers follow the order: TFSI > BF<sub>4</sub> > Tf > PF<sub>6</sub>, where the difference in conductivity for TFSI compared to the other anions is not as significant compared to the

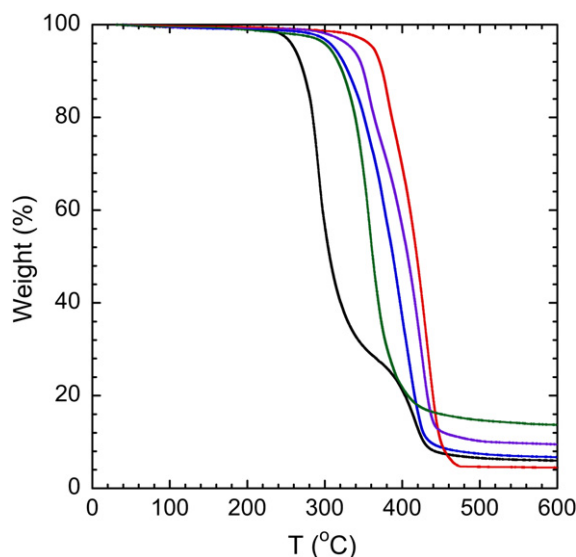


**Fig. 4.** Thermal stability of PILs: poly(MEBIm–Br) (black), poly(MEBIm–BF<sub>4</sub>) (blue), poly(MEBIm–PF<sub>6</sub>) (green), poly(MEBIm–Tf) (magenta), poly(MEBIm–TFSI) (red). (For interpretation of the references to color in this figure legend, the reader is referred to the web version of this article).

**Table 3**  
Thermal degradation temperatures ( $T_d$ ) and glass transition temperatures ( $T_g$ ) of PILs.

PIL	$T_d$ (K)	$T_g$ (K)
Poly(MEBIm–Br)	534	375
Poly(MEBIm–BF <sub>4</sub> )	586	358
Poly(MEBIm–TFSI)	636	280
Poly(MEBIm–Tf)	608	337
Poly(MEBIm–PF <sub>6</sub> )	579	367

PILs. Also, the order in conductivity differs from the PILs, where the differences in  $T_g$  (see Supplementary data Table S4) are minor compared to the PILs; maximum difference of 11 K for the IL monomers compared to 95 K for the PILs. Unlike the glass transition-dependant PIL system, the IL monomer conductivity differences are dictated by other factors; most probably liquid viscosity, which has been shown by many other investigators for common ILs [37,38].

The glass transition dependence for the PIL system can be seen more clearly in Fig. 5b, where conductivity is plotted versus a normalized temperature,  $T_g/T$ . However, the data does not collapse onto one single curve. This suggests that other factors in addition to  $T_g$  can impact ion transport. After normalizing for  $T_g$ , poly(MEBIm–TFSI) has the lowest conductivity, where it shows the highest conductivity in Fig. 5a (before normalization). The differences in conductivity may be attributed to the symmetry and size of the anions and the dissociation energy of the ion pairs, where the PILs with BF<sub>4</sub> and PF<sub>6</sub> have the highest conductivities when the effects of  $T_g$  are removed [39].

#### 3.3.1. VFT regression

For a solid polymer electrolyte system, the temperature dependent ionic conductivity is often regressed to the Vogel-Fulcher-Tammann (VFT) equation [40–42]:

$$\sigma(T) = \sigma_0 \exp\left(-\frac{b}{T - T_0}\right) \quad (1)$$

where  $\sigma_0$  (S cm<sup>-1</sup>) is the infinite temperature conductivity,  $b$  (K) is a constant that can be related to the Arrhenius activation energy, and  $T_0$  (K) is the Vogel temperature.  $T_0$  has been interpreted as the temperature at which the configurational entropy vanishes, [43] the polymer relaxation time becomes infinite, [44] or the mobility of ions goes to zero [45] and is typically ~ 50 K below the measured  $T_g$  of the polymer [46]. The physical meaning of the VFT equation is not straightforward, but has been explained in terms of the free volume model [47] and the configurational entropy model [43]. Fig. 6a shows the temperature dependant ionic conductivity for the PILs regressed to the VFT equation (solid lines), which requires three fitting parameters (regressed values listed in Table 4).

Alternatively, Eq. (1) can be recast into the following form:

$$\sigma(T) = \sigma(T_r) \exp\left(-b \left(\frac{1}{T - T_0} - \frac{1}{T_r - T_0}\right)\right) \quad (2)$$

where  $\sigma(T_r)$  is the conductivity at a reference temperature,  $T_r$ . In this study, we choose an experimentally measured value for the reference temperature,  $T_r = T_g + 50$  K. The introduction of  $T_r$  in Eq. (2) reduces the number of fitting parameters in the VFT equation from three to two,  $b$  and  $T_0$ . Fig. 6b shows the PIL conductivity data regressed to Eq. (2), where the resulting fitting constants are also listed in Table 4. Interestingly, the three-parameter regression results in  $T_g - T_0$  values close to the expected 50 K, whereas the two-parameter regression results in  $T_g - T_0$  values that are much larger (ranging from 116 to 146 K).



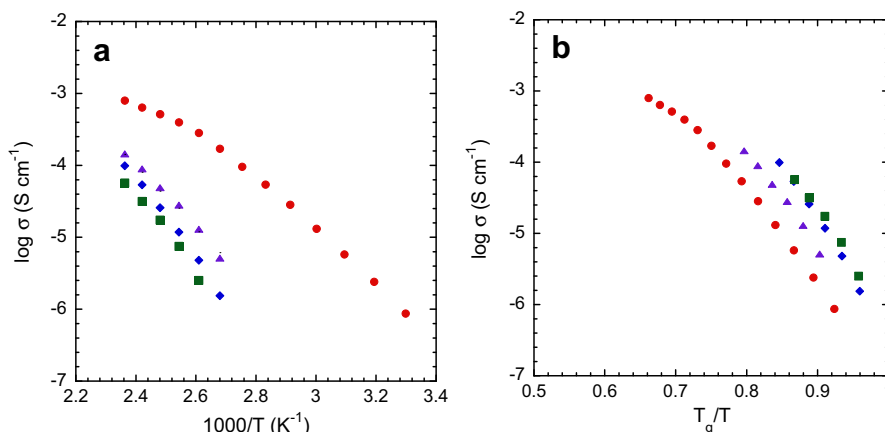


**Fig. 5.** Ionic conductivity versus (a)  $1000/T$  ( $K^{-1}$ ) and (b)  $T_g/T$  of PILs: poly(MEBIm-BF<sub>4</sub>) (blue diamonds), poly(MEBIm-PF<sub>6</sub>) (green squares), poly(MEBIm-Tf) (magenta triangles), poly(MEBIm-TFSI) (red circles). (For interpretation of the references to color in this figure legend, the reader is referred to the web version of this article).

### 3.3.2. WLF regression

The temperature dependence of ionic conductivity for solid polymer electrolytes (e.g., Li salt-poly(ethylene oxide) (PEO) mixtures) can also be regressed to the Williams-Landel-Ferry (WLF) equation:

$$\log\left(\frac{\sigma(T)}{\sigma(T_g)}\right) = \frac{C_1^g(T - T_g)}{C_2^g + (T - T_g)} \quad (3)$$

where  $\sigma(T)$  and  $\sigma(T_g)$  are the conductivities at a given temperature,  $T$ , and the glass transition temperature,  $T_g$ , and  $C_1^g$  and  $C_2^g$  (K) are fitting parameters. Similarly, the WLF equation can be recast in terms of an experimentally measurable reference temperature,  $T_r$ :

$$\log\left(\frac{\sigma(T)}{\sigma(T_r)}\right) = \frac{C_1^r(T - T_r)}{C_2^r + (T - T_r)} \quad (4)$$

where  $C_1^g$  and  $C_2^g$  in Eq. (3) can be related to  $C_1^r$  and  $C_2^r$  with the following equations:

$$C_1^g = \frac{C_1^r C_2^r}{C_2^r + (T_g - T_r)} \quad (5)$$

$$C_2^g = C_2^r + T_g - T_r \quad (6)$$

Fig. 7 shows a master regression of all the PIL conductivity data to the modified WLF equation (Eq. (4)) and Table 5 lists the regressed values,  $C_1^r$  and  $C_2^r$ , from this master regression and also each individual PIL (individual regressions not shown here). Table 5 also lists the  $C_1^g$  and  $C_2^g$  values calculated from Eqs. (5) and (6). Note that although the WLF (Eq. (3)) and VFT (Eq. (1)) equations have different origins, they are actually mathematically equivalent, where  $b = 2.303C_1^g C_2^g$  and  $T_0 = T_g - C_2^g$ . Therefore, the  $C_2^g$  and  $2.303C_1^g C_2^g$  values listed in Table 5 determined from the WLF regression are in a good agreement with the  $T_g - T_0$  and  $b$  values listed in Table 4 determined from the two-parameter VFT regression. This analysis confirms the high  $T_g - T_0$  ( $C_2^g$ ) value observed from the two-parameter VFT regression. Actually, the master WLF regression shows that  $C_1^g$  and  $C_2^g$  values are 9.03 and 168 K, respectively, which greatly deviate from the classical values originally obtained from mechanical relaxation of uncharged polymers ( $C_1^g = 17.44$ ,  $C_2^g = 51.6$  K).

Based on the free volume theory developed by Doolittle [48], Williams et al. [46] interpreted the physical meaning of  $C_1^g$  and  $C_2^g$  by relating them to the fractional free volume,  $f$ , and the thermal expansion coefficient,  $\alpha$ , at  $T_g$ .

$$f(T_g) = \frac{B}{2.303 C_1^g} \quad (7)$$

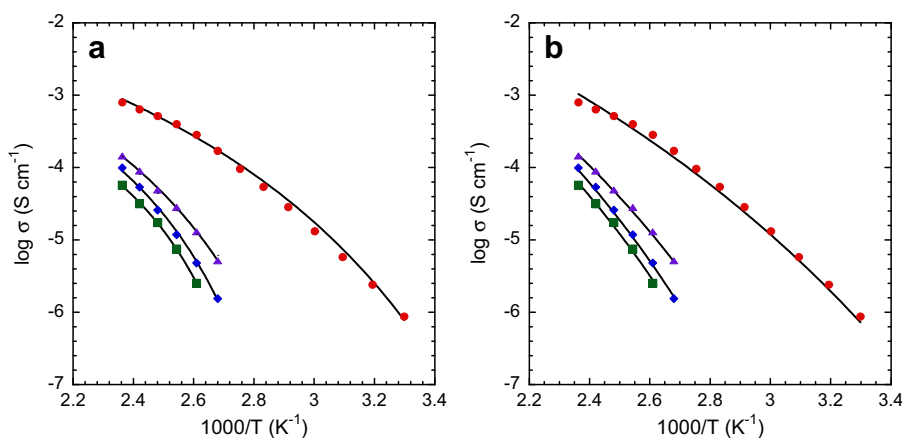


**Fig. 6.** VFT regression of the temperature dependent ionic conductivity of PILs: (a) three-parameter regression (Eq. (1)) and (b) two-parameter regression (Eq. (2)). PILs: poly(MEBIm-BF<sub>4</sub>) (blue diamonds), poly(MEBIm-PF<sub>6</sub>) (green squares), poly(MEBIm-Tf) (magenta triangles), poly(MEBIm-TFSI) (red circles). (For interpretation of the references to color in this figure legend, the reader is referred to the web version of this article).

**Table 4**  
VFT equation regression values of temperature dependent conductivity data for PILs.

PIL	Three-parameter regression (Eq. (1))				Two-parameter regression (Eq. (2))		
	$\sigma_0$ (S cm <sup>-1</sup> )	$b$ (K)	$T_0$ (K)	$T_g - T_0$ (K)	$b$ (K)	$T_0$ (K)	$T_g - T_0$ (K)
Poly(MEBIm-BF <sub>4</sub> )	0.029	302	303	55	2507	220	138
Poly(MEBIm-TFSI)	0.152	466	215	65	2187	164	116
Poly(MEBIm-Tf)	0.061	373	282	55	2323	216	121
Poly(MEBIm-PF <sub>6</sub> )	0.009	232	318	49	2550	221	146

$$\alpha(T_g) = \frac{B}{2.303 C_1^g C_2^g} \quad (8)$$

In Eqs. (7) and (8), we assume  $B = 1$ . Originally, Doolittle also assumed  $B = 1$  [48]. Others have calculated  $B$  from volume-temperature data of polymers (without pressure dependence) and estimated  $B = 0.9 \pm 0.3$  or  $1.6 \pm 0.6$  depending on the estimation method [49]. Most reports, however, have adopted  $B$  equal to unity, including reports on charged polymers [50]. The values for  $f(T_g)$  and  $\alpha(T_g)$ , calculated from the WLF regressed  $C_1^g$  and  $C_2^g$  values, are listed in Table 5, where the fractional free volumes for the PILs are on average double that of what has been classically observed for uncharged polymers ( $f(T_g) = 0.025$ ).

One should note the universal parameters for uncharged polymers ( $C_1^g = 17.44$  and  $C_2^g = 51.6$  K,  $f(T_g) = 0.025$ ) are based on a master regression of data from many polymers. If one were to determine these parameters from regressing data for each polymer individually (data in Ref. [51]), the average and standard deviation of all of these individual regressed values are  $C_1^g = 16.79 \pm 5.43$ ;  $C_2^g = 63.7 \pm 28.1$  K;  $f(T_g) = 0.028 \pm 0.01$ . For our PILs, regressions from both individual polymers and a master regression are listed in Table 5. The average and standard deviation from our individual regressions are  $C_1^g = 7.92 \pm 0.28$ ;  $C_2^g = 131 \pm 13$  K;  $f(T_g) = 0.055 \pm 0.001$ . Therefore, despite the high deviation of the WLF regressed values for uncharged polymers, there is still a significant difference compared to the WLF values obtained in this study on PILs.

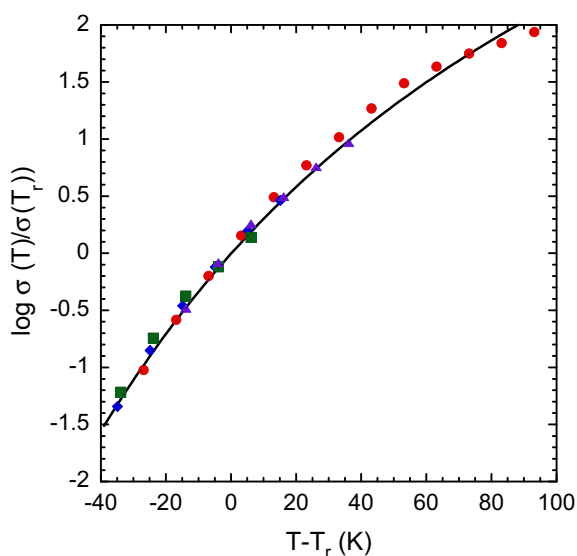


**Fig. 7.** WLF master regression (Eq. (4)) of the temperature dependent ionic conductivity of all PILs: poly(MEBIm-BF<sub>4</sub>) (blue diamonds), poly(MEBIm-PF<sub>6</sub>) (green squares), poly(MEBIm-Tf) (magenta triangles), poly(MEBIm-TFSI) (red circles). (For interpretation of the references to color in this figure legend, the reader is referred to the web version of this article).

**Table 5**  
WLF equation regression values of temperature dependent conductivity data for PILs.

PIL	$C_1^g$	$C_2^g$	$C_1^g$	$C_2^g$	2.303 $C_1^g C_2^g$	$f(T_g)$	$\alpha(T_g)$
Poly(MEBIm-BF <sub>4</sub> )	5.79	188	7.89	138	2508	0.055	$4.0 \times 10^{-4}$
Poly(MEBIm-TFSI)	5.72	166	8.18	116	2185	0.053	$4.5 \times 10^{-4}$
Poly(MEBIm-Tf)	5.75	175	8.05	125	2318	0.054	$4.3 \times 10^{-4}$
Poly(MEBIm-PF <sub>6</sub> )	5.61	196	7.53	146	2532	0.057	$4.0 \times 10^{-4}$
All PILs	6.97	218	9.03	168	3494	0.049	$2.9 \times 10^{-4}$

Understanding the considerable deviation of  $C_1^g$  (9.03) and  $C_2^g$  (168 K) for the PILs studied here compared to classical values determined from uncharged polymers ( $C_1^g = 17.44$  and  $C_2^g = 51.6$  K) is of great interest. WLF constants obtained from charged polymer systems (solid polymer electrolytes) would serve as a better comparison. There are few reports of WLF regressions to PIL conductivity data. However, there are a number of studies that have examined WLF behavior of Li salt-PEO polymer electrolyte systems. The  $C_1^g$  and  $C_2^g$  values were examined as a function of salt type [52], salt concentration [53,54], as well as, polymer chain length [55]. However, there is no universal agreement on the  $C_1^g$  and  $C_2^g$  values for these systems. Although some studies showed that  $C_1^g$  values are close to 17.44 [56] or  $C_2^g$  values are close to 51.6 [57], most studies showed deviations of  $C_1^g$  or  $C_2^g$  from these classical values. Specifically, numerous studies report values for  $C_1^g$  at  $\sim 7$ –12 for the Li salt-PEO system (8.5–10.6 [58], 7.8–12.5 [52], 9.6–11.8 [59], 8.0 [60], 8.1–12.0 [50]). In particular, Watanabe et al. [53] studied the effect of Li salt concentration in PEO on  $C_1^g$  and  $C_2^g$  values, where  $C_1^g$  decreased from 13.5 to 10.1 and  $C_2^g$  increased from 39.4 to 97.9 with increasing salt concentration from 0.015 to 0.062 ([salt]/[EO unit]). However, a detailed explanation for the reason behind these deviations has not yet been presented.

In this work, we report  $C_1^g$  values that are far from uncharged polymers [46]. This suggests a higher fractional free volume at  $T_g$  for PILs. Also, the  $C_2^g$  value for the PILs in this study deviates significantly from both uncharged polymers and the Li salt-PEO charged polymer system, suggesting a lower Vogel temperature (the temperature at which free volume becomes zero). At temperatures below  $T_g$ , the interaction of the bulky cation and anion in imidazolium-based PILs results in increased free volume due to the impact of steric hindrance on polymer chain packing [61]. It is interesting to note that the typical Li salt-PEO systems investigated has a salt concentration on the order of 0.1 mol Li salt/mol EO repeat unit, whereas the PIL system in this study has an ionic concentration on the order of 1 mol IL salt/mol MMA repeat unit. It is also important to note that Li salt-PEO systems is PEO doped with a Li salt, where both cation (Li) and anion (e.g., TFSI) are both mobile compared to the PIL in this study, where the cation is tethered to the polymer backbone and therefore is a single anion conductor. Therefore, these results suggest that the higher ion concentration and tethered cations (single anion conductor) in PILs may be key factors that result in lower Vogel temperatures compared to salt doped polymer electrolytes.

#### 4. Conclusions

In this study, imidazolium-based PIL single ion conductors of constant average chain length were paired with different anions, BF<sub>4</sub>, TFSI, Tf, and PF<sub>6</sub>, at the polymer stage to solely explore the effect of anion type on the chemical structures, thermal properties, and ion conduction. Chemical analysis confirms that the anion exchange reactions for both PILs and IL monomers in water resulted in nearly fully exchanged PILs and IL monomers. GPC results show that the molecular weights of PILs measured against PEG/PEO

standards are closer to their true molecular weights when compared to PS standards, which interact with column packing materials. Anion type had a significant effect on the degradation and glass transition temperatures, where poly(MEBIm–TFSI) had the highest degradation temperature and the lowest glass transition temperature, indicating a much wider operating temperature window for practical applications. The ionic conductivity of PILs scales with the glass transition temperature, where poly(MEBIm–TFSI) had a significantly lower glass transition temperature and a significantly higher ionic conductivity compared with PILs exchanged with other anions. Ion transport was also influenced by other factors, including the size and symmetry of the anion and dissociation energy of the ion pair.

The temperature dependent ionic conductivity of all PILs studied follows VFT behavior. Interestingly, the results obtained from a three-parameter VFT regression were different from those obtained from a two-parameter VFT regression, where the latter was consistent with the results obtained from a mathematically equivalent WLF regression. The  $C_1^g$  (9.03) and  $C_2^g$  (168 K) values obtained from the WLF regression for these PILs deviate significantly from the classical values obtained from the mechanical relaxation of uncharged polymers ( $C_1^g = 17.44$ ,  $C_2^g = 51.6$  K). The fractional free volume for the PILs at the glass transition temperature, calculated from  $C_1^g$  value, was on average double that of what has been classically observed for uncharged polymers. While  $C_1^g$  value obtained here for PIL single ion conductors was close to some Li salt-PEO charged polymer systems, the  $C_2^g$  value was significantly higher than any other charged polymer systems reported in the literature. This suggests that the salt or ionic concentration in charged polymers can affect free volume and the Vogel temperature ( $T_0 = T_g - C_2^g$ ), where ion mobility at temperatures farther below the glass transition temperature can be achieved at higher salt or ionic concentrations in single ion conductors. Therefore, anion type and salt or ion concentration are two key parameters that can be tuned to affect the temperature dependent ionic conductivity in PILs.

## Acknowledgments

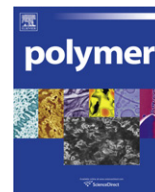
The authors gratefully acknowledge the financial support of the U.S. Army Research Office under Grant W911NF-07-1 0452; Ionic Liquids in Electro-Active Devices (ILEAD) MURI.

## Appendix. Supplementary data

Supplementary data associated with this article can be found online at doi:10.1016/j.polymer.2011.01.031. <http://www.elsevier.com/>.

## References

- [1] Green O, Grubjesic S, Lee S, Firestone MA. *Polym Rev* 2009;49:339–60.
- [2] Armand M, Endres F, MacFarlane DR, Ohno H, Scrosati B. *Nat Mater* 2009;8:621–9.
- [3] Hirao M, Ito K, Ohno H. *Electrochim Acta* 2000;45:1291–4.
- [4] Ohno H, Yoshizawa M, Ogihara W. *Electrochim Acta* 2004;50:255–61.
- [5] Shovskiy A, Varga I, Makuska R, Claesson PM. *Langmuir* 2009;25:6113–21.
- [6] Chen H, Choi JH, Salas-de la Cruz D, Winey KI, Elabd YA. *Macromolecules* 2009;42:4809–16.
- [7] Bhowmik PK, Burchett RA, Han H, Cebe JJ. *J Polym Sci Part A Polym Chem* 2001;39:2710–5.
- [8] Yoshizawa M, Ohno H. *Chem Lett* 1999;28:889–90.
- [9] Yoshizawa M, Ohno H. *Electrochim Acta* 2001;46:1723–8.
- [10] Ohno H, Ito K. *Chem Lett* 1998;27:751–2.
- [11] Ohno H, Nakai Y, Ito K. *Chem Lett* 1998;27:15–6.
- [12] Matsumi N, Sugai K, Miyake M, Ohno H. *Macromolecules* 2006;39:6924–7.
- [13] Brylev O, Alloin F, Duclot M, Souquet JL, Sanchez JY. *Electrochim Acta* 2003;48:1953–9.
- [14] Vygodskii YS, Shaplov AS, Lozinskaya EI, Filippov OA, Shubina ES, Bandari R, et al. *Macromolecules* 2006;39:7821–30.
- [15] Sato T, Marukane S, Narutomi T, Akao T. *J Power Sources* 2007;164:390–6.
- [16] Marcilla R, Blazquez JA, Rodriguez J, Pomposo JA, Mecerreyes D. *J Polym Sci Part A Polym Chem* 2004;42:208–12.
- [17] Collins KD. *Biophys J* 1997;72:65–76.
- [18] Gwee L. Ph.D. dissertation. Drexel University; June 2010.
- [19] Holomb R, Martinelli A, Albinsson I, Lassègues JC, Johansson P, Jacobsson P. *J Raman Spectrosc* 2008;39:793–805.
- [20] Seki T, Grunwaldt JD, Baiker A. *J Phys Chem B* 2009;113:114–22.
- [21] Sanders RA, Frech R, Khan MA. *J Phys Chem B* 2003;107:8310–5.
- [22] Iwahashi T, Miyamae T, Kanai K, Seki K, Kim D, Ouchi Y. *J Phys Chem B* 2008;112:11936–41.
- [23] Domard A, Rinaudo M, Rochas C. *J Polym Sci Polym Phys Ed* 1979;17:673–81.
- [24] Schuster M, de Araujo CC, Atanasov V, Andersen HT, Kreuer KD, Maier J. *Macromolecules* 2009;42:3129–37.
- [25] Tang H, Tang J, Ding S, Radosz M, Shen Y. *J Polym Sci Part A Polym Chem* 2005;43:1432–43.
- [26] Dubin P, Koontz S, Wright III KL. *J Polym Sci Polym Chem Ed* 1977;15:2047–57.
- [27] Tokuda T, Mori M, Yamada T. *J Chromatogr A* 1996;722:123–7.
- [28] McEwen AB, Ngo HL, LeCompte K, Goldman JL. *J Electrochem Soc* 1999;146:1687–95.
- [29] Ngo HL, LeCompte K, Hargens L, McEwen AB. *Thermochim Acta* 2000;357–358:97–102.
- [30] Fredlake CP, Crosthwaite JM, Hert DG, Aki SNVK, Brennecke JF. *J Chem Eng Data* 2004;49:954–64.
- [31] Chowdhury A, Thynell ST. *Thermochim Acta* 2006;443:159–72.
- [32] Kroon MC, Buijs W, Peters CJ, Witkamp G. *Thermochim Acta* 2007;465:40–7.
- [33] Vygodskii YS, Mel'nik OA, Shaplov AS, Lozinskaya EI, Malyshkina IA, Gavrilova ND. *Polym Sci Ser A* 2007;49:256–61.
- [34] Chang TC, Wang YT, Hong YS, Chen HB, Yang JC. *Polym Degrad Stabil* 2000;69:317–22.
- [35] Benrabah D, Arnaud R, Sanchez JY. *Electrochim Acta* 1995;40:2437–43.
- [36] Arnaud R, Benrabah D, Sanchez JY. *J Phys Chem* 1996;100:10882–91.
- [37] Okoturo OO, VanderNoot TJ. *J Electroanal Chem* 2004;568:167–81.
- [38] Tokuda H, Tsuzuki S, Susan MABH, Hayamizu K, Watanabe M. *J Phys Chem B* 2006;110:19593–600.
- [39] Fragiadakis D, Dou S, Colby RH, Runt J. *Macromolecules* 2008;41:5723–8.
- [40] Vogel HZ. *Phys* 1921;22:645–6.
- [41] Fulcher GS. *J Am Ceram Soc* 1925;8:339–55.
- [42] Tammann G, Hesse GZ. *Anorg Allg Chem* 1926;156:245–57.
- [43] Adam G, Gibbs JH. *J Chem Phys* 1965;43:139–46.
- [44] Rault J. *J Non-Cryst Solids* 2000;271:177–217.
- [45] Klein RJ, Zhang S, Dou S, Jones BH, Colby RH, Runt J. *J Chem Phys* 2006;124:144903–8.
- [46] Williams ML, Landel RT, Ferry JD. *J Am Chem Soc* 1955;77:3701–7.
- [47] Cohen MH, Turnbull D. *J Chem Phys* 1959;31:1164–9.
- [48] Doolittle AK. *J Appl Phys* 1951;22:1471–5.
- [49] Berry GC, Fox TG. *Adv Polym Sci* 1967;5:261.
- [50] Ikeda Y, Masui H, Matoba Y. *J Appl Polym Sci* 2005;95:178–84.
- [51] Ferry JD. *Viscoelastic properties of polymers*. 3rd ed. Wiley; 1980. pp. 277–89.
- [52] Watanabe M, Itoh M, Sanui K, Ogata N. *Macromolecules* 1987;20:569–73.
- [53] Watanabe M, Ohashi S, Sanui K, Ogata N, Kobayashi T, Ohtaki Z. *Macromolecules* 1985;18:1945–50.
- [54] Carvalho LM, Guegan P, Cheradame H, Gomes AS. *Eur Polym J* 2000;36:401–9.
- [55] Saito M, Ikuta H, Uchimoto Y, Wakihara M, Yokoyama S, Yabe T, et al. *J Electrochem Soc* 2003;150:A726–31.
- [56] Qi L, Lin Y, Jing X, Wang F. *Solid State Ionics* 2001;139:293–301.
- [57] Ikeda Y, Masui H, Matoba Y. *J Appl Polym Sci* 2005;95:178–84.
- [58] Watanabe M, Sanui K, Ogata N. *Macromolecules* 1986;19:815–9.
- [59] Tabata S, Hirakimoto T, Tokuda H, Susan MABH, Watanabe M. *J Phys Chem B* 2004;108:19518–26.
- [60] Wang SJ, Wang B, Li SQ, Peng ZL. *J Radioanal Nucl Chem* 1996;211:127–35.
- [61] Bamford D, Dlubek G, Reiche A, Alam MA, Meyer W, Galvosas P, et al. *J Chem Phys* 2001;115:7260–70.



# Hetero-stereocomplex formation of stereoblock copolymer of substituted and non-substituted poly(lactide)s

Hideto Tsuji\*, Kenta Shimizu, Yuzuru Sakamoto, Ayaka Okumura

Department of Environmental and Life Sciences, Graduate School of Engineering, Toyohashi University of Technology, Tempaku-cho, Toyohashi, Aichi 441-8580, Japan

## ARTICLE INFO

### Article history:

Received 18 October 2010

Received in revised form

13 January 2011

Accepted 18 January 2011

Available online 26 January 2011

### Keywords:

Hetero-stereocomplexation

Poly(lactic acid)

Poly(2-hydroxybutanoic acid)

## ABSTRACT

The crystallization behavior of the stereoblock copolymer of substituted and non-substituted poly(lactide)s, i.e., poly(*D*-2-hydroxybutyrate) and poly(*L*-lactide) chains having the opposite configurations [P(*D*-2HB)-*b*-PLLA] and the reference block copolymer of poly(*D*-2-hydroxybutyrate) and poly(*D*-lactide) chains with the identical configurations [P(*D*-2HB)-*b*-PDLA] was investigated. At the crystallizable temperature range of 60–160 °C, the crystallized P(*D*-2HB)-*b*-PLLA contained solely the hetero-stereocomplex crystallites as a crystalline species, without formation of poly(*D*-2-hydroxybutyrate) or poly(*L*-lactide) homo-crystallites, in contrast with their polymer blends. On the other hand, at the crystallizable temperature range of 60–140 °C, the crystallized P(*D*-2HB)-*b*-PDLA had only PDLA homo-crystallites as crystalline species, reflecting no co-crystallites formation between poly(*D*-2-hydroxybutyrate) and poly(*D*-lactide) chains having the same configurations. The equilibrium melting temperature of hetero-stereocomplex crystallites in P(*D*-2HB)-*b*-PLLA was 189.0 °C, which was higher than 171.3 °C of PDLA homo-crystallites in P(*D*-2HB)-*b*-PDLA. Although the final crystallinity of P(*D*-2HB)-*b*-PLLA was higher than those of P(*D*-2HB)-*b*-PDLA, the spherulite growth rate of P(*D*-2HB)-*b*-PLLA was lower. The regime analysis indicated unusual nucleation mechanism of P(*D*-2HB)-*b*-PLLA.

© 2011 Elsevier Ltd. All rights reserved.

## 1. Introduction

Homo-stereocomplex (HMSC) formation between isotactic and syndiotactic polymers and between *L*- and *D*-polymers (*S*- and *R*-configured polymers) are reported for some polymers including poly(methyl methacrylate), poly(propiolactone), and non-substituted and substituted poly(lactide)s (PLAs) [1,2,3,4,5,6,7]. In the case of PLA, HMSC formation enhances the mechanical performance, heat- and hydrolysis-resistance [1,2,3,4,5,6,7]. Also, the polymers having different chemical structures and the opposite configurations are known to form hetero-stereocomplex (HTSC). Such polymer pairs reported so far are isotactic and syndiotactic vinyl polymers—*isotactic* PMMA and *syndiotactic* poly(isobutyl-methacrylate) [8], optically active and isotactic *S*- and *R*-polyketones-(+)-poly(propylene-carbon monoxide) and (-)-poly(1-butene-carbon monoxide) [9], and optically active and isotactic *S*- and *R*-polyesters—poly(*D*-lactide) (PDLA) and poly(*L*-2-hydroxybutyrate) [10]. HTSC formation between substituted and non-substituted PLAs can be used as a versatile preparation method for biodegradable materials

having a wide range of physical properties and biodegradability [10]. However, with the polymer blending method, the biodegradable materials containing only HTSC crystallites as a crystalline species can be prepared by the crystallization at a limited temperature range from the melt.

On the other hand, stereoblock copolymers of poly(*L*-lactide) (PLLA) and PDLA are known to form HMSC [1,2,3,4,5,11]. The neighboring PLLA and PDLA chains in stereoblock copolymers is reported to facilitate the HMSC formation. However, as far as we are aware, there has been no report for HTSC formation of stereoblock copolymers. In the present study, we first report the HTSC formation of a stereoblock copolymer, i.e., poly(*D*-2-hydroxybutyrate)-*b*-poly(*L*-lactide) [P(*D*-2HB)-*b*-PLLA] (Fig. 1), and the crystallization behavior of P(*D*-2HB)-*b*-PLLA having two types of blocks with different chemical structures and opposite configurations, in comparison with that of poly(*D*-2-hydroxybutyrate)-*b*-poly(*D*-lactide) [P(*D*-2HB)-*b*-PDLA] having two types of blocks with different chemical structures and the identical configurations. The crystallization behavior including HTSC formation was investigated by differential scanning calorimetry (DSC), wide-angle X-ray scattering (WAXS), and polarized optical microscopy (POM). The finding in the present study indicated that the stereoblock copolymerization is a very effective method for HTSC formation, avoiding the formation of P(*D*-2HB) or PLLA homo-crystallites.

\* Corresponding author.

E-mail address: [tsuji@ens.tut.ac.jp](mailto:tsuji@ens.tut.ac.jp) (H. Tsuji).



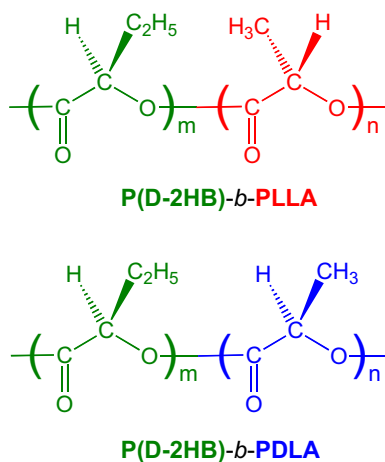


Fig. 1. Molecular structures of P(D-2HB)-b-PLLA and P(D-2HB)-b-PDLA copolymers.

## 2. Experimental part

### 2.1. Materials

Synthesis of P(D-2HB)-b-PLLA and P(D-2HB)-b-PDLA copolymers was performed in bulk according to the procedure reported for the synthesis of PLLA-b-PDLA by Yui et al. [12] and by ourselves [13,14]. A relatively low-molecular-weight poly(D-2-hydroxybutyrate) [P(D-2HB)] prepolymer was synthesized by polycondensation of D-2-hydroxybutanoic acids (hydroxybutyric acids) ( $\geq 97.0\%$ , enantiomeric ratio  $\geq 99:1$ , Sigma-Aldrich Co.) [7,15] and purified [7,16,17] according to the previous literature. Ring-opening polymerization of L- or D-lactide in the presence of stannous octoate (0.03 wt% of lactide) and P(D-2HB) [ $M_w = 1.3 \times 10^4$  g mol $^{-1}$ ,  $M_w$ /number-average molecular weight ( $M_n$ ) = 3.7] as the initiator and coinitiator, respectively, at 140 °C for 10 h [16,17]. L- or D-lactide/P(D-2HB) (w/w) ratio was 1/1, which ratio was determined by repeated experiments for the synthesis of blockcopolymers having the equimolar lactyl and hydroxybutyrate units. During polymerization, P(D-2HB) [melting temperature ( $T_m$ ) = 100 °C] and L- or D-lactide ( $T_m = 95$ –99 °C) were in the melt and dissolved with each other. Also, PLLA and PDLA homopolymers having  $M_w$  of about  $1$ – $2 \times 10^4$  g mol $^{-1}$  were synthesized for evaluating the specific optical rotation values. Synthesized polymers were purified using chloroform and methanol as the solvent and non-solvent, respectively. The synthesized polymers dissolved in chloroform were precipitated into the stirred methanol. The purified polymers were dried under reduced pressure for at least 7 days. For preparation of melt-quenched and crystallized specimens, each of block copolymers was packed in a DSC aluminum cell was sealed in a test-tube under reduced pressure, melted at 200 °C for 3 min, and quenched at 0 °C for 5 min (melt-quenched specimens) or crystallized at

a predetermined  $T_c$  of 50–170 °C for 10 h, and quenched at 0 °C for 5 min (crystallized specimens).

### 2.2. Physical measurements and observation

The  $M_w$  and  $M_n$  of the polymers were evaluated in chloroform at 40 °C with a Tosoh GPC system (refractive index monitor: RI-8020) with two TSK Gel columns (GMH $_{XL}$ ) using polystyrene standards. The 400 MHz  $^1\text{H}$  NMR spectra of synthesized P(D-2HB)-b-PLLA and P(D-2HB)-b-PDLA copolymers were obtained in deuterated chloroform (50 mg mL $^{-1}$ ) by a Bruker Biospin (Yokohama, Japan) AVANCE III 400 Spectrometer using tetramethylsilane as the internal standard. The methine triplet, methylene multiplet, and methyl triplet peaks of P(2HB) segments were observed at around 5.1, 2.0, and 1.0 ppm, respectively [7], whereas the methine quartet and methyl doublet peaks of PLA segments were observed at around 5.2 and 1.6 ppm, respectively. Using the peak areas of methyl groups of PLA and P(2HB) segments, the mol fraction of lactyl monomer units were obtained. The specific optical rotation ( $[\alpha]_{589}^{25}$ ) of the polymers was measured in chloroform at a concentration of 1 g dL $^{-1}$  and 25 °C using a JASCO (Tokyo, Japan) P-2100 polarimeter at a wave length of 589 nm. The mol fractions of lactyl and hydroxybutyrate monomer units of the copolymers ( $x_L$  and  $x_B$ , respectively) were estimated by the flowing two equations:

$$x_L + x_B = 1 \quad (1)$$

$$\begin{aligned} &([\alpha]_{25}^{589} \text{ per gram}) \times (72.1x_L + 86.1x_B) \\ &= \{[\alpha]_{25}^{589}(\text{PLLA or PDLA}) \text{ per mol}\}x_L \\ &+ \{[\alpha]_{25}^{589}[\text{P(D-2HB)}] \text{ per mol}\}x_B \end{aligned} \quad (2)$$

where 72.1 and 86.1 are molecular weights of lactyl and hydroxybutyrate monomer units in the polymer, respectively.  $-1.17 \times 10^4$ ,  $1.16 \times 10^4$ , and  $9.8 \times 10^3$  deg dm $^{-1}$  mol $^{-1}$  cm $^3$  were used for  $[\alpha]_{25}^{589}(\text{PLLA})$  per mol,  $[\alpha]_{25}^{589}(\text{PDLA})$  per mol, P(D-2HB) per mol (Table 1), which are very similar to those reported in the literature [7,10]. The evaluated molecular characteristics of the polymers are shown in Table 1.

The glass transition and cold crystallization ( $T_g$  and  $T_{cc}$ , respectively), melting temperatures of PLLA or PDLA homo-crystallites [ $T_m(\text{PLA})$ ] and HTSC crystallites [ $T_m(\text{SC})$ ], and enthalpies of melting of PLLA or PDLA homo-crystallites [ $\Delta H_m(\text{PLA})$ ] and HTSC [ $\Delta H_m(\text{SC})$ ] of the specimens were determined by a Shimadzu (Kyoto, Japan) DSC-50 differential scanning calorimeter with a cooling cover (LTC-50). The specimens were heated from 0 to 200 °C at a rate of 10 °C min $^{-1}$  under a nitrogen gas flow of 50 mL min $^{-1}$  for DSC measurements. The  $T_g$ ,  $T_{cc}$ ,  $T_m(\text{PLA})$ ,  $T_m(\text{SC})$ ,  $\Delta H_m(\text{PLA})$  and  $\Delta H_m(\text{SC})$  of the specimens were calibrated using tin, indium, and benzophenone as standards. In the present study,  $T_{cc}$  is defined as a peak

Table 1

Characteristics and properties of homopolymers and block copolymers synthesized in the present study.

Code	$M_w^a$ (g mol $^{-1}$ )	$M_w/M_n^a$	$[\alpha]_{25}^{589b}$ (deg dm $^{-1}$ g $^{-1}$ cm $^3$ )	$[\alpha]_{25}^{589}/10^{4b}$ (deg dm $^{-1}$ mol $^{-1}$ cm $^3$ )	$x_L(\text{P})^c$	$x_L(\text{NMR})^c$
P(D-2HB)	$1.3 \times 10^4$	3.7	114	0.98	–	–
PLLA	$1.9 \times 10^4$	1.2	–162	–1.17	–	–
PDLA	$1.6 \times 10^4$	1.9	161	1.16	–	–
P(D-2HB)-b-PLLA	$3.5 \times 10^4$	1.4	–14	–0.11	0.51	0.56
P(D-2HB)-b-PDLA	$3.0 \times 10^4$	1.4	136	1.07	0.52	0.56

<sup>a</sup>  $M_n$  and  $M_w$  are number- and weight-average molecular weights, respectively.

<sup>b</sup> Specific optical rotation.

<sup>c</sup>  $x_L(\text{P})$  and  $x_L(\text{NMR})$  are lactyl unit mol fractions estimated by polarimetry and  $^1\text{H}$  NMR spectroscopy, respectively.

temperature. As stated in the Results and Discussion sections, the melting temperature and enthalpies of P(D-2HB) homo-crystallites were not observed.

The crystallinity of PLLA or PDLA [ $X_c(\text{PLA})$ ] and HTSC [ $X_c(\text{SC})$ ] of isothermally crystallized specimens were estimated by the use of WAXS. As stated in the Results and Discussion sections, the no crystalline diffraction of P(D-2HB) homo-crystallites was observed in the present study, indicating the no significant homo-crystallite formation of P(D-2HB). The WAXS measurements were performed at 25 °C using a RINT-2500 equipped with a Cu-K $\alpha$  source ( $\lambda = 0.1542$  nm), which was operated at 40 kV and 200 mA (Rigaku Co., Tokyo, Japan). In a  $2\theta$  range of 10–25°, the crystalline peak areas for PLLA or PDLA  $\alpha$ - or  $\alpha'$ -form crystallites at  $2\theta$  values around 16.5 and 19° and for HTSC crystallites at  $2\theta$  values around 11, 19.5, and 22.5° relative to the total area between a diffraction profile and a baseline were used to estimate  $X_c(\text{PLA})$  and  $X_c(\text{SC})$ , respectively [2,10]. We did not calculate the crystallinity from the DSC results, because the HTSC crystallites can be formed during DSC heating, as reported previously for the HMSC crystallites in the PLLA/PDLA blend [18], which will disturb the accurate evaluation of  $X_c(\text{PLA})$  and  $X_c(\text{SC})$ .

The spherulite morphology and growth in the P(D-2HB)-*b*-PLLA and P(D-2HB)-*b*-PDLA copolymers were observed by an Olympus (Tokyo, Japan) polarization optical microscope (BX50) equipped with a heating-cooling stage and temperature controller (LK-600PM, Linkam Scientific Instruments, Surrey, UK) under a constant nitrogen gas flow. The P(D-2HB)-*b*-PLLA and P(D-2HB)-*b*-PDLA copolymers were first heated from room temperature to 200 °C at 100 °C min<sup>-1</sup>, held at the same temperature for 3 min to erase thermal history, cooled to an arbitrary  $T_c$  in the range of 50–170 °C at 100 °C min<sup>-1</sup>, and then held at the same  $T_c$  (spherulite growth was observed here).

### 3. Results and discussion

#### 3.1. Synthesis of block copolymers

The P(D-2HB)-*b*-PLLA and P(D-2HB)-*b*-PDLA copolymers were synthesized with the previously reported procedure [12,13,14]. Fig. 2 shows the GPC curves of the P(D-2HB) prepolymer before and after second polymerization of L- or D-lactide. Evidently, the molecular weight of the GPC curves of the P(D-2HB) prepolymer as a coinitiator shifted to higher molecular weights after L- or D-lactide polymerization. This figure indicates that the PLLA or PDLA chain grew from the P(D-2HB) coinitiator and thereby block copolymers, the P(D-2HB)-*b*-PLLA and P(D-2HB)-*b*-PDLA copolymers were synthesized. Fig. 3 shows the <sup>1</sup>H NMR spectrum of the P(D-2HB)-*b*-PLLA copolymer. Here, only the <sup>1</sup>H NMR spectrum of the P(D-2HB)-*b*-PLLA copolymer is shown because the <sup>1</sup>H NMR spectrum of the P(D-2HB)-*b*-PDLA copolymer is very similar with that of

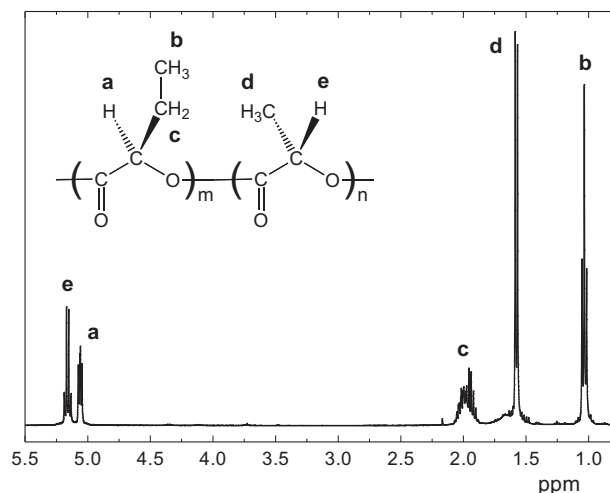


Fig. 3. <sup>1</sup>H NMR spectrum of P(D-2HB)-*b*-PLLA copolymer.

the P(D-2HB)-*b*-PLLA copolymer. Each resonance line of lactyl and hydroxybutyl units in the P(D-2HB)-*b*-PLLA and P(D-2HB)-*b*-PDLA copolymers had the same chemical shift value as that of their homopolymers. This supports the formation of the block copolymers. However, the fractions of these block copolymers may have had the multi-block structure, in addition to the non-trans-esterified diblock structure because of the high catalytic effect on polymerization utilized in the present study, which may have induced transesterification [14]. The molecular characteristics of synthesized P(D-2HB)-*b*-PLLA and P(D-2HB)-*b*-PDLA copolymers were tabulated in Table 1. The L- or D-lactyl unit fractions of the copolymers estimated from <sup>1</sup>H NMR spectroscopy and polarimetry are around 50 mol%, indicating that the block copolymers contained equimolar L- or D-lactyl units and D-hydroxybutyrate units.

#### 3.2. Wide-angle X-ray scattering

Fig. 4 shows the WAXS profiles of the P(D-2HB)-*b*-PLLA and P(D-2HB)-*b*-PDLA copolymers quenched at 0 °C or crystallized at different  $T_c$  values from the melt. In Fig. 4(a), the crystalline peaks were observed at  $2\theta$  values of around 11, 19.5, and 22.5° for HTSC crystallites [10], but neither peaks at  $2\theta$  values of around 16.5 and 19° for PLLA  $\alpha$ - or  $\alpha'$ -form crystallites nor those at  $2\theta$  values of 14.7 and 17.2° for pure P(D-2HB) [7,10]. This is indicative of the fact that the P(D-2HB)-*b*-PLLA copolymer contained only HTSC crystallites as a crystalline species. This is in marked contrast with the result of solution- and melt-crystallized polymer blends of P(L-2HB) and

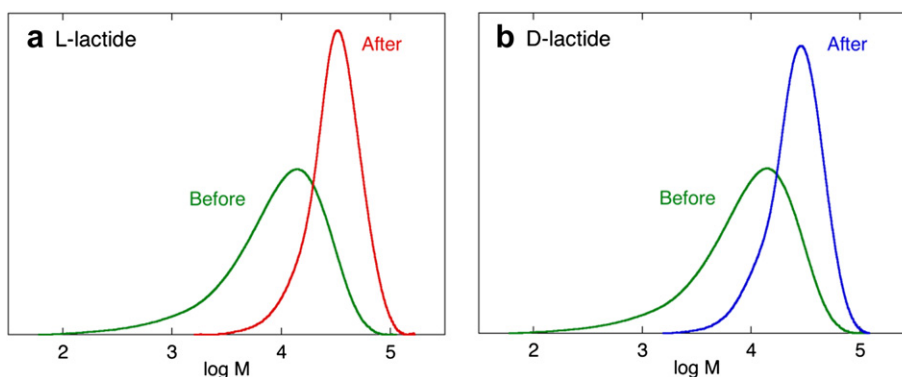


Fig. 2. GPC curves of P(D-2HB) before and after second polymerization of L-lactide (a) and D-lactide (b).

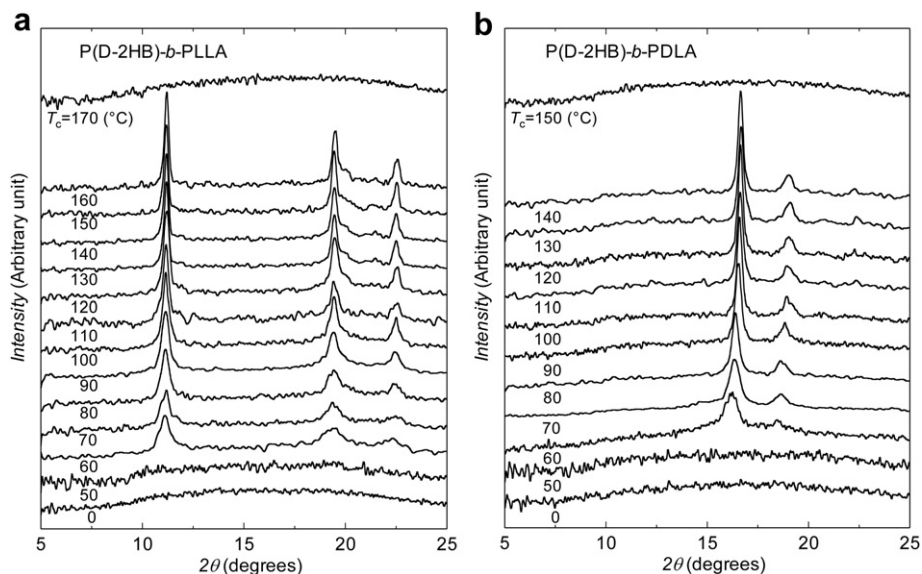


Fig. 4. WAXS profiles of P(D-2HB)-b-PLLA (a) and P(D-2HB)-b-PDLA (b) copolymers crystallized at different  $T_c$  or quenched at 0 °C from the melt.

PDLA [10] which should have the crystallization behavior identical with that of P(D-2HB)/PLLA blends. In the blends, P(L-2HB) and PDLA homo-crystallites were formed in addition to HTSC crystallites, except for that crystallized at a selected  $T_c$ . Therefore, the block copolymerization can be a very effective method for the HTSC formation, avoiding the formation of poly(D-2HB) or PLLA homo-crystallites, in agreement with ready HMSC formation in stereoblock copolymers of PLLA and PDLA [5,11–13]. On the other hand, the P(D-2HB)-b-PDLA copolymer had only crystalline diffraction peaks for PDLA  $\alpha$ - or  $\alpha'$ -form homo-crystallites but no peaks for P(D-2HB) homo-crystallites, indicating only PDLA  $\alpha$ - or  $\alpha'$ -form homo-crystallites were formed as a crystalline species. This is very similar to the solution-cast blend of P(L-2HB) and PLLA, but in contrast with the melt-crystallized P(L-2HB) and PLLA blend [10] which should have the crystallization behavior identical with that of P(D-2HB)/PDLA

blends. In these blends, both P(L-2HB) and PLLA homo-crystallites were formed [10]. The difference in the crystallization behavior between the block copolymers in the present study and the polymer blends in the previous study may be ascribed to the multi-block structure in the copolymers caused by transesterification during synthesis of the block copolymers. The multi-block structure in the copolymers may have reduced the monomer sequence lengths of L- or D-lactide units and D-2-hydroxybutyrate units below crystallizable lengths.

### 3.3. Differential scanning calorimetry

Fig. 5 shows the DSC thermograms of the P(D-2HB)-b-PLLA and P(D-2HB)-b-PDLA copolymers crystallized at different  $T_c$  values or quenched at 0 °C from the melt. The glass transition, cold

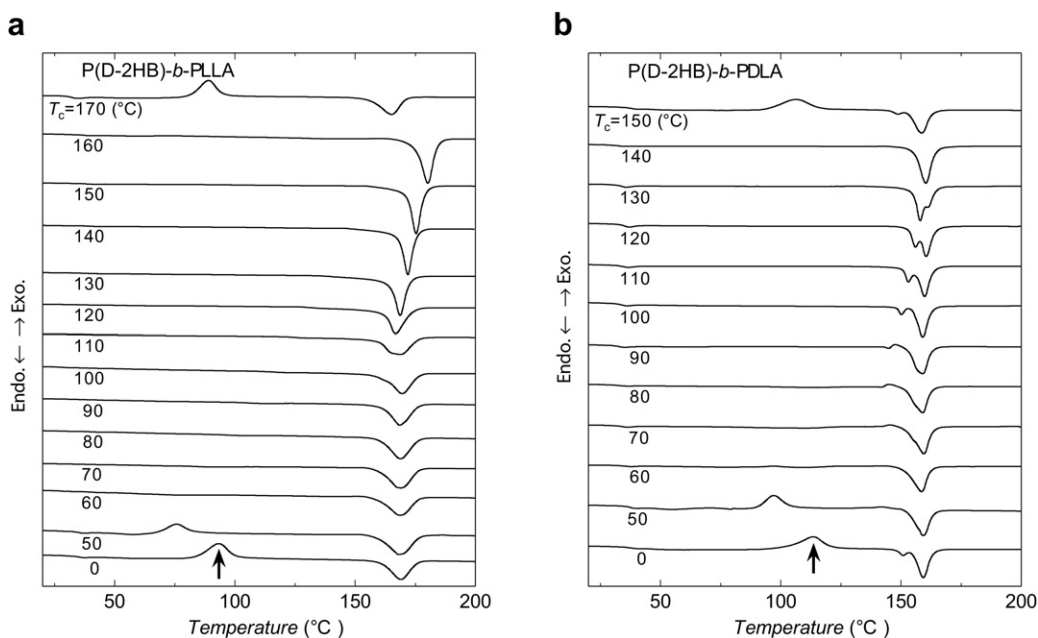


Fig. 5. DSC thermograms of P(D-2HB)-b-PLLA (a) and P(D-2HB)-b-PDLA (b) copolymers crystallized at different  $T_c$  or quenched at 0 °C from the melt. Arrows show the cold crystallization peaks of the melt-quenched specimens.

**Table 2**  
Thermal properties of melt-quenched P(D-2HB)-*b*-PLLA and P(D-2HB)-*b*-PDLA copolymers.

Code	$T_g^a$ (°C)	$T_{cc}^a$ (°C)	$T_m(\text{PLA})^a$ (°C)	$T_m(\text{SC})^a$ (°C)	$\Delta H_{cc}^b$ (J g <sup>-1</sup> )	$\Delta H_m(\text{PLA})^b$ (J g <sup>-1</sup> )	$\Delta H_m(\text{SC})^b$ (J g <sup>-1</sup> )
P(D-2HB)- <i>b</i> -PLLA	31.5	93.2	—	169.0	36.1	0	35.4
P(D-2HB)- <i>b</i> -PDLA	33.8, 44.5	114.0	151.0	—	28.3	27.5	0

<sup>a</sup>  $T_g$ ,  $T_{cc}$ , and  $T_m$  are glass transition, cold crystallization, and melting temperatures, respectively. No melting peak of P(D-2HB) was observed.

<sup>b</sup>  $\Delta H_{cc}$  and  $\Delta H_m$  are cold crystallization and melting enthalpies, respectively.

crystallization, and melting of HSC crystallites or PDLA  $\alpha$ - or  $\alpha'$ -form homo-crystallites are observed at 20–60, 70–120, and 150–180 °C, respectively. The P(D-2HB)-*b*-PLLA and P(D-2HB)-*b*-PDLA copolymers quenched at 0 °C or crystallized at 50 °C and at the highest  $T_c$  had the cold crystallization peak, reflecting an amorphous nature or an imperfectly crystallized state of these specimens. For the melt-quenched specimens ( $T_c = 0$  °C), the cold crystallization of the P(D-2HB)-*b*-PLLA copolymer was observed at the lower  $T_c$  compared with that of the P(D-2HB)-*b*-PDLA copolymer, meaning the higher crystallizability of the copolymer which can form HTSC crystallites (See the arrows in Fig. 5). In the case of the melt-quenched specimens,  $T_m$  was higher for the P(D-2HB)-*b*-PLLA copolymer (169 °C) than for the P(D-2HB)-*b*-PDLA copolymer (151 °C) (Table 2). The presence of melting peak of PDLA homo-crystallites at around 160 °C and the absence of melting peak of P(D-2HB) homo-crystallites at around 100 °C in the DSC thermograms of the P(D-2HB)-*b*-PDLA copolymer confirmed the WAXS finding that only PDLA chains were crystallizable in the copolymer. On the other hand, we could not specify which crystallites (PLLA homo-crystallites or HTSC crystallites) melted at around 170 °C in the P(D-2HB)-*b*-PLLA copolymer only from the DSC thermograms, because the  $T_m$  values of PDLA homo-crystallites and HSC crystallites were close to each other. However, based on the WAXS result, the melting peak at around 170 °C was ascribed to that of HTSC crystallites, not to that of PDLA homo-crystallites.

### 3.4. Crystallinity and melting temperature

The  $X_c(\text{SC})$ ,  $X_c(\text{PLA})$ ,  $T_m(\text{SC})$ , and  $T_m(\text{PLA})$  of P(D-2HB)-*b*-PLLA and P(D-2HB)-*b*-PDLA copolymers were estimated from Figs. 4 and 5, respectively, and are plotted in Fig. 6 as a function of  $T_c$ . When double melting peak was observed in the DSC thermograms, the first peak temperature is assumed to be  $T_m$ , because the second melting peak should be due to the melting of crystallites re-crystallized during heating. The most of  $X_c(\text{SC})$  and  $X_c(\text{PLA})$  values of the P(D-2HB)-*b*-PLLA and P(D-2HB)-*b*-PDLA copolymers increased with an increase

in  $T_c$  and the gave maximum values (59 and 33%, respectively) at the  $T_c$  values of 150–160 and 130–140 °C, respectively. Similar to  $X_c$ , the  $T_m$  values of the P(D-2HB)-*b*-PLLA and P(D-2HB)-*b*-PDLA copolymers gave maxima (180 and 160 °C, respectively) at  $T_c = 160$  and 140 °C, respectively. Here, seemingly high  $T_m$  values of the P(D-2HB)-*b*-PDLA copolymers for  $T_c$  range of 50–70 °C could not be considered as a real  $T_m$  values, because these  $T_m$  values are melting temperatures of the crystallites re-crystallized during DSC heating, as observed for other  $T_c$  values. Such difference in  $T_c$  values giving maximum  $X_c$  and  $T_m$  values should be due to the higher  $T_m$  value of the P(D-2HB)-*b*-PLLA copolymer compared to that of the P(D-2HB)-*b*-PDLA copolymers. The  $X_c$  values of the P(D-2HB)-*b*-PDLA copolymer were lower than those of P(D-2HB)-*b*-PLLA copolymer, when compared at the same  $T_c$ . This is attributable to the fact that in P(D-2HB)-*b*-PLLA copolymer both P(D-2HB) and PLLA chains with the opposite configuration should have co-crystallized to form HTSC crystallites, whereas in P(D-2HB)-*b*-PDLA copolymer only PDLA chains could crystallize.

The  $T_c$ -sensitive  $T_m$  values are expected to reflect the crystalline sizes depending on  $T_c$ . In contrast, the  $T_c$ -insensitive  $T_m$  values of P(D-2HB)-*b*-PLLA and P(D-2HB)-*b*-PDLA copolymers in the  $T_c$  ranges of 50–110, and 170 °C and of 50–70, and 150 °C, respectively, are not actual  $T_m$  values but those of the crystallites re-crystallized during DSC heating. Therefore, we carried out the Hoffman-Weeks plot of  $T_m$  values in  $T_c$  ranges of 120–160 °C and 80–140 °C for the P(D-2HB)-*b*-PLLA and P(D-2HB)-*b*-PDLA copolymers, respectively (Fig. 7). The extrapolation of the experimental  $T_m$  lines to  $T_m = T_c$  gives equilibrium melting temperature ( $T_m^0$ ) values. The thus obtained  $T_m^0$  values are 189.0 and 171.3 °C for HTSC crystallites and PDLA homo-crystallites of the P(D-2HB)-*b*-PLLA and P(D-2HB)-*b*-PDLA copolymers, respectively. The  $T_m^0$  value of PDLA homo-crystallites in the P(D-2HB)-*b*-PDLA copolymer is much lower than the  $T_m^0$  values reported for PLLA homo-crystallites (191–227 °C) [19,20,21,22,23,24,25]. This can be ascribed to the low molecular weight of PDLA chain ( $M_w < 3.0 \times 10^4$  g mol<sup>-1</sup>). Similar to this, the  $T_m^0$  value of HTSC crystallites of P(D-2HB)-*b*-PLLA copolymer should be much lower than actual value. Also, the  $T_m^0$

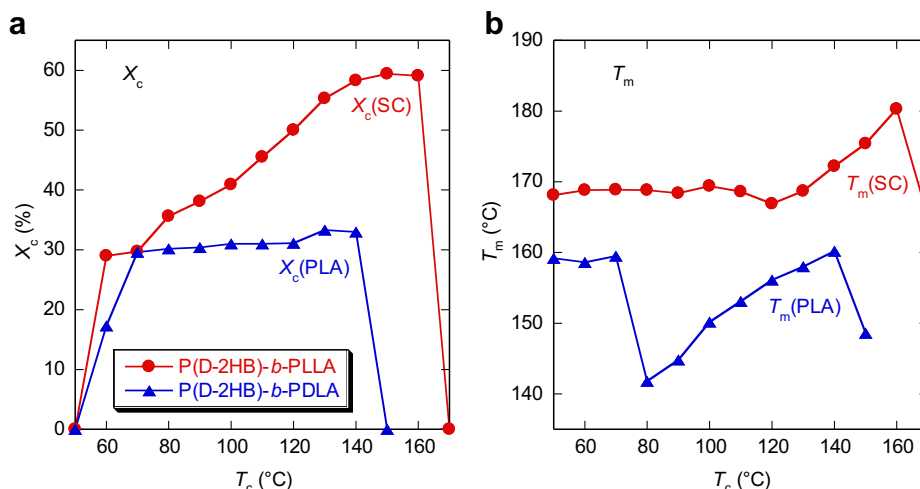


**Fig. 6.** Crystallinity ( $X_c$ ) (a) and melting temperature ( $T_m$ ) (b) of P(D-2HB)-*b*-PLLA and P(D-2HB)-*b*-PDLA copolymers as a function of  $T_c$ .



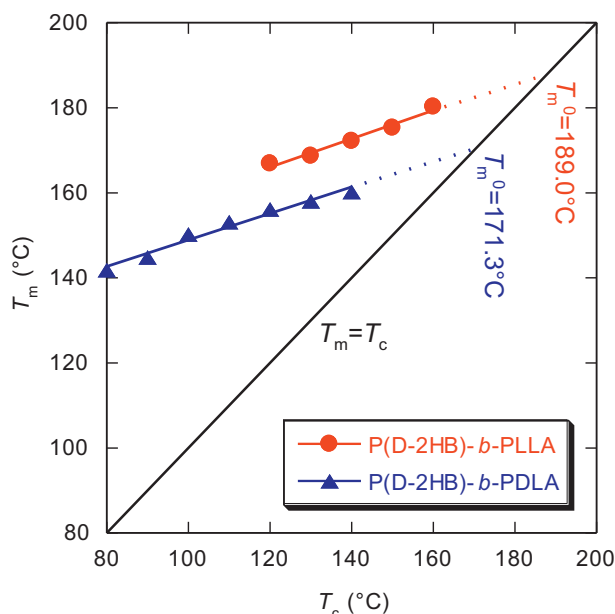


Fig. 7. Hoffman-Weeks plot of P(D-2HB)-b-PLLA and P(D-2HB)-b-PDLA copolymers.

value of HTSC crystallites is lower than those reported for HMSC crystallites of PLLA and PDLA (233–237 and 279 °C) [26,27].

### 3.5. Spherulite morphology and growth

Fig. 8 shows the polarized optical photomicrographs of the P(D-2HB)-b-PLLA and P(D-2HB)-b-PDLA copolymers crystallized at different  $T_c$ . The maximum radii of the P(D-2HB)-b-PLLA spherulites were ca. 6 and 3  $\mu\text{m}$  at  $T_c$  of 160 and 130 °C, respectively, whereas those of the P(D-2HB)-b-PDLA spherulites were ca. 140 and 10  $\mu\text{m}$  at  $T_c$  of 130 and 100 °C, respectively. A smaller, supercooling ( $\Delta T = T_m^0 - T_c$ ) will decrease the number of spherulite nuclei per unit

mass, resulting in the formation of larger spherulites. However, despite the smaller  $\Delta T$  of the P(D-2HB)-b-PLLA copolymer (29.0 °C at  $T_c = 160$  °C) compared with that of the P(D-2HB)-b-PDLA copolymer (41.3 °C at  $T_c = 130$  °C), the maximum radius of spherulites was smaller for the former (ca. 6  $\mu\text{m}$ ) than the latter (ca. 140  $\mu\text{m}$ ). The same trend was observed for P(D-2HB)-b-PLLA at  $T_c = 130$  °C and P(D-2HB)-b-PDLA at  $T_c = 100$  °C. The observed lower maximum radius of the P(D-2HB)-b-PLLA copolymer than that of the P(D-2HB)-b-PDLA copolymer can be ascribed to the higher nucleus density of HTSC spherulites of the former. Well-defined Maltese crosses were observed only for the P(D-2HB)-b-PDLA spherulites at the relatively higher  $T_c$  of 130 °C, meaning the PDLA lamella was well-oriented along the radius direction.

Fig. 9 shows the radius growth rate of spherulites ( $G$ ) and the induction period for spherulite growth ( $t_i$ ) of the P(D-2HB)-b-PLLA and P(D-2HB)-b-PDLA copolymers. The  $G$  values of the P(D-2HB)-b-PLLA copolymer were lower than those of the P(D-2HB)-b-PDLA copolymer in the  $T_c$  range of 100–140 °C. It is interesting to note that despite the lower  $G$  values of the P(D-2HB)-b-PLLA copolymer, the final  $X_c$  values of the P(D-2HB)-b-PLLA copolymer were higher than those of the P(D-2HB)-b-PDLA copolymer. On the other hand, the  $t_i$  values were practically zero for  $T_c$  range below 135 °C and showed significant non-zero values when  $T_c$  approached  $T_m$ . The  $T_c$  which caused a significant increase in  $t_i$  was lower for the P(D-2HB)-b-PDLA copolymer than for the P(D-2HB)-b-PLLA copolymer because the  $T_m^0$  was lower for the former (171 °C) than the latter (189 °C).

We estimated the nucleation constant ( $K_g$ ) and the front constant ( $G_0$ ) for the P(D-2HB)-b-PLLA and P(D-2HB)-b-PDLA copolymers by the use of the nucleation theory established by Hoffman et al. [28,29], in which  $G$  can be expressed by the following equation:

$$G = G_0 \exp[-U^*/R(T_c - T_\infty)] \exp[-K_g/(T_c \Delta T f)] \quad (3)$$

where  $U^*$  is the activation energy for transportation of segments to the crystallization site,  $R$  is the gas constant,  $T_\infty$  is the hypothetical temperature where all motion associated with viscous flow ceases, and  $f$  is the factor expressed by  $2T_c/(T_m + T_c)$  that accounts for the change in heat of fusion as the temperature is decreased below  $T_m^0$ .

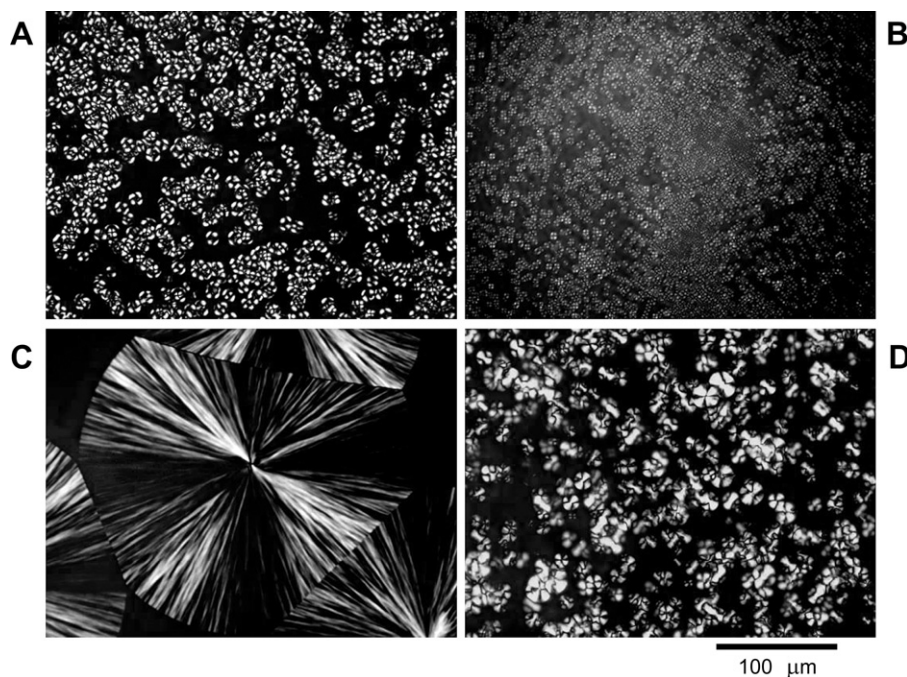


Fig. 8. The polarized optical photomicrographs of P(D-2HB)-b-PLLA copolymer crystallized at 160 °C for 30 min (A) and 130 °C for 1 min (B) and of P(D-2HB)-b-PDLA copolymer crystallized at 130 °C for 20 min (C) and 100 °C for 3 min (D).

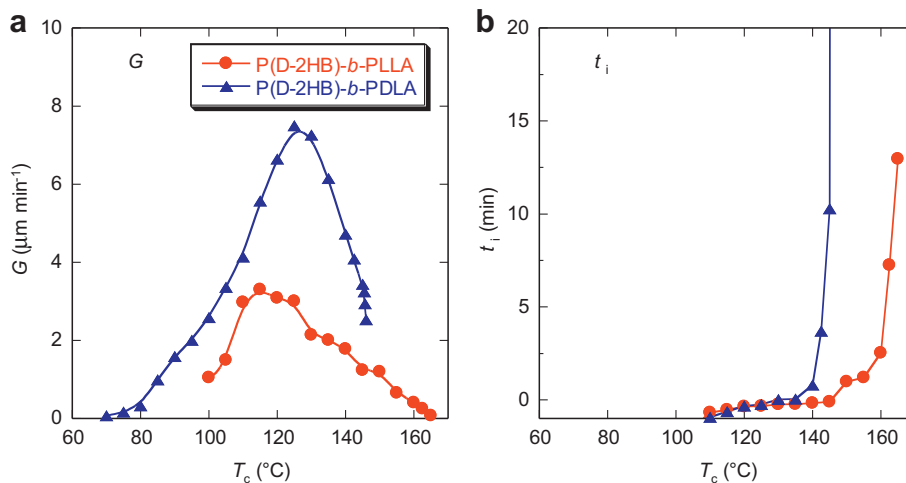


Fig. 9. Radius growth rate of spherulites ( $G$ ) (a) and induction period for spherulite growth ( $t_i$ ) (b) of P(D-2HB)-b-PLLA and P(D-2HB)-b-PDLA copolymers as a function of  $T_c$ .

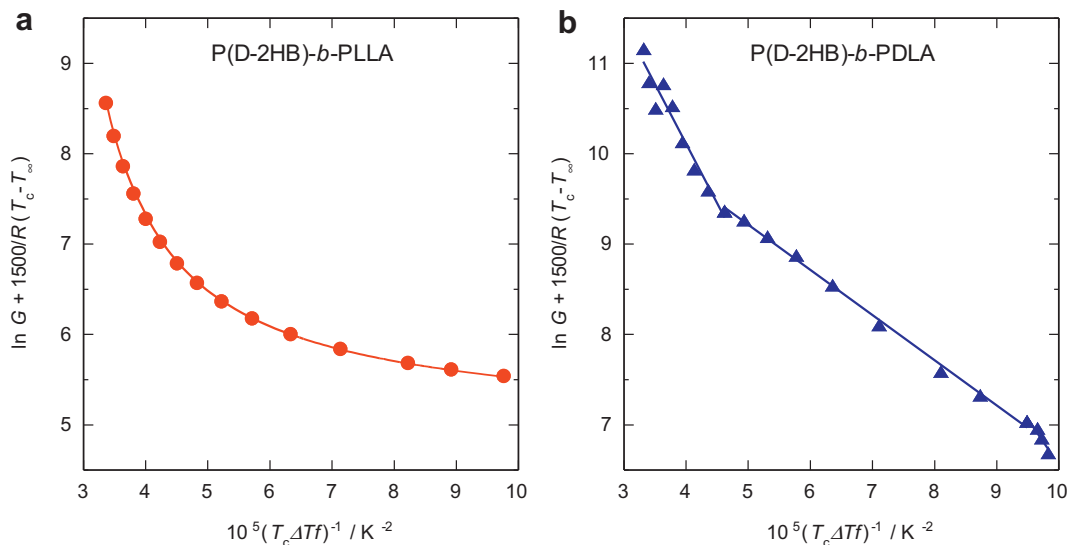


Fig. 10.  $\ln G + 1500/R(T_c - T_{\infty})$  of P(D-2HB)-b-PLLA and P(D-2HB)-b-PDLA copolymers as a function of  $1/(T_c \Delta T_f)$ .

Fig. 10 illustrates the  $\ln G + 1500/R(T_c - T_{\infty})$  of the P(D-2HB)-b-PLLA and P(D-2HB)-b-PDLA copolymers as a function of  $1/(T_c \Delta T_f)$ , using the  $T_m^0$  values of HTSC and PDLA crystallites (189 and 171  $^{\circ}\text{C}$ ) and the  $T_g$  values of the melt-quenched polymers in the present study (Table 2). Also, we used the universal values of  $U^* = 1500 \text{ cal mol}^{-1}$  and  $T_{\infty} = T_g - 30 \text{ K}$ .

Normally, the plot as in Fig. 10 gives  $K_g$  as a slope and the intercept  $\ln G_0$ . The thus obtained values for the P(D-2HB)-b-PDLA copolymer are summarized in Table 3. However, for the P(D-2HB)-b-PLLA copolymer,  $K_g$  and  $G_0$  values could not be determined due to the continuous change of the slope of the curve, reflecting the persistent change of nucleating mechanism. Such unusual behavior was not reported for PLLA-*b*-PDLA stereoblock copolymers [13]. Three  $K_g$  values observed for the P(D-2HB)-b-PDLA copolymer, indicating the presence of three different nucleation mechanisms,

Table 3  
Front constant ( $G_0$ ) and nucleation constant ( $K_g$ ) of P(D-2HB)-b-PDLA copolymer.

$T_c$ range ( $^{\circ}\text{C}$ )	$G_0$ ( $\mu\text{m min}^{-1}$ )	$K_g$ ( $\text{K}^2$ )	Regime
70–110	$4.88 \times 10^6$	$1.32 \times 10^5$	III
110–145	$1.21 \times 10^5$	$0.50 \times 10^5$	II
145–146	$1.62 \times 10^7$	$1.00 \times 10^5$	I

depending  $T_c$ . The smaller  $K_g$  value ( $0.50 \times 10^5 \text{ K}^2$ ) was about a half of the larger  $K_g$  values ( $1.32$  and  $1.00 \times 10^5 \text{ K}^2$ ), strongly suggesting that the smaller and larger  $K_g$  values are those for Regime II and for Regimes I and III kinetics.

#### 4. Conclusions

The conclusions derived from present study on the crystallization of the block copolymers of substituted and non-substituted PLAs, i.e., P(D-2HB)-*b*-PLLA and P(D-2HB)-*b*-PDLA having two optically active blocks with the opposite and identical configurations are summarized as follows:

- (1) The P(D-2HB)-*b*-PLLA copolymer can crystallize in the  $T_c$  range of 60–160  $^{\circ}\text{C}$  and the isothermally crystallized P(D-2HB)-*b*-PLLA contained solely the HTSC crystallites as a crystalline species, without formation of poly(D-2HB) or PLLA homo-crystallites, regardless of  $T_c$ , in marked contrast with the polymer blends. This indicates that the block copolymerization is the very effective method for HTSC formation, avoiding the formation of poly(D-2HB) or PLLA homo-crystallites.

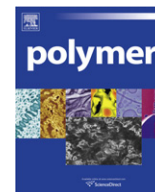
- (2) The P(D-2HB)-*b*-PDLA copolymer can crystallize in the  $T_c$  range of 60–140 °C and the isothermally crystallized P(D-2HB)-*b*-PDLA copolymer had only PDLA homo-crystallites as crystalline species, irrespective of  $T_c$ , reflecting no-cocrySTALLITES formation between poly(D-2HB) and PDLA chains having the same configurations.
- (3) The  $T_m^0$  of HTSC crystallites of the P(D-2HB)-*b*-PLLA copolymer was estimated to be 189.0 °C, which was higher than 171.3 °C evaluated for PDLA homo-crystallites in the P(D-2HB)-*b*-PDLA.
- (4) Although the final  $X_c$  was higher for the P(D-2HB)-*b*-PLLA copolymer than for the P(D-2HB)-*b*-PDLA copolymer, the  $G$  was lower for the P(D-2HB)-*b*-PLLA copolymer. The regime analysis indicated that the nucleation mechanism of the P(D-2HB)-*b*-PLLA copolymer persistently changed, depending on  $T_c$ , whereas the P(D-2HB)-*b*-PDLA copolymer had three types of Regimes I, II, and III.

### Acknowledgments

This research was supported by a Grand-in-Aid for Scientific Research, Category "C", No. 19500404, from Japan Society for the Promotion of Science (JSPS).

### References

- [1] Slager J, Domb A. *J Adv Drug Deliv Rev* 2003;55:549–83.
- [2] Tsuji H. *Macromol Biosci* 2005;5:569–97.
- [3] Fukushima K, Kimura Y. *Polym Int* 2006;55:626–42.
- [4] Tsuji H, Ikada Y. In: Yu L, editor. *Biodegradable polymer blends and composites from renewable resources*. NJ: John Wiley & Sons, Inc.; 2009. p. 165–90.
- [5] Kakuta M, Hirata M, Kimura Y. *Polym Rev* 2009;49:107–40.
- [6] Marín R, Alla A, Muñoz-Guerra S. *Macromol Rapid Commun* 2006;27:1955–61.
- [7] Tsuji H, Okumura A. *Macromolecules* 2009;42:7263–6.
- [8] Bosscher F, Keekstra D, Challa G. *Polymer* 1981;22:124–6.
- [9] Jiang Z, Boyer MT, Sen A. *J Am Chem Soc* 1995;117:7037–8.
- [10] Tsuji H, Yamamoto S, Okumura A, Sugiura Y. *Biomacromolecules* 2010;11:252–8.
- [11] Fukushima K, Hirata M, Kimura Y. *Macromolecules* 2007;40:3049–55.
- [12] Yui N, Dijkstra PJ, Feijen J. *Makromol Chem* 1990;191:481–8.
- [13] Tsuji H, Wada T, Sakamoto Y, Sugiura Y. *Polymer* 2010;51:4937–47.
- [14] Tsuji H, Nishikawa M, Sakamoto Y, Itsuno S. *Biomacromolecules* 2007;8:1730–8.
- [15] Tsuji H, Matsuoka H, Itsuno S. *J Appl Polym Sci* 2008;110:3954–62.
- [16] Tsuji H, Tezuka Y. *Biomacromolecules* 2004;5:1181–6.
- [17] Tsuji H, Hyon S-H, Ikada Y. *Macromolecules* 1991;24:5651–6.
- [18] Tsuji H, Del Carpio CA. *Biomacromolecules* 2003;4:7–11.
- [19] Tsuji H, Ikada Y. *Polymer* 1995;36:2709–16.
- [20] Tsuji H, Ikada Y. *J Polym Sci Part A Polym Chem* 1998;36:59–66.
- [21] Tsuji H, Ikada Y. *Polym Degrad Stab* 2000;67:179–89.
- [22] Tsuji H, Ikarashi K. *Polym Degrad Stab* 2001;71:415–24.
- [23] Abe H, Kikkawa Y, Inoue Y, Doi Y. *Biomacromolecules* 2001;2:1007–14.
- [24] Abe H, Harigaya M, Kikkawa Y, Tsuge T, Doi Y. *Biomacromolecules* 2005;6:457–67.
- [25] Tsuji H, Ikarashi K. *Biomacromolecules* 2004;5:1021–8.
- [26] Tsuji H, Ikada Y. *Macromol Chem Phys* 1996;197:3483–99.
- [27] Tsuji H, Tsuruno T. *Polym Degrad Stab* 2010;95:477–84.
- [28] Hoffman JD, Davis GT, Lauritzen JI. In: Hannay NB, editor. *Treatise on solid state chemistry*, vol. 3. Crystalline and noncrystalline solids. New York: Plenum Press; 1976 [Chapter 7].
- [29] Hoffman JD, Davis GT, Lauritzen JI. *J Res Na Bur Std-A Phys Chem* 1975;79A: 671–99.



# Electrospun-fiber induced transcrystallization of isotactic polypropylene matrix

Chi Wang\*, Fwu-Hung Liu, Wei-Hung Huang

Department of Chemical Engineering, National Cheng Kung University, Tainan 70101, Taiwan, ROC

## ARTICLE INFO

### Article history:

Received 22 September 2010

Received in revised form

2 January 2011

Accepted 18 January 2011

Available online 26 January 2011

### Keywords:

Electrospun fiber

Nucleating ability

Transcrystallization

## ABSTRACT

To reveal the influences of fiber diameter and characteristics on the surface-induced matrix crystallization, four different fibers, i.e. syndiotactic polystyrene (sPS), Nylon 6, and polyhydroxyamide (PHA) and poly(p-phenylene benzobisoxazole) (PBO) fibers, were used to study their nucleating abilities towards isotactic polypropylene (iPP) matrix. Among them, micron-sized PBO fibers were obtained from the supplier, whereas submicron-sized fibers of sPS, Nylon 6 and PHA were prepared by the solution electrospinning process developed in this laboratory. To resolve the observation difficulty due to the fast nucleation rate and crystal growth at high supercooling degrees ( $>60$  °C), a high speed camera was mounted on the polarized optical microscope equipped with a hot stage to successfully snapshot the corresponding processes at various crystallization temperatures ( $T_c$ ) in the range of 96–120 °C. For all the active fibers, only  $\alpha$ -form iPP transcrystallites were observed at the fiber/matrix interface. Two crucial parameters were proposed for characterizing the fiber nucleating ability, i.e. the interfacial free energy difference ( $\Delta\sigma$ ) based on the heterogeneous nucleation from a thermodynamic point of view, and the maximum temperature for transcrystalline layer observed ( $T_{max}$ ) based on a kinetic consideration. Values of  $\Delta\sigma$  for different fibers were derived on the basis of the tertiary nucleation taking place in the selective “grooves” at the fiber surface. It was found that the nucleating rate of sPS fibers was scaled with the fiber diameter, and  $\Delta\sigma$  showed a negligible diameter dependence, but  $T_{max}$  slightly increased with increasing fiber diameter. For all the fibers investigated, an intimate relation between the  $\Delta\sigma$  and  $T_{max}$  was derived and used to compare their nucleating abilities.

© 2011 Elsevier Ltd. All rights reserved.

## 1. Introduction

When fibers are introduced in a semicrystalline polymer matrix, under certain circumstances, a highly oriented crystal layer with the chain axis parallel to the fiber axis is observed at the fiber/matrix interface. This distinct morphology is termed the transcrystalline layer (TCL) and is resulting from a profound nucleation density at the fiber interface in comparison with that in the bulk, in which conventional spherulites are developed. TCL exhibits a higher Young's modulus but less ductile behavior than the bulk spherulites [1,2]. Due to the restricted lamellar growth in a direction perpendicular to the fiber surface, anisotropic modulus in the TCL has recently been measured using the nano-scale shear and indentation technique [3]. On the basis of the heterogeneous nucleation theory, the interfacial free energy difference of the crystallizing polymer chains at the fiber surface ( $\Delta\sigma_{TCL}$ ), and that in the bulk ( $\Delta\sigma_B$ ) are readily determined and compared with each other for predicting the TCL formation from a thermodynamic point

of view. By studying the ultra drawn PE fibers embedded in the PE matrix, Ishida and Bussi [4] proposed that TCL is likely to develop at the fiber surface provided that  $\Delta\sigma_{TCL}$  is lower than  $\Delta\sigma_B$ . However, several investigations demonstrated that this criterion is merely a sufficient condition, not a necessary one [5,6]. In other words, TCL is also observed for a system with  $\Delta\sigma_{TCL}$  larger than  $\Delta\sigma_B$ , suggesting that other kinetic factors should be taken into account for the TCL development. Similar with the PE fibers/PE system, Sun *et al.* [7] recently reported that isotactic polypropylene (iPP) fibers could also induce the transcrystallization of iPP matrix at its surface. Thomason and Van Rooyen [8] have carried out a detailed study on the iPP transcrystallization on various fibers and they concluded that TCL formation is relevant with the magnitude of thermal stress at the fiber/matrix interface induced by the mismatch of thermal expansion coefficient between the *solid fiber* and *melt*. In addition to the fiber-pulling [8], temperature gradient is also a practical means to generation TCL at various fiber surfaces [9]. Many mechanisms have been suggested with an attempt to account for the plausible origin for the TCL formation; however, none of them could be successfully applied to all the cases reported. A review article of the recent progress of TCL research provided a good comparison among them [10]. Regarding the TCL effect on the

\* Corresponding author. Tel.: +886 6 2757575x62645; fax: +886 6 2344496.  
E-mail address: [chiwang@mail.ncku.edu.tw](mailto:chiwang@mail.ncku.edu.tw) (C. Wang).



interfacial strength, moreover, controversial results obtained from different analytical techniques were often found in various fiber/polymer composites. Basically, two principles are frequently applied for characterizing the interfacial strength; one is based on the stress criterion which is more readily to apply due to its simplicity, the other is based on the fracture energy criterion, which possesses more underlying physics and is independent of the specimen geometry. Using the micro-debonding test, Chen and Hsiao [11] showed that the presence of TCL could increase ca. 40% in the debonding force in the poly-ether-ketone-ketone composites with various fibers such as Kevlar, pitch-based carbon, and PAN-based carbon fibers. However, the matrix crystallinity was varied in the single-fiber composites with TCL (~28%) from that without TCL (0%), suggesting the difference in the mechanical strength for a comparison basis. Using a sophisticated method of asymmetric double cantilever beam test, Cho *et al.* [12] were able to determine the adhesive fracture energy ( $G_a$ ) between iPP and the surface-modified silicone substrate with the presence of TCL at the interface. They found that the thicker the TCL thickness, the higher the measured  $G_a$  due to the variation of failure locus. By means of the micro-bond test, Gati and Wagner [13] reported that the presence of TCL produces little, if any, effect on the measured  $G_a$  in the Kevlar 149/poly(caprolactone) single-fiber composites. Based on the conventional single-fiber pull-out test with the introduction of frictional stress at the debonded region, we have shown that the presence of TCL does not promote the level of adhesion in the PTFE fiber/iPP single-fiber composites, whereas the frictional stress at the interface is enhanced when samples are crystallized at high temperatures [14].

Discovered by Iijima in 1991 [15], carbon nanotubes (CNTs) are known as the strongest materials with a Young's modulus of  $\sim 10^3$  GPa, and a diameter of  $\sim 2$  nm for single-walled CNTs and  $\sim 20$  nm for multi-walled CNTs. The nano-scale diameter together with a large aspect ratio ( $\sim 1000$ ) makes the CNT-related composites more attractive in the practical applications than the conventional carbon fibers, which possess a diameter of  $\sim 10$   $\mu\text{m}$ . Although development of TCL at the single CNT surface has been occasionally reported using electron microscopy [16], difficulties have been encountered to monitor the evolution of TCL at the CNT surfaces due to its extremely tiny diameter. Zhang *et al.* [17] have used CNT bundles, instead of single CNT, with a diameter of 10  $\mu\text{m}$  to readily nucleate a columnar structure of iPP. An intriguing question is immediately raised: what is the effect of fiber diameter on the crystallizing matrix? Or, does the nucleation ability of fibers depend upon its diameter? To resolve this unexplored issue left to date, in this study a series of syndiotactic polystyrene (sPS) fibers with various diameters in a range from 300 nm to 6  $\mu\text{m}$  are prepared using the electrospinning technique operated at an elevated temperature. Fibers in such a diameter range make it more feasible to trace the crystallization kinetics of TCL, if occurs, under optical microscopy. In addition to electrospun sPS fibers, electrospun Nylon, and polyhydroxyamide (PHA) fibers together with the commercial poly(*p*-phenylene benzobisoxazole) (PBO) fibers are also used to investigate their abilities to induce the nucleation of iPP. PBO fibers are noted for their better tensile strength and modulus than the Kevlar fibers, whereas their nucleation ability towards polypropylene matrix is still unknown yet. Combined with previous findings on other fiber types (Kevlar, carbon, PET and PTFE) [5], nucleation abilities of seven active fibers towards the same batch of iPP are compared and the results will be discussed in terms of  $\Delta\sigma$ . Although plausible mechanisms for the TCL formation have been offered by various authors in the past, none of them could be applicable to all the reported circumstances. In this paper we shall show that in quiescent crystallization the transient thermal stress, which is associated with the transient temperature

evolution in the fibers, is the driving force to induce the aligned segments of iPP chains adjacent to fibers. These oriented chain segments are parallel with the fiber surface, serving as the nucleation precursors for TCL formation. Since fiber surface consists of many "grooves" (or steps) of various heights, the potential nuclei are most likely to locate in these grooves provided that the groove length is sufficiently larger than the critical lamellar thickness,  $l^*$ , to fulfill the tertiary nucleation, which is a less energy process than the secondary nucleation.

## 2. Experimental

### 2.1. Materials

The same batch of iPP powder used for our previous TCL studies [5] was applied in this study; it had a viscosity average molecular weight (MW) of  $2.8 \times 10^5$  g/mol. Commercial PBO fibers with a diameter of 15  $\mu\text{m}$  were supplied by Dow Chemical Co. Electrospinning process developed in this laboratory [18] has been successfully performed to obtain sPS, Nylon, and PHA fibers. To prepare sPS fibers with various diameters, electrospinning of sPS/*ortho*-dichlorobenzene (*o*-DCB) solutions with various concentrations was carried out at a solution temperature of  $\sim 140$  °C. The sPS pellets were provided by Dow Chemical Co. with a weight average MW of  $2.0 \times 10^5$  g/mol. The as-electrospun sPS fibers possessed a diameter ranging from 0.3 to 6.0  $\mu\text{m}$ . For Nylon fibers, room-temperature electrospinning of 18 wt.% Nylon/formic acid solutions was conducted under the processing conditions of 0.1 mL/h, 15 kV and 7 cm for the tip-to-collector distance. The diameter of electrospun Nylon fibers was  $0.37 \pm 0.12$   $\mu\text{m}$ . The pellets of Nylon 6 were purchased from Polysciences, Inc. and its weight average MW was  $3.5 \times 10^4$  g/mol. BisAPAF-IC PHA powders kindly provided by Prof. Hsu (NCKU) were synthesized from a low temperature polymerization of 2,2'-bis(3-amino-4-hydroxyphenyl) hexafluoropropane (BisAPAF) and isophthaloyl chloride (IC). They were dissolved in the DMAc/THF co-solvent with a volume ratio of 1/9 to form a 20 wt.% solution first, then the homogeneous solution was electrospun at room temperature to prepare PHA fibers with a diameter of  $0.33 \pm 0.12$   $\mu\text{m}$  [19].

### 2.2. Measurements

The testing fibers were covered with iPP powders and placed in a well-controlled hot stage (Linkam, THMS600) at a temperature of 200 °C for 10 min to homogenize the iPP melts. Then, the samples were cooled at a rate of 100 °C/min to the desired temperature ( $T_c$ ) for isothermal crystallization. Dry nitrogen was introduced to eliminate the plausible thermal degradation. Crystallization of iPP on the fibers was monitored with a polarized optical microscope (POM, Leica DMLP) equipped with phase contrast lens and two different CCD systems. For the high  $T_c$  range above 125 °C, a conventional CCD (Leica, DFC420) with a frame speed of 4 frames/10 s was sufficient to catch the nucleation evolution of iPP at the fiber surface. In contrast, a high speed CCD camera (Redlake, Motion Pro 10000) was used for the low  $T_c$  range due to the rapid nucleation and crystal growth of iPP at high supercooling degrees. The number of iPP nuclei at the fiber surface was accounted at selected time, and the nucleation density on fibers was expressed by number of nuclei per unit length of fiber. The sample thickness was controlled to be ca. 20  $\mu\text{m}$  in all cases. At a given  $T_c$ , the nucleation rate ( $I$ ) was determined from the linear slope of the plots of nucleation density versus elapsed time, and the intercept of the time axis provided the induction time ( $t_i$ ). Experimental details have been reported in our previous paper [5]. Fiber surface was investigated by atomic force microscopy (AFM) in the tapping mode

of operation. The AFM observations were performed in air at room temperature with a Nanoscope Multimode IIIa (Digital instruments) apparatus. FTIR spectra of samples were obtained at  $1\text{ cm}^{-1}$  resolution by a Perkin Elmer Spectrum 100 spectrometer equipped with a Mettler FP900 hot stage.

### 3. Results and discussion

#### 3.1. Transcrystallization of iPP on electrospun sPS fibers

By the high-temperature electrospinning apparatus developed in this laboratory [18], electrospinning of sPS/o-DCB solutions with various concentrations became feasible to prepare sPS fibers having different diameters. Fig. 1 shows the morphology of sPS fibers electrospun from a 14 wt.% solution, together with the corresponding histogram for the fiber diameter distribution. The fiber diameter ranged from 100 to 450 nm, and the average fiber diameter was  $178 \pm 59\text{ nm}$ . The average fiber diameter was found to be increased with increasing sPS concentration; for example, electrospinning of a 25 wt.% solution yielded sPS fibers with a diameter of  $\sim 1190 \pm 340\text{ nm}$ . Detailed effects of the electrospinning conditions on fiber formation are provided in our previous article [18]. In this paper, selected fibers with a pre-determined diameter ( $d_f$ ) ranging from 0.3 to  $6.0\text{ }\mu\text{m}$  became available to study the  $d_f$  effect on the iPP transcrystallization.

sPS is a polymorphic material possessing various crystal modifications, e. g. thermodynamically stable  $\beta$ -form with orthorhombic lattices and kinetically favored  $\alpha$ -form with hexagonal lattices [20]. Due to the rapid solvent evaporation resulting from the high-temperature electrospinning process, the as-spun sPS fibers were amorphous according to their FTIR spectra shown in Fig. 2 (curve a). It has been demonstrated that the absorbance peak at  $1222\text{ cm}^{-1}$  is associated with the crystalline phase with TTTT chain conformation existing in both the  $\alpha$ - and  $\beta$ -form sPS [21]. On the other hand, three absorbance peaks are seen in the  $870\text{--}920\text{ cm}^{-1}$  range, and the corresponding peaks at  $901$ ,  $911$ , and  $906\text{ cm}^{-1}$  are attributed to the  $\alpha$ -form,  $\beta$ -form and amorphous phase, respectively. Thermal treatments on the as-spun amorphous fibers were performed at various  $T_c$  and the corresponding FTIR spectra are also displayed in Fig. 2 to detect the variation of fiber microstructure. After being held at  $200\text{ }^\circ\text{C}$  for 10 min then cooling down to  $25\text{ }^\circ\text{C}$ , the as-spun sPS fibers undergo the cold crystallization process and give rise to formation of the  $\alpha$ -form crystals (curve b). Repeatedly annealing by the same thermal procedure (as that used for transcrystallization process) does not alter the crystal structure and fiber crystallinity; that is the  $\alpha$  form is always preserved provided that the holding

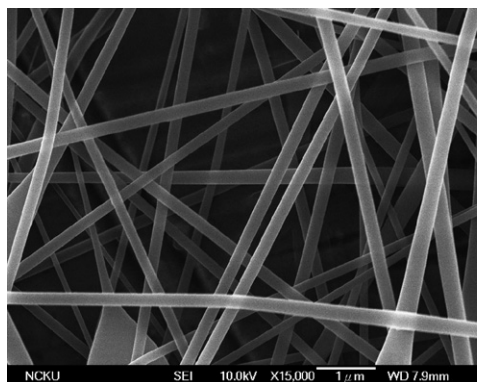


Fig. 1. Typical SEM micrograph and corresponding fiber diameter distribution of electrospun sPS fibers obtained by electrospinning of 14 wt.% sPS/o-DCB solutions at  $110\text{ }^\circ\text{C}$ . The average fiber diameter is  $178 \pm 59\text{ nm}$ .

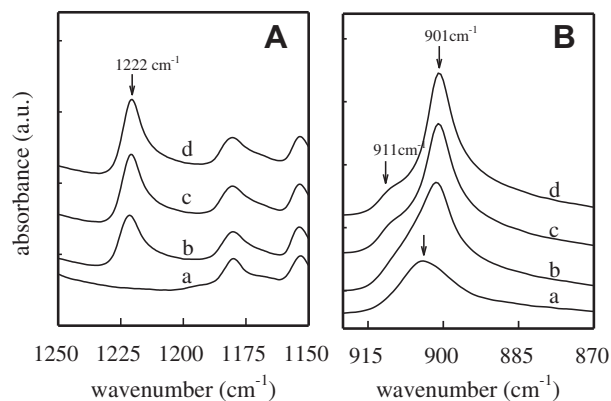
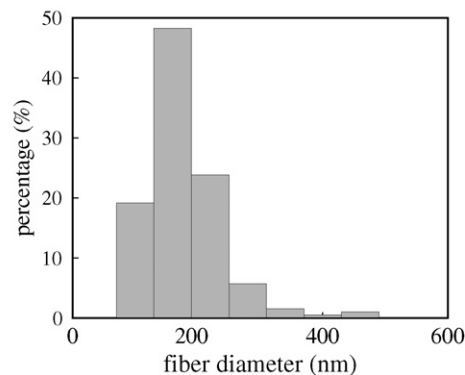
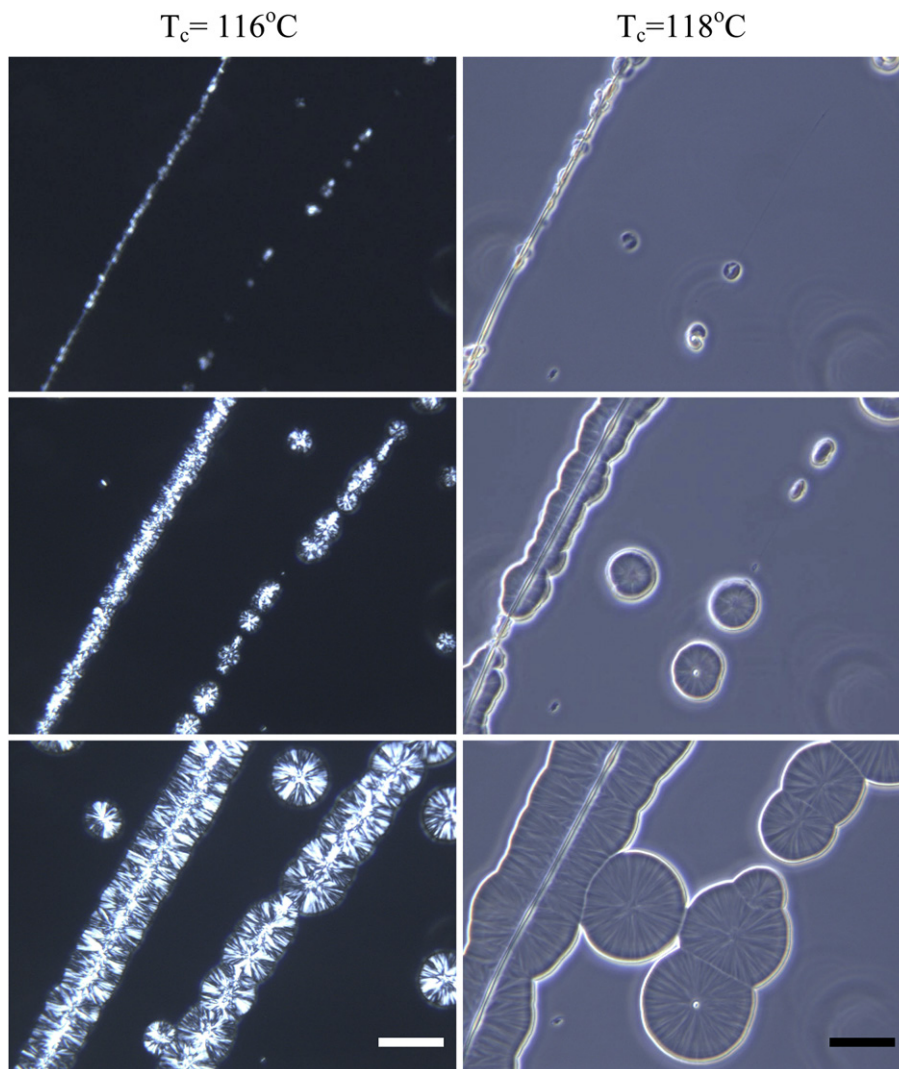


Fig. 2. FTIR spectra of the electrospun sPS fibers experienced different annealing history. Curve a: as-spun sPS fibers, b: after annealing at  $200\text{ }^\circ\text{C}$  for 60 min and then cooling to  $25\text{ }^\circ\text{C}$ , c: heating to  $260\text{ }^\circ\text{C}$  and then cooling to  $25\text{ }^\circ\text{C}$ , d: heating to  $270\text{ }^\circ\text{C}$  and then cooling to  $25\text{ }^\circ\text{C}$ . The heating rate is  $100\text{ }^\circ\text{C}/\text{min}$  and the cooling rate is  $10\text{ }^\circ\text{C}/\text{min}$ . The absorbance peak at  $1222\text{ cm}^{-1}$  is relevant with the crystalline phase with the TTTT conformation, whereas the peaks at  $901$  and  $911\text{ cm}^{-1}$  are related to the  $\alpha$ - and  $\beta$ -form crystals, respectively. The absorbance peak at  $906\text{ cm}^{-1}$  is due to the amorphous phase.

temperature is maintained at  $200\text{ }^\circ\text{C}$ . On the other hand, some trace of  $\beta$ -form crystals is detected as-revealed by the presence of absorbance peak at  $911\text{ cm}^{-1}$  (curve c) when the as-spun fibers are rapidly raised to  $260\text{ }^\circ\text{C}$  and then are cooled at a rate of  $10\text{ }^\circ\text{C}/\text{min}$  to room temperature. More  $\beta$ -form crystals are developed when the fibers are annealed to  $270\text{ }^\circ\text{C}$  (curve d). The transformation from the as-spun amorphous fibers to the  $\alpha$ -form crystalline fibers at low temperatures (below  $240\text{ }^\circ\text{C}$ ), and to the  $\alpha/\beta$ -mixed form fibers at high temperatures (above  $260\text{ }^\circ\text{C}$ ) has been confirmed as well by the electron diffraction technique conducted on the single thermally-treated fiber [18]. Under SEM observations, however, the as-spun fibers annealed at  $270\text{ }^\circ\text{C}$  exhibited a partial melting of the skin layer, whereas those annealed at  $260\text{ }^\circ\text{C}$  kept their round shape. Thus, the as-spun sPS fibers annealed respectively to  $200$  and  $260\text{ }^\circ\text{C}$  were used in the following studies with an attempt to reveal the effect of fiber microstructure (crystal modification) on the TCL formation.

Fig. 3 shows the TCL evolution of iPP on two sPS fibers with different diameters at  $116\text{ }^\circ\text{C}$  (left column, under cross-polar) and at  $118\text{ }^\circ\text{C}$  (right column, under phase contrast) after  $200\text{ }^\circ\text{C}$  annealing. It is evident that the fatter fiber on the left possesses higher iPP nucleating density than the thinner fiber on the right. In addition, the nucleating density of iPP is eventually lower at a higher  $T_c$ . Since





**Fig. 3.** The evolution of iPP transcrystallization on two sPS fibers with different diameters. The diameter of fiber on the left is 2.0  $\mu\text{m}$  and that on the right is 0.2  $\mu\text{m}$ . Left column shows the process at 116  $^{\circ}\text{C}$  under cross-polarized light, and right column is the results obtained at 118  $^{\circ}\text{C}$  under phase contrast. The scale bar is 50  $\mu\text{m}$ .

the nucleating rate of iPP on the fibers is rather fast, a high speed camera is mounted on the OM to trace the time variation of iPP nuclei. The number of iPP nuclei per unit fiber length is then counted and plotted against the elapsed time as shown in Fig. 4, from which the nucleating parameters are obtained. At a given  $T_c$ , the nucleating rate ( $I$ ) is determined from the linear slope, the time-axis intercept gives the induction time ( $t_i$ ), and the saturated nucleating density ( $N_{\infty}$ ) is derived as well. For TCL formation at a higher  $T_c$ ,  $t_i$  is increased, but both  $I$  and  $N_{\infty}$  are decreased. Similar results are obtained for sPS fibers having different diameters. Fig. 5 shows the  $T_c$  dependence of  $I$  for fibers with different diameters. It is of interest to note that  $I$  is increased with increasing  $d_f$  at a given  $T_c$ . However, when the nucleating rate per unit fiber area ( $I_s = I/\pi d_f$ ) is calculated for each fiber, they are all superimposed to one another to form a master curve as shown in the inset, suggesting that the difference in the nucleating density in Fig. 3 is simply due to the diameter variation. It is intriguing to note that there exist a highest temperature referred to  $T_{\text{max}}$ , above which no preferential nucleation of iPP at the fiber surface is observed, and TCL formation is not seen.  $T_{\text{max}}$  is slightly increased with increasing fiber diameter, being 118 and 121  $^{\circ}\text{C}$  for fibers with a diameter of 0.3 and 6.0  $\mu\text{m}$ , respectively. To further characterize the fiber nucleating ability,

heterogeneous nucleation theory should be applied because the fiber surface provides the active sites to transcrystallize iPP. Thus, it is essential to address the surface morphologies of the sPS fibers prior to further quantitative attempts. Hata *et al.* [2] concluded that

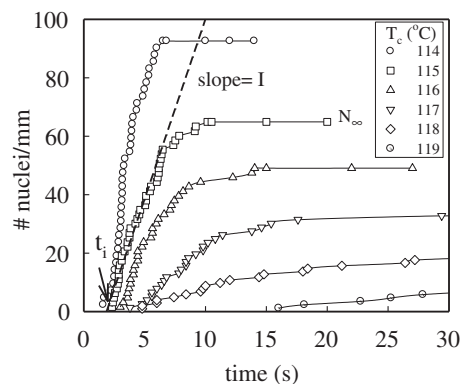


**Fig. 4.** Nucleating density of iPP at sPS fiber surface as a function of time at different crystallization temperatures,  $T_c$ . The diameter of sPS fibers is 0.7  $\mu\text{m}$ .



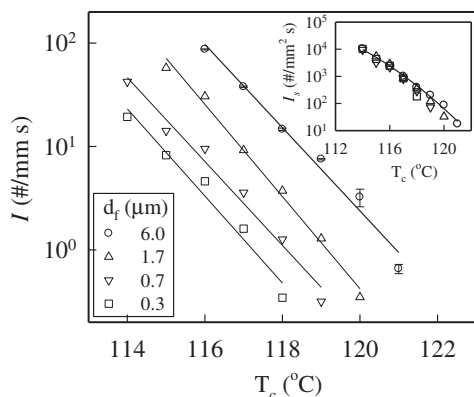


**Fig. 5.** Effect of crystallization temperature on the nucleation rate,  $I$ , for sPS fibers with various diameters,  $d_f$ . The inset shows the  $T_c$  dependence of surface nucleation rate,  $I_s$ , for sPS with various diameters;  $I_s = I/\pi d_f$ .

it is surface roughness of substrate rather than the substrate species or surface energy that plays the critical role in determining the formation of TCL. Similar conclusions have been reported in various systems [5,6,22]. Fig. 6(a) shows the typical AFM image of the electrospun sPS fibers, in which two morphological features can be seen. In addition to the “groove” extending along the fiber axis, many protruding “ridges” surrounded by “valleys” are randomly distributed at the surface, indicating the non-even characteristics of the fiber surface. The random orientation of these ridges/valleys in the electrospun sPS fibers is in striking contrast with the surface of conventional fibers, such as Kevlar or carbon fibers [5], which exclusively exhibit the presence of groove feature. In the conventional spinning processes, mechanical stretching along the spinning line is generally required to obtain a better chain orientation, leading to the development of microfibrillar structure within fibers. These microfibrils, in turn, potentially produce the groove morphology at the fiber surface with its length parallel to the fiber axis. In the electrospinning process, on the other hand, violent whipping of the electrified jets associated with the repulsive electric forces takes place in the bending instability region due to the excess surface charges [18]. In the absence of a global stretching direction, solvent evaporation of the local liquid segments becomes the dominant role in determining the surface morphology of electrospun fibers. Fig. 6(b) shows the  $d_f$  dependence of the root-

mean-square roughness ( $R_q$ ) of fiber surface, which is used to present the groove height.  $R_q$  is found to increase with fiber diameter, and can be scaled by a power law relation:  $R_q \sim d_f^{0.61}$  for a  $d_f$  lower than 10  $\mu\text{m}$ .  $R_q$  for the fibers with a diameter of 0.3  $\mu\text{m}$  is  $\sim 3$  nm but that for the 6.0  $\mu\text{m}$  fiber is  $\sim 15$  nm. In order to incubate the iPP nucleus, the height and length of an active groove should be larger than the nucleus dimensions, as shown in Fig. 6(c).

To take account of the energy change caused by the creation of new surfaces on the top of foreign substrates, a quantity called interfacial free energy difference,  $\Delta\sigma$ , is incorporated and essentially applied to determine the nucleating ability of the studied substrate [23]; the lower value of  $\Delta\sigma$ , the more likely for the polymer chains to deposit on this active surface. Based on the surface thermodynamics,  $\Delta\sigma$  is theoretically derived to be  $2(\sigma_s^{1/2} - \sigma_m^{1/2})(\sigma^{1/2} - \sigma_m^{1/2})$ , where  $\sigma_m$ ,  $\sigma_s$  and  $\sigma$  are the surface energies of the melt, substrate, and lateral surface of lamellar crystals, respectively [23]. From a pure thermodynamic standpoint, it has been long considered that a substrate with a high surface energy ( $\sigma_s$ ) should promote its nucleating ability due to the possession of low  $\Delta\sigma$ . Such a concept contradicts the common observations that PTFE fibers (or films) with a quite low  $\sigma_s$  are readily induce the TCL in comparison with high energy metallic fibers (or films) [2,5,24,25]. This fact implies that other factors should be taken into account in consideration of the transcrystallization mechanism. According to the heterogeneous nucleation theory, the nucleation rate  $I$  is expressed as follows [23,26],

$$I = I_0 \exp\left[-U^*/R(T_c - T_\infty)\right] \exp\left[-K_n T_m^{02}/kT_c(\Delta T \Delta h_f)^2\right] \quad (1)$$

where  $I_0$  is a constant,  $U^*$  is the activation energy related to molecules transporting across the phase boundary,  $R$  is the gas constant,  $T_c$  is the crystallization temperature,  $T_\infty$  is the temperature below which crystallization ceases,  $T_m^0$  is the equilibrium melting temperature of iPP,  $\Delta T$  is the degree of supercooling ( $=T_m^0 - T_c$ ),  $\Delta h_f$  is the heat of fusion per unit volume of iPP, and  $f$  is a correction factor given by  $2T_c/(T_c + T_m^0)$  to estimate the heat of fusion at large supercoolings. Although a different form of  $f$  has recently been suggested for iPP to cover the whole temperature range from glass transition to  $T_m^0$  [27], the present form still offers a good approximation at a  $T_c$  higher than 100  $^\circ\text{C}$ .  $K_n$  is a parameter associated with the type of heterogeneous nucleation; it can be expressed by  $16\sigma\sigma_e\Delta\sigma$  for nucleation taking place on a flat substrate

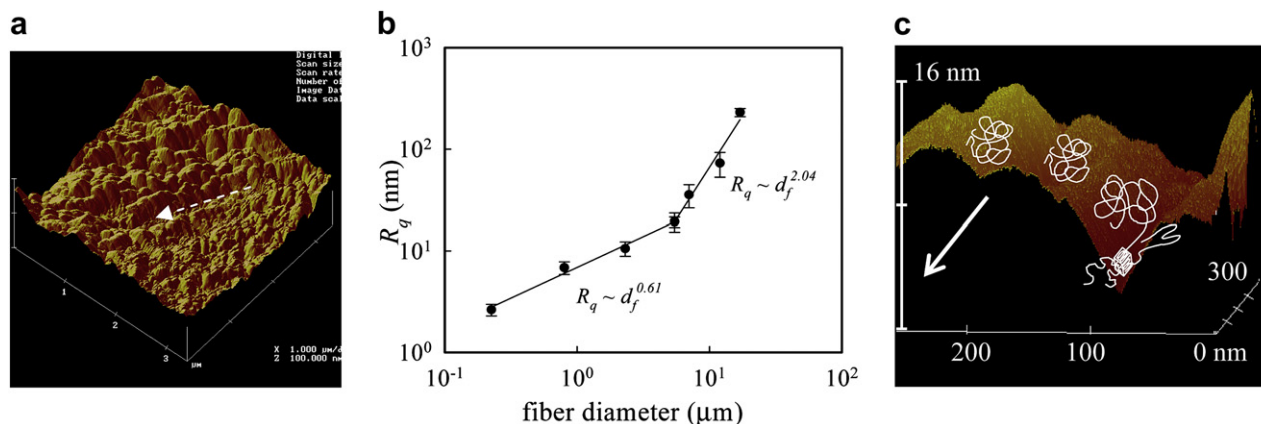


**Fig. 6.** (a) AFM height image of sPS fibers to reveal the presence of ridge and valley morphologies. The scan size is  $3 \times 3 \mu\text{m}$  and the fiber diameter is ca.  $1.1 \mu\text{m}$ . The arrow shows the fiber axis and indicates the presence of the groove. (b) The fiber diameter dependence of surface roughness. (c) Schematic illustration of random coils, at the fiber surface, with chain segments to develop a stable nucleus in a suitable groove having the height and length of  $\sim 6$  and  $\sim 100$  nm, respectively. The nucleus size is  $3 \times 3 \times 10$  nm. The fiber diameter is ca.  $1.2 \mu\text{m}$ , and the arrow shows the fiber axis.



for secondary nucleation, but becomes  $8\sigma_e(\Delta\sigma)^2$  for tertiary nucleation taking place in a step (groove) [23].  $\sigma_e$  is the fold surface energy of the lamellar crystals. The ratio of free energy required for formation of stable nuclei,  $\Delta G^*$ , by the primary, secondary and tertiary nucleation is 1:  $\Delta\sigma/2\sigma_e(\Delta\sigma/2\sigma)^2$ . Provided that  $\Delta\sigma$  is lower than  $2\sigma$ , tertiary nucleation is always a preferred process since a lower energy barrier is needed [23]. In order to apply Equation (1), values of  $T_m^0$ ,  $T_\infty$ ,  $U^*$  and  $\Delta h_f$  are taken from the literature [28,29] to be 458 K, 232 K,  $6.28 \times 10^{10}$  erg/mol and  $1.96 \times 10^9$  erg/cm<sup>3</sup>, respectively. A plot of  $\log I + U^*/2.303R(T_c - T_\infty)$  versus  $1/T_c(\Delta Tf)^2$  should give a straight line with a slope producing the value of  $8\sigma_e(\Delta\sigma)^2$ . Fig. 7 shows the corresponding plots of sPS fibers with different  $d_f$ s. In spite of twenty times difference in the fiber diameter, their deduced  $\sigma_e(\Delta\sigma)^2$  values are similar, and the average value is  $19,840 \pm 1100$  erg<sup>3</sup>/cm<sup>6</sup>. To exclusively derive the  $\Delta\sigma$  value, the determination of  $\sigma_e$  from the TCL growth kinetic is necessary.

Growth rates of TCL at the fiber interface as well as those of spherulites in the bulk were determined from the linear slopes of the plots of the measured crystal sizes versus elapsed time. When  $T_c$  was lower than 105 °C, however, measurement difficulties were encountered by using a conventional CCD since a quite limited time for the snapshots was available due to the fast growth of profound spherulites. A non-isothermal technique at a given cooling rate has been proposed to obtain the isothermal growth rates of iPP at low  $T_c$ s; however the lowest  $T_c$  feasible for measurements was  $\sim 104$  °C [30,31]. To resolve this difficulty and obtain isothermal growth data at high supercooling degrees, a high speed camera CCD was attempted in this study for acquiring sufficient snapshots in a short period of few seconds in the low  $T_c$  region; the results are shown in Fig. 8. For the present setup, the minimum  $T_c$  accessible is 96 °C. Fig. 9 shows the  $T_c$  dependence of crystal growth rate of iPP in the spherulitic form (triangles) and in the TCL form (inverted triangles) determined in this manner from 96 to 126 °C. In spite of the difference in crystal morphologies, both the spherulite and TCL possess the same rate of growth at a given  $T_c$ , which is consistent with previous findings at high  $T_c$ s [32]. Also included in Fig. 9 are the growth rates of iPP (circles) obtained from ref. 32 in a temperature range of 126–147 °C. It is of interest to note that for the accessible  $T_c$  as low as 96 °C we are still unable to reach the “diffusion controlled region” by the melt crystallization process [30]. To derive the surface energy parameters of iPP crystals, the classical kinetic theory [28] is applied to analyze the TCL (spherulitic) growth rate data according to Equation (2).

$$G = G_0 \exp \left[ -U^*/R(T_c - T_\infty) \right] \exp \left[ -K_g/T_c \Delta Tf \right] \quad (2)$$

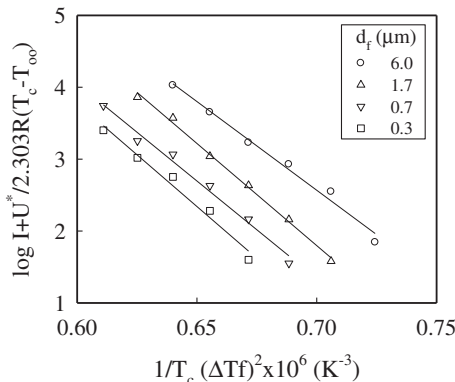


Fig. 7. Variation of nucleation rate with supercooling degree, according to Equation (1), to determine the  $\sigma_e(\Delta\sigma_{TCL})^2$  parameters for sPS with different diameters,  $d_f$ .

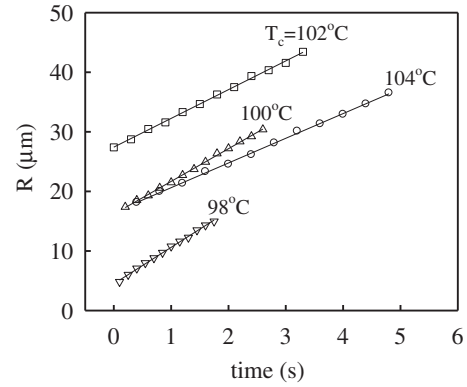


Fig. 8. Determination of crystal growth rate of iPP at low temperatures by a high speed camera to trace the time variation of spherulitic radius in a short period. Spherical growth of  $\alpha$ -form crystals is followed.

where  $G_0$  is a constant and  $K_g$  is a kinetic parameter. Based on Equation (2), the corresponding plot is displayed in the inset of Fig. 9. An evident slope change from  $0.7443 \times 10^5$  K<sup>2</sup> in the high  $T_c$  regime to  $1.5740 \times 10^5$  K<sup>2</sup> in the low  $T_c$  regime is observed at 137 °C, indicating the growth transition from the regime II to regime III. The derived slopes and transition temperature of II  $\rightarrow$  III regime are similar with those reported previously [28,29,31]. It is of importance to note that regime III growth is prevailing down to a temperature of 96 °C (a supercooling of 90 K), suggesting the intactness of  $\sigma_e$  in the  $T_c$  range. The slope ( $K_g$ ) was used to estimate  $\sigma_e$  by the simple relation expressed:  $K_g = j b_0 \sigma_e T_m^0 / k \Delta h_f$  with  $j = 2$  for regime II and 4 for regime III, and  $b_0$  is the width of polymer chains. For the (110) growing plane with  $b_0 \sim 0.626$  nm [28], the calculated values for  $\sigma_e$  are 855.6 and 809.2 erg<sup>2</sup>/cm<sup>4</sup> for the regime III and II growth, respectively. After substituting the reported value of  $\sigma$  ( $\sim 11.5$  erg/cm<sup>2</sup>) [28], the determined  $\sigma_e$  for iPP is *ca.*  $72.4 \pm 2.0$  erg/cm<sup>2</sup>, which is in agreement with previous results [28,29,31]. Thus, the value of  $\Delta\sigma$  for iPP to nucleate on the electrospun sPS fibers is determined to be  $16.6 \pm 0.4$  erg/cm<sup>2</sup> by the ratio of  $[\sigma_e(\Delta\sigma)^2/\sigma_e]^{1/2}$ , in which the numerator and denominator are derived from the nucleation and crystal growth data, respectively. In a short summary, we conclude that thicker fibers yield a higher nucleating density of iPP due to its possession of larger fiber surface, but the nucleating ability of fibers characterized by the magnitude of  $\Delta\sigma$  is independent of the fiber diameter.

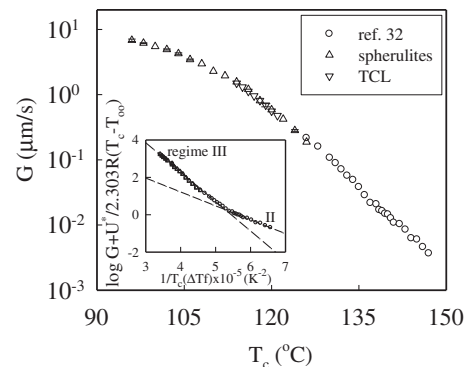


Fig. 9.  $T_c$  dependence of crystal growth rate of iPP in a wide temperature range from 96 to 145 °C. The data measured at the high temperature regime ( $\circ$ ) are obtained from ref. [32]. The inset shows the Hoffman–Lauritzen plot of the growth rate data to determine the  $\sigma_e$  parameter for iPP crystals.

Fig. 10 shows the  $T_c$  dependence of the dimensions of a stable nucleus calculated on the basis of secondary nucleation on a flat substrate (a), and the tertiary nucleation in the groove of a rough substrate (b). Previous data for PTFE fibers [5] are also included for a comparison with those for the present sPS fibers. Based on the secondary heterogeneous nucleation [5], the  $\Delta\sigma$  value for the PTFE fiber was derived to be  $0.75 \text{ erg/cm}^2$ , giving a derived from the, the magnitude of) is about several nanometers, but  $b^*$  ( $= 2\Delta\sigma T_m^0 / \Delta h_f \Delta T_f \sim 0.05\text{--}0.1 \text{ nm}$ ) is *ca.* one order lower than the thickness of mono-molecular layer ( $b_0$ ) as shown in Fig. 10a. Recalculation based on the tertiary heterogeneous nucleation leads to a reasonable and comparable value of  $b^*$  ( $= a^* \sim 0.3\text{--}0.6 \text{ nm}$ ) with respect to  $b_0$  (Fig. 10b), suggesting that mono-molecular layer of iPP is formed on the highly active PTFE surfaces. In contrast, *ca.* 2–4 molecular layers of iPP are required for the relatively inactive sPS fibers to develop a stable nucleus. It should be noted that the dimensions of  $a^*$  and  $b^*$  are in the range of 1–3 nm, which are generally smaller than the surface roughness of common substrates used, but a relatively large magnitude of  $l^*$  ( $= 4\sigma_e T_m^0 / \Delta h_f \Delta T_f \sim 10\text{--}15 \text{ nm}$ ) is seen in Fig. 10, suggesting that  $l^*$  is the most important length scale to be considered. As expected,  $l^*$  is independent of the type of heterogeneous nucleation and its magnitude is increased with increasing  $T_c$ . If the length of the groove is smaller than  $l^*$ , development of stable nuclei through tertiary heterogeneous nucleation is never possible.

In addition to fibers possessing the  $\alpha$ -form crystals, sPS fibers with the mixed  $\alpha/\beta$ -form crystals yielded by thermal annealing to a temperature of  $260 \text{ }^\circ\text{C}$  (Fig. 2) were also used to investigate their ability towards iPP nucleation. In spite of a slight increase in fiber crystallinity, surface roughness of the annealed fibers remains unchanged as-revealed by AFM results. The  $T_c$  dependence of nucleation rate,  $I$ , is displayed by the bottom line in Fig. 11. The

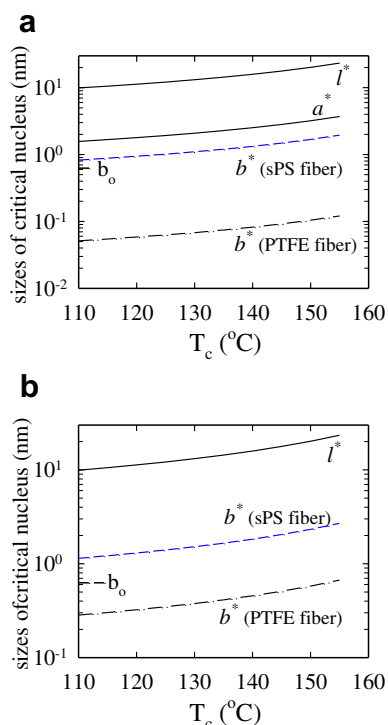


Fig. 10.  $T_c$  dependence of critical dimensions of stable lamellar nucleus ( $a^*$ ,  $b^*$ ,  $l^*$ ) calculated on the basis of (a) secondary nucleation;  $a^*$  is estimated by  $4\sigma_e T_m^0 / \Delta h_f \Delta T_f$ , (b) tertiary nucleation;  $a^* = b^*$ . Only the  $\alpha$ -form of iPP crystals is considered.  $b_0$  is the layer thickness of iPP crystals. sPS and PTFE fibers are used for a comparison.

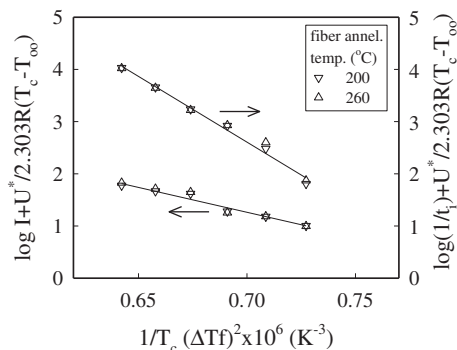


Fig. 11. A comparison of nucleation rate and induction time approaches used to determine  $\sigma_e(\Delta\sigma_{TCL})^2$ . The results show that the Ishida's hypothesis, i.e.  $I \times t_i \sim \text{constant}$ , is not applicable to the present sPS fiber/iPP system ( $d_f$ :  $6.0 \mu\text{m}$ ). Effect of thermal annealing on the nucleating ability of fibers is also elucidated. According to Fig. 2, fibers annealed to  $200 \text{ }^\circ\text{C}$  possess the  $\alpha$ -form crystals; whereas mixed  $\alpha/\beta$ -form crystals are developed for fibers annealed to  $260 \text{ }^\circ\text{C}$ .

inverse triangle symbols are for sPS fibers with the  $\alpha$ -form crystals, and the triangle symbols are for sPS fibers with the mixed  $\alpha/\beta$ -form crystals. For sPS fibers prior to and post to  $260 \text{ }^\circ\text{C}$  annealing, the measured data are superimposed to form a straight line. It is evident that crystal modification exhibits a negligible effect on the nucleating ability of fibers. Ishida and Bussi proposed a simple relation between  $I$  and  $t_i$  as [4]:

$$I(T_c) \times t_i(T_c) = \text{invariant} \quad (3)$$

Provided that Equation (3) is held valid,  $\log(1/t_i)$  could be used, instead of using  $\log I$ , to derive the  $\Delta\sigma$  value according to Equation (1). This simple relation has been verified for the PE fiber/PE matrix composites [4] as well as the iPP composites consisting of high modulus (HM) carbon fibers and PTFE fibers [5]. To test this hypothesis for the present sPS fibers, the corresponding  $\log(1/t_i)$  plots are also included in Fig. 11 (upper line). Compared to the line constructed by the nucleation rate data, however, a different slope is readily seen. It indicates that Ishida's hypothesis is not applicable to the sPS fiber/iPP system and an over-estimated  $\Delta\sigma$  will be obtained if the induction time approach is used. The inapplicability of Equation (3) for the present sPS fibers is attributable to the non-uniformity in the fiber roughness as shown in Fig. 6(a). Similar findings and conclusions have been reported for the Kevlar fiber/iPP and PET fiber/iPP systems [5].

### 3.2. Transcrystallization of iPP on Nylon, PBO and PHA fibers

Previous results have already demonstrated that melt-spun Nylon fibers with a diameter of several tens micrometers showed good nucleating ability towards iPP matrix to develop TCL at the interface [33]. In contrast, Nylon fibers with a diameter of sub-micrometers only become available recently by the electrospinning process and their nucleating ability is still unknown. Fig. 12a shows the SEM micrograph of the studied Nylon fibers here by solution electrospinning at room temperature and a higher magnification is displayed in the inset. The as-electrospun fibers are uniform with an average diameter of  $\sim 0.37 \mu\text{m}$ , and possess the major  $\gamma$ -form crystals with monoclinic lattices according to their FTIR spectra and electron diffraction patterns (not shown here for brevity). The fiber crystallinity fraction determined from wide-angle X-ray diffraction is  $\sim 0.37$ . After being embedded in the iPP matrix, Nylon fibers readily induce the TCL formation as evidenced in Fig. 12b.  $T_{max}$  for the electrospun Nylon fibers is found to be  $140 \text{ }^\circ\text{C}$ , which is higher than that of the electrospun sPS fibers ( $118 \text{ }^\circ\text{C}$ ) having a similar

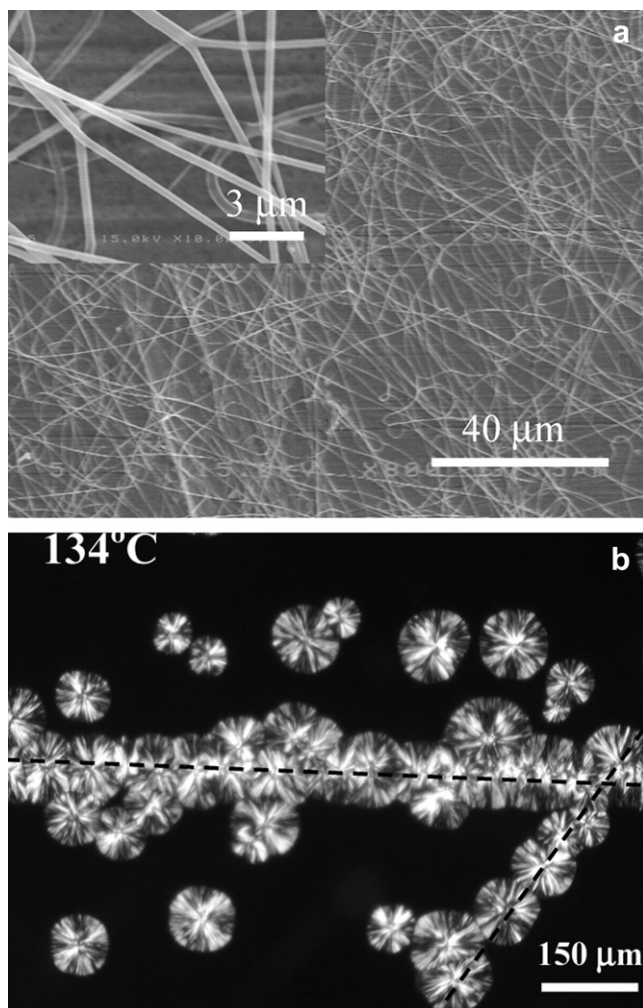


**Fig. 12.** (a) SEM images of electrospun Nylon fibers and the inset providing a higher magnification, (b) transcrystallization of iPP on Nylon fibers at 134 °C. The dashed lines show the fiber position. [ $d_f = 0.37 \mu\text{m}$ , fibers prepared by electrospinning of 18 wt.% Nylon solutions under processing variables of 0.1 mL/hr, 15.06 kV, and tip-to-collector distance of 7 cm].

diameter. It suggests that nucleation of iPP is more likely to take place at the surface of Nylon fibers than sPS fibers. As shown in Fig. 13, indeed, a lower slope is obtained for the Nylon fibers when the nucleation rate is plotted against the supercooling parameter,

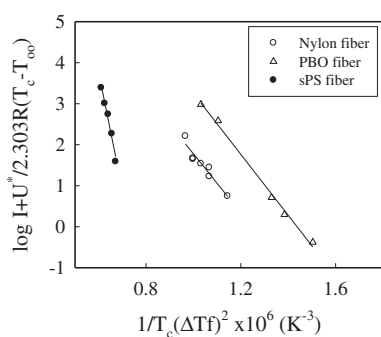


**Fig. 13.** Variation of nucleation rate with supercooling degree, according to Equation (1), to determine the  $\sigma_e(\Delta\sigma_{TCL})^2$  parameters for Nylon fibers (open circles), PBO fibers (open triangles) and sPS fibers with a  $d_f$  of 0.3  $\mu\text{m}$  (filled circles).

$T_c(\Delta T)^2$ , according to Equation (1). The derived  $\Delta\sigma$  for the electrospun Nylon fiber is  $9.36 \pm 0.32 \text{ erg/cm}^2$ , which is lower than that for the sPS fiber. It seems that there is an intimate correlation between  $\Delta\sigma$  and  $T_{\text{max}}$  in determining the nucleating ability of fibers. This issue will be addressed in the later section.

Compared to the well-documented Kevlar fiber used as a reinforcement material in advanced composites, PBO fibers also possess outstanding mechanical properties, long-term stability and excellent resistance to high temperature due to its rigid-rod molecular structure. Several studies showed that the mechanical properties of PBO fibers are even superior to those of Kevlar fibers; however, whether PBO fibers can induce the TCL formation of iPP is still not explored yet. As shown in Fig. 14, PBO fibers are found to be able to induce the nucleation and growth of iPP at its surface without difficulties. For a higher  $T_c$ , the nucleation density is lower, but a thicker TCL is observed.  $T_{\text{max}}$  for the PBO fiber/iPP system is  $\sim 143 \text{ }^\circ\text{C}$ , which is identical to that for the Kevlar fiber [5]. Similar data analyses have been conducted on the PBO fibers and the results are displayed in Fig. 13 (triangle symbols). From the linear slope, the corresponding  $\Delta\sigma$  is determined to be  $8.48 \pm 0.45 \text{ erg/cm}^2$  for the PBO fibers. Moreover, it was found that Equation (3) was not applicable to the PBO fiber/iPP system, attributable to the non-uniform fiber surface possessing the microfibrillar structure covered partially by contaminant layers [34]. The microfibrils in the PBO fibers were reported to be 10–20 nm wide, stretching parallel

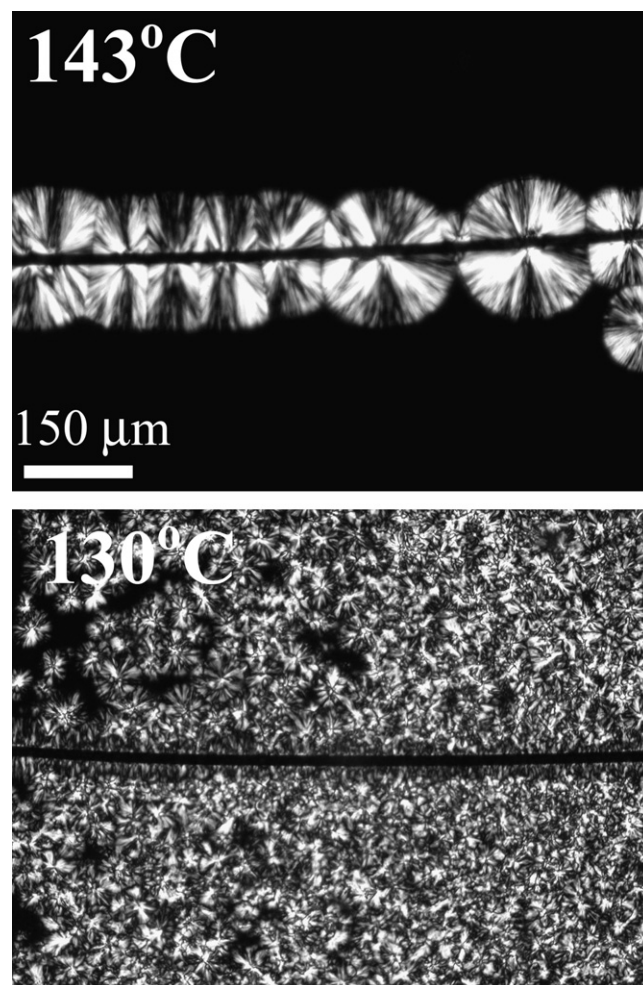


**Fig. 14.** iPP transcrystallization on the PBO fibers at 143 °C (top) and 130 °C (bottom) [ $T_{\text{max}} = 143 \text{ }^\circ\text{C}$ ,  $d_f = 15.1 \mu\text{m}$ ].



to the fiber axis over several tens of nanometers [34]. The microfibrils provide the necessarily sized grooves at the fiber surface to host the crystallizing iPP segments.

The electrospun PHA fibers used for TCL studies are amorphous [19]. Its glass transition temperature ( $T_g$ ) is  $\sim 280$  °C and fiber diameter is  $\sim 0.33$   $\mu\text{m}$ . TCL formation was not seen in a wide temperature range, 120–140 °C, suggesting that no preferential nucleation of iPP takes place on the fibers in comparison with that in the bulk. Despite of its inability to induce TCL for a single PHA fiber, PHA fiber bundles are found to be capable of induce the iPP nucleation between individual fibers as shown in Fig. 15, in which the top row images are taken at 24 min after isothermal crystallization at 145 °C, and those at the bottom are snapshot at 80 min. Within the right dense bundle, many iPP crystals are nucleated, and gradually grow outwards to the bundle surface. In contrast, the left branch consisting of loosely packed fibers is unable to induce iPP nucleation. This finding suggests that the mobility of iPP chains in the constrained region set by the densely packed fibers could be greatly reduced and incubation of stable nuclei therein becomes feasible. Similar observation was reported by Zhang *et al.* who provided the direct evidence of TCL formation on the carbon nanotube bundle, instead of single CNT [17]. After step-wise cyclization to a high temperature of  $\sim 350$  °C, the as-spun PHA fibers were converted to become BisAPAF-IC PBO fibers having a  $T_g$  of 314 °C [19]. In contrast with the commercial PBO fibers, our BisAPAF-IC PBO fibers were unable to induce the TCL formation of iPP.

### 3.3. Roles of fiber surface–height and length of grooves

At the fiber surface, morphological features of grooves and ridge/valley are often observed. A roughness distribution of fiber surface is expected, and its average is denoted by  $R_q$ . AFM conveniently provides the groove height by  $R_q$ , but a quantitative analysis

of groove length is not readily available. For most studied fibers,  $R_q$  is generally larger than the  $b^*$  dimension of the stable nuclei (Table 1 and Fig. 10), thereby suggesting that length of grooves with respect to  $l^*$  is the determining factor for the tertiary nucleation to take place. To the first approximation, fibers with a rough surface are more likely to possess a long groove length, implying that the population of active grooves may be increased for fibers with a larger  $R_q$ . In the absence of appropriate roughness to accommodate the stable nuclei, TCL formation becomes unlikely. Such a case is often seen for the un-treated glass fibers. In contrast, TCL is readily seen for the chemically treated glass fibers, attributable to the creation of rough surface with at least a length scale larger than  $l^*$  [35].

For the present iPP chains in the melt state, the estimated diameter of random coils ( $D_g$ ) is  $\sim 37$  nm [36], and the width of an iPP chain stem ( $W_s$ ) is  $\sim 0.5$  nm [28]. A preferred substrate to proceed the tertiary nucleation is the presence of surface grooves with a width smaller than  $D_g$  but larger than  $W_s$ . In these particular sites only portion of the chain coil is able to penetrate into the small grooves to form the nuclei. After deposition of first crystalline layer on the substrate, the stable nuclei readily grow in a manner according to the classical growth theory given by Equation (2).

Surface nucleation can also be preferentially induced by the epitaxial mechanism [24,25,37–39], which is widely investigated and used to account for the TCL formation. True epitaxy (an atomistic level of epitaxy) suggests one or two-dimensional lattice match at the interface between the epitaxial crystals and the underlying substrate. Without taking the nucleation into consideration, the major requirement for true epitaxy is that the discrepancy between the lattice parameters is less than 10–15%. For iPP, three active substrate surfaces characterized by topological regularity of 0.5, 0.65 and 0.56 nm are reported to give rise to the either homo- or hetero-epitaxies [24]. It can be considered as

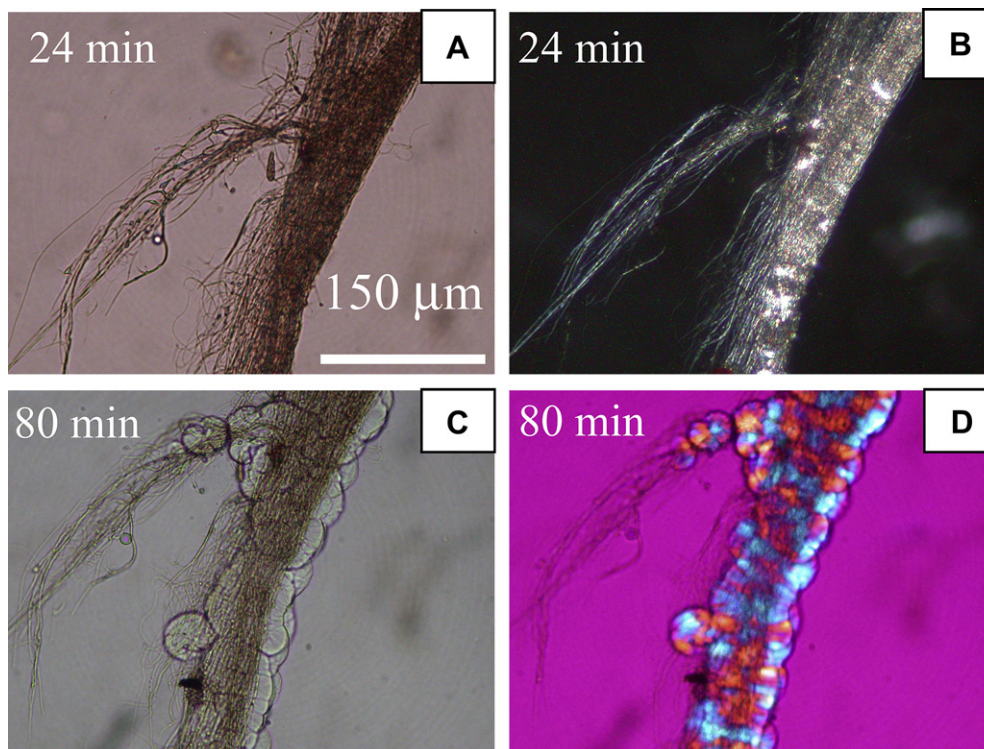


Fig. 15. Transcrystallization process of iPP in the PHA fiber bundle at 145 °C. Note the absence of TCL formation on the left branch consisting of loosely packed fibers. (A, C): parallel-polarized, (B) cross-polarized, (D) cross-polarized with  $\lambda$ -plate. The individual fiber in the bundle has a diameter of  $\sim 0.33$   $\mu\text{m}$ .



**Table 1**  
Fiber characteristics to induce iPP transcrystallization.

fiber type	$d_f$ ( $\mu\text{m}$ )	$\Delta\sigma$ ( $\text{erg}/\text{cm}^2$ )	$T_{\text{max}}$ ( $^{\circ}\text{C}$ )	$I \times t_i$ = Const.	$R_q$ (nm)	source
PTFE	30	$4.15 \pm 0.33$	156	Yes	40	ref. [5]
Carbon	8	$5.12 \pm 0.56$	141	Yes	10	ref. [5]
PBO	15	$8.48 \pm 0.45$	143	No	$15^{34}$	this work
Kevlar	15	$8.78 \pm 0.24$	143	No	10	ref. [5]
Nylon	0.37	$9.36 \pm 0.32$	134	No	NA	this work
PET	12	$11.6 \pm 0.5$	136	No	8	ref. [5]
sPS	0.3–6.0	$16.7 \pm 0.3$	118–121	No	3–15	this work

$\Delta\sigma$  is derived on the basis of tertiary nucleation theory. Re-calculation of nucleation data in ref. [5] is carried out to derive the present value of  $\Delta\sigma$ .

a special case of our phenomenal model for tertiary nucleation that the chain segments are trapped in the shallow grating-like grooves set by the crystal planes of the underlying substrate. On the basis of secondary nucleation, a template model was alternatively proposed by Greso and Phillips to account for true epitaxial growth of polymers [37]. The requirement for the formation of secondary nuclei on the flat substrate is that the crystal dimension of the substrate in the matching direction must be larger than  $l^*$  of the epitaxially grown crystals. There are many evidences to support the true epitaxy of iPP on the thin film substrate using electron diffraction technique [24,25,38,39]. A correct analysis of epitaxy has to be carefully done at the atomic scale. For the present fibers used for TCL formation, it should be reminded that the crystal structure at the fiber surface may be more disordered than that in the fiber core.

### 3.4. Role of transient thermal stress

When the fiber/iPP sample is rapidly cooled from  $T_m$  (200  $^{\circ}\text{C}$  in this study) to  $T_c$ , transient thermal stress ( $tTS$ ) is likely to establish at the solid fiber surface as a result of temperature gradient across the fiber, in that the fiber surface changes temperature more rapidly than the interior. The magnitude of the transient thermal stresses is dependent upon a temperature change ( $\Delta T = T_m - T_c$ ) as well as temperature distribution inside the fiber [5,40,41]. The induced thermal stress should become vanished when the temperature of fiber center reaches  $T_c$  since there is no constrains set at the fiber surface, i.e. the fiber is a free body surrounded by the iPP melt. The direction of  $tTS$  is parallel with the fiber surface and  $tTS$  is null perpendicular to the fiber surface, i.e. the  $r$ -component strain is relieved by the radial expansion (or shrinkage). Conceptually, these normal stresses are more effective to pre-align the polymer chain segments adjacent to the solid fiber for producing the stable nuclei in the vicinity of the fibers. The stretched segments could serve as the potential nuclei for later TCL growth provided that its relaxation process is slow. Due to the possession of a longer relaxation time, iPP with a higher molecular weight was verified to be able to develop TCL at a higher temperature than the low MW species under the same crystallization condition [8]. Thus, TCL formation is kinetically associated with the competition and the resultant balance between the chain orientation induced by  $tTS$  and relaxation process of these oriented segments. For a given fiber, TCL is more readily seen at a lower  $T_c$  and there exists a  $T_{\text{max}}$  above which TCL formation becomes difficult due to a small  $tTS$  and fast segment relaxation.

Our proposed model is based on the quiescent crystallization process, which is different from shear-induced crystallization by continuous fiber-pulling experiment [9,42,43]. In the fiber-pulling process, the driving force for the TCL formation is the mechanical shear stress, which is uniformly transferred from the solid fiber to iPP melt. The melt chains are thus engaged in local networks of aligned and ordered clusters [42], which act as crystallization

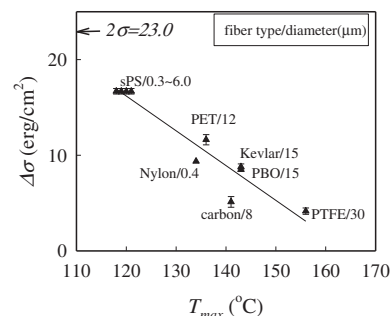


**Fig. 16.** A plot of  $\Delta\sigma$  versus  $T_{\text{max}}$  for various fibers to reveal their nucleating abilities for iPP crystallization. The data of PTFE, Kevlar, PET and high modulus carbon fibers are obtained from ref. [5]. Fiber diameters are also displayed for a comparison.

nuclei. In this manner, the substrate plays no role for the heterogeneous nucleation, but just fulfills the stress-transfer means. Glass fibers are known to be unable to induce TCL in the quiescent crystallization due to its smooth surface, but become capable of producing thick TCL through application of shear stress by fiber-pulling since the surface roughness is not an issue [8,9,44].

### 3.5. Nucleating ability of various fibers

The nucleation results obtained from the present study are displayed in Table 1. Using the same batch of iPP matrix, other fibers reported previously are also included for a detailed comparison of their ability to induce TCL formation [5]. For all the active fibers, only  $\alpha$ -form iPP transcrystallites were observed at the fiber/matrix interface. From a thermodynamic point of view, fibers with a lower  $\Delta\sigma$  can transcrystallize iPP more easily since the total free energy required to develop the stable nuclei at the fiber surface is lower. Thus, the ability of PTFE fibers to nucleate TCL growth is the best in spite of its lowest surface energy, whereas the sPS fiber exhibits the least nucleation ability toward iPP. Fig. 16 shows the plot of  $\Delta\sigma$  versus  $T_{\text{max}}$  for all the active fibers, obtained from the commercial and electrospun ones, with  $d_f$  in a wide range of 0.3–30  $\mu\text{m}$ . It should be reminded that  $\Delta\sigma$  is independent of  $d_f$  (Fig. 7), but  $T_{\text{max}}$  is slightly increased with  $d_f$  (Fig. 5, ca. 3  $^{\circ}\text{C}$  difference in  $T_{\text{max}}$  for sPS fibers with 20 times difference in  $d_f$ ). Based on Fig. 16, a general correlation can be seen: a higher  $T_{\text{max}}$  is expected for fibers with a lower  $\Delta\sigma$ . Thus, the parameter  $T_{\text{max}}$  also provides a measure of the nucleating ability of a given fiber.

## 4. Conclusion

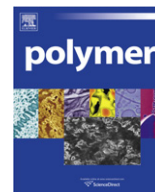
In combination with previous studies [5], seven different fibers were used for a comparison of their nucleating ability towards iPP by evaluating the nucleation rate of iPP at the fiber/matrix interface at various  $T_c$ . Under a quiescent melt crystallization condition, only  $\alpha$ -form iPP transcrystallites were observed at the interface for those fibers, which were capable of producing TCL. The driving force to pre-align chain segments as the stable nucleus is associated with the thermal stress induced at the fiber surface during cooling by the transient temperature gradient, not the mismatch of thermal expansion coefficient between the solid fiber and melt matrix as proposed by Thomason *et al* [8]. In addition, surface grooves with sufficient dimensions to adapt the stable nuclei seem necessary for tertiary heterogeneous nucleation to take place, leading to the formation of TCL.

## Acknowledgments

The authors are grateful to Prof. S. L. C. Hsu (NCKU) for providing the PHA powders, and to the National Science Council of the Republic of China (Taiwan) for supporting this study. Financial support from the National Cheng Kung University through the “Landmark Program of the NCKU top University Project” is also highly appreciated.

## References

- [1] Kewi TK, Schonhorn H, Frisch HL. *J Appl Phys* 1967;38:2512–6.
- [2] Hata T, Ohsaka K, Yamada T, Nakamae K, Shibata N, Matsumoto T. *J Adhes* 1994;45:125–35.
- [3] Amitay-Sadovsky E, Cohen SR, Wagner HD. *Macromolecules* 2001;34:1252–7.
- [4] Ishida H, Bussi P. *Macromolecules* 1991;24:3569–77.
- [5] Wang C, Liu CR. *Polymer* 1999;40:289–98.
- [6] Lin CW, Ding SY, Hwang YW. *J Mater Sci* 2001;36:4943–8.
- [7] Sun X, Li H, Zhang X, Wang J, Wang D, Yan S. *Macromolecules* 2006;39:1087–92.
- [8] Thomason JL, Van Rooyen AA. *J Mater Sci* 1992;27:889–96.
- [9] Cai Y, Petermann J, Wittich H. *J Appl Polymer Sci* 1997;65:67–75.
- [10] Quan H, Li ZM, Yang MB, Huang R. *Compos Sci Technol* 2005;65:999–1021.
- [11] Chen EJH, Hsiao BS. *Polymer Eng Sci* 1992;32:280–6.
- [12] Cho K, Kim D, Yoon S. *Macromolecules* 2003;36:7652–60.
- [13] Gati A, Wagner HD. *Macromolecules* 1997;30:3933–5.
- [14] Wang C, Hwang LM. *J Polymer Sci Part B Polymer Phys* 1996;34:1435–42.
- [15] Iijima S. *Nature* 1991;354:56–8.
- [16] Miltner HE, Grossiord N, Lu K, Loos J, Koning CE, Van Mele B. *Macromolecules* 2008;41:5753–62.
- [17] Zhang S, Minus ML, Zhu L, Wong CP, Kumar S. *Polymer* 2008;49:1356–64.
- [18] Cheng YW, Lu HA, Wang YC, Thierry A, Lotz B, Wang C. *Macromolecules* 2010;43:2371–6.
- [19] Hsu SLC, Lin KS, Wang C. *J Polymer Sci Part A Polymer Chem* 2008;46:8159–69.
- [20] Guerra G, Vitagliano VM, De Rosa C, Petraccone V, Corradian P. *Macromolecules* 1990;23:1539–44.
- [21] Reynolds NM, Stidham HD, Hsu SL. *Macromolecules* 1991;24:3662–5.
- [22] Sukhanova TE, Lednický F, Urban J, Baklagina YG, Mikhailov GM, Kudryavtsev VV. *J Mater Sci* 1995;30:2201–14.
- [23] Wunderlich B. *Macromolecular physics*, vol. 2. New York: Academic Press; 1976 [chap. 5].
- [24] Yan S, Katzenberg F, Petermann J, Yang D, Shen Y, Straupé C, et al. *Polymer* 2000;41:2613–25.
- [25] Wittmann JC, Smith P. *Nature* 1991;352:414–7.
- [26] Binsbergen FL. *J Polymer Sci Part B Polymer Phys* 1973;11:117–35.
- [27] Shanbhag S, Alamo RG. *Polymer* 2008;49:2515–9.
- [28] Clark EJ, Hoffman JD. *Macromolecules* 1984;17:878–85.
- [29] Cheng SZD, Janimak JJ, Zhang A, Cheng HN. *Macromolecules* 1990;23:298–303.
- [30] Di Lorenzo ML, Silvestre C. *Thermochim Acta* 2003;396:67–73.
- [31] Shangguan Y, Song Y, Zheng Q. *Polymer* 2007;48:4567–77.
- [32] Wang C, Hwang LM. *J Polymer Sci Part B Polymer Phys* 1996;34:47–56.
- [33] Lopez-Manchado MA, Arroyo M. *Polymer* 1999;40:487–95.
- [34] Tamargo-Martinez K, Villar-Rodil S, Paredes JI, Martinez-Alonso A, Tasóon JMD, Montes-Morán MA. *Macromolecules* 2003;36:8662–72.
- [35] Li Y, Chen L, Zhou X. *J Mater Sci* 2008;43:5083–91.
- [36] Wignall GD, Mandelkern L, Edwards C, Glotin M. *J Polymer Sci Part B Polymer Phys* 1982;20:245–58 [The radius of gyration ( $R_g$ ) of iPP chains was related to the molecular weight (MW) by the equation of  $R_g/MW^{1/2}=0.035 \text{ nm}/(\text{g/mol})^{1/2}$ ].
- [37] Greso AJ, Phillips PJ. *Polymer* 1994;35:3373–6.
- [38] Yan S, Yang D, Petermann J. *Polymer* 1998;39:4569–78.
- [39] Beekmans LGM, Vallée R, Vancso GJ. *Macromolecules* 2002;35:9383–90.
- [40] Boley BA, Weiner JH. *Theory of thermal stresses*. New York: John Wiley & Sons, Inc; 1960 [chap. 9].
- [41] Timoshenko SP, Doodier JN. *Theory of elasticity*. Singapore: McGraw-Hill; 1970 [p. 447].
- [42] Azzurri F, Alfonso GC. *Macromolecules* 2005;38:1723–8.
- [43] Varga J, Karger-Kocsis J. *J Polymer Sci Part B Polymer Phys* 1996;34:657–70.
- [44] Gray DG. *J Polymer Sci Polymer Lett* 1974;12:645.



## Functional thiol ionic liquids as novel interfacial modifiers in SBR/HNTs composites

Yanda Lei, Zhenghai Tang, Lixin Zhu, Baochun Guo\*, Demin Jia

Department of Polymer Materials and Engineering, South China University of Technology, Guangzhou 510640, China

### ARTICLE INFO

#### Article history:

Received 30 August 2010

Received in revised form

11 January 2011

Accepted 13 January 2011

Available online 20 January 2011

#### Keywords:

Ionic liquid

Halloysite nanotubes

Interface

### ABSTRACT

Two kinds of thiol ionic liquids (ILs), 1-methylimidazolium mercaptopropionate (MimMP) and bis (1-methylimidazolium) mercaptosuccinate (BMimMS), were investigated as novel interfacial modifiers for styrene butadiene rubber/halloysite nanotubes (SBR/HNTs) composites. According to model compounds, it was found that their affinities toward HNTs were originated from hydrogen bonding and that they could be grafted onto SBR chains via thiol-ene reactions. The ILs addition could promote vulcanization and effectively facilitate HNTs dispersion in rubber matrix. The interfacial interaction, quantitatively evaluated by a proposed equation based on rubber elasticity and reinforcement theory, was consistently increased. Mechanical properties of SBR/HNTs vulcanizates were largely improved and better than those of the 3-mercaptopropyl trimethoxysilane modified system. The BMimMS's efficiency on modifying SBR/HNTs vulcanizates was higher than the other for its Gemini structure. Significantly mechanical improvements and lowered mechanical loss in the range of 50–80 °C were correlated to the improved HNTs dispersion and strengthened interfacial interactions.

© 2011 Elsevier Ltd. All rights reserved.

### 1. Introduction

Halloysite nanotubes (HNTs), as one type of naturally occurring clays with nanotubular structure, were extensively studied as promising filler for polymer composites with remarkable improved mechanical properties, thermal stability and flammability [1]. The functional group of HNTs such as hydroxyl group is mainly located in the internal surface and the tube end. The distribution of functional groups was considered to be helpful for the fine dispersion of HNTs in polymer composites. However, the interfacial interaction between HNTs and polymer was not satisfied. Therefore, the interfacial modification is still one of the great challenges in fabrication of polymer/HNTs nanocomposites with desired performance [2–5].

Ionic liquid (IL), as one kind of versatile agents, could be utilized to improve the conductivity of polymers [6–8] and promisingly to be explored for fabricating protic conductor [7], actuator [8], and other functional devices [9]. ILs were considered to be potential modifiers in filled polymer composites for their high affinities toward carbon nanotubes [10–13], silica [14,15] and clays [14]. The versatile interactions between ILs and fillers have confirmed to be cation- $\pi$  [11,13,16],  $\pi$ - $\pi$  [15,17], van der Waals [18], hydrogen

bonding [10,19] and delocalized electron interactions [20]. ILs/silica interactions were widely employed in controlling their morphologies [15,21,22], fabricating stationary phase for HPLC [23,24], improving thermal stability [14] and enhancing the extracting efficiency [25].

One kind of common ILs, 1-butyl-3-methyl-imidazolium hexafluorophosphate (BMimPF<sub>6</sub>), was previously found to be able to strongly adsorb onto HNTs surface and acknowledged to be one of promising agents to improve filler dispersion and strength interfacial bonding [26]. Recently, designing ILs with functional groups has been expected for tailoring the interface of polymer composites. Introducing functional groups, such as double bond group [27,28] and thiol group [29], into IL was highlighted for improving the performance of rubber composites. The thiol-ene chemistry, which was widely focused for its mild reaction condition, high reactivity and excellent yielding, is now under extensive investigation in the technology of photocrosslinking [30,31] and in fabricating functional materials [31–36]. In the present work, two kinds of functional IL, 1-methylimidazolium mercaptopropionate (MimMP) and bis (1-methylimidazolium) mercaptosuccinate (BMimMS), were investigated as modifiers for tailoring the interfacial structure of SBR/HNTs composites. The influences of functional ILs on vulcanization behavior, mechanical performance and morphology were studied. With a proposed equation on evaluating the interfacial interaction by stress–strain curves, interfacial interactions induced by thiol-containing ILs were quantitatively

\* Corresponding author. Tel.: +86 20 8711 3344; fax: +86 20 2223 6688.  
E-mail address: [psbcguo@scut.edu.cn](mailto:psbcguo@scut.edu.cn) (B. Guo).

compared and correlated to the morphology and the HNTs dispersion in SBR/HNTs vulcanizates.

## 2. Experimental

### 2.1. Materials

N-methylimidazole (99% purity), 3-mercaptopropionic acid (98% purity) and mercaptosuccinic acid (99% purity) were purchased from Alfa Aesar, Tianjin, China. Styrene butadiene rubber (SBR), with trade name SBR1502 (styrene content 23.5 wt%), was manufactured by Jilin Chemical Industry Company, China. HNTs was mined from Hubei, China and purified according to the procedure [37]. The Brunauer–Emmett–Teller (BET) value of HNTs was determined to be 50.4 m<sup>2</sup>/g by an ASAP 2020 surface area/porosity analyser (Micromeritics, America). Other rubber additives were industrial grade and used as received.

### 2.2. Synthesis of MimMP and BMimMS

The synthesis of MimMP was followed by another work [29]. Typically, stoichiometrical 3-mercaptopropionic acid was slowly added into 1-methylimidazole under stirring at ambient temperature. After a reaction for 4 h, the liquid product of bis(1-methylimidazolium) mercaptosuccinate (BMimMS) was obtained. MimMP was characterized elsewhere [29] and BMimMS was characterized by <sup>13</sup>C NMR and FTIR [38–40]. These NMR and FTIR spectra were collected on the Bruker Avance Digital NMR spectrometer (300 MHz, Buchen, Germany) and Bruker Vertex 70 FTIR spectrometer (Buchen, Germany), respectively. <sup>13</sup>C NMR (BMimMS, D<sub>2</sub>O): 180.1 (–CH<sub>2</sub>–COO), 179.0 (–CH–COO), 134.9 (–N–C=N–), 122.8 (–C=C–N(CH<sub>3</sub>)–), 120.0 (=N–C=CH–N(CH<sub>3</sub>)–), 43.9 (–CH–SH), 41.2 (–CH<sub>2</sub>–COO), 35.3 (–N–CH<sub>3</sub>). FTIR (BMimMS, KBr): 3414(N–H), 3140(imidazolium–H), 2959(CH<sub>2</sub>), 2557(S–H), 1688(C=O), 1525 and 1576 (imidazolium conjugate). The structure of BMimMS, MimMP and a typical thiol-containing silane (3-mercaptopropyl trimethoxysilane, MPTS) were shown in Table 1.

### 2.3. Affinity of functional ILs toward HNTs and their reactivity toward SBR chains

Interactions between ILs and HNTs were determined by X-ray photoelectron spectroscopy (XPS, Kratos Axis Ultra DLD; Kratos

Analytical, Eppstein, Germany). A monochromated Aluminum K $\alpha$  source (1486.6 eV) was used and all XPS spectra were individually calibrated to its reference C1s component at 285.0 eV [41]. Shirley background and Gaussian function were employed in the fitting program to distinguish the delicate difference of the chemical environment. For the preparation of model compounds (HNTs/MimMP, HNTs/BMimMS and HNTs/MPTS) used for XPS experiment, HNTs with a loading of 10 wt% modifier in a solution of acetone was subjected to sonication, centrifugation and vacuum drying. The reactivity of ILs toward rubber chains could be verified by a model compound [29]. The reaction of SBR/MimMP (or BMimMS)/AIBN (1/1/0.02, wt/wt/wt) was performed at 65 °C for 12 h. The crude product was first washed with plenty water and then extracted by water for 2 days. After vacuum dried at 80 °C, their graft products, SBR-g-MimMP and SBR-g-BMimMS, were characterized by Attenuated total reflection fourier transform infrared (ATR-FTIR) spectroscopy. These ATR-FTIR spectra were collected on the Bruker FTIR spectrometer.

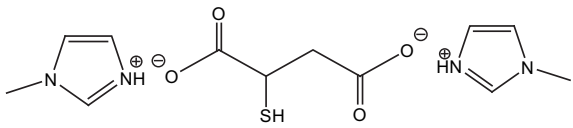
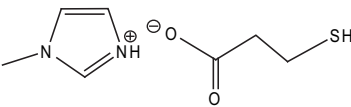
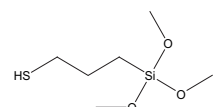
### 2.4. Preparation of SBR/HNTs compounds and characterizations

All the rubber compositions were summarized in Table 2. SBR and other additives were mixed on an open two-mill mill. The curing characteristics of the rubber compounds were determined using a UR-2030 vulcameter (U-CAN, Taiwan) at 150 °C. The rubber compounds were vulcanized at 150 °C  $\times$  Tc90. For a comparison with MPTS, the rubber compound with a 4 phr of MPTS was coded as R4MPTS to ease following discussion.

Tensile, tear and hardness tests of the vulcanizates were performed following ISO 37-2005, ISO 34-2004 and ISO 7619-2004, respectively. Crosslink density ( $V_e$ ) of the vulcanizates was determined by the equilibrium swollen method [42]. Dynamic mechanical analysis was performed on an EPLEXOR dynamic mechanical analyzer (Gabo Qualimeter Testanlagen GmbH; Germany). The samples are scanned from –100 to 100 °C at 3 °C/min. A tensile mode was adopted.

The specimens of vulcanizates were ultramicrotomed into thin pieces of about 300 nm in thickness with Leica EMUC6 in liquid nitrogen. The transition electron microscopy (TEM) observations were done using a Philips Tecnai 12 transmission electron microscope (Eindhoven, Netherlands) with an accelerating voltage of 30 kV.

**Table 1**  
Structure of BMimMS, MimMP and MPTS.

Sample	Composition	M. W. (g/mol)	Structure
BMimMS	C <sub>12</sub> H <sub>18</sub> O <sub>4</sub> N <sub>4</sub> S	314.4	
MimMP	C <sub>7</sub> H <sub>12</sub> O <sub>2</sub> N <sub>2</sub> S	188.2	
MPTS	C <sub>6</sub> H <sub>16</sub> O <sub>3</sub> SiS	196.3	



**Table 2**  
Composition of SBR/HNTs rubber composites.<sup>a</sup>

SBR	HNTs	MimMP	Sample code	BMimMS	Sample code
100	40	0	Blank	/	/
100	40	1	R1MimMP	1	R1BMimMS
100	40	2	R2MimMP	2	R2BMimMS
100	40	3	R3MimMP	3	R3BMimMS
100	40	4	R4MimMP	4	R4BMimMS

<sup>a</sup> rubber ingredients: zinc oxide 5, stearic acid 1, N-cyclohexyl-2-benzothiazole sulfenamide (CZ) 1.5, dibenzothiazole disulfide (DM) 0.5, 2-mercaptobenzimidazole 1.5, sulfur 1.5 (all in parts per hundred parts of rubber, phr).

### 3. Results and discussion

#### 3.1. Reactivity of MimMP and BMimMS toward SBR chains

Thiol-ene reaction is versatile in photocrosslinking elastomers and fabrication of functional materials [30,35,43]. The reactivity of MimMP and BMimMS toward rubber chains is revealed by FTIR spectra of their grafts as shown in Fig. 1. The aromatic hydrogen (3025 and 3061  $\text{cm}^{-1}$ ), the  $\text{CH}_2$  (2917 and 2847  $\text{cm}^{-1}$ ), the *trans*  $>\text{C}=\text{CH}<$  (965  $\text{cm}^{-1}$ ), the vinyl ( $>\text{C}=\text{CH}_2$ ; 913  $\text{cm}^{-1}$ ) and the phenyl (699  $\text{cm}^{-1}$ ) are assigned to the SBR backbone [44,45]. In the lower two curves, the presence of characteristic groups of ILS, such as carbonyl (1708  $\text{cm}^{-1}$ ),  $\text{C}=\text{N}$  (1553  $\text{cm}^{-1}$ ) and  $\text{C}=\text{C}-\text{H}$  (3149  $\text{cm}^{-1}$ ) in the imidazolium cation [40,46], indicates the successful grafting onto SBR chains.

Still, from the FTIR spectra, the grafting sites could be found and the difference on their grafts could be compared according to the integration of absorption peaks of different groups. The integration result is tabulated in Table 3. For SBR-g-MimMP, the intensity ratio of  $I_{(913, >\text{C}=\text{CH}_2)}/I_{(699, \text{phenyl})}$  is obviously decreased from 79% for SBR to 61% with a decrement about 22%. The  $I_{(965, >\text{C}=\text{CH}-)}/I_{(699, \text{phenyl})}$  ratio, however, is decreased but in a limited degree about 14%. It implies that the reactivity of thiol toward vinyl is much higher than that toward double bond ( $-\text{CR}=\text{CH}-$ ) in the backbone [31,33,35]. For SBR-g-BMimMS, the ratio values of  $I_{(913, >\text{C}=\text{CH}_2)}/I_{(699, \text{phenyl})}$  and  $I_{(965, >\text{C}=\text{CH}-)}/I_{(699, \text{phenyl})}$  are decreased by 12% and 7%, respectively. The lower activity for BMimMS toward SBR estimated by this method may be related to the higher molecular weight of BMimMS. Noticeably, the thiol content of MimMP (1/344  $\text{mol g}^{-1}$ ) is much higher than that for BMimMS (1/188  $\text{mol g}^{-1}$ ).

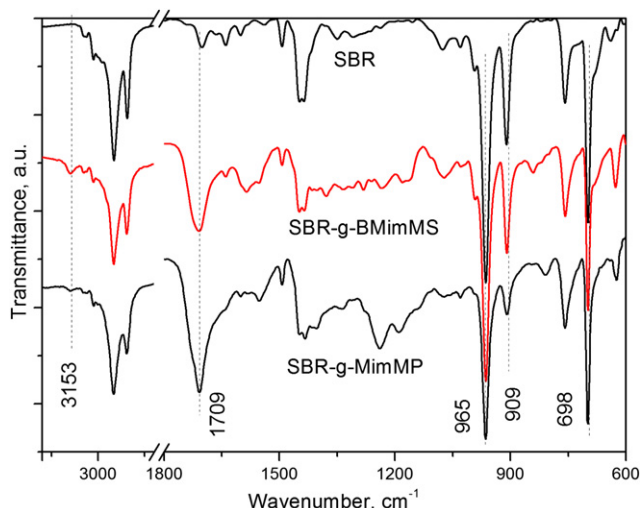


**Fig. 1.** FTIR spectra of SBR, SBR-g-BMimMS and SBR-g-MimMP.

**Table 3**  
Integration results of FTIR spectra.

	Phenyl	$-\text{CH}=\text{CH}_2$	$-\text{CH}=\text{CH}-$	$I_{(>\text{C}=\text{CH}_2)}/I_{(\text{phenyl})}$	$I_{(>\text{C}=\text{CH}-)}/I_{(\text{phenyl})}$
SBR	63.01	49.89	87.87	0.79	1.39
SBR-g-BMimMS	39.43	33.79	56.84	0.69	1.30
SBR-g-MimMP	58.41	35.63	69.40	0.61	1.19

#### 3.2. Affinities of ILS toward HNTs

A peak fitting program on XPS spectra of Al 2p and Si 2p was performed to detect the possible interaction between functional ILS and HNTs. The XPS spectra, together with their fitting curves, are shown in Fig. 2. The binding energy (BE) of Al 2p in aluminol (Al–OH) is at 74.6 eV. The content of Al–OH, locating at the inner side of HNTs lumens, is lower than that of aluminum–oxygen (Al–O) bond (74.5 eV). The content of silanol (Si–OH) at 103.1 eV on HNTs outer surface is quite low and the silicon–oxygen (Si–O) bond is dominant in the existing forms of Si atoms. When treated with MimMP, their binding energy (BE) values for Al in Al–O and Al–OH are shifted to 74.7 and 74.9 eV, respectively, indicating that two different kinds of hydrogen bonding may exist. One is Al–O/imidazolium cation hydrogen bonding and the other is Al–OH/anion one, both of which can reduce the electron screening effect

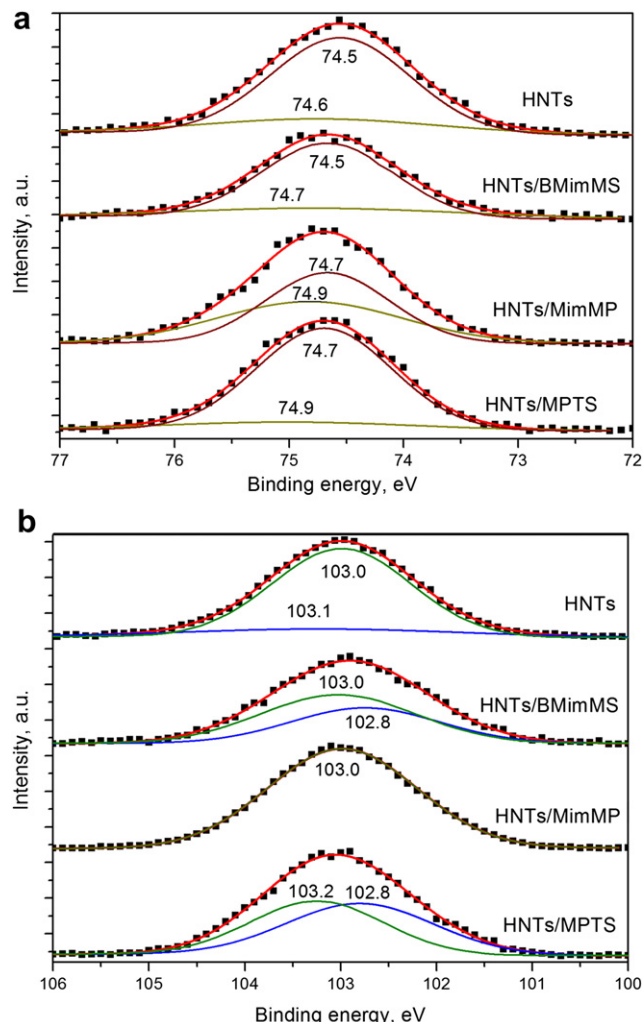


**Fig. 2.** XPS spectra of Al 2p (up) and Si 2p (down) in HNTs model compounds.

and therefore increase the BE values for Al atoms. As regard for Si–OH on the outside of HNTs, it is not distinguished by the fitting program. It may also relate to the hydrogen bonding between Si–OH and anion. But the BE value for Si atom in Si–O is not changed at all, implying that the affinity of HNTs toward MimMP is not due to Si–O and MimMP. So, MimMP could be interacted with Al–OH, Si–OH and Al–O in HNTs via different hydrogen bondings.

When HNTs is treated with BMimMS, the phenomena are a little different. The XPS spectra of Al 2p show that the BE value of Al atom in Al–OH is obviously shifted to 74.7 eV and that in Al–O is not changed. According to the spectra of Si 2p, the Si atoms in Si–OH with a low content cannot be distinguished by the fitting program. It may be ascribed to the Si–OH/anion hydrogen bonding. The BE value of Si in Si–O is partially moved to 102.8 eV. This may be related to the hydrogen bonding between Si–O and imidazolium cation in BMimMS. The other part of Si–O bonding, locating at 103.0 eV, may be assigned to the unreacted Si–O bonds in the region where is geometrically unavailable. Accordingly, the affinity of BMimMS toward HNTs may be mainly resulted from the Al–OH, Si–OH and part of Si–O bond.

The different affinities for MimMP and BMimMS toward HNTs may be resulted from the structure differences for ILs. For BMimMS, its Gemini structure is ended with two imidazolium cations and two anions. Both the cations and the anions, affinitive toward Si–O and Si–OH, may prevent BMimMS molecules from diffusing into the lumen of HNTs. However, smaller MimMP molecules possibly enter into the lumen via the strong interaction between Al–OH and anion of MimMP.

For the MPTS treated HNTs, the obviously changed BE values for Al and Si atoms may be related to coupling reaction between methoxy group in MPTS and hydroxyls (Al–OH and Si–OH) on HNTs [47,48]. As substantiated above, the interactions between ILs and HNTs are mainly composed of hydrogen bonding. Compared with the functional ILs, the covalently bonding between MPTS and HNTs is possibly responsible for the bigger BE shifts.

### 3.3. Vulcanization behavior of the SBR/HNTs rubber compounds

Vulcanization behavior of the SBR/HNTs rubber compounds is studied and showed in Fig. 3. For the unmodified rubber compounds, a long marching cure is observed. It is possibly related to the high absorbability of rubber additives such as accelerator onto the outer surface and the lumen of HNTs, which was observed elsewhere [3]. Once either of these functional ILs is loaded, the scorching time ( $T_{s2}$ ) is cut down and consistently decreased with

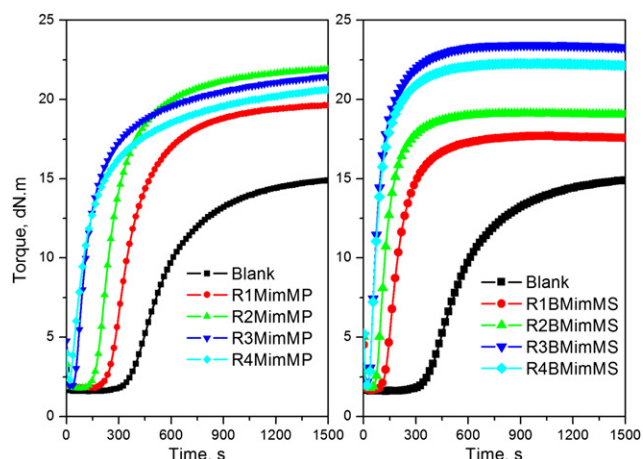


Fig. 3. Vulcanization curves for SBR/HNTs rubber compounds.

increasing incorporation. Several possible reasons are proposed. First, the hydrogen bonding between HNTs and ILs could restrict the additive adsorption and increase the concentration of curing additives. Second, the thiol group may largely activate the vulcanization via effectively lowering the corresponding activation energy ( $E_a$ ) of rubber vulcanization [49]. Third, the high active thiol-ene reaction leads to the grafting of MimMP onto the rubber chains. The ions in SBR-g-MimMP could be interacted with HNTs and could accelerate the crosslinking, because thiol-ene addition could be further activated when the thiol substance bearing a catalyzing agents such as the imidazolium cation [30,33].

From the curing curves, both the minimum torque ( $T_{min}$ ) and the maximum torque ( $T_{max}$ ) during vulcanization are changed.  $T_{min}$  is changed in a quite limited extent because it is largely dependent on the properties of uncured rubber matrix. Incorporation of functional ILs can effectively increase the  $T_{max}$  values, which are mainly dependent on filler networking, rubber network and filler-rubber interfacial interaction in vulcanizates. There are two factors in regulating the values of  $T_{max}$ . First, the crosslink density of rubber ( $V_r$ ), as indicated in Table 4, is increased with an increasing loading of ILs. This is possibly due to the constrained ingredients absorption, thiol-ene activation on vulcanization [30,33] and thiol evolved crosslinking during vulcanization. Second, the grafts generated during vulcanization can strengthen the rubber-filler interfacial interaction via the hydrogen bondings. As a result, both the increased  $V_r$  and the strengthened interfacial interactions are mainly responsible for the increasing values of  $T_{max}$ .

### 3.4. Morphology and interfacial interaction on SBR/HNTs composites

Generally speaking, filler dispersion in polymer based composites is of great importance in governing their performance. From the TEM photo of original HNTs in Fig. 4, it can be seen that their lengths range from several hundred nanometers to about 1  $\mu\text{m}$ , their outer and inner diameter is about 50 and 20 nm, respectively. Once HNTs were incorporated into rubber matrix, the HNTs dispersion was checked by TEM observation. As typically shown in Fig. 4, HNTs are seriously agglomerated in the unmodified sample. When SBR/HNTs are incorporated with MimMP or BMimMS, the agglomeration of HNTs is effectively restrained. A quantitative comparison was performed via analyzing the gray level of the pixel on figure [50]. A higher value of gray could be used to recognize the existence of filler. In the gray curve for blank, a peak with a width of 0.4  $\mu\text{m}$  is observed, corresponding to agglomerate with several HNTs stacked in parallel. The dispersion of HNTs in R3MimMP is considered to be finer than that of blank because no wide peak exists in the gray curve. Although a wide peak is also observed in the gray curve for R3MimMP, it is due to the observation of gray along the longitudinal direction of the tube. According to the gray curve of R3BMimMS, the peaks are sharp, indicating the finest dispersion state among these samples. Furthermore, the HNTs dispersion in R3BMimMS is obviously finer than that in R3MimMP. This may be resulted from the different interactions between functional ILs and HNTs.

Since the HNTs dispersion improvement in rubber matrix was disclosed by TEM, the HNTs rubber interaction, also another critical

Table 4  
Crosslink densities of SBR/HNTs vulcanizates.

	MimMP				BMimMS				MPTS	
Loading, phr	0	1	2	3	4	1	2	3	4	4
$V_r$ , $10^{-4}$ mol $\text{cm}^{-3}$	1.94	2.27	2.52	2.48	2.87	2.05	2.19	2.50	2.37	2.31

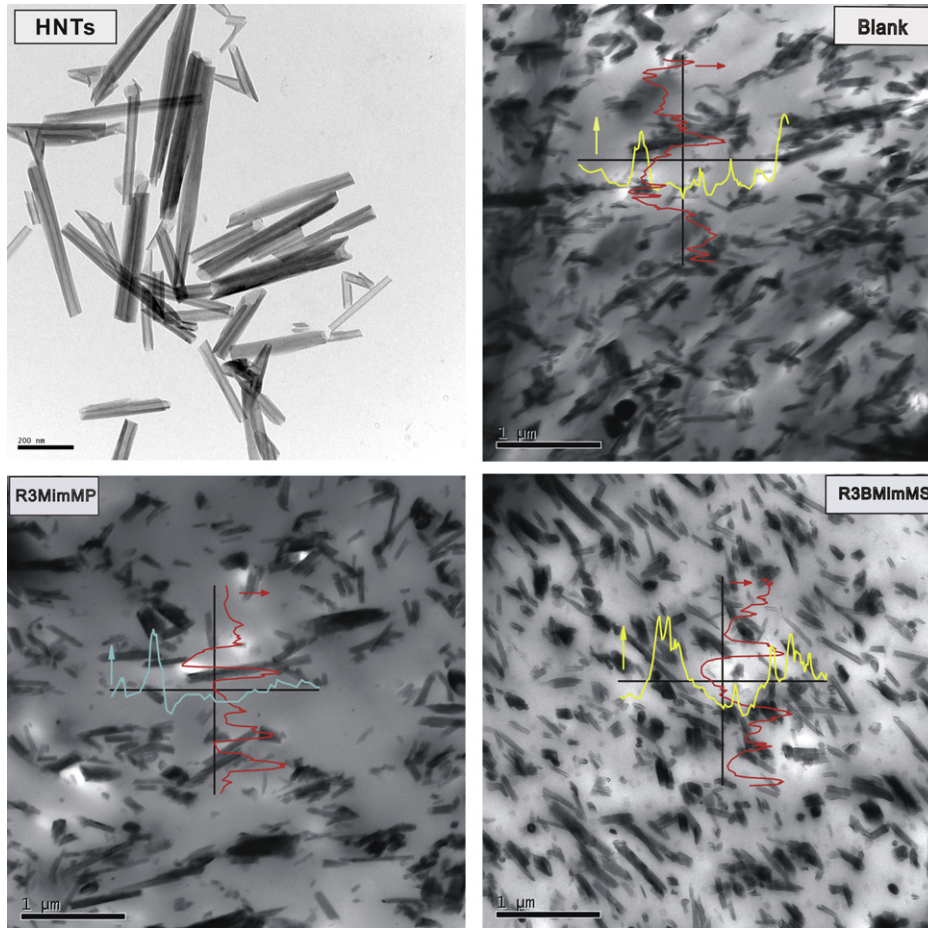


Fig. 4. TEM photos of HNTs and SBR/HNTs vulcanizates, where the insets were curves for the gray level (a.u.) of the cross solid lines.

factor in governing the ultimate performance of polymer/clay nanocomposites [51–53], should be further studied. Within various methods on evaluating the interfacial interaction with the stress–strain relationship, the slopes at certain strains and/or certain ranges of strains were always utilized [54–56]. However, ignoring the significant impact of crosslink density ( $V_r$ ) on the modulus may be not reasonable [56]. For example, the  $V_r$  values in Table 4 are obviously different from each other. What is meant by this is that measuring the rubber/filler interactions exclusively by the rubber modulus is not adequate. In following, a method based on the theory of rubber elasticity and reinforcement is to be provided with detailed descriptions.

Stress in filled vulcanizates ( $\sigma_{com}$ ) is greatly influenced by multi factors including filler, rubber and the interfacial interactions. A possible equation can be proposed to describe  $\sigma_{com}$  as:

$$\sigma_{com} = \psi(\sigma_r, \sigma_f, \sigma_{int}) \quad (1)$$

where  $\sigma_r$ ,  $\sigma_f$  and  $\sigma_{int}$  are the stress resulting from rubber network, filler and interfacial phase, respectively. The contributions of these three components to  $\sigma_{com}$  were dependent on strains. Under lower strains,  $\sigma_f$ , which is possibly related to the formation of filler network, has an important impact on  $\sigma_{com}$ . However, for the poor deformability of rigid filler network, its contribution to  $\sigma_{com}$  at large strains may be ignored. Thus, at large strains, the strong interaction between rubber chains and filler can be regarded as physical and/or chemical crosslinks [57,58].

According to the rubber elastics, stress of unfilled rubber vulcanizate ( $\sigma_r$ ) can be expressed as following:

$$\sigma_r = N_r RT \left( \lambda - \frac{1}{\lambda^2} \right) \left( 1 - \frac{2\overline{M}_c}{\overline{M}_n} \right), \quad (2)$$

where  $R$  is the universal gas constant,  $\lambda$  is the tensile ratio,  $N_r$  is the density of chain segments,  $T$  is the absolute temperature,  $\overline{M}_c$  and  $\overline{M}_n$  are the average molecular weight between two neighboring crosslink points and the average molecular weight of the rubber chains before vulcanization, respectively.

Given that the interfacial phase could have a similar mechanism under tensile and that the contribution of  $\sigma_f$  is treated as negligible at large strains,  $\sigma_{com}$  at large strains can be approximated by following [28]:

$$\sigma_{com} = (N_r + N_{int}) RT \left( \lambda - \frac{1}{\lambda^2} \right) \left( 1 - \frac{2\overline{M}_c}{\overline{M}_n} \right). \quad (3)$$

$N_{int}$  in Equation (3) is the density of chain segments introduced by the interfacial phase.  $N_r$  could be expressed by  $V_r$  and its functionality of the crosslink points ( $X_r$ ). Supposed that functionality of crosslink point in the present system is 3 and  $X_r$  is therefore to be 3/2 in present system, Equation (3) can be rearranged as:

$$N_{int} = \left[ \frac{\sigma_{com}}{RT(\lambda - \lambda^{-2})} - \frac{3}{2}V_r + \frac{3\rho_r}{\overline{M}_n} \right] / \left( 1 - \frac{2\overline{M}_c}{\overline{M}_n} \right) \approx \frac{\sigma_{com}}{RT(\lambda - \lambda^{-2})} - \frac{3}{2}V_r + \frac{3\rho_r}{\overline{M}_n}, \quad (4)$$



where  $\rho_r$  is the density of the rubber. Therefore,  $N_{\text{int}}$ , which excludes the contribution from chemical crosslink, could be reasonably utilized to evaluate the interfacial interaction between rubber chains and filler. The term for chain ends effect ( $3\rho_r/\overline{M}_n$ ), is based on the supposition that the chain ends of SBR is not interacted with filler and negatively contribute to the stress. Theoretically, this term could be calculated by measuring the molecular weights for the uncured rubber compounds. Differently, the modified SBR/silica vulcanizates, bearing active side chains (i.e. MimMP or BMimMS) on rubber backbone, are not consistent with the supposition. It means that for the different structure, the end effect for these five samples could not be equally treated by measuring the average molecular weight before vulcanization ( $\overline{M}_n$ ) as well as their polydispersity index. Another important factor influencing the estimation of the chain end effect is the high concentration of non cured ingredients added in polymerization (i.e. up to 10 wt% for SBR1502 in this work). Therefore, in order to simplify the complex situation, the term  $3\rho_r/\overline{M}_n$  is considered to be a constant ( $\overline{M}_n = 30\,000\text{ g mol}^{-1}$  and  $C = 3\rho_r/\overline{M}_n = 1.0 \times 10^{-4}\text{ mol cm}^{-3}$ ), independent of rubber structures. Equation (4) can be further approximated by:

$$N_{\text{int}} \approx \frac{\sigma_{\text{com}}}{RT(\lambda - \lambda^{-2})} - \frac{3}{2}V_r + C. \quad (5)$$

Curves of stress–strain and  $N_{\text{int}}$  versus strain for SBR/HNTs vulcanizates are selectively plotted in Fig. 5.  $\sigma_{\text{com}}$  and  $N_{\text{int}}$  are largely dependent on the deformation of the filled vulcanizates because of the different contributions from  $\sigma_r$ ,  $\sigma_f$  and  $\sigma_{\text{int}}$ . Within a range of lower strains, the unreasonable high value of  $N_{\text{int}}$  may be ascribed to the HNTs network formation. At higher strains, the  $N_{\text{int}}$  values are obviously increased with increasing loading of functional ILs, which is well consistent with our previous reports [28,29]. This strongly indicates that the interfacial interaction between rubber and HNTs is largely improved. The improved filler dispersion, which could increase the volume of interphase, and the improved polymer–filler compatibility due to the hydrogen bonding between filler and SBR grafting chains are possibly responsible [59].

However, the SBR/HNTs interfacial interaction introduced by different ILs is a little different. From the curves in Fig. 5b, the SBR/HNT interfacial interaction of R3BMimMS is higher than that of R3MimMP. It may be related to their structure for ILs. BMimMS with a Gemini structure could be more affinitive toward HNTs via the hydrogen bonding between BMimMS and Si–O on the outer surface of HNTs. While the interaction between MimMP and HNTs

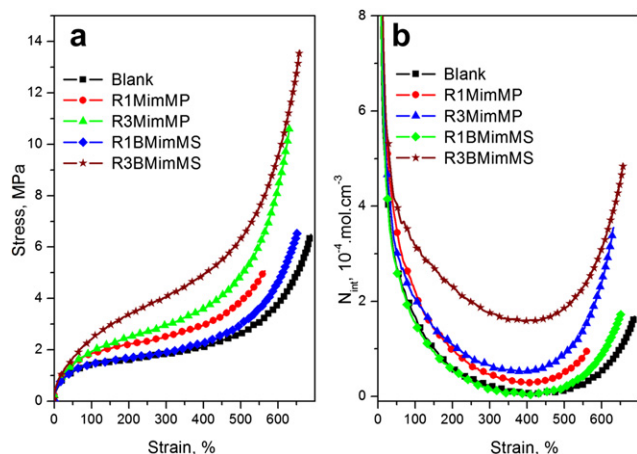


Fig. 5. Dependence of stress (a) and interfacial interaction (b) on strains for SBR/HNTs vulcanizates.

Table 5  
Mechanical performance of SBR/HNTs vulcanizates.

	Stress at 300%, MPa	Elongation at break, %	Tensiles stress, MPa	Tear strength, $\text{kN m}^{-1}$	Shore A hardness
Blank	$1.9 \pm 0.1$	$676 \pm 26$	$6.4 \pm 1.4$	$20.4 \pm 1.2$	53
R1MimMP	$2.5 \pm 0.1$	$590 \pm 17$	$5.5 \pm 1.1$	$27.8 \pm 0.3$	55
R2MimMP	$2.7 \pm 0.1$	$559 \pm 11$	$5.4 \pm 0.9$	$29.1 \pm 1.9$	55
R3MimMP	$2.9 \pm 0.1$	$642 \pm 12$	$10.7 \pm 0.5$	$30.7 \pm 1.1$	55
R4MimMP	$4.1 \pm 0.1$	$595 \pm 15$	$10.9 \pm 0.8$	$37.0 \pm 1.6$	55
R1BMimMS	$1.9 \pm 0.1$	$655 \pm 11$	$6.5 \pm 0.7$	$21.4 \pm 1.6$	53
R2BMimMS	$2.2 \pm 0.1$	$648 \pm 29$	$8.2 \pm 0.5$	$25.6 \pm 1.8$	54
R3BMimMS	$4.1 \pm 0.2$	$626 \pm 28$	$13.4 \pm 3.5$	$40.7 \pm 2.3$	57
R4BMimMS	$3.7 \pm 0.1$	$638 \pm 13$	$12.2 \pm 1.5$	$36.9 \pm 1.4$	57
R4MPTS	$6.2 \pm 0.2$	$616 \pm 14$	$11.0 \pm 0.5$	$35.8 \pm 2.0$	51

is mainly functionalized through the hydrogen bonding between inner aluminol and the MimMP. The geometry characteristic may also be responsible for the different interfacial interactions among different ILs. Therefore the introduced interfacial interaction between HNTs and BMimMS is much higher.

### 3.5. Mechanical performance and dynamical performance of SBR/HNTs vulcanizates

Mechanical performance of the SBR/HNTs vulcanizates is summarized in Table 5. The addition of functional ILs can largely improve the mechanical properties. Comparing with that of blank sample, the modulus (stress at 300%) is increased to 4.1 MPa for R4MimMP and 4.1 MPa for R3BMimMS, with an increment up to 110%. The tensile strength for these two samples with 3 phr IL is increased by 70% and 109%, respectively. Also, the tear strength for these two samples with 3 phr IL is effectively increased to 37.0 and 40.7  $\text{kN m}^{-1}$ . Several possible reasons are proposed to explain these phenomena. First, the increased crosslink density, which is one of the factors determining the deformability of the rubber network, is responsible for the increased modulus. Second, HNTs dispersion in rubber matrix is largely improved according to the morphology observation. Last and more importantly, the interfacial interaction between rubber and HNTs is much strengthened as substantiated above.

Comparing with MPTS in this work (as included in Table 5) and other modifiers [60], the efficiency of functional ILs on modifying SBR/HNTs vulcanizates is also enhanced according to the mechanical data. The modification mechanism of the present systems was different from those for the silane modified ones. Here, we take MPTS for example. MPTS could be chemically bonded with HNTs and grafted onto rubber matrix. But the reactive functional groups toward MPTS are mainly located at the inner surface of HNTs lumens [3,61,62]. Through a simple *in situ* method for rubber compounding, MPTS cannot easily creep into the HNTs lumen. So the effective interfacial junctions induced by MPTS are mainly confined at the lumen ends. For functional ILs, the interfacial interaction could be strengthened by the hydrogen bonding between functional groups and the outer surface of HNTs. The high density of interfacial hydrogen bonding may be attributed to the higher modification efficiency comparing with the systems with covalently bonded interface. The modulus at 300% for MPTS modified sample is higher than that of these modified by ILs, because the interfacial interaction of the latter one is originated from hydrogen bonding.

### 3.6. Dynamic mechanical analysis (DMA) for SBR/HNTs vulcanizates

For tread application of rubber compounds, the dynamic performance is important. The dynamic performance of the



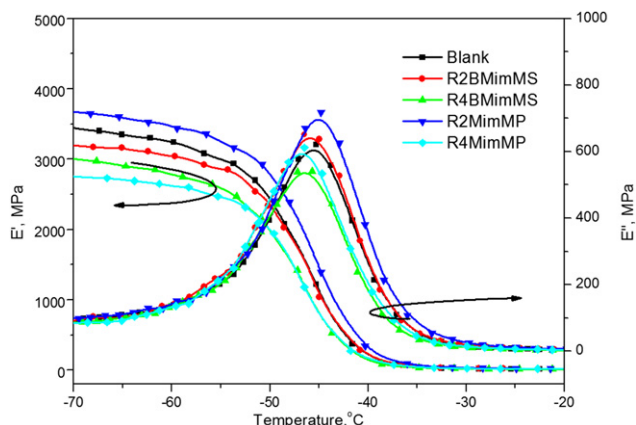


Fig. 6. Temperature dependence of storage and loss modulus of SBR/HNTs vulcanizates.

modified SBR/HNTs vulcanizates is also examined. The storage modulus ( $E'$ ) and loss modulus ( $E''$ ) at the range of  $-70\text{ }^{\circ}\text{C}$  to  $-20\text{ }^{\circ}\text{C}$  are showed in Fig. 6. It can be seen that at lower temperature, the  $E'$  curves are slightly changed. Three reasons may be responsible. First, the rubber networking, typically represented by its crosslink density, is changed. Second, the weakened filler–filler interaction due to the ILs' high affinities toward HNTs can effectively restrain the filler networking and lower the effective volume of filler [27,28]. Last, the IL grafted rubber chains could tune the origin polymer matrix into a softer one by endowing side chains. When the first one is dominant, the value of  $E'$  is slightly increased for R2MimMP. While the latter two are the key factor, the  $E'$  values at lower temperature is slightly lower than that of blank.

For both ILs modified SBR/HNTs vulcanizates with a higher loading of ILs, the  $E''$  value is lowered and peak value is shifted to a lower temperature in comparison to that of blank sample. The restrained mechanical loss is due to the strong hydrogen bonding between HNTs and polymer matrix. The peak shift toward lower temperature may be resulted from the grafted segments favorable for local motion [63].

The dependence of tangent delta is showed in Fig. 7. The temperature of glass transition ( $T_g$ ) for the functional ILs modified SBR/HNTs is depressed a little. It seems to be contradicted with the increased crosslink density, which could restrain polymer segments [64]. The increased polymer segmental mobility is ascribed to the negative pressure in the polymer–filler interfacial phase due to the

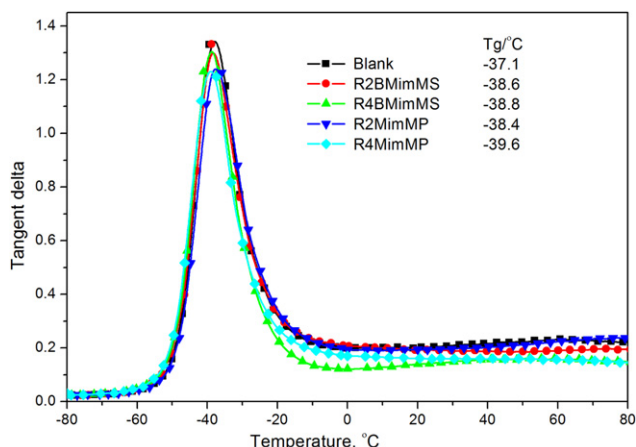


Fig. 7. Dependence of tangent delta ( $\tan \delta$ ) on temperature of SBR/HNTs vulcanizates.

dilation stress [63]. Also, it can be observed that the mechanical loss in transition zone, indicated by  $\tan \delta$ , is effectively lowered. This is possibly due to the restrained mobility of the rubber chains. Furthermore, the remarkably decreased mechanical loss at the range of  $50\text{--}80\text{ }^{\circ}\text{C}$  indicates that this novel modification method can be potentially utilized to fabricating green tire material with a lower roll resistance [65]. The lowered mechanical loss may be mainly ascribed to the largely improved HNTs dispersion and the effectively strengthened interfacial interactions.

#### 4. Conclusion

Functional ILs bearing thiol group was investigated as novel modifiers for SBR/HNTs composites. Two novel ILs, 1-methylimidazolium mercaptopropionate (MimMP) and bis (1-methylimidazolium) mercaptosuccinate (BMimMS), were synthesized. Their affinities toward HNTs were substantiated to originate from hydrogen bonding. The grafting reactivity onto SBR chains were mainly ascribed to the thiol-ene reaction. The restrained adsorption of rubber ingredients by HNTs and the presence of thiol and imidazolium cation groups in the ILs may be responsible for the promoted vulcanization. Substantiated hydrogen bond between HNTs and ILs largely facilitates the HNTs dispersion in the rubber matrix. The quantitatively evaluated interfacial interaction was found to be consistently increased with the increasing loading of functional ILs. Significant improvement in mechanical properties was correlated to the improved HNTs dispersion and the hydrogen bonding. The IL modified systems also possessed remarkably decreased mechanical loss at the range of  $50\text{--}80\text{ }^{\circ}\text{C}$ , suggesting potential applications in fabricating tread with a lower roll resistance.

#### Acknowledgments

The authors thank the financial supports from the National Natural Science Foundation of China (50873035 and 50933001), the Doctorate Foundation of South China University of Technology to Mr. Yanda Lei, Guangdong Natural Science Foundation (151008901000137), Fundamental Research for the Central Universities (2009ZZ0007) and National High-tech R & D Program (863 Program; 2009AA03Z338).

#### References

- [1] Du ML, Guo BC, Jia DM. *Polym Int* 2010;59:574.
- [2] Du ML, Guo BH, Liu MX, Jia DM. *Polym Polym Compos* 2007;15:321.
- [3] Du ML, Guo BC, Lei YD, Liu MX, Jia DM. *Polymer* 2008;49:4871.
- [4] Liu MX, Guo BC, Lei YD, Du ML, Jia DM. *Appl Surf Sci* 2009;255:4961.
- [5] Guo BC, Chen F, Lei YD, Jia DM. *J Macromol Sci. Phys* 2010;49:111.
- [6] Gwee L, Choi J, Winey K, Elabd Y. *Polymer* 2010;51:5516.
- [7] Vilkmann M, Lankinen A, Volk N, Kostamo P, Ikkala O. *Polymer* 2010;51:4095.
- [8] Lin JH, Liu Y, Zhang QM. *Polymer* 2011;52:540.
- [9] Lu JM, Yan F, Texter J. *Prog Polym Sci* 2009;34:431.
- [10] Zhang H, Wang ZG, Zhang ZN, Wu J, Zhang J, He HS. *Adv Mater* 2007;19:698.
- [11] Fukushima T, Kosaka A, Ishimura Y, Yamamoto T, Takigawa T, Ishii N, et al. *Science* 2003;300:2072.
- [12] Haggenueller R, Rahatekar SS, Fagan JA, Chun J, Becker ML, Naik RR, et al. *Langmuir* 2008;24:5070.
- [13] Fukushima T, Asaka K, Kosaka A, Aida T. *Angew Chem. Int Ed* 2005;44:2410.
- [14] Byrne C, McNally T. *Macromol Rapid Commun* 2007;28:780.
- [15] Zhou Y, Schattka JH, Antonietti M. *Nano Lett* 2004;4:477.
- [16] Lei YD, Guo BC, Liu XL, Jia DM. *Appl Surf Sci* 2009;255:8488.
- [17] Maleki N, Safavi A, Tajabadi F. *Anal Chem* 2006;78:3820.
- [18] Wang JY, Chu HB, Li Y. *ACS Nano* 2008;2:2540.
- [19] Dong K, Zhou GH, Liu XM, Yao XQ, Zhang SJ, Lyubartsev A. *J Phys Chem C* 2009;113:10013.
- [20] Zhang YJ, Shen YF, Li JH, Niu L, Dong SJ, Ivaska A. *Langmuir* 2005;21:4797.
- [21] Trewyn BC, Whitman CM, Lin VSY. *Nano Lett* 2004;4:2139.
- [22] Zhou Y, Antonietti M. *Adv Mater* 2003;15:1452.
- [23] Wang Q, Baker GA, Baker SN, Colon LA. *Analyst* 2006;131:1000.
- [24] Van Meter DS, Stuart OD, Carle AB, Stalcup AM. *J Chromatogr A* 2008;1191:67.

- [25] Liu Y, Zhu L, Sun X, Chen J, Luo F. *Ind Eng Chem Res* 2009;48:7308.
- [26] Guo BC, Liu XL, Zhou WY, Lei YD, Jia DM. *J Macromol Sci. Phys* 2010;49:1029.
- [27] Lei YD, Guo BC, Tang ZH, Jia DM. *Polym J* 2010;42:555.
- [28] Lei YD, Tang ZH, Guo BC, Zhu LX, Jia DM. *Express Polym Lett* 2010;4:692.
- [29] Lei YD, Guo BC, Tang ZH, Jia DM. *J Appl Polym Sci* in press.
- [30] Decker C, Viet TNT. *Macromol Chem Phys* 1999;200:1965.
- [31] Hoyle CE, Lee TY, Roper T. *J Polym Sci Part A Polym Chem* 2004;42:5301.
- [32] Killops KL, Campos LM, Hawker CJ. *J Am Chem Soc* 2008;130:5062.
- [33] Rim C, Lahey LJ, Patel VG, Zhang H, Son DY. *Tetrahedron Lett* 2009;50:745.
- [34] Mansur HS, Orefice RL, Vasconcelos WL, Lobato ZP, Machado LJC. *J Mater Sci Mater Med* 2005;16:333.
- [35] Justynska J, Hordyjewicz Z, Schlaad H. *Polymer* 2005;46:12057.
- [36] Ide Y, Fukuoka A, Ogawa M. *Chem Mater* 2007;19:964.
- [37] Liu MX, Guo BC, Du ML, Cai XJ, Jia DM. *Nanotechnology* 2007;18:455703.
- [38] Uygun M, Tasdelen MA, Yagci Y. *Macromol Chem Phys* 2010;211:103.
- [39] Jerman I, Jovanovski V, Vuk AS, Hocevar SB, Gaberscek M, Jesih A, et al. *Electrochim Acta* 2008;53:2281.
- [40] Vuk AS, Jovanovski V, Pollet-Villard A, Jerman I, Orel B. *Sol Energy Mater Sol Cells* 2008;92:126.
- [41] Watts JF, Wolstenholme J. *An introduction to surface analysis by XPS and AES. West Sussex (England): John Wiley & Sons, Ltd; 2003.*
- [42] Guo BC, Lei YD, Chen F, Liu XL, Du ML, Jia DM. *Appl Surf Sci* 2008;255:2715.
- [43] Hoyle CE, Bowman CN. *Angew Chem. Int Ed* 2010;49:1540.
- [44] Yu JJ, Ryu SH. *J Appl Polym Sci* 1999;73:1733.
- [45] Romero-Sanchez MD, Pastor-Blas MM, Martin-Martinez JM. *Int J Adhes Adhes* 2001;21:325.
- [46] Rajkumar T, Rao GR. *Mater Chem Phys* 2008;112:853.
- [47] Jesionowski T, Krysztafkiewicz A. *Appl Surf Sci* 2001;172:18.
- [48] Lassiaz S, Galarneau A, Trems P, Labarre D, Mutin H, Brunel D. *New J Chem* 2010;34:1424.
- [49] Poh BT, Ng CC. *Eur Polym J* 1998;34:975.
- [50] Kornmann X, Lindberg H, Berglund LA. *Polymer* 2001;42:4493.
- [51] Ali Z, Le H, Ilisch S, Thurn-Albrecht T, Radusch H. *Polymer* 2010;51:4580.
- [52] Choudhury A, Bhowmick A, Ong C. *Polymer* 2009;50:201.
- [53] Dohi H, Horiuchi S. *Langmuir* 2007;23:12344.
- [54] Ayala JA, Hess WM, Dotson AO, Joyce GA. *Rubber Chem Technol* 1990;63:747.
- [55] Ayala JA, Hess WM, Kistler FD, Joyce GA. *Rubber Chem Technol* 1991;64:19.
- [56] Zhang HM, Datta RN, Talma AG, Noordermeer JWM. *Macromol Mater Eng* 2010;295:76.
- [57] Cai JJ, Salovey RJ. *Mater Sci* 2001;36:3947.
- [58] Litvinov VM, Steeman PAM. *Macromolecules* 1999;32:8476.
- [59] Stöckelhuber KW, Das A, Jurk R, Heinrich G. *Polymer* 2010;51:1954.
- [60] Lei YD, Chen F, Liu XL, Wan JJ, Zou QL, Du ML, et al. *Special purpose rubber products*, vol. 30; 2009. p. 1.
- [61] Du ML, Guo BC, Jia DM. *Polym Int*; 2010.
- [62] Yuan P, Southon PD, Liu ZW, Green MER, Hook JM, Antill SJ, et al. *J Phys Chem C* 2008;112:15742.
- [63] Hashima K, Nishitsuji S, Inoue T. *Polymer* 2010;51:3934.
- [64] Thomas R, Yumei D, Yuelong H, Le Y, Moldenaers P, Weimin Y, et al. *Polymer* 2008;49:278.
- [65] Wang MJ, Mahmud K, Murphy LJ, Patterson WJ. *Kautsch Gummi Kunstst* 1998;51:348.